

DECEMBER 2020

**AJNR**

VOLUME 41 • PP 2173–2383

# AJNR

## AMERICAN JOURNAL OF NEURORADIOLOGY

DECEMBER 2020  
VOLUME 41  
NUMBER 12  
WWW.AJNR.ORG

THE JOURNAL OF DIAGNOSTIC AND  
INTERVENTIONAL NEURORADIOLOGY

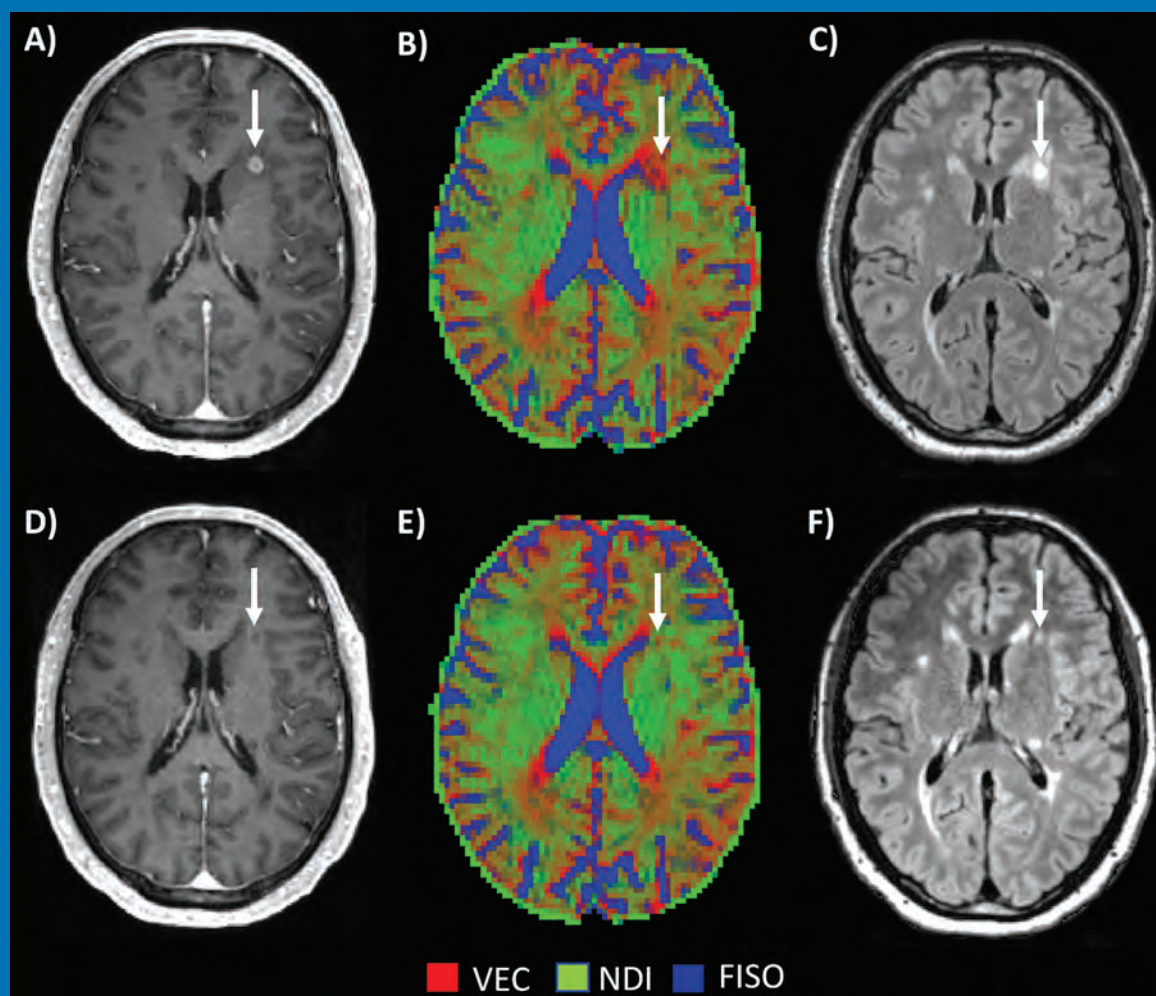
Neuroimaging of COVID-19

Neurite orientation dispersion and density imaging for MS

Recent iodinated contrast and core infarct estimation using RAPID software

Dural arteriovenous fistulas with an angiographic pseudophlebitic pattern

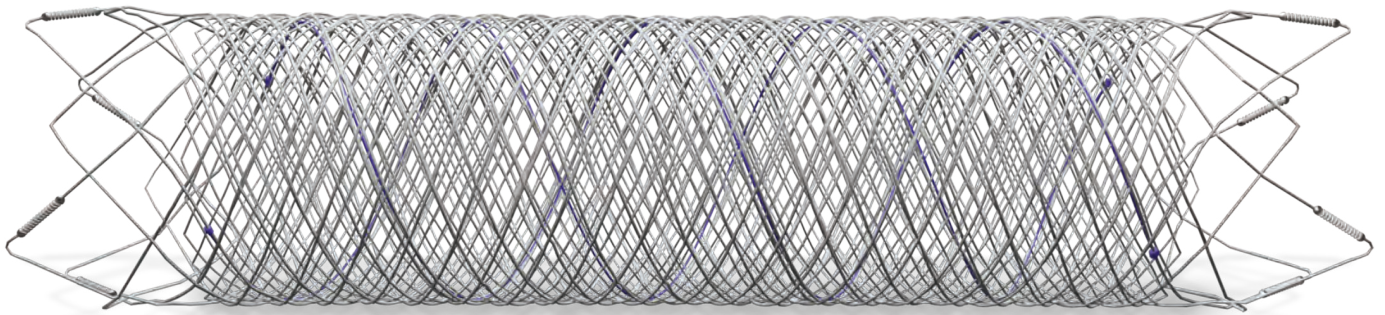
Official Journal ASNR • ASFNR • ASHNR • ASPNR • ASSR



# FRED™

Flow Re-Direction  
Endoluminal Device

## FLOW DIVERSION.



## SIMPLIFIED.



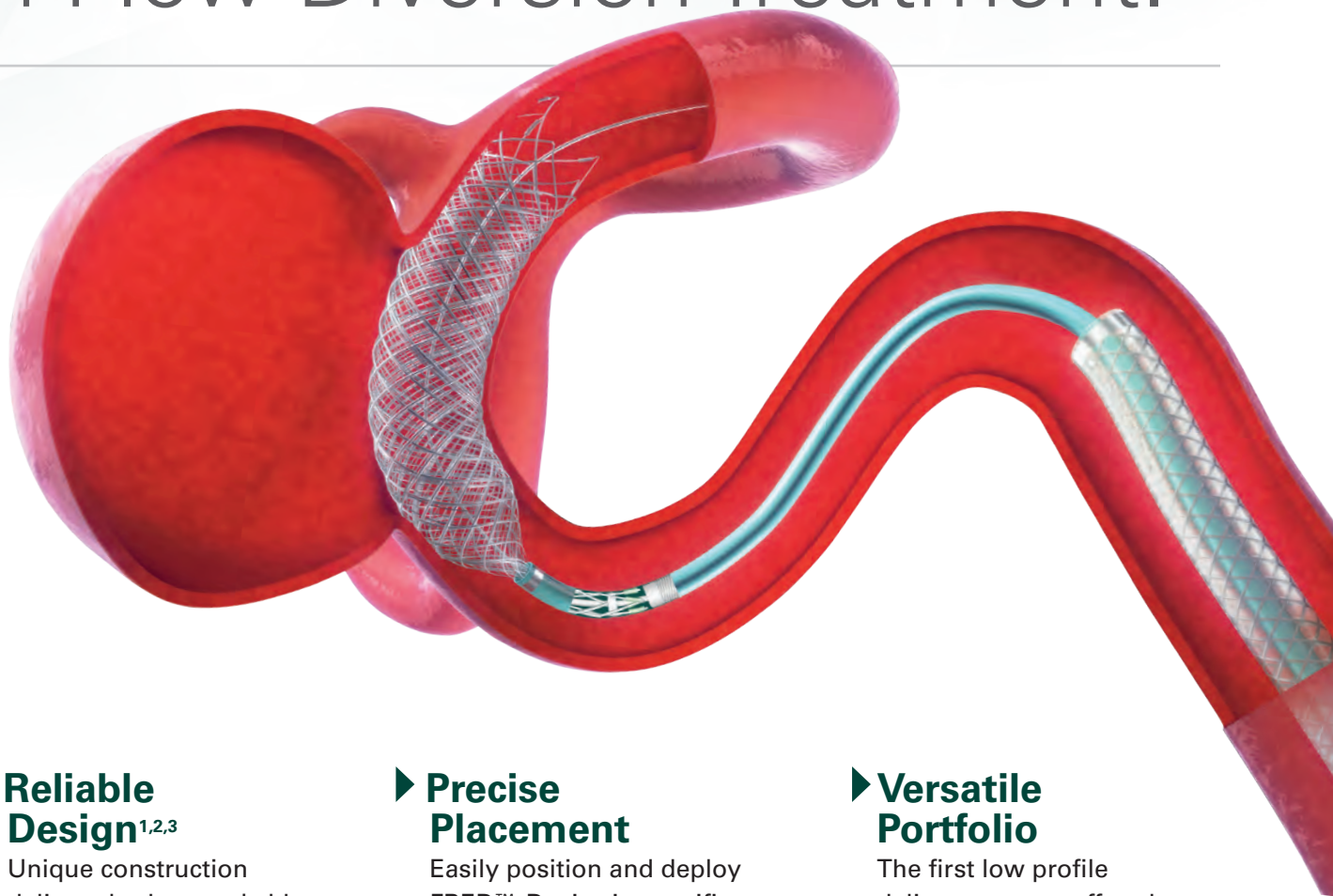
**MicroVention Worldwide**  
**Innovation Center**  
35 Enterprise  
Aliso Viejo, CA 92656 USA  
**MicroVention UK Limited**  
**MicroVention Europe S.A.R.L.**  
**MicroVention Deutschland GmbH**  
**Web**

PH +1 714.247.8000

PH +1 44 (0) 191 258 6777  
PH +33 (1) 39 21 77 46  
PH +49 211 210 798-0  
[microvention.com](http://microvention.com)



# The New Standard of **Ease and Simplicity** in Flow Diversion Treatment.



## ► **Reliable Design**<sup>1,2,3</sup>

Unique construction delivers both remarkable ease of use and excellent flow diversion<sup>1,2,3</sup>

## ► **Precise Placement**

Easily position and deploy FRED™ Device in specific, targeted locations<sup>4,5,6</sup>

## ► **Versatile Portfolio**

The first low profile delivery system offered in combination with large diameter and long length options

#### References:

1. TR11-211 2. TR13-171 3. TR15-055 4. TR13-192 5. TR15-072 6. TR19-145

The Flow Re-Direction Endoluminal Device (FRED™) System is indicated for use in the internal carotid artery from the petrous segment to the terminus for the endovascular treatment of adult patients (22 years of age or older) with wide-necked (neck width  $\geq 4$  mm or dome-to-neck ratio  $< 2$ ) saccular or fusiform intracranial aneurysms arising from a parent vessel with a diameter  $\geq 2.0$  mm and  $\leq 5.0$  mm.

Use of the FRED™ System is contraindicated under these circumstances: Patients in whom anticoagulant, anti-platelet therapy, or thrombolytic drugs are contraindicated. Patients with known hypersensitivity to metal such as nickel-titanium and metal jewelry. Patients with anatomy that does not permit passage or deployment of the FRED™ System. Patients with an active bacterial infection. Patients with a pre-existing stent in place at the target aneurysm. Patients in whom the parent vessel size does not fall within the indicated range. Patients who have not received dual anti-platelet agents prior to the procedure. For complete indications, contraindications, potential complications, warnings, precautions, and instructions, see instructions for use (IFU provided in the device).

**RX Only:** Federal (United States) law restricts this device to sale by or on the order of a physician.

MICROVENTION™ and FRED™ are registered trademarks of MicroVention, Inc. in the United States and other jurisdictions. © 2020 MicroVention, Inc. 04/2020.





## **Simplify** the MOC Process



## **Manage** your CME Credits Online

# **CMEgateway.org**

### **Available to Members of Participating Societies**

American Board of Radiology (ABR)  
American College of Radiology (ACR)  
American Roentgen Ray Society (ARRS)  
American Society of Neuroradiology (ASNR)  
Commission on Accreditation of Medical  
Physics Educational Programs, Inc. (CAMPEP)  
Radiological Society of North America (RSNA)  
Society of Interventional Radiology (SIR)  
SNM  
The Society for Pediatric Radiology (SPR)

### **It's Easy and Free!**

Log on to CME Gateway to:

- View or print reports of your CME credits from multiple societies from a single access point.
- Print an aggregated report or certificate from each participating organization.
- Link to SAMs and other tools to help with maintenance of certification.

### **American Board of Radiology (ABR) participation!**

By activating ABR in your organizational profile, your MOC-fulfilling CME and SAM credits can be transferred to your own personalized database on the ABR Web site.

### **Sign Up Today!**

go to [CMEgateway.org](http://CMEgateway.org)

# *We're Inside Every Great Neuroradiologist!*

## **ASNR MEMBERS RECEIVE**

### ***American Journal of Neuroradiology (AJNR)***

The leading neuroradiology research journal, published monthly

### ***Neurographics***

Bimonthly educational journal with CME for members

### **ASNR Annual Meeting**

Discounts for members on the field's premier conference

### **eCME**

Online collection of lectures and articles with SA-CME and Category 1 credit

### **Advocacy**

Coding/reimbursement, quality standards and practice guidelines; demonstrating neuroradiology's value!

### **Networking**

Access to 5,000 peers

... And More!

## **Join the leaders in neuroradiology today!**

## **Learn more at [www.asnr.org/join](http://www.asnr.org/join)**

# **ASNR**

## **American Society of Neuroradiology**

800 Enterprise Dr., Suite 205, Oak Brook, IL 60523 • (630)574-0220 • [membership@asnr.org](mailto:membership@asnr.org) • [www.asnr.org](http://www.asnr.org)



# AJNR *go green*

***AJNR* urges American Society of Neuroradiology members to reduce their environmental footprint by voluntarily suspending their print subscription.**

The savings in paper, printing, transportation, and postage directly fund new electronic enhancements and expanded content.

The digital edition of *AJNR* presents the print version in its entirety, along with extra features including:

- Publication Preview
- Case Collection
- Podcasts
- The *AJNR* News Digest
- The *AJNR* Blog

It also reaches subscribers much faster than print. An electronic table of contents will be sent directly to your mailbox to notify you as soon as it publishes.

Readers can search, reference, and bookmark current and archived content 24 hours a day on [www.ajnr.org](http://www.ajnr.org).

ASNR members who wish to opt out of print can do so by using the *AJNR* Go Green link on the *AJNR* Website (<http://www.ajnr.org/content/subscriber-help-and-services>). Just type your name in the email form to stop print and spare our ecosystem.



# CALL FOR AJNR EDITORIAL FELLOWSHIP CANDIDATES

## 2021 Candidate Information and Requirements

ASNR and AJNR are pleased once again to join efforts with other imaging-related journals that have training programs on editorial aspects of publishing for trainees or junior staff (<5 years on staff), including Radiology (Olmsted fellowship), AJR (Figley and Rogers fellowships), JACR (Bruce J. Hillman fellowship), and Radiologia.

### GOALS

- Increase interest in editorial and publication-related activities in younger individuals.
- Increase understanding and participation in the AJNR review process.
- Incorporate into AJNR's Editorial Board younger individuals who have previous experience in the review and publication process.
- Fill a specific need in neuroradiology not offered by other similar fellowships.
- Increase the relationship between "new" generation of neuroradiologists and more established individuals.
- Increase visibility of AJNR among younger neuroradiologists.

### ACTIVITIES OF THE FELLOWSHIP

- Serve as Editorial Fellow for one year. This individual will be listed on the masthead as such.
- Review at least one manuscript per month for 12 months. Evaluate all review articles submitted to AJNR.
- Learn how electronic manuscript review systems work.
- Be involved in the final decision of selected manuscripts together with the Editor-in-Chief.
- Participate in all monthly Senior Editor telephone conference calls.
- Participate in all meetings of the Editors during the annual meetings of ASNR and RSNA and the Radiology Editors Forum as per candidate's availability. The Foundation of the ASNR will provide \$2000 funding for this activity.
- Evaluate progress and adjust program to specific needs in annual meeting or telephone conference with the Editor-in-Chief.
- Embark on an editorial scientific or bibliometric project that will lead to the submission of an article to AJNR or another appropriate journal as determined by the Editor-in-Chief. This project will be presented by the Editorial Fellow at the ASNR annual meeting.
- Recruit trainees as reviewers as determined by the Editor-in-Chief.
- Organize and host a Fellows' Journal Club podcast.
- Serve as Guest Editor for an issue of AJNR's News Digest with a timely topic.

### QUALIFICATIONS

- Be a fellow in neuroradiology from North America, including Canada (this may be extended to include other countries).
- Be a junior faculty neuroradiology member (< 5 years) in either an academic or private environment.
- Be an "in-training" or member of ASNR in any other category.

### APPLICATION

- Include a short letter of intent with statement of goals and desired research project. CV must be included.
- Include a letter of recommendation from the Division Chief or fellowship program director. A statement of protected time to perform the functions outlined is desirable.
- Applications will be evaluated by AJNR's Senior Editors prior to the ASNR annual meeting. The name of the selected individual will be announced at the meeting.
- Applications should be received by March 1, 2021 and sent to Ms. Karen Halm, AJNR Managing Editor, electronically at [khalm@asnir.org](mailto:khalm@asnir.org).

# AJNR

## AMERICAN JOURNAL OF NEURORADIOLOGY

DECEMBER 2020  
VOLUME 41  
NUMBER 12  
WWW.AJNR.ORG

Publication Preview at [www.ajnr.org](http://www.ajnr.org) features articles released in advance of print.  
Visit [www.ajnrblog.org](http://www.ajnrblog.org) to comment on AJNR content and chat with colleagues  
and AJNR's News Digest at <http://ajnrndigest.org> to read the stories behind the  
latest research in neuroimaging.

2173 **PERSPECTIVES** *T.R. Meling*

### EDITORIAL

2174 **Changing the Rules of the Game: The Problem of Surrogate Angiographic Outcomes in the Evaluation of Aneurysm Treatments** *T.E. Darsaut, et al.* **INTERVENTIONAL**

### REVIEW ARTICLES

 2176 **Imaging Review of Paraneoplastic Neurologic Syndromes**  
*A.A. Madhavan, et al.*


 2188 **Secondary Otalgia: Referred Pain Pathways and Pathologies**  
*C.D. Norris, et al.* **HEAD & NECK**

### GENERAL CONTENTS

 2199 **MRI Brain Findings in 126 Patients with COVID-19: Initial Observations from a Descriptive Literature Review** *E. Gulko, et al.* **ADULT BRAIN**

 2204 **Unusual Brain MRI Pattern in 2 Patients with COVID-19 Acute Respiratory Distress Syndrome** *S. Toledano-Massiah, et al.* **ADULT BRAIN**

 2206 **COVID-19–Associated PRES–like Encephalopathy with Perivascular Gadolinium Enhancement** *G. Conte, et al.* **ADULT BRAIN**

 2209 **NAA is a Marker of Disability in Secondary-Progressive MS: A Proton MR Spectroscopic Imaging Study** *B.S. Solanky, et al, for the MS-SMART Investigators* **ADULT BRAIN FUNCTIONAL**

   2219 **Neurite Orientation Dispersion and Density Imaging for Assessing Acute Inflammation and Lesion Evolution in MS** *S. Sacco, et al.* **ADULT BRAIN FUNCTIONAL**

 2227 **Development and Validation of a Deep Learning–Based Automatic Brain Segmentation and Classification Algorithm for Alzheimer Disease Using 3D T1-Weighted Volumetric Images** *C.H. Suh, et al.* **ADULT BRAIN FUNCTIONAL**







  2235 **Recent Administration of Iodinated Contrast Renders Core Infarct Estimation Inaccurate Using RAPID Software** *A.Z. Copelan, et al.* **ADULT BRAIN FUNCTIONAL**

  2243 **Cortical Distribution of Fragile Periventricular Anastomatic Collateral Vessels in Moyamoya Disease: An Exploratory Cross-Sectional Study of Japanese Patients with Moyamoya Disease** *A. Miyakoshi, et al.* **ADULT BRAIN**

AJNR (Am J Neuroradiol ISSN 0195–6108) is a journal published monthly, owned and published by the American Society of Neuroradiology (ASNR), 800 Enterprise Drive, Suite 205, Oak Brook, IL 60523. Annual dues for the ASNR include approximately 21% for a journal subscription. The journal is printed by Cadmus Journal Services, 5457 Twin Knolls Road, Suite 200, Columbia, MD 21045; Periodicals postage paid at Oak Brook, IL and additional mailing offices. Printed in the U.S.A. POSTMASTER: Please send address changes to American Journal of Neuroradiology, P.O. Box 3000, Denville, NJ 07834, U.S.A. Subscription rates: nonmember \$410 (\$480 foreign) print and online, \$320 online only; institutions \$470 (\$540 foreign) print and basic online, \$935 (\$1000 foreign) print and extended online, \$380 online only (basic), \$825 online only (extended); single copies are \$35 each (\$40 foreign). Indexed by PubMed/MEDLINE, BIOSIS Previews, Current Contents (Clinical Medicine and Life Sciences), EMBASE, Google Scholar, HighWire Press, Q-Sensei, RefSeek, Science Citation Index, SCI Expanded, Meta/CZI, ReadCube, and Semantic Scholar. Our content is discoverable via EBSCOhost. Copyright © American Society of Neuroradiology.


	2250	Clinical and Radiologic Findings of Acute Necrotizing Encephalopathy in Young Adults <i>H.A. Vanjare, et al.</i>	ADULT BRAIN
	2255	<b>Commentary</b> Acute Necrotizing Encephalopathy: A Disease Meriting Greater Recognition <i>H. Kidokoro</i>	ADULT BRAIN
	2257	Safety Profile of Infinity Deep Brain Stimulation Electrode Placement in a 1.5T Interventional MRI Suite: Consecutive Single-Institution Case Series <i>N. Gravbrot, et al.</i>	ADULT BRAIN INTERVENTIONAL
	2263	Characteristics of Large-Vessel Occlusion Associated with COVID-19 and Ischemic Stroke <i>S. John, et al.</i>	INTERVENTIONAL
	2269	<b>Commentary</b> The Forest and the Trees <i>T.M. Leslie-Mazwi, et al.</i>	INTERVENTIONAL
	2271	The Impact of COVID-19 on Emergent Large-Vessel Occlusion: Delayed Presentation Confirmed by ASPECTS <i>D.J. Altschul, et al.</i>	INTERVENTIONAL
	2274	Considerations for Antiplatelet Management of Carotid Stenting in the Setting of Mechanical Thrombectomy: A Delphi Consensus Statement <i>M. Goyal, et al.</i>	INTERVENTIONAL
	2280	Treatment of Ruptured Blister-Like Aneurysms with the FRED Flow Diverter: A Multicenter Experience <i>M.A. Möhlenbruch, et al.</i>	INTERVENTIONAL
	2285	Clinical Presentation and Imaging Findings of Patients with Dural Arteriovenous Fistulas with an Angiographic Pseudophlebitic Pattern <i>W. Brinjikji, et al.</i>	INTERVENTIONAL
	2292	Endovascular Cerebral Venous Sinus Imaging with Optical Coherence Tomography <i>C.R. Pasarikovski, et al.</i>	INTERVENTIONAL
	2298	Patients Requiring Conversion to General Anesthesia during Endovascular Therapy Have Worse Outcomes: A Post Hoc Analysis of Data from the SAGA Collaboration <i>C.Z. Simonsen, et al.</i>	INTERVENTIONAL
	2303	Interrater Reliability in the Measurement of Flow Characteristics on Color-Coded Quantitative DSA of Brain AVMs <i>K.H. Narsinh, et al.</i>	INTERVENTIONAL
	2311	Selection of Patients for Treatment of Brain Arteriovenous Malformations by the Transvenous Approach: Relationship with Venous Anatomy and Risk of Hemorrhagic Complications <i>J.M.B. De Sousa, et al.</i>	INTERVENTIONAL
	2317	Can a Stent Retriever Damage the JET 7 Reperfusion Catheter? <i>J. Pearly Ti, et al.</i>	INTERVENTIONAL
	2320	MRI-Based Assessment of the Pharyngeal Constrictor Muscle as a Predictor of Surgical Margin after Transoral Robotic Surgery in HPV-Positive Tonsillar Cancer <i>Y.J. Kim, et al.</i>	HEAD & NECK
	2327	Radioanatomic Characteristics of the Posteromedial Intraconal Space: Implications for Endoscopic Resection of Orbital Lesions <i>A. Jafari, et al.</i>	HEAD & NECK
	2333	Gadolinium-Enhanced 3D T1-Weighted Black-Blood MR Imaging for the Detection of Acute Optic Neuritis <i>I. Riederer, et al.</i>	HEAD & NECK
	2339	Quantitative T1ρ MRI of the Head and Neck Discriminates Carcinoma and Benign Hyperplasia in the Nasopharynx <i>Q.Y.H. Ai, et al.</i>	HEAD & NECK FUNCTIONAL
	2345	Design of 3D-Printed Nasopharyngeal Swabs for Children is Enabled by Radiologic Imaging <i>Z. Starosolski, et al.</i>	PEDIATRICS
	2348	Vessel Wall Enhancement and Focal Cerebral Arteriopathy in a Pediatric Patient with Acute Infarct and COVID-19 Infection <i>E. Gulko, et al.</i>	PEDIATRICS
	2351	Variations of Intracranial Dural Venous Sinus Diameters from Birth to 20 Years of Age: An MRV-Based Study <i>A.S. Larson, et al.</i>	PEDIATRICS



- 2358 **Risk Factors for Early Brain AVM Rupture: Cohort Study of Pediatric and Adult Patients** *L. Garzelli, et al.* **PEDIATRICS**
-  2364 **Longitudinal Assessment of Neuroradiologic Features in Wolfram Syndrome** *A. Samara, et al.* **PEDIATRICS**
-   2370 **Neonatal Developmental Venous Anomalies: Clinicoradiologic Characterization and Follow-Up** *A.F. Geraldo, et al.* **PEDIATRICS**
-    2377 **Perinatal Arterial Ischemic Stroke in Fetal Vascular Malperfusion: A Case Series and Literature Review** *A.F. Geraldo, et al.* **PEDIATRICS**

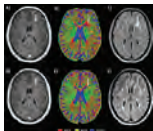
## ONLINE FEATURES

### LETTERS

-  E95 **Ocular MR Imaging as a Substitute for Ultrasound during the COVID-19 Pandemic** *Y.M. Purcell, et al.*
- E97 **Gadolinium Deposition and the Patient's View on the Problem** *I.B. Böhm*

## BOOK REVIEWS *R.M. Quencer, Section Editor*

Please visit [www.ajnrblog.org](http://www.ajnrblog.org) to read and comment on Book Reviews.



From: Neurite Orientation Dispersion and Density Imaging for Assessing Acute Inflammation and Lesion Evolution in MS by S. Sacco, et al.



Indicates Editor's Choices selection



Indicates Fellows' Journal Club selection



Indicates open access to non-subscribers at [www.ajnr.org](http://www.ajnr.org)



Indicates article with supplemental on-line table



Indicates article with supplemental on-line photo



Indicates article with supplemental on-line video



Evidence-Based Medicine Level 1



Evidence-Based Medicine Level 2

### EDITOR-IN-CHIEF

**Jeffrey S. Ross, MD**

Professor of Radiology, Department of Radiology,  
Mayo Clinic College of Medicine, Phoenix, AZ

### SENIOR EDITORS

**Harry J. Cloft, MD, PhD**

Professor of Radiology and Neurosurgery,  
Department of Radiology, Mayo Clinic College of  
Medicine, Rochester, MN

**Christopher G. Filippi, MD**

Professor and Alice Ettinger-Jack R. Dreyfuss  
Chair of Radiology,  
Tufts University School of Medicine,  
Radiologist-in-Chief  
Tufts University Medical Center

**Thierry A.G.M. Huisman, MD**

Radiologist-in-Chief, Texas Children's Hospital,  
Houston, TX

**Yvonne W. Lui, MD**

Associate Professor of Radiology,  
Chief of Neuroradiology,  
New York University School of Medicine,  
New York, NY

**C.D. Phillips, MD, FACR**

Professor of Radiology, Weill Cornell Medical  
College, Director of Head and Neck Imaging,  
New York-Presbyterian Hospital, New York, NY

**Lubdhra M. Shah, MD, MS**

Professor of Radiology and Director of Spine  
Imaging, University of Utah Department of  
Radiology and Imaging Sciences, Salt Lake City, UT

### STATISTICAL SENIOR EDITOR

**Bryan A. Comstock, MS**

Senior Biostatistician,  
Department of Biostatistics,  
University of Washington, Seattle, WA

### ARTIFICIAL INTELLIGENCE DEPUTY EDITOR

**Peter D. Chang, MD**

Assistant Professor-in-Residence,  
Departments of Radiological Sciences,  
Computer Sciences, and Pathology,  
Director, Center for Artificial Intelligence in  
Diagnostic Medicine (CAIDM),  
University of California, Irvine, Irvine, CA

### EDITORIAL BOARD

Ashley H. Aiken, Atlanta, GA

Lea M. Alhilali, Phoenix, AZ

Mohammed A. Almekhlafi, Calgary, Alberta,  
Canada

Joachim Berkefeld, Frankfurt, Germany

Aashim Bhatia, Pittsburgh, PA

Waleed Brinjikji, Rochester, MN

Judah Burns, New York, NY

Danielle Byrne, Dublin, Ireland

Federico Cagnazzo, Montpellier, France

J. Levi Chazen, New York, NY

James Y. Chen, San Diego, CA

Gloria C. Chiang, New York, NY

Daniel Chow, Irvine, CA

Kars C.J. Compagne, Rotterdam, The Netherlands

Arturo Consoli, Suresnes, France

Seena Dehkharghani, New York, NY

Nilesh K. Desai, Houston, TX

Yonghong Ding, Rochester, MN

Birgit Ertl-Wagner, Toronto, Ontario, Canada

Clifford J. Eskey, Hanover, NH

Massimo Filippi, Milan, Italy

Nils D. Forkert, Calgary, Alberta, Canada

Ana M. Franceschi, New York, NY

Frank Gaillard, Melbourne, Australia

Joseph J. Gemmete, Ann Arbor, Michigan

Wende N. Gibbs, Phoenix, AZ

Philipp Gölitz, Erlangen, Germany

Brent Griffith, Detroit, MI

Joseph M. Hoxworth, Phoenix, Arizona

Raymond Y. Huang, Boston, MA

Gábor Janiga, Magdeburg, Germany

Christof Karmonik, Houston, TX

Timothy J. Kaufmann, Rochester, MN

Hillary R. Kelly, Boston, MA

Toshibumi Kinoshita, Akita, Japan

Alexander W. Korutz, Chicago, IL

Stephen F. Kralik, Houston, TX

Alexander Lerner, Los Angeles, CA

Yinsheng Li, Madison, WI

Franklin A. Marden, Chicago, IL

Markus A. Möhlenbruch, Heidelberg, Germany

Kambiz Nael, Los Angeles, CA

Renato Hoffmann Nunes, Sao Paulo, Brazil

Sasan Partovi, Cleveland, OH

Johannes A.R. Pfaff, Heidelberg, Germany

Laurent Pierot, Reims, France

Alireza Radmanesh, New York, NY

Prashant Raghavan, Baltimore, MD

Eytan Raz, New York, NY

Paul M. Ruggieri, Cleveland, OH

Sebastian Schafer, Madison, WI

Maksim Shapiro, New York, NY

Timothy Shepherd, New York, NY

James Shin, New York, NY

Mark S. Shiroishi, Los Angeles, CA

Bruno P. Soares, Baltimore, MD

Jason F. Talbott, San Francisco, CA

Ruth Thiex, Everett, Washington

Vincent Thijs, Melbourne, Victoria, Australia

Anderanik Tomasian, Los Angeles, CA

Fabio Triulzi, Milan, Italy

Anja G. van der Kolk, Utrecht, the Netherlands

Arastoo Vossough, Philadelphia, PA

Elysa Widjaja, Toronto, Ontario, Canada

Leonard Yeo, Singapore

Woong Yoon, Gwangju, South Korea

David M. Yousem, Evergreen, CO

Carlos Zamora, Chapel Hill, NC

Chengcheng Zhu, Seattle, WA

### EDITORIAL FELLOW

Matthew D. Alvin, Baltimore, MD

### SPECIAL CONSULTANTS TO THE EDITOR

**AJNR Blog Editor**

Neil Lall, Denver, CO

**Case of the Month Editor**

Nicholas Stence, Aurora, CO

**Case of the Week Editors**

Juan Pablo Cruz, Santiago, Chile

Matylda Machnowska, Toronto, Ontario, Canada

Sapna Rawal, Toronto, Ontario, Canada

**Classic Case Editor**

Sandy Cheng-Yu Chen, Taipei, Taiwan

**Health Care and Socioeconomics Editor**

Pina C. Sanelli, New York, NY

**Physics Editor**

Greg Zaharchuk, Stanford, CA

**Podcast Editor**

Wende N. Gibbs, Phoenix, AZ

**Twitter Editor**

Roger Jordan, Houston, TX

### Official Journal:

American Society of Neuroradiology

American Society of Functional Neuroradiology

American Society of Head and Neck Radiology

American Society of Pediatric Neuroradiology

American Society of Spine Radiology

Founding Editor  
Juan M. Taveras

Editors Emeriti  
Mauricio Castillo, Robert I. Grossman,  
Michael S. Huckabee, Robert M. Quencer

Managing Editor  
Karen Halm

Assistant Managing Editor  
Laura Wilhelm

Editorial Assistant  
Margaret B. Sabato

Executive Director, ASNR  
Mary Beth Hepp



Title: Melancholic Sunset from Norway. This photo from Hafrsfjord, outside Stavanger on the southwestern coast of Norway, shows a simplistic, yet beautiful, traditional boat-house in the sunset.

*Torstein R. Meling, Professor of Neurosurgery, Geneva University Hospitals, Geneva, Switzerland*



# Changing the Rules of the Game: The Problem of Surrogate Angiographic Outcomes in the Evaluation of Aneurysm Treatments

T.E. Darsaut, R. Chapot, and J. Raymond

Surrogate outcomes (indicators or signs used in place of the true clinical outcome measure) are often used in the evaluation of neurovascular treatments, but there are many pitfalls.<sup>1</sup> The various ways surrogate angiographic outcomes are handled in our literature can be sources of confusion, particularly when new endovascular devices are introduced or when attempts are made to compare the results of different treatments.

One danger in focusing on a surrogate measure is losing sight of the goal of therapy: a good clinical outcome. In the case of aneurysm treatments, this means minimizing treatment-related morbidity and efficacy in the prevention of rupture. Angiographic outcomes are still important for at least 2 reasons. First, in clinical care, we cannot wait for ruptures to occur before we decide whether treatment was a success or a failure. Doctors need some indicator of the results of their actions so that they can, for example, offer a second treatment if need be. Second, and this is particularly true for unruptured aneurysms, the number of ruptures that occur during follow-up are few. An inordinately large number of patients followed for many years would be required for a randomized trial to show clinical outcomes are improved. A surrogate angiographic outcome measure can be obtained much sooner and can then be used to show superiority of a treatment with a smaller number of patients, provided the surrogate outcome truly predicts patients' future clinical outcomes. Surrogate angiographic outcomes are thus often used in randomized controlled trials (RCTs) that compare different endovascular devices.<sup>2-5</sup>

A famous example of the classic pitfall comes from cardiology: arrhythmias were known to cause death after myocardial infarction, and antiarrhythmic agents were found to decrease the incidence of arrhythmias,<sup>6</sup> but they were then shown to cause more deaths!<sup>7</sup> To avoid drawing the wrong conclusion about a treatment, clinical trials must always include hard clinical end points, and the "primary outcome" of a trial should be simple, clinical, and meaningful.<sup>8</sup> For neurovascular treatments, the problem is that these larger trials are infrequently done.

One exception is the International Subarachnoid Aneurysm Trial (ISAT),<sup>9</sup> which compared surgical clipping and coiling of ruptured aneurysms. The primary outcome was appropriately clinical (mRs  $\geq 3$  at 1 year), but it required the enrollment of 2143 patients. Angiographic outcomes were not recorded in ISAT, but it was known that the angiographic results of coiling were not as good or as durable, as advocates of surgical clipping complained: clipping achieved complete occlusion in 90% of cases compared with 45%–50% for endovascular treatment at best.<sup>10</sup> The appropriate response

to that concern is that the clinical results are what count; they were better with coiling in ISAT.<sup>9</sup> In the meantime, because complete occlusions were infrequent with coiling, we learned to accept a residual neck as "acceptable" because rebleeding was rare compared with patients with residual aneurysms.<sup>10</sup>

Now flow diverters are introduced; how can the case be made that they should be used instead of coiling? A randomized trial with a clinical outcome measure, say, to ensure the complication rate of flow diversion was not double that of coiling (ie, 5% to 10%), would require at least 865 patients. So, we use a surrogate angiographic outcome. But because we now consider residual necks as "satisfactory" and we can obtain this result in 80%–90% of cases,<sup>11</sup> even this strategy won't work: a trial of 1000–1500 patients would be necessary to show that flow diversion can improve already good results. What's left to do? Well, what was done is that the threshold for what constitutes a good angiographic outcome was changed to no longer accept residual necks; in other words, the rules of the game were changed.

With this altered definition, flow diversion can be made to look good. Consider how simple it would have been to do an RCT with success defined as "complete aneurysm occlusion": a trial of approximately 110 patients or so could have been sufficient to show that flow diversion improved complete occlusions rates from 50% to 75%. With a trial this size, of course, no one would be able to properly evaluate clinical outcomes: whether the improvement in the surrogate imaging finding (from near-complete to complete occlusion) was worth the added risk of flow diversion or whether it translated into better clinical outcomes in the long run. But was this simple trial even done? The unfortunate reality is that an RCT was not required to introduce flow diverters; flow diverter complete occlusion rates were simply "compared" with historical controls.<sup>12</sup>

The latest iteration of the changing-of-the-rules-as-you-go-along problem is to adapt the classification of angiographic results to the needs of the new device, as was recently done for the WEB device. If by design the device regularly leaves a residuum at its base, it is now proposed to consider that result akin to "complete occlusion." "Adequate occlusion" is now a broad class that subsumes complete occlusions, including "complete occlusions with opacification of the recess, in addition to neck remnants need to close."<sup>13,14</sup> In this scheme, aneurysm necks are "acceptable" (post-ISAT), then "not acceptable" (to justify flow diversion), and then "acceptable" again (to justify WEB) (Figure). Advocates of surgical clipping especially should decry that the rules of the game keep on changing. Had complete occlusion consistently stayed the reason to choose one treatment over the other (without ever properly checking impacts on clinical outcomes as was done in ISAT), clipping would still be the treatment of choice for most aneurysm patients!

One final related pitfall should be mentioned: attempts to compare treatments are further encumbered now because device-specific scales are used to evaluate angiographic results for each treatment.<sup>13,15-17</sup> Using a different scale for every different treatment only ensures that the results of aneurysm treatments can no longer be compared.

Angiographic results	Interpretation of Aneurysm Neck	Evidence of Angiographic Outcome	Evidence of Clinical Outcome
Pre-ISAT: Clipping better (>90% complete occlusion) compared with coiling (~45% complete occlusion)		Bad	Historical only
<b>ISAT (2002)</b>			
Post-ISAT: Coiling not better than clipping, but angiographic outcomes trumped by clinical outcome results (for ruptured aneurysms only)	Acceptable	None	Better 1 year clinical outcomes with coiling (ISAT)
Flow diversion better (90% complete occlusion) compared with coiling (~45% complete occlusion)		Bad	Compared with historical controls only
WEB (new device-specific scale):	Acceptable (+ recesses, too!)	Comparisons difficult and historical	Not powered to verify clinical outcomes

**FIGURE.** Changing the rules of the game.

Pitfalls notwithstanding, angiographic outcomes will continue to play an important role in the evaluation of neurovascular treatments. However, clinicians must remain wary of how they can be manipulated to show treatment results in a good light.

Disclosures: Rene Chapot—UNRELATED: Consultancy: Microvention, Stryker\*; Payment for Lectures Including Service on Speakers Bureaus: Balt, Medtronic, Microvention, Siemens, Stryker.\* \*Money paid to the institution.

## REFERENCES

- Fleming TR, DeMets DL. Surrogate end points in clinical trials: are we being misled? *Ann Intern Med* 1996;125:605–13 CrossRef Medline
- McDougall CG, Johnston SC, Gholkar A, et al. Bioactive versus bare platinum coils in the treatment of intracranial aneurysms: the MAPS (Matrix and Platinum Science) trial. *AJNR Am J Neuroradiol* 2014;35:935–42 CrossRef Medline
- Raymond J, Darsaut TE, Guilbert F, et al. Flow diversion in aneurysms trial: the design of the FIAT study. *Interv Neuroradiol* 2011;17:147–53 CrossRef Medline
- Raymond J, Roy D, White PM, et al. A Randomized Trial Comparing Platinum and Hydrogel-coated Coils in Patients Prone to Recurrence after Endovascular Treatment (the PRET trial). *Interv Neuroradiol* 2008;14:73–83 CrossRef Medline
- White PM, Lewis SC, Gholkar A, et al. Hydrogel-coated coils versus bare platinum coils for the endovascular treatment of intracranial aneurysms (HELPS): a randomised controlled trial. *Lancet* 2011;377:1655–62 CrossRef Medline
- The Cardiac Arrhythmia Pilot Study. The CAPS investigators. *Am J Cardiol* 1986;57:91–95 CrossRef
- Ruskin JN. The cardiac arrhythmia suppression trial (CAST). *N Engl J Med* 1989;321:386–88 CrossRef Medline
- Haynes BR, Sackett DL, Guyatt GH, et al. *Clinical Epidemiology: How to Do Clinical Practice Research*. 3rd ed. Lippincott Williams & Wilkins; 2005
- Molyneux A, Kerr R, Stratton I, International Subarachnoid Aneurysm Trial (ISAT) Collaborative Group, et al. International Subarachnoid Aneurysm Trial (ISAT) of neurosurgical clipping versus endovascular coiling in 2143 patients with ruptured intracranial aneurysms: a randomised trial. *Lancet* 2002;360:1267–74 CrossRef Medline
- Roy D, Milot G, Raymond J. Endovascular treatment of unruptured aneurysms. *Stroke* 2001;32:1998–2004 CrossRef Medline
- Raymond J, Guilbert F, Weill A, et al. Long-term angiographic recurrences after selective endovascular treatment of aneurysms with detachable coils. *Stroke* 2003;34:1398–1403 CrossRef Medline
- Becske T, Kallmes DF, Saatci I, et al. Pipeline for uncoilable or failed aneurysms: results from a multicenter clinical trial. *Radiology* 2013;267:858–68 CrossRef Medline
- Lubicz B, Klisch J, Gauvrit JY, et al. WEB-DL endovascular treatment of wide-neck bifurcation aneurysms: short- and midterm results in a European study. *AJNR Am J Neuroradiol* 2014;35:432–38 CrossRef Medline
- Pierot L, Szikora I, Barreau X, et al. Aneurysm treatment with WEB in the cumulative population of two prospective, multicenter series: 3-year follow-up. *J Neurointerv Surg* 2020 Jun 12 [Epub ahead of print] CrossRef Medline
- Cekirge HS, Saatci I. A new aneurysm occlusion classification after the impact of flow modification. *AJNR Am J Neuroradiol* 2016;37:19–24 CrossRef Medline
- Kotowski M, Farzin B, Fahed R, et al. Residual cerebral aneurysms after microsurgical clipping: a new scale, an agreement study, and a systematic review of the literature. *World Neurosurg* 2019;121:e302–21 CrossRef Medline
- O'Kelly CJ, Krings T, Fiorella D, et al. A novel grading scale for the angiographic assessment of intracranial aneurysms treated using flow diverting stents. *Interv Neuroradiol* 2010;16:133–37 CrossRef Medline

# Imaging Review of Paraneoplastic Neurologic Syndromes

 A.A. Madhavan,  C.M. Carr,  P.P. Morris,  E.P. Flanagan,  A.L. Kotsenas,  C.H. Hunt,  L.J. Eckel,  E.P. Lindell, and  F.E. Diehn



## ABSTRACT

**SUMMARY:** Paraneoplastic syndromes are systemic reactions to neoplasms mediated by immunologic or hormonal mechanisms. The most well-recognized paraneoplastic neurologic syndrome, both clinically and on imaging, is limbic encephalitis. However, numerous additional clinically described syndromes affect the brain, spinal cord, and peripheral nerves. Many of these syndromes can have imaging findings that, though less well described, are important in making the correct diagnosis. Moreover, imaging in these syndromes frequently mimics more common pathology, which can be a diagnostic challenge for radiologists. Our goal is to review the imaging findings of paraneoplastic neurologic syndromes, including less well-known entities and atypical presentations of common entities. Specifically, we discuss limbic encephalitis, paraneoplastic cerebellar degeneration, paraneoplastic brain stem encephalitis, cranial neuropathy, myelitis, and polyneuropathy. We also demonstrate common diagnostic pitfalls that can be encountered when imaging these patients.

**ABBREVIATIONS:** ANNA = antineuronal nuclear autoantibody; PNS = paraneoplastic neurologic syndrome; PCD = paraneoplastic cerebellar degeneration

Paraneoplastic syndromes (PNSs) result from systemic reactions to neoplasms, often mediated by immunologic or hormonal mechanisms. PNSs include limbic encephalitis, encephalomyelitis, paraneoplastic cerebellar degeneration (PCD), brain stem encephalitis, polyneuropathy, stiff-person syndrome, retinopathy, myasthenia gravis, Lambert-Eaton myasthenic syndrome, and enteric nervous system dysfunction (Fig 1). These syndromes are often associated with serum or CSF positivity of onconeural or neuronal cell surface antibodies. Onconeural antibodies are more directly associated with underlying neoplasms and cause neuronal dysfunction by recruitment of cytotoxic T cells. In contrast, neuronal cell surface antibodies are less commonly associated with an underlying neoplasm and mediate pathology by directly binding to neurons. PNSs can occur in the presence or absence of paraneoplastic antibodies and are ultimately a clinical diagnosis. Conversely, antibody-mediated neurologic syndromes can occur in the absence of malignancy, though these are separately classified.<sup>1</sup>

Many PNSs have salient imaging features. Although some of these are well described, particularly those of limbic encephalitis, others are not. Additionally, the spectrum of imaging findings for many PNSs is more variable than what is currently reported in the literature, which can frequently lead to incorrect or delayed diagnoses. Imaging is frequently obtained before the formal diagnosis of a PNS or underlying malignancy.<sup>2</sup> Therefore, it is important to be aware of imaging features of these syndromes and common pitfalls.

This review illustrates the typical imaging findings of paraneoplastic neurologic syndromes in a pictorial essay format and briefly discusses the differential diagnosis for each syndrome when encountered on imaging (On-line Table). Although prior reviews have comprehensively discussed the clinical features of these syndromes, their associated imaging features have not been widely demonstrated, with the notable exception of limbic encephalitis. The patients presented were ultimately diagnosed with paraneoplastic syndromes based on a combination of clinical, laboratory, and imaging findings. Several of the patients also highlight potential imaging pitfalls that can obfuscate the correct diagnosis.

## PARANEOPLASTIC NEUROLOGIC SYNDROMES BY ANATOMIC LOCATION


### Brain: Limbic Encephalitis


Limbic encephalitis refers to inflammatory changes involving the limbic system, which includes the hippocampus, amygdala, hypothalamus, and cingulate cortex. Symptoms include mood and

Received May 19, 2020; accepted after revision June 29.

From the Division of Neuroradiology, Department of Radiology (A.A.M., C.M.C., P.P.M., A.L.K., C.H.H., L.J.E., E.P.L., F.E.D.) and the Department of Neurology (E.P.F.), Mayo Clinic, Rochester, Minnesota.

Please address correspondence to Ajay Madhavan, MD, Department of Radiology, Mayo Clinic, 200 First Street SW, Rochester, MN 55905, e-mail: madhavan.ajay@mayo.edu

 Indicates open access to non-subscribers at [www.ajnr.org](http://www.ajnr.org)

 Indicates article with supplemental on-line table.

<http://dx.doi.org/10.3174/ajnr.A6815>



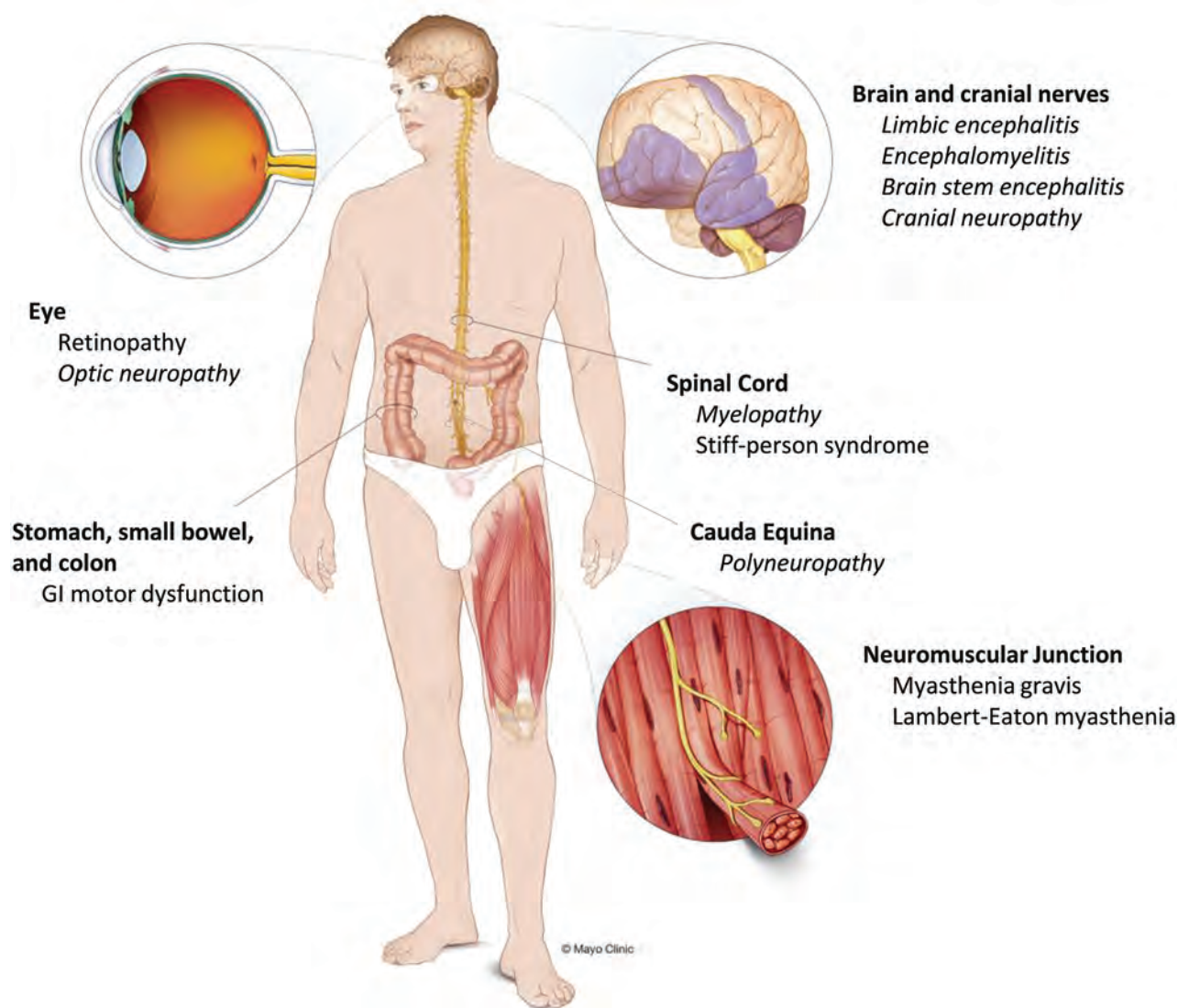


**FIG 1.** Illustration of the diverse array of paraneoplastic neurologic syndromes affecting a wide variety of anatomic structures. Most of these syndromes (in italics) can have salient imaging findings that can be important in making the correct diagnosis. Used with permission of Mayo Foundation for Medical Education and Research, all rights reserved.

behavioral changes, cognitive dysfunction, memory loss, and seizure activity. Limbic encephalitis may be associated with various onconeural paraneoplastic antibodies, including antineuronal nuclear autoantibody type 1 (ANNA-1)/anti-Hu, anti-collapsin response mediator protein-5 (CRMP5)/anti-CV2, and anti-Ma2. Although the syndromes associated with these antibodies all characteristically involve the limbic system, some can have extralimbic involvement. For example, anti-Ma2 can involve the brain stem and cerebellum, and anti-CRMP5 can have spinal cord involvement. Common tumor associations for limbic encephalitis in general include small cell lung cancer and breast cancer. Alternatively, limbic encephalitis can be seen in association with nonparaneoplastic neuronal cell surface antibodies, causing an autoimmune encephalitis. These include leucine-rich glioma-inactivated-1 (LGI1) autoantibodies, GAD65 autoantibodies, and anti-contactin-associated proteinlike 2 (CASPR2) antibodies.<sup>3,4</sup> Patients with autoimmune encephalitis often have typical limbic system involvement, but

sometimes different imaging findings such as subcortical T2 hyperintensities are seen.<sup>5</sup> Imaging findings in paraneoplastic limbic encephalitis are ultimately not reliably distinguishable from nonparaneoplastic autoimmune causes, so it is important to be aware of autoantibodies that are more associated with nonparaneoplastic limbic encephalitis. Additionally, even autoimmune encephalitis associated with a typically nonparaneoplastic antibody have been uncommonly seen with underlying malignancy. Therefore, malignancy screening is nearly always appropriate.<sup>6</sup>

Typical imaging findings of limbic encephalitis include T2 hyperintensity and swelling of the mesial temporal lobes with FDG avidity on PET (Fig 2A, -B), sometimes with associated enhancement. These findings can also involve other parts of the limbic system. For example, paraneoplastic limbic encephalitis can have striking involvement of the hypothalamus and mammillary bodies with relative sparing of the remaining limbic system (Fig 2C-F). Sometimes limbic encephalitis can have a masslike appearance that

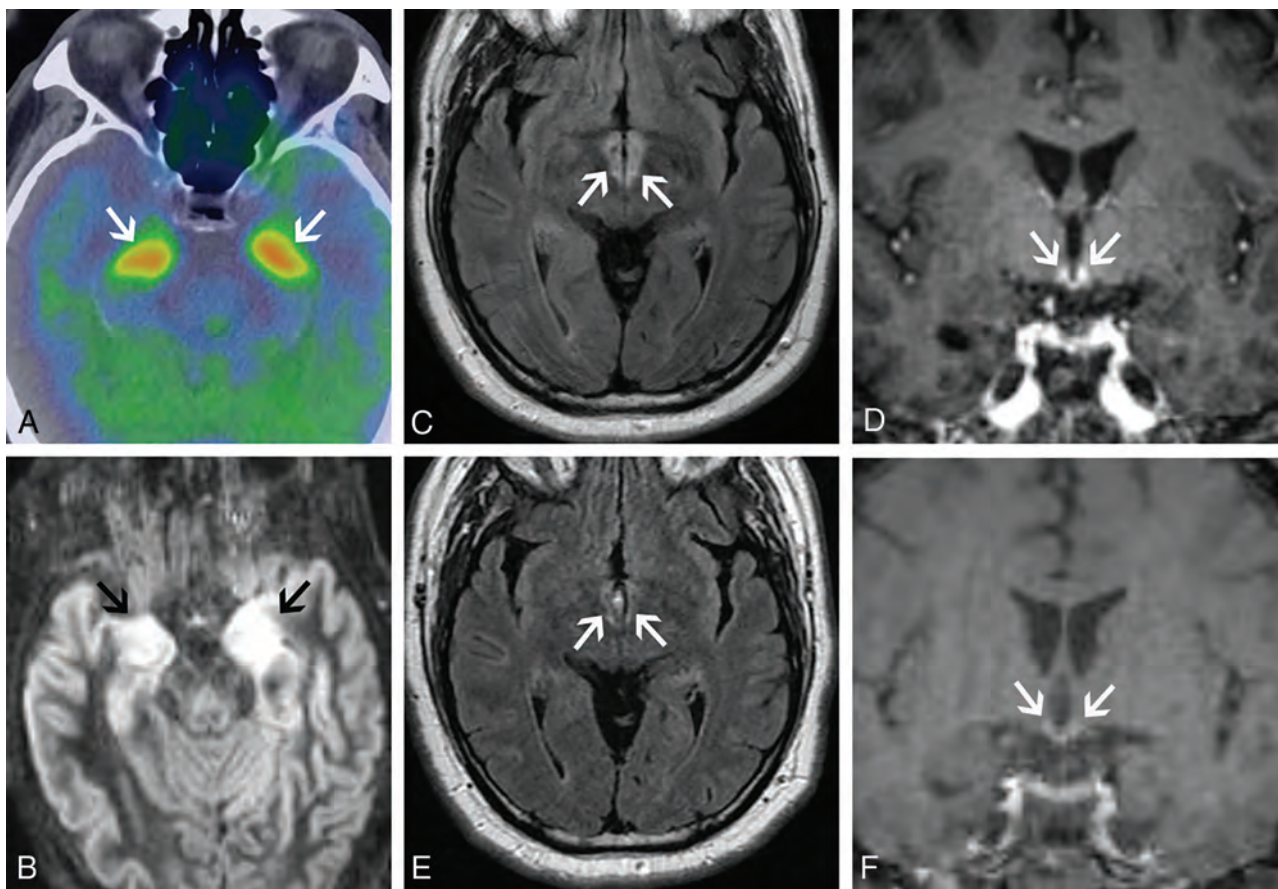


**FIG 2.** Classic limbic encephalitis (A and B). A 75-year-old healthy man presented with abrupt onset of memory loss and staring spells over several days. CSF analysis was positive for LGII autoantibodies. FDG-PET/CT axial image (A) shows marked hypermetabolism in the bilateral mesial temporal lobes (A, arrows). Axial double inversion recovery MR imaging image (B) shows corresponding increased T2 signal in both mesial temporal lobes (B, arrows). Atypical limbic encephalitis (C–F). A 29-year-old man with a history of resected nongerminoma testicular cancer presented months after treatment with worsening memory, diminished executive function, hypogonadism, and hypothyroidism. CSF analysis showed increased total protein but was otherwise normal. Axial FLAIR (C) and coronal T1-weighted postcontrast (D) images show abnormal T2 signal in the hypothalamus (C, arrows) and enhancement of the mammillary bodies (D, arrows). He was diagnosed with paraneoplastic limbic encephalitis with atypical involvement of the hypothalamus and mammillary bodies. He opted for observation with symptomatic improvement over months. Follow-up MR imaging shows improved mild residual hypothalamic T2 signal (E, arrows) and decreased enhancement of the mammillary bodies (F, arrows).

can be mistaken for tumors such as low- or high-grade gliomas or even lymphoma (Fig 3A–C). The imaging findings in such cases can dramatically improve with treatment, and FDG hypometabolism may be seen after recovery (Fig 3D–F). Overall, limbic encephalitis has more complex imaging features than previously appreciated and should be considered even in cases that do not involve typical areas such as the hippocampus and amygdala. Atypical patterns of involvement can be seen in nonparaneoplastic limbic encephalitis as well.<sup>1,6</sup>

The primary differential to exclude in limbic encephalitis with mesial temporal lobe involvement is herpes simplex viral encephalitis. Ancillary findings such as cortical petechial hemorrhages, or rarely intracerebral hematomas, can suggest herpes infection. CSF testing and prophylactic antiviral treatment are necessary if infection is a clinical possibility. Other differential considerations include status epilepticus, neurosyphilis, and low- or high-grade glioma.<sup>4</sup> When limbic encephalitis has hypothalamic involvement, inflammatory conditions such as sarcoidosis or lymphocytic hypophysitis should be considered.

Diagnostic criteria for limbic encephalitis include subacute symptom onset over less than 3 months, limbic system abnormalities on brain MR imaging, EEG showing epileptic or slow-wave activity in the temporal lobes or CSF pleocytosis, and reasonable exclusion of other etiologies.<sup>7</sup> Thus, the work-up for limbic encephalitis, in addition to a thorough neurologic history and physical examination, typically includes brain MR imaging, paraneoplastic antibody testing, EEG, and oncologic work-up, including FDG-PET/CT. Brain biopsy is rarely needed but can be difficult to avoid when imaging shows a masslike abnormality. After the diagnosis is established, the most important next step is management of any underlying malignancy.<sup>8</sup> However, immunosuppression and plasma exchange can be helpful, too.

#### **Brain: Paraneoplastic Cerebellar Degeneration**

PCD is clinically characterized by limb and truncal ataxia, nystagmus, and dysarthria.<sup>9</sup> These symptoms are often progressive over weeks to months. Pathologically, patients have progressive loss of Purkinje cells in the cerebellum.<sup>10</sup> CSF analysis can show pleocytosis and elevated oligoclonal bands. PCD is associated with a variety of paraneoplastic antibodies, including anti-Yo (Purkinje cell autoantibody type-1



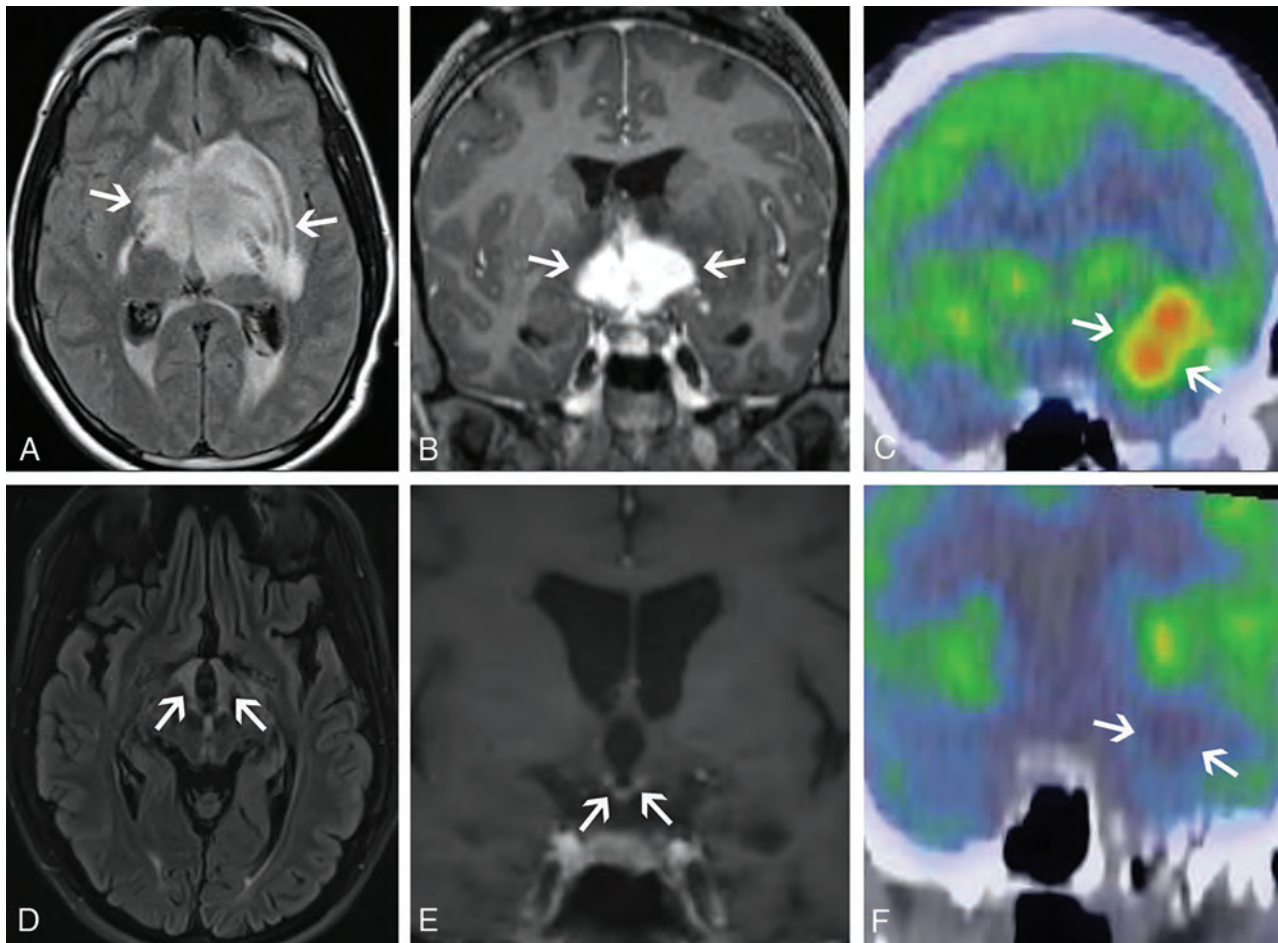


**FIG 3.** Limbic encephalitis mimicking a tumor. A 31-year-old man presented after being found unconscious while doing repair work on his home. He had multiple neurologic symptoms, including impaired thermoregulation, hypersexuality, and depression. Axial FLAIR (A) and coronal T1-weighted postgadolinium (B) images show extensive increased T2 signal and masslike enhancement centered in the region of the hypothalamus (A and B, arrows). The findings were initially considered worrisome for a neoplastic process, such as lymphoma, versus an inflammatory lesion, such as lymphocytic hypophysitis. Biopsy of this region showed a nonspecific macrophage-rich demyelinating lesion with no evidence of tumor. He was later found to have anti-Ma2 serum positivity and a mediastinal germ cell tumor. Images of the brain from his staging FDG-PET/CT show asymmetric FDG uptake in the left mesial temporal lobe (C, arrows), separate from the affected regions on his MR imaging. He was treated with chemotherapy and high-dose corticosteroids with gradual improvement in his symptoms. Axial FLAIR (D) and coronal postgadolinium (E) MR imaging obtained 1 year later show marked improvement in the prior findings, with mild residual hypothalamic T2 signal (D, arrows) and mild enhancement of the tuber cinereum (E, arrows). His subsequent FDG-PET/CT shows decreased FDG avidity in the previously involved left mesial temporal lobe (F, arrows). Ultimately, his intracranial findings were consistent with limbic encephalitis rather than malignancy.

[PCA-1]), anti-Ri (ANNA-2), and anti-Purkinje cell autoantibody-Tr/DNER (delta/notchlike epidermal growth factor-related receptor). About 60% of cases have an associated onconeural antibody.<sup>9</sup> Common associated malignancies include ovarian cancer, breast cancer, and Hodgkin lymphoma.

Imaging findings of PCD depend on the phase of the syndrome. In the acute phase, increased T2 signal within the cerebellar hemispheres can be seen (Fig 4A, -B). At this stage, the differential diagnosis includes infectious or inflammatory cerebellitis. In the chronic phase, T2 hyperintensity improves, and cerebellar FDG-PET hypometabolism, atrophy, or both may be seen (Fig 4C-F). The differential diagnosis for chronic PCD includes alcoholic degeneration, neurodegenerative disorders such as multiple system atrophy (cerebellar subtype), and sequelae from infectious/inflammatory cerebellitis. Careful attention to patient history, such as prior alcohol use disorder or cerebellar infection, is most important in distinguishing these entities.

As with limbic encephalitis, brain MR imaging, paraneoplastic antibody testing, and oncologic work-up are key to diagnosis. Pelvic sonography or MR imaging should also be considered in women because PCD is associated with gynecologic malignancies.<sup>11</sup> Treatment of any identifiable malignancy is critical, but immunosuppressive agents are also used, ranging from corticosteroids to cyclophosphamide for severe cases. Treatment response is generally poor if antibodies to intracellular antigens are detected (eg, PCA-1/anti-Yo), and most of these patients progress to wheelchair dependence. If an antibody to a cell surface antigen is instead found (eg, metabotropic glutamate receptor [mGluR1]), the prognosis is better.

#### **Brain: Brain Stem Encephalitis**

Brain stem encephalitis, or rhombencephalitis, refers to inflammation predominantly involving the brain stem, though the cerebellar peduncles and hemispheres can be affected too. Paraneoplastic

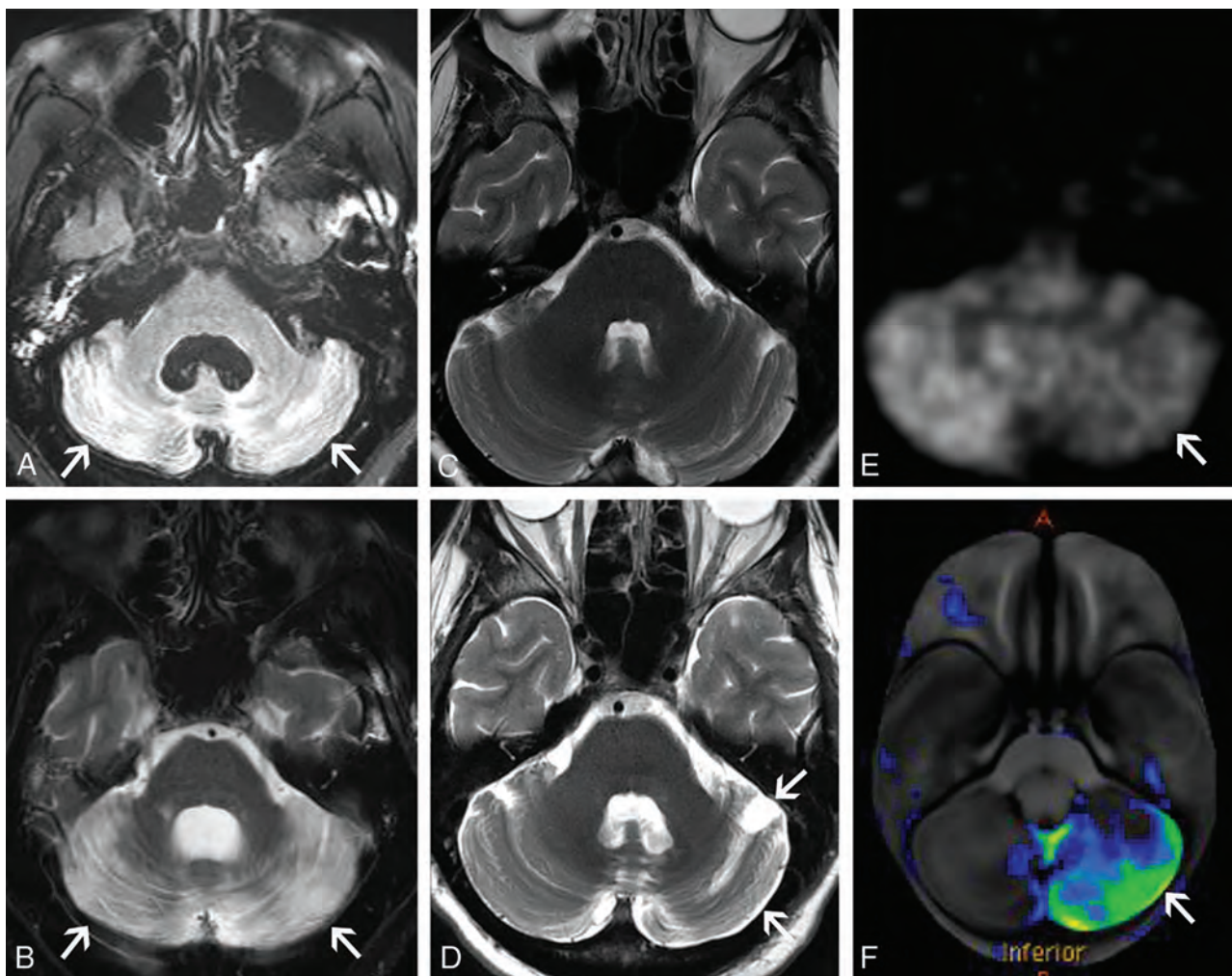


**FIG 4.** Subacute paraneoplastic cerebellar ataxia (A and B). A 58-year-old woman presented with headaches, vertigo, and ataxia that had progressed over a period of weeks. CSF analysis showed a high titer of PCA-1 autoantibodies. After additional work-up, she was found to have metastatic breast adenocarcinoma. Axial FLAIR (A) and T2-weighted (B) images of the brain show marked T2 hyperintensity diffusely involving both cerebellar hemispheres (A and B, arrows). No enhancement was seen on postgadolinium images (not shown). The patient was diagnosed with paraneoplastic cerebellar degeneration. She had mild improvement in her neurologic symptoms with high-dose corticosteroids but remained wheelchair dependent. Chronic paraneoplastic cerebellar ataxia (C–F). A 56-year-old woman presented with progressive ataxia over a period of several months. Paraneoplastic serum antibody panel revealed anti-G-AChR (ganglionic acetylcholine receptor) antibodies, and CSF analysis revealed increased protein concentration and high IgG levels. Initial axial T2-weighted image of the brain (C) and subsequent axial T2-weighted image from an examination several months later (D) show interval development of mild left cerebellar atrophy (D, arrows). FDG-PET axial source image of the brain (E) and processed surface rendering of the brain compared with age-matched control participants (F) show marked hypometabolism within the left cerebellar hemisphere (E and F, arrows). No cerebral lesion was present to suggest crossed cerebellar diaschisis. Review of prior records noted an FDG-avid thyroid lesion found to be a follicular neoplasm on resection. She was diagnosed with paraneoplastic cerebellar degeneration with chronic atrophic features. Her symptoms have been stable on cyclophosphamide with pulsed corticosteroids.

brain stem encephalitis has a variable clinical presentation that may include ataxia, dysarthria, and ophthalmoplegia.<sup>12</sup> It is most commonly associated with the anti-Ma2 antibody but has also recently been identified with antibodies to Kelchlike protein 11.<sup>13</sup> The syndrome is most associated with testicular germ cell tumors such as seminomas.<sup>9</sup> However, it can also be seen with neuroendocrine and other tumors.<sup>14</sup>

Imaging findings can be normal in these patients. When present, findings vary depending on the phase of illness. Acutely, T2 hyperintensity and/or enhancement of the cerebellum, cerebellar peduncles, and brain stem are seen. Importantly, there can be isolated involvement of the brain stem in the acute phase, which can be mistaken for other entities, including tumor (Fig 5A, -B). As

the disease progresses, cerebellar and brain stem atrophy are often seen. Additionally, cruciform T2 hyperintensity in the pons and T2 hyperintensity in the middle cerebellar peduncles can occur with this syndrome secondary to Wallerian degeneration, quite similar to the imaging findings seen in multiple system atrophy (Fig 5C, -D). Hypertrophic olivary degeneration can also be seen as a result of paraneoplastic brain stem encephalitis (Fig 5E, -F), presumably caused by disruption of the dentato-rubro-olivary pathway.

Differential considerations for the acute phase are broad, though certain conditions are known to have a predilection for the brain stem. These include *Listeria* and herpes simplex virus infection as well as inflammatory disorders such as Behçet disease, systemic



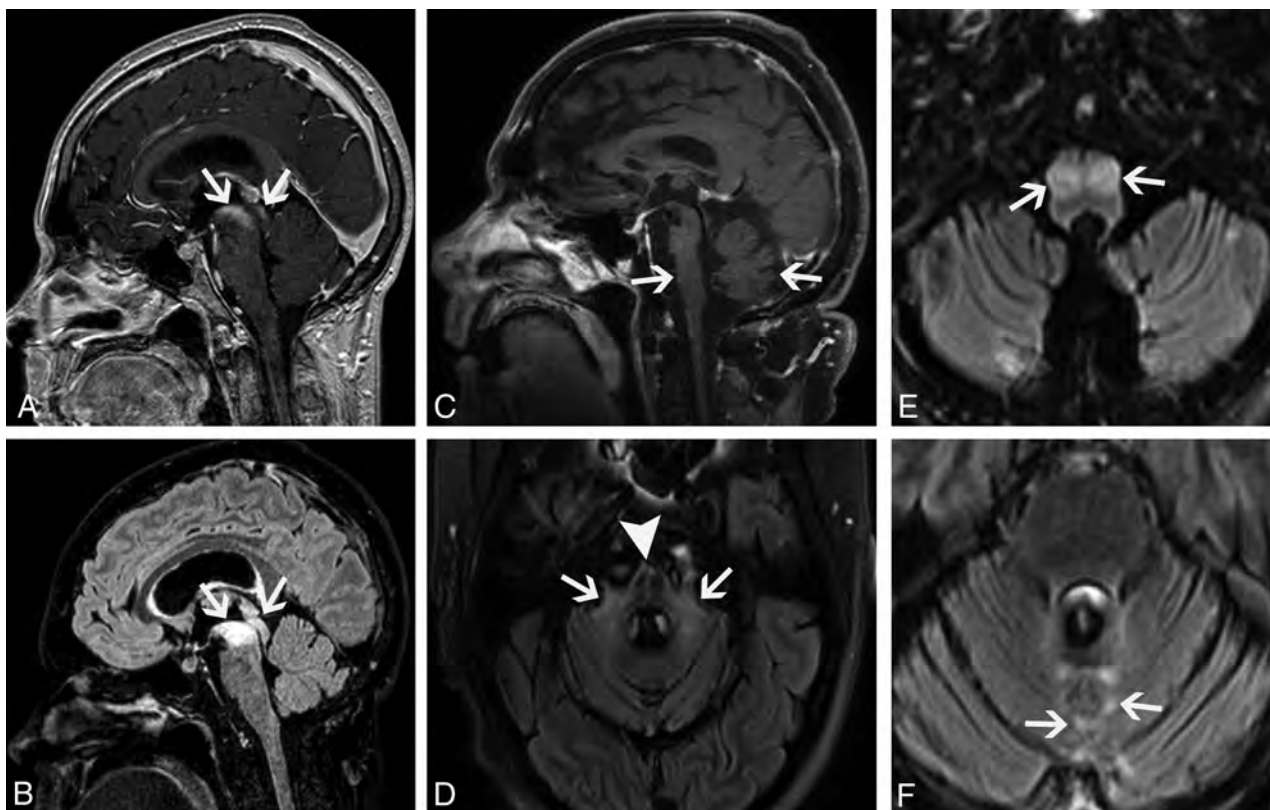


**FIG 5.** Paraneoplastic brain stem encephalitis mimicking a tumor (A–D). A 29-year-old man presented with tinnitus, hearing loss, diplopia, and imbalance that had progressed over at least 1 year. After extensive clinical work-up, the patient was diagnosed with metastatic seminoma to the mediastinum and noted to have elevated CSF IgG. Serum and CSF were positive for Kelchlike protein 11 autoantibodies. Sagittal T1-weighted postcontrast (A) and sagittal FLAIR (B) images show enhancing, T2 hyperintense lesions in the midbrain and tectum (A and B, arrows), initially believed to be worrisome for metastases. He was treated with chemotherapy, and his symptoms transiently improved but then worsened over the next several years. Sagittal T1-weighted postcontrast (C) and axial FLAIR (D) images from a subsequent MR imaging 4 years later show new marked cerebellar and brain stem atrophy (C, arrows), as well as new T2 signal in the middle cerebellar peduncles (D, arrows) and cruciform T2 signal in the pons (D, arrowhead). He was diagnosed with paraneoplastic brain stem encephalitis rather than multiple system atrophy given the clinical context of the findings. The patient's symptoms mildly improved after treatment with multiple immunosuppressive agents. Brain stem encephalitis associated with hypertrophic olivary degeneration (E and F). A 45-year-old man presented with progressive aural fullness and hearing loss, initially thought to be caused by otitis media. Over the next 2 years, he had progressive gait ataxia and diplopia. CSF analysis showed antibodies to Kelchlike protein 11. Testicular sonography, performed as part of his oncologic work-up, showed a right testicular mass. Right orchiectomy revealed a germ cell neoplasm. Axial FLAIR images (E and F) from his brain MR imaging show enlargement and T2 hyperintensity of both inferior olives (E, arrows) consistent with bilateral hypertrophic olivary degeneration. Additionally, there is patchy T2 hyperintensity in the cerebellar vermis (F, arrows). He was diagnosed with paraneoplastic rhombencephalitis with associated hypertrophic olivary degeneration. He has had a partial response to multiple immunotherapies.

lupus erythematosus, Bickerstaff encephalitis, or Miller Fischer syndrome.<sup>12,15</sup> Demyelinating diseases such as multiple sclerosis, neuromyelitis optica spectrum disorder, and myelin oligodendrocyte glycoprotein antibody-associated disease are additional considerations. In the chronic phase, this syndrome can be mistaken for multiple system atrophy and other neurodegenerative disorders.

In addition to brain MR imaging and usual paraneoplastic antibody screening, screening for the newly discovered KLHL11 autoantibodies should be done when diagnosing these patients. Furthermore, testicular sonography should be done in men given the association with testicular seminoma.<sup>11</sup> The mainstay of management is treatment of any identifiable malignancy, with immunomodulatory therapy used in refractory cases.

### Head: Cranial Neuropathy

Paraneoplastic cranial neuropathies are rare but have been previously described in several reports.<sup>16,17</sup> Symptoms depend on the cranial nerves involved. For example, deteriorating balance and sensorineural hearing loss have been observed with paraneoplastic involvement of the eighth cranial nerves.<sup>17</sup> Symptoms may be more extensive when there is involvement of multiple cranial nerves, as seen in 1 report of paraneoplastic neuropathy of the third, sixth, and seventh cranial nerves in a patient with gallbladder carcinoma.<sup>18</sup> Anti-Hu/ANNA-1 and the newly described antibodies to Kelchlike protein-11 associated with seminoma are especially associated with paraneoplastic cranial neuropathy.

Possible imaging findings include enhancement and/or enlargement of the affected cranial nerves (Fig 6). The differential

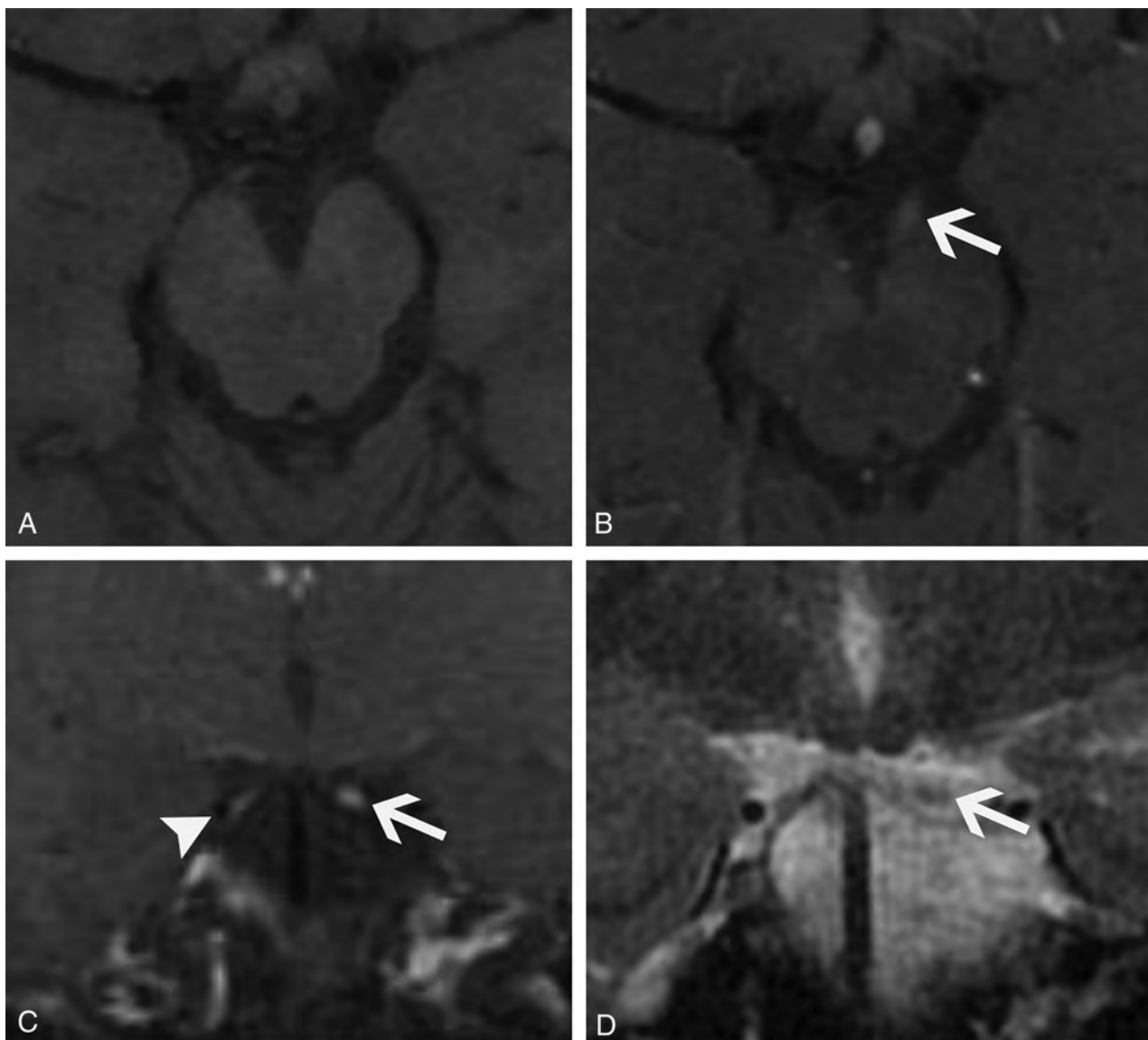


**FIG 6.** Paraneoplastic cranial neuropathy mimicking leptomeningeal carcinomatosis. A 54-year-old woman recently diagnosed with small cell lung cancer presented with diplopia that slowly progressed over a period of days. Her examination showed left eye ptosis and gaze abnormalities consistent with oculomotor palsy. The primary clinical concern was metastatic leptomeningeal carcinomatosis. Lumbar puncture showed elevated CSF IgG index and IgG synthesis rate with no specific findings for malignancy. No specific paraneoplastic antibodies were detected. Axial T1-weighted pre- (A) and postcontrast (B) images and the coronal postcontrast image (C) from her brain MR imaging show enlargement and enhancement of the left third cranial nerve cisternal segment (B and C, arrows) and mild enhancement of the right third cranial nerve cisternal segment (C, arrowhead). Coronal T1-weighted image (D) confirms mild enlargement of the left third cranial nerve (arrow). Based on the lack of other widespread intracranial disease, non-nodular nerve enhancement, and CSF findings, she was diagnosed with paraneoplastic cranial neuropathy and had rapid symptomatic improvement with methylprednisolone.

diagnosis includes infection, acute inflammatory demyelinating polyneuropathy (Guillain-Barré syndrome), and chronic inflammatory demyelinating polyneuropathy.<sup>19,20</sup> Entities such as neurosarcoidosis, lymphoma, and carcinomatous meningitis tend to have more nodular enhancement and likely other areas of involvement, whereas chronic inflammatory demyelinating polyneuropathy tends to have mainly nerve root enlargement without enhancement. Notably, leptomeningeal metastases are a frequent clinical concern in patients with cancer who have new cranial neuropathy, so imaging can play an important role in potentially suggesting a paraneoplastic rather than malignant cause (Fig 6).

Diagnosis requires a thorough neurologic work-up, and ophthalmologic consultation is helpful if ophthalmoplegia is identified. Brain MR imaging with thin-section imaging is particularly useful to assess the cranial nerves and patterns of pathologic enhancement. The treatment for paraneoplastic cranial neuropathy is not well studied and mainly involves management of the underlying malignancy. In our experience, patients have improved with short-term corticosteroids.

#### **Spine: Myelitis**

Paraneoplastic myelitis is a rare but likely underreported entity. It may occur in isolation or in conjunction with other involved regions

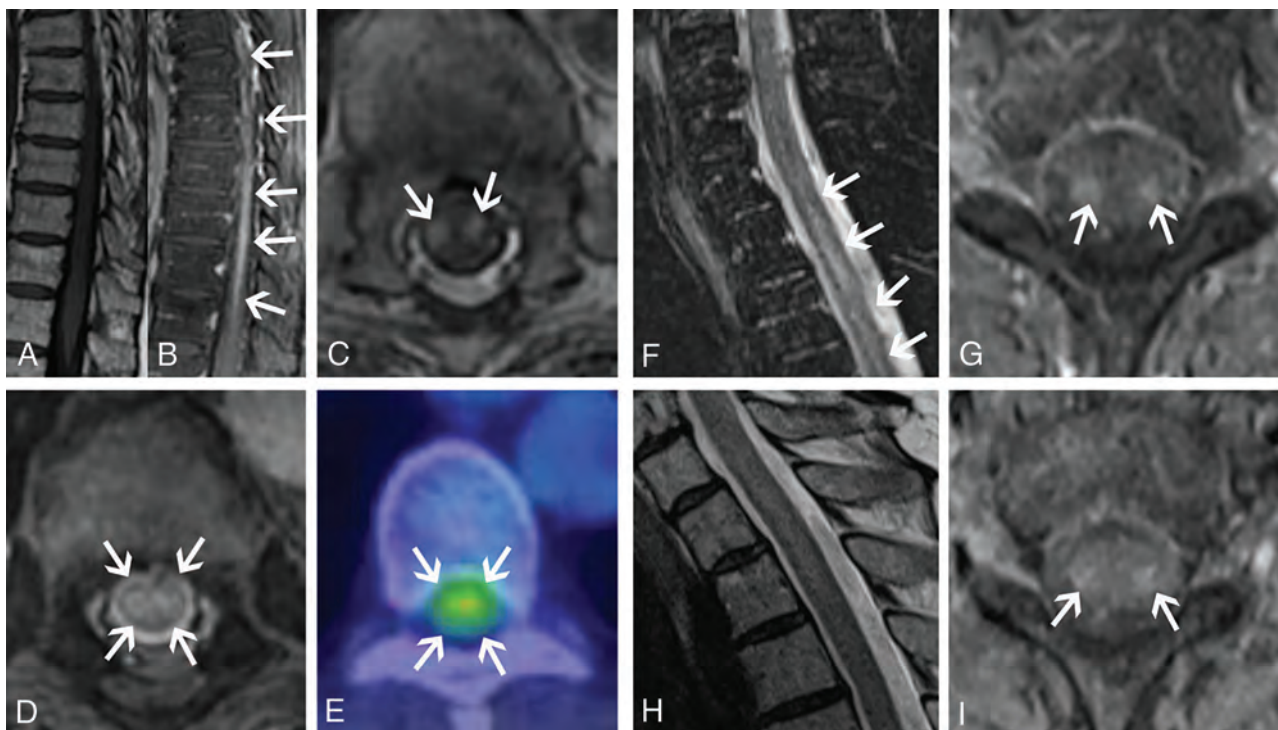


**FIG 7.** Paraneoplastic myelitis (A–E). A 52-year-old woman recently diagnosed with small cell lung cancer presented with progressive bilateral lower extremity weakness over weeks. Lumbar puncture was remarkable for elevated CSF IgG index and IgG synthesis rate, though no specific paraneoplastic antibody was identified. Sagittal T1-weighted pre- (A) and postcontrast (B) images and an axial postcontrast image (C) from her thoracic spine MR imaging show a long segment of enhancement involving the lateral columns of the thoracic spinal cord. Corresponding axial T2-weighted (D) and FDG-PET/CT (E) images show increased T2 signal (D, arrows) and marked abnormal FDG uptake (E, arrows) in the spinal cord. She was diagnosed with paraneoplastic myelopathy and had transient improvement with methylprednisolone. Paraneoplastic myelitis with treatment response (F–I). A 64-year-old woman recently diagnosed with small cell lung cancer presented with gait difficulties and progressive bilateral lower extremity weakness lasting several months. Serum and CSF were positive for CRMP5 autoantibodies. Sagittal T2-weighted (F) and axial T1-weighted postcontrast (G) images of the cervical cord show increased T2 signal (F, arrows) and enhancement of the lateral columns (G, arrows). She was treated with 6 months of cyclophosphamide and had partial symptomatic improvement. Follow-up sagittal T2-weighted image (H) shows near resolution of abnormal signal. There is mild residual patchy cord enhancement, greatest in the lateral columns (I, arrows).

(eg, paraneoplastic encephalomyelitis).<sup>9,21</sup> Even in such cases, it differs from limbic encephalitis insofar as it has more generalized cerebral abnormalities not confined to the limbic system. Patients can have an acute myelitis or more insidious progressive myelopathy with combinations of weakness, numbness, and bowel or bladder dysfunction. Other symptoms can include headache, seizures, and agitation, attributable to the associated intracranial involvement.<sup>6</sup> A variety of paraneoplastic antibodies can be seen, but anti-CRMP5/anti-CV2 and anti-amphiphysin are the most common. Small cell lung and breast cancer are the most frequently associated malignancies. A paraneoplastic aquaporin-4 IgG seropositive neuromyelitis optica spectrum disorder is also recognized.<sup>22</sup>

When confined to the spinal cord, imaging findings include longitudinally extensive T2 hyperintensity and enhancement (Fig 7). Tract-specific abnormalities, particularly along the lateral columns, are characteristic (Fig 7C, -G). Abnormal FDG uptake can also be present in the involved area of the spinal cord with this syndrome (Fig 7E), which could potentially be mistaken for metastatic tumor involvement.<sup>23</sup> Differential considerations for this entity include neuromyelitis optica spectrum disorder, neurosarcoïdosis, spinal dural AVF, radiation myelitis, and cord infarct. The presence of perimedullary flow voids usually suggests an

AVF, whereas preferential involvement of the anterior horns often suggests cord infarct. Multiple sclerosis would not generally have longitudinally extensive involvement.

In addition to the usual paraneoplastic work-up, MR imaging of the entire spine is particularly helpful in these patients because of the longitudinally extensive nature of spinal cord involvement. Imaging of the brain is also usually indicated to assess for associated encephalitis, which is frequently seen with anti-CRMP5 syndromes. Typical treatment includes management of the underlying malignancy and immunosuppression. Despite treatment, the outcome is overall poor with most patients becoming wheelchair dependent. Although follow-up of patients with paraneoplastic myelitis is not well documented in the literature, clinical improvement and improvement in imaging findings can occur (Fig 7F–I).

### Spine: Polyneuropathy

Paraneoplastic polyneuropathy is rare but usually manifests clinically as a sensory neuropathy.<sup>9</sup> This is characterized by pain, paresthesias, and loss of vibratory sensation, often with ANNA-1/anti-Hu or anti-CRMP5 antibody positivity. Much less commonly, paraneoplastic syndromes can also have other combinations of motor, sensory, and



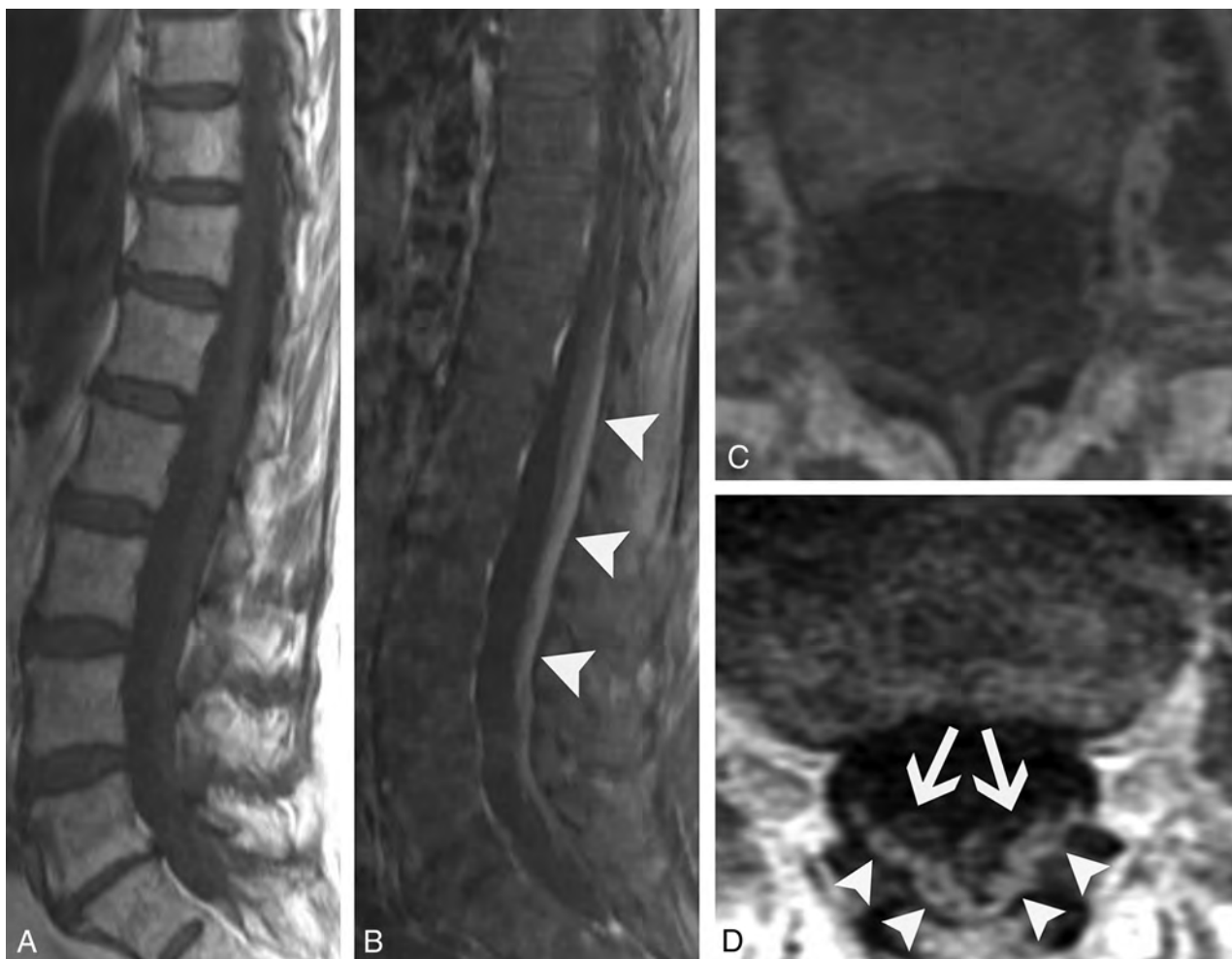


**FIG 8.** Paraneoplastic polyneuropathy mimicking Guillain-Barré syndrome. A 69-year-old woman presented with rapidly progressive ascending weakness and paresthesias. CSF analysis was remarkable for albuminocytologic dissociation, and the patient was initially diagnosed with Guillain-Barré syndrome. Sagittal T1-weighted pre- (A) and postcontrast (B) and axial T1-weighted pre- (C) and postcontrast (D) images from the patient's lumbar spine MR imaging show enhancement of the predominantly dorsal cauda equina nerve roots (B–D, arrowheads). There is relative sparing of the ventral nerve roots (D, arrows), somewhat atypical for Guillain-Barré syndrome. The patient's CSF was later found to be ANNA-1/anti-Hu antibody positive, and she was ultimately found to have small cell lung cancer.

autonomic deficits.<sup>24</sup> As examples, paraneoplastic syndromes associated with Hodgkin lymphoma and prostate cancer causing motor and sensory deficits were recently reported.<sup>25–27</sup> Autonomic dysfunction was also previously reported from a syndrome related to a carcinoid tumor.<sup>28</sup>

Reports of imaging findings of paraneoplastic polyneuropathy involvement are scarce. To our knowledge, there are only 5 published cases of paraneoplastic polyneuropathy showing cauda equina abnormalities. These have demonstrated variable patterns of enhancement, with 2 patients having ANNA-1 positivity.<sup>27,29–32</sup> We have found that enhancement can predominantly involve the dorsal (Fig 8) or ventral nerve roots (Fig 9), and the pattern of enhancement does not always correlate with symptoms. The clinical presentation can frequently mimic Guillain-Barré syndrome with a similar rapidly ascending weakness (Fig 8). Additionally, polyneuropathy may be seen with osteosclerotic multiple myeloma in the setting of POEMS syndrome (polyneuropathy, organomegaly, endocrinopathy, monoclonal plasma proliferative disorder, skin

changes).<sup>33</sup> Although POEMS syndrome is not always described among the classic forms of PNS, many authors consider its peripheral nerve involvement to be paraneoplastic. The presence of sclerotic bone lesions and peripheral nerve root enhancement are the most important imaging features to suggest POEMS syndrome (Fig 10).

Differential diagnoses for paraneoplastic polyneuropathy mainly include Guillain-Barré syndrome and infection. Guillain-Barré syndrome classically, but not always, has ventral predominant nerve enhancement. Chronic inflammatory demyelinating polyneuropathy could be considered but is less likely to show any enhancement and would have more prominent nerve enlargement. Entities such as neurosarcoidosis or leptomeningeal carcinomatosis tend to have more nodular enhancement. Ventral cauda equina enhancement has also recently been described in association with cord infarct.<sup>34</sup>

The diagnostic work-up should include a thorough history to elicit any antecedent infection that may suggest Guillain-Barré



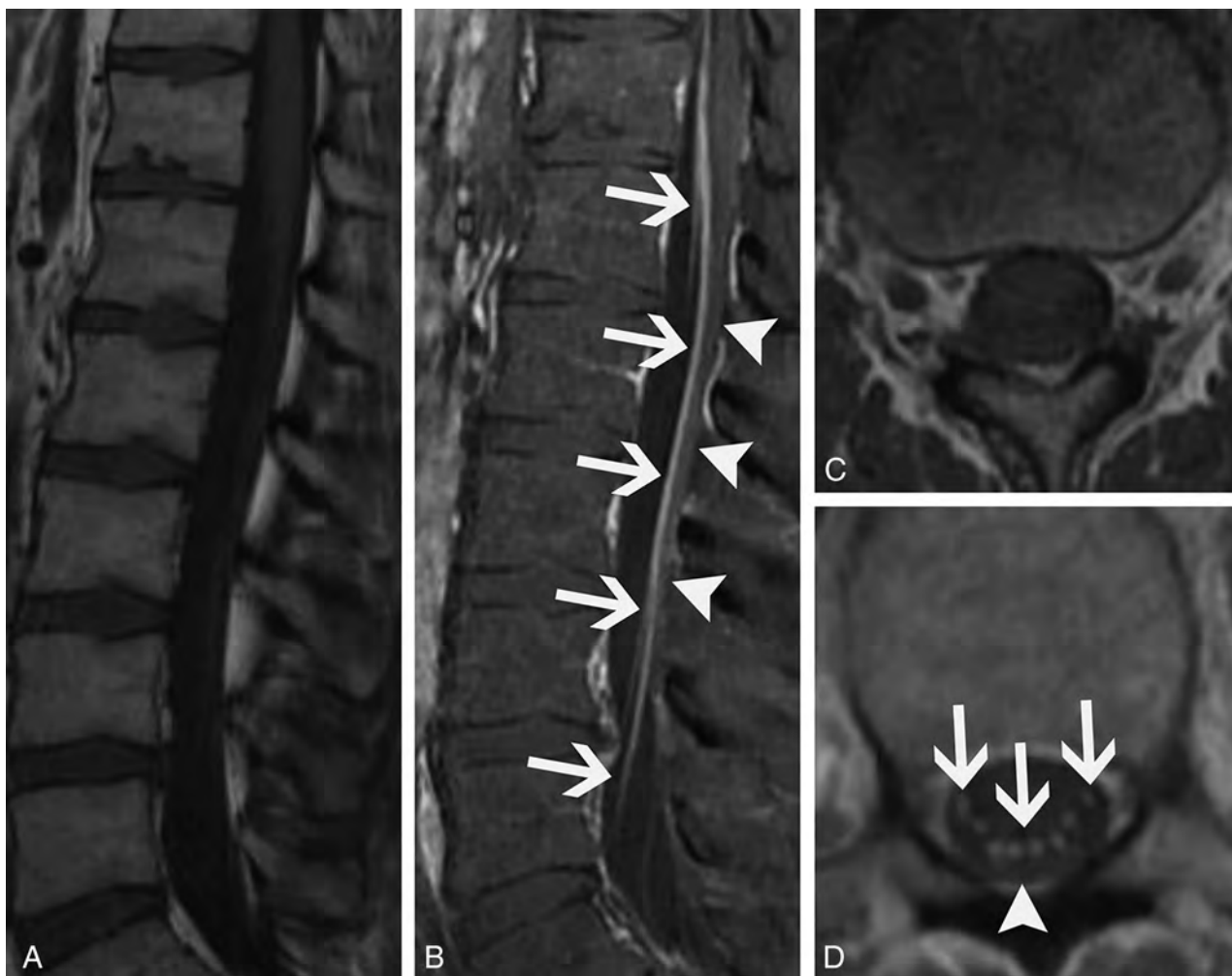


**FIG 9.** Ventral predominant paraneoplastic polyneuropathy. A 29-year-old man with a history of mediastinal seminoma presented with progressive lower extremity weakness and frequent falls over months. Lumbar puncture showed elevated CSF IgG. Serum and CSF were positive for Kelchlike protein 11 autoantibodies. Sagittal T1-weighted pre- (A) and postcontrast (B) images, as well as corresponding axial T1-weighted pre- (C) and postcontrast (D) images from his lumbar spine MR imaging demonstrate smooth enhancement of the cauda equina nerve roots with a predilection for the ventral roots (B and D, arrows). There is clear sparing of the dorsal roots (B and D, arrowheads). He was diagnosed with paraneoplastic polyneuropathy and had mild symptomatic improvement with numerous immunosuppressive agents.

syndrome, a complete neurologic examination, paraneoplastic antibody testing, electromyography, and lumbar spine MR imaging. Treatment is not well studied, but we have observed symptomatic improvement with corticosteroids and plasma exchange.

## CONCLUSIONS

Paraneoplastic neurologic syndromes can cause a wide range of imaging abnormalities throughout the central and peripheral nervous systems. Prior reports have focused on the imaging findings of limbic encephalitis, but as we have shown, PNSs involving other parts of the nervous system can have characteristic imaging findings. We have described the imaging findings of paraneoplastic limbic encephalitis, cerebellar degeneration, brain stem encephalitis, cranial neuropathy, myelitis, and polyneuropathy. Additionally, we have highlighted the fact that these entities can have variable imaging findings resulting in many potential diagnostic pitfalls. Because imaging features of each entity are sometimes nonspecific, consideration of

paraneoplastic syndromes based on imaging findings combined with review of patient history are important. Although serum and CSF paraneoplastic antibody positivity can be helpful, they may be absent, as illustrated in many of our cases. Importantly, many of these syndromes respond to treatment of underlying malignancy or immunotherapy. Therefore, timely diagnosis is likely to significantly impact patient outcomes. Last, it should be noted that PNSs are relatively rare disorders compared with various conditions in the differential diagnosis. The diagnosis of PNS often requires exclusion of these more common entities.

## ACKNOWLEDGMENT

The authors acknowledge the assistance of Desiree J. Lanzino, PT, PhD, in editing the manuscript.

Disclosures: Eoin Flanagan—*UNRELATED: Other:* Viela Bio, Comments: I am a site principal investigator in a placebo-controlled randomized controlled phase 3 trial on inebilizumab in neuromyelitis optica spectrum disorder.

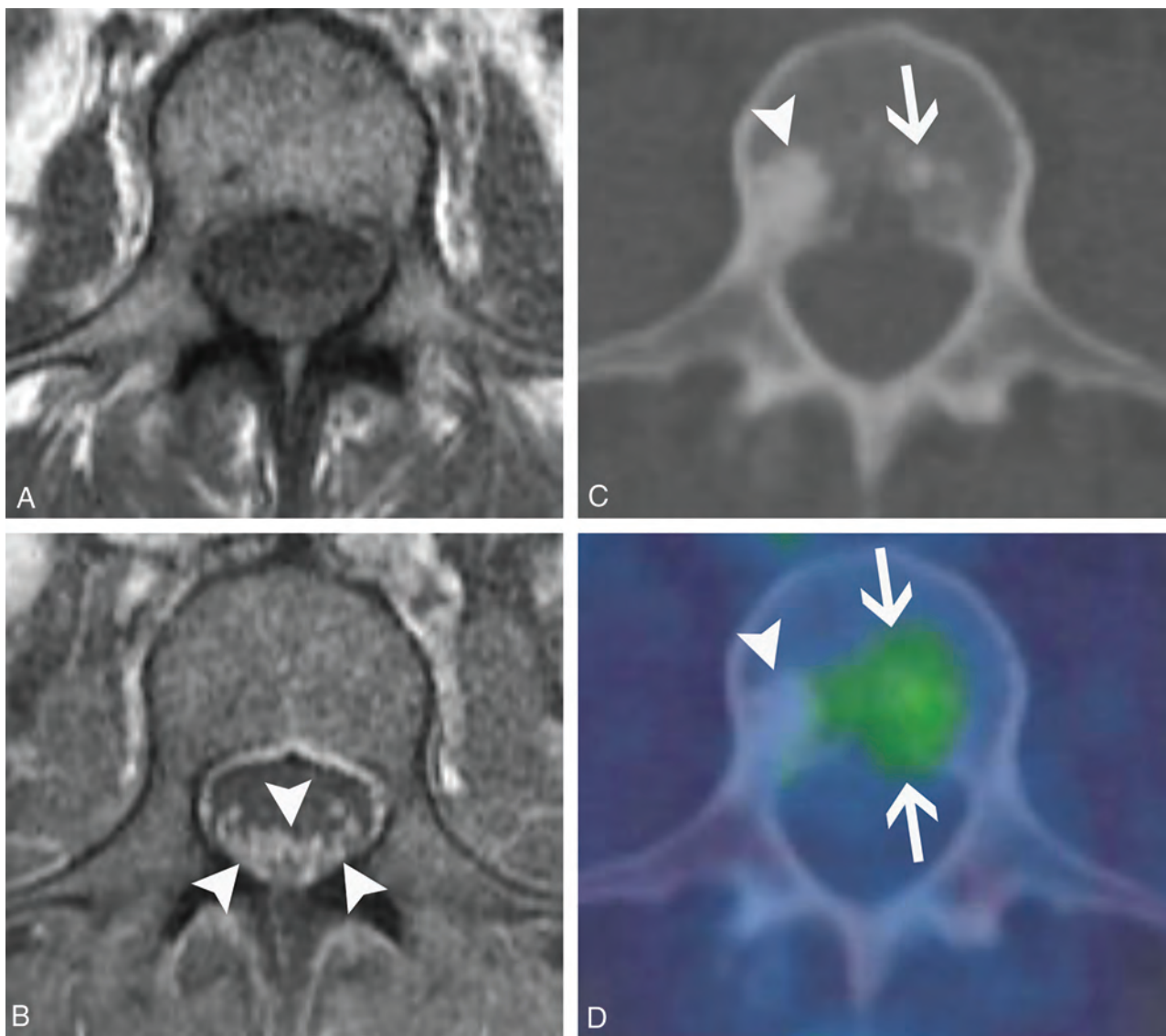


**FIG 10.** POEMS syndrome. A 50-year-old woman presented with weakness, burning, and tingling in her extremities that had waxed and waned over 4 years. Axial T1-weighted pre- (A) and postcontrast (B) images from her lumbar spine MR imaging show diffuse enlargement and enhancement of the cauda equina nerve roots (B, arrowheads). Axial CT (C) and fused FDG-PET/CT (D) images show a non-FDG-avid lumbar vertebral sclerotic lesion (C and D, arrowheads) and an adjacent mildly FDG-avid sclerotic lesion (C and D, arrows). After additional work-up, she was diagnosed with osteosclerotic multiple myeloma, which is characterized by osteosclerotic lesions with variable FDG avidity. Her MR imaging findings were ultimately attributed to polyneuropathy in the setting of POEMS syndrome.

## REFERENCES

- Kelley BP, Patel SC, Marin HL, et al. **Autoimmune encephalitis: pathophysiology and imaging review of an overlooked diagnosis.** *AJNR Am J Neuroradiol* 2017;38:1070–78 CrossRef Medline
- Leyppoldt F, Wandinger KP. **Paraneoplastic neurological syndromes.** *Clin Exp Immunol* 2014;175:336–48 CrossRef Medline
- Lancaster E, Huijbers MG, Bar V, et al. **Investigations of caspr2, an auto-antigen of encephalitis and neuromyotonia.** *Ann Neurol* 2011;69:303–11 CrossRef Medline
- da Rocha AJ, Nunes RH, Maia AC Jr, et al. **Recognizing autoimmune-mediated encephalitis in the differential diagnosis of limbic disorders.** *AJNR Am J Neuroradiol* 2015;36:2196–205 CrossRef Medline
- Fredriksen JR, Carr CM, Koeller KK, et al. **MRI findings in glutamic acid decarboxylase associated autoimmune epilepsy.** *Neuroradiology* 2018;60:239–45 CrossRef Medline
- Guerin J, Watson RE, Carr CM, et al. **Autoimmune epilepsy: findings on MRI and FDG-PET.** *Br J Radiology* 2019;92:20170869 CrossRef Medline
- Dutra LA, Abrantes F, Toso FF, et al. **Autoimmune encephalitis: a review of diagnosis and treatment.** *Arq Neuropsiquiatr* 2018;76:41–49 CrossRef Medline
- Lancaster E. **The diagnosis and treatment of autoimmune encephalitis.** *J Clin Neurol* 2016;12:1–13 CrossRef Medline
- Hofberger R, Rosenfeld MR, Dalmau J. **Update on neurological paraneoplastic syndromes.** *Curr Opin Oncol* 2015;27:489–95 CrossRef Medline
- Jarius S, Wildemann B. **“Medusa head ataxia”: the expanding spectrum of Purkinje cell antibodies in autoimmune cerebellar ataxia. Part 3: anti-Yo/CDR2, anti-Nb/AP3B2, PCA-2, anti-Tr/DNER, other antibodies, diagnostic pitfalls, summary and outlook.** *J Neuroinflammation* 2015;12:168 CrossRef Medline
- Mahta A, Vijayvergia N, Bhavsar TM, et al. **Diagnostic approach to a patient with paraneoplastic neurological syndrome.** *World J Oncol* 2012;3:243–46 CrossRef Medline
- Campos LG, Trindade RA, Faistauer A, et al. **Rhombencephalitis: pictorial essay.** *Radiology Bras* 2016;49:329–36 CrossRef Medline

13. Mandel-Brehm C, Dubey D, Kryzer TJ, et al. **Kelch-like protein 11 antibodies in seminoma-associated paraneoplastic encephalitis.** *N Engl J Med* 2019;381:47–54 CrossRef Medline
14. Boch M, Rinke A, Rexin P, et al. **Paraneoplastic brainstem encephalitis in a patient with exceptionally long course of a metastasized neuroendocrine rectum neoplasm.** *BMC Cancer* 2014;14:691 CrossRef Medline
15. Jubelt B, Mihai C, Li TM, et al. **Rhombencephalitis/brainstem encephalitis.** *Curr Neurol Neurosci Rep* 2011;11:543–52 CrossRef Medline
16. Cheung SSL, Lau GKK, Chan KH, et al. **Optic neuritis as the initial clinical presentation of limbic encephalitis: a case report.** *J Med Case Rep* 2018;12:357 CrossRef Medline
17. Renna R, Plantone D, Batocchi AP. **Teaching NeuroImages: a case of hearing loss in a paraneoplastic syndrome associated with anti-Hu antibody.** *Neurology* 2012;79:e134 CrossRef Medline
18. Kaido M, Yuasa Y, Yamamoto T, et al. **A case of possible paraneoplastic neurological syndrome presenting as multiple cranial nerve palsies associated with gallbladder cancer.** *Rinsho Shinkeigaku* 2016;56:617–21 CrossRef Medline
19. Nanda SK, Jayalakshmi S, Ruikar D, et al. **Twelfth cranial nerve involvement in Guillain Barre syndrome.** *J Neurosci Rural Pract* 2013;4:338–40 CrossRef Medline
20. Inoue H, Tsuboi Y, Tsugawa J, et al. **Hypertrophic cranial nerve roots in CIPD.** *Neurology* 2004;63:1481 CrossRef Medline
21. Flanagan EP, McKeon A, Lennon VA, et al. **Paraneoplastic isolated myelopathy: clinical course and neuroimaging clues.** *Neurology* 2011;76:2089–95 CrossRef Medline
22. Pittock SJ, Lennon VA, de Seze J, et al. **Neuromyelitis optica and non organ-specific autoimmunity.** *Arch Neurol* 2008;65:78–83 CrossRef Medline
23. Keegan BM, Flanagan EP. **In reply—Sensitivity of [18F]-fluorodeoxyglucose-positron emission tomography in patients with active myelopathy.** *Mayo Clin Proc* 2014;89:859 CrossRef Medline
24. Graus F, Santamaría J, Obach J, et al. **Sensory neuropathy as remote effect of cancer.** *Neurology* 1987;37:1266–67 CrossRef Medline
25. Al IO, Koc B, Bayram C, et al. **Variant Guillain-Barré syndrome in a patient with Hodgkin lymphoma: AMSAN.** *Turk Pediatri Ars* 2019;53:263–66 CrossRef
26. Choi JK, Kim WJ, Jeon JY. **Paraneoplastic sensorimotor polyneuropathy in prostatic adenocarcinoma: a case report.** *Medicine (Baltimore)* 2018;97:e0030 CrossRef Medline
27. Nomiya K, Uchino A, Yakushiji Y, et al. **Diffuse cranial nerve and cauda equina lesions associated with breast cancer.** *Clin Imaging* 2007;31:202–05 CrossRef Medline
28. Veilleux M, Bernier JP, Lamarche JB. **Paraneoplastic encephalomyelitis and subacute dysautonomia due to an occult atypical carcinoid tumour of the lung.** *Can J Neurol Sci* 1990;17:324–28 CrossRef Medline
29. Kumar N, Dyck PJ. **Hypertrophy of the nerve roots of the cauda equina as a paraneoplastic manifestation of lymphoma.** *Arch Neurol* 2005;62:1776–77 CrossRef Medline
30. Flanagan EP, Sandroni P, Pittock SJ, et al. **Paraneoplastic lower motor neuronopathy associated with Hodgkin lymphoma.** *Muscle Nerve* 2012;46:823–27 CrossRef Medline
31. Shibata M, Uchida M, Tsukagoshi S, et al. **Anti-Hu antibody-associated paraneoplastic neurological syndrome showing peripheral neuropathy and atypical multifocal brain lesions.** *Intern Med* 2015;54:3057–60 CrossRef Medline
32. Madhavan AA, Guerin JB, Eckel LJ, et al. **Dorsal cauda equina nerve root enhancement on magnetic resonance imaging due to ANNA-1-associated paraneoplastic polyneuropathy.** *Neuroradiol J* 2020 Apr 15 [Epub ahead of print] CrossRef Medline
33. Paravitane S, Gooneratne L, Chang T. **Polyneuropathy, organomegaly, endocrinopathy, monoclonal band, and skin (POEMS) changes syndrome presenting with a pseudosensory level: a case report.** *J Med Case Rep* 2019;13:384 CrossRef Medline
34. Diehn FE, Hunt CH, Lehman VT, et al. **Vertebral body infarct and ventral cauda equina enhancement: two confirmatory findings of acute spinal cord infarct.** *J Neuroimaging* 2015;25:133–35 CrossRef Medline

# Secondary Otalgia: Referred Pain Pathways and Pathologies

C.D. Norris and N.A. Koontz



## ABSTRACT

**SUMMARY:** Otalgia is very common, and when the cause of ear pain is not identified on otoscopy and physical examination, cross-sectional imaging is routinely used to evaluate for potential sources of referred ear pain (secondary otalgia). Innervation of the ear structures is complex, involving multiple upper cervical, lower cranial, and peripheral nerves, which transit and innervate a large anatomic territory involving the brain, spine, skull base, aerodigestive tract, salivary glands, paranasal sinuses, face, orbits, deep spaces of the neck, skin, and viscera. Interpreting radiologists must be familiar with these neural pathways and potential sources of secondary otalgia. The purposes of this review are to detail the currently proposed mechanisms of referred ear pain, review the salient neuroanatomy of the complex pathways responsible for secondary otalgia, highlight important benign and malignant etiologies of referred ear pain, and provide a structured search pattern for approaching these challenging cases on cross-sectional imaging.

**ABBREVIATION:** CN = cranial nerve; TMJ = temporomandibular joint

Otalgia is common and indiscriminate, affecting persons of all ages with nearly a 100% lifetime prevalence.<sup>1,2</sup> Frequently, the cause of otalgia can be identified with otoscopy, and when the pathoetiology localizes to the affected ear, it is referred to as a primary otalgia. Common causes of primary otalgia include otitis media, external otitis, folliculitis, cerumen impaction, mastoiditis, myringitis, and neoplasm.<sup>3</sup> Primary otalgia is far more common in children than in adults.<sup>1,4</sup> When the pain generator cannot be localized to the affected ear on physical examination and otoscopy, it is referred to as secondary otalgia. Although most secondary otalgia is caused by biomechanical issues of the neck, cervical spine, and temporomandibular joints (TMJs),<sup>5</sup> one must be vigilant to exclude more ominous causes, such as occult malignancy. Because of the complex innervation of head and neck structures,

which may yield referred pain from sources outside the ear, it is imperative that a complete history and comprehensive physical examination be performed on patients with otalgia.

When the cause of otalgia is not identified after an appropriate history and physical examination, cross-sectional imaging becomes the primary tool of investigation. Temporal bone CT is the first-line technique for assessing causes within the ear and temporal bone. Assessment of the pharynx, larynx, and other neck sites is typically best accomplished with contrast-enhanced CT of the neck, although MR imaging plays a complementary role and may be superior to CT for some entities. Severity of otalgia rarely correlates with the significance of the pathology. Thus, performing imaging should be based on the patient's history, presence of other symptoms, or other concerning physical examination findings rather than the severity of pain.<sup>4,6,7</sup>

Because of the complex interplay of multiple upper cervical, lower cranial, and peripheral nerves providing sensory information to and from the ear, localizing the source of referred ear pain is challenging. This complexity is magnified by the diverse anatomic territory transited and innervated by these nerves, which spans portions of the brain, spine, skull base, aerodigestive tract, salivary glands, paranasal sinuses, face, orbits, deep spaces of the neck, skin, and viscera. These cases require a thorough and thoughtful search pattern, scrutinizing the course of potential culprit neural pathways from origin nuclei to end organs.

In this review, which serves as a current update to the classic *AJNR* review article "The Radiology of Referred Otalgia" by Chen et al,<sup>8</sup> we detail the currently proposed mechanisms of referred ear

Received April 28, 2020; accepted after revision July 18.

From the Department of Radiology and Imaging Sciences, Indiana University School of Medicine, Indianapolis, Indiana.

Levels of contribution: Dr. Norris (first author) and Dr. Koontz (senior author).

Previously presented as an electronic education exhibit at: Annual Meeting of the American Society of Head & Neck Radiology (ASHNR) 2018, September 26-30, 2018, The Westin Savannah Harbor Golf Resort & Spa, Savannah, Georgia.

Retrospective review of PACS and RIS at our institution for the purposes of this manuscript was performed in a HIPAA-compliant manner and with review and approval of the IRB at our institution (Indiana University IRB#1604478948A001).

Please address correspondence to Nicholas A. Koontz, MD, 550 N. University Blvd, Room 0663, Indianapolis, IN 46202; e-mail: nakoontz@iupui.edu; @nakoontz; @CarrieDNorrisMD

Indicates open access to non-subscribers at [www.ajnr.org](http://www.ajnr.org)

<http://dx.doi.org/10.3174/ajnr.A6808>



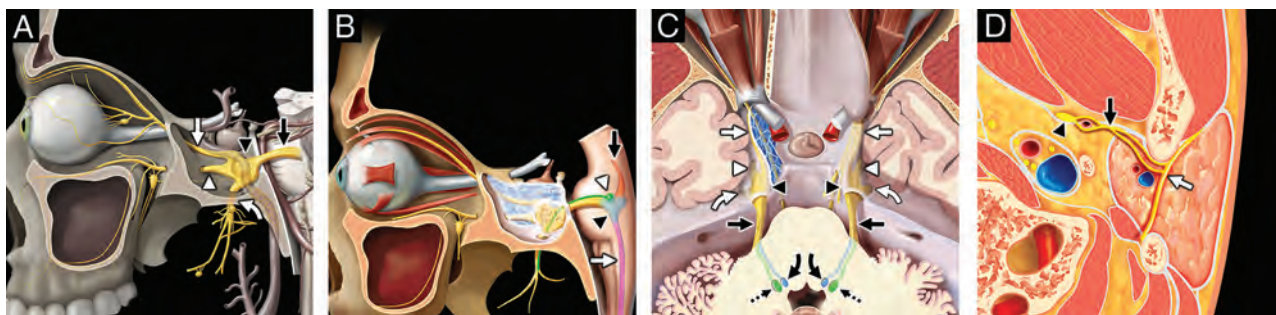


**FIG 1.** Trigeminal nerve, associated nuclei, and major branches. Sagittal graphic (A) shows the major branches of the trigeminal nerve (CN V), including the preganglionic or cisternal segment (*black straight arrow*), trigeminal ganglion (*black arrowhead*) in the trigeminal cave, ophthalmic division (*white straight arrow*, CN V1) entering the orbit via the superior orbital fissure, maxillary division (*white arrowhead*, CN V2) exiting at the foramen rotundum, and mandibular division (*white curved arrow*, CN V3) exiting the skull base at the foramen ovale before transiting the infrazygomatic masticator space. Sagittal graphic (B) highlights the brain stem nuclei of the trigeminal nerve, including the mesencephalic nucleus (*orange shading*, *black straight arrow*), main sensory nucleus (*blue shading*, *black arrowhead*), spinal nucleus (*pink shading*, *white straight arrow*), and motor nucleus (*green shading*, *white arrowhead*). Axial graphic (C) demonstrates the course of the trigeminal nerves, including the preganglionic segments (*black straight arrows*), trigeminal ganglia (*black arrowheads*), ophthalmic divisions (*white straight arrows*, CN V1), maxillary divisions (*white arrowheads*, CN V2), and mandibular divisions (*white curved arrows*, CN V3), as well as the sensory (*blue shading*, *black curved arrows*) and motor (*green shading*, *black dashed arrows*) nuclei. Axial graphic (D) shows the relationship of the auriculotemporal nerve (*black straight arrow*), a complex branch of the mandibular nerve (*black arrowhead*, CN V3) that transits the infrazygomatic masticator space and parotid space, serving as an extracranial “bridge” linking CN V3 and the intraparotid facial nerve (*white straight arrow*, CN VII). Graphics are reproduced with permission from *Imaging Anatomy: Brain and Spine* and *Specialty Imaging: Head and Neck Cancer*. Copyright Elsevier.

pain, review the salient neuroanatomy, report important benign and malignant etiologies of secondary otalgia, and provide a structured search pattern for approaching secondary otalgia on cross-sectional imaging.

### MECHANISMS OF REFERRED PAIN

Pain may be elicited from heat, chemical, and mechanical stimuli, which are perceived by primary afferent nociceptors in the skin, muscles, and viscera in a process known as transduction.<sup>9</sup> This nociceptive pseudounipolar neuron typically has its cell body in the dorsal root ganglion (or respective sensory ganglion for select cranial nerves [CNs]), 1 axonal branch in the peripheral tissues, and 1 axonal branch in the dorsal horn of the spinal cord or medulla (if the primary afferent is in the head).<sup>10,11</sup> In a process known as transmission, the primary afferent nociceptors release neurotransmitters to activate second-order neurons, which may decussate immediately and travel via the anterolateral spinal cord (spinothalamic and spinothalamic tracts) or travel along the dorsal cord and decussate in the medulla (medial lemniscus tract).<sup>9,12</sup> In the head and neck, the primary nociceptive neuron has its cell body in a nucleus of a CN and ascends via a specific neural pathway (eg, trigeminothalamic tract).<sup>13</sup> With both somatic and CNs, the second-order neurons terminate on different parts of the thalami, and from there third-order neurons transmit to different locations of the brain cortex (projection).<sup>9,12,13</sup> Throughout the peripheral and central nervous systems, complex and dynamic excitatory and inhibitory pathways alter the nociceptive signal in a process known as modulation<sup>12</sup> before the painful stimulus reaches the cortex and is appreciated (perception).<sup>11</sup>

The mechanisms of referred otalgia are incompletely understood and challenging to study because pain is subjective and difficult to measure scientifically. For example, there can be subjective pain without activity in primary afferent nociceptors, and there can be activity in primary afferent nociceptors without subjective pain.<sup>9</sup> Furthermore, afferents innervating deep structures are difficult to

localize and can be misperceived as arising from a site distant from the actual site of stimulation. The elusive phenomenon of referred pain has been widely theorized, and several underlying mechanisms are hypothesized. Some postulate that a single nociceptor may synapse on multiple second-order neurons, and under normal conditions, most of the second-order neurons are latent, and the nociceptive information is not transmitted.<sup>14</sup> However, with prolonged or intense nociceptive stimulation, previously latent second-order neurons become activated, and information from regions unrelated to the source of the noxious peripheral stimulus may be conveyed to higher centers of the brain.<sup>9,14</sup> Others postulate that sympathetic nerves may cause referred pain by sensitizing nociceptors or restricting blood flow in the region of referred pain.<sup>15</sup> One theory widely considered as a cause of hyperalldynia, the central sensitization theory, may also play a role in referred pain. This theory asserts that through a series of complex molecular interactions and neuroplasticity, previously subthreshold synaptic inputs are recruited and stimulated to generate an action potential output, which allows “hyperexcitable” neurons to send nociceptive information to the brain, even if they innervate areas not directly stimulated.<sup>16–20</sup> Last, the theory of convergence postulates that a single second-order neuron may receive nociceptive input from multiple primary somatic or visceral afferents from separate sites (eg, the heart and the muscles of the left shoulder), but the brain cannot accurately decipher which site the stimulus originated from, thus it misinterprets and incorrectly localizes the sensation.<sup>20–23</sup>

### NEUROANATOMY OF SECONDARY OTALGIA

Afferent innervation of the ear is complex and involves multiple cranial and somatic nerves. There is considerable overlap and ambiguity within the nervous supply both within the ear and the related areas of innervation in the head and neck, which includes contributions from cervical nerves (C II and C III), CN V (Fig 1),

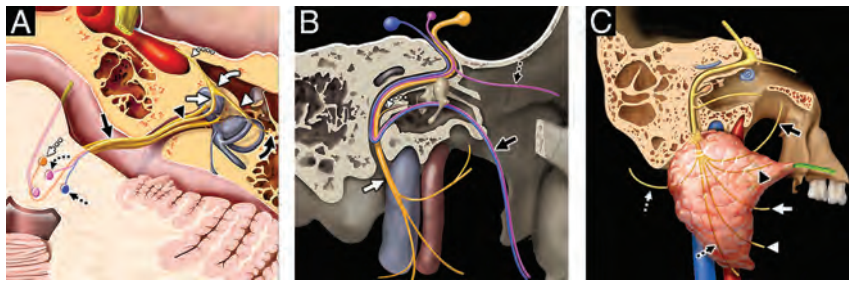


**FIG 2.** Facial nerve, associated nuclei, and major branches. Axial graphic (A) shows the segments of the facial nerve (CN VII), including the cisternal (black solid arrow), canalicular (black arrowhead), labyrinthine (white solid arrow), tympanic (white arrowhead), and proximal descending mastoid (black solid curved arrow) segments. Note additionally the geniculate ganglion (white solid curved arrow) and greater superficial petrosal nerve (white dashed curved arrow). The 3 brain stem nuclei of CN VII are seen at the level of the pons, including the motor (orange shading, white dashed straight arrow), superior salivatory (pink shading, black dashed curved arrow), and solitary tract nuclei (blue shading, black dashed straight arrow). Sagittal graphic (B) shows the motor, sensory, and parasympathetic fibers of the facial nerve and its major branches. Motor fibers (orange shading) give off the small stapedius motor nerve (white dashed curved arrow) before exiting the skull base at the stylomastoid foramen as the extracranial CN VII (white solid arrow), which is purely motor. Parasympathetic fibers (shaded pink) give off the greater superficial petrosal nerve (black dashed straight arrow) that innervates the lacrimal gland and contribute to the chorda tympani nerve (black solid arrow). The chorda tympani nerve also receives special sensory fibers, providing taste to the anterior two-thirds of the tongue in addition to providing parasympathetic innervation of the submandibular and sublingual glands. Sagittal graphic (C) shows the extracranial motor branches of CN VII, including the temporal (black solid arrow), zygomatic (black arrowhead), buccal (white solid arrow), mandibular (white arrowhead), cervical (black dashed straight arrow), and posterior auricular (white dashed straight arrow) branches. Graphics are reproduced with permission from *Imaging Anatomy: Brain and Spine*. Copyright Elsevier.

CN VII (Fig 2), CN IX (Fig 3), and CN X (Fig 4).<sup>6-8</sup> To thoroughly evaluate a patient with otalgia, one must be familiar with the sensory innervation of the ear, as well as the shared neural pathways outside the ear that may contribute to referred ear pain (Table 1).

### Cervical Nerves (C II and C III)

The great auricular and lesser occipital nerves serve as the major cervical nerve origins for sensory innervation of the ear. Both the great auricular and lesser occipital nerves are derived from the cervical plexus of C II and C III. Together these nerves innervate most of the inferomedial and lateral surfaces of the pinna, ear lobule, skin in front of and behind the external ear, and angle of the mandible.<sup>24</sup> The great auricular nerve courses behind the sternocleidomastoid before ascending along its superficial surface just deep to the platysma to the level of the parotid gland, where it bifurcates into an anterior branch, innervating skin of the preauricular face overlying the parotid gland, and a posterior branch, innervating the postauricular skin overlying the mastoid process, as well as the skin of the posterior external ear. The lesser occipital nerve ascends from the cervical plexus along the posterior margin of the sternocleidomastoid, eventually innervating the postauricular skin and scalp.

Primary otogenic pathologies may stimulate pain along the course of these cervical nerve branches, including folliculitis, chondritis, neoplasm, and cellulitis.<sup>3</sup> In the absence of otogenic pathology, other structures receiving afferent innervation of cervical nerves C2 and C3 may cause referred pain through sensory “cross-talk.”<sup>25</sup> These structures include the nerve roots, facet joints, overlying skin, and muscles of the ipsilateral anterior, lateral, and

posterior neck.<sup>26-28</sup> Therefore, when imaging a patient with unexplained otalgia, it is critical to scrutinize the upper spine, including the spinal canal, neural foramina, facet joints (Fig 5), and surrounding soft tissues, as well as along the expected courses of the great auricular and lesser occipital nerves (Fig 6) as potential sites of pathology that may serve as a pain generator.

### Cranial Nerve V

One of the most common neural pathways involved with both primary and secondary otalgia is via the trigeminal nerve (CN V).<sup>2,29,30</sup> CN V is a mixed nerve, containing both motor efferents and sensory afferents with 4 origin nuclei (motor, main sensory, mesencephalic, and spinal) whose locations span the midbrain, pons, medulla, and upper cervical cord<sup>31</sup> (Fig 1). The trigeminal nerve exits the brain stem along the lateral pons near its junction with the brachium pontis, transits the prepontine cistern (cisternal or preganglionic segment), and enters the trigeminal cistern (Meckel cave), forming the trigeminal ganglion. The postganglionic

CN V trifurcates into CN V1 (ophthalmic nerve), CN V2 (maxillary nerve), and CN V3 (mandibular nerve) branches with CN V1 and CN V2, continuing anteriorly through the cavernous sinus and CN V3 immediately exiting the skull base via the foramen ovale. Distal to the cavernous sinus, CN V1 exits the skull via the superior orbital fissure and its branches supply sensory innervation to orbits, face, scalp, nasal structures, sphenoid sinus mucosa, and posterior ethmoid sinus mucosa. After transiting the cavernous sinus, CN V2 exits the skull via the foramen rotundum, transits the pterygopalatine fossa, travels along the floor of the orbit via the infraorbital nerve canal, and then exits the orbit at the infraorbital foramen providing sensory innervation to the cheek, maxillary teeth, and maxillary sinus mucosa. Small sensory branches of CN V2 also transit the pterygopalatine fossa, including those contributing to the greater palatine nerve (a mixed nerve supplying the posterior hard palate and posterior maxillary gingiva), lesser palatine nerve (a mixed nerve supplying portions of the soft palate and tonsil), and nasopalatine nerve (a mixed nerve supplying the anterior hard palate, anterior maxillary teeth, and nasal septum). After the mandibular branch (CN V3) exits the cranial cavity through the foramen ovale, it passes through the infrazygomatic masticator space between the tensor veli palatini and the lateral pterygoid, and it begins giving off muscular (motor to the muscles of mastication, tensor veli palatini, and tensor tympani) and sensory branches.

The trigeminal nerve supplies the anterosuperior pinna and external auditory canal, as well as the lateral aspect of the tympanic membrane via the auriculotemporal nerve (Fig 1), a major branch of CN V3 that also provides secretomotor innervation to



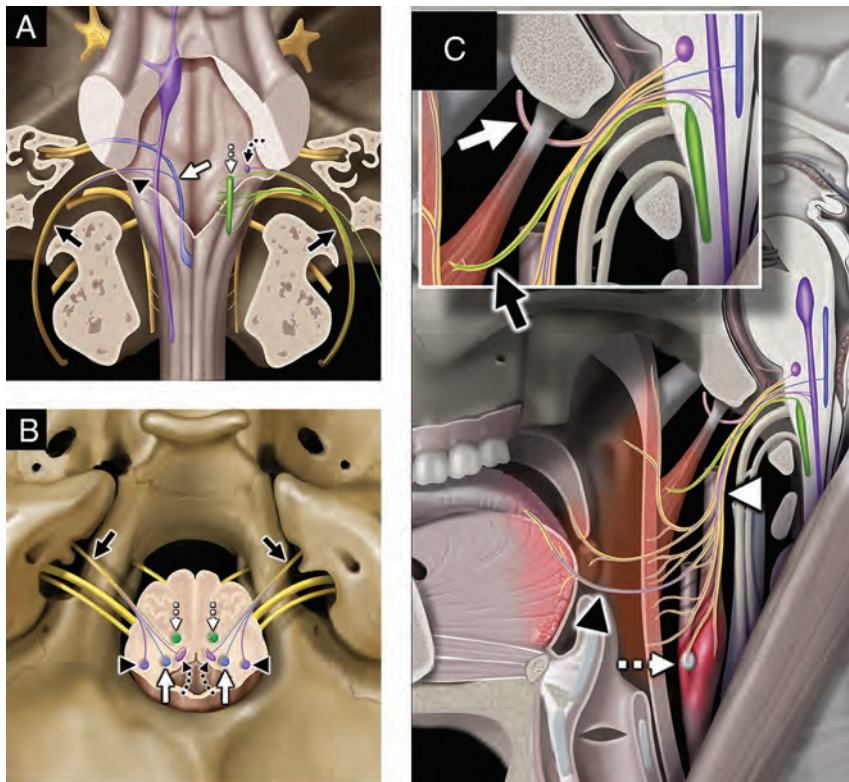


**FIG 3.** Glossopharyngeal nerve, associated nuclei, and major branches. Coronal graphic (A) shows the glossopharyngeal nerves (black solid arrows, CN IX) exiting the skull base at the jugular foramina. CN IX is a mixed nerve, including afferent sensory fibers to the spinal nucleus of CN V (purple shading, black arrowhead), afferent special sensory fibers (taste from posterior two-thirds of the tongue) to the solitary tract nucleus (blue shading, white solid arrow), efferent motor fibers from the nucleus ambiguus (green shading, white dashed straight arrow), and efferent parasympathetic fibers from the inferior salivatory nucleus (lavender shading, black dashed curved arrow). Axial graphic (B) shows CN IX (black solid arrows) departing the medulla laterally at the postolivary sulcus and exiting the skull base at the pars nervosa segment of the jugular foramina. Note the brain stem nuclei of CN IX, including the spinal nucleus of CN V (purple shading, black arrowheads), solitary tract nucleus (blue shading, white solid arrows), inferior salivatory nucleus (pink shading, black dashed curved arrows), and nucleus ambiguus (green shading, white dashed straight arrows). Sagittal graphic (C) demonstrates the complex extracranial innervation provided by CN IX, including motor innervation of the stylopharyngeus muscle (black solid arrow, magnified inset), sensory innervation from the middle ear and parasympathetic innervation to the parotid gland via the tympanic (Jacobson) nerve (white solid arrow, magnified inset), sensory and taste from the posterior two-thirds of the tongue (black arrowhead), sensory from the soft palate and oropharynx (white arrowhead), and viscerosensory to the carotid sinus and body (white dashed straight arrow). Graphics are reproduced with permission from *Imaging Anatomy: Brain and Spine*. Copyright Elsevier.

the parotid gland.<sup>32</sup> The auriculotemporal nerve acts as an extracranial bridge linking the facial (CN VII) and trigeminal (CN V3) nerves, thus may serve as a conduit for perineural tumor spread between CN VII and CN V<sup>33</sup> (Fig 7). Other important branches of CN V3 with regard to secondary otalgia include the lingual, buccal, and inferior alveolar nerves, which together provide sensory innervation to the oral cavity, gingival and buccal mucosa, palate, floor of the mouth, anterior two-thirds of the tongue (general sensory; not gustatory, which is supplied by the chorda tympani branch of CN VII), mandibular teeth, and mandible, including the TMJ.<sup>32</sup>

Primary pathologies that may stimulate CN V3 overlap those that affect the aforementioned C II and C III cervical nerves, specifically including pathologies affecting the external auditory canal, such as otitis externa, foreign body, cerumen impaction, keratosis obturans, and squamous cell carcinoma.<sup>3</sup> However, any pathology involving the anatomic distribution of CN V3 may cause ear pain through sensory “cross-talk”<sup>25</sup>; therefore, one must scrutinize the full course of CN V3 and its branches from origin nuclei to end organs for pathology when assessing patients with secondary otalgia. Common culprits include TMJ dysfunction (Fig 8); sialolithiasis (Fig 9), sialadenitis, sialodochitis, and other sublingual, submandibular, and parotid infections; salivary gland neoplasms (Fig 7); oral cavity neoplasms; and odontogenic infection<sup>32,34–37</sup> (Fig 10).

### Cranial Nerve VII

The facial nerve (CN VII) is a mixed nerve that transmits motor fibers to the muscles of facial expression, special sensory (taste) to the anterior two-thirds of the tongue, and parasympathetic innervation to the submandibular, sublingual, and lacrimal glands.<sup>38</sup> Accordingly, it has 3 distinct brain stem nuclei (motor, solitary tract, and superior salivatory nuclei for motor, taste, and salivation or lacrimation, respectively) located in the pons (Fig 2). After exiting the lateral pontomedullary junction, distinct motor and sensory roots of CN VII merge together and transit the cerebello-pontine angle cistern (cisternal segment of CN VII), course through the internal auditory canal anterosuperiorly, and then travel through the labyrinthine segment of the facial nerve canal to the level of the geniculate ganglion. At the

geniculate ganglion, the greater superficial petrosal nerve branches from CN VII and courses anteromedially, and CN VII proper turns posterolateral and descends through the temporal bone via tympanic and descending mastoid segments before exiting the base of the temporal bone into the parotid space at the stylomastoid foramen.

Branches of CN VII function to directly innervate parts of the ear, including the posterior auricular nerve (Fig 2), which joins with branches of CN IX and CN X to provide sensory information from the conchal bowl, external ear canal, and tympanic membrane.<sup>32</sup> The posterior auricular nerve originates from the proximal extracranial facial nerve, just below the stylomastoid foramen,



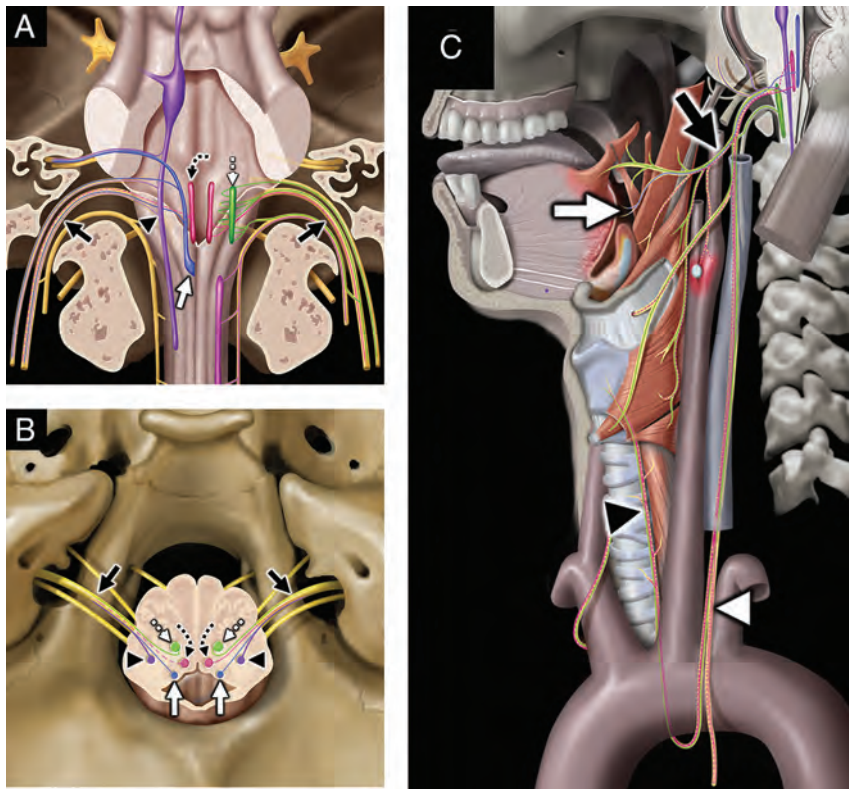


**FIG 4.** Vagus nerve, associated nuclei, and major branches. Coronal graphic (A) shows the vagus nerves (black solid arrows, CN X) exiting the skull base at the jugular foramina. CN X is a mixed nerve, including afferent sensory fibers to the spinal nucleus of CN V (purple shading, black arrowhead), afferent special sensory fibers (taste from epiglottis and valleculae) to the solitary tract nucleus (blue shading, white solid arrow), efferent motor fibers from the nucleus ambiguus (green shading, white dashed straight arrow), and both efferent parasympathetic fibers from and afferent viscerosensory fibers to the dorsal vagal nucleus (rose shading, black dashed curved arrow). Axial graphic (B) shows CN X (black solid arrows) departing the medulla laterally at the postolivary sulcus and exiting the skull base at the pars vascularis segment of the jugular foramina. Note the brain stem nuclei of CN X, including the spinal nucleus of CN V (purple shading, black arrowheads), solitary tract nucleus (blue shading, white solid arrows), dorsal vagal nuclei (rose shading, black dashed curved arrows), and nucleus ambiguus (green shading, white dashed straight arrows). Sagittal graphic (C) demonstrates the complex extracranial innervation provided by CN X, including motor innervation of the soft palate and constrictors via the pharyngeal plexus (black solid arrow); motor innervation of the muscles of the larynx (except cricothyroid) via the recurrent laryngeal nerve (black arrowhead); special sensory (taste) from the epiglottis and valleculae (white solid arrow); afferent sensory from the external ear and skull base; parasympathetic innervation of the cervical, thoracic, and abdominal viscera; and viscerosensory afferents (white arrowhead) from the larynx, visceral space, chest, and abdomen. Graphics are reproduced with permission from *Imaging Anatomy: Brain and Spine*. Copyright Elsevier.

where it ascends ventral to the mastoid tip before communicating with branches of the great auricular and lesser occipital nerves (see “Cervical Nerves”) to innervate the ear. The complex anatomic relationships between cranial and cervical nerve branches serve as a substrate for “cross-talk” and propagation of referred pain from pathology along the course of any of these nerves.

Other portions of the facial nerve complex that can contribute to referred otalgia include the geniculate ganglion, which relays a complex array of general sensory, special sensory (taste, via chorda tympani fibers), parasympathetic, and motor fibers; the greater superficial petrosal nerve; and the nerve of the pterygoid canal (Vidian nerve). Herpes virus reactivation from the geniculate

ganglion can involve additional segments of the facial nerve, resulting in facial palsy, hearing loss, and ear pain, as well as vesicular rash in zoster oticus.<sup>39</sup> The nerve of the pterygoid canal (Vidian nerve) and greater superficial petrosal nerve provide parasympathetic innervation to the nasal mucosa, sphenoid and ethmoid sinuses, portions of the palate, and lacrimal glands, which can also be a source referred otalgia in the setting of mucosal inflammation, sinusitis (Fig 11), large nasal septal bone spurs, or dacryoadenitis.<sup>8,40</sup>

### Cranial Nerve IX

The glossopharyngeal nerve (CN IX) is a mixed nerve with motor, general sensory, special sensory (taste), viscerosensory, and parasympathetic innervation.<sup>41</sup> CN IX has 4 discrete brain stem nuclei, all of which are in part located in or extend through the medulla, including the nucleus ambiguus (motor), spinal nucleus of CN V (sensory), solitary tract nucleus (taste), and inferior salivatory nucleus (parasympathetic) (Fig 3). CN IX departs the medulla laterally at the postolivary sulcus, courses anterolaterally through the basal cistern along with CN X and the accessory nerve (CN XI), exits the skull base via the pars nervosa portion of the jugular foramen, and descends within the carotid space lateral to the internal carotid artery at the level of the nasopharynx before providing its constituent branches.

In addition to contributing to direct sensory innervation of the inner surface of the tympanic membrane and the middle ear through sensory fibers of the tympanic nerve (Jacobson nerve, Fig 3), CN IX also provides mixed sensory, motor, parasympathetic, and viscerosensory innervation to portions of the

head and neck, including innervation of the stylopharyngeus muscle, posterior third of the tongue, palatine tonsils, carotid body and sinus, pharyngeal mucosa, parapharyngeal space, and retropharyngeal space.<sup>32</sup>

Causes of secondary otalgia may originate anywhere along the geographically extensive pathway of the glossopharyngeal nerve, necessitating thorough imaging review of the expected course of CN IX and its branches from origin nuclei to end organs. Perhaps the most ominous cause of secondary otalgia is malignancy, particularly squamous cell carcinoma, which may trigger referred pain via CN IX through its involvement of the pharyngeal mucosal space (Figs 6 and 12). Additionally, CN IX afferents may further be

**Table 1: Sensory innervation of the ear and potential referred pain origin sites**

Nerve	Primary Ear Sensory Innervation	Origin Site of Referred Pain
CN II and CN III	Inferomedial and lateral pinna Pre- and postauricular skin Lobule	Skin overlying angle of mandible Lateral neck Muscles of neck Upper cervical facet joints and nerve roots Atlantoaxial joint
CN V	Anterosuperior pinna External auditory canal Tympanic membrane	Gingival and buccal mucosa of oral cavity Palate Floor of the mouth Anterior two-thirds of the tongue (sensory nerves) Mandibular teeth TMJ Mandible Nasal mucosa (sensory nerves) Paranasal sinus mucosa (sensory nerves) Parotid gland
CN VII	Conchal bowl External auditory canal Tympanic membrane	Nasal mucosa (parasympathetic nerves) Sphenoid and ethmoid sinuses (parasympathetic nerves) Anterior two-thirds of the tongue (taste fibers)
CN IX	Tympanic membrane	Stylopharyngeus muscle Posterior third of the tongue Palatine tonsil Carotid body Pharyngeal mucosa Parapharyngeal space Retropharyngeal space
CN X	Concha Postauricular skin Posterior external auditory canal Tympanic membrane	Oropharynx (vallecula and constrictor muscles) Larynx Hypopharynx (pyriform sinus) Visceral space (thyroid, esophagus, and trachea)



**FIG 5.** A 55-year-old man with secondary otalgia due to cervical spondylosis. Axial bone algorithm CT shows marked left-sided facet arthropathy (white arrow), which along with uncovertebral hypertrophy (black arrow) results in narrowing of the C II to C III neural foramen (white arrowhead). Impingement of the C III nerve root can lead to otalgia via referred pain along the *great auricular* or *lesser occipital* nerves.

stimulated via metastatic lymphadenopathy encroaching on the retropharyngeal or carotid spaces<sup>2,32,42</sup> (Figs 6 and 12).

Benign processes can also cause secondary ear pain through stimulation of CN IX afferents, including nonsuppurative tonsillitis, tonsillar or peritonsillar abscess, suppurative retropharyngeal

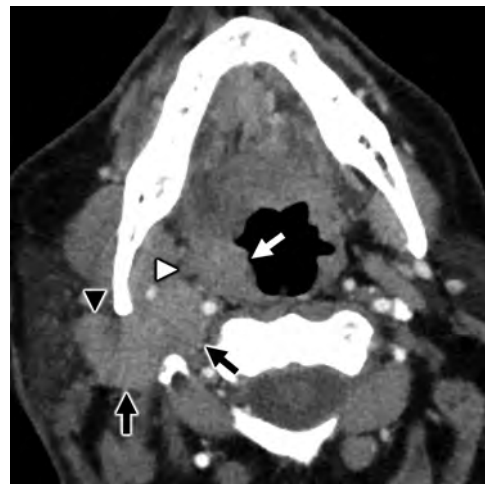


**FIG 6.** A 64-year-old man with secondary otalgia caused by palatine tonsil squamous cell carcinoma. Axial contrast-enhanced CT shows a right palatine tonsil mass (white arrow) with deep invasion through the superior constrictor (white arrowhead) into the parapharyngeal space. Conglomerate right level II cervical adenopathy (black arrows) with extracapsular spread displaces the carotid space and invades the parotid tail (black arrowhead). In this case, the patient's referred otalgia may be caused by involvement of CN IX, CN X, and/or upper cervical nerve branches (*great auricular* or *lesser occipital*).

adenopathy, transient perivascular inflammation of the carotid syndrome (Fig 13), and stylohyoid (Eagle) syndrome.<sup>17,43-46</sup> Additionally, patients with neurovascular compression of the

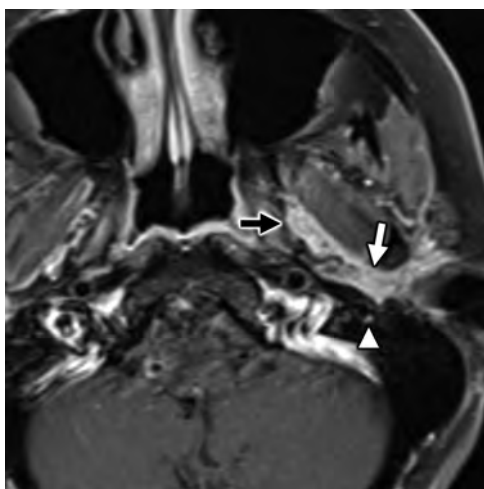


**FIG 7.** A 35-year-old man with secondary otalgia caused by perineural tumor spread from parotid adenoid cystic carcinoma. Axial T1-weighted postcontrast fat-saturated MR imaging shows cordlike enhancement (*white arrow*) along the course of the *auriculotemporal nerve*, which serves as an extracranial bridge linking the intraparotid *facial nerve* to CN V3 (*black arrow*) in the infrazygomatic masticator space. Note hyperenhancement along the descending mastoid segment of CN VII (*white arrowhead*) from additional perineural tumor spread. In this case, referred otalgia may occur along the *auriculotemporal nerve*, CN V3, and/or CN VII.



**FIG 9.** Benign parotid pathology presenting with secondary otalgia. Axial contrast-enhanced CT in a 75-year-old man with right-sided ear pain shows obstructive calculous parotitis and sialodochitis with marked intraparotid ductal dilation (*white arrow*) and wall enhancement upstream of an obstructing sialolith (*white arrowhead*). Referred otalgia from intraparotid pathologies is thought to occur via the *auriculotemporal nerve*, a branch of CN V3.



**FIG 8.** A 58-year-old woman with secondary otalgia caused by TMJ derangement. Oblique sagittal T1-weighted image in open-mouth position demonstrates irregularity and loss of normal biconcave morphology of the articular disk (*white arrow*), which has been displaced anteriorly. The disk does not recapture upon mouth opening, which prevents normal anterior translation of the mandibular condyle (*white arrowhead*) with respect to the articular eminence (*black arrow*). TMJ degeneration is a very common etiology of secondary otalgia with pain likely referred along CN V3.

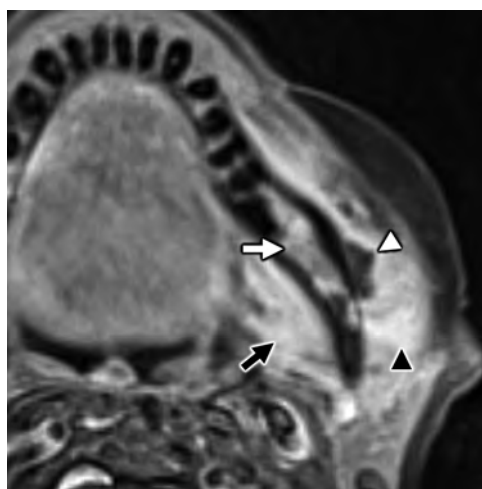


**FIG 10.** A 42-year-old woman with secondary otalgia due to odontogenic infection. Axial T1-weighted postcontrast fat-saturated MR imaging shows a rim-enhancing subperiosteal abscess (*white arrowhead*). Note the corresponding hyperenhancing marrow (*white arrow*) from osteitis and hyperenhancing medial pterygoid (*black arrow*) and masseter (*black arrowhead*) muscles from myositis. Odontogenic infection is a common source of referred otalgia via CN V3 and its branches.

### Cranial Nerve X

The vagus nerve (CN X) is a mixed nerve, transmitting motor, general sensory, special sensory (taste), viscerosensory, and parasympathetic nerve connections to geographically diverse regions of the body, spanning the brain stem, head and neck, chest, and abdomen to the level of the colon.<sup>48</sup> Similar to CN IX, the vagus nerve is supported by 4 brain stem nuclei that are located in or extend through the medulla, including the nucleus ambiguus

proximal root entry zone of CN IX (typically by the posterior inferior cerebellar artery or anterior inferior cerebellar artery) may uncommonly manifest glossopharyngeal neuralgia, a rare entity consisting of paroxysmal pain involving the external ear, posterior tongue, and tonsil.<sup>47</sup>





**FIG 11.** A 64-year-old woman with secondary otalgia caused by sinus mucosal disease. Axial bone algorithm CT shows a partially opacified right sphenoid sinus with marked hyperostosis and sclerosis of the sinus walls from long-standing mucoperiosteal reaction (*white arrow*) related to sinus mucosal disease. Note an air-fluid level (*white arrowhead*), which is a nonspecific finding that can be seen in the setting of acute inflammation related to the sinus mucosal disease. Sinus disease is a common source of secondary otalgia, thought to yield referred pain via CN VII parasympathetic branches or via CN VI sensory branches.

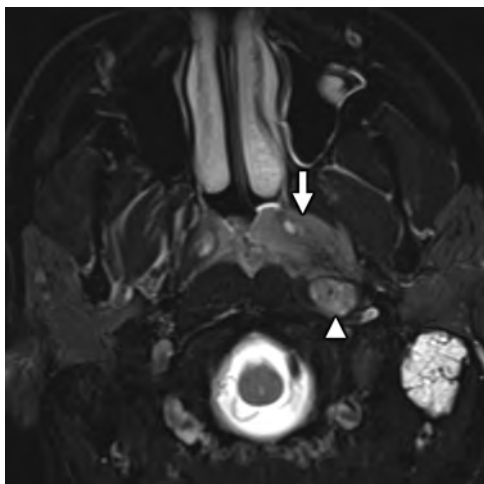


**FIG 12.** A 52-year-old man with secondary otalgia caused by nasopharyngeal carcinoma (NPC). Axial T2-weighted fat-saturated MR imaging shows an intermediate signal intensity nasopharyngeal mass (*white arrow*) consistent with a cellular tumor, which extends laterally into the parapharyngeal space. Note the additional metastatic retropharyngeal adenopathy (*white arrowhead*) and left mastoid effusion. NPC may present with primary and secondary otalgia caused by mastoid–middle ear effusion (primary otalgia) and referred pain along CN IX (secondary otalgia).

(motor), solitary tract nucleus (taste), dorsal vagal nucleus (viscerosensory afferents and parasympathetic efferents), and spinal nucleus of CN V (general sensory) (Fig 4). CN X departs the medulla laterally at the postolivary sulcus, courses anterolaterally through the basal cistern along with CN IX and CN XI, and travels through the jugular foramen, where it transits the superior



**FIG 13.** Transient perivascular inflammation of the carotid artery (TIPIC) syndrome presenting as otalgia. Axial contrast-enhanced CT in a 44-year-old woman with TIPIC syndrome shows characteristic segmental, eccentric soft tissue thickening (*white arrow*) around the wall of the common carotid artery. Note the lack of associated arterial stenosis (*white arrowhead*). TIPIC syndrome may yield referred otalgia via CN IX and/or CN X branches, depending on which segments of the carotid artery are involved.

vagal ganglion and exits the skull base via the pars vascularis portion of the jugular foramen. Below the skull base, CN X descends in the carotid space, transiting the nodose ganglion before descending posterolateral to the carotid artery and into the chest.

Primary sensory innervation of the ear via CN X is complex and variable but generally includes portions of the concha, postauricular skin, the posterior external auditory canal, and the tympanic membrane via the auricular branch of the vagus nerve (Arnold nerve), which relays from CN X via the superior vagal ganglion in the jugular foramen, as well as receives some innervation via CN IX.<sup>48</sup> The vagus nerve also provides branches to the oropharynx (vallecula), supraglottic larynx (laryngeal and lingual surfaces of the epiglottis), hypopharynx (pyriform sinus), thyroid, cervical esophagus, and trachea via the superior and inferior laryngeal nerves.<sup>32</sup> This complex CN X innervation pathway involving the ear and other geographically remote regions of the body is exemplified by the ear-cough (Arnold nerve) reflex, which can result in the induction of cough as a result of stimulation or manipulation of the external ear.<sup>49</sup>

Many neoplastic causes of referred ear pain can be directly attributed to the CN X sensory pathway. Therefore, these structures must be carefully inspected on cross-sectional imaging, particularly if the patient has a history of dysphonia, dysphagia, or dyspnea.<sup>50</sup> Glottic and supraglottic laryngeal cancer, esophageal carcinoma (Fig 14), and apical lung cancer may all present with otalgia.<sup>51–53</sup> Benign pathologies, including TIPIC syndrome (Fig 13), thyroiditis, and cricoarytenoid arthropathy, may also cause referred ear pain via CN X afferents.<sup>43,54,55</sup>

## APPROACH TO IMAGING

The approach to imaging referred ear pain should be driven by clinical history and physical examination findings, and it is incumbent on the interpreting radiologist to review the medical record of

patients evaluated for otalgia. Protocolling of examinations for all permutations of clinical presentations of otalgia is beyond the scope of this review, but in general, the choice of imaging technique and examination is predicated on clinical features, and imaging protocols should be targeted to address specific examination abnormalities. For patients with “red flags,” such as weight loss, dysphagia, odynophagia, dyspnea, adenopathy, and advanced age, cross-sectional imaging serves a primary role in screening for occult head and neck malignancy as a potential source of referred ear pain. In

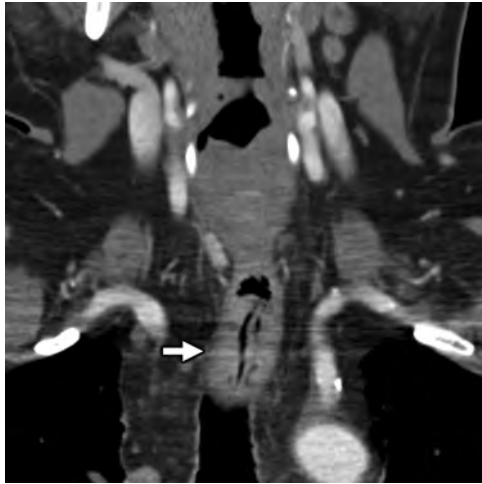


**FIG 14.** A 58-year-old man with secondary otalgia caused by esophageal carcinoma. Coronal contrast-enhanced CT image shows segmental wall thickening (white arrow) of the distal cervical esophagus corresponding to the esophageal carcinoma. In this case, the referred otalgia likely occurred via CN X branches.

this population, contrast-enhanced CT of the neck is an appropriate first-line imaging technique. For patients with otalgia and symptoms of chronic rhinosinusitis or eustachian tube dysfunction, targeted imaging of the paranasal sinuses with high-resolution CT is a reasonable first-line technique. If ear pain is associated with lower cranial neuropathies, high-resolution CT and MR imaging of the temporal bones are complementary in evaluating for potential skull base causes, such as jugular foramen masses, skull base metastases, and osteomyelitis. In general, contrast-enhanced CT of the soft tissues of the neck is a practical starting point if clinical history and physical examination are noncontributory.

When approaching secondary otalgia on cross-sectional imaging, it is useful to heed the classic head and neck imaging mantra of “image from origin nuclei to end organs” for the search pattern. Under this paradigm, the interpreting radiologist systematically evaluates for central (ie, brain stem or spine) causes and then scans the expected courses of the potentially affected nerves all the way out to their constituent innervation targets for referable pathology. Because multiple upper cervical and lower CNs may be involved, it is imperative to systematically approach the imaging of these complex cases. Regardless of technique, we advocate by using a standard search pattern, which allows the interpreting radiologist to operate in a consistent and strategic manner.

A checklist of our suggested search pattern for secondary otalgia is summarized in Table 2, which is based on a modification of the classic “10 Ts of referred otalgia” mnemonic.<sup>5,56</sup> First focus on the ear, evaluating the external, middle, and inner ear structures; surrounding periauricular soft tissues; and overlying skin for pathology. Next, assess for pathology affecting the brain stem and upper cervical cord. Scrutinize the upper cervical (C II and C

III) nerve courses, noting spinal canal and thecal sac stenoses and neural foramina compromise, as well as scan the expected extraspinal course of the great auricular and lesser occipital nerves. Then, evaluate the course of CN V, CN VII, CN IX, and CN X and their major branches for pathology, starting with the origin nuclei that span the brain stem and upper cervical cord and then assessing their respective cisternal, skull base and temporal bone, and extracranial segments. Special attention is paid to their courses through the masticator, parotid, and carotid spaces, as well as the major CN waystations (eg, pterygopalatine fossa). Evaluate the major end organs 1 at a time, including the major salivary glands, orbits, nose and paranasal sinuses, oral cavity and tongue, teeth, TMJ, nasopharynx, oropharynx, hypopharynx, larynx, visceral space, and carotid space, making sure to assess for cervical, retropharyngeal, and intraparotid adenopathy. Finally, review imaged portions of the brain and upper chest,

**Table 2: Suggested cross-sectional imaging search pattern for secondary otalgia**

Component	Specific Sites of Interest
Ear and temporal bone	External ear External auditory canal Middle ear, mastoid Inner ear, otic capsule, and petrous apex Periauricular soft tissues
Central nervous system	Midbrain, pons, and medulla Upper cervical spinal cord
Upper cervical nerves (C II and C III)	Occipitocervical and atlantoaxial joints Spinal canal and neural foramina (C II and C III) Extracranial course of great auricular and lesser occipital nerves
CN V, CN VII, CN IX, and CN X	Cisternal segments Skull base or temporal bone segments Extracranial segments (masticator, parotid, and carotid spaces) Major waystations (pterygopalatine fossa and geniculate ganglion)
“End organs” of innervation	Major salivary glands (parotid, submandibular, and sublingual) Orbits Nose and sinonasal cavity Oral cavity (tongue, mucosa, and palate) Maxilla and mandible (teeth and TMJ) Pharynx (nasopharynx, oropharynx, and hypopharynx) Larynx Visceral space (thyroid, esophagus, and trachea) Carotid space (carotid artery and internal jugular vein) Lymph nodes (cervical, retropharyngeal, and intraparotid)
“Corners” of the examination	Imaged portions of the brain Imaged portions of the chest

which can serve as sites of meningeal or visceral referred pain to the ear.

## CONCLUSIONS

Otalgia is common, and when no source is identified on physical examination, a more complete diagnostic work-up is warranted, including medical imaging. Such causes of secondary otalgia may often be identified on cross-sectional imaging (CT and MR imaging), and it is critical for radiologists to be familiar with the complex sensorineural pathways that innervate the ear because referred pain from numerous head and neck sites can manifest as otalgia.

Disclosures: Nicholas Koontz—UNRELATED: Royalties: Amirsys-Elsevier.








## REFERENCES

- Harrison E, Cronin M. **Otalgia.** *Aust Fam Physician* 2016;45:493–97 Medline
- Olsen KD. **The many causes of otalgia. Infection, trauma, cancer.** *Postgrad Med* 1986;80:50–52, 55–56, 61–63 CrossRef Medline
- Neilan RE, Roland PS. **Otalgia.** *Med Clin North Am* 2010;94:961–71 CrossRef Medline
- Kim SH, Kim TH, Byun JY, et al. **Clinical differences in types of otalgia.** *J Audiol Otol* 2015;19:34–38 CrossRef Medline
- Fenton JE, Uzomefuna V, O'Rourke C, et al. **Applying the Ts of referred otalgia to a cohort of 226 patients.** *Clin Otolaryngol* 2018;43:937–40 CrossRef Medline
- Yanagisawa K, Kveton JF. **Referred otalgia.** *Am J Otolaryngol* 1992;13:323–27 CrossRef Medline
- Shah RK, Blevins NH. **Otalgia.** *Otolaryngol Clin North Am* 2003;36:1137–51 CrossRef Medline
- Chen RC, Khorsandi AS, Shatzkes DR, et al. **The radiology of referred otalgia.** *AJNR Am J Neuroradiol* 2009;30:1817–23 CrossRef Medline
- Osterweis M, Kleinman A, Mechanic D, eds. **The anatomy and physiology of pain.** In: *Pain and Disability: Clinical, Behavioral, and Public Policy Perspectives.* National Academies Press; 1987:123–45
- Hao J, Bonnet C, Amsalem M, et al. **Transduction and encoding sensory information by skin mechanoreceptors.** *Pflugers Arch* 2015;467:109–19 CrossRef Medline
- Bell A. **The neurobiology of acute pain.** *Vet J* 2018;237:55–62 CrossRef Medline
- Marchand S. **The physiology of pain mechanisms: from the periphery to the brain.** *Rheum Dis Clin North Am* 2008;34:285–309 CrossRef Medline
- Ralston HJ, 3rd. **Pain and the primate thalamus.** *Prog Brain Res* 2005;149:1–10 CrossRef Medline
- Murray GM. **Guest editorial: referred pain.** *J Appl Oral Sci* 2009;17:i
- Proacci P, Zoppi M, Maresca M, et al. **Analgesic action of tetracosactide in chronic pain syndromes.** *Clin Ter* 1981;98:643–46 Medline
- Pace MC, Passavanti MB, De Nardis L, et al. **Nociceptor plasticity: a closer look.** *J Cell Physiol* 2018;233:2824–38 CrossRef Medline
- Asherson N. **Glossopharyngeal neuralgia (otalgia) and the elongated styloid process: a record of five cases.** *J Laryngol Otol* 1957;71:453–70 CrossRef Medline
- Latremoliere A, Woolf CJ. **Central sensitization: a generator of pain hypersensitivity by central neural plasticity.** *J Pain* 2009;10:895–926 CrossRef Medline
- Woolf CJ. **Central sensitization: implications for the diagnosis and treatment of pain.** *Pain* 2011;152:S2–15 CrossRef Medline
- Giamberardino MA. **Referred muscle pain/hyperalgesia and central sensitization.** *J Rehabil Med* 2003;35:85–88 CrossRef Medline
- Foreman RD, Schmidt RF, Willis WD. **Effects of mechanical and chemical stimulation of fine muscle afferents upon primate spinothalamic tract cells.** *J Physiol (Lond)* 1979;286:215–31 CrossRef Medline
- Milne RJ, Foreman RD, Giesler GJ, Jr, et al. **Convergence of cutaneous and pelvic visceral nociceptive inputs onto primate spinothalamic neurons.** *Pain* 1981;11:163–83 CrossRef Medline
- Lynn RB. **Mechanisms of esophageal pain.** *Am J Med* 1992;92:11S–19S CrossRef Medline
- Alvord LS, Farmer BL. **Anatomy and orientation of the human external ear.** *J Am Acad Audiol* 1997;8:383–90 Medline
- Woolf CJ, Salter MW. **Neuronal plasticity: increasing the gain in pain.** *Science* 2000;288:1765–69 CrossRef Medline
- Jaber JJ, Leonetti JP, Lawrason AE, et al. **Cervical spine causes for referred otalgia.** *Otolaryngol Head Neck Surg* 2008;138:479–85 CrossRef Medline
- Danish SF, Zager EL. **Cervical spine meningioma presenting as otalgia: case report.** *Neurosurgery* 2005;56:E621 CrossRef Medline
- Gamrath DJ. **Consider atlanto-occipital joint dysfunction as a cause of secondary otalgia.** *Am Fam Physician* 2018;98:142 Medline
- Holt JJ. **Otalgia: the many causes.** *Wis Dent Assoc J* 1987;63:551 Medline
- Taziki MH, Behnampour N. **A study of the etiology of referred otalgia.** *Iran J Otorhinolaryngol* 2012;24:171–76 Medline
- Vattoth S. **CNV (trigeminal nerve).** In: Chapman PR, Harnsberger HR, Vattoth S, eds. *Imaging Anatomy: Head and Neck.* Elsevier; 2019:152–63
- Scarborough TJ, Day TA, Williams TE, et al. **Referred otalgia in head and neck cancer: a unifying schema.** *Am J Clin Oncol* 2003;26:e157–62 CrossRef Medline
- Schmalzuss IM, Tart RP, Mukherji S, et al. **Perineural tumor spread along the auriculotemporal nerve.** *AJNR Am J Neuroradiol* 2002;23:303–11 Medline
- Bush FM, Harkins SW, Harrington WG. **Otalgia and aversive symptoms in temporomandibular disorders.** *Ann Otol Rhinol Laryngol* 1999;108:884–92 CrossRef Medline
- Erkalp K, Erkalp KN, Ozdemir H. **Acute otalgia during sleep (live insect in the ear): a case report.** *Agri* 2009;21:36–38 Medline
- Kim DS, Cheang P, Dover S, et al. **Dental otalgia.** *J Laryngol Otol* 2007;121:1129–34 CrossRef Medline
- Kim SH. **A case of bruxism-induced otalgia.** *J Audiol Otol* 2016;20:123–26 CrossRef Medline
- Chapman PR, Harnsberger HR. **CNVII (facial nerve).** In: Chapman PR, Harnsberger HR, Vattoth S, eds. *Imaging Anatomy: Head and Neck.* Elsevier; 2019:168–75
- Charlett SD, Coatesworth AP. **Referred otalgia: a structured approach to diagnosis and treatment.** *Int J Clin Pract* 2007;61:1015–21 CrossRef Medline
- Nanda MS, Kaur M, Bhatia S. **Impact of septoplasty on hearing and middle ear function.** *Int J Res Med Sci* 2018;6:135–39 CrossRef Medline
- Singhal A, Harnsberger HR. **CNIX (glossopharyngeal nerve).** In: Chapman PR, Harnsberger HR, Vattoth S, eds. *Imaging Anatomy: Head and Neck.* Elsevier; 2019:182–87
- Grosskopf CC, Kuperstein AS, O'Malley BW Jr, et al. **Parapharyngeal space tumors: another consideration for otalgia and temporomandibular disorders.** *Head Neck* 2013;35:E153–56 CrossRef Medline
- Hill LM, Hastings G. **Carotidynia: a pain syndrome.** *J Fam Pract* 1994;39:71–75 Medline
- Kim KS. **Referred otalgia induced by a large tonsillolith.** *Korean J Fam Med* 2013;34:221–23 CrossRef Medline
- Naraev BG, Linthicum FH, Jr. **Traumatic neuroma of the tympanic (Jacobson's) nerve as a possible cause of otalgia.** *Otolaryngol Head Neck Surg* 2008;138:735–37 CrossRef Medline
- Lecler A, Obadia M, Savatovsky J, et al. **TIPIC syndrome: beyond the myth of carotidynia, a new distinct unclassified entity.** *AJNR Am J Neuroradiol* 2017;38:1391–98 CrossRef Medline
- Haller S, Etienne L, Kovari E, et al. **Imaging of neurovascular compression syndromes: trigeminal neuralgia, hemifacial spasm, vestibular paroxysmia, and glossopharyngeal neuralgia.** *AJNR Am J Neuroradiol* 2016;37:1384–92 CrossRef Medline
- Singhal A, Harnsberger HR. **CNX (vagus nerve).** In: Chapman PR, Harnsberger HR, Vattoth S, eds. *Imaging Anatomy: Head and Neck.* Elsevier; 2019:188–93
- Dicpinigaitis PV, Kantar A, Enilari O, et al. **Prevalence of Arnold nerve reflex in adults and children with chronic cough.** *Chest* 2018;153:675–79 CrossRef Medline



50. Thaller SR, De Silva A. **Otalgia with a normal ear.** *Am Fam Physician* 1987;36:129–36 Medline
51. Kellerhals B. **Pain syndromes of the head, neck and locomotor system—determining current status.** *HNO* 1984;32:181–89 Medline
52. Kuo YW, Chen KY, Chang YL, et al. **Small-cell lung carcinoma presenting with otalgia and hearing impairment.** *J Clin Oncol* 2008;26:4690–92 CrossRef Medline
53. Rareshide EH, Amedee RG. **Referred otalgia.** *J La State Med Soc* 1990;142:7–10 Medline
54. Jajić I, Dubravica M, Jajić Z. **Rheumatoid arthritis in the cricoarytenoid joint.** *Reumatizam* 1994;41:13–14 Medline
55. Stevenson J. **Acute bacterial thyroiditis presenting as otalgia.** *J Laryngol Otol* 1991;105:788–89 CrossRef Medline
56. Harvey H. **Diagnosing referred otalgia: the ten Ts.** *Cranio* 1992;10:333–34 CrossRef Medline

# MRI Brain Findings in 126 Patients with COVID-19: Initial Observations from a Descriptive Literature Review

 E. Gulko,  M.L. Oleksk,  W. Gomes,  S. Ali,  H. Mehta,  P. Overby,  F. Al-Mufti, and  A. Rozenshtein



## ABSTRACT

**BACKGROUND AND PURPOSE:** Recently, numerous investigational studies, case series, and case reports have been published describing various MR imaging brain findings in patients with COVID-19. The purpose of this literature review was to compile and analyze brain MR imaging findings in patients with COVID-19-related illness.

**MATERIALS AND METHODS:** Literature searches of PubMed, publicly available Internet search engines, and medical journal Web sites were performed to identify articles published before May 30, 2020 that described MR imaging brain findings in patients with COVID-19.

**RESULTS:** Twenty-two articles were included in the analysis: 5 investigational studies, 6 case series, and 11 case reports, encompassing MR imaging of the brain in 126 patients. The articles originated from 7 different countries and were published in 14 medical journals. MR imaging brain findings included specific diagnoses (such as acute infarct, posterior reversible encephalopathy syndrome) or specific imaging features (such as cortical FLAIR signal abnormality, microhemorrhages).

**CONCLUSIONS:** The most frequent diagnoses made on brain MR imaging in patients with COVID-19 were acute and subacute infarcts. Other common findings included a constellation of leukoencephalopathy and microhemorrhages, leptomeningeal contrast enhancement, and cortical FLAIR signal abnormality.

**ABBREVIATIONS:** COVID-19 = coronavirus disease 2019; PRES = posterior reversible encephalopathy syndrome; SARS-CoV-2 = Severe Acute Respiratory Syndrome coronavirus 2

Growing evidence suggests that coronavirus disease 2019 (COVID-19), secondary to infection with Severe Acute Respiratory Syndrome coronavirus 2 can manifest with a multitude of neurologic conditions including ataxia, seizure, acute stroke, and impaired consciousness.<sup>1,2</sup> Since the World Health Organization declared coronavirus disease 2019 (COVID-19) a global pandemic on March 11, 2020,<sup>3</sup> the medical literature describing COVID-19 mechanisms, manifestations, and treatments has expanded with extraordinary speed. In concordance with the World Health Organization's efforts for rapid

distribution of data by biomedical journals during public health emergencies,<sup>4</sup> this rapid pace has been aided by the expedited peer-review processes instituted by multiple medical journals.<sup>5</sup> Consequently, journals representing multiple disciplines simultaneously have published numerous articles describing imaging findings in COVID-19 illness. While pulmonary disease is the best recognized morbidity associated with COVID-19, there are many reported neurologic manifestations of this infection. The purpose of this literature review was to collect, analyze, and summarize the findings on brain MR imaging reported to date in patients with COVID-19.


## MATERIALS AND METHODS


Due to the rapid pace of COVID-19-related publications, many relevant articles were not yet represented on the public data bases, including PubMed, and a standard systematic review was not possible. We, therefore, adopted an ad hoc approach that included queries of PubMed, other publicly available Internet search engines (such as Google, Google Scholar, and Bing), as well as a review of journal Web sites. Our review includes only articles published before May 30, 2020. Search terms included "brain MR imaging,"

Received June 4, 2020; accepted after revision July 28.

From the Department of Radiology (E.G., W.G., S.A., H.M.), Division of Neuroradiology; Department of Pediatrics (P.O.); Department of Neurology (F.A.M.); and Department of Radiology (A.R.), Division of Cardiothoracic Imaging, Westchester Medical Center, Valhalla, New York; and New York Medical College (M.L.O.), Valhalla, New York.

Please address correspondence to Edwin Gulko, MD, Division of Neuroradiology, Department of Radiology, Westchester Medical Center, 100 Woods Rd, Valhalla New York, 10595; e-mail: Edwin.Gulko@wmchealth.org

 Indicates open access to non-subscribers at [www.ajnr.org](http://www.ajnr.org)

 Indicates article with supplemental on-line table.

<http://dx.doi.org/10.3174/ajnr.A6805>

“COVID-19,” “neuro,” “neurology,” “neurologic,” and “stroke.” The Web sites of major radiology journals such as *Radiology*, *JAMA Neurology*, *New England Journal of Medicine*, and *American Journal of Neuroradiology* were also reviewed to identify relevant articles. Articles were included in the review if they discussed brain MR imaging findings in patients with COVID-19. Articles were excluded if they were not yet accepted by a peer-reviewed journal, pertained to pediatric patients, were not written in English, or mentioned MR imaging of the brain performed in patients with COVID-19 but did not discuss the imaging findings. All included articles were reviewed by 2 fellowship-trained neuroradiologists with Certificates of Added Qualification (E.G. and W.G.).

## RESULTS

### Articles

Twenty-two published articles met the inclusion criteria. There were 5 investigational studies, 6 case series, and 11 case reports (Table 1 and On-line Table). The articles originated from 7 different countries (United States,  $n = 6$ ; Turkey,  $n = 4$ ; France,  $n = 4$ ; Italy,  $n = 4$ ; United Kingdom,  $n = 2$ ; Japan,  $n = 1$ ; Canada,  $n = 1$ ) and were published in 14 medical journals. Some articles focused primarily on neuroimaging findings in COVID-19, while others reported neuroimaging in the context of a broader clinical report. Three of the 5 investigational studies included specifically evaluated MR neuroimaging findings in hospitalized patients with COVID-19.<sup>6-8</sup> The other 2 studies evaluated neurologic features in patients with Severe Acute Respiratory Syndrome coronavirus 2 (SARS-CoV-2) infection<sup>1</sup> and thrombotic complications in patients with COVID-19 with Acute Respiratory Distress Syndrome.<sup>9</sup>

**Table 1: Articles describing MR imaging brain findings in patients with COVID-19**

Manuscripts Describing MRI Brain Findings in COVID-19 Patients	
Articles	22
Journals	14
Countries	7
Patients with MR imaging of the brain described	126
Investigational studies	5
Case series	6
Case report	11

**Table 2: Findings on brain MR imaging in 126 patients with COVID-19**

Imaging Finding	No. of Cases
Acute or subacute infarcts	32
Leukoencephalopathy	17
Cortical FLAIR signal abnormality	15
Microhemorrhages	14
Leptomeningeal enhancement	14
PRES	4
Demyelinating lesions or exacerbation of MS	3
Dural venous thrombosis	2
Signal abnormality and/or enlargement of the olfactory bulbs	2
Acute hemorrhagic necrotizing encephalopathy	1
Rhombencephalitis	1
Miller-Fisher Guillain-Barré syndrome	1
Hypoxic-ischemic encephalopathy	1
Normal findings on brain MR imaging	19

### Imaging Findings

The reported brain MR imaging findings in 126 patients are summarized in Table 2. In some cases, the authors made a specific diagnosis (eg, acute infarct) without describing the specific features supporting the diagnosis. In other cases, specific imaging features were provided (such as white matter hyperintensity on FLAIR images), sometimes with a presumptive diagnosis based on these findings (eg, leukoencephalopathy). In total, there were 32 cases with acute or subacute infarcts, 4 cases of parenchymal abnormality attributed to posterior reversible encephalopathy syndrome (PRES) 2 of which were hemorrhagic, 2 cases of dural venous sinus thrombosis, 3 cases of demyelinating lesions or exacerbation of MS, 1 case of acute hemorrhagic necrotizing encephalopathy, and 1 case of hypoxic-ischemic encephalopathy. With respect to specific imaging features, there were 17 reported cases of diffuse white matter signal abnormality, broadly consistent with leukoencephalopathy, described as subcortical and deep white matter signal abnormality (3 cases), diffuse abnormality (10 cases), extensive frontal and parietal white matter signal abnormality (1 case), subcortical distribution with callosal involvement (1 case), diffuse and confluent posterior predominant white matter T2/FLAIR hyperintensities (1 case), and confluent regions of restricted diffusion with subcortical and deep hemispheric white matter (1 case). Petechial parenchymal microhemorrhages with varying distributions (cortical, juxtacortical, corpus callosum, or tracking along small cortical veins) were present in 14 cases. Leptomeningeal contrast enhancement was described in 14 cases, and cortical FLAIR signal abnormality, in 15 cases. There were 2 cases of signal abnormality and/or enlargement of the olfactory bulbs and 1 case each of T2 hyperintensity in the right inferior cerebellar peduncle extending into the upper spinal cord, attributed to rhombencephalitis, and cranial nerve enhancement in the setting of Miller-Fisher Guillain-Barré syndrome. There were 19 reported cases of normal brain MR imaging findings.

### DISCUSSION

The most common imaging finding described across all articles was acute or subacute infarction (Figure). Acute stroke is a strong prognostic marker of poor outcome in patients hospitalized with COVID-19.<sup>10</sup> Multiple recent reports suggest that COVID-19 is associated with acute cerebrovascular disease, including intracranial hemorrhage, large-vessel occlusion, acute ischemic stroke, and dural venous sinus thrombosis.<sup>11-13</sup> The apparent association of COVID-19 with cerebrovascular disease may reflect an increased risk of vessel thrombosis secondary to endothelial dysfunction, inflammation, platelet activation, and stasis.<sup>14</sup> However, the exact pathophysiology of stroke in COVID-19 remains poorly understood. For example, it is presently unknown to what extent arterial thrombosis in COVID-19 is associated with pre-



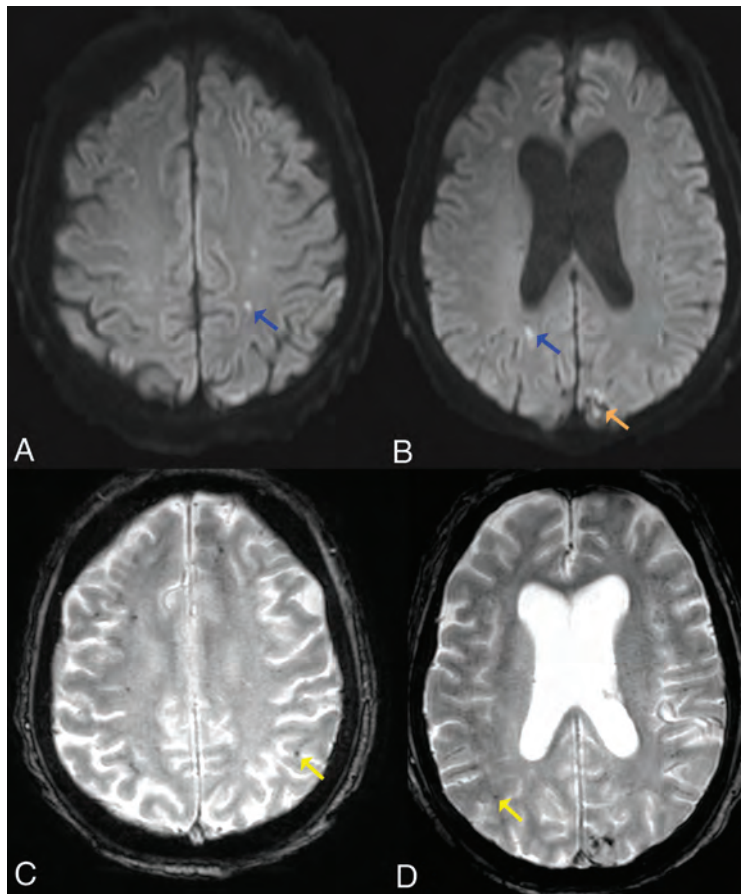


**FIGURE.** Acute infarcts and microhemorrhages. Axial diffusion (A and B) and gradient-echo (C and D) sequences in a 61-year-old man with COVID-19 infection. There are acute infarcts within the bilateral cerebral white matter (blue arrows) and a left occipital hemorrhagic infarct (orange arrow). There are innumerable microhemorrhages throughout the bilateral cerebral hemispheres (yellow arrows).

existing atheromatous plaque versus an entirely *de novo* phenomenon. It is also unclear whether thrombosis predominantly occurs in large or small arteries and, to what extent, if any, nonthrombotic vascular stenosis may contribute to the incidence of infarction.

Other commonly described findings were diffuse white matter abnormality, consistent with leukoencephalopathy, in association with parenchymal microhemorrhages. As suggested by Radmanesh et al,<sup>7</sup> COVID-19 may be associated with a form of leukoencephalopathy that is particularly characterized by the presence of microhemorrhage. This could be the direct consequence of SARS-CoV-2 CNS infection or a secondary effect of a generalized COVID-19 phenomenon (such as hypercoagulability). In addition, as postulated by Radmanesh et al, it may be a late complication of critically ill patients with COVID-19 secondary to hypoxia and possibly a manifestation of delayed posthypoxic leukoencephalopathy. Of note, all patients described by Radmanesh et al and most studied by Kandemirli et al<sup>6</sup> were intubated. Furthermore, the cohort studied by Radmanesh et al was mechanically ventilated for a mean duration of 27 days. In their study, Radmanesh et al observed mild restricted diffusion within white matter regions of T2 hyperintensities, the same imaging characteristics seen with delayed posthypoxic leukoencephalopathy.<sup>15</sup>

Nicholson et al<sup>16</sup> observed multifocal, predominantly petechial hemorrhages in patients with COVID-19 and speculated that they may have resulted from diffuse thrombotic microangiopathy, which has previously been reported to cause similar abnormalities<sup>17</sup> and can lead to PRES.<sup>18</sup> Several studies have recently described cytokine storms in COVID-19 infection,<sup>19,20</sup> with resultant vascular endothelial damage,<sup>21</sup> which can result in thrombotic microangiopathy. Nicholson et al<sup>16</sup> further suggested that extracorporeal membrane oxygenation therapy may contribute to parenchymal brain abnormalities in COVID-19 due to obligatory anticoagulation with resultant hemorrhage. However, Radmanesh et al<sup>7</sup> described extensive microhemorrhage in a cohort that did not receive extracorporeal membrane oxygenation.

Other brain MR imaging findings in patients with COVID-19 were leptomeningeal contrast enhancement and cortical FLAIR signal abnormality, either separately or in combination. Leptomeningeal contrast enhancement is a known manifestation of leptomeningitis and has been seen in other viral illnesses such as H1N1-associated encephalitis.<sup>22</sup> Cortical FLAIR signal abnormality has a broad differential diagnosis and can include encephalitis, postictal state, PRES, as well as acute ischemia.

Despite the global reach of the pandemic and the vast number of critically ill patients, the small number of reported cases with brain MR imaging abnormalities is likely due to stringent policies on the use of MR imaging in patients with COVID-19. The American College of Radiology recently issued recommendations for practitioners to minimize the use of MR imaging in patients infected or suspected of having COVID-19 infection unless absolutely necessary.<sup>23</sup> Similar policies are likely to be in effect worldwide, limiting MR imaging use to patients with COVID-19 with the highest clinical urgency. This policy may, at least in part, explain most of the patients in the published reports being severely ill, many of them mechanically ventilated. It would be necessary to perform brain MR imaging examinations in symptomatic patients with COVID-19 with mild and moderate illness to determine the full spectrum of central nervous system involvement in this disease.

In addition to the small number of reported cases, our study is necessarily limited by data accessibility. Our searches of the main on-line data bases missed a substantial portion of existing COVID-19-related reports. Therefore, we added manual

searches of multiple journal Web sites. As a result, our search results are likely not reproducible. Articles were often identified ahead of publication and before assignment of a PubMed number. Consequently, some relevant articles may have been missed.

## CONCLUSIONS

In this descriptive literature review, the most frequent diagnoses made at brain MR imaging in patients with COVID-19 were acute and subacute infarcts. Other common findings included a constellation of leukoencephalopathy and microhemorrhages, leptomeningeal contrast enhancement, and cortical FLAIR signal abnormality. Because these results are preliminary, a formalized systematic review following the Preferred Reporting Items for Systematic Reviews and Meta-Analyses guidelines will be needed as more articles are published.

## REFERENCES

- Helms J, Kremer S, Merdji H, et al. **Neurologic features in severe SARS-CoV-2 infection.** *N Engl J Med* 2020;382:2268–70 CrossRef Medline
- Mao L, Jin H, Wang M, et al. **Neurologic manifestations of hospitalized patients with coronavirus disease 2019 in Wuhan, China.** *JAMA Neurol* 2020 April 10. [Epub ahead of print] CrossRef Medline
- Cucinotta D, Vanelli M. **WHO declares COVID-19 a pandemic.** *Acta Biomed* 2020;91:157–60 CrossRef Medline
- Modjarrad K, Moorthy VS, Millett P, et al. **Developing global norms for sharing data and results during public health emergencies.** *PLoS Med* 2016;13:e1001935 CrossRef Medline
- Li X, Qian Y, Liu B, et al. **Helping the radiologist: the role of scientific journals to help prevent the spread of COVID-19.** *Radiology* 2020;295:E4 CrossRef Medline
- Kandemirli SG, Dogan L, Sarikaya ZT, et al. **Brain MRI findings in patients in the intensive care unit with COVID-19 infection.** *Radiology* 2020 May 8. [Epub ahead of print] CrossRef Medline
- Radmanesh A, Derman A, Lui YW, et al. **COVID-19-associated diffuse leukoencephalopathy and microhemorrhages.** *Radiology* 2020 May 21. [Epub ahead of print] CrossRef Medline
- Mahammed A, Saba L, Vagal A, et al. **Imaging in neurological disease of hospitalized patients with COVID-19: an Italian multicenter retrospective observational study.** *Radiology* 2020 May 21. [Epub ahead of print] CrossRef Medline
- Helms J, Tacquard C, Severac F, et al; CRICS TRIGGERSEP Group (Clinical Research in Intensive Care and Sepsis Trial Group for Global Evaluation and Research in Sepsis). **High risk of thrombosis in patients with severe SARS-CoV-2 infection: a multicenter prospective cohort study.** *Intensive Care Med* 2020;46:1089–98 CrossRef
- Jain R, Young M, Dogra S, et al. **COVID-19 related neuroimaging findings: a signal of thromboembolic complications and a strong prognostic marker of poor patient outcome.** *J Neurol Sci* 2020;414:116923 CrossRef Medline
- Radmanesh A, Raz E, Zan E, et al. **Brain imaging use and findings in COVID-19: a single academic center experience in the epicenter of disease in the United States.** *AJNR Am J Neuroradiol* 2020;41:1179–83 CrossRef Medline
- Oxley TJ, Mocco J, Majidi S, et al. **Large-vessel stroke as a presenting feature of COVID-19 in the young.** *N Engl J Med* 2020;382:e60 CrossRef Medline
- Hughes C, Nichols T, Pike M, et al. **Cerebral venous sinus thrombosis as a presentation of COVID-19.** *Eur J Case Rep Intern Med* 2020;7:001691 CrossRef Medline
- Bikdeli B, Madhavan MV, Jimenez D, et al; Global COVID-19 Thrombosis Collaborative Group, Endorsed by the ISTH, NATE, ESVM, and the IUA, Supported by the ESC Working Group on Pulmonary Circulation and Right Ventricular Function. **COVID-19 and thrombotic or thromboembolic disease: implications for prevention, antithrombotic therapy, and follow-up: JACC state-of-the-art review.** *J Am Coll Cardiol* 2020;75:2950–73 CrossRef Medline
- Zamora CA, Nauen D, Hynecek R, et al. **Delayed posthypoxic leukoencephalopathy: a case series and review of the literature.** *Brain Behav* 2015;5:e00364 CrossRef Medline
- Nicholson P, Alshafai L, Krings T. **Neuroimaging findings in patients with COVID-19.** *AJNR Am J Neuroradiol* 2020 June 11. [Epub ahead of print] CrossRef Medline
- Ellchuk TN, Shah LM, Hewlett RH, et al. **Suspicious neuroimaging pattern of thrombotic microangiopathy.** *AJNR Am J Neuroradiol* 2011;32:734–38 CrossRef Medline
- Hawley JS, Ney JP, Swanberg MM. **Thrombotic thrombocytopenic purpura-induced posterior leukoencephalopathy in a patient without significant renal or hypertensive complications.** *J Postgrad Med* 2004;50:197–99
- Ye Q, Wang B, Mao J. **The pathogenesis and treatment of the “cytokine storm” in COVID-19.** *J Infect* 2020;80:607–13 CrossRef Medline
- Mehta P, McAuley DF, Brown M, et al. HLH Across Speciality Collaboration, UK. **COVID-19: consider cytokine storm syndromes and immunosuppression.** *Lancet* 2020;395:1033–34 CrossRef Medline
- Teijaro JR, Walsh KB, Cahalan S, et al. **Endothelial cells are central orchestrators of cytokine amplification during influenza virus infection.** *Cell* 2011;146:980–91 CrossRef Medline
- Haktanir A. **MR imaging in novel influenza A(H1N1)-associated meningoencephalitis.** *AJNR Am J Neuroradiol* 2010;31:394–95 CrossRef Medline
- ACR Guidance on COVID-19 and MR Use. <https://www.acr.org/Clinical-Resources/Radiology-Safety/MR-Safety/COVID-19-and-MR-Use>. Accessed May 31, 2020
- Dogan L, Kaya D, Sarikaya T, et al. **Plasmapheresis treatment in COVID-19-related autoimmune meningoencephalitis: case series.** *Brain Behav Immun* 2020;87:155–58 CrossRef Medline
- Tunç A, Ünlübaş Y, Alemdar M, et al. **Coexistence of COVID-19 and acute ischemic stroke report of four cases.** *J Clin Neurosci* 2020;77:227–29 CrossRef Medline
- Beyroui R, Adams ME, Benjamin L, et al. **Characteristics of ischemic stroke associated with COVID-19.** *J Neurol Neurosurg Psychiatry* 2020;91:889–91 CrossRef Medline
- Franceschi AM, Ahmed O, Giliberto L, et al. **Hemorrhagic posterior reversible encephalopathy syndrome as a manifestation of COVID-19 infection.** *AJNR Am J Neuroradiol* 2020;41:1173–76 CrossRef Medline
- Cavalcanti DD, Raz E, Shapiro M, et al. **Cerebral venous thrombosis associated with COVID-19.** *AJNR Am J Neuroradiol* 2020 June 18. [Epub ahead of print] CrossRef Medline
- Moriguchi T, Harii N, Goto J, et al. **A first case of meningitis/encephalitis associated with SARS-coronavirus-2.** *Int J Infect Dis* 2020;94:55–58 CrossRef Medline
- Sachs JR, Gibbs KW, Swor DE, et al. **COVID-19-associated leukoencephalopathy.** *Radiology* 2020 May14. [Epub ahead of print] CrossRef Medline
- Pilotto A, Odolini S, Masciocchi S, et al. **Steroid-responsive encephalitis in coronavirus disease 2019.** *Ann Neurol* 2020 May17. [Epub ahead of print] CrossRef Medline
- Poyiadji N, Shahin G, Noujaim D, et al. **COVID-19-associated acute hemorrhagic necrotizing encephalopathy: CT and MRI features.** *Radiology* 2020;296:E119–20 CrossRef Medline
- Wong PF, Craik S, Newman P, et al. **Lessons of the month 1: a case of rhombencephalitis as a rare complication of acute COVID-19 infection.** *Clin Med* 2020;20:293–94 CrossRef Medline

34. Zanin L, Saraceno G, Panciani PP, et al. **SARS-CoV-2 can induce brain and spine demyelinating lesions.** *Acta Neurochir (Wien)* 2020;162:1491–94 CrossRef Medline
35. Kaya Y, Kara S, Akinci C, et al. **Transient cortical blindness in COVID-19 pneumonia; a PRES-like syndrome: case report.** *J Neurol Sci* 2020;413:116858 CrossRef Medline
36. Laurendon T, Radulesco T, Mugnier J, et al. **Bilateral transient olfactory bulbs edema during COVID-19-related anosmia.** *Neurology* 2020;95:224–25 CrossRef Medline
37. Chougar L, Mathon B, Weiss N, et al. **Atypical deep cerebral vein thrombosis with hemorrhagic venous infarction in a patient positive for COVID-19.** *AJNR Am J Neuroradiol* 2020 June18. [Epub ahead of print] CrossRef Medline
38. Avula A, Nalleballe K, Narula N, et al. **COVID-19 presenting as stroke.** *Brain Behav Immun* 2020;87:115–19 CrossRef Medline
39. Politi LS, Salsano E, Grimaldi M. **Magnetic resonance imaging alteration of the brain in a patient with coronavirus disease 2019 (COVID-19) and anosmia.** *JAMA Neurol* 2020 May 29. [Epub ahead of print] CrossRef Medline



# Unusual Brain MRI Pattern in 2 Patients with COVID-19 Acute Respiratory Distress Syndrome

 S. Toledano-Massiah,  N. Badat,  A. Leberre,  C. Bruel,  A. Ray,  S. Gerber,  M. Zins, and  J. Hodel



## ABSTRACT

**SUMMARY:** We report the cases of 2 patients hospitalized in our intensive care unit with confirmed coronavirus disease 2019 infection in whom brain MR imaging showed an unusual DWI pattern with nodular and ring-shaped lesions involving the periventricular and deep white matter. We discuss the possible reasons for these findings and their relationship to the infection.

**ABBREVIATIONS:** COVID-19 = coronavirus disease 2019; SARS-CoV-2 = Severe Acute Respiratory Syndrome coronavirus disease 2

Severe Acute Respiratory Syndrome coronavirus 2 (SARS-CoV-2) is responsible for the coronavirus disease 2019 (COVID-19) pandemic. Although the most common and important presentation of SARS-CoV-2 is respiratory disease, reports of associated neurologic complications are increasing.<sup>1</sup> A wide spectrum of neurologic symptoms has been described, ranging from nonspecific symptoms such as headache to encephalitis and cerebrovascular disease, either due to direct viral infection or as secondary complications of SARS-CoV-2.<sup>1</sup> This brief report presents 2 patients in our intensive care unit with confirmed COVID-19 infection, in whom brain MR imaging showed an unusual DWI pattern with nodular and ring-shaped lesions of the white matter.

## Case Reports

We report 2 cases of patients admitted to our hospital because of Acute Respiratory Distress Syndrome due to COVID-19. For both of them, CT revealed an interstitial pneumonia, and real-time polymerase chain reaction for SARS-CoV-2 was positive. Endotracheal intubation and mechanical ventilation were required because of severe respiratory failure. Patient 1 was a 52-year-old man with a medical history of hypertension, and patient 2, a 44-year-old man with a medical history of diabetes.

During their stay in intensive care unit, both patients presented with sepsis secondary to ventilated-associated pneumonia. Both presented with delayed recovery of consciousness after prolonged sedation. Brain MR imaging was performed at day 31 from intensive care unit hospitalization for patient 1 (day 12 after the interruption of the sedation) and at day 22 for patient 2 (day 10 after the interruption of the sedation).

In both cases, brain MR imaging revealed an unusual pattern, with nodular and ring-shaped lesions involving the periventricular and deep white matter, hyperintense on DWI and FLAIR (Fig 1). The corpus callosum was also involved. There was no involvement of the cortical-subcortical regions. Ring-shaped diffusion restriction was observed in some lesions without postcontrast enhancement. The lesions were larger on FLAIR images than they were on DWI, corresponding to surrounding vasogenic edema. Of note, subtle hemorrhage was also present in some of the lesions in patient 1 (Fig 2). There was no intracranial or supra-aortic trunk vessel obstruction or stenosis on TOF-MRA, or on CT angiography of the supra-aortic vessels.

The CSF real-time polymerase chain reaction for SARS-CoV-2 was negative for both patients. Both patients presented with progressive improvement of their neurologic state.

## DISCUSSION

The mechanism of action for SARS-CoV-2 neurologic invasion could be multiple: direct invasion, blood circulation pathway, neuronal pathway, hypoxia injury, immune injury, or related to cytokine storm syndromes and angiotensin-converting enzyme 2 receptor expression.<sup>2,3</sup>

The occurrence of acute stroke in patients with COVID-19 (as suggested in our cases by diffusion restriction) has been previously reported, suggesting either an excessive systemic proinflammatory response in COVID-19 causing dysregulation of

Received June 9, 2020; accepted after revision August 3.

From the Departments of Radiology (S.T.-M., N.B., A.L., S.G., M.Z., J.H.), Intensive Care (C.B.), and Neurology (A.R.), Fondation Hôpital Saint-Joseph, Paris, France.

Please address correspondence to Sarah Toledano-Massiah, MD, Fondation Hôpital Saint-Joseph, Department of Radiology, 185 Rue Raymond Losserand, 75014 Paris, France; e-mail: stoledano@hpsj.fr

 Indicates open access to non-subscribers at [www.ajnr.org](http://www.ajnr.org)

<http://dx.doi.org/10.3174/ajnr.A6817>

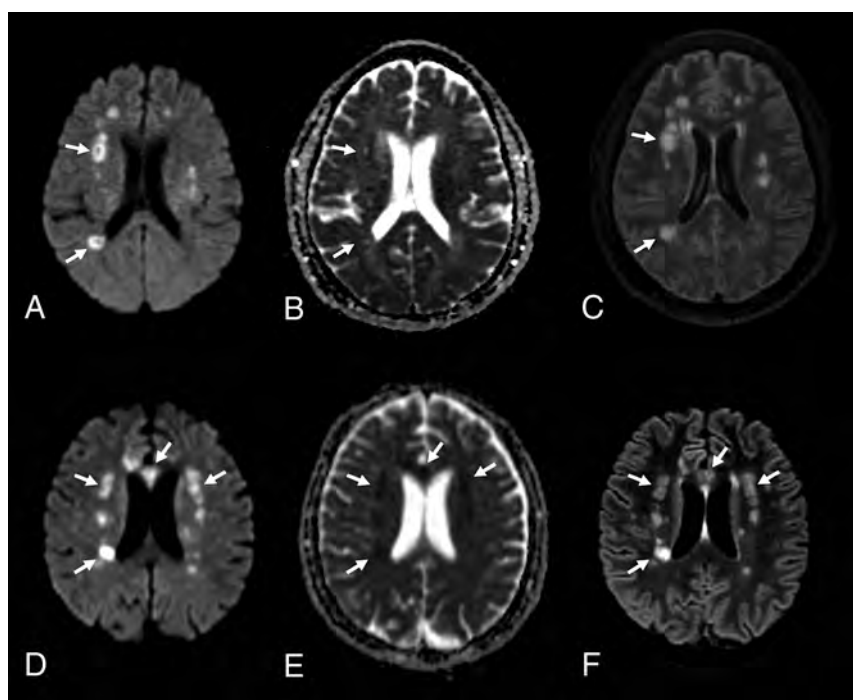


**FIG 1.** Brain MR imaging in 2 critically ill patients with COVID-19 with delayed recovery of consciousness after prolonged sedation, including a 52-year-old man (A–C), and a 44-year-old man (D–F). Axial diffusion-weighted (A and D), apparent diffusion coefficient (B and E), and 3D-FLAIR (C and F) images in both patients demonstrate nodular and ring-shaped lesions (arrows), involving the periventricular and deep white matter.

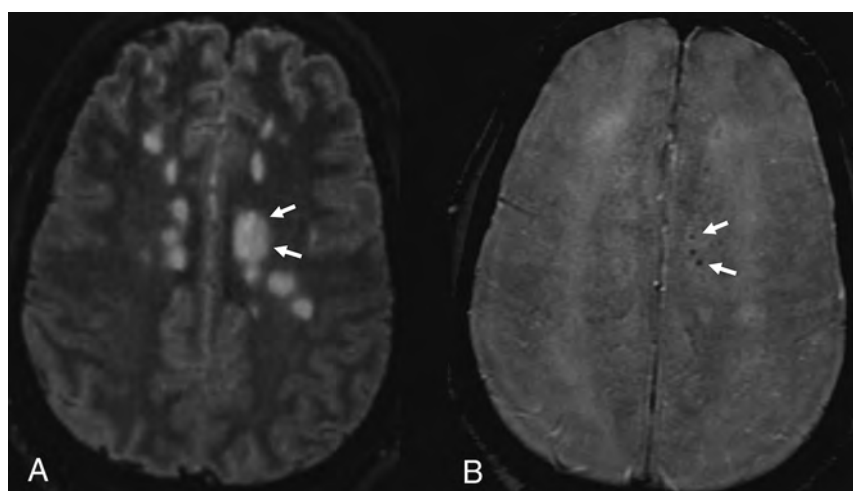


**FIG 2.** 3D FLAIR image (A) and susceptibility-weighted image (B) show mild hemorrhage within some of the lesions in patient 1 (arrows).

homeostasis with coagulopathy or cardioembolism from virus-related cardiac injury.<sup>4,5</sup>

However, in our case series, brain MR imaging appeared unusual considering the nodular ring shape as well as the topography (ie, asymmetric involvement of corpus callosum, deep and periventricular white matter) of the lesions. Indeed, such imaging findings could have potentially suggested inflammatory lesions such as acute disseminated encephalomyelitis, which is thought

to occur from cross-reactivity in immunity to viral antigens, triggering an autoimmune attack on the CNS.


One patient showed mild punctuated magnetic susceptibility artifacts within some of the brain lesions, suggesting hemorrhage. This could be due to necrosis or microthrombosis, which have both been described in SARS-CoV-2, in the brain or in the lung, and could be an additional argument for stroke lesions. Hemorrhagic lesions are also seen in acute necrotizing encephalopathy, which has been described in 1 patient with COVID-19.<sup>6</sup> Furthermore, the association of microhemorrhages with stroke lesions is suggestive of vasculitis, which has been histologically proved in several other organs including the lung, liver, kidney, or skin, in patients diagnosed with COVID-19.<sup>7</sup>

In conclusion, the etiology and physiopathology of these unusual brain lesions are still not clarified. Neurologists and neuroradiologists should be familiar with the broad spectrum of neuroimaging patterns associated with COVID-19.

## REFERENCES

1. Mao L, Jin H, Wang M, et al. **Neurologic manifestations of hospitalized patients with coronavirus disease 2019 in Wuhan, China.** *JAMA Neurol* 2020;77:1–9 CrossRef Medline
2. Baig AM, Khaleeq A, Ali U, et al. **Evidence of the COVID-19 virus targeting the CNS: tissue distribution, host-virus interaction, and proposed neurotropic mechanisms.** *ACS Chem Neurosci* 2020;11:995–98 CrossRef Medline
3. Gu J, Gong E, Zhang B, et al. **Multiple organ infection and the pathogenesis of SARS.** *J Exp Med* 2005;202:415–24 CrossRef Medline
4. Madjid M, Safavi-Naeini P, Solomon SD, et al. **Potential effects of coronaviruses on the cardiovascular system: a review.** *JAMA Cardiol* 2020 Mar 27. [Epub ahead of print] CrossRef Medline
5. Wang D, Hu B, Hu C, et al. **Clinical characteristics of 138 hospitalized patients with 2019 novel coronavirus-infected pneumonia in Wuhan, China.** *JAMA* 2020 Feb 7. [Epub ahead of print] CrossRef Medline
6. Poyiadji N, Shahin G, Noujaim D, et al. **COVID-19-associated acute hemorrhagic necrotizing encephalopathy: CT and MRI features.** *Radiology* 2020;296:E119–20 CrossRef Medline
7. Xu Z, Shi L, Wang Y, et al. **Pathological findings of COVID-19 associated with acute respiratory distress syndrome.** *Lancet Respir Med* 2020;8:420–42 CrossRef Medline

# COVID-19–Associated PRES–like Encephalopathy with Perivascular Gadolinium Enhancement

 G. Conte,  S. Avignone,  M. Carbonara,  M. Meneri,  F. Ortolano,  C. Cinnante, and  F. Triulzi



## ABSTRACT

**SUMMARY:** We describe the case of a 63-year-old woman who developed a coronavirus disease 2019–associated acute encephalopathy with perivascular gadolinium enhancement.

**ABBREVIATIONS:** ICU = intensive care unit; PRES = posterior reversible encephalopathy syndrome; SARS-Cov-2 = Severe Acute Respiratory Syndrome coronavirus 2

A 63-year-old woman was admitted to our hospital on day 7 (day 1 is the first day of symptoms) with fever, dry cough, fatigue, and subjective dyspnea. A nasopharyngeal swab for Severe Acute Respiratory Syndrome coronavirus 2 (SARS-Cov-2) was positive. Arterial blood gas analysis in room air showed mild hypoxemia (partial pressure of carbon dioxide, 31), causing mild respiratory alkalosis (pH = 7.48) and a low level of oxygen (partial pressure of carbon dioxide, 67). A chest x-ray was performed, showing bilateral ground-glass opacities. The patient had hypertension, but no other comorbidities were identified.

She was first admitted to the emergency ward and treated with a continuous positive airway pressure helmet; lopinavir/ritonavir was started as compassionate use approved by the ethics committee, as well as empirical piperacillin-tazobactam. Her respiratory parameters progressively worsened during the next days until she showed dyspnea, and her PaO<sub>2</sub>/FiO<sub>2</sub> ratio was 110 with a continuous positive airway pressure helmet at 15 cm of water and an inspiratory fraction of oxygen of 70%. On day 11, she was intubated and transferred to the intensive care unit (ICU). During her ICU stay, she initially received mechanical ventilation at a medium level of positive end-expiratory pressure (up to 14) and inhaled nitric oxide and underwent two 20-hour prone-position cycles. She also developed a moderately acute

kidney injury (measured creatinine clearance of 28 mL/minute), which never required replacement therapy, and high levels of hepatic enzymes and bilirubin, which caused us to stop lopinavir/ritonavir. An angiotensin-converting-enzyme inhibitor was introduced to reduce blood pressure in the ventilator weaning phase after 15 days on sedative drugs and opioids.

Regarding the treatment given in the ICU that was different from the usual care, she received anakinra (an interleukin 1 antagonist) due to a persistent high level of C-reactive Protein and ferritin and a high dose of subcutaneous heparin to target an activated partial thromboplastin time ratio of 2. On day 24, antibiotics were suspended until she developed ventilator-associated pneumonia by methicillin-sensitive *Staphylococcus aureus*, and cefazolin was given. Gradually, her clinical conditions improved, and she was weaned from the ventilator on day 28, after 24 hours of spontaneous breathing. On day 29, she was transferred back to medium intensity care in relatively good condition: afebrile, low-flow oxygen therapy via nasal cannula with normal peripheral capillary oxygen saturation and respiratory mechanics, normal blood pressure, and diuresis with acute kidney and hepatic injuries improving.


On day 30, she presented with left head and eye deviation and continuous tonic seizures on the left side of the body. After ineffective treatment with diazepam and lacosamide, the patient was sedated, intubated, and transferred again to the ICU. A phenytoin IV load was started, followed by enteral maintenance dosages, associated with diazepam infusion with clinical resolution. An electroencephalogram showed periodic lateralized epileptiform discharges in the right posterior regions, without clinical correlation. A lumbar puncture revealed only a slightly elevated protein level (70 mg/dL). A polymerase chain reaction test for virus

Received June 6, 2020; accepted after revision July 14.

From the Neuroradiology Unit (G.C., S.A., C.C., F.T.), Neuroscience Intensive Care Unit (M.C., F.O.), Department of Anesthesia and Critical Care, and Neurology Unit (M.M.), Fondazione IRCCS Ca' Granda Ospedale Maggiore Policlinico, Milan, Italy.

Please address correspondence to Giorgio Conte, MD, Fondazione IRCCS Ca' Granda Ospedale Maggiore Policlinico, Neuroradiology Unit, Via F. Sforza 35, Milan 20122, Italy; e-mail: giorgioconte.unimed@gmail.com; @GiorgioConte86

 Indicates open access to non-subscribers at [www.ajnr.org](http://www.ajnr.org)

 Indicates article with supplemental on-line photo.

<http://dx.doi.org/10.3174/ajnr.A6762>



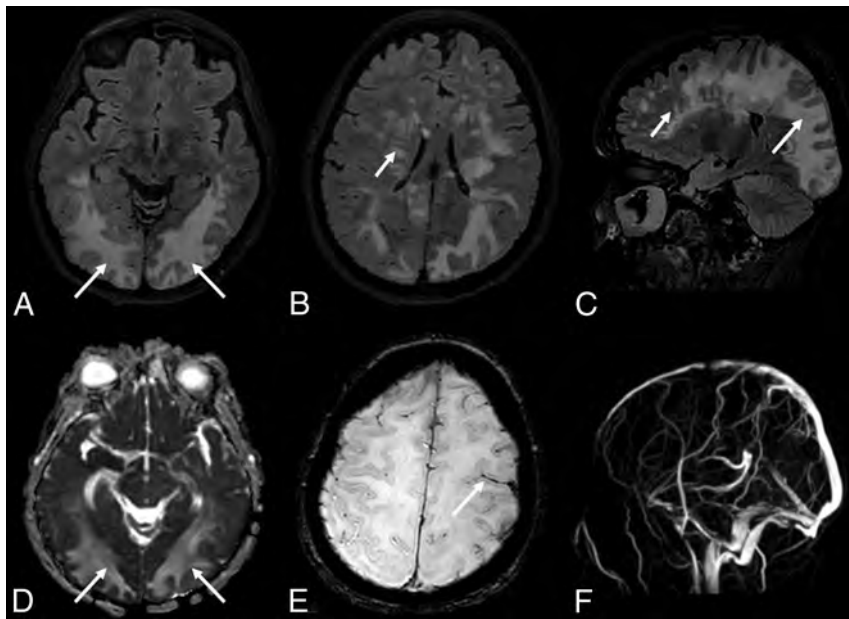


**FIG 1.** The FLAIR sequence shows multiple lesions of the white matter of both hemispheres (A–C), more striking in the posterior regions with a tumefactive appearance (*long arrows*) and with a multifocal perivascular pattern in the deep white matter regions (*short arrows*). The lesions (*arrows*) show high values on the apparent diffusion coefficient map (D), suggesting increased water content in the parenchyma. The SWI sequence (E) shows a subarachnoid blood effusion along the left precentral sulcus (*arrow*). MR venography (F) excludes intracranial thrombosis.

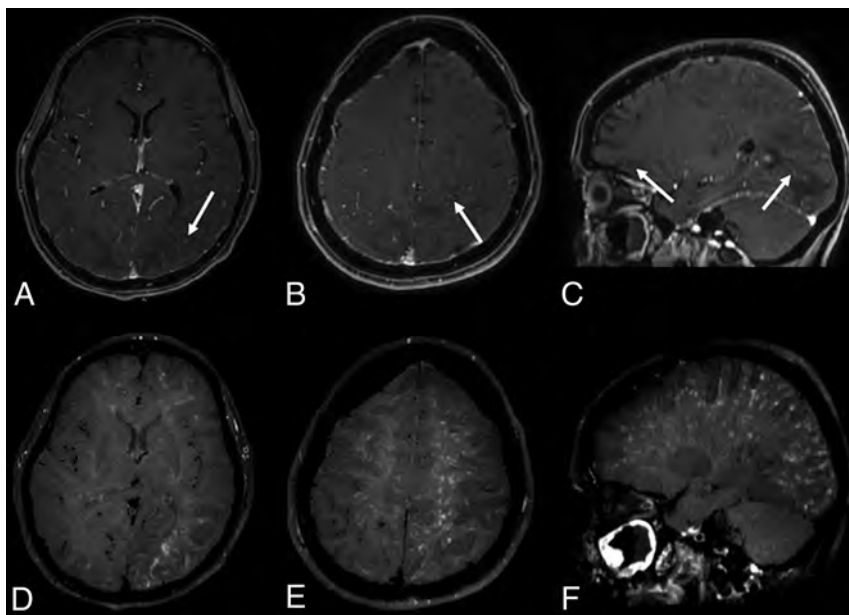


**FIG 2.** The contrast-enhanced 3D conventional T1-weighted sequence (A–C) shows multiple spotlike gadolinium enhancement (*arrows*) in the posterior white matter and left hemisphere. The postcontrast 3D-T1-weighted black-blood sequence (D–F) shows a stratiform perivascular gadolinium enhancement in the white matter of both cerebral hemispheres. Neither wall enhancement of the large intracranial arterial vessels nor leptomeningeal enhancement are observed on postcontrast sequences.

detection in the CSF, including SARS-Cov-2, was negative. MR imaging showed cortical swelling and restricted diffusivity in the posterior regions of the right hemisphere, corresponding to the epileptic focus (On-line Figure). We observed multiple, partially confluent, tumefactive lesions of the sub- and supratentorial white matter hemispheres, with prevalence in the posterior hemisphere regions, which appeared as increased signal intensity on T2-weighted images, consistent with brain edema. The susceptibility-weighted images showed a subarachnoid blood effusion along the left precentral sulcus and excluded intraparenchymal hemorrhagic petechiae. MR venography excluded intracranial thrombosis (Fig 1). The contrast-enhanced T1-weighted black-blood sequence showed a miliari-form perivascular gadolinium enhancement in the supra- and subtentorial white matter. Neither wall enhancement of the large intracranial arterial vessels nor leptomeningeal enhancement was observed on postcontrast sequences (Fig 2).

The patient gradually improved. On day 41, she was extubated and was discharged to the ward 2 days later with residual mild left hemiparesis and left lateral hemianopsia. A control electroencephalogram showed only sporadic sharp waves and spikes in the right posterior regions. At follow-up, on MR imaging on day 49, the cerebellar lesions disappeared, cerebral lesions were markedly reduced, perivascular enhancement was not detected, and diffusion-weighted imaging findings were negative. On day 61, the patient was discharged from the hospital and referred to rehabilitation. At 180-day follow-up, the patient was at home, without motor deficits but with partial visual loss in the left eye (extended Glasgow Outcome Scale, 4; mRS score, 3).

We made a diagnosis of posterior reversible encephalopathy syndrome

















(PRES)-like encephalopathy with peculiar MR imaging findings. The miliaryform perivascular postgadolinium enhancement has not previously been reported among typical and atypical MR imaging findings in PRES.<sup>1,2</sup> The perivascular enhancement might be a sign of immune-mediated small-vessel damage, leading to altered integrity of the blood-brain barrier and brain edema, as supposed in PRES.<sup>3</sup>

Disclosures: Marco Carbonara—**UNRELATED:** *Travel/Accommodations/Meeting Expenses Unrelated to Activities Listed:* European Union, *Comments:* In the context of CENTER-TBI-related activities.

## REFERENCES

1. Bartynski WS. **Posterior reversible encephalopathy syndrome, Part 1: fundamental imaging and clinical features.** *AJNR Am J Neuroradiol* 2008;29:1036–42 CrossRef Medline
2. Saad AF, Chaudhari R, Wintermark M. **Imaging of atypical and complicated posterior reversible encephalopathy syndrome.** *Front Neurol* 2019;10:964 CrossRef Medline
3. Fugate JE, Rabinstein AA. **Posterior reversible encephalopathy syndrome: clinical and radiological manifestations, pathophysiology, and outstanding questions.** *Lancet Neurol* 2015;14:914–25 CrossRef Medline

# NAA is a Marker of Disability in Secondary-Progressive MS: A Proton MR Spectroscopic Imaging Study

 B.S. Solanky,  N.A. John,  F. DeAngelis,  J. Stutters,  F. Prados,  T. Schneider,  R.A. Parker,  C.J. Weir,  A. Monteverdi,  D. Plantone,  A. Doshi,  D. MacManus,  I. Marshall,  F. Barkhof,  C.A.M. Gandini Wheeler-Kingshott, and  J. Chataway, for the MS-SMART Investigators



## ABSTRACT

**BACKGROUND AND PURPOSE:** The secondary progressive phase of multiple sclerosis is characterised by disability progression due to processes that lead to neurodegeneration. Surrogate markers such as those derived from MRI are beneficial in understanding the pathophysiology that drives disease progression and its relationship to clinical disability. We undertook a 1H-MRS imaging study in a large secondary progressive MS (SPMS) cohort, to examine whether metabolic markers of brain injury are associated with measures of disability, both physical and cognitive.

**MATERIALS AND METHODS:** A cross-sectional analysis of individuals with secondary-progressive MS was performed in 119 participants. They underwent <sup>1</sup>H-MR spectroscopy to obtain estimated concentrations and ratios to total Cr for total NAA, mIns, Glx, and total Cho in normal-appearing WM and GM. Clinical outcome measures chosen were the following: Paced Auditory Serial Addition Test, Symbol Digit Modalities Test, Nine-Hole Peg Test, Timed 25-foot Walk Test, and the Expanded Disability Status Scale. The relationship between these neurometabolites and clinical disability measures was initially examined using Spearman rank correlations. Significant associations were then further analyzed in multiple regression models adjusting for age, sex, disease duration, T2 lesion load, normalized brain volume, and occurrence of relapses in 2 years preceding study entry.

**RESULTS:** Significant associations, which were then confirmed by multiple linear regression, were found in normal-appearing WM for total NAA (tNAA)/total Cr (tCr) and the Nine-Hole Peg Test ( $p = 0.23$ ; 95% CI, 0.06–0.40); tNAA and tNAA/tCr and the Paced Auditory Serial Addition Test ( $p = 0.21$ ; 95% CI, 0.03–0.38) ( $p = 0.19$ ; 95% CI, 0.01–0.36); mIns/tCr and the Paced Auditory Serial Addition Test, ( $p = -0.23$ ; 95% CI, -0.39 to -0.05); and in GM for tCho and the Paced Auditory Serial Addition Test ( $p = -0.24$ ; 95% CI, -0.40 to -0.06). No other GM or normal-appearing WM relationships were found with any metabolite, with associations found during initial correlation testing losing significance after multiple linear regression analysis.

**CONCLUSIONS:** This study suggests that metabolic markers of neuroaxonal integrity and astrogliosis in normal-appearing WM and membrane turnover in GM may act as markers of disability in secondary-progressive MS.

**ABBREVIATIONS:** CSI = chemical shift imaging; EDSS = Expanded Disability Status Scale; 9HPT = Nine-Hole Peg Test; IPS = information processing speed; NAWM = normal-appearing white matter; PASAT3 = Paced Auditory Serial Addition Test (3-second); PPMS = primary-progressive MS; SDMT = Symbol Digit Modalities Test; SPMS = secondary-progressive MS; T25-FW = Timed 25-foot Walk; tCho = total Cho; tCr = total Cr; tNAA = total NAA; WML = white matter lesions; PMS = Progressive forms of MS

Received June 3, 2020; accepted after revision July 24.


From the Department of Neuroinflammation (B.S.S., N.A.J., F.D., J.S., F.P., D.P., A.D., D.M., C.A.M.G.W.-K., J.C.), Faculty of Brain Sciences, Queen Square Multiple Sclerosis Centre, UCL Queen Square Institute of Neurology, and Centre for Medical Image Computing (F.P., F.B.), Department of Medical Physics and Biomedical Engineering, University College London, London, UK; Edinburgh Clinical Trials Unit (R.A.P., C.J.W.), Usher Institute, and Centre for Clinical Brain Sciences (I.M.), University of Edinburgh, Edinburgh, UK; Brain MRI 3T Research Center (C.A.M.G.W.-K.), Scientific Institute for Research, Hospitalization and Healthcare Mondino National Neurological Institute Foundation, Pavia, Italy; Department of Brain and Behavioural Sciences (A.M., C.A.M.G.W.-K.), University of Pavia, Pavia, Italy; National Institute for Health Research (F.B.), University College London Hospitals Biomedical Research Centre, London, UK; and Department of Radiology and Nuclear Medicine (F.B., J.C.), MS Center Amsterdam, Amsterdam, the Netherlands; Philips UK (T.S.), Guildford, Surrey, UK; and Universitat Oberta de Catalunya (F.P.), Barcelona, Spain.


Bhavana S. Solanky and Nevin A. John are joint first authors and contributed equally to this work.

This work was funded by the Efficacy and Mechanism Evaluation program as project number 11/30/11. MS-SMART is an investigator-led project sponsored by University College London. This independent research is awarded by and funded by the Medical Research Council, the UK MS Society, and the National MS Society and is managed by the National Institute for Health Research on behalf of the Medical Research Council–National Institute for Health partnership. Additional support comes from the University of Edinburgh; the National Institute for Health Research University College London Hospitals Biomedical Research Centre and University College London; and the National Institute for Health Research Leeds Clinical Research Facility (Dental Translational and Clinical Research Unit).

C.J.W. and R.A.P. were supported in this work by National Health Service Lothian via the Edinburgh Clinical Trials Unit.

Please address correspondence to Nevin Alex John, MD, Queen Square Institute of Neurology, University College London, Queen Square, London, WC1N 3BG, United Kingdom; e-mail: nevin.john@ucl.ac.uk

 Indicates open access to non-subscribers at [www.ajnr.org](http://www.ajnr.org)

 Indicates article with supplemental on-line tables.

<http://dx.doi.org/10.3174/ajnr.A6809>



Secondary-progressive MS (SPMS) is the dominant progressive form of multiple sclerosis that is characterized by accumulating disability due to a variety of neurodegenerative processes.<sup>1</sup> These include microglial activation with subsequent formation of reactive oxygen species inducing mitochondrial damage, sodium channel dysfunction leading to histotoxic hypoxia and axonal energy failure, and glutaminergic excitotoxicity.<sup>2-4</sup>

Surrogate markers of brain injury are valuable in improving our understanding of the pathophysiology driving clinical disability in progressive forms of MS (PMS). Surrogate imaging-based markers such as MR imaging–based lesional and atrophy metrics can identify existing inflammatory injury and axonal loss and provide adjunctive prognostic information. Yet existing imaging based-measures are relatively limited in their ability to demonstrate metabolic or microstructural changes and show only a modest association with clinical disability outcomes in PMS.<sup>5</sup> This is where advanced nonstructural MR imaging techniques such as <sup>1</sup>H-MR spectroscopy are attractive to further understand this neuropathology and its association with clinical disability in progressive forms of MS.

By means of <sup>1</sup>H-MR spectroscopy, neurometabolites of interest in MS include the following: *N*-acetylaspartate plus *N*-acetylaspartylglutamate (total NAA = tNAA), a marker of neuroaxonal integrity and mitochondrial function;<sup>6,7</sup> Glx, the sum of the excitatory neurotransmitter glutamate and its precursor glutamine;<sup>4</sup> myo-inositol (mIns), a marker of glial cell activity, most likely astrogliosis; and total choline (tCho = glycerophosphocholine and phosphocholine), a marker of membrane turnover.<sup>7,8</sup> Many studies have demonstrated decreases in tNAA and tNAA/tCr and increases in total creatine (tCr = creatine and phosphocreatine) and inositol in normal-appearing white matter (NAWM) and GM in SPMS.<sup>9</sup> In a recent meta-analysis of <sup>1</sup>H-MR spectroscopy studies, effect sizes for a reduction in NAA and NAA/Cr were larger in PMS compared with relapsing-remitting MS.<sup>9</sup> There have been conflicting results from studies examining disability associations in PMS: Several studies showed no association between metabolites (NAA, Glx, mIns, tCho) and the Expanded Disability Status Scale score (EDSS),<sup>10-13</sup> while others showed moderate associations with EDSS, the Nine-Hole Peg Test (9HPT), and the Timed 25-foot Walk Test (T25-FW) in cortical GM and NAWM.<sup>14-16</sup> Of the studies examining cognitive performance (including information processing speed [IPS]) in PMS, no associations were found in sample sizes ranging from 14 to 31, with only 2 of these studies containing pure SPMS cohorts.<sup>13,14,16-18</sup>

The rationale for this cross-sectional study was to further define metabolite levels and their associations with disability in a much larger sample of individuals with SPMS than has been achieved before.

## MATERIALS AND METHODS

### Participants and Measures

Participants were recruited from the MS-Secondary Progressive Multi-Arm Randomization Trial (MS-SMART) (NCT01910259), a Phase IIb double-blind, placebo-controlled, multiarm, multicenter study assessing the neuroprotective potential of amiloride, fluoxetine, and riluzole in SPMS. Details of the trial protocol and final

trial results were recently published.<sup>19,20</sup> Participants recruited into the study were individuals with SPMS, 25–65 years of age with an EDSS score of 4.0–6.5, which showed evidence of progression independent of relapses during the past 2 years. Participants were randomized 1:1:1:1 to amiloride, fluoxetine, riluzole, or placebo, and the primary outcome measure was the percentage brain volume change over 96 weeks.

Participants involved in the MS-SMART study at our site (Queen Square MS Center, University College London) were invited to take part in an optional “Advanced MR imaging sub-study” inclusive of <sup>1</sup>H-MR spectroscopy scans. Recruited participants had their MR imaging and clinical assessments before randomization and commencing study medication. They underwent a series of clinical assessments including EDSS, T25-FW, 9HPT, and 2 standard measures of IPS: the Paced Auditory Serial Addition Test-3 (PASAT3) and the Symbol Digit Modalities Test (SDMT).<sup>21-23</sup> MR imaging measures included normalized brain volume, NAWM, cortical GM, and T2 lesion volume.

Consent was obtained for all participants according to the Declaration of Helsinki and ethical approval for the study was provided by the Scotland A Research Ethics Committee (13/SS/0007).

### MR Imaging Acquisition

Neurometabolite spectra from multiple voxels within 1 scan were acquired using a technique known as chemical shift imaging (CSI) to determine estimated neurometabolite concentrations and ratios by obtaining average metabolite concentrations from a slice of neuronal tissue.<sup>24</sup> Imaging was acquired using an Achieva 3T MR imaging scanner (Philips Healthcare) with a 16-channel neurovascular coil.

All participants underwent the following scans:

**MRS.** A 210 × 160 mm<sup>2</sup> VOI with a 15-mm slice thickness was selected for CSI, placed superior to the lateral ventricles (Fig 1). The inferior margin of the slice was positioned at the superior margin of the corpus callosum, angulated to the anterior/posterior commissure line. At the baseline visit, a screen shot of the exact positioning of the CSI was saved (Fig 1) to be used as a reference for subsequent time points. The slice placement was chosen to avoid the ventricles to ensure that all voxels were of consistent quality and shim. The CSI VOI was subdivided into a 21 × 16 grid, with a voxel size of 10 × 10 × 15 mm<sup>3</sup>. Spectra were acquired using the manufacturer’s 2D point-resolved spectroscopic sequence (short TE = 35 ms, TR = 2000 ms). Outer volume suppression using fat saturation was applied to limit artifacts, and the VOI was shimmed using the pencil beam-automatic technique.<sup>25</sup> Chemical shift selective saturation pulses were used for water suppression. A reference scan with no water suppression was also performed with identical parameters during the same examination for quantification. tNAA (total NAA = *N*-acetylaspartate and *N*-acetylaspartylglutamate), mIns, Glx (sum of glutamate and glutamine), tCho (total choline = glycerophosphocholine and phosphocholine), and each of their ratios to total creatine (sum of creatine and phosphocreatine) were calculated.

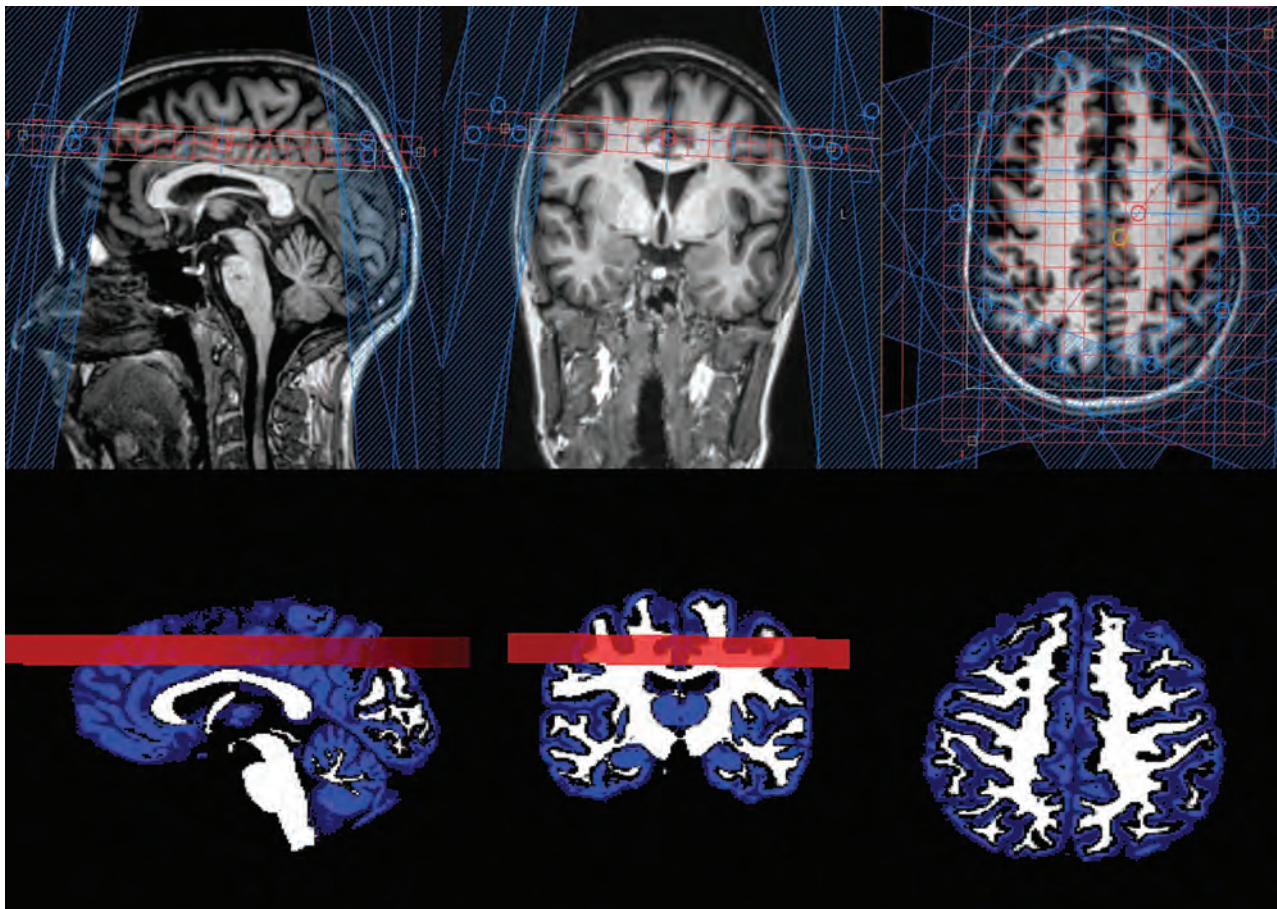


**FIG 1.** Proton MR spectroscopy slice placement and mask. The *upper panel* demonstrates slice placement in the sagittal, coronal, and axial planes. The *lower panel* shows an example of the chemical shift mask for normal-appearing white matter and gray matter.

**Structural MR Imaging.** Scans for structural information and lesion assessment were collected before MR spectroscopy as detailed below and were also used for planning purposes. A sagittal 3D-T1WI with matrix =  $256 \times 256$ , FOV =  $256 \times 256$  mm<sup>2</sup>, 180 sagittal slices 1 mm thick, flip angle =  $8^\circ$ , TR/TI/TE = 7/840/3.2 ms (turbo factor = 230) was acquired for structural information. An axial proton-density T2 (TR/TE1/TE2 = 3500/19/85 ms, turbo factor = 10) and FLAIR sequences (TR/TI/TE = 8000/2400/125 ms, turbo factor = 24) with matrix =  $240 \times 180$ , FOV =  $240 \times 180$  mm<sup>2</sup>, and 50 slices 3 mm thick) were acquired for lesion assessment.

### MR Imaging Analysis

**Brain and WM Lesion Segmentation.** To obtain segmentations of WM, GM, and CSF, a NIfTI image was created in the same space as the axial proton-density T2 to represent the positioning of the CSI matrix and to act as a mask for the MR spectroscopy volume (Fig 1). The axial proton-density T2 image was rigidly registered and resampled to the 3D T1 image space using Nifty Reg (<https://sourceforge.net/projects/niftyreg/>),<sup>26</sup> and an identical transform was applied to the CSI mask to get the matrix in the desired space for segmentation. WM lesions were semimanually delineated using Jim 7 software (<http://www.xinapse.com/home.php>) on the T2WI using the FLAIR image as a reference. After lesion-filling,<sup>27</sup> the 3D-T1WI was segmented using Geodesical Information Flows, enabling the calculation of T2 lesion volume.<sup>28</sup>

**Brain Volume Measures.** Normalized brain volume was calculated using the FSL SIENAX (<http://fsl.fmrib.ox.ac.uk/fsl/fslwiki/SIENAX>) method from the segmented 3D-T1WI.<sup>29</sup> SIENAX rescales each subject head to a Montreal Neurological Institute atlas size, hence correcting each individual brain volume. Thus, the normalized brain volume is the volume of the rescaled brain, and it allows us to correct brain volume for variations in head size, effectively resulting in a measure of cross-sectional atrophy.<sup>29</sup>

**CSI Spectra and Image Postprocessing.** Following the acquisition, postprocessing of spectra were completed using Linear Combination of Model spectra (LCModel, Version 6.3-1A; <http://www.lcmodel.com>), a program used to fit MR spectroscopy data to a basis set, which, together with the water reference scan, enabled estimated quantification of metabolites as well as providing a set of parameters to perform quality assurance for each voxel.<sup>30</sup> The LCModel basis set was provided by S. Provencher (personal written communication, 24 October 2010).

The water reference scan was used to find a scaling factor for the basis set, as detailed in the LCmodel manual.<sup>30</sup> This carries with it the assumption that the concentration of water in the spectrum is equivalent to that of healthy white matter (35880 mM), which, in the absence of a specific measure per patient, is often used as the default.<sup>30,31</sup> In addition, to correct for T2 relaxation, we set the default water density to 0.7, based on TE = 30 and on Ernst



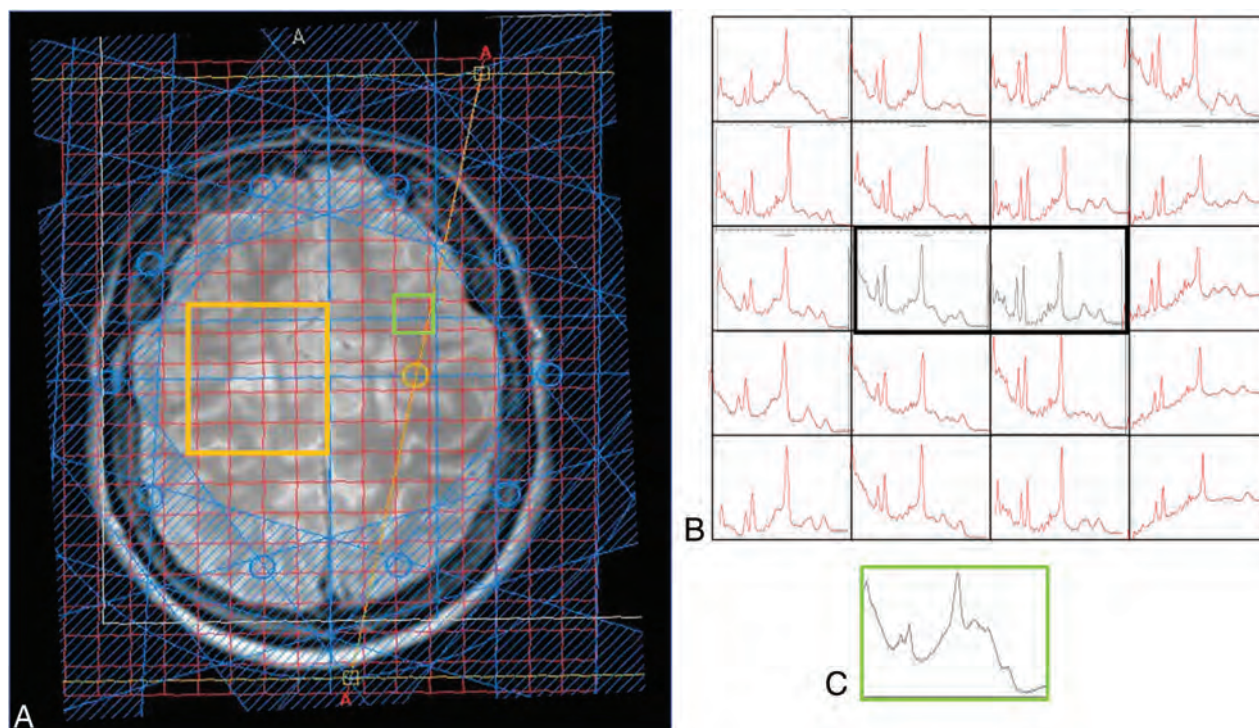


**FIG 2.** Sample spectra and the chemical shift grid show the position where representative spectra originate, including a lesion (A), accepted spectra in red and lesion in black (B), and spectra from a rejected voxel (C). The position is shown in green in A.

et al,<sup>31</sup> who found that the major water compartment in brain has  $T2 \approx 80$  ms [ $\exp(-TE/T2) = \exp(-30/80) \approx 0.7$ ].<sup>30</sup> If substituted for  $TE = 35$  ms, this reduces to 0.65; however, in the absence of an accurate  $T2$  in pathology, the default was again kept (Section 11.2; LCmodel manual). Because we used a long TR and water scaling, no correction for  $T1$  was made.

Spectra from individual voxels were automatically rejected if any neurometabolite Cramer-Rao lower bounds were  $>20\%$ , the full width at half maximum of the tNAA spectral peak was  $>15$ Hz, or the SNR was  $<9$ . All voxels that passed the automated step were visually inspected by an experienced assessor (B.S.S.) to look for baseline artifacts, nonrandom residuals, or outer volume contamination that may prevent the accurate measurement of neurometabolites. The resulting set of voxels made up a clean dataset, which passed the automated and visual quality assurance.

Figure 2 is a sample spectrum from a single voxel of brain tissue and spectra from the chemical shift imaging grid.

**Neurometabolite Analysis.** Neurometabolites were analyzed in the following 2 ways:

1. Estimated metabolite concentrations: The mean metabolite concentrations (tNAA, mIns, Glx, tCho) of all voxels that passed the automatic and visual quality assurance (clean data) were averaged for each participant to calculate a per-patient estimated metabolite concentration reported in institutional units.
2. Metabolite ratios: Mean neurometabolite ratios (tNAA, mIns, Glx, tCho) to tCr were calculated from the clean data for each participant.

Metabolite concentrations and ratios were then calculated in the following 2 tissue types: NAWM and GM.

To eliminate contamination by white matter lesions (WML) and CSF, we first removed any voxels containing  $>1\%$  WML and  $>15\%$  CSF. Linear regression models were used to explore the association between the concentration of each metabolite and the white or gray matter fraction on a voxel-by-voxel basis. These models were then extrapolated to find the value for each metabolite in which the GM or WM fraction was 100%, to find the metabolite concentration for each tissue type. Metabolite outliers were removed from the regression models, leaving us with per-patient metabolite values. This method has been previously described.<sup>32</sup> Owing to the small lesion load in the acquired slice (average WML fraction in the SPMS cohort was 0.01), calculation of metabolite values in WML could not be completed.

### Statistical Analyses

Neurometabolic data and distribution over the cohort were summarized descriptively. Statistical analysis was completed using R statistical and computing software (Version 3.5.1; <http://www.r-project.org/>).<sup>33</sup> All  $P$  values were 2-tailed and reported using a .05 significance level.

### Neurometabolite Correlations with Clinical Disability Measures

To examine the association between tissue-specific neurometabolites and clinical disability measures (EDSS, T25-FW, 9HPT, PASAT3, SDMT), we calculated Spearman rank correlation coefficients, given the non-normal distribution of the clinical disability measures. The scope of the analysis was to analyze the association between our key metabolites in NAWM and GM



(tNAA, mIns, Glx, tCho, and their ratios to tCr) and the disability measures listed above. During correlation testing, 60 comparisons were prespecified, but here we report 80 after tCho and tCho/tCr were added following a post hoc request by a peer reviewer. These are reported in On-line Table 1. In reporting multiple analyses, we were guided by considerations outlined in Patel et al.<sup>34</sup> Multiplicity adjustment is not required when a list of hypotheses of primary importance are prespecified; emphasis is placed on being explicit and transparent about the extent of multiplicity; and the magnitude of observed associations is interpreted in the context of the background literature.

When statistically significant correlations were found in the Spearman rank correlation analysis, a subsequent multivariable linear regression analysis was performed, adjusting for age, sex, disease-duration from onset, occurrence of relapses in the preceding 2 years, T2 lesion volume, and normalized brain volume. Model diagnostics undertaken to assess the regression model included the following: calculation of variance inflation factors to determine

multicollinearity, the Cook's distance to determine effect of leveraged data points, and plots of studentized residuals against adjusted predicted values to check residual homoscedasticity.

## RESULTS

One hundred fifty-four participants gave consent for the Advanced MR Imaging substudy from January 2015 to June 2016. Of these 154 participants, 6 failed the CSI quality assurance, leaving 148 participants in the CSI arm of the Advanced MR Imaging substudy at baseline.

In total, there were 8361 CSI voxels for the analysis that passed both automatic and visual quality assurance; 3035 voxels remained after excluding voxels that contained >1% WML and >15% CSF (mean, 20.5 ± 9.2 voxels per patient). After calculating metabolite values and removing metabolic outliers, 119 participants with SPMS remained for analysis. Cohort demographics are provided for the cohort of 119 participants who underwent correlation testing and regression analysis; 81/119 (68%) were women and 108/119 (91%) had not experienced a relapse in the 2 years before randomization. Further details of the cohort are shown in Table 1.

Estimated neurometabolite concentrations (in institutional units) and metabolite ratios to tCr can be found in the On-line Table 2.

Metabolite concentrations/ratios that showed statistically significant correlations to disability measures in NAWM and GM are shown in On-line Table 1.

Table 2 shows the results of the regression analysis for neurometabolites that were significantly associated with clinical disability measures after adjusting for covariates. Neurometabolites that showed a statistically significant association on the Spearman rank correlation but lost statistical significance after regression analysis are not shown in Table 2. In NAWM, associations were seen between tNAA/tCr and 9HPT ( $\beta = 0.19$ ,  $P = .04$ ); tNAA and tNAA/tCr and PASAT3 ( $\beta = 0.17$ ,  $P = .04$ ) ( $\beta = 0.19$ ,  $P = .02$ ), respectively; and mIns/tCr and PASAT3 ( $\beta = -0.22$ ,  $P = .007$ ). In GM, tCho was associated with PASAT3 ( $\beta = -0.17$ ,  $P = .04$ ).

## DISCUSSION

This is the largest reported cohort of individuals with SPMS undergoing <sup>1</sup>H-MR spectroscopy. On-line Table 1 shows all of the correlations that were statistically significant indicated. These were then explored in a multiple regression analysis (Table 2). The results suggest a relationship in NAWM between tNAA (tNAA/tCr) and mIns/tCr and IPS performance (PASAT3) and between tNAA/tCr and upper limb

**Table 1: Baseline demographics and characteristics (n = 119)**

Clinical Variable	Mean (SD)
Age (yr)	54.2 (6.7)
EDSS <sup>a</sup>	6.0 (4.0–6.5)
Normalized brain volume (mL)	1418 (87.3)
Nine-Hole Peg Test (sec <sup>-1</sup> ) <sup>b</sup>	0.035 (0.01)
SPMS duration (yr)	22.3 (9.2)
PASAT3 score (of 60)	43.0 (11.5)
SDMT score (of 110)	46.9 (11.0)
T2 lesion volume (mL) <sup>a</sup>	9.7 (0.3–34.6)
T25–FW (sec) <sup>a</sup>	10.6 (4.3–180.0)

<sup>a</sup> Median (range).

<sup>b</sup> The Nine-Hole Peg Test was calculated by taking the reciprocal of the average of 2 trials for each arm and taking the mean.

**Table 2: Results from multiple regression analysis examining associations between neurometabolites and clinical disability measures<sup>a</sup>**

Predictors	Standardized $\beta$	Standardized 95% CI	P
Nine-Hole Peg Test (n = 118) <sup>b</sup>			
NAWM tNAA/tCr	0.19	0.01–0.36	.04
Paced Auditory Serial Addition Test (n = 119)			
NAWM tNAA	0.17	0.01–0.34	.04
Sex <sup>c</sup>	–0.23	–0.42 to –0.05	.01
T2 lesion volume	–0.47	–0.64 to –0.30	<.001
Paced Auditory Serial Addition Test (n = 118) <sup>d</sup>			
NAWM tNAA/tCr	0.19	0.03–0.35	.02
Sex <sup>c</sup>	–0.26	–0.44 to –0.08	.006
T2 lesion volume	–0.46	–0.63 to –0.29	<.001
Paced Auditory Serial Addition Test (n = 119)			
NAWM mIns/tCr	–0.22	–0.39 to –0.06	.007
Sex <sup>c</sup>	–0.25	–0.43 to –0.07	.008
T2 lesion volume	–0.47	–0.64 to –0.30	<.001
Paced Auditory Serial Addition Test (n = 119)			
GM tCho	–0.17	–0.33 to –0.01	.04
T2 lesion volume	–0.48	–0.65 to –0.31	<.001

<sup>a</sup> Covariates in the model include age, sex, duration from onset, occurrence of relapse in the 2 years preceding randomization, T2 lesion volume, and normalized brain volume. The table highlights only the predictor variables that were significant from the multiple regression models.

<sup>b</sup> The Nine-Hole Peg Test was calculated by taking the reciprocal of the average of 2 trials for each arm and taking the mean.

<sup>c</sup> Male is reference category.

<sup>d</sup> One hundred eighteen participants in this cohort because 1 case was removed due to a highly leveraged point.

function (9HPT). In GM, tCho was associated with IPS performance. While a number of other correlations were identified in the correlation analysis, no associations with EDSS or T25-FW were found in GM or NAWM after multiple regression analysis.

### **Relationships between Neurometabolites and Clinical Disability**

**Upper Limb Function.** Previous smaller studies examining tNAA or tNAA/tCr in NAWM in PMS have not demonstrated statistically significant associations between neuroaxonal integrity and upper limb function (Table 2).<sup>14,16</sup> Our study suggests that as neuroaxonal integrity (and mitochondrial function) decreases, upper limb function, as reflected by 9HPT, also decreases. The association found between tNAA/tCr and 9HPT during the correlation analysis (On-line Table 1) and multiple regression is in the expected direction with decreased tNAA/tCr associated with decreased upper limb function (as reflected by the 9HPT). It remains of interest whether this association is reflective of regional changes in NAWM that affect specific tracts related to upper limb and hand function or more reflective of generalized changes throughout the NAWM. With the association being seen with 9HPT but not T25-FW, it may suggest that changes in neuroaxonal integrity and mitochondrial function in the brain play a more important role in upper limb dysfunction in the progressive stage of the disease. This could be further explained by the hypothesis that PMS is a length-dependent central axonopathy, whereby the legs are affected earlier due to greater susceptibility of spinal cord motor neurons and the greater reserve capacity of shorter neuronal pathways such as the upper limb earlier in progressive disease.<sup>35</sup>

Sastre-Garriga et al<sup>14</sup> found an association between tNAA and 9HPT in cortical GM ( $r = -0.48$ ,  $P = .03$ ), and in this context, the correlation in this study of 0.22 (On-line Table 1) is lower, though our association was in NAWM rather than cortical GM. Our result contrasts with previous studies, but this contrast could be explained by the differences in cohort characteristics, whereby Sastre-Garriga et al examined 43 predominantly male participants with early PPMS with a lower median EDSS of 4.5 and Obert et al<sup>16</sup> analyzed 15 participants with SPMS with a median EDSS score of 4.5.<sup>14</sup>

**Information Processing Speed.** The aforementioned study by Obert et al examined measures of IPS (PASAT3) and its relationship to in vivo neurometabolites in NAWM in SPMS ( $n = 15$ ). This study did not show any associations.<sup>16</sup> Several other studies reported results in the form of standardized scores such as multiple sclerosis functional composite or the Brief Repeatable Battery Neuropsychological Tests, making it difficult to discern the true relationship between IPS and neurometabolites in PMS.<sup>13,14,18</sup> First, our findings of an association between NAWM tNAA and tNAA/tCr with PASAT3 scores (On-line Table 1 and Table 2 and Fig 3) are in the expected direction, with decreased neuroaxonal integrity in NAWM associated with decreased performance on the PASAT3. We were unable to determine whether there was a predilection to a specific region of NAWM or whether it was possibly associated with altered functional or structural connectivity. Solana et al<sup>32</sup> examined this issue in a mixed cohort of relapsing-remitting MS and SPMS, demonstrating that tNAA/tCr and mIns/tCr in

WM were associated with abnormal efficiency in the frontoparietal network, with abnormalities in this network associated with impaired attention and processing speed (compared with healthy controls).

Our findings differed from those of Obert et al,<sup>16</sup> who used a similar <sup>1</sup>H-MR spectroscopy acquisition to calculate tNAA and tNAA/tCr, but their SPMS cohort of 15 undergoing <sup>1</sup>H-MR spectroscopy may not have had sufficient power to detect an association. Sex is also associated with IPS with women being associated with decreased PASAT3 scores compared with men, adjusting for the other covariates (Table 2). Neurometabolic differences between men and women in SPMS were examined by De Stefano et al,<sup>36</sup> who did not find differences in NAA/Cr in NAWM. There was also no difference in tNAA or tNAA/tCr in NAWM between men and women in our SPMS cohort (Welch  $t$  test:  $P = .3$ ,  $P = .7$ , respectively). Penny et al<sup>37</sup> examined the longitudinal association between tNAA and IPS in PPMS and did not identify sex as being associated with 5-year measures of IPS. Their results, however, may differ because they studied a cohort of patients with PPMS who had a predominance of men and a lower baseline median EDSS score of 4.5. T2 lesion volume reflecting the inflammatory lesion burden was also associated with IPS and cognitive performance, findings that have been demonstrated before confirming the strong association between inflammatory lesion burden and clinical disability in PMS.<sup>18,37</sup>

We also found that mIns/tCr in NAWM had a negative association with PASAT3 scores (On-line Table 1 and Table 2). This relationship is in the expected direction, with increased astrogliosis (as reflected by higher mIns/tCr) associated with decreased performance on PASAT3. mIns values were not associated with tests of IPS, but the ratio between the 2 showed a weak negative association, which suggests that as the mIns/tCr ratio increases, PASAT3 scores decrease (Fig 3). This finding could be driven by either an increased mIns or a decreased tCr (tCr is more commonly used a reference metabolite) and reflective of increased astrogliosis in SPMS causing IPS dysfunction.

There was a correlation between tNAA in NAWM and the SDMT. However, this association was not significant after adjusting for covariates in the regression analysis. While both PASAT3 and SDMT measure IPS, PASAT3 involves verbal working memory compared with SDMT, which involves visuospatial memory, and this difference may explain the association between neuroaxonal integrity in NAWM and PASAT3, but not SDMT.<sup>38</sup> A separate study comparing PASAT with SDMT using fMRI found that PASAT activated more frontal areas and the left inferior parietal lobe, suggesting that PASAT required more working memory capacity and executive function to execute compared with SDMT.<sup>39</sup> However, studies in those with relapsing-remitting MS suggest a strong correlation between the PASAT3 and SDMT, with similar sensitivity and specificity between the 2 tests, so our lack of association with SDMT should be interpreted with caution.<sup>40</sup>

A previous study of choline levels in cortical GM did not show any difference between those with primary-progressive MS and healthy controls, nor was there any association with clinical disability measures.<sup>14</sup> Our results suggest an association between GM tCho (a surrogate marker of membrane turnover) and IPS: As GM tCho levels increase, IPS performance (reflected by PASAT3

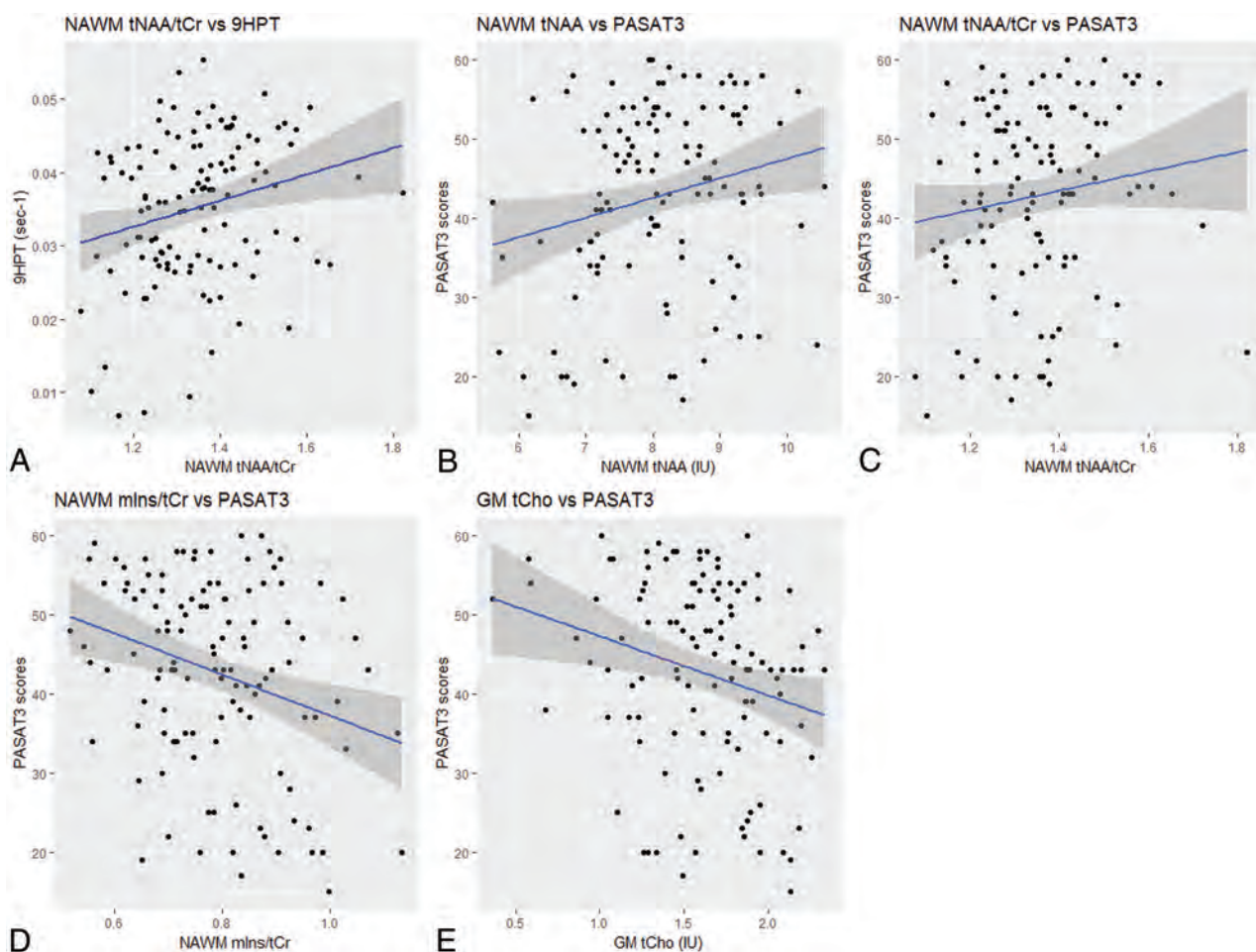


**FIG 3.** Associations between neurometabolites and clinical disability measures. The scatterplots with the line of best fit and 95% confidence intervals are shown for the associations in normal-appearing white matter among the following: A, tNAA/tCr and 9HPT ( $\rho = 0.23$ ; 95% CI, 0.06–0.40). B, tNAA and Paced Auditory Serial Addition Test ( $\rho = 0.21$ ; 95% CI, 0.03–0.38). C, tNAA/tCr and Paced Auditory Serial Addition Test ( $\rho = 0.19$ ; 95% CI, 0.01–0.36). D, mIns/tCr and Paced Auditory Serial Addition Test ( $\rho = -0.23$ ; 95% CI, -0.39 to -0.05) and in gray matter between tCho and Paced Auditory Serial Addition Test ( $\rho = -0.24$ ; 95% CI, -0.40 to -0.06) (E).

scores) decreases (On-line Table 1 and Table 2 and Fig 3). Phosphatidylcholine is one of the major choline-containing compounds within cell membranes, and there is evidence that this, along with its precursor molecule phosphocholine and the breakdown product glycerophosphocholine, is measured by the tCho peak in  $^1\text{H}$ -MR spectroscopy.<sup>41</sup> In addition, the consistent finding of increased tCho (tCho/tCr) in active MS lesions suggests that tCho is a marker of membrane turnover.<sup>9</sup> Recent findings have demonstrated that meningeal lymphoid follicles release proinflammatory molecules that can lead to cortical GM inflammation in SPMS, and our findings may support this finding, with a surrogate marker of increased membrane turnover in cortical GM being associated with IPS.<sup>42,43</sup> However, this association should be interpreted with caution because tCho was not associated with other measures of clinical disability. Our findings may have differed from those in the previous study because Sastre-Garriga et al<sup>14</sup> examined a cohort of 41 participants with early and lower disability (median EDSS score = 4.5; mean disease duration = 3.31 years).

Previous studies exploring the relationship between brain neurometabolites and measures of IPS in PMS did not report the correlation coefficients, making it difficult to place our results from

this study in the context of previously reported results.<sup>14,16,18,44</sup> Examining the associations in these studies between metabolites and other clinical disability measures (eg, EDSS) would suggest that the size of our correlations (On-line Table 1) is generally in keeping with previously reported work.<sup>14,16</sup>

There were statistically significant correlations in GM between mIns and PASAT3 scores, mIns/tCr and SDMT scores, and mIns/tCr and T25-FW (On-line Table 1), however these were not significant in the regression analysis after adjusting for other covariates and were generally in keeping with previous studies that have examined associations between cortical GM metabolites and clinical disability measures such as EDSS and the Brief Repeatable Battery Neuropsychological Tests in SPMS cohorts.<sup>13,45–47</sup> A single study found that tNAA was decreased in cortical GM compared with controls and tNAA in cortical GM showed a moderate association with EDSS and 9HPT, but this was in early PPMS.<sup>14</sup> When calculating GM metabolites, several studies used careful placement of the VOI using single-voxel spectroscopy,<sup>13,46</sup> while the remaining studies used CSI followed by automated or manual tissue segmentation.<sup>45,47</sup> These differing techniques reflect the technical challenges in GM metabolite calculation in which the partial volume effect can result



in contamination of the VOI or leave insufficient pure GM voxels. The other issue is that previous studies have reported clinical measures that reflect general disability or composite scores (eg, EDSS and Brief Repeatable Battery Neuropsychological Tests), making it difficult to determine associations with specific functional measures such as upper limb function or ambulation. We attempted to address these issues using CSI followed by segmentation, then using a regression method to calculate GM metabolite values, and then examining these associations with specific functional measures of clinical disability.

### Measures of Ambulation and General Disability

While there were several associations seen between metabolites and T25-FW and EDSS (On-line Table 1), after multiple regression analysis, we did not find any significant associations between the T25-FW performance or the EDSS score and any neurometabolite levels. Previous studies examining SPMS cohorts have shown relationships between total choline and EDSS in NAWM and tNAA/Cr in cortical GM and EDSS in a cohort of PPMS ( $n = 15$ ).<sup>16</sup> The lack of association between metabolites and the EDSS could be due to the limited distribution of scores in the cohort in which 106/148 had an EDSS score of 6.0–6.5, compounded by the ceiling effect and nonlinear characteristics of the EDSS.<sup>35</sup> EDSS scores, particularly between 4.0–6.5, are defined by ambulatory distance, and there is a moderate-to-strong correlation between the T25-FW and EDSS;<sup>48</sup> or there is no relationship to be found.

There were statistically significant correlations between GM Glx (Glx/tCr) and EDSS and with T25-FW (On-line Table 1), but after multiple regression analysis, we did not find any significant relationships between Glx or Glx/tCr and measures of clinical disability. Glutaminergic excitotoxicity has been shown to be involved in the pathogenesis of PMS.<sup>4</sup> When glutamate values were measured separate from glutamine using a TE-averaged MR spectroscopic imaging technique, glutamate was associated with a decline in neuroaxonal integrity in a mixed cohort of MS (number of PMS = 31/343).<sup>49</sup> We measured Glx (glutamine + glutamate) due to the difficulty in resolving glutamate from its precursor glutamine at 3T. It also seems unlikely that we can measure glutaminergic excitotoxicity directly because most Glx signal arises from the intracellular compartment and thereby is more likely to reflect neuroaxonal integrity.

### Methodologic and Analytic Considerations

The demographics and characteristics ( $n = 119$ ) of the cohort analyzed in this study were consistent with those reported from the main MS-SMART study ( $n = 445$ ).<sup>20</sup> The placement of the CSI grid above the ventricles was designed to limit the effect of ventricles from which there is no metabolite signal, decrease the partial volume effect, and ensure consistency of shimming across the CSI slice. The predilection of WML to periventricular regions led to voxels containing predominantly WM and GM, which meant we were unable to obtain metabolite values from WML. When determining metabolite values for NAWM and GM, we attempted to limit contamination by WML and CSF by excluding voxels that contained 1% WML and 15% CSF. These parameters kept the best balance between the loss of CSI voxels while minimizing WML and CSF contamination of voxels used in NAWM

and GM calculations. During the calculation of metabolite values in NAWM and GM, 29 participants were excluded as metabolite outliers. No formal statistical comparison was undertaken, but the characteristics of these 29 participants were generally similar to those in the cohort that underwent analysis ( $n = 119$ ), except to note that the median T2 lesion volume was higher in the excluded group (15.6 versus 9.7 mL). While we outline a rationale for dealing with multiple comparisons, some caution is advised during interpretation of the associations due to the multiple comparisons being undertaken. Owing to technical difficulties in GM lesion detection, GM lesions were not segmented, and this feature should be acknowledged when interpreting metabolite values and results pertaining to GM.

The neurometabolite ratios to tCr need careful interpretation because tCr is also affected by neuropathology.<sup>11</sup> There are, however, benefits to using tCr as a stable reference because it removes the need to adjust for head-coil loading and T1 and T2 effects.<sup>9</sup> Estimated concentrations are reported using a water reference for scaling, which can be used to produce absolute concentrations; this process, in turn, carries assumptions within LCModel about the water content of tissue, which is based on reports from healthy volunteers.<sup>31</sup> Given this assumption and the fact that at TR = 2000 ms, T1 effects may still be present, we chose to present an estimated (rather than absolute) concentration in institutional units. The use of estimated concentrations allows the possibility that errors between the LCModel “absolute” concentrations and the true metabolite concentrations may be present.

### CONCLUSIONS

After multiple regression analysis, tNAA, tNAA/tCr, and mIns/tCr in NAWM and tCho in GM are associated with clinical disability in upper limb function and information processing speed. These metabolites are therefore of interest as surrogate markers of brain injury in SPMS.

### ACKNOWLEDGMENTS

The authors would like to thank all the participants of the MS-SMART trial and all the collaborators involved in the trial, particularly, Tiggy Beyene, Vanessa Bassan, Marios Yiannakis, Almudena Garcia Gomez, Alvin Zapata, Rebecca Samson, Alberto Calvi, and Marcello Moccia.

Disclosures: Bhavana S. Solanky—RELATED: Grant: Efficacy and Mechanism Evaluation, Comments: funding reference number 11/30/11\*; UNRELATED: Employment: University College London; Grants/Grants Pending: Wings for Life.\* Nevin A. John—RELATED: Grant: Efficacy and Mechanism Evaluation, Comments: funding reference number 11/30/11.\* Jonathan Stutters—RELATED: Grant: Efficacy and Mechanism Evaluation, Comments: funding reference number 11/30/11.\* Ferran Prados—RELATED: Grant: Guarantors of Brain, Comments: nonclinical Guarantors of Brain fellowship; UNRELATED: Employment: University College London. Torben Schneider—UNRELATED: Employment: employee at Philips Healthcare, Comments: During the time of the study, I was employed by Philips Healthcare; Patents (Planned, Pending or Issued): patents with Philips Healthcare. Richard A. Parker—RELATED: Grant: Efficacy and Mechanism Evaluation, Comments: funding reference number 11/30/11.\* Other: National Health Service Lothian, Comments: support for the salary of Dr Parker via the Edinburgh Clinical Trials Unit.\* Christopher J. Weir—RELATED: Grant: Efficacy and Mechanism Evaluation, Comments: funding reference number 11/30/11.\* Other: National Health Service Lothian, Comments: support for the salary of Professor Weir via the Edinburgh Clinical Trials Unit.\* Anita Monteverdi—RELATED: Grant: Efficacy and Mechanism Evaluation, Comments: funding reference number 11/30/11.\* Anisha Doshi—RELATED: Grant: Efficacy and Mechanism Evaluation,

Comments: funding reference number 11/30/11\*; UNRELATED: Employment: Queen Square MS Center Institute for Neurology. David MacManus—RELATED: Grant: Efficacy and Mechanism Evaluation, Comments: funding reference number 11/30/11\* Frederik Barkhof—UNRELATED: Board Membership: Roche, Biogen, Bayer AG, Merck, Comments: Steering committee and Independent data monitoring committee membership; Consultancy: IXICO; Grants/Grants Pending: European Union—Internal Market Information System.\* Jeremy Chataway—RELATED: Grant: Efficacy and Mechanism Evaluation Program and Health Technology Assessment Program (National Institute for Health Research); UK Multiple Sclerosis Society and National Multiple Sclerosis Society; National Institute for Health Research University College London Hospitals Biomedical Research Center, Comments: funding reference number 11/30/11\*; UNRELATED: Consultancy: Azadyne, Biogen, Celgene, MedDay Pharma, Merck, and Roche; Grants/Grants Pending: Novartis, Comments: investigator grant from Novartis\*; Other: a local Principal Investigator for commercial trials funded by Actelion, Biogen, Novartis, and Roche.\* Ian Marshall—RELATED: Grant: Efficacy and Mechanism Evaluation, Comments: funding reference number 11/30/11\* Claudia A.M. Gandini Wheeler-Kingshott—RELATED: Grant: Efficacy and Mechanism Evaluation program, Comments: funding reference number 11/30/11\*; UNRELATED: Grants/Grants Pending: MS Society, Wings for Life, International Spinal Research Trust, Craig H. Neilsen Foundation, Horizon2020\*; Royalties: Elsevier. \*Money paid to the institution.

## REFERENCES

1. Ontaneda D, Thompson AJ, Fox RJ, et al. **Progressive multiple sclerosis: prospects for disease therapy, repair, and restoration of function.** *Lancet* 2017;389:1357–66 CrossRef Medline
2. Mahad DH, Trapp BD, Lassmann H. **Pathological mechanisms in progressive multiple sclerosis.** *Lancet Neurol* 2015;14:183–93 CrossRef Medline
3. Paling D, Golay X, Wheeler-Kingshott C, et al. **Energy failure in multiple sclerosis and its investigation using MR techniques.** *J Neurol* 2011;258:2113–27 CrossRef Medline
4. Macrez R, Stys PK, Vivien D, et al. **Mechanisms of glutamate toxicity in multiple sclerosis: biomarker and therapeutic opportunities.** *Lancet Neurol* 2016;15:1089–102 CrossRef Medline
5. Brown JW, Chard DT. **The role of MRI in the evaluation of secondary progressive multiple sclerosis.** *Expert Rev Neurother* 2016;16:157–71 CrossRef Medline
6. Ciccarelli O, Toosy AT, De Stefano N, et al. **Assessing neuronal metabolism in vivo by modeling imaging measures.** *J Neurosci* 2010;30:15030–33 CrossRef Medline
7. Rovira À, Alonso J. **1H magnetic resonance spectroscopy in multiple sclerosis and related disorders.** *Neuroimaging Clin N Am* 2013;23:459–74 CrossRef Medline
8. Bitsch A, Bruhn H, Vougioukas V, et al. **Inflammatory CNS demyelination: histopathologic correlation with in vivo quantitative proton MR spectroscopy.** *AJNR Am J Neuroradiol* 1999;20:1619–27 Medline
9. Swanberg KM, Landheer K, Pitt D, et al. **Quantifying the metabolic signature of multiple sclerosis by in vivo proton magnetic resonance spectroscopy: current challenges and future outlook in the translation from proton signal to diagnostic biomarker.** *Front Neurol* 2019;10:1173 CrossRef Medline
10. Narayana PA, Wolinsky JS, Rao SB, et al; PROMiSe Trial MRSI Group. **Multicentre proton magnetic resonance spectroscopy imaging of primary progressive multiple sclerosis.** *Mult Scler* 2004;10 (Suppl 1):S73–78 CrossRef Medline
11. Vrenken H, Barkhof F, Uitendhaag BMJ, et al. **MR spectroscopic evidence for glial increase but not for neuro-axonal damage in MS normal-appearing white matter.** *Magn Reson Med* 2005;53:256–66 CrossRef Medline
12. Rovaris M, Gallo A, Falini A, et al. **Axonal injury and overall tissue loss are not related in primary progressive multiple sclerosis.** *Arch Neurol* 2005;62:898–902 CrossRef Medline
13. Geurts JGG, Reuling IEW, Vrenken H, et al. **MR spectroscopic evidence for thalamic and hippocampal, but not cortical, damage in multiple sclerosis.** *Magn Reson Med* 2006;55:478–83 CrossRef Medline
14. Sastre-Garriga J, Ingle GT, Chard DT, et al. **Metabolite changes in normal-appearing gray and white matter are linked with disability in early primary progressive multiple sclerosis.** *Arch Neurol* 2005;62:569 CrossRef Medline
15. Hannoun S, Bagory M, Durand-Dubief F, et al. **Correlation of diffusion and metabolic alterations in different clinical forms of multiple sclerosis.** *PLoS One* 2012;7:e32525 CrossRef Medline
16. Obert D, Helms G, Sättler MB, et al. **Brain metabolite changes in patients with relapsing-remitting and secondary progressive multiple sclerosis: a two-year follow-up study.** *PLoS One* 2016;11:e0162583 CrossRef Medline
17. Foong J, Rozewicz L, Davie CA, et al. **Correlates of executive function in multiple sclerosis.** *J Neuropsychiatry Clin Neurosci* 1999;11:45–50 CrossRef Medline
18. Cox D, Pelletier D, Genain C, et al. **The unique impact of changes in normal appearing brain tissue on cognitive dysfunction in secondary progressive multiple sclerosis patients.** *Mult Scler* 2004;10:626–29 CrossRef Medline
19. Connick P, Angelis FD, Parker RA, et al; UK Multiple Sclerosis Society Clinical Trials Network. **Multiple Sclerosis-Secondary Progressive Multi-Arm Randomisation Trial (MS-SMART): a multiarm phase IIb randomised, double-blind, placebo-controlled clinical trial comparing the efficacy of three neuroprotective drugs in secondary progressive multiple sclerosis.** *BMJ Open* 2018;8:e021944 CrossRef Medline
20. Chataway J, De Angelis F, Connick P, et al; MS-SMART Investigators. **Efficacy of three neuroprotective drugs in secondary progressive multiple sclerosis (MS-SMART): a phase 2b, multiarm, double-blind, randomised placebo-controlled trial.** *Lancet Neurol* 2020;19:214–25 CrossRef Medline
21. Kurtzke JF. **Rating neurologic impairment in multiple sclerosis: an Expanded Disability Status Scale (EDSS).** *Neurology* 1983;33:1444–52 CrossRef Medline
22. Cutter GR, Baier ML, Rudick RA, et al. **Development of a multiple sclerosis functional composite as a clinical trial outcome measure.** *Brain* 1999;122:871–82 CrossRef Medline
23. Benedict RH, DeLuca J, Phillips G, et al; Multiple Sclerosis Outcome Assessments Consortium. **Validity of the Symbol Digit Modalities Test as a cognition performance outcome measure for multiple sclerosis.** *Mult Scler* 2017;23:721–33 CrossRef Medline
24. Brink HF, Buschmann MD, Rosen BR. **NMR chemical shift imaging.** *Comput Med Imaging Graph* 1989;13:93–104 CrossRef Medline
25. Shen J, Rothman DL, Hetherington HP, et al. **Linear projection method for automatic slice shimming.** *Magn Reson Med* 1999;42:1082–88 CrossRef Medline
26. Modat M, Ridgway GR, Taylor ZA, et al. **Fast free-form deformation using graphics processing units.** *Comput Methods Programs Biomed* 2010;98:278–84 CrossRef Medline
27. Prados F, Cardoso MJ, Kanber B, et al. **A multi-time-point modality-agnostic patch-based method for lesion filling in multiple sclerosis.** *Neuroimage* 2016;139:376–84 CrossRef Medline
28. Cardoso MJ, Modat M, Wolz R, et al. **Geodesic Information Flows: spatially-variant graphs and their application to segmentation and fusion.** *IEEE Trans Med Imaging* 2015;34:1976–88 CrossRef Medline
29. Smith SM, Zhang Y, Jenkinson M, et al. **Accurate, robust, and automated longitudinal and cross-sectional brain change analysis.** *Neuroimage* 2002;17:479–89 CrossRef Medline
30. LCMModel & LCMgui User's Manual. <http://s-provencher.com/pub/LCMModel/manual/manual.pdf>. Accessed 6th October, 2020
31. Ernst T, Kreis R, Ross BD. **Absolute quantitation of water and metabolites in the human brain, I: compartments and water.** *J Magn Reson Ser B* 1993;102:1–8 CrossRef
32. Solana E, Martinez-Heras E, Martinez-Lapiscina EH, et al. **Magnetic resonance markers of tissue damage related to connectivity disruption in multiple sclerosis.** *NeuroImage Clin* 2018;20:161–68 CrossRef Medline
33. R Core Team. **R: A language and environment for statistical computing.** 2017. <https://cran.r-project.org/doc/manuals/r-release/fullrefman.pdf>. Accessed March 12, 2020

34. Patel CJ, Ioannidis JP. **Placing epidemiological results in the context of multiplicity and typical correlations of exposures.** *J Epidemiol Community Health* 2014;68:1096–100 CrossRef Medline
35. Giovannoni G, Cutter G, Pia-Sormani M, et al. **Is multiple sclerosis a length-dependent central axonopathy? The case for therapeutic lag and the asynchronous progressive MS hypotheses.** *Mult Scler Relat Disord* 2017;12:70–78 CrossRef Medline
36. De Stefano N, Narayanan S, Francis GS, et al. **Evidence of axonal damage in the early stages of multiple sclerosis and its relevance to disability.** *Arch Neurol* 2001;58:65–70 CrossRef Medline
37. Penny S, Khaleeli Z, Cipolotti L, et al. **Early imaging predicts later cognitive impairment in primary progressive multiple sclerosis.** *Neurology* 2010;74:545–52 CrossRef Medline
38. Sonder JM, Burggraaff J, Knol DL, et al. **Comparing long-term results of PASAT and SDMT scores in relation to neuropsychological testing in multiple sclerosis.** *Mult Scler* 2014;20:481–88 CrossRef Medline
39. Forn C, Belenguer A, Belloch V, et al. **Anatomical and functional differences between the paced auditory serial addition test and the symbol digit modalities test.** *J Clin Exp Neuropsychol* 2011;33:42–50 CrossRef Medline
40. López-Góngora M, Querol L, Escartín A. **A one-year follow-up study of the Symbol Digit Modalities Test (SDMT) and the Paced Auditory Serial Addition Test (PASAT) in relapsing-remitting multiple sclerosis: an appraisal of comparative longitudinal sensitivity.** *BMC Neurol* 2015;15:40 CrossRef Medline
41. Miller BL. **A review of chemical issues in 1H NMR spectroscopy: N-acetyl-L-aspartate, creatine and choline.** *NMR Biomed* 1991;4:47–52 CrossRef Medline
42. James RE, Schalks R, Browne E, et al. **Persistent elevation of intrathecal pro-inflammatory cytokines leads to multiple sclerosis-like cortical demyelination and neurodegeneration.** *Acta Neuropathol Commun* 2020;8:66 CrossRef Medline
43. Magliozzi R, Howell O, Vora A, et al. **Meningeal B-cell follicles in secondary progressive multiple sclerosis associate with early onset of disease and severe cortical pathology.** *Brain* 2007;130:1089–104 CrossRef Medline
44. MacMillan E, Tam R, Zhao Y, et al. **Progressive multiple sclerosis exhibits decreasing glutamate and glutamine over two years.** *Mult Scler J* 2016;22:112–16 CrossRef Medline
45. Caramanos Z, DiMaio S, Narayanan S, et al. **1H-MRSI evidence for cortical gray matter pathology that is independent of cerebral white matter lesion load in patients with secondary progressive multiple sclerosis.** *J Neurol Sci* 2009;282:72–79 CrossRef Medline
46. Sarchielli P, Presciutti O, Tarducci R, et al. **Localized (1)H magnetic resonance spectroscopy in mainly cortical gray matter of patients with multiple sclerosis.** *J Neurol* 2002;249:902–10 CrossRef Medline
47. Adalsteinsson E, Langer-Gould A, Homer RJ, et al. **Gray matter N-acetyl aspartate deficits in secondary progressive but not relapsing-remitting multiple sclerosis.** *AJNR Am J Neuroradiol* 2003;24:41–45 Medline
48. Motl RW, Cohen JA, Benedict R, et al; Multiple Sclerosis Outcome Assessments Consortium. **Validity of the timed 25-foot walk as an ambulatory performance outcome measure for multiple sclerosis.** *Mult Scler* 2017;23:704–10 CrossRef Medline
49. Azevedo CJ, Kornak J, Chu P, et al. **In vivo evidence of glutamate toxicity in multiple sclerosis.** *Ann Neurol* 2014;76:269–78 CrossRef Medline



# Neurite Orientation Dispersion and Density Imaging for Assessing Acute Inflammation and Lesion Evolution in MS

S. Sacco, E. Caverzasi, N. Papinutto, C. Cordano, A. Bischof, T. Gundel, S. Cheng, C. Asteggiano, G. Kirkish, J. Mallott, W.A. Stern, S. Bastianello, R.M. Bove, J.M. Gelfand, D.S. Goodin, A.J. Green, E. Waubant, M.R. Wilson, S.S. Zamvil, B.A. Cree, S.L. Hauser, R.G. Henry, and University of California, San Francisco MS-EPIC Team



## ABSTRACT

**BACKGROUND AND PURPOSE:** MR imaging is essential for MS diagnosis and management, yet it has limitations in assessing axonal damage and remyelination. Gadolinium-based contrast agents add value by pinpointing acute inflammation and blood-brain barrier leakage, but with drawbacks in safety and cost. Neurite orientation dispersion and density imaging (NODDI) assesses microstructural features of neurites contributing to diffusion imaging signals. This approach may resolve the components of MS pathology, overcoming conventional MR imaging limitations.

**MATERIALS AND METHODS:** Twenty-one subjects with MS underwent serial enhanced MRIs ( $12.6 \pm 9$  months apart) including NODDI, whose key metrics are the neurite density and orientation dispersion index. Twenty-one age- and sex-matched healthy controls underwent unenhanced MR imaging with the same protocol. Fifty-eight gadolinium-enhancing and non-gadolinium-enhancing lesions were semiautomatically segmented at baseline and follow-up. Normal-appearing WM masks were generated by subtracting lesions and dirty-appearing WM from the whole WM.

**RESULTS:** The orientation dispersion index was higher in gadolinium-enhancing compared with non-gadolinium-enhancing lesions; logistic regression indicated discrimination, with an area under the curve of 0.73. At follow-up, in the 58 previously enhancing lesions, we identified 2 subgroups based on the neurite density index change across time: Type 1 lesions showed increased neurite density values, whereas type 2 lesions showed decreased values. Type 1 lesions showed greater reduction in size with time compared with type 2 lesions.

**CONCLUSIONS:** NODDI is a promising tool with the potential to detect acute MS inflammation. The observed heterogeneity among lesions may correspond to gradients in severity and clinical recovery after the acute phase.

**ABBREVIATIONS:** AD = axial diffusivity; DAWM = dirty-appearing white matter; FA = fractional anisotropy; FU = follow-up; GEL = gadolinium-enhancing lesion; HC = healthy control; MD = mean diffusivity; NAWM = normal-appearing white matter; NDI = neurite density index; NGEL = non-gadolinium-enhancing lesion; NODDI = neurite orientation dispersion and density imaging; nODI = normalized orientation dispersion index; ODI = orientation dispersion index; RD = radial diffusivity; VEC = extra-neurite compartment

Conventional MR imaging is essential for MS diagnosis and management, specifically for demonstrating WM lesion dissemination in space (involvement of >1 CNS region) and time (across time accumulation).<sup>1</sup> Conventional MR imaging, however,

lacks specificity in characterizing MS WM lesions after the acute phase; all lesions show a similar radiologic appearance on T2WI, irrespective of the degree of inflammation, axonal loss, gliosis,

Received May 4, 2020; accepted after revision July 29.

From the Department of Neurology (S.S., E.C., N.P., C.C., A.B., T.G., S.C., C.A., G.K., J.M., W.A.S., R.M.B., J.M.G., D.S.G., A.J.G., E.W., M.R.W., S.S.Z. B.A.C., S.L.H., and R.G.H.), University of California, San Francisco Weill Institute for Neurosciences, University of California, San Francisco, California; Institute of Radiology (S.S., C.A.), Department of Clinical Surgical Diagnostic and Pediatric Sciences, and Department of Brain and Behavioral Sciences (S.B.), University of Pavia, Pavia, Italy; and Neuroradiology Department (S.B.), Istituto Di Ricovero e Cura a Carattere Scientifico Mondino Foundation, Pavia, Italy.

This work was supported by a gift from the Ostby Foundation (R.G.H.); the National Institute of Neurological Diseases and Stroke (R35NS11644, S.L.H.; ROINS26799, S.L.H.; K23 NS048869, B.A.C.); the National MS Society (RG-1707-28775, R.G.H.); the Valhalla Foundation; and gifts from Friends of the Multiple Sclerosis Research Group at UCSF.

Paper previously presented at: 56th annual meeting of the ASNR (American society of Neuroradiology), June 2–7, 2018, Vancouver, Canada; NAIMS, North American Imaging in Multiple Sclerosis Cooperative workshop meeting, February 27, 2019, Dallas; ACTRIMS, Annual americas committee for treatment and research in multiple sclerosis Forum, February 28–March 2, 2019, Dallas; and Annual Meeting of the International Society of Magnetic Resonance in Medicine, May 11–16, 2019, Montreal, Quebec, Canada.

Please address correspondence to Simone Sacco, MD, Department of Neurology, UCSF Weill Institute for Neurosciences, University of California San Francisco, 675 Nelson Rising Ln, San Francisco, CA 94158; e-mail: saccoosimone88@gmail.com

Indicates open access to non-subscribers at www.ajnr.org

Indicates article with supplemental online appendix and table.

Indicates article with supplemental online photo.

<http://dx.doi.org/10.3174/ajnr.A6862>

demyelination, and remyelination.<sup>2,3</sup> Furthermore, clinical disability shows limited correlation with volume and the number of detectable WM lesions. The different neuropathologic characteristics of WM lesions as well as the accumulation of tissue damage within normal-appearing WM (NAWM) are some of the other factors possibly playing a role in the development of MS disability.<sup>4</sup>

Gadolinium-based imaging improves the utility of conventional MR imaging in MS because gadolinium-enhancing lesions (GELs) represent a radiologic correlate of acute inflammation, corresponding to active lesions associated with blood-brain barrier disruption. However, despite its importance for diagnosis (fulfillment of dissemination in time criteria), the application of gadolinium-based contrast agents has raised a number of safety concerns.<sup>5</sup> Therefore, alternative MR imaging markers of acute inflammation are needed.

Neurite orientation dispersion and density imaging (NODDI) is a clinically feasible diffusion MR imaging technique, incorporating multiple shells with different b-values to model brain tissue into 3 compartments showing different diffusion properties.<sup>6</sup> According to this orientation-dispersed cylindric model, the isotropic diffusion fraction is highly represented only within CSF, whereas within brain parenchyma, the diffusion signal can be either hindered (Gaussian displacement pattern) or restricted (non-Gaussian displacement pattern). The hindered signal is attributed to the extraneurite compartment (VEC), defining the extracellular volume fraction whereas the restricted signal is attributed to intraneurite spaces and is thought to correspond to the neurite density index (NDI). A Watson distribution is then used to compute the orientation distribution of the cylinders, quantified from 0 to 1 by the orientation dispersion index (ODI). Highly compacted and parallel WM bundles, such as the corpus callosum, generally show lower ODI values compared with the cortical and subcortical regions, characterized by multidirectional dendritic structures.

Even though NODDI applications are novel in MS, this technique appears promising in detecting and modeling the complexity of MS pathology, being potentially more specific than DTI in capturing microstructural substrates.<sup>7-12</sup> NODDI has never been used, however, to assess longitudinal changes within MS lesions and NAWM. For animal studies, only a single work, based on a murine model, longitudinally assessed induced demyelinated lesions, correlating NODDI abnormalities with histopathologic changes.<sup>13</sup> The authors suggested that after a demyelinating event, the combination of decreasing ODI and increasing NDI with time might reflect improvement in fiber coherency due to remyelination.

The aim of this work was to cross-sectionally assess the role of NODDI in indicating gadolinium enhancement in acute lesions and to longitudinally assess NODDI and conventional DTI changes in MS lesions and NAWM in the transition from detectable to undetectable gadolinium enhancement. We hypothesized that NODDI-derived metrics may be promising markers to detect acute inflammation as well as heterogeneity among lesions and their evolution with time.

## MATERIALS AND METHODS

### Subjects

A subgroup of subjects with MS participating in the UCSF EPIC study<sup>14,15</sup> was identified on the basis of the following inclusion

criteria: 1) confirmed MS or clinically isolated syndrome diagnosis; 2) at least 2 longitudinal 3T MR imaging scans during 2 years, including a NODDI multishell dedicated protocol of adequate quality; 3) the presence of at least 1 enhancing lesion at baseline that had to be resolved at the follow-up examination; and 4) absence of new enhancing lesions at follow-up. The Committee on Human Research at our institution (UCSF) approved the study protocol. Written informed consent was obtained from all participants.

Of 290 subjects assessed from 2015 to 2018, 21 met the study entry requirements (mean age,  $36.4 \pm 8.7$  years, 17 women). Sixteen of them had relapsing-remitting MS, 3 had clinically isolated syndrome, and 2 had primary-progressive MS with an average Expanded Disability Status Scale score of  $2.6 \pm 1.6$ . For each subject, we chose as follow-up MRI ( $12.6 \pm 9$  months apart) the first MRI showing complete resolution of enhancement and absence of new enhancing lesions.

We studied 21 age- and sex-matched healthy controls (HCs) (mean age,  $36.4 \pm 8.7$  years; 17 women).

### MRI Protocol

Subjects underwent longitudinal (2 or 3 time points) 3T MRIs (Magnetom Skyra; Siemens) with a high-angular-resolution diffusion imaging 2-shell acquisition protocol (simultaneous multi-section sequence, section acceleration factor of two, 30 directions at  $b = 700 \text{ s/mm}^2$ , and 64 directions at  $b = 2000 \text{ s/mm}^2$  with TR/TE = 4300/96 ms, along with 10  $b = 0$  scans, 1 of which was acquired using a reversed phase-encoding direction, posterior to anterior;  $2.2\text{-mm}^3$  isotropic voxels; 66 axial slices; FOV =  $220 \times 220 \text{ mm}$ ). The NODDI protocol was added to the conventional MR imaging sequences (pre- and postcontrast 3D T1WI  $1\text{-mm}^3$  cubic voxel MPRAGE and FLAIR) performed at each visit. HCs underwent 1 unenhanced 3T MR imaging with the same protocol.

### NODDI and DTI Processing and Imaging Coregistration

First, susceptibility-induced distortions were estimated from image pairs acquired with reversed phase-encoding directions (resulting in distortions with opposite directions), analogous to Andersson et al,<sup>16</sup> using the “TOPUP” tool of the FMRIB Software Library (FSL; <http://fsl.fmrib.ox.ac.uk/fsl/fslwiki/topup>).<sup>17</sup> Additionally, eddy current-induced distortions and head motion were estimated and corrected using “eddy” from the same toolbox (<https://fsl.fmrib.ox.ac.uk/fsl/fslwiki/eddy>); b-vectors were accordingly rotated to account for the corrections.

NODDI fitting was performed with the NODDI Matlab Toolbox (Version 1.0.1; MathWorks) and DTI using DIPY, Version 0.13.<sup>18</sup> To analyze the NODDI and DTI metrics within the same ROIs for both time points, we performed a linear registration using FMRIB's Linear Image Registration Tool (FLIRT; <http://www.fmrib.ox.ac.uk/fsl/fslwiki/FLIRT>) for aligning the T1WI MPRAGE, FLAIR, and postgadolinium T1WI MPRAGE images to their baseline time point. For each time point and for the HC scans, the Anisotropic Power Map derived from the high-angular-resolution diffusion imaging data was then registered to the T1WI MPRAGE images using the ANTS (<http://stnava.github.io/ANTs/>) multidimensional registration tool. The same transformation used to register the Anisotropic Power Map was then applied to each of the

NODDI and DTI maps to register the images into the same space. Visual quality checks of the registration results were performed.

### **Selection of ROIs in Subjects with MS**

**Acute Lesions:** GELs. Acute lesions were studied longitudinally at both baseline and follow-up.

Specifically, at baseline S.S. semiautomatically segmented 140 GELs on 21 subjects using Jim (<http://www.xinapse.com/home.php>) on postgadolinium T1WI. The results were reviewed by E.C., and consensus was eventually achieved. The ROIs were subsequently checked on the baseline FLAIR and manually edited to include any voxel of abnormal FLAIR hyperintensity. We used these modified GEL ROIs for analysis. Each lesion in each subject was indexed.

Starting from GEL baseline masks, we created GEL follow-up masks (GEL-FU) by manually modifying the ROIs on the follow-up FLAIR. The manual editing was performed to take into account the evolution in size of a lesion after enhancement resolution to avoid inclusion of contiguous NAWM within GEL-FU ROIs. All GEL-FU lesions were nonenhancing.

NODDI data were registered to the T1-weighted image that had a higher resolution. Only lesions that had at least twenty-five 1-mm<sup>3</sup> voxels at both baseline and follow-up were included to avoid inaccuracies due to partial volume effects.

**Chronic Lesions: Non-Gadolinium-Enhancing Lesions.** Chronic lesions were studied longitudinally at both baseline and follow-up.

For comparison, we selected 58 nonenhancing lesions, >25 voxels from the same subjects who showed the GELs used in our final analysis. We refer to this last mask as non-gadolinium-enhancing lesions (NGELs). NGEL follow-up masks (NGEL-FU) were created with manual edits as described above. Each lesion in each subject was indexed.

**Normal-Appearing White Matter and Dirty-Appearing White Matter.** An in-house-developed algorithm was applied to delineate dirty-appearing white matter (DAWM). DAWM was defined as having a T2-weighted signal intensity intermediate between lesions and NAWM.<sup>19</sup> The first step of this algorithm uses FSL SIENAX (<http://fsl.fmrib.ox.ac.uk/fsl/fslwiki/SIENAX>)<sup>20</sup> to segment WM and cortical GM as well as FreeSurfer (<http://surfer.nmr.mgh.harvard.edu>) to segment subcortical GM. FMRIB's Integrated Registration and Segmentation Tool (FIRST; <http://fsl.fmrib.ox.ac.uk/fsl/fslwiki/FIRST>) was then used within the boundaries of the WM mask created from the steps above to separate the WM into 2 tissue types: NAWM and DAWM. E.C. and S.S. reviewed the DAWM probability maps and chose a 0.95 threshold to obtain a final DAWM ROI. The final NAWM masks were generated by subtracting lesions, DAWM masks, subcortical GM, and infratentorial regions from SIENAX WM masks.

### **Extraction of NODDI and DTI Metrics from NAWM, DAWM, GELs, GEL-FU, NGELs, and NGEL-FU**

Median values of ODI, NDI, and DTI metrics were extracted within GELs at the time of enhancement and GEL-FU after resolution of enhancement. Median values of ODI, NDI, and DTI metrics were extracted at both time points within the NAWM

and DAWM masks. As values of reference for chronic lesions, we extracted ODI, NDI, and DTI metrics from NGEL masks at baseline and NGEL-FU masks at follow-up.

For ODI values, an upper threshold of 0.5 was used to minimize potential partial volume effects with CSF and GM. Isotropic volume fraction differences between lesions and NAWM, DAWM, and healthy control WM (HCWM) were too small to be estimated. The fraction of water able to move isotopically within brain WM is indeed generally low. To potentially account for isotropic volume fraction variation, however, we corrected NDI and VEC values, dividing them for the global amount of anisotropic diffusion (VEC + NDI). In this context, VEC and NDI become exactly specular within each voxel of the brain; therefore, in the current study, we only report NDI values to avoid redundant information.

### **Healthy Control WM Values**

HC MRIs were used to furnish NODDI and DTI WM values of reference in the healthy control population as described in the Online Appendix.

### **Statistical Analysis**

To compare values across different brain regions, we normalized ODI values (nODI) by computing the percentage change from HC values extracted as described in the Online Appendix (ie, the subject's ODI/HC ODI in the same ROI).

We used a 2-sided *t* test to assess differences in NODDI and DTI metrics among GELs, NGELs, NAWM, DAWM, and HCWM. Longitudinal differences in NODDI and DTI metrics within NAWM, DAWM, GEL, and NGEL masks were assessed using a 2-sided paired *t* test.

Logistic regression analysis was performed using nODI to calculate the NODDI power to discriminate GELs from NGELs at baseline as well as the gadolinium-enhancing phase (GEL) from a phase without gadolinium enhancement (GEL-FU) within the same lesions.

## **RESULTS**

### **Subject Treatments**

At the baseline scan, 11 subjects were treatment-naïve. Of the 10 treated subjects, 6 had received glucocorticoids 30 days before MR imaging, 3 were on disease-modifying therapies but had not received glucocorticoids, and 1 was on disease-modifying therapies and had received glucocorticoids. At follow-up, 17/21 subjects were on disease-modifying therapies; no subjects received glucocorticoids within 30 days preceding the follow-up scans.

### **Lesions**

Fifty-eight GELs of >25 voxels, distributed among 17 subjects (mean, 3.47 ± 4.35; minimum 1, maximum 18 per subject), were identified and matched to 58 NGELs.

**Cross-Sectional Analysis of ODI Values.** In the contrast-enhancing phase at baseline, GEL ODI was higher than that in HCWM (0.28 ± 0.07 versus 0.22 ± 0.07; *P* < .001), whereas at follow-up in the nonenhancing phase, GEL-FU ODI had values similar to those in HCWM (0.23 ± 0.08 versus 0.23 ± 0.08; *P* = .4).



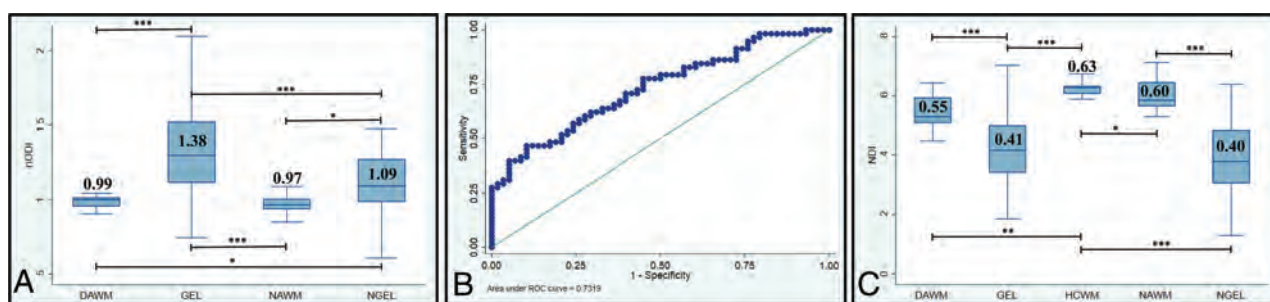


**FIG 1.** A, nODI (ODI pt/ODI HC) values within DAWM, GEL, NAWM, and NGEL masks at baseline with a respective 2-sided *t* test. Only statistically significant differences are reported (asterisk = *P* < .05; 2 asterisks = *P* < .005; 3 asterisks = *P* < .0005). B, Receiver operating characteristic for logistic regression using nODI for discriminating between GELs and NGELs at baseline. C, NDI values within DAWM, GELs, HCWM, NAWM, and NGELs at baseline with respective 2-sided *t*-tests. Only statistically significant differences are reported (asterisk = *P* < .05; 2 asterisks = *P* < .005; 3 asterisks = *P* < .0005). pt, subject.

Across all subjects, we compared ODI values within different ROIs using nODI to eliminate the influence of location. As shown in Fig 1A, baseline nODI was higher in GELs than NGELs ( $1.38 \pm 0.39$  versus  $1.09 \pm 0.22$ ; *P* < .001). Logistic regression indicated that nODI was the best discriminator between GELs and NGELs among NODDI and DTI metrics (the area under curve for nODI is equal to 0.73, whereas the area under curve for fractional anisotropy (FA) is equal to 0.64) (Fig 1B).

**ODI Change with Time.** nODI decreased within GELs from baseline to follow-up ( $1.38 \pm 0.39$  versus  $1.02 \pm 0.24$ ; *P* < .001). nODI decreased even within NGELs from baseline to follow-up ( $1.09 \pm 0.22$  versus  $1.02 \pm 0.26$ ; *P* < .05). Logistic regression indicated that nODI was the best discriminator between GELs and GEL-FU among NODDI and DTI metrics (the area under curve for nODI is equal to 0.83, whereas the area under curve for FA is equal to 0.71).

**Cross-Sectional Analysis of NDI Values.** As shown in Fig 1C, NDI was lower within lesions than in HCWM, NAWM, and DAWM ( $0.41 \pm 0.12$  versus  $0.63 \pm 0.02$ ,  $0.60 \pm 0.05$ ,  $0.55 \pm 0.05$ ; *P* < .001). There was no difference in the NDI between GELs and NGELs at baseline ( $0.42 \pm 0.11$  versus  $0.4 \pm 0.14$ ; *P* = .4).

**NDI Change with Time, Definition of Lesion Types 1 and 2, and Post Hoc Analyses.** On average, there was no NDI change with time within lesions in the transition from the enhancing to non-enhancing phase. However, after resolution of enhancement, 30/58 lesions showed an increased NDI compared with baseline, whereas 28/58 showed a decreased NDI.

In a post hoc analysis, we separated these lesions into 2 groups, lesion type 1 “increasing NDI with time,” and lesion type 2, “decreasing NDI with time” using a 2-sided *t* test to look for differences in NODDI and DTI metrics at baseline and follow-up, as well as shrinkage in lesion size, distribution among subjects, and treatment.

During gadolinium enhancement, NDI was lower in lesion type 1 than in lesion type 2 ( $0.37 \pm 0.09$  versus  $0.47 \pm 0.1$ ; *P* < .001), whereas, most interesting, NDI was higher in lesion type 1 than in lesion type 2 following enhancement disappearance ( $0.48 \pm 0.11$  versus  $0.39 \pm 0.11$ ; *P* < .005). Specifically, in lesion type 1, NDI increased with time along with a decrease in ODI,

whereas in lesions type 2, NDI decreased with time along with a decrease in ODI (Online Table).

Lesion type 1 showed more pronounced shrinkage compared with lesion type 2 (*P* < .05), decreasing on average by  $50\% \pm 20\%$ , whereas lesion type 2 decreased on average by  $38\% \pm 22\%$  (Online Table).

Of 17 subjects, 8 demonstrated only type 1 lesions, 6 showed both lesion types, and 3 had only type 2 lesions. No statistically significant differences among these groups of subjects were detected regarding glucocorticoid use or disease-modifying therapies before scanning, either at baseline or follow-up.

#### Differences in DTI Parameters between GELs/GEL-FU and NGELs

NGELs showed lower FA compared with GEL-FU ( $0.3 \pm 0.04$  versus  $0.37 \pm 0.02$ ; *P* < .01), higher radial diffusivity (RD) compared with GEL-FU ( $702 \pm 84 \times 10^{-6}$  versus  $665 \pm 14 \times 10^{-6}$ ; *P* < .005), higher mean diffusivity (MD) compared with GEL and GEL-FU ( $840 \pm 8 \times 10^{-6}$  versus  $790 \pm 14 \times 10^{-6}$ ,  $770 \pm 16 \times 10^{-6}$ ; *P* < .05), and higher axial diffusivity (AD) compared with GEL ( $1180 \pm 180$  versus  $1003 \pm 240 \times 10^{-6}$ ; *P* < .005). The Online Figure shows the comparison of NODDI and DTI metrics between GELs and GEL-FU as well as GELs and NGELs.

Regarding lesion subtypes, type 1 lesions showed decreases with time in MD, RD, and AD and an increase in FA, whereas type 2 lesions showed increases in all the metrics (Online Table).

#### NAWM and DAWM Changes

**ODI.** NAWM showed lower ODI compared with HCWM ( $0.228 \pm 0.0002$  versus  $0.234 \pm 0.0001$ ; *P* < .05) at both baseline and follow-up. No difference was detected between HCWM and DAWM ODI at both baseline and follow-up. At baseline, nODI was lower in NAWM and DAWM compared with both GELs and NGELs ( $0.97 \pm 0.06$ ,  $0.99 \pm 0.07$  versus  $1.38 \pm 0.39$ ,  $1.09 \pm 0.22$ ; *P* < .05) (Fig 1A), whereas at follow-up, no difference was detectable.

Differences in nODI between NAWM and DAWM were not significant at baseline or follow-up.

There was also no difference for change in nODI from baseline to follow-up within NAWM or DAWM.

NDI. NAWM and DAWM had lower NDIs compared with HCWM ( $0.60 \pm 0.05$ ,  $0.55 \pm 0.05$  versus  $0.63 \pm 0.02$ ;  $P < .05$ ,  $P < .005$ ), and the NDI was lower in DAWM compared with NAWM ( $0.55 \pm 0.05$  versus  $0.60 \pm 0.05$ ;  $P < .05$ ) (Fig 1C).

Longitudinally, the NDI decreased by  $4\% \pm 5\%$  within NAWM from the enhancing-to-nonenhancing phase ( $P < .005$ ; 2-sided paired  $t$  test). For lesion subgroups, NAWM NDI decreased by  $6\% \pm 4\%$  among the 9 subjects with any type 2 lesions (NDI decreasing lesions) ( $P < .005$ ; 2-sided paired  $t$  test), whereas no significant NAWM NDI change was detectable among the 8 subjects without type 2 lesions ( $2\% \pm 5\%$ ,  $P = .11$ ; 2-sided paired  $t$  test).

No significant longitudinal change was detected within DAWM in the transition from baseline to follow-up.

**DTI Metrics.** There was no difference in FA between NAWM and HCWM (Online Figure). DAWM showed lower FA compared with HCWM ( $0.45 \pm 0.03$  versus  $0.48 \pm 0.02$ ;  $P < .005$ ). NAWM and DAWM showed higher RD compared with HCWM ( $440 \pm 25 \times 10^{-6}$ ,  $474 \pm 37 \times 10^{-6}$  versus  $0.426 \pm 14 \times 10^{-6}$ ;  $P < .05$ ,  $P < .005$ ). NAWM and DAWM, compared with HCWM, showed higher MD ( $616 \pm 22 \times 10^{-6}$ ,  $649 \pm 36 \times 10^{-6}$  versus  $597 \pm 15 \times 10^{-6}$ ;  $P < .005$ ) and AD ( $961 \pm 28 \times 10^{-6}$ ,  $996 \pm 39 \times 10^{-6}$  versus  $934 \pm 26 \times 10^{-6}$ ;  $P < .005$ ). Across time within the NAWM, there was an increase in RD ( $440 \pm 25 \times 10^{-6}$  versus  $448 \pm 33 \times 10^{-6}$ ;  $P < .05$ ) and MD ( $616 \pm 22 \times 10^{-6}$  versus  $623 \pm 24 \times 10^{-6}$ ;  $P < .005$ ).

## DISCUSSION

Diffuse and focal WM microstructural changes were assessed across time in the transition from detectable to undetectable gadolinium enhancement. nODI values were consistently higher during the acute enhancing phase of a lesion compared with a later time point after resolution of enhancement (GELs versus GEL-FU) as well as within acute-versus-chronic lesions (GELs versus NGELs). The ODI might, therefore, represent a new potential marker of acute inflammation. Changes in NODDI parameters with time correlate with long-term evolution of lesion size.

### nODI as a Marker of Acute Inflammation

Compared with HCs, markedly higher ODI values within MS lesions were observed during the acute inflammatory phase, indicated by gadolinium enhancement. These ODI values reduced toward HCWM values after the resolution of the enhancement. The association of higher ODI values with gadolinium enhancement suggests that ODI, when normalized for HC values (nODI), could be used as a potential radiologic marker of acute inflammation. The underlying histopathologic reasons for the nODI increase in the acute phase remain unknown.

A positive correlation between ODI and increased microglial density was reported in mice after withdrawal of colony-stimulating factor 1 receptor inhibition.<sup>21</sup> Likewise, the presence of a higher number of inflammatory cells within the core of acute-versus-chronic MS lesions<sup>22</sup> might partially explain the different ODI values detectable during gadolinium enhancement.

To date, only 1 longitudinal study assessed demyelinating lesions combining NODDI and histologic data. This work

focused on a mouse model of toxic demyelination (injection of lysolecithin), characterized mainly by myelin content changes rather than inflammatory activity.<sup>13</sup> Most interesting, even in this model, focal lesions showed higher ODI values compared with healthy WM only at the peak of demyelination. These values, then, decreased with time to values similar to those in healthy WM.<sup>13</sup> This change suggests that the increased nODI within lesions in the acute phase might be connected not only with inflammatory changes but also the active demyelination detectable during gadolinium enhancement.<sup>22</sup>

Despite its possible association with inflammation, increased nODI is not unique to acute (gadolinium-enhancing) lesions but can sometimes also be detected in nonenhancing lesions. This finding may indicate that part of the pathophysiologic processes underlying an increase in nODI in the acute phase (ie, acute demyelination/inflammatory changes) might still be ongoing during the subacute phase, after blood-brain barrier closure. The fact that we detected decreasing nODI with time even within lesions that did not enhance at baseline (NGELs) indicates that nODI (and perhaps inflammation) keeps decreasing after enhancement resolution.

The existing NODDI literature on nonenhancing lesions is controversial. Our findings are consistent with the work of Granberg et al<sup>10</sup> comparing nonenhancing lesions with the contralateral NAWM. In contrast, a previous study found ODI to be lower in nonenhancing lesions than in HCWM.<sup>7</sup> This discrepancy might result from differences in location when comparing lesions. As a result of the dispersion and architectonic organization of the fibers, ODI varies across the normal brain, with lower values within main WM pathways (ie, corpus callosum, superior longitudinal fascicle) and higher values in the subcortical regions. We specifically addressed this issue in building a WM ODI atlas (see the Online Appendix for detailed technical description) to extract reference values for each lesion, thereby accounting for lesion location variability.

Only 1 study to date correlated NGEL ODI with pathology in subjects with MS. Specifically, Grussu et al<sup>9</sup> detected reduced ODI within chronic WM lesions confirmed by a histology-derived ODI, suggesting that neurites can have reduced orientation variability compared with healthy tissue within areas of focal demyelination and profound axonal loss. This finding is in contrast with our results, though differences in patient characteristics and anatomic sites investigated confound direct comparison of these studies.

### Association of NDI and ODI Changes Over-Time as a Marker of Recovery and Possibly Remyelination

In line with previous cross-sectional studies,<sup>7,10</sup> we observed that NDI was consistently lower in WM lesions than in NAWM and HCWM. When we considered all GELs, NDI did not change during the transition from the acute-to-subacute phase, but at a single lesion level, we noticed a heterogeneity in the NDI changes with time. Approximately half (52%) of the lesions (type 1) showed increasing NDI over time along with decreasing ODI (Fig 2), whereas lesion type 2 (48% of the lesions) showed decreasing ODI and NDI with time (Fig 3).

In a toxic model of demyelination, remyelinating lesions showed a decreasing ODI and increasing NDI with time following the injury.<sup>13</sup> The authors suggested that these changes were

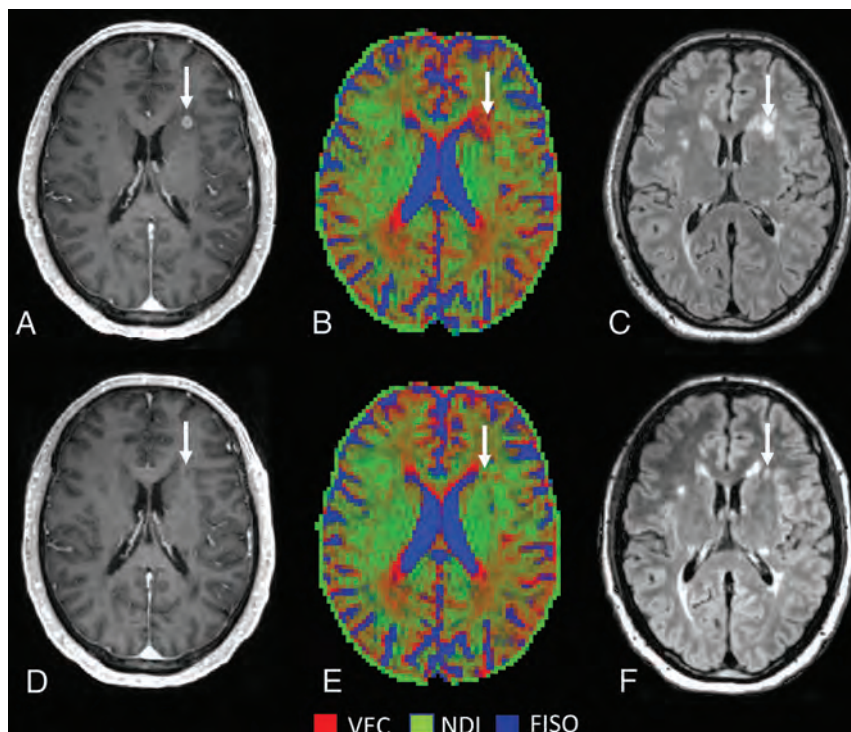


**FIG 2.** Lesion type 1 NODDI color map<sup>8</sup> graphically representing NDI (green) or VEC (red) compartment prevalence in voxels within a focal WM lesion (white arrows) at baseline (A–C) and at follow-up (after 12 months) (D–F). The green within the lesion is represented more at follow-up, after the disappearance of the enhancement, with a relative decrease of the red voxels. FLAIR sequences (C and F) show an important reduction in size with time. VEC and NDI are fractions in each voxel: If NDI increases, VEC decreases and vice versa. FISO indicates isotropic volume fraction.

due to increasing fiber coherency occurring along with the histologically-identified remyelination. With the precaution of translating these findings to MS, we speculate that the type 1 lesions we found might have a higher degree of remyelination compared with type 2 lesions, which might, in contrast, demonstrate ongoing tissue destruction. This hypothesis is supported by the finding that type 2 lesions also showed less shrinkage with time compared with type 1 lesions. Prior histopathologic data in MS suggest that remyelination occurs in approximately half of the lesions, a value similar in proportion to type 1 lesions in this study.<sup>23</sup>

#### NODDI Metrics in NAWM and DAWM

Even the longitudinal changes of NDI within the NAWM seem to depend on the predominant subtype of GEL. Specifically, subjects presenting exclusively with type 1 lesions did not show NDI changes with time within NAWM, whereas subjects with lesion type 2 (decreasing NDI with time, solely or combined with lesion type 1) showed decreasing NAWM NDI with time.

A report on scan-rescan reliability of NODDI showed that small biologic changes (<5%) may be detected with feasible sample sizes ( $n < 6-10$ ).<sup>24</sup> The presence of type 2 lesions may, therefore, identify a subset of subjects characterized both by partial lack of focal remyelination and progressive ongoing NAWM damage. The latter may be a consequence of anterograde and retrograde degeneration secondary to axonal and neuronal damage within focal lesions.<sup>25,26</sup> In our study, only 3/17 participants showed

exclusively type 2 lesions. Most interesting, 2 of them were the only primary-progressive cases included in the study, which might possibly indicate an association between type 2 lesions and a progressively worsening disease course.

Controversial results were reported for ODI changes within NAWM. We found lower ODI compared with HCWM, probably driven by predominant axonal loss rather than inflammation within NAWM.<sup>27</sup> In line with our findings, De Santis et al<sup>12</sup> found a trend for lower ODI in NAWM compared with HCWM, and a recent voxel-based-analysis study identified decreased ODI within the posterior and anterior limbs of the internal capsule with concomitant increased ODI in subcortical regions.<sup>11</sup> Another work, in contrast, found higher ODI in NAWM than in HCWM, possibly due to the limitations in ODI assessment as discussed above.<sup>7</sup> In the current study, we limited our analysis to the WM; therefore, our finding of slightly decreased ODI in NAWM might be mainly driven by changes in the major WM tracts.

#### Limitations

The present work shows several limitations: among them, the small number of subjects, the variable follow-up time, the absence of secondary-progressive MS participants, the convenience sampling, the lack of replication, and the possible confounding effect of various treatments.

Nonetheless, the lack of correlation with histopathologic data represents the most important limitation of our study. MR imaging/histopathology correlations are rarely performed in early relapsing-remitting MS due to limited tissue availability from biopsy, whereas postmortem studies mostly assess late disease stages. Our findings, however, are consistent with previous histologic studies. The higher ODI in the acute phase is likely to represent a combined result of inflammatory changes<sup>21</sup> and demyelination.<sup>13</sup> Regarding changes with time, our results are comparable with the only longitudinal work correlating NODDI metrics with histopathologic changes within focal demyelinated plaques.<sup>13</sup> The current work, however, only suggests speculative hypotheses that should be further confirmed with histopathologic correlation studies.

An additional important limitation of this work is that NDI does not represent an absolute but rather represents a relative measurement of neurite density. NODDI models the relative contribution of the intraneurite compartment (NDI) to the total diffusion signal in each voxel. Within brain tissue voxels, this compartment is mainly distinguished from the extra-neurite compartment (VEC), whereas the purely isotropic contribution does not play a major role. An increase in NDI might, therefore, indicate either a higher density of neurites or a reduced contribution by extracellular



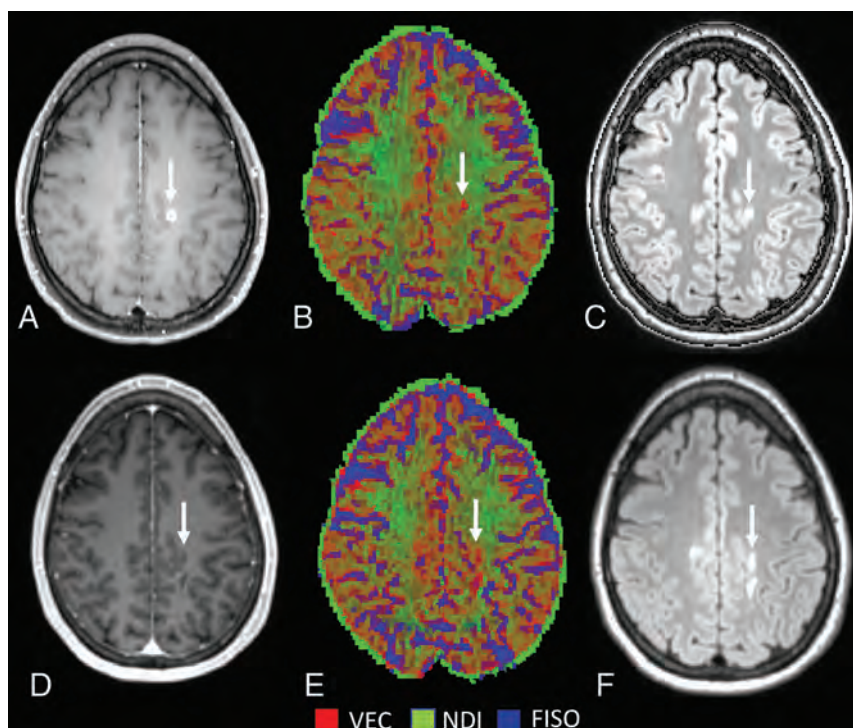


**FIG 3.** Lesion type 2 NODDI color map<sup>8</sup> graphically representing NDI (green) or VEC (red) compartment prevalence in voxels within a focal WM lesion (white arrows) at baseline (A–C) and at follow-up (after 15 months) (D–F). The green within the lesion is less represented at follow-up after the disappearance of the enhancement, with a relative increase of the red voxels. FLAIR sequences (C and F) show a moderate reduction in size with time. VEC and NDI are fractions in each voxel: If NDI decreases, VEC increases and vice versa. FISO indicates isotropic volume fraction.

spaces or other cell types. An increase in NDI with time is, indeed, theoretically consistent with both remyelination (NDI increases indicating recovery of axonal integrity) and reduction of inflammation (VEC decreases associated with reduction of edema and inflammatory cells).

## CONCLUSIONS

NODDI-derived metrics showed an intriguing potential in detecting acute inflammation and ongoing inflammatory disease activity. Assessing their changes with time might permit categorization of subacute and chronic lesion evolution in MS. The consistency of our MR imaging findings in subjects with MS with previous findings in animal models and the histopathologic correlation between NDI/ODI changes with time with remyelination suggest that NODDI imaging is also a potential tool to assess responses to neuroprotective or remyelinating therapies in vivo.

**Disclosures:** Simone Sacco—UNRELATED: Employment: University of Pavia, Italy, University of California, San Francisco. Riley M. Bove—UNRELATED: Comments: research; Provision of Writing Assistance, Medicines, Equipment, or Administrative Support: Genzyme Sanofi, Comments: writing assistance; Consultancy: Alexion, Biogen, EMD Serono, Roche Genentech, Genzyme Sanofi, Novartis; Grants/Grants Pending: Akili Interactive.\* Jeffrey M. Gelfand—UNRELATED: Consultancy: Biogen, Alexion Pharmaceuticals; Grants/Grants Pending: Genentech, Comments: research support for a clinical trial.\* Douglas S. Goodin—UNRELATED: Board Membership: Biogen Idec, Bayer Schering Pharma, Novartis, EMD Serono, Genzyme, and Teva Pharmaceuticals; Consultancy: Biogen Idec, Bayer Schering Pharma, Novartis, EMD Serono, Genzyme, and Teva Pharmaceuticals; Employment: Biogen Idec, Bayer

Schering Pharma, Novartis, EMD Serono, Genzyme, and Teva Pharmaceuticals; Grants/Grants Pending: Biogen Idec, Bayer Schering Pharma, Novartis, EMD Serono, Genzyme, and Teva Pharmaceuticals; Payment for Lectures Including Service on Speakers Bureaus: Biogen Idec, Bayer Schering Pharma, Novartis, EMD Serono, Genzyme, and Teva Pharmaceuticals. Roland G. Henry—RELATED: Grant: Roche/Genentech, Atara Biotherapeutics; Consulting Fee or Honorarium: Roche/Genentech, Novartis, Sanofi/Genzyme, QIA Consulting; UNRELATED: Board Membership: AbbVie, Roche, and Novartis; Employment: UCSF; Expert Testimony: StemCells Inc, Hoffmann-La Roche, and Sanofi Genzyme\*; Grants/Grants Pending: Ari J. Green—UNRELATED: Board Membership: Biogen and Medimmune, Novartis and Scientific Advisory Board for Bionure; Consultancy: Inception Sciences and Mylan Pharmaceuticals; Employment: UCSF; Grants/Grants Pending: National MS Society, Novartis, University of California San Francisco, CTSI, That Man May See. Bruce A. Cree—UNRELATED: Consultancy: Akili Interactive, Alexion, Atara Biotherapeutics, Biogen, EMD Serono, Novartis, Sanofi, and TG Therapeutics. Stephen L. Hauser—RELATED: Grant: National Institutes of Health/National Institute of Neurological Disorders and Stroke, National MS Society, Valhalla Charitable Foundation, Comments: R35NS111644, RR 2005-A-13; UNRELATED: Dr Hauser serves on the Board of Directors and received stock options for Neurona Therapeutics and serves on the Scientific Advisory Board and received stock options for Accure, Alector, Annexon Biosciences, and Molecular Stethoscope; he has also received nonfinancial support from Hoffmann-La Roche and Novartis (travel reimbursement and writing support for anti-CD20 meetings and presentations). Michael R. Wilson—UNRELATED: Grants/Grants Pending:

Roche/Genentech.\* Scott S. Zamvil—UNRELATED: Board Membership: Deputy Editor, *Neurology*, *Neuroimmunology and Neuroinflammation*; Consultancy: Alexion, Biogen Idec, Genzyme, Novartis, Roche/Genentech, Teva Pharmaceuticals; Grants/Grants Pending: National Institutes of Health 1 R01 AI13624-01-A1, National Institutes of Health R21 NS1081590-01, 1R21 AI142186-01\*; Payment for Lectures Including Service on Speakers Bureaus: Alexion, Genzyme, Novartis.\*Money paid to the institution.

## REFERENCES

- Thompson AJ, Banwell BL, Barkhof F, et al. **Diagnosis of multiple sclerosis: 2017 revisions of the McDonald criteria.** *Lancet Neurol* 2018;17:162–73 CrossRef Medline
- Filippi M, Rocca MA, Ciccarelli O, et al. **MRI criteria for the diagnosis of multiple sclerosis: MAGNIMS consensus guidelines.** *Lancet Neurol* 2016;15:292–303 CrossRef
- De Groot CJ, Bergers E, Kamphorst W, et al. **Post-mortem MRI-guided sampling of multiple sclerosis brain lesions: increased yield of active demyelinating and (p)reactive lesions.** *Brain* 2001;124:1635–45 CrossRef Medline
- Cercignani M, Bozzali M, Iannucci G, et al. **Intra-voxel and inter-voxel coherence in patients with multiple sclerosis assessed using diffusion tensor MRI.** *J Neurol* 2002;249:875–83 CrossRef Medline
- Gulani V, Calamante F, Shellock FG, et al; International Society for Magnetic Resonance in Medicine. **Gadolinium deposition in the brain: summary of evidence and recommendations.** *Lancet Neurol* 2017;16:564–70 CrossRef Medline
- Zhang H, Schneider T, Wheeler-Kingshott CA, et al. **NODDI: practical in vivo neurite orientation dispersion and density imaging of the human brain.** *Neuroimage* 2012;61:1000–16 CrossRef Medline

7. Schneider T, Brownlee W, Zhang H, et al. **Sensitivity of multi-shell NODDI to multiple sclerosis white matter changes: a pilot study.** *Funct Neurol* 2017;32:97–101 CrossRef Medline
8. Caverzasi E, Papinutto N, Castellano A, et al. **Neurite orientation dispersion and density imaging color maps to characterize brain diffusion in neurologic disorders.** *J Neuroimaging* 2016;26:494–98 CrossRef Medline
9. Grussu F, Schneider T, Tur C, et al. **Neurite dispersion: a new marker of multiple sclerosis spinal cord pathology?** *Ann Clin Transl Neurol* 2017;4:663–79 CrossRef Medline
10. Granberg T, Fan Q, Treaba CA, et al. **In vivo characterization of cortical and white matter neuroaxonal pathology in early multiple sclerosis.** *Brain* 2017;140:2912–26 CrossRef Medline
11. Spanò B, Giulietti G, Pisani V, et al. **Disruption of neurite morphology parallels MS progression.** *Neurol Neuroimmunol Neuroinflamm* 2018;5:e502 CrossRef Medline
12. De Santis S, Bastiani M, Droby A, et al. **Characterizing microstructural tissue properties in multiple sclerosis with diffusion MRI at 7T and 3T: the impact of the experimental design.** *Neuroscience* 2019;403:17–26 CrossRef Medline
13. Luo T, Oladosu O, Rawji KS, et al. **Characterizing structural changes with devolving remyelination following experimental demyelination using high angular resolution diffusion MRI and texture analysis.** *J Magn Reson Imaging* 2019;49:1750–59 CrossRef Medline
14. University of California, San Francisco MS-EPIC Team, Cree BA, Gourraud PA, et al. **Long-term evolution of multiple sclerosis disability in the treatment era.** *Ann Neurol* 2016;80:499–510
15. University of California, San Francisco MS-EPIC Team, Cree BAC, Hollenbach JA, et al. **Silent progression in disease activity-free relapsing multiple sclerosis.** *Ann Neurol* 2019;85:653–66
16. Andersson JL, Skare S, Ashburner J. **How to correct susceptibility distortions in spin-echo echo-planar images: application to diffusion tensor imaging.** *Neuroimage* 2003;20:870–88 CrossRef Medline
17. Smith SM, Jenkinson M, Woolrich MW, et al. **Advances in functional and structural MR image analysis and implementation as FSL.** *Neuroimage* 2004;23(Suppl 1):S208–19 CrossRef Medline
18. Garyfallidis E, Brett M, Amirbekian B, et al; DIPY Contributors. **DIPY, a library for the analysis of diffusion MRI data.** *Front Neuroinform* 2014;8:8 CrossRef Medline
19. Moore GR, Laule C, Mackay A, et al. **Dirty-appearing white matter in multiple sclerosis: preliminary observations of myelin phospholipid and axonal loss.** *J Neurol* 2008;255:1802–11 CrossRef Medline
20. Smith SM, Zhang Y, Jenkinson M, et al. **Accurate, robust and automated longitudinal and cross-sectional brain change analysis.** *Neuroimage* 2002;17:479–49 CrossRef Medline
21. Yi SY, Barnett BR, Torres-Velázquez M, et al. **Detecting microglial density with quantitative multi-compartment diffusion MRI.** *Front Neurosci* 2019;13:81 CrossRef Medline
22. Popescu BF, Pirko I, Lucchinetti CF. **Pathology of multiple sclerosis: where do we stand?** *Continuum (Minneapolis Minn)* 2013;19:901–21 CrossRef Medline
23. Barkhof F, Brück W, De Groot CJ, et al. **Remyelinated lesions in multiple sclerosis: magnetic resonance image appearance.** *Arch Neurol* 2003;60:1073–81 CrossRef Medline
24. McCunn P, Gilbert KM, Zeman P, et al. **Reproducibility of neurite orientation dispersion and density imaging (NODDI) in rats at 9.4 Tesla.** *PLoS One* 2019;14:e0215974 CrossRef Medline
25. Lassmann H. **Multiple sclerosis pathology.** *Cold Spring Harb Perspect Med* 2018;8:a028936 CrossRef Medline
26. Haider L, Zrzavy T, Hametner S, et al. **The topography of demyelination and neurodegeneration in the multiple sclerosis brain.** *Brain* 2016;139:807–15 CrossRef Medline
27. Thompson AJ, Baranzini SE, Geurts J, et al. **Multiple sclerosis.** *Lancet* 2018;391:1622–36 CrossRef Medline

# Development and Validation of a Deep Learning–Based Automatic Brain Segmentation and Classification Algorithm for Alzheimer Disease Using 3D T1-Weighted Volumetric Images

C.H. Suh, W.H. Shim, S.J. Kim, J.H. Roh, J.-H. Lee, M.-J. Kim, S. Park, W. Jung, J. Sung, and G.-H. Jahng, for the Alzheimer's Disease Neuroimaging Initiative



## ABSTRACT

**BACKGROUND AND PURPOSE:** Limited evidence has suggested that a deep learning automatic brain segmentation and classification method, based on T1-weighted brain MR images, can predict Alzheimer disease. Our aim was to develop and validate a deep learning–based automatic brain segmentation and classification algorithm for the diagnosis of Alzheimer disease using 3D T1-weighted brain MR images.

**MATERIALS AND METHODS:** A deep learning–based algorithm was developed using a dataset of T1-weighted brain MR images in consecutive patients with Alzheimer disease and mild cognitive impairment. We developed a 2-step algorithm using a convolutional neural network to perform brain parcellation followed by 3 classifier techniques including XGBoost for disease prediction. All classification experiments were performed using 5-fold cross-validation. The diagnostic performance of the XGBoost method was compared with logistic regression and a linear Support Vector Machine by calculating their areas under the curve for differentiating Alzheimer disease from mild cognitive impairment and mild cognitive impairment from healthy controls.

**RESULTS:** In a total of 4 datasets, 1099, 212, 711, and 705 eligible patients were included. Compared with the linear Support Vector Machine and logistic regression, XGBoost significantly improved the prediction of Alzheimer disease ( $P < .001$ ). In terms of differentiating Alzheimer disease from mild cognitive impairment, the 3 algorithms resulted in areas under the curve of 0.758–0.825. XGBoost had a sensitivity of 68% and a specificity of 70%. In terms of differentiating mild cognitive impairment from the healthy control group, the 3 algorithms resulted in areas under the curve of 0.668–0.870. XGBoost had a sensitivity of 79% and a specificity of 80%.

**CONCLUSIONS:** The deep learning–based automatic brain segmentation and classification algorithm allowed an accurate diagnosis of Alzheimer disease using T1-weighted brain MR images. The widespread availability of T1-weighted brain MR imaging suggests that this algorithm is a promising and widely applicable method for predicting Alzheimer disease.

**ABBREVIATIONS:** AD = Alzheimer disease; ADNI = Alzheimer's Disease Neuroimaging Initiative; AUC = area under the curve; CNN = convolutional neural network; MCI = mild cognitive impairment; OASIS = Open Access Series of Imaging Studies; SVM = Support Vector Machine

Alzheimer disease (AD) is the most common cause of dementia, with mild cognitive impairment (MCI) regarded as a

transitional state between normal cognition and early stages of dementia.<sup>1</sup> Although current therapeutic and preventive options are only moderately effective, a reliable decision-making diagnostic approach is important during early stages of AD.<sup>2,3</sup> The guidelines of the National Institute on Aging–Alzheimer's Association suggest that MR imaging is a supportive imaging tool in the diagnostic work-up of patients with AD and MCI.<sup>2,3</sup> Imaging biomarkers play an important role in the diagnosis of AD, both in

Received March 4, 2020; accepted after revision August 7.

From the Department of Radiology and Research Institute of Radiology (C.H.S., W.H.S., S.J.K.), Department of Neurology (J.H.R., J.-H.L.), and Health Screening and Promotion Center (M.-J.K.), Asan Medical Center, University of Ulsan College of Medicine, Seoul, Republic of Korea; Department of Physiology (J.H.R.), Korea University College of Medicine, Seoul, Republic of Korea; VUNO Inc (S.P., W.J., J.S.), Seoul, Republic of Korea; and Department of Radiology (G.-H.J.), Kyung Hee University Hospital at Gangdong, College of Medicine, Kyung Hee University, Seoul, Republic of Korea.

C.H. Suh and W.H. Shim contributed equally to this article.

This work was supported by a grant from the Institute for Information and Communications Technology Promotion, funded by the Korean government (C0510-18-1001; Intelligent SW Technology Development for Medical Data Analysis); a grant from the Korean Health Technology R&D Project, Ministry of Health and Welfare, Republic of Korea (H111C1238 or A111282); and a grant from the Basic Science Research Program through the National Research Foundation of Korea grant funded by the Korea government (2014RIA2A2A01002728).

Please address correspondence to Sang Joon Kim, MD, PhD, Department of Radiology and Research Institute of Radiology, Asan Medical Center, University of Ulsan College of Medicine, 88 Olympic-ro 43-gil, Songpa-Gu, Seoul 05505, Republic of Korea; e-mail: sjkimjb5@gmail.com

Indicates open access to non-subscribers at www.ajnr.org

Indicates article with supplemental online appendix and table.

<http://dx.doi.org/10.3174/ajnr.A6848>



**Table 1: Characteristics of the development and datasets<sup>a</sup>**

	Asan Medical Center	Kyung Hee University Hospital in Gangdong	ADNI	OASIS
No. of patients	1099	212	711	705
Age (mean) (yr)	65 ± 13	70 ± 9	76 ± 7	68 ± 10
No. of male patients	500 (45)	52 (25)	412 (58)	403 (57)
No. of female patients	599 (55)	160 (75)	299 (42)	302 (43)
Classification				
AD	161 (15)	68 (32)	178 (25)	145 (21)
Education (yr)	9.9 (4.8)	NA	14.5 (3.4)	14.0 (3.2)
MMSE score	18.5 (4.7)	17.4 (5.3)	22.8 (3.1)	24.4 (5.1)
Clinical Dementia Rating	1.00 (0.49)	1.10 (0.47)	0.73 (0.34)	0.68 (0.28)
Global Deterioration Scale	NA	NA	1.7 (1.4)	3.2 (7.3)
MCI	363 (33)	63 (30)	317 (45)	0
Education (yr)	10.1 (5.0)	NA	15.9 (2.5)	
MMSE score	24.9 (3.6)	25.7 (3.7)	26.4 (2.1)	
Clinical Dementia Rating	0.51 (0.09)	0.61 (1.16)	0.5	
Global Deterioration Scale	NA	NA	1.5 (1.3)	
Healthy control	575 (52)	81 (38)	216 (30)	560 (79)
Education (yr)	NA	NA	16.2 (2.8)	15.2 (2.7)
MMSE score	29.5 (0.5)	27.7 (2.5)	29.1 (1.0)	28.8 (3.2)
Clinical Dementia Rating	NA	0.24 (0.26)	0	0
Global Deterioration Scale	NA	NA	0.8 (1.1)	1.3 (4.0)

**Note:**—MMSE indicates Mini-Mental State Examination; NA, not available.

<sup>a</sup> Unless otherwise indicated, data are reported as number (%).

the research field and in clinical practice. The identification of amyloid and the  $\tau$  PET ligand provided huge advances in understanding the pathophysiologic mechanisms underlying AD and its early diagnosis, even in the preclinical or prodromal stage.<sup>4–6</sup> Although amyloid and  $\tau$  PET are more sensitive and specific for the diagnosis of AD, they are expensive to perform, have limited availability, and require ionizing radiation, limiting their use in clinical practice. CSF amyloid and  $\tau$  are also important biomarkers that could be used for AD diagnostics in the clinical research setting.<sup>3,7–9</sup> However, CSF AD biomarkers also have limited availability. MR imaging, however, is widely available and used in standard practice to support the diagnosis of AD and to exclude other causes of cognitive impairment, including stroke, vascular dementia, normal-pressure hydrocephalus, and inflammatory and neoplastic conditions.

3D T1-weighted volumetric MR imaging is the most important MR imaging tool in the diagnosis of AD. 3D volumetry has long been used as a morphologic diagnostic tool for AD, not only as a visual assessment or manual segmentation but for semiautomatic and automatic segmentation. Examples include semiautomatic structural changes on MR imaging,<sup>10</sup> automated hippocampal volumetry,<sup>11</sup> entorhinal cortex atrophy,<sup>12</sup> and changes in pineal gland volume.<sup>13</sup> Although user-friendly automated segmentation algorithms were first introduced 20 years ago, evidence supporting the use of 3D volumetry in clinical practice is currently insufficient. Visual assessment requires experience, and automatic 3D volumetry requires a long acquisition time.

To our knowledge, limited evidence has suggested that a deep learning automatic brain segmentation and classification method,

based on T1-weighted brain MR images, can predict AD.<sup>14</sup> Currently available algorithms have low clinical feasibility because of the long processing time for brain segmentation, and the classification algorithm based on T1-weighted brain MR images needs to be validated in a large external dataset. The purpose of this study was to develop and validate a deep learning–based automatic brain segmentation and classification algorithm for the diagnosis of AD using 3D T1-weighted brain MR images.

## MATERIALS AND METHODS

This study was approved by the institutional review boards of all participating institutions, which waived the requirement for informed consent due to the retrospective design of this study.

### Development and Validation Dataset

The deep learning–based automatic brain segmentation and classification algorithm was developed using a dataset of T1-weighted brain MR images from consecutive patients with AD and MCI who met the diagnostic criteria. This dataset was derived from consecutive patients who were referred to a neurology memory clinic and underwent brain MR imaging at Asan Medical Center between December 2014 and March 2017. Patients were considered eligible if their electronic medical records were available, and they had no treatment history of antedementia or psychoactive drugs and no history of neurologic or psychiatric disorders other than AD or MCI. Clinical diagnosis served as the reference standard for AD and MCI, which were diagnosed in all patients by 2 experienced neurologists on the basis of the diagnostic guidelines of the National Institute on Aging–Alzheimer’s Association workgroups.<sup>3,7</sup> During the same period, healthy controls were enrolled at Asan Medical Center Health Screening and Promotion Center. Healthy controls were recruited with the following inclusion criteria: no memory impairment, no history of neurologic or psychiatric disorders, and no history of being treated with antedementia or psychoactive drugs.

The patients and healthy controls from Kyung Hee University Hospital in Gangdong who met the same eligibility criteria were evaluated. To externally validate the algorithm using public datasets, we used the Alzheimer Disease Neuroimaging Initiative (ADNI) and the Open Access Series of Imaging Studies (OASIS) datasets. Their final diagnoses were downloaded from the ADNI web portal ([adni.loni.ucla.edu](http://adni.loni.ucla.edu))<sup>15</sup> and the OASIS web portal ([oasis-brains.org](http://oasis-brains.org)), respectively. Patients included in these datasets met the same eligibility criteria. None of the brain MR images in datasets overlapped the images in the other datasets. The characteristics of the datasets are shown in Table 1.

All classification experiments were performed using 5-fold cross-validation. Each of the 4 datasets was divided into 5 folds. For each fold containing 4/5 and 1/5 of the training and validation split, respectively, the training set was further partitioned evenly into 5 segments to obtain an ensemble of 5 models, which was then evaluated on the remaining 1/5 validation data. Areas under the curve (AUCs), sensitivity, specificity, positive predictive value, and negative predictive value were used as the evaluation metrics.

### **MR Imaging Protocol**

The MR imaging data in this study were obtained using various MR imaging machines at multiple institutions. MRIs at Asan Medical Center were performed on 3T units (Ingenia; Philips Healthcare) using a 32-channel sensitivity encoding head coil. High-resolution anatomic 3D volume images were obtained in the sagittal plane using a 3D gradient-echo T1-weighted sequence. The detailed parameters included a TR of 9.6 ms, TE of 4.6 ms, a flip angle of 8°, an FOV of  $224 \times 224$  mm, section thickness of 1 mm with no gap, and a matrix size of  $224 \times 224$ .

MRIs at Kyung Hee University Hospital in Gangdong were performed on a 3T MR imaging scanner (Achieva; Philips Healthcare) using a dedicated 8-element phased array sensitivity encoding head coil. 3D T1-weighted sagittal images were acquired using an MPRAGE sequence with imaging parameters that included a TR of 9.9 ms, a TE of 4.6 ms, a flip angle of 8°, an FOV of  $240 \times 240$  mm, a section thickness of 1 mm, a matrix size of  $240 \times 240$ , and a resolution of  $1.00 \times 1.00 \times 1.00$  mm.<sup>3</sup> In the ADNI dataset, the section thickness was 1.2 mm with no gaps. In the OASIS dataset, the section thickness was 1.25 mm with no gaps.

### **Development of Deep Learning–Based Automatic Classification Algorithm**

**Brain Parcellation Module.** The proposed deep learning–based AD classification system consisted of a deep convolutional neural network (CNN) module and an XGBoost module (<https://hackernoon.com/want-a-complete-guide-for-xgboost-model-in-python-using-scikit-learn-sc11f31bq>). The deep CNN module parcellated each brain into 82 areas. The proposed deep CNN had a 2.5 channel HighResnet architecture ([https://github.com/NifTK/NiftyNet/tree/dev/demos/brain\\_parcellation](https://github.com/NifTK/NiftyNet/tree/dev/demos/brain_parcellation)), consisting of 44 convolution layers without a strided convolution or pooling layer. The HighResnet architecture, in which layers were stacked as deep as possible using atrous convolution rather than pooling or stride, has been shown to perform brain parcellation well.<sup>16</sup> 2.5D CNN is a method designed to use 3D information while still using 2D CNN architecture. This method concatenates a target section and other slices around the target in the channel dimension and uses it as the input to the network. This method is widely used for medical images that include 3D imaging data.<sup>17</sup>

HighResnet is a network of deeply stacked blocks with residual connections. The residual connection is a method proposed to solve the degradation problem, in which accuracy is saturated as the depth of the network increases.<sup>18</sup> The residual connection helps in effective training, even if the layer blocks are deeply stacked. A neural network with  $n$  residual connections was found to have  $2^n$  unique pathways.<sup>19</sup> Thus, a network with residual

connections has the same effect as using receptive fields of various sizes without having a fixed receptive field.<sup>20</sup> Details of the brain parcellation module are described in the On-line Appendix.

**Volume-Based AD Classification Algorithm.** On the basis of this parcellated brain volume information, the XGBoost module classified patients into the AD, MCI, and healthy control groups. We compared our AD classification method against logistic regression and the linear Support Vector Machine (SVM). Both methods have been implemented by Scikit-learn (Version 0.21.0; <https://scikit-learn.org/>). The detailed network structure of the parcellation CNN module is summarized in Fig 1. The 2 modules were cascaded for use as a fully automated classification system. The network was trained using an ADAM optimizer<sup>21</sup> with an initial learning rate of 0.001. The exponential decay rates for the first- and second-moment estimates were 0.9 and 0.999, respectively.

Both modules were coded in Python (Version 2.7; Python Software Foundation). The parcellation CNN module was implemented using Tensorflow libraries (Version 1.12; <https://www.tensorflow.org>), whereas the classification XGBoost module was implemented using DMLC XGBoost packages (Version 0.80; <https://xgboost.ai/> and <https://github.com/dmlc/xgboost/blob/master/CITATION>).

This study did not use an end-to-end approach to classify AD. Rather, the entire system was divided into a parcellation module using a CNN and a classification module using XGBoost. The features extracted from the CNN activation maps are difficult to interpret medically, whereas the volumes of brain regions are directly associated with the degree of cortical atrophy due to AD. In addition, differently distributed volumes can distinguish among AD, MCI, and healthy controls. In neurodegeneration research, normalization of regional volume by intracranial volume is crucial to reduce interindividual variation. To measure whole-brain volumes, we developed a brain-extraction method, which is another deep learning–based semantic segmentation algorithm. We divided raw volumes of brain parcellation by the whole-brain volume. In addition, to remove the age-related effects of brain volumes and reflect sex matching, we composed 82 volumes, age, and sex (0 or 1) as input data for classification. It is a multivariate approach of age and sex matching. Transformation of each T1-weighted brain MR image into the volume of each brain region reduces the dimensionality of the data. When the data dimensionality is relatively small, a classifier using the boosting technique is efficient.<sup>22</sup> Therefore, AD, MCI, and healthy controls were classified using XGBoost.

Boosting is a method by which weak classifiers can be grouped into sets, with these ensembles used to predict results. XGBoost is a tree-boosting algorithm, using an ensemble model called a classification and a regression tree to create a tree classifier. Tree boosting is a highly effective and widely used machine learning method. The hyperparameters for XGBoost learning were set at a maximum depth of 5, 102 estimators, and a learning rate of 0.9.

### **Evaluation of Algorithms and Statistical Analyses**

On the basis of T1-weighted brain MR images, the trained deep learning–based automatic classification algorithm generated continuous probabilities, ranging from 0 to 1, that patients had AD. The primary outcome was to investigate the diagnostic performance of

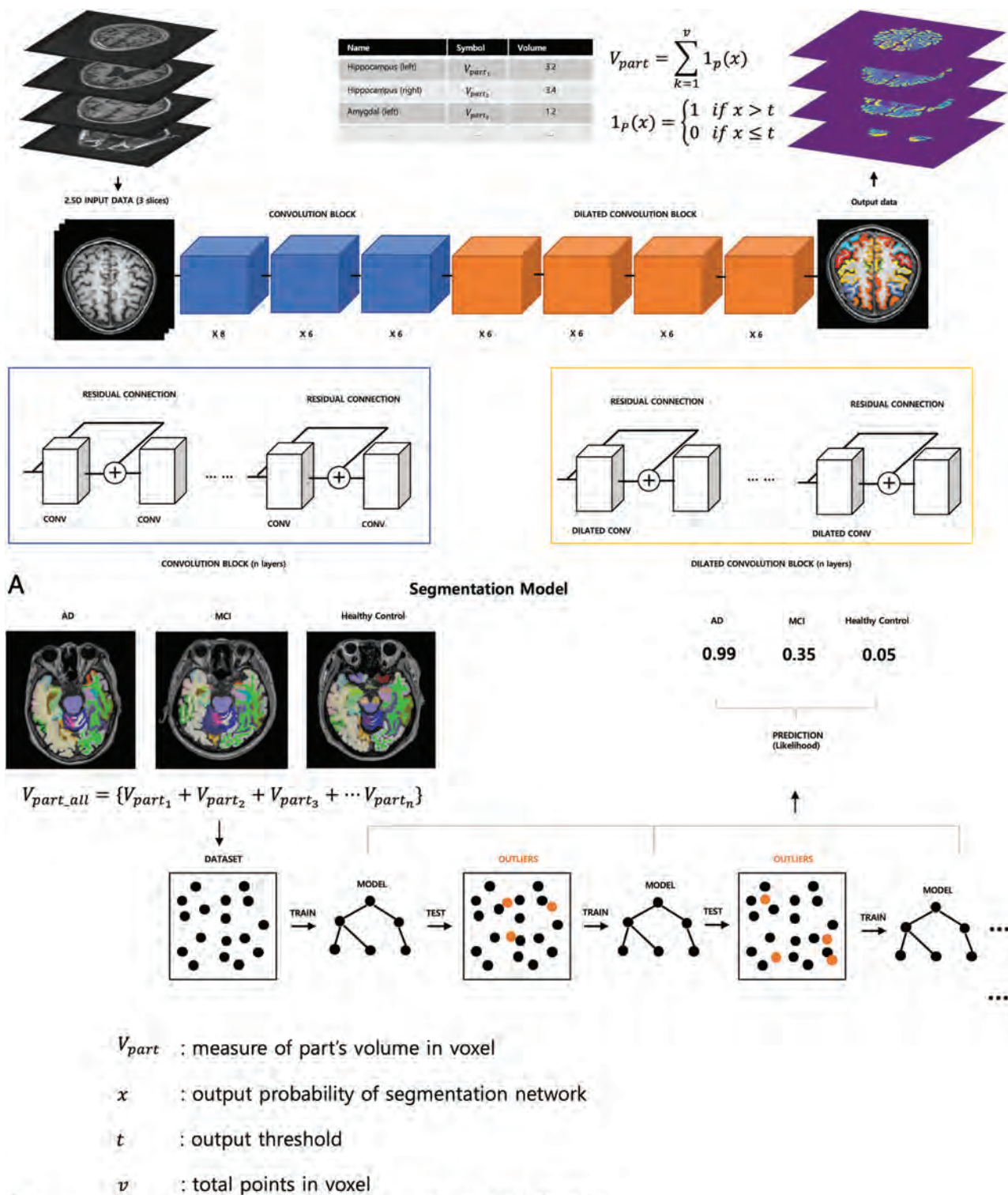


**FIG 1.** Network architecture of the brain parcellation and classification model. CONV indicates convolution.

the algorithm in differentiating AD from MCI and MCI from healthy controls. The secondary outcome was to investigate the diagnostic performance of the algorithm in differentiating AD from healthy controls. The impact of each feature (volume of each brain region) on the AD prediction model was reported using Shapley values (Fig 2), in which the impact of a feature is defined as the

change in the expected output of the model when a feature is, compared with when it is not, observed.<sup>23</sup>

The XGBoost method was compared with 2 other commonly used classification methods for the prediction of AD, logistic regression and linear SVM. The diagnostic performance of the 3 methods was compared using the method of Delong et al<sup>24</sup> to



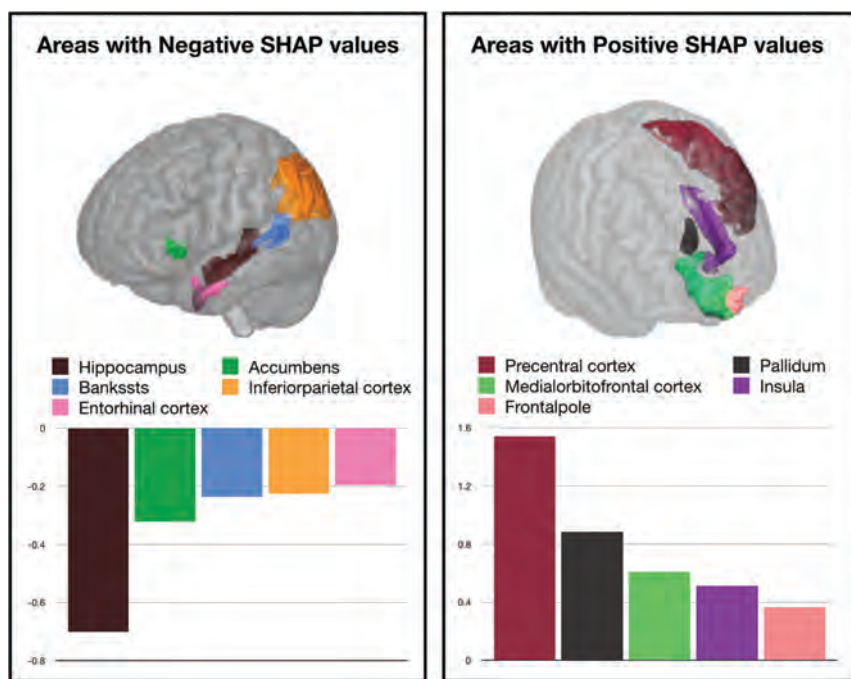


**FIG 2.** The impact of feature (volume of each brain region) on the AD prediction model, as represented by Shapley values, in which the impact of a feature is defined as the change in the expected output of the model when a feature is observed versus unknown. A, Visualization of the top 5 brain regions representing feature impacts pushing the decision of the model to AD, along with average feature impact. B, Visualization of the top 5 brain regions representing feature impacts pushing the decision of the model to healthy controls, along with average feature impact. Bankssts indicates banks of the superior temporal sulcus; SHAP, Shapley Additive Explanations (<https://pbiecek.github.io/ema/shapley.html>).

calculate the standard error of the AUC and the difference among the 3 AUCs. Optimal cutoff probabilities for differentiating AD or MCI were obtained from receiver operating characteristic curves, with the sensitivity, specificity, positive predictive value, negative predictive value, and AUC calculated using the Youden index,<sup>25</sup> defined as sensitivity + specificity - 1, with values ranging from -1 to +1. The parcellation module was evaluated with a mean Dice Similarity Coefficient using the ground truth segmentation mask of FreeSurfer (<http://surfer.nmr.mgh.harvard.edu>). All statistical analyses were performed using MedCalc, Version 18.6 (MedCalc Software), with  $P < .05$  defined as statistically significant.

## RESULTS

### Patient Demographics

Of the 1099 eligible patients who underwent T1-weighted MR imaging at the Asan Medical Center, 161 were diagnosed with probable AD, 363 were diagnosed with MCI, and 575 were classified as healthy controls (Table 1). The mean ages of these 3 groups were  $75 \pm 8$  years,  $69 \pm 10$  years, and  $57 \pm 9$  years, respectively, and there was a statistically difference ( $P < .01$ ). In 212 patients from the dataset of Kyung Hee University Hospital in Gangdong, 68 patients were diagnosed with probable AD, 63 were diagnosed with MCI, and 81 were classified as healthy controls. The mean ages of these 3 groups were  $75 \pm 8$  years,  $70 \pm 8$  years, and  $65 \pm 9$  years, respectively, and there was a statistically

significant difference ( $P < .01$ ). The ADNI dataset included 178 patients diagnosed with AD, 317 diagnosed with MCI, and 216 healthy controls; their mean ages were  $76 \pm 8$  years,  $75 \pm 8$  years, and  $77 \pm 5$  years, respectively. The OASIS dataset included 145 patients diagnosed with AD and 560 healthy controls; their mean ages were  $74 \pm 8$  years and  $70 \pm 9$  years, respectively.

### Diagnostic Performance in AD versus MCI

In the Asan Medical Center dataset, the AUCs for logistic regression, linear SVM, and XGBoost were 0.770 (95% CI, 0.761–0.779), 0.772 (95% CI, 0.761–0.782), and 0.803 (95% CI, 0.802–0.805), respectively (Table 2). Use of XGBoost significantly improved the prediction of AD compared with the linear SVM ( $P < .001$ ) and logistic regression ( $P < .001$ ). Because XGBoost showed the highest AUC, this method was chosen to provide the optimal cutoff value. XGBoost had a sensitivity of 71% (95% CI, 69%–72%) and a specificity of 74% (95% CI, 74%–74%), with an optimal cutoff value of 0.613 (On-line Table).

In the dataset of the Kyung Hee University Hospital in Gangdong, the AUCs for logistic regression, linear SVM, and XGBoost were 0.798 (95% CI, 0.775–0.822), 0.804 (95% CI, 0.783–0.824), and 0.825 (95% CI, 0.810–0.840). In the ADNI dataset, the AUCs for logistic regression, linear SVM, and XGBoost were 0.706 (95% CI, 0.702–0.710), 0.700 (95% CI, 0.695–0.704), and 0.758 (95% CI, 0.755–0.760), respectively.

### Diagnostic Performance in MCI versus Healthy Controls

In the Asan Medical Center dataset, the AUCs for logistic regression, linear SVM, and XGBoost were 0.812 (95% CI, 0.806–0.817), 0.830 (95% CI, 0.821–0.840), and 0.870 (95% CI, 0.868–0.872), respectively (Table 2). Use of XGBoost significantly improved the prediction of AD compared with the linear SVM ( $P < .001$ ) and logistic regression ( $P < .001$ ). XGBoost had a sensitivity of 79% (95% CI, 78%–79%) and a specificity of 80% (95% CI, 79%–81%), with an optimal cutoff value of 0.016 (On-line Table).

In the dataset of the Kyung Hee University Hospital in Gangdong, the AUCs for logistic regression, linear SVM, and XGBoost were 0.692 (95% CI, 0.678–0.706), 0.687 (95% CI, 0.669–0.706), and 0.705 (95% CI, 0.699–0.712), respectively. In the ADNI dataset, the AUCs for logistic regression, linear SVM, and XGBoost were 0.698 (95% CI, 0.686–0.710), 0.702 (95% CI, 0.697–0.708), and 0.668 (95% CI, 0.664–0.671), respectively. The diagnostic performance of the algorithm in differentiating AD from healthy controls is shown in Table 2 and the On-line Table.

**Table 2: Diagnostic performance of logistic regression, the linear Support Vector Machine, and the deep learning-based automatic classification algorithm in the datasets<sup>a</sup>**

	Logistic Regression	Linear SVM	XGBoost	P Value <sup>b</sup>	P Value <sup>c</sup>
AD vs MCI					
Asan Medical Center	0.770 (0.761–0.779)	0.772 (0.761–0.782)	0.803 (0.802–0.805)	<.001	<.001
Kyung Hee University Hospital at Gangdong	0.798 (0.775–0.822)	0.804 (0.783–0.824)	0.825 (0.810–0.840)	.018	.030
ADNI	0.706 (0.702–0.710)	0.700 (0.695–0.704)	0.758 (0.755–0.760)	<.001	<.001
MCI vs healthy control					
Asan Medical Center	0.812 (0.806–0.817)	0.830 (0.821–0.840)	0.870 (0.868–0.872)	<.001	<.001
Kyung Hee University Hospital at Gangdong	0.692 (0.678–0.706)	0.687 (0.669–0.706)	0.705 (0.699–0.712)	.029	.023
ADNI	0.698 (0.686–0.710)	0.702 (0.697–0.708)	0.668 (0.664–0.671)	<.001	<.001
AD vs healthy controls					
Asan Medical Center	0.953 (0.949–0.958)	0.960 (0.958–0.963)	0.982 (0.980–0.985)	<.001	<.001
Kyung Hee University Hospital at Gangdong	0.905 (0.889–0.921)	0.911 (0.903–0.920)	0.940 (0.933–0.947)	<.001	<.001
ADNI	0.863 (0.856–0.870)	0.860 (0.857–0.863)	0.885 (0.879–0.891)	<.001	<.001
OASIS <sup>d</sup>	0.826 (0.817–0.835)	0.820 (0.809–0.832)	0.840 (0.837–0.844)	.001	<.001

<sup>a</sup> Data are AUC (95% CI).

<sup>b</sup> P values: between logistic regression and XGBoost.

<sup>c</sup> P values: between linear SVM and XGBoost.

<sup>d</sup> OASIS dataset included only AD and healthy controls.

### Performance Evaluation of Brain Parcellation Module

Dice Similarity Coefficients for Asan Medical Center, ADNI, and OASIS datasets were 82.0 (95% CI, 81.6–82.4), 82.3 (95% CI, 81.5–83.1), and 82.0 (95% CI, 81.6–82.4), respectively. This performance is almost identical to the 82.05, on average, reported by Li et al.<sup>16</sup>

## DISCUSSION

The present study describes the development and validation of a deep learning-based automatic brain segmentation and classification algorithm using T1-weighted brain MR images for the diagnosis of AD. This algorithm resulted in the accurate diagnosis of AD, with AUCs of 0.758–0.825 in differentiating AD from MCI and AUCs of 0.668–0.870 in differentiating MCI from healthy controls. Because of the widespread availability of T1-weighted brain MR imaging, the deep learning-based automatic brain segmentation and classification algorithm is a promising and widely applicable method for prediction of AD.

The CNN parcellation module developed in this study successfully mimicked FreeSurfer,<sup>26</sup> with only 20 seconds required for parcellation and classification of each MR image. One of the disadvantages of previous methods for parcellation, including FreeSurfer and NeuroQuant (CorTechs Labs), was their long processing times (FreeSurfer, 7 hours; NeuroQuant, 5–7 minutes).<sup>27,28</sup> In addition, our deep learning-based automatic brain segmentation and classification algorithm (XGBoost) was robust across various clinical settings, even in public datasets, showing improved diagnostic performance for the prediction of AD compared with the linear SVM and logistic regression. XGBoost can easily handle sparse data using sparsity-aware algorithms and is scalable to various tasks<sup>22</sup> in medicine, including AD classification, medical text data, and temporal data. The gradient-boosting algorithm constructed the new base learners to be maximally correlated with the negative gradient of the loss function, which is associated with many decision trees (weak learners). The gradient boosting algorithm consistently provided greater accuracy than conventional single, strong, machine learning models. Because the Dice Similarity Coefficients for the Asan Medical Center, ADNI, and OASIS datasets were similar, XGBoost

may contribute to performance differences among XGBoost, SVM, and logistic regression.

The algorithm we developed was based on brain volumes determined on T1-weighted brain MR images. This algorithm yielded probabilities of 0–1 for each patient. The optimal cutoff value was 0.613, showing a sensitivity of 71% (95% CI, 69%–72%) and a specificity of 74% (95% CI, 74%–74%) in predicting AD differentiation from MCI. In clinical practice, it is difficult to predict AD using MR imaging, though several imaging findings may be predictive of advanced AD. MR imaging findings during the early stages of AD are subtle, with visual assessments of these findings being subjective. Use of our high-speed, accurate deep learning-based automatic brain segmentation and classification algorithm could predict the likelihood of AD in patients with cognitive impairment or when screening individuals in daily clinical practice. Moreover, the present study demonstrated high diagnostic performance of the algorithm in differentiating AD from healthy controls (AUC = 0.840–0.982) and MCI from healthy controls (AUC = 0.668–0.870). Thus, our results may broaden the clinical utility of a deep learning-based automatic brain segmentation and classification algorithm for patients with memory impairment.

Among the various imaging methods available for evaluating AD, T1-weighted brain MR imaging and FDG-PET MR imaging have been widely validated and have shown clinical efficacy.<sup>14,29</sup> For example, an ensemble learning system for classification of AD, MCI, and healthy controls was developed using an ADNI dataset, and a parameter-efficient deep learning approach was found to be highly accurate (AUC = 0.925) in predicting conversion from MCI to AD in an ADNI dataset.<sup>14</sup> Similarly, the accuracy of a deep learning algorithm for early prediction of AD using <sup>18</sup>F-FDG-PET results was found to be 0.98 (95% CI, 0.94–1.00).<sup>29</sup> These studies mainly focused on predicting the early conversion to AD among patients with MCI. By contrast, our study demonstrated that our algorithm was accurate in differentiating AD from MCI (AUCs = 0.758–0.825) and MCI from healthy controls (AUC = 0.668–0.870), which may be due to the large overlap between AD and MCI. However, our findings were validated externally in large patient cohorts. In the Kaggle 2016 competition (a machine learning neuroimaging

challenge for automated diagnosis of mild cognitive impairment), the winner of the competition attempted to quantify the prediction accuracy of multiple morphologic MR imaging features and achieved a precision of 76% for the class AD and a precision of 45%–64% for the class MCI, which was lower than our results.<sup>30</sup>

This study externally validated our deep learning–based automatic brain segmentation and classification algorithm using 3 different test datasets. A recent analysis reported that only 31 of 516 (6%) studies included external validation.<sup>31</sup> Evaluation of the clinical performance of a diagnostic or predictive artificial intelligence model requires the analysis of external data from a clinical cohort that appropriately represents the target patient population, avoiding overestimation of the initial results because of overfitting and spectrum bias.<sup>32</sup> Our results showed that the diagnostic performance of our algorithm was similar for internal (AUC = 0.803) and external (AUC = 0.758–0.825) datasets, indicating no overfitting.

The present study had several limitations. First, this study was based on retrospective data from selected patient groups and did not include patients with non-AD neurodegenerative diseases. This study, however, was not intended to develop an all-inclusive tool to differentiate various causes of cognitive impairment, suggesting that application of this algorithm to such populations may be limited. Further validation with larger, prospectively collected test datasets may be necessary to determine whether our algorithm is applicable to various types of cognitive impairment.<sup>33</sup> Second, the diagnostic criteria of AD were based on the clinical diagnosis; therefore, these might be different from a diagnosis based on amyloid PET or  $\tau$  PET. However, our study was based on retrospective data from the clinical field; thus, we could use only diagnostic criteria of AD based on clinical diagnosis. Third, further research is required to assess the clinical benefits of the deep learning–based automatic classification algorithm in predicting the prognosis and helping to manage patients with AD. In addition, longitudinal outcome studies evaluating the likelihood of decline or progression to MCI or AD in an individual using longitudinal MR imaging data are necessary.

## CONCLUSIONS

The deep learning–based automatic brain segmentation and classification algorithm developed in this study was accurate in diagnosing AD using T1-weighted brain MR images. The widespread availability of T1-weighted brain MR imaging indicates that this algorithm may be a promising and widely applicable method for prediction of AD.

Disclosures: Sang Joon Kim—RELATED: Grant: funded by the Korean government (C0510-18-1001). Jee Hoon Roh—RELATED: Grant: from the Korea Health Technology Research and Development Project through the Korea Health Industry Development Institute funded by the Ministry of Health and Welfare, Republic of Korea (H14C3319).\* Sejin Park—UNRELATED: Employment: VUNO Inc. Jinkyong Sung—UNRELATED: Employment: VUNO Inc. Wonmo Jung—UNRELATED: Money paid to the institution.




















## REFERENCES

- Petersen RC, Negash S. **Mild cognitive impairment: an overview.** *CNS Spectr* 2008;13:45–53 CrossRef Medline
- Dubois B, Feldman HH, Jacova C, et al. **Research criteria for the diagnosis of Alzheimer's disease: revising the NINCDS-ADRDA criteria.** *Lancet Neurol* 2007;6:734–46 CrossRef Medline
- McKhann GM, Knopman DS, Chertkow H, et al. **The diagnosis of dementia due to Alzheimer's disease: recommendations from the National Institute on Aging-Alzheimer's Association workgroups on diagnostic guidelines for Alzheimer's disease.** *Alzheimers Dement* 2011;7:263–69 CrossRef Medline
- Jack CR Jr, Bennett DA, Blennow K, et al; Contributors. **NIA-AA research framework: toward a biological definition of Alzheimer's disease.** *Alzheimers Dement* 2018;14:535–62 CrossRef Medline
- Johnson KA, Schultz A, Betensky RA, et al. **Tau positron emission tomographic imaging in aging and early Alzheimer disease.** *Ann Neurol* 2016;79:110–19 CrossRef Medline
- Jack CR Jr, Bennett DA, Blennow K, et al. **A/T/N: an unbiased descriptive classification scheme for Alzheimer disease biomarkers.** *Neurology* 2016;87:539–47 CrossRef Medline
- Albert MS, DeKosky ST, Dickson D, et al. **The diagnosis of mild cognitive impairment due to Alzheimer's disease: recommendations from the National Institute on Aging-Alzheimer's Association workgroups on diagnostic guidelines for Alzheimer's disease.** *Alzheimers Dement* 2011;7:270–79 CrossRef Medline
- Sperling RA, Aisen PS, Beckett LA, et al. **Toward defining the preclinical stages of Alzheimer's disease: recommendations from the National Institute on Aging-Alzheimer's Association workgroups on diagnostic guidelines for Alzheimer's disease.** *Alzheimers Dement* 2011;7:280–92 CrossRef Medline
- Jack CR Jr, Albert MS, Knopman DS, et al. **Introduction to the recommendations from the National Institute on Aging-Alzheimer's Association workgroups on diagnostic guidelines for Alzheimer's disease.** *Alzheimers Dement* 2011;7:257–62 CrossRef Medline
- McEvoy LK, Fennema-Notestine C, Roddey JC, et al; Alzheimer's Disease Neuroimaging Initiative. **Alzheimer disease: quantitative structural neuroimaging for detection and prediction of clinical and structural changes in mild cognitive impairment.** *Radiology* 2009;251:195–205 CrossRef Medline
- Colliot O, Chetelat G, Chupin M, et al. **Discrimination between Alzheimer disease, mild cognitive impairment, and normal aging using automated segmentation of the hippocampus.** *Radiology* 2008;248:194–201 CrossRef Medline
- Enkirsch SJ, Traschutz A, Muller A, et al. **The ERICA score: an MR imaging-based visual scoring system for the assessment of entorhinal cortex atrophy in Alzheimer disease.** *Radiology* 2018;288:226–333 CrossRef Medline
- Matsuoka T, Imai A, Fujimoto H, et al. **Reduced pineal volume in Alzheimer disease: a retrospective cross-sectional MR imaging study.** *Radiology* 2018;286:239–48 CrossRef Medline
- Spasov S, Passamonti L, Duggento A, et al; Alzheimer's Disease Neuroimaging Initiative. **A parameter-efficient deep learning approach to predict conversion from mild cognitive impairment to Alzheimer's disease.** *Neuroimage* 2019;189:276–87 CrossRef Medline
- Mueller SG, Weiner MW, Thal LJ, et al. **The Alzheimer's Disease Neuroimaging Initiative.** *Neuroimaging Clin N Am* 2005;15:869–77. xi-xii CrossRef Medline
- Li W, Wang G, Fidon L, et al. **On the compactness, efficiency, and representation of 3D convolutional networks: brain parcellation as a pretext task.** In: *Proceedings of the International Conference on Information Processing in Medical Imaging*, Boone, North Carolina; June 25–30, 2017
- Roth HR, Lu L, Seff A, et al. **A new 2.5 D representation for lymph node detection using random sets of deep convolutional neural network observations.** In: *Proceedings of International Conference on Medical Image Computing and Computer-Assisted Intervention*; Springer; 2014;520–27
- He K, Zhang X, Ren S, et al. **Deep residual learning for image recognition.** In: *Proceedings of the IEEE Conference on Computer Vision and Pattern Recognition*, Las Vegas, Nevada; June 27–30, 2016 CrossRef



19. Veit A, Wilber M, Belongie S. **Residual networks are exponential ensembles of relatively shallow networks**. October 2016. *arXiv.org*. <https://arxiv.org/abs/1605.06431v1>. Accessed Aug 1, 2019
20. Luo W, Li Y, Urtasun R, et al. **Understanding the effective receptive field in deep convolutional neural networks**. January 2017. *arXiv.org*. <https://arxiv.org/abs/1701.04128>. Accessed Aug 1, 2019
21. Kingma DP, Ba J. **Adam: a method for stochastic optimization**. December 2014. *arXiv.org* <https://arxiv.org/abs/1412.6980>. Accessed Aug 1, 2019
22. Chen T, Guestrin C. **XGBoost: a scalable tree boosting system**. In: *Proceedings of the 22nd ACM SIGKDD International Conference on Knowledge Discovery and Data Mining*, San Francisco, California. August 2016; 785–94
23. Strumbelj E, Kononko I. **An efficient explanation of individual classifications using game theory**. *Journal of Machine Learning Research* 2010;11:1–18 CrossRef
24. DeLong ER, DeLong DM, Clarke-Pearson DL. **Comparing the areas under two or more correlated receiver operating characteristic curves: a nonparametric approach**. *Biometrics* 1988;44:837–45 Medline
25. Youden WJ. **Index for rating diagnostic tests**. *Cancer* 1950;3:32–35 CrossRef Medline
26. Dale AM, Fischl B, Sereno MI. **Cortical surface-based analysis, I: segmentation and surface reconstruction**. *Neuroimage* 1999;9:179–94 CrossRef Medline
27. Ochs AL, Ross DE, Zannoni MD, et al; Alzheimer's Disease Neuroimaging Initiative. **Comparison of automated brain volume measures obtained with NeuroQuant and FreeSurfer**. *J Neuroimaging* 2015;25:721–27 CrossRef Medline
28. Persson K, Barca ML, Cavallin L, et al. **Comparison of automated volumetry of the hippocampus using NeuroQuant and visual assessment of the medial temporal lobe in Alzheimer's disease**. *Acta Radiol* 2018;59:997–1001 CrossRef Medline
29. Ding Y, Sohn JH, Kawczynski MG, et al. **A deep learning model to predict a diagnosis of Alzheimer disease using (18)F-FDG PET of the brain**. *Radiology* 2019;290:456–64 CrossRef Medline
30. Dimitriadis SI, Liparas D, Tsolanki MN, et al. **Random forest feature selection, fusion and ensemble strategy: combining multiple morphological MRI measures to discriminate among healthy elderly, MCI, cMCI and alzheimer's disease patients: from the alzheimer's disease neuroimaging initiative (ADNI) database**. *Journal of Neuroscience Methods* 2018;302:14–23
31. Kim DW, Jang HY, Kim KW, et al. **Design characteristics of studies reporting the performance of artificial intelligence algorithms for diagnostic analysis of medical images: results from recently published papers**. *Korean J Radiol* 2019;20:405–10 CrossRef Medline
32. Park SH, Han K. **Methodologic guide for evaluating clinical performance and effect of artificial intelligence technology for medical diagnosis and prediction**. *Radiology* 2018;286:800–09 CrossRef Medline
33. Park SH. **Diagnostic case-control versus diagnostic cohort studies for clinical validation of artificial intelligence algorithm performance**. *Radiology* 2019;290:272–73 CrossRef Medline

# Recent Administration of Iodinated Contrast Renders Core Infarct Estimation Inaccurate Using RAPID Software

 A.Z. Copelan,  E.R. Smith,  G.T. Drocton,  K.H. Narsinh,  D. Murph,  R.S. Khangura,  Z.J. Hartley,  A.A. Abba,  W.P. Dillon,  C.F. Dowd,  R.T. Higashida,  V.V. Halbach,  S.W. Hetts,  D.L. Cooke,  K. Keenan,  J. Nelson,  D. McCoy,  M. Ciano, and  M.R. Amans



## ABSTRACT

**BACKGROUND AND PURPOSE:** Automated CTP software is increasingly used for extended window emergent large-vessel occlusion to quantify core infarct. We aimed to assess whether RAPID software underestimates core infarct in patients with an extended window recently receiving IV iodinated contrast.

**MATERIALS AND METHODS:** We reviewed a prospective, single-center data base of 271 consecutive patients who underwent CTA  $\pm$  CTP for acute ischemic stroke from May 2018 through January 2019. Patients with emergent large-vessel occlusion confirmed by CTA in the extended window ( $>6$  hours since last known well) and CTP with RAPID postprocessing were included. Two blinded raters independently assessed CT ASPECTS on NCCT performed at the time of CTP. RAPID software used relative cerebral blood flow of  $<30\%$  as a surrogate for irreversible core infarct. Patients were dichotomized on the basis of receiving recent IV iodinated contrast ( $<8$  hours before CTP) for a separate imaging study.

**RESULTS:** The recent IV contrast and contrast-naïve cohorts comprised 23 and 15 patients, respectively. Multivariate linear regression analysis demonstrated that recent IV contrast administration was independently associated with a decrease in the RAPID core infarct estimate (proportional increase = 0.34; 95% CI, 0.12–0.96;  $P = .04$ ).

**CONCLUSIONS:** Patients who received IV iodinated contrast in proximity ( $<8$  hours) to CTA/CTP as part of a separate imaging study had a much higher likelihood of core infarct underestimation with RAPID compared with contrast-naïve patients. Over-reliance on RAPID postprocessing for treatment disposition of patients with extended window emergent large-vessel occlusion should be avoided, particularly with recent IV contrast administration.

**ABBREVIATIONS:** ELVO = emergent large-vessel occlusion; LKW = last known well; MT = mechanical thrombectomy; PI = proportional increases; rCBF = relative cerebral blood flow

Quantifying core infarction versus viable ischemic penumbra is at the crux of patient selection for mechanical thrombectomy (MT) in the setting of anterior circulation emergent large-vessel occlusion (ELVO). While patients with large infarcts tend to demonstrate worse clinical outcomes following reperfusion, successful recanalization of sizable ischemic penumbra, indicative of salvageable tissue, may result in drastic clinical improvement.<sup>1</sup>

Segregation of core infarction from ischemic penumbra is particularly relevant for extended window ELVOs ( $>6$  hours since last known well [LKW]).<sup>2,3</sup>

The semiquantitative ASPECTS system is highly predictive of clinical outcome with ELVO but demonstrates high inter- and intrareader variability.<sup>4,5</sup> Additionally, ASPECTS regions are volumetrically weighted unequally; consequently, patients with the same ASPECTS may have different core infarct volumes depending on the regions involved. The automated quantitative Rapid processing of Perfusion and Diffusion (RAPID; iSchemaView) CTP platform offers standardized and numeric estimation of core infarct and ischemic penumbra, lessening reliance on neuroradiologic ASPECTS interpretation. RAPID estimates a variety of


Received January 24, 2020; accepted after revision August 1.

From the Departments of Diagnostic and Interventional Neuroradiology (A.Z.C., E.R.S., G.T.D., K.H.N., D.M., R.S.K., Z.J.H., A.A.A., W.P.D., C.F.D., R.T.H., V.V.H., S.W.H., D.L.C., J.N., D.M., M.C., M.R.A.), and Neurosurgery (A.A.A.), University of California, San Francisco, San Francisco, California; Department of Radiology (E.R.S.), Medical College of Wisconsin, Milwaukee, Wisconsin; and Department of Neurology (K.K.), University of California Davis, Sacramento, California.

Paper previously presented at: Annual Meeting of the Society of Neurointerventional Surgery, July 21–26, 2019; Miami, Florida.

Research reported in this publication was supported by the National Institute on Deafness and Other Communication Disorders of the National Institutes of Health under award No. R21DC016087-01A1 and the National Heart, Lung, and Blood Institute of the National Institutes of Health under award number R56HL149124-01.

Please address correspondence to Matthew R. Amans, MD, MSc, Department of Diagnostic and Interventional Neuroradiology, 505 Parnassus Ave, San Francisco, CA 94143; e-mail: Matthew.amans@ucsf.edu; @UCSFimaging

 Indicates open access to non-subscribers at [www.ajnr.org](http://www.ajnr.org)

<http://dx.doi.org/10.3174/ajnr.A6908>

perfusion parameters indicative of cerebral hemodynamics at the moment of scanning. Accordingly, RAPID may predict tissue fate in the hyperacute setting (<1 hour since LKW). NCCT, however, is dependent on parenchymal hypoattenuation, which becomes apparent at least several hours from symptom onset.

RAPID software has been validated in multiple clinical trials, notably in DAWN (DWI or CTP Assessment with Clinical Mismatch in the Triage of Wake-Up and Late Presenting Strokes Undergoing Neurointervention with Trevo) and DEFUSE-3 (Endovascular Therapy Following Imaging Evaluation for Ischemic Stroke 3), both using RAPID for patient selection for MT in extended window ELVOs. Patients allocated to MT versus best medical therapy alone in the DAWN and DEFUSE-3 trials demonstrated markedly better clinical outcomes with unprecedented numbers needed to treat (NNT) of 2.8 and 4, respectively, to achieve functional independence at 90 days.<sup>2,3</sup>

Through more ubiquitous RAPID use, we encountered a recurrent phenomenon in which transfer patients with extended window ELVO demonstrated MCA territory hypoattenuation on NCCT but with disproportionately small and, in some instances, zero RAPID estimated core infarct. Essentially, all ELVO transfers to our institution are recent recipients of IV iodinated contrast. Given this imaging incongruity and our ongoing need to optimize patient selection for MT, we aimed to assess whether RAPID software underestimated core infarct volume in patients who received recent (<8 hours) IV contrast for a separate imaging study, most commonly CTA ± CTP at an outside hospital before transfer.

## MATERIALS AND METHODS

These study data contain sensitive personal information and cannot be made publicly available according to local data-protection regulations.

### Patient Selection

We performed a retrospective review of a prospectively maintained acute ischemic stroke data base from a tertiary care academic institution (University of California, San Francisco). We reviewed 271 consecutive patients presenting with acute ischemic stroke symptoms who underwent CTA ± CTP at our institution from May 2018 to January 2019. Inclusion criteria comprised extended window presentation; baseline NCCT, CTA confirming ELVO (ICA terminus, MCA M1 and M2 segments); and technically adequate CTP imaging (absence of excessive patient motion, poor cardiac output, or incorrect selection of arterial input function or venous output function on review of arterial input function/venous output function time plots), with RAPID postprocessing and availability of demographic and clinical data. Three transfer patients received IV tPA at an outside institution; however, all 3 had persistent ELVO on repeat imaging at our institution. An ASPECTS of 10 was excluded because by definition, these patients could not harbor a falsely low RAPID estimated core infarct volume. Thirty-eight patients met the inclusion criteria, with most exclusions due to absence of ELVO on CTA, imaging performed within 6 hours since LKW, and an ASPECTS of 10. This study was approved by the local institutional review board, with the board waiving the need for patient consent.

Two neurointerventional radiologists (A.Z.C., G.T.D.) with subspecialty neuroradiology fellowship training, blinded to

clinical data as well as additional imaging and therapeutic interventions at the time of review, independently assigned an ASPECTS (0–10) to NCCTs and collateral scores to corresponding CTAs (1 = excellent, 2 = intermediate, 3 = poor).<sup>6</sup> CTP imaging was processed with fully automated, commercially available RAPID software, Version 4.5.0., to define tissue state, with ischemic core defined as relative CBF (rCBF) of <30% of the corresponding contralateral territory (ie, CBF is comparatively reduced >70%).<sup>7</sup>

Demographic and clinical data were collected including, age, sex, hours since LKW, serum creatinine level, and whether MT was performed. In addition, CT ASPECTS, CTA collaterals grade, and core infarct volume (milliliters) by RAPID were collected for each patient. We also obtained the time from CTP to reperfusion.

### Imaging Protocols

**Imaging Acquisition.** Patients underwent an institutional stroke imaging protocol, including NCCT, CTA, and CTP performed on a 40-mm, 64-detector row clinical system (LightSpeed VCT; GE Healthcare). Helical NCCT (120 kV; 300–355 auto-mA) was performed from the foramen magnum to the vertex at a 3.75-mm section thickness. Helical CTA (120 kV; 200–700 auto-mA) was performed from the mid-cardiac level to the vertex (section thickness/interval, 0.625/0.5 mm) after intravenous administration of 70 mL of iodinated contrast, power-injected at 5 mL/s through an 18- or 20-ga antecubital IV access and followed by a 25-mL saline flush. After 1–2 minutes, 2 contiguous CTP slabs were obtained for 8-cm combined supratentorial coverage, obtained at eight 5-mm sections per slab. For each of the 2 slabs, obtained approximately 90 seconds apart, cine mode acquisition (80 kV; 100 mA) permitting high-temporal resolution (1-second sampling interval) dynamic bolus passage imaging was obtained after the administration of 40-mL of iodinated contrast, power-injected at 5 mL/s. Contrast administration was followed by a 25-mL saline flush at the same rate. Subsequently, delayed contrast-enhanced CT (120 kV; 300–355 auto-mA) was performed from the foramen magnum to the vertex at 3.75-mm thickness. In total, 150 mL of iodinated contrast was administered.

**Imaging Processing.** Images were processed with fully automated, commercially available CTP software (RAPID, Version 4.5.0.) to identify and distinguish potentially salvageable ischemic penumbra (delay of the maximum of the tissue residue function longer than 6 seconds, time-to-maximum of >6 seconds) from irreversibly infarcted core (rCBF of <30% compared with normal tissue). We also manually obtained final infarct volumes in patients treated with embolectomy with TICI 2b, 2c, or 3 results using OsiriX Imaging Software 11.0 (<http://www.osirix-viewer.com>), blinded to each patient's cohort (contrast-naïve versus received prior contrast).

**Statistical Analysis.** Patients were dichotomized into 2 cohorts: recent (<8 hours) recipients of IV iodinated contrast before CTP at our institution versus contrast-naïve patients. Power analysis was performed on both cohorts, with a 1-to-1 enrollment ratio and binomial end points. We assumed 5% overestimation in the non-contrast group and 50% core infarct overestimation in the contrast



**Table 1: Baseline characteristics**

Characteristic	Recent IV Contrast <sup>a</sup>	No Recent IV Contrast <sup>a</sup>	Overall <sup>a</sup>	P Value <sup>b</sup>
Count	23	15	38	NA
Age (yr)	70.5 ± 16.0	76.5 ± 18.4	72.9 ± 17.0	.32
Serum creatinine level (mg/dL)	1.08 ± 0.34	1.12 ± 0.29	1.10 ± 0.32	.78
Female	15 (65%)	7 (47%)	22 (58%)	.32
Time since last known well (hr)	12.5 ± 5.6	9.3 ± 7.8	11.2 ± 6.6	.19
ASPECTS	5.4 ± 2.0	7.5 ± 2.2	6.2 ± 2.3	.005
CTP core (median) (range) (mL)	4 (0–234)	13 (0–208)	6 (0–234)	.28
Collateral grade				.71
1	15 (65%)	9 (60%)	24 (63%)	
2	6 (26%)	3 (20%)	9 (24%)	
3	2 (9%)	3 (20%)	5 (13%)	
Thrombectomy	11 (48%)	12 (80%)	23 (61%)	.09

**Note:**—NA indicates not applicable.

<sup>a</sup> Values are No., No. (%), or mean ± SD.

<sup>b</sup> P values are from the Fisher exact test or 2-sample t test with unequal variances.

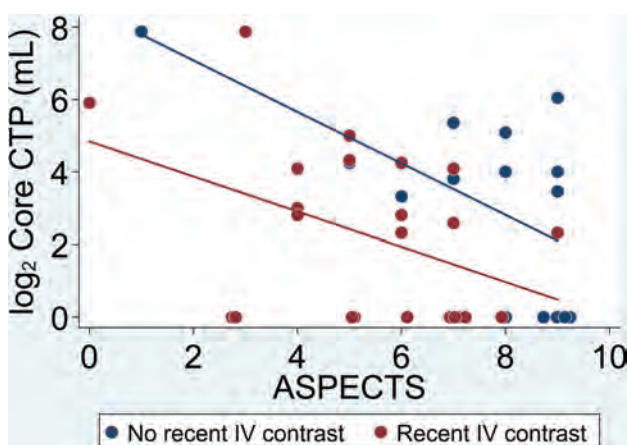


**FIG 1.** Scatterplot of CT-ASPECTS versus log-transformed CTP-estimated core infarct for the recent IV contrast group (red) and the contrast-naïve group (blue) with lines of best fit. For the same CT-ASPECTS, the CTP-estimated core infarct is consistently less in the recent IV contrast group with divergence of the lines of best fit toward the lower ASPECTS indicative of more substantial differences between the 2 cohorts and more significant underestimation of estimated core infarct for lower CT-ASPECTS.

group based on prior experience, resulting in 14 patients in each cohort with an  $\alpha$  level of .05, a  $\beta$  level of 0.2, and power of 80%. The Fischer exact test and unequal variances 2-sample *t* test were used for categoric and continuous variables, respectively, to assess differences between the groups.

A multivariate linear regression model was produced to test whether RAPID-estimated core infarct was associated with recent IV contrast administration, while including variables that met a predetermined statistical significance threshold ( $P = .05$ ). Core infarct estimated by RAPID values underwent log-transformation before analysis to accommodate overly influential outliers and allow improved adherence to the assumption of the linear regression model of homoscedasticity and normally distributed residuals. An absolute value of 1 was added to the core infarct estimated value before log-transformation because a log-transformation of zero is not possible.

Regression results are presented as exponentiated regression coefficients labeled as proportional increases (PIs). For example, a

PI of 1.2 would indicate a 20% increase, whereas a PI of 0.8 would indicate a 20% decrease. Data analysis was conducted on STATA 15.1 (StataCorp [2017], STATA Statistical Software, Release 15).

In an effort to determine whether RAPID was underestimating the presentation core infarct value, we used multivariable regression analysis to determine whether there was a difference in final infarct volumes compared with that estimated by RAPID in patients who were contrast-naïve and those who received prior contrast, while adjusting for the time from CTP to reperfusion. For this particular analysis, core infarct values were not log-transformed.

## RESULTS

Of the 38 patients who met the inclusion criteria, 23 received recent IV contrast and 15 were contrast-naïve. Table 1 summarizes group and overall characteristics.

The average age was 72.9 years, and 58% were female, with no significant difference between groups for either. There was no difference in serum creatinine levels, a marker of renal function, between those who received recent IV contrast and the contrast-naïve group ( $1.08 \pm 0.34$  versus  $1.12 \pm 0.29$ ,  $P = .78$ ). The recent IV contrast group tended to have longer times since LKW at the time of CTP imaging but not significantly so ( $12.5$  versus  $9.3$  hours,  $P = .19$ ). While those who received recent IV contrast demonstrated significantly lower ASPECTS ( $5.4$  versus  $7.5$ ,  $P = .005$ ), there was not a statistically significant baseline difference in core infarct estimates by RAPID between the 2 cohorts ( $P = .28$ ) (Fig 1). There was no significant difference in CTA collateral grades ( $P = .71$ ). Contrast-naïve patients were more likely to be selected for MT but not significantly so ( $80\%$  versus  $48\%$ ,  $P = .09$ ).

Final multivariable linear regression results are shown in Table 2, with the log-transformed core infarct estimated by RAPID as the outcome, and included the following predictors: 1) recent IV contrast administration, 2) ASPECTS, and 3) collateral grade. Recent IV contrast administration was associated with decreased (about two-thirds) RAPID-estimated core infarct (PI = 0.34; 95% CI, 0.12–0.96;  $P = .04$ ). Most important, analysis of the data before logarithmic transformation demonstrated an even more significant decrease in RAPID-estimated core infarct with recent IV contrast administration. There was an inverse relationship between the ASPECTS and core infarct estimated by RAPID, with each point increase in the ASPECTS resulting in 26% lower core infarct estimated by RAPID (PI = 0.74; 95% CI, 0.59–0.93;  $P = .01$ ). Patients with intermediate and poor collaterals (grades 2 and 3, respectively) demonstrated higher core infarcts by RAPID than patients with excellent collaterals (PI = 2.27; 95% CI, 0.78–6.60;  $P = .13$  and PI = 8.46; 95% CI, 2.10–34.06;  $P = .004$ , respectively). There were no associations between RAPID-estimated core infarct with other variables, including age, sex, and time since LKW, and these variables were therefore excluded.

Seventeen patients met the inclusion criteria for analysis comparing final infarct volume with the core infarct estimated by RAPID (8 received prior contrast and 9 were contrast-naïve) (Fig 2). The average times from CTP to reperfusion were not significantly different

**Table 2: Multivariable linear regression results**

Characteristic	PI <sup>a</sup>	95% Confidence Interval	P Value
Recent IV contrast	0.34	(0.12–0.96)	.04
ASPECTS	0.74	(0.59–0.93)	.01
Collateral grade (1 = reference group)			
2	2.27	(0.78–6.60)	.13
3	8.46	(2.10–34.06)	.004

<sup>a</sup> Outcome is log2 core CTP.

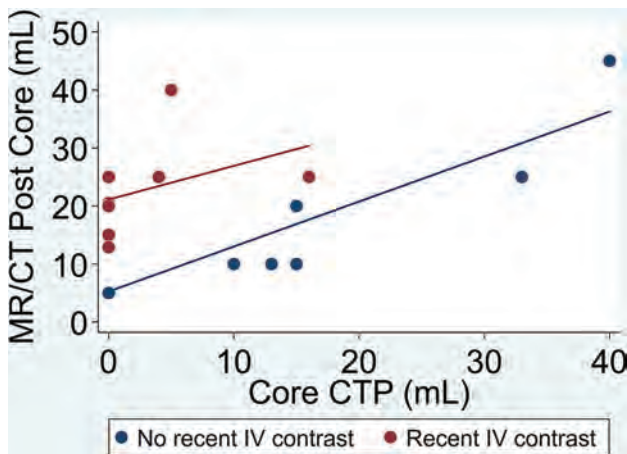


**FIG 2.** Scatterplot of CTP-measured core infarct volume versus postoperative core infarct volume as measured by MR imaging or CT for the recent IV contrast group (red) and the contrast-naïve group (blue) with lines of best fit. For the same preoperative CTP-measured core, the postoperative core infarct is greater in the recent IV contrast group, suggesting that recent IV contrast underestimates CTP-measured core infarct volume at presentation.

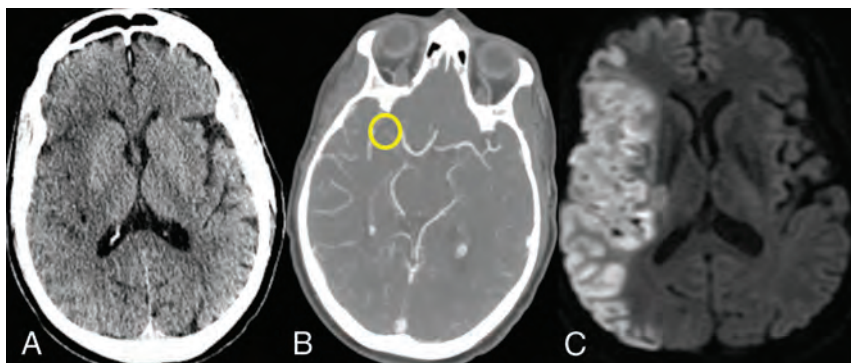


**FIG 3.** A 56-year-old man who presented to an outside hospital with a right MCA syndrome and ELVO confirmed on CTA. Last known well was approximately 11 hours before imaging at our institution. A, NCCT demonstrates loss of gray-white matter differentiation, in keeping with acute infarct, involving the right insula as well as the frontal and temporal opercula. B, CTA confirms a right M1 segment (yellow circle) occlusion. C, DWI reveals an extensive area of acute infarct correlating with the areas of hypoattenuation on the NCCT. TICI 3 reperfusion was achieved within 60 minutes of the CTP study, and the MR imaging was obtained later in the day.

( $P = .37$ ). While the slopes of the regression lines were similar ( $P = .61$ ), final infarct volume was higher for any given core infarct volume estimated by RAPID in patients who received prior contrast (coefficient = 14.4; 95% CI, 5.7–23.0;  $P = .003$ ). In other words, in patients who received contrast before CTP at our institution, RAPID underestimated the infarct volume.

## DISCUSSION

In early 2018, synchronous with rapidly increasing CTP imaging using RAPID postprocessing, our team observed a repeat phenomenon: Extended window ELVOs with conspicuous MCA territory hypoattenuation on NCCT (Fig 3) were frequently demonstrating disproportionately small core infarcts as predicted by RAPID (Fig 4), in contradistinction to patients presenting directly to our institution (Fig 5) who underwent CTP (Fig 6). This seemingly occurred exclusively in our acute ischemic stroke transfers, essentially all of whom received IV iodinated contrast for CTA to confirm ELVO before transfer.

The results of this study corroborate our hypothesis: RAPID postprocessing tends to underestimate core infarct volume (defined as rCBF of  $<30\%$ ) in patients receiving IV contrast for a separate imaging study within 8 hours of CTP imaging. While multifarious pitfalls of RAPID software have been described, particularly overestimation of core infarct in the hyperacute setting, this is, to our knowledge, the first description of underestimation of core infarct related to recent IV contrast administration.<sup>8–10</sup>

Our findings have impacted our team's algorithm for transfer patients with ELVO by decreasing our reliance on RAPID output. This may additionally impact other stroke centers as we continue learning which patients will benefit from this life-saving procedure.

In this era of perpetually increasing extended window MT volumes, clinicians must be cognizant of this pitfall because estimation of core infarct is clinically relevant. First, in patients with extended windows eligible for MT by the DAWN criteria, the baseline ASPECTS appears to modify the treatment effect of MT, with significantly greater benefit in patients with higher ASPECTS of 7–10.<sup>11</sup> Second, MT in the setting of an ASPECTS

of 0–5 is often more complex, is associated with worse clinical outcomes, and has an increased symptomatic intracranial hemorrhage risk.<sup>5</sup> While some neurointerventionalists advocate MT even in the presence of ASPECTS of 3–5, awareness of this phenomenon may augment the accuracy of patient prognostication, leading to a more informed decision to intervene, family discussion, and procedural consent.

RAPID-generated mismatch maps comprise the following: time-to-maximum of  $>6.0$  seconds, indicative of ischemic penumbra likely to infarct without reperfusion; and rCBF of  $<30\%$ , a surrogate for irreversibly injured parenchyma. RAPID software, however, does not directly identify infarcted tissue; rather, the perfusion



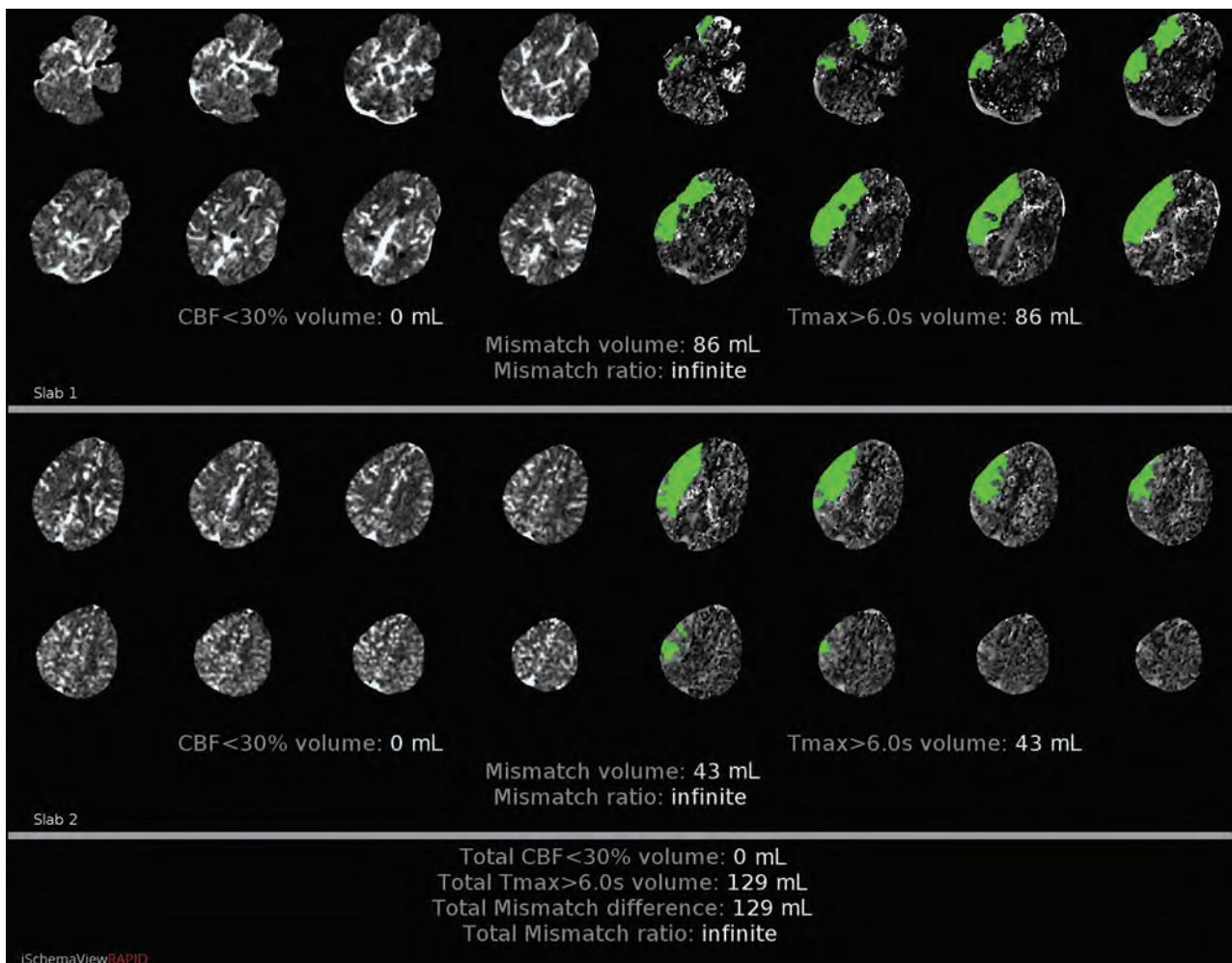


**FIG 4.** CTP with RAPID postprocessing from the same patient as in Fig 3 suggests no core infarct (lack of pink color-coding and an rCBF of  $<30\%$  volume of 0 mL) with a large area of ischemic penumbra (green color-coding with time-to-maximum [Tmax] of  $>6$  seconds of 129 mL).

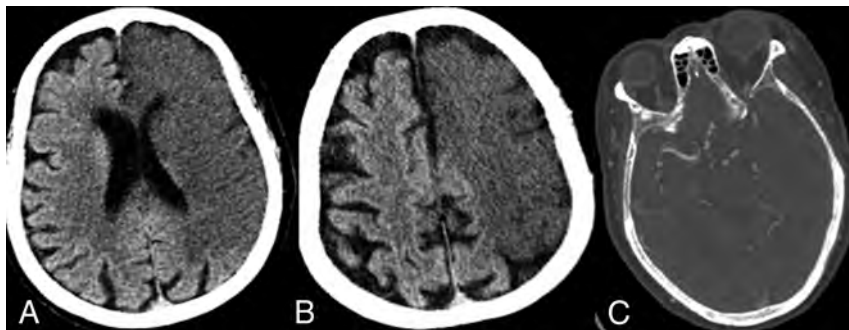


**FIG 5.** A 67-year-old man who presented directly to our institution (no recent IV contrast) with a left MCA syndrome and last known well approximately 8 hours before imaging. A and B, NCCT demonstrates hypoattenuation involving a large volume of the left MCA and anterior cerebral artery territories. C, CTA demonstrates a internal carotid terminus occlusion with involvement of the carotid terminus and A1 and M1 segments.

maps reflect cerebral hemodynamics at the moment the scan was performed. Spontaneous or posttherapeutic recanalization to a recently infarcted territory may result in failure of the RAPID software to detect core infarct using the rCBF of  $<30\%$  threshold;

however, all our included patients had confirmed ELVO at the time of imaging at our institution (Figs 3 and 5). Alternatively, recruitment of leptomeningeal collaterals to acutely infarcted parenchyma may result in a false-negative core on RAPID due to similar principles affecting CTP parameters. The automated suppression of markedly hypoattenuating regions in RAPID, such as chronic infarcts or CSF-containing structures, may lead to suppression of acutely infarcted tissue, particularly in the late extended window with more of a subacute infarct CT appearance. These pitfalls, however, cannot explain the striking discrepancy between our cohorts.

The ideal rCBF threshold should err on the side of underestimating core infarct to avoid inappropriate exclusion of potential MT candidates. Accordingly, rCBF of  $<30\%$  underestimates infarcts present on DWI by an average of 12 mL but demonstrates



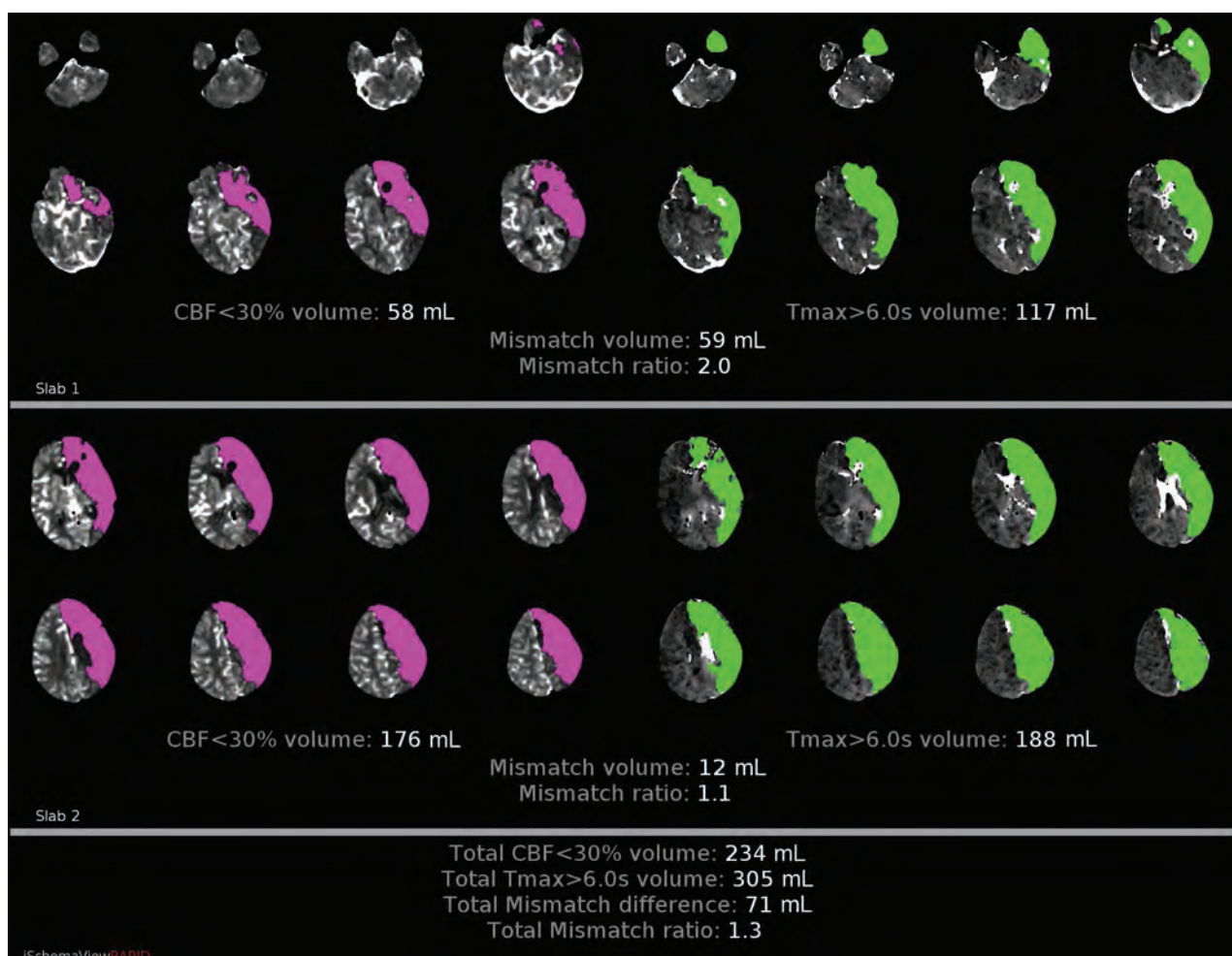


**FIG 6.** CTP imaging with RAPID postprocessing from the same patient as in Fig 5 suggests an extensive area of core infarct (pink color-coding and an rCBF of <30% volume of 234 mL) corresponding to the large volume of hypodensity on NCCT. Tmax indicates time-to-maximum.

greater specificity in predicting DWI-positive voxels compared with an rCBF of <38%, which is actually more accurate, on average, in estimating core infarct.<sup>7</sup> No perfusion parameter should be assessed in isolation. rCBF should be analyzed in conjunction with the NCCT, CTA, as well as the additionally provided perfusion parameters, particularly CBV. CBV of <40% of the contralateral hemisphere, absolute CBV of <2 mL/100 g<sup>-1</sup>, and relative CBV of 0.32 have all been shown to be predictive of core infarct.<sup>12-14</sup> Multiple studies, however, have demonstrated rCBF to be the optimal parameter for estimating irreversible infarction, including studies using concurrent DWI performing significantly better than CBV.<sup>7,15,16</sup> More important, rCBF of <30% is the surrogate for core infarct used in multiple contemporary thrombectomy trials and is endorsed by the major endovascular societies.<sup>2,3,17-20</sup> We therefore used rCBF of <30% for our analysis; however, we routinely assess NCCT for ASPECTS, CTA for collaterals, as well as additional perfusion parameters, depending on specific clinical scenarios.

While the recent IV contrast group presented with significantly lower CT ASPECTS, likely due to a longer time from LKW to CTP, there was no significant difference in RAPID core infarct estimates. When we controlled for ASPECTS and other associated variables, recent IV contrast administration was associated with a two-thirds

decrease in the RAPID-predicted core infarct volume for the same ASPECTS. This may result in inappropriately selecting patients for MT on the basis of the DAWN or DEFUSE-3 inclusion criteria.<sup>2,3</sup>

Multitudinous factors contribute to CTP variability, including timing and volume of IV contrast administration, postprocessing algorithm (eg, definition of arterial input/venous output function, motion correction, and smoothing), and parameter threshold. Although CTP use is increasing, consensus has not been achieved among manufacturers as to which parameter optimally defines core infarct. Significant variability in calculated core infarct volumes has been demonstrated among various software packages.<sup>21</sup>

In our limited series, postprocessing of the CTP data using the AW Server software package (GE Healthcare; <https://www.gehealthcare.com/products/advanced-visualization/platforms/aw-server>) without a smoothing algorithm resulted in more conspicuous reduction of rCBF in the ischemic core than the RAPID software package maps, which do use a smoothing algorithm (Fig 7).

The precise mechanism of recent IV contrast resulting in falsely low core infarcts by RAPID remains a conundrum. The sequence of CTA and CTP in stroke CT protocols has been shown to have no significant influence on quantitative parameters of CTP.<sup>22</sup>

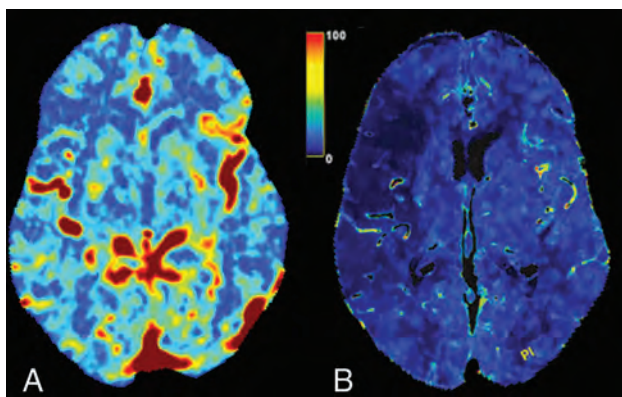


**FIG 7.** The same 56-year-old man with right M1 segment occlusion as presented in Fig 3. A, rCBF map from the RAPID postprocessing of CTP data demonstrates subtle decreased blood flow to the right MCA territory corresponding to the suggested core infarct volume of 0 mL. B, rCBF map from GE Healthcare processing of the CTP data demonstrates much more conspicuous decreased blood flow within the right MCA territory (scale bar = 0–100 mL/g/min).

However, IV contrast administered several hours before CTP, as opposed to several minutes, may allow sufficient time for the contrast to circulate to alter perfusion parameters. Our group and others have previously described contrast staining of acutely infarcted brain parenchyma on NCCT following digital subtraction angiography.<sup>23–26</sup> Similarly, contrast administered several hours before CTP may lead to progressive accumulation in the infarcted tissue, thereby elevating the Hounsfield units. The underlying mechanism for such contrast staining is likely disruption of the blood-brain barrier.<sup>27</sup>

The authors are cognizant of ASPECTS shortcomings and readily acknowledge that it is not the criterion standard for estimating core infarction. CT lacks the sensitivity and specificity of MR imaging in the detection of acute infarction.<sup>28,29</sup> Nevertheless, the ASPECTS remains pertinent because it allows expeditious assessment and prognostication before treatment. Several of the major ELVO thrombectomy trials excluded ASPECTS of <6 from MT, and the ACR-ASNR-SIR-SNIS practice parameter<sup>20</sup> supports the same exclusion criterion.<sup>17–19</sup> Although individual ASPECTS regions are weighted unequally in regard to volume, several studies have shown correlation between ASPECTS and CTP-estimated ischemic core.<sup>11,30</sup> While CTP measures collateral perfusion and does not directly measure tissue viability, ASPECTS scoring is based on hypoattenuation, which is highly specific for irreversible parenchymal injury and becomes more apparent in the extended window.<sup>31,32</sup> Nevertheless, our final infarct volume subanalysis in patients who had a good result from thrombectomy also supports the hypothesis. While the slopes of the regression lines for each cohort were similar, the y-intercept was significantly higher in patients who received prior contrast while controlling for the time between CTP acquisition and time to reperfusion. In other words, RAPID was underestimating the final infarct volume in patients who had received prior contrast.

This study has limitations inherent in its retrospective nature and relatively small sample size. Many patients who underwent CT stroke protocol imaging were ultimately diagnosed with distal branch occlusions, lacunar infarcts, intracranial hemorrhage, as well

as nonvascular conditions and were therefore excluded. In addition, patients with ASPECTS of 10 were excluded. Heterogeneity in follow-up imaging at our institution, largely at the discretion of the neurology team, also limited our sample sizes for final infarct analysis. Given the small sample size, we could not analyze matched ASPECTS strata between the 2 cohorts. The small sample size is largely due to the narrow time window (May 2018 to January 2019) for inclusion in this study. Rather than delay the reporting of such a clinically relevant pitfall to augment our sample size, we thought it pertinent to alert our neuroradiology and neurointerventional colleagues to our findings.

Another limitation is our lack of a criterion standard reference for core infarct estimation. This is due to the nature of the study because no patients underwent MR imaging simultaneous with the baseline NCCT. Patients excluded from thrombectomy would likely have a more significant interval growth of core infarct on follow-up compared with those who were successfully recanalized; therefore, a direct comparison on follow-up imaging would be misleading. Regardless, our results are striking irrespective of the sample, and it is, therefore, critical that all centers relying on RAPID as part of their selection criteria for MT be cognizant of this phenomenon.

## CONCLUSIONS

Recent administration of IV iodinated contrast, omnipresent among stroke transfers undergoing CTA to confirm ELVO before transfer, may result in falsely low core infarcts as predicted by RAPID software. It is critical for neurointerventionalists and clinicians to peruse the NCCT for evidence of hypoattenuated parenchyma and to estimate a baseline ASPECTS, particularly in the extended window with recent administration of IV iodinated contrast.

**Disclosures:** Steven W. Hetts—*UNRELATED: Consultancy:* Route 92 Medical, *Comments:* clinical trial clinical event evaluator for thrombectomy device company; *Grants/Grants Pending:* Siemens, Stryker, MicroVention, Terumo, *Comments:* research contract for advanced angiography suites, core imaging lab for aneurysm treatment clinical trials\*; *Stock/Stock Options:* ThrombX, *Comments:* investor in startup thrombectomy device company. Jeffrey Nelson—*RELATED: Grant:* National Institutes of Health.\* Matthew R. Amans—*RELATED: Grant:* National Institutes of Health, *Comments:* Research reported in this publication was supported by the National Institute of Deafness and Other Communication Disorders R21DC016087-01A1 and the National Heart, Lung, and Blood Institute R56HL149124-01\*; *UNRELATED: Consultancy:* Covidien, Stryker, MicroVention; *Expert Testimony:* various medicolegal consulting. \*Money paid to the institution.

## REFERENCES

1. Cagnazzo F, Derraz I, Dargazanli C, et al. **Mechanical thrombectomy in patients with acute ischemic stroke and ASPECTS ≤6: a meta-analysis.** *J Neurointerv Surg* 2020;12:350–55 CrossRef Medline
2. Nogueira RG, Jadhav AP, Haussen DC, et al; DAWN Trial Investigators. **Thrombectomy 6 to 24 hours after stroke with a mismatch between deficit and infarct.** *N Engl J Med* 2018;378:11–21 CrossRef Medline
3. Albers GW, Lansberg MG, Kemp S, et al. **A multicenter randomized controlled trial of endovascular therapy following imaging evaluation for ischemic stroke (DEFUSE 3).** *Int J Stroke* 2017;12:896–905 CrossRef Medline
4. Yoo AJ, Zaidat OO, Chaudhry ZA, et al; Penumbra Pivotal and Penumbra Imaging Collaborative Study (PICS) Investigators. **Impact of pretreatment noncontrast CT Alberta Stroke Program Early CT Score on clinical outcome after intra-arterial stroke therapy.** *Stroke* 2014;45:746–51 CrossRef Medline

5. Schröder J, Thomalla G. A critical review of Alberta Stroke Program Early CT Score for evaluation of acute stroke imaging. *Front Neurol* 2016;7:245 CrossRef Medline
6. Nambiar V, Sohn SI, Almekhlafi MA, et al. CTA collateral status and response to recanalization in patients with acute ischemic stroke. *AJNR Am J Neuroradiol* 2014;35:884–90 CrossRef Medline
7. Cereda CW, Christensen S, Campbell BC, et al. A benchmarking tool to evaluate computer tomography perfusion infarct core predictions against a DWI standard. *J Cereb Blood Flow Metab* 2016;36:1780–89 CrossRef Medline
8. Boned S, Padroni M, Rubiera M, et al. Admission CT perfusion may overestimate initial infarct core: the ghost infarct core concept. *J Neurointerv Surg* 2017;9:66–69 CrossRef Medline
9. Angermaier A, Khaw AV, Kirsch M, et al. Influence of recanalization and time of cerebral ischemia on tissue outcome after endovascular stroke treatment on computed tomography perfusion. *J Stroke Cerebrovasc Dis* 2015;24:2306–12 CrossRef Medline
10. Silvennoinen HM, Hamberg LM, Lindsberg PJ, et al. CT perfusion identifies increased salvage of tissue in patients receiving intravenous recombinant tissue plasminogen activator within 3 hours of stroke onset. *AJNR Am J Neuroradiol* 2008;29:1118–23 CrossRef Medline
11. Bhuva P, Yoo AJ, Jadhav AP, et al; DAWN Trial Investigators. Noncontrast computed tomography Alberta Stroke Program Early CT Score may modify intra-arterial treatment effect in DAWN. *Stroke* 2019;50:2404–12 CrossRef Medline
12. Srinivasan A, Goyal M, Al Azri F, et al. State-of-the-art imaging of acute stroke. *Radiographics* 2006;26(Suppl 1):S75–95 CrossRef Medline
13. Wintermark M, Flanders AE, Velthuis B, et al. Perfusion-CT assessment of infarct core and penumbra: receiver operating characteristic curve analysis in 130 patients suspected of acute hemispheric stroke. *Stroke* 2006;37:979–85 CrossRef Medline
14. Mokin M, Levy EI, Saver JL, et al; SWIFT PRIME Investigators. Predictive value of RAPID assessed perfusion thresholds on final infarct volume in SWIFT PRIME (Solitaire With the Intention for Thrombectomy as Primary Endovascular Treatment). *Stroke* 2017;48:932–38 CrossRef Medline
15. Amukotuwa S, Straka M, Aksoy D, et al. Cerebral blood flow predicts the infarct core: new insights from contemporaneous diffusion and perfusion imaging. *Stroke* 2019;50:2783–89 CrossRef Medline
16. Campbell BC, Christensen S, Levi CR, et al. Cerebral blood flow is the optimal CT perfusion parameter for assessing infarct core. *Stroke* 2011;42:3435–40 CrossRef Medline
17. Demchuk AM, Goyal M, Menon BK, et al; ESCAPE Trial Investigators. Endovascular Treatment for Small Core and Anterior Circulation Proximal Occlusion with Emphasis on Minimizing CT to Recanalization Times (ESCAPE) trial: methodology. *Int J Stroke* 2015;10:429–38 CrossRef Medline
18. Saver JL, Goyal M, Bonafe A, et al; SWIFT PRIME Investigators. Solitaire<sup>TM</sup> with the Intention for Thrombectomy as Primary Endovascular Treatment for Acute Ischemic Stroke (SWIFT PRIME) trial: protocol for a randomized, controlled, multicenter study comparing the Solitaire revascularization device with IV tPA with IV tPA alone in acute ischemic stroke. *Int J Stroke* 2015;10:439–48 CrossRef Medline
19. Molina CA, Chamorro A, Rovira À, et al. REVASCAT: a randomized trial of revascularization with SOLITAIRE FR device vs best medical therapy in the treatment of acute stroke due to anterior circulation large vessel occlusion presenting within eight-hours of symptom onset. *Int J Stroke* 2015;10:619–26 CrossRef Medline
20. ACR-ASNR-SIR-SNIS Practice Parameter for the Performance of Endovascular Embolectomy and Revascularization in Acute Stroke. 2018. <https://www.acr.org/-/media/ACR/Files/Practice-Parameters/Acute-Stroke.pdf?la=en>. Accessed February 25, 2020
21. Koopman MS, Berkhemer OA, Geuskens RR, et al; MR CLEAN Trial Investigators. Comparison of three commonly used CT perfusion software packages in patients with acute ischemic stroke. *J Neurointerv Surg* 2019;11:1249–56 CrossRef Medline
22. Dorn F, Liebig T, Muenzel D, et al. Order of CT stroke protocol (CTA before or after CTP): impact on image quality. *Neuroradiology* 2012;54:105–12 CrossRef Medline
23. Amans MR, Cooke DL, Vella M, et al. Contrast staining on CT after DSA in ischemic stroke patients progresses to infarction and rarely hemorrhages. *Interv Neuroradiol* 2014;20:106–15 CrossRef Medline
24. Nakano S, Iseda T, Yoneyama T, et al. Early CT signs in patients with acute middle cerebral artery occlusion: incidence of contrast staining and haemorrhagic transformations after intra-arterial reperfusion therapy. *Clin Radiol* 2006;61:156–62 CrossRef Medline
25. Nakano S, Iseda T, Kawano H, et al. Parenchymal hyperdensity on computed tomography after intra-arterial reperfusion therapy for acute middle cerebral artery occlusion: incidence and clinical significance. *Stroke* 2001;32:2042–48 CrossRef Medline
26. Parrilla G, García-Villalba B, Espinosa de Rueda M, et al. Hemorrhage/contrast staining areas after mechanical intra-arterial thrombectomy in acute ischemic stroke: imaging findings and clinical significance. *AJNR Am J Neuroradiol* 2012;33:1791–96 CrossRef Medline
27. Numaguchi Y, Fleming MS, Hasuo K, et al. Blood-brain barrier disruption due to cerebral arteriography: CT findings. *J Comput Assist Tomogr* 1984;8:936–39 CrossRef Medline
28. Jaillard A, Hommel M, Baird AE, et al. Significance of early CT signs in acute stroke: a CT scan-diffusion MRI study. *Cerebrovasc Dis* 2002;13:47–56 CrossRef Medline
29. Kim EY, Ryoo JW, Roh HG, et al. Reversed discrepancy between CT and diffusion-weighted MR imaging in acute ischemic stroke. *AJNR Am J Neuroradiol* 2006;27:1990–95 Medline
30. Haussen DC, Dehkharghani S, Rangaraju S, et al. Automated CT perfusion ischemic core volume and noncontrast CT ASPECTS (Alberta Stroke Program Early CT Score): correlation and clinical outcome prediction in large vessel stroke. *Stroke* 2016;47:2318–22 CrossRef Medline
31. Lev MH, Farkas J, Gemmete JJ, et al. Acute stroke: improved non-enhanced CT detection—benefits of soft-copy interpretation by using variable window width and center level settings. *Radiology* 1999;213:150–55 CrossRef Medline
32. Dzialowski I, Weber J, Doerfler A, et al. Brain tissue water uptake after middle cerebral artery occlusion assessed with CT. *J Neuroimaging* 2004;14:42–48 CrossRef Medline



# Cortical Distribution of Fragile Periventricular Anastomotic Collateral Vessels in Moyamoya Disease: An Exploratory Cross-Sectional Study of Japanese Patients with Moyamoya Disease

A. Miyakoshi, T. Funaki, Y. Fushimi, T. Nakae, M. Okawa, T. Kikuchi, H. Kataoka, K. Yoshida, Y. Mineharu, M. Matsuhashi, E. Nakatani, and S. Miyamoto



## ABSTRACT

**BACKGROUND AND PURPOSE:** Collateral vessels in Moyamoya disease represent potential sources of bleeding. To test whether these cortical distributions vary among subtypes, we investigated cortical terminations using both standardized MR imaging and MRA.

**MATERIALS AND METHODS:** Patients with Moyamoya disease who underwent MR imaging with MRA in our institution were enrolled in this study. MRA was spatially normalized to the Montreal Neurological Institute space; then, collateral vessels were measured on MRA and classified into 3 types of anastomosis according to the parent artery: lenticulostriate, thalamic, and choroidal. We also obtained the coordinates of collateral vessel outflow to the cortex. Differences in cortical terminations were compared among the 3 types of anastomosis.

**RESULTS:** We investigated 219 patients with Moyamoya disease, and a total of 190 collateral vessels (lenticulostriate anastomosis,  $n = 72$ ; thalamic anastomosis,  $n = 21$ ; choroidal anastomosis,  $n = 97$ ) in 46 patients met the inclusion criteria. We classified the distribution patterns of collateral anastomosis as follows: lenticulostriate collaterals outflowing anteriorly ( $P < .001$ ; 95% CI, 67.0–87.0) and medially ( $P < .001$ ; 95% CI, 11.0–24.0) more frequently than choroidal collaterals; lenticulostriate collaterals outflowing anteriorly more frequently than thalamic collaterals ( $P < .001$ ; 95% CI, 34.0–68.0); and choroidal collaterals outflowing posteriorly more frequently than thalamic collaterals ( $P < .001$ ; 95% CI, 14.0–34.0). Lenticulostriate anastomoses outflowed to the superior or inferior frontal sulcus and interhemispheric fissure. Thalamic anastomoses outflowed to the insular cortex and cortex around the central sulcus. Choroidal anastomoses outflowed to the cortex posterior to the central sulcus and the insular cortex.

**CONCLUSIONS:** Cortical distribution patterns appear to differ markedly among the 3 types of collaterals.

**ABBREVIATIONS:** choA = choroidal artery; LSA = lenticulostriate artery; MNI = Montreal Neurological Institute; PcomA = posterior communicating artery

Collateral vessels in Moyamoya disease develop as the disease progresses.<sup>1</sup> Lenticulostriate arteries (LSAs), perforators from the posterior communicating artery (PcomA), and anterior and posterior choroidal arteries (choAs) are representative collateral vessels that supply the cortex.<sup>2–4</sup> Development of such collateral

vessels represents a risk factor for intracerebral hemorrhage,<sup>3,5–7</sup> and these vessels have frequently been considered as the vessels responsible for bleeding in recent reports.<sup>8–10</sup> These collateral vessels connect with medullary arteries near the lateral ventricle and thus supply the cortex via the medullary arteries.<sup>3,4</sup> However, no reports have addressed the cortical distributions of these collateral vessels.

Bypass surgery reduces the risk of rebleeding in patients with hemorrhagic onset of Moyamoya disease<sup>7,11–13</sup> and also shrinks collateral vessels in Moyamoya disease.<sup>7,12,14,15</sup> Augmentation of cerebral blood flow via bypass seems to decrease the necessity for development of collateral flow and shrinks existing collaterals.<sup>15</sup> To shrink risky collateral vessels effectively and prevent hemorrhage, well-designed and planned bypass surgeries may be required.<sup>16</sup> Comprehension of the nature and cortical distribution of collateral vessels may thus be clinically useful.

Received May 1, 2020; accepted after revision August 6.

From the Departments of Neurosurgery (A.M., T.F., M.O., T.K., H.K., K.Y., Y.M., S.M.), Diagnostic Imaging and Nuclear Medicine (Y.F.), and Epilepsy, Movement Disorders and Physiology (M.M.), Kyoto University Graduate School of Medicine, Kyoto, Japan; Department of Neurosurgery (A.M.), and Division of Statistical Analysis (E.N.), Shizuoka General Hospital, Shizuoka, Japan; and Department of Neurosurgery (T.N.), Shiga General Hospital, Shiga, Japan.

Please address correspondence to Akinori Miyakoshi, MD, Department of Neurosurgery, Shizuoka General Hospital, Shizuoka, Japan, 4-27-1, Kita Ando, Aoi-ku Shizuoka City, Shizuoka, 420-8527, Japan; e-mail: myks-kr@umin.ac.jp

Indicates open access to non-subscribers at www.ajnr.org

Indicates article with supplemental on-line video.

<http://dx.doi.org/10.3174/ajnr.A6861>

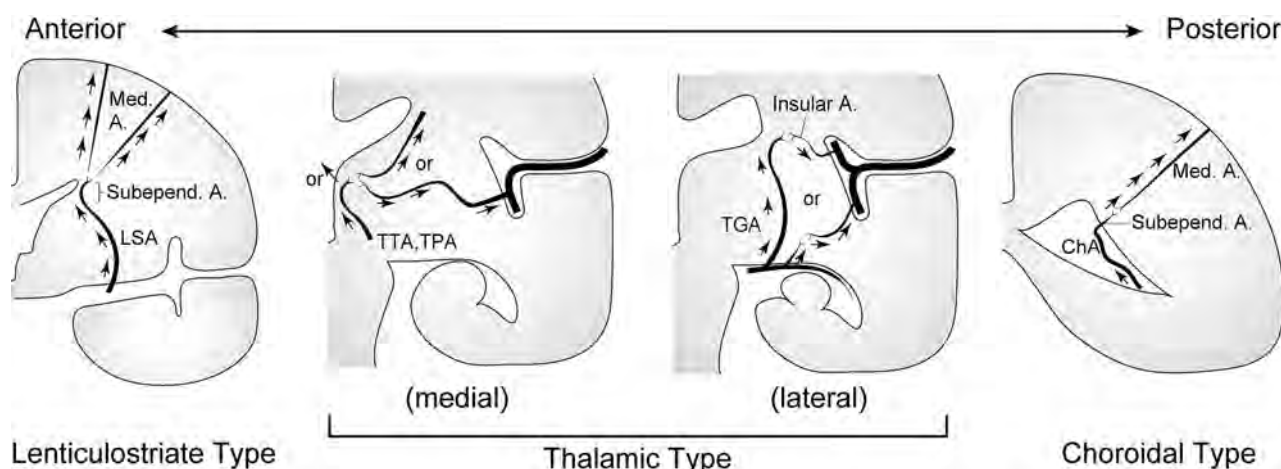


**FIG 1.** Schematic illustration showing a coronal plane of the left cerebral hemisphere and 3 subtypes of collateral anastomoses: lenticulostriate, thalamic, and choroidal anastomoses. A indicates artery; Med, medullary; Subepend, subependymal; TGA, thalamogeniculate artery; TPA, thalamoperforating artery; TTA, thalamotuberal artery. Reprinted with permission from Funaki et al.<sup>18</sup>

MRA performed using a 3T scanner has proved useful for detecting the abnormally extended collateral vessels in Moyamoya disease.<sup>2</sup> We investigated the cortical distribution of collateral vessels using 3T MR imaging and MRA to clarify whether cortical distributions vary among anastomotic subtypes and to better understand collateral networks.

## MATERIALS AND METHODS

### Study Design and Patients

This investigation was designed as a cross-sectional study. The study protocols were reviewed and approved by the ethics committee at the Kyoto University Graduate School of Medicine (R1600). Informed consent was obtained by an opt-out method on the institutional Web site. In accordance with the ethical standards of the institutional and national research committees, this retrospective, noninvasive study did not require formal consent. Instead, the outline of the study was open to the public on the institutional homepage and provided an opportunity for patients to decline to participate in the research. We retrospectively enrolled consecutive patients diagnosed with Moyamoya disease who visited our institution between January 2009 and April 2018. The diagnosis of Moyamoya disease was determined according to the proposed criteria.<sup>1</sup> Patients were excluded from the analysis if they had been diagnosed with quasi-Moyamoya disease (secondary Moyamoya phenomenon due to underlying disease). Patients who had undergone craniotomy (ie, hematoma-evacuation craniotomy or indirect or direct bypass surgery) were excluded, as were cases in which brains showed a change in shape from a normal structure because of massive infarction or hemorrhage. This exclusion was because an abnormal structure of the brain was considered to affect standardization of the brain. Patients who had not undergone imaging that met the imaging protocols were also excluded.

### Imaging Protocol and Postimaging Processing

A 3T MR imaging scanner (Magnetom Trio, Skyra, or Prisma; Siemens) using a 32-channel head coil was introduced in 2009. Whole-brain 3D-T1WI was performed in all cases for anatomic standardization. Imaging parameters for 3D-T1WI and TOF-MRA

in this study were as follows—T1-weighted MPRAGE: TR, 1900 ms; TE, 2.58 ms; flip angle, 9°; TI, 900 ms; FOV, 230 × 230 mm; matrix, 256 × 256; section thickness, 0.9 mm; generalized auto calibrating partially parallel acquisitions, 2; scan time, 4 minutes 26 seconds; TOF-MRA: TR, 20–21 ms; TE, 3.69 ms; flip angle, 20°; FOV, 220 × 187 mm; matrix, 384 × 328; section thickness, 0.7 mm; generalized auto calibrating partially parallel acquisitions, 3; scan time, 5 minutes 48 seconds. The imaging field extended from the level of the foramen magnum to the top of the head.

Images from MRA were registered to the corresponding T1WI. Subsequently, images from 3D-T1WI and MRA were anatomically standardized into the Montreal Neurological Institute (MNI) space using SPM12 software (<https://www.fil.ion.ucl.ac.uk/spm/>). To retain vessel information from MRA, we applied a 0.5-mm Gaussian smoothing kernel to these spatially normalized images from T1WI and MRA. Thus, all images from T1WI and MRA were created as 0.5-mm isotropic images in MNI coordinates.

### Measurement of Collateral Vessels That Are Continuously Detectable from Origin to the Cortex

We placed standardized MRA and T1WI from all axial, coronal, and sagittal views obtained in the same scanning session on the viewer of ITK-SNAP, Version 3.6, software (<https://www.itksnap.org/>).<sup>17</sup> Next, we detected collateral anastomoses on MRA and included collateral vessels for which signals could be identified all the way from the origin to the cerebral cortex without interruption. We classified the origin of anastomosis in 3 types (LSA, PcomA, or choA) on MRA according to previous reports<sup>2,18</sup> (Fig 1) and identified the point at which the anastomosis outflowed to the cortex. In brief, these types were the following: 1) lenticulostriate anastomosis, beginning at an LSA and connecting to the medullary or insular arteries; 2) thalamic anastomosis, beginning at the thalamotuberal, thalamoperforating, or thalamogeniculate arteries and connecting to the medullary or insular arteries; and 3) choroidal anastomosis, beginning at the anterior or posterior choroidal arteries and connecting to medullary or insular arteries. Thin-section T1WI was more favorable for detecting the edge of the cortex than MRA. Voxel coordinates of the outflow point were recorded, and the type

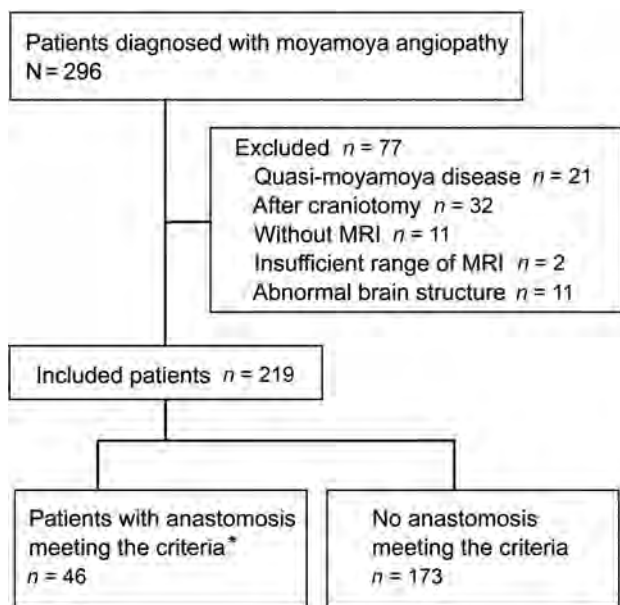


**FIG 2.** Flowchart for patient inclusion. Asterisk indicates that the patients have the anastomoses for which signals could be identified all the way from the origin to the cerebral cortex without interruption on MR angiography.

#### Patient characteristics

	Included Patients with Moyamoya Disease (n = 46)
Median age (range) (yr)	28.5 (3–56)
Male sex (No.) (%)	14 (30.4)
Clinical presentation (No.) (%)	
Ischemic symptoms	28 (60.9)
Hemorrhagic symptoms	11 (23.9)
Other symptoms	7 (15.2)

of anastomosis was classified according to the consensus decision of 2 neurosurgeons (A.M. and T.F.). An independent neuroradiologist (Y.F.) then identified the anastomosis on the basis of the coordinates recorded by the 2 neurosurgeons, tracked its signal to the origin, and then classified the type of anastomosis. In cases of disagreement between the neurosurgeons and the neuroradiologist, another neurosurgeon (M.O.) judged the type of anastomosis. In cases of an anastomosis joined to another type of anastomosis, we counted the case as 2 anastomoses for 1 outflow point. Interrater agreement for the origin of collateral vessels between the consensus decision of the 2 neurosurgeons and the neuroradiologist was then evaluated. The actual measurement process is shown in the Online Video.

Voxel coordinates on ITK-SNAP ranged from 1 to 361 (right to left) for the x-axis, 1 to 395 (back to front) for the y-axis, and 1 to 345 (caudal to cranial) for the z-axis. To treat all coordinates as being on the left hemisphere, we performed a horizontal mirroring of coordinates—that is, we calculated x-axis coordinates on the right hemisphere as  $362 - x$ .

#### Mapping Cortical Distribution of Perforating Arteries onto the Standardized Brain Model

Once we determined the cortical distributions of collateral arteries in individual brains, we converted voxel coordinates

into the MNI space. For visualization in 3D space, we created a standard brain surface model from the T1WI provided as `MNI152_T1_2mm_brain.nii.gz` in the FSL package (<https://fsl.fmrib.ox.ac.uk/fsl/fslwiki/FSL>). To obtain an isosurface of the standard brain, we chose a threshold of 5400 to visualize sulci keeping the visibility of the cerebral cortex. The surface model was loaded and displayed in 3D, together with the coordinates of cortical distributions. These procedures were performed by our in-house script in Matlab software (MathWorks).

#### Statistical Analysis

Interrater agreement for the classification of collateral vessels between the consensus decision of the neurosurgeons (A.M. and T.F.) and the decision of the neuroradiologist (Y.F.) was evaluated using the unweighted  $\kappa$  statistic and the corresponding 95% CI. We compared x, y, and z voxel coordinates among the 3 types of anastomoses to evaluate differences in distributions. The Kruskal-Wallis test was used to compare the 3 types of anastomoses, and the Mann-Whitney *U* test was used for every 2 anastomoses using Bonferroni-corrected *P* values.  $P < .05$  was considered significant in  $\kappa$  statistics and the Kruskal-Wallis test, and  $P < .016$  (ie,  $.05/3$ ) was used for the Mann-Whitney *U* test. We assumed that measurements from each anastomosis were independent along with patient characteristics and performed statistical analyses. All statistical analyses were conducted using R statistical and computing software, Version 3.5.2 (<http://www.r-project.org>).

## RESULTS

#### Patients and Anastomoses

Between January 2009 and April 2018, a total of 296 patients diagnosed with Moyamoya disease visited our institution. Seventy-seven patients were excluded (quasi-Moyamoya disease,  $n = 21$ ; after craniotomy including bypass surgery,  $n = 32$ ; patients who had not undergone MR imaging,  $n = 11$ ; insufficient range of MR imaging,  $n = 2$ ; and abnormal brain structure,  $n = 11$ ). We investigated the remaining 219 patients, with 46 of these 219 patients showing anastomoses for which uninterrupted signals could be identified all the way from the origin to the cerebral cortex (Fig 2).

A total of 190 anastomoses (lenticulostriate anastomosis,  $n = 72$ ; thalamic anastomosis,  $n = 21$ ; choroidal anastomosis,  $n = 97$ ) were detected in 46 Japanese patients. Six anastomoses were counted as 2 different types of anastomosis joined (lenticulostriate and thalamic,  $n = 2$ ; lenticulostriate and choroidal,  $n = 2$ ; thalamic and choroidal,  $n = 2$ ). Interrater agreement for the judgment of anastomosis origin was high ( $\kappa = 0.95$ ; 95% CI, 0.90–0.99). Six cases showed a discrepancy in the judgment between the neurosurgeons and the neuroradiologist. As examples, 4 anastomoses counted as a lenticulostriate type by neurosurgeons had been classified as a choroidal type by the neuroradiologist. Those 4 anastomoses were finally judged as lenticulostriate types by the final neurosurgeon.

#### Background Characteristics of Patients

Fourteen male and 32 female patients with Moyamoya disease were included (median age, 28.5 years; range, 3–56 years) (Table). Among 46 patients, 28 patients had ischemic symptoms at onset, 11



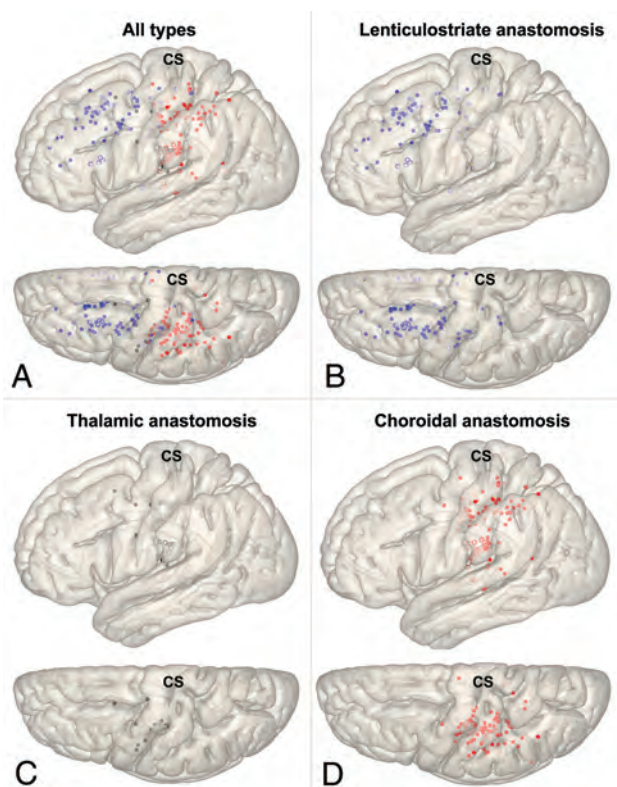


**FIG 3.** Cortical distributions for each type of collateral depicted on a standard brain surface model (A, All types; B, Lenticulostriate anastomosis; C, Thalamic anastomosis; D, Choroidal anastomosis). Each dot shows the point of anastomosis outflow to the cortex (blue dot, lenticulostriate anastomosis; black dot, thalamic anastomosis; red dot, choroidal anastomosis). Unfilled circles represent outflow on the insular cortex. Pale dots represent outflow located in a sulcus. CS indicates central sulcus.

from hemorrhagic symptoms, with the remaining 7 patients presenting with other symptoms.

#### Cortical Distributions of Collateral Types on the Brain Surface

We demonstrated spatial distribution patterns of the “collateral anastomosis” or collateral vessels reaching the cerebral cortex without interruption. Cortical distributions of each type of collateral on the standard brain surface model are depicted in Figs 3 and 4. Lenticulostriate anastomoses developed from LSAs and showed outflow mainly to the superior and inferior frontal sulcus and cingulate sulcus (interhemispheric fissure) via medullary arteries. Thalamic anastomoses developed from PcomA perforators and showed outflow to the insular cortex and sulcus around the central sulcus via medullary arteries. Choroidal anastomoses developed from the anterior and posterior choroidal arteries and showed outflow to the sulci posterior to the central sulcus and the insular cortex via the medullary arteries.

#### Spatial Distribution Patterns of Collateral Anastomoses

For the x-axis (mediolateral direction), distributions among the 3 types of anastomosis differed significantly ( $P < .001$ ). LSA anastomoses showed outflow to the cortex more medially than choroidal anastomoses ( $P < .001$ ; 95% CI, 11.0–24.0) (Fig 5). For the y-axis

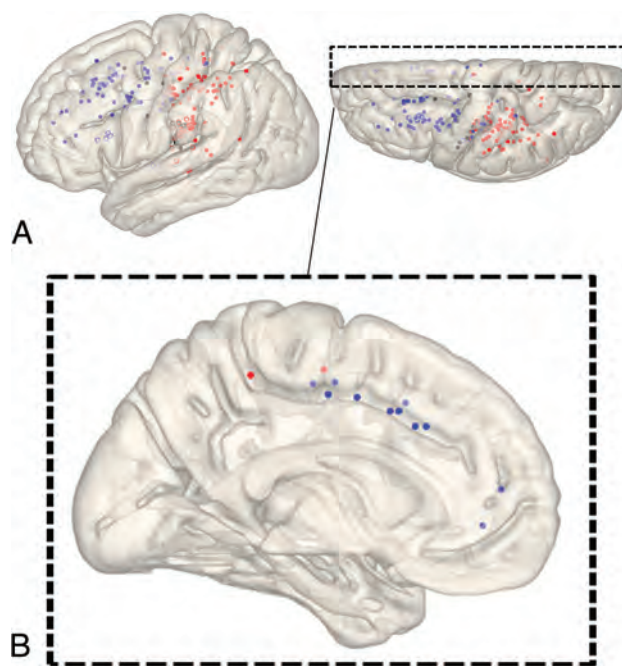


**FIG 4.** Cortical distributions of each type of collateral depicted on a standard brain surface model. Each dot shows the point where each anastomosis outflowed to the cortex (blue dot, lenticulostriate anastomosis; black dot, thalamic anastomosis; red dot, choroidal anastomosis). White circles (circles without fill) show dots located on the insular cortex. A, All dots are depicted on a brain surface model. B, The view from the medial surface of a 3D brain surface model. Dots were extracted that exist within 15 mm from the midline.

(posterior-anterior direction), distributions among the 3 types of anastomosis also differed significantly ( $P < .001$ ). LSA anastomoses showed outflow to the cortex more anteriorly than thalamic ( $P < .001$ ; 95% CI, 34.0–68.0) or choroidal anastomoses ( $P < .001$ ; 95% CI, 67.0–87.0) (Fig 6). Thalamic anastomoses showed outflow to the cortex more anteriorly than choroidal anastomoses ( $P < .001$ ; 95% CI, 14.0–34.0) (Fig 6). For the z-axis (caudocranial direction), no significant differences in distribution were evident among the 3 types (Fig 7).

#### DISCUSSION

We demonstrated that lenticulostriate anastomoses showed outflow to the cortex more anteriorly and medially than choroidal anastomoses. Choroidal anastomoses showed outflow to the cortex more posteriorly than thalamic or lenticulostriate anastomoses.

We finally analyzed data from 46 of 219 patients with Moyamoya disease. The detection rate of abnormally dilated collaterals using MRA is equal to that using conventional DSA, as previously reported.<sup>10</sup> MRA is also superior for identifying positions of vessels relative to the brain. However, we processed MRA data to standardize the images using software, and this process slightly decreased the spatial resolution. We, therefore, only included obviously dilated collaterals with uninterrupted signals. This was 1 reason why most of the initial patient cohort was excluded.

Unlike the PcomA and choAs, abnormal dilation and extension of the LSA has not been proved to be associated with intracranial hemorrhage in Moyamoya disease. Two previous studies

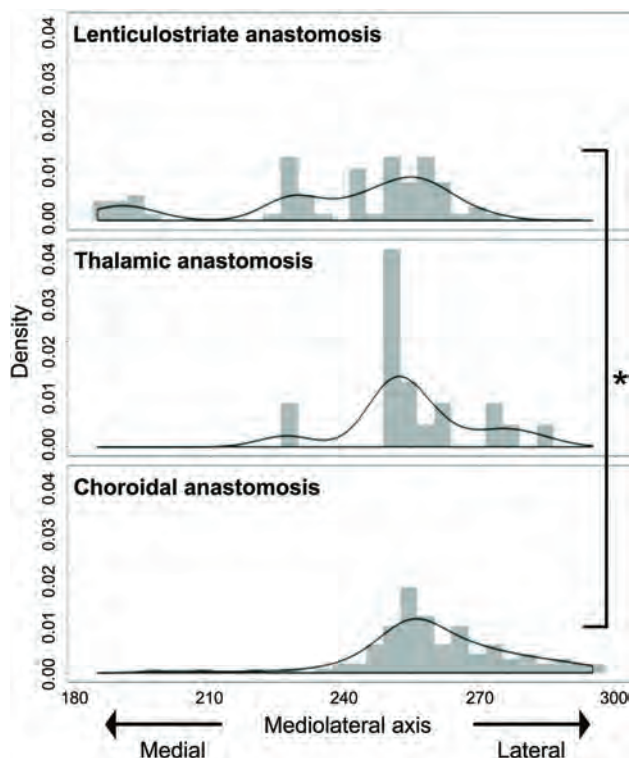


**FIG 5.** Mediolateral (x-coordinate) distribution of outflow to the cortex for each type of anastomosis. The value for the midline of images is 181, and the value for the lateral edge of images is 361. Values for x-coordinates are shown as density estimations. The asterisk indicates  $P < .001$ .

compared the development of LSA collaterals between ischemic and hemorrhagic-onset Moyamoya disease, and no significant difference in the development of LSA collaterals was identified, unlike PcomA and choA collaterals.<sup>4,19</sup> However, a dilated and extended LSA is suggested as a vessel responsible for hemorrhage.<sup>10</sup> Some reports have also discussed ruptured aneurysms arising on dilated and extended LSAs.<sup>9,20,21</sup> These aneurysms supposedly develop due to an increase in the hemodynamic burden, to supply the cortex via collaterals in place of shrunken major arteries.<sup>9,20,21</sup> Furthermore, Takahashi et al<sup>22</sup> estimated LSAs as possible sources of anterior hemorrhage in a subanalysis of the Japan Adult Moyamoya Trial. Such findings suggest that lenticulostriate anastomosis is associated with anterior hemorrhage in Moyamoya disease.<sup>3,22</sup> Prospective cohort studies are expected to clarify the potential risk of LSA dilation in patients with Moyamoya disease.

Thalamic anastomosis was the least-detected anastomosis (21/190) among the 3 types of anastomosis seen in this study. Dilation and extension of the PcomA and its perforators represent a risk factor for hemorrhage in patients with Moyamoya disease.<sup>5,7,19</sup> Furthermore, a recent study suggested that dilated thalamic perforators represented a source of thalamic hemorrhage.<sup>10</sup> In the present study, thalamic anastomoses mainly showed outflow to the insular cortex, and less commonly to the cortex without joining with other types of anastomosis. Matsushige et al<sup>23</sup> evaluated the collateral networks in 15 patients with Moyamoya disease using 7T MRA and classified anastomoses of the thalamic perforators as PcomA perforators anastomosing with thalamostriate arteries and

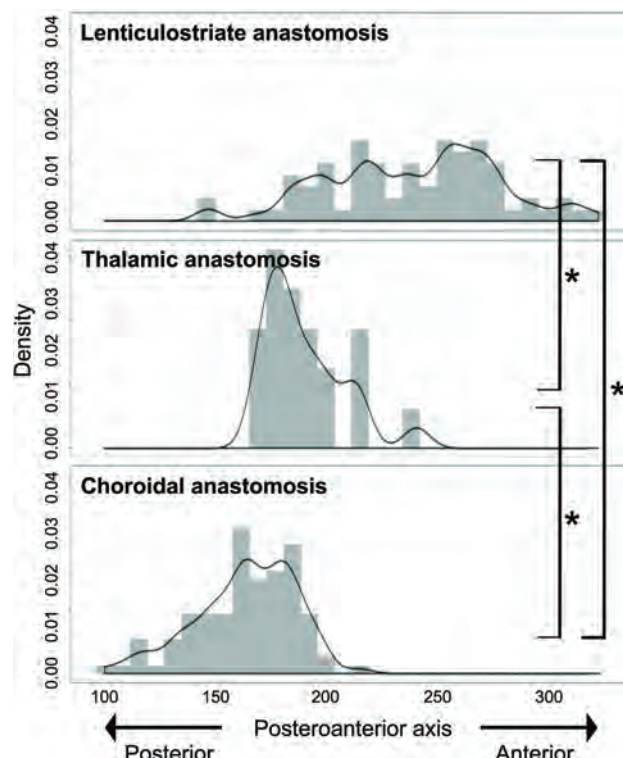


**FIG 6.** Posteroanterior (y-coordinate) distribution of outflow to the cortex for each type of anastomosis. The value for the posterior edge of images is 1, and the value for the frontal edge of images is 395. Values for y-coordinates are shown as density estimations. The asterisk indicates  $P < .001$ .

intrathalamic anastomoses among thalamic arteries. Those findings suggest that thalamic perforators less commonly outflow to the cortex independently and tend to anastomose with other collateral vessels. Thalamic collaterals might be strongly involved in thalamic hemorrhage<sup>10</sup> and may be less involved in periventricular hemorrhage at sites other than the thalamus.

In hemorrhagic-onset Moyamoya disease, choroidal anastomosis is the most frequently detected type of anastomosis and represents a strong risk factor for rebleeding.<sup>3,6,7,24</sup> Recent studies have suggested choroidal anastomosis as a risk factor for de novo hemorrhage in Moyamoya disease,<sup>8</sup> and choroidal anastomosis is mainly associated with posterior hemorrhage and periventricular hemorrhage in Moyamoya disease.<sup>8,10,25</sup> On the other hand, choroidal anastomoses frequently shrink after bypass surgery,<sup>7,14,15</sup> though the reasons remain poorly understood. We hypothesize that choroidal anastomoses may outflow to the cortex around the recipient site for ordinary bypass surgery. Collateral flow via direct bypass is thought to reduce the burden on abnormally developed collateral vessels and thus contribute to prevention of rebleeding.<sup>3,7,13,15</sup> On the basis of this concept, the anastomotic site of bypass might affect such preventative effects. In this study, choroidal anastomoses showed outflow to the cortex posterior to the central sulcus, in an area corresponding to the recipient site in bypass surgery.<sup>26-29</sup>

Takahashi et al<sup>22</sup> reported that the preventative effects of bypass surgery on rebleeding were not detected in an anterior hemorrhage group. The area of lenticulostriate anastomosis



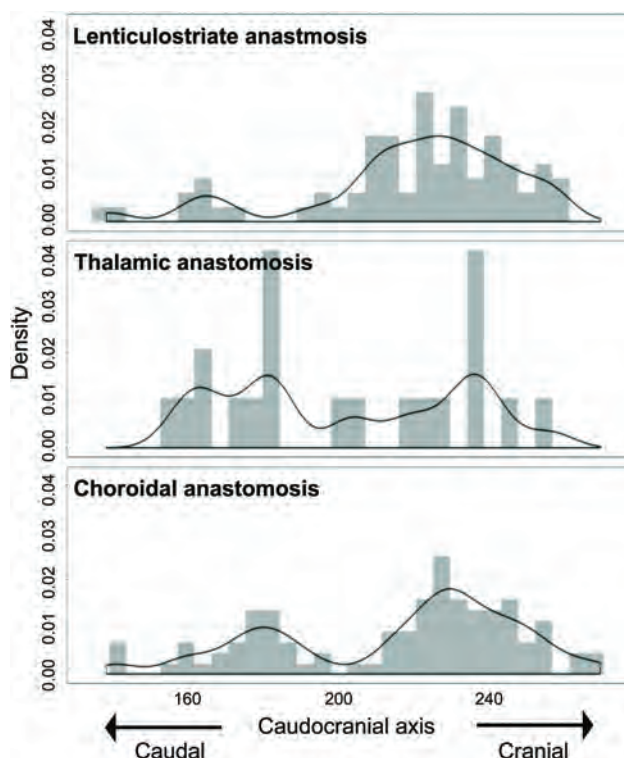


**FIG 7.** Caudocranial (z-coordinate) distribution of outflow to the cortex for each type of anastomosis. The value for the caudal edge of images is 1, and the value for the cranial edge of images is 345. Values for z-coordinates are shown as density estimations.

outflow is less likely to be the recipient site under usual bypass surgery because outflow is more anterior or to the interhemispheric fissure, unlike other anastomoses. This anatomic feature may explain the lack of preventative effects from bypass surgery among the anterior hemorrhage group.

Some limitations to this study must be considered. First, although we used spatially standardized MR imaging, anatomic differences in each patient would likely have had a small effect on the results. Second, although interrater agreement was high, both misclassification (measurement error) and observer bias are essential limitations and may have impacted the internal validity of this study. Third, although we analyzed 190 anastomoses in 46 patients among the cohort of 219 patients, these patients might represent an insufficient cohort to allow generalization of the results. Fourth, because all patients in this study were of Japanese ethnicity, the results are most generalizable to Japanese or Asian patients. Differences in the development of collateral vessels between Japanese and European white patients have already been reported.<sup>30</sup>

We believe the findings obtained from this study will contribute to understanding the pathology of hemorrhagic Moyamoya disease and to the establishment of better bypass surgeries to prevent bleeding among patients with Moyamoya disease.

## CONCLUSIONS

Outflow of lenticulostriate anastomoses was more anterior than that of thalamic and choroidal anastomoses. Outflow of lenticulostriate anastomoses was more medial than that of choroidal anastomoses.

Outflow of choroidal anastomoses was more posterior than that of lenticulostriate and thalamic anastomoses. Lenticulostriate anastomosis outflow to the cortex was anterior to the central sulcus and to the interhemispheric fissure. Thalamic anastomosis outflow was to the insular cortex and cortex around the central sulcus. Choroidal anastomosis outflow was to the cortex posterior to the central sulcus and the insular cortex. A more detailed understanding of each pattern of cortical distribution from abnormal collateral vessels may contribute to designing treatment strategies, allowing tailored bypass surgery optimized to prevent hemorrhage among patients with Moyamoya disease.<sup>16</sup>

**Disclosures:** Masao Matsushashi—RELATED: Grant: KAKENHI, Comments: Ministry of Education, Culture, Sports, Science and Technology KAKENHI grant No. 15H05875; UNRELATED: Grants/Grants Pending: KAKENHI, Comments: 19H03574, 19H01091, 18H02709, 17H02121, 26330175, 21700288; OTHER RELATIONSHIPS: Department of Epilepsy, Movement Disorders and Physiology, Kyoto University, is the Industry-Academia Collaboration Courses, supported by Eisai Co, Nihon Kohden Corp, Otsuka Pharmaceutical Co, and UCB Japan Co. Eiji Nakatani—UNRELATED: Consultancy: Sagamihiro National Hospital, Osaka University; Expert Testimony: Osaka University; Grants/Grants Pending: Shionogi & Co. Shizuoka Prefecture, Japan Society for the Promotion of Science\*; Payment for Lectures Including Service on Speakers Bureaus: Celgene Japan. \*Money paid to the institution.

## REFERENCES

1. Research Committee on the Pathology and Treatment of Spontaneous Occlusion of the Circle of Willis; Health Labour Sciences Research Grant for Research on Measures for Intractable Diseases. **Guidelines for diagnosis and treatment of moyamoya disease (spontaneous occlusion of the circle of Willis).** *Neurol Med Chir (Tokyo)* 2012;52:245–66 CrossRef Medline
2. Funaki T, Takahashi JC, Yoshida K, et al. **Periventricular anastomosis in moyamoya disease: detecting fragile collateral vessels with MR angiography.** *Japan Neurosurg* 2016;124:1766–72 CrossRef Medline
3. Funaki T, Takahashi JC, Houkin K, et al. **Angiographic features of hemorrhagic moyamoya disease with high recurrence risk: a supplementary analysis of the Japan Adult Moyamoya Trial.** *J Neurosurg* 2018;128:777–84 CrossRef Medline
4. Yamamoto S, Hori S, Kashiwazaki D, et al. **Longitudinal anterior-to-posterior shift of collateral channels in patients with moyamoya disease: an implication for its hemorrhagic onset.** *J Neurosurg* 2018;130:884–90 CrossRef Medline
5. Morioka M, Hamada JI, Kawano T, et al. **Angiographic dilatation and branch extension of the anterior choroidal and posterior communicating arteries are predictors of hemorrhage in adult moyamoya patients.** *Stroke* 2003;34:90–95 CrossRef Medline
6. Liu P, Han C, Li DS, et al. **Hemorrhagic moyamoya disease in children: clinical, angiographic features, and long-term surgical outcome.** *Stroke* 2016;47:240–43 CrossRef Medline
7. Jiang H, Ni W, Xu B, et al. **Outcome in adult patients with hemorrhagic moyamoya disease after combined extracranial-intracranial bypass.** *J Neurosurg* 2014;121:1048–55 CrossRef Medline
8. Funaki T, Takahashi JC, Houkin K, et al. **Effect of choroidal collateral vessels on de novo hemorrhage in moyamoya disease: analysis of nonhemorrhagic hemispheres in the Japan Adult Moyamoya Trial.** *J Neurosurg* 2019;132:408–14 CrossRef Medline
9. Sasagasako T, Funaki T, Tanji M, et al. **Intractable medial anastomotic branches from the lenticulostriate artery causing recurrent hemorrhages in moyamoya disease.** *World Neurosurg* 2019;127:279–83 CrossRef Medline
10. Miyakoshi A, Funaki T, Fushimi Y, et al. **Identification of the bleeding point in hemorrhagic moyamoya disease using fusion images of susceptibility-weighted imaging and time-of-flight MRA.** *AJNR Am J Neuroradiol* 2019;40:1674–80 CrossRef Medline



11. Miyamoto S, Yoshimoto T, Hashimoto N, et al; JAM Trial Investigators. **Effects of extracranial-intracranial bypass for patients with hemorrhagic moyamoya disease: results of the Japan Adult Moyamoya Trial.** *Stroke* 2014;45:1415–21 CrossRef Medline
12. Liu X, Zhang D, Shuo W, et al. **Long-term outcome after conservative and surgical treatment of haemorrhagic moyamoya disease.** *J Neurol Neurosurg Psychiatry* 2013;84:258–65 CrossRef Medline
13. Jang DK, Lee KS, Rha HK, et al. **Bypass surgery versus medical treatment for symptomatic moyamoya disease in adults.** *J Neurosurg* 2017;127:492–502 CrossRef Medline
14. Irikura K, Miyasaka Y, Kurata A, et al. **The effect of encephalo-myo-synangiosis on abnormal collateral vessels in childhood moyamoya disease.** *Neurol Res* 2000;22:341–46 CrossRef Medline
15. Miyakoshi A, Funaki T, Takahashi JC, et al. **Restoration of periventricular vasculature after direct bypass for moyamoya disease: intra-individual comparison.** *Acta Neurochir* 019;161:947–54 CrossRef Medline
16. Funaki T, Kataoka H, Yoshida K, et al. **The targeted bypass strategy for preventing hemorrhage in moyamoya disease: technical note.** *Neurol Med Chir (Tokyo)* 2019;59:517–22 CrossRef Medline
17. Yushkevich PA, Piven J, Hazlett HC, et al. **User-guided 3D active contour segmentation of anatomical structures: significantly improved efficiency and reliability.** *Neuroimage* 2006;31:1116–28 CrossRef Medline
18. Funaki T, Fushimi Y, Takahashi JC, et al. **Visualization of periventricular collaterals in moyamoya disease with flow-sensitive black-blood magnetic resonance angiography: preliminary experience.** *Neurol Med Chir (Tokyo)* 2015;55:204–09 CrossRef Medline
19. Fujimura M, Funaki T, Houkin K, et al. **Intrinsic development of choroidal and thalamic collaterals in hemorrhagic-onset moyamoya disease: case-control study of the Japan Adult Moyamoya Trial.** *J Neurosurg* 2019;130:1453–59 CrossRef Medline
20. Liu P, Lv XL, Liu AH, et al. **Intracranial aneurysms associated with moyamoya disease in children: clinical features and long-term surgical outcome.** *World Neurosurg* 2016;94:513–20 CrossRef Medline
21. Ni W, Jiang H, Xu B, et al. **Treatment of aneurysms in patients with moyamoya disease: a 10-year single-center experience.** *J Neurosurg* 2018;128:1813–22 CrossRef Medline
22. Takahashi JC, Funaki T, Houkin K, et al; JAM Trial Investigators. **Significance of the hemorrhagic site for recurrent bleeding: pre-specified analysis in the Japan Adult Moyamoya Trial.** *Stroke* 2016;47:37–43 CrossRef Medline
23. Matsushige T, Kraemer M, Sato T, et al. **Visualization and classification of deeply seated collateral networks in moyamoya angiopathy with 7T MRI.** *AJNR Am J Neuroradiol* 2018;39:1248–54 CrossRef Medline
24. Funaki T, Takahashi JC, Houkin K, et al. **High rebleeding risk associated with choroidal collateral vessels in hemorrhagic moyamoya disease: analysis of a nonsurgical cohort in the Japan Adult Moyamoya Trial.** *J Neurosurg* 2019;130:525–30 CrossRef Medline
25. Wang J, Yang Y, Li X, et al. **Lateral posterior choroidal collateral anastomosis predicts recurrent ipsilateral hemorrhage in adult patients with Moyamoya disease.** *AJNR Am J Neuroradiol* 2019;40:1665–71 CrossRef Medline
26. Guzman R, Steinberg GK. **Direct bypass techniques for the treatment of pediatric moyamoya disease.** *Neurosurg Clin N Am* 2010;21:565–73 CrossRef Medline
27. Houkin K, Kamiyama H, Takahashi A, et al. **Combined revascularization surgery for childhood moyamoya disease: STA-MCA and encephalo-duro-arterio-myo-synangiosis.** *Childs Nerv Syst* 1997;13:24–29 CrossRef Medline
28. Kim DS, Yoo DS, Huh PW, et al. **Combined direct anastomosis and encephaloduroarteriogaleosynangiosis using inverted superficial temporal artery-galeal flap and superficial temporal artery-galeal pedicle in adult moyamoya disease.** *Surg Neurol* 2006;66:389–94 CrossRef Medline
29. Acker G, Fekonja L, Vajkoczy P. **Surgical management of Moyamoya disease.** *Stroke* 2018;49:476–82 CrossRef Medline
30. Hori S, Kashiwazaki D, Yamamoto S, et al. **Impact of interethnic difference of collateral angioarchitectures on prevalence of hemorrhagic stroke in Moyamoya disease.** *Neurosurgery* 2019;85:134–46 CrossRef Medline

# Clinical and Radiologic Findings of Acute Necrotizing Encephalopathy in Young Adults

H.A. Vanjare, B.T. Selvi, R. Karuppusami, A. Manesh, K. Gunasekaran, A.T. Prabhakar, P. Mannam, and A. Jasper



## ABSTRACT

**SUMMARY:** Acute necrotizing encephalopathy after an acute febrile illness, although initially described exclusively in the pediatric age group, has been recently shown to have an adult onset as well. In this study, we describe 10 patients (16 years of age or older) with acute necrotizing encephalopathy. In our study, bilateral thalamic involvement with the trilaminar pattern of diffusion restriction on MR imaging was the predominant finding seen in all of the patients reviewed. Ancillary findings of cerebral white matter, brain stem, and cerebellum involvement with sparing of the basal ganglia were also noted. A poorer outcome was observed in patients with a higher degree of thalamic involvement. The cause of an underlying infection was identified in 4 patients (dengue in 3 and influenza in 1). Overall, a sizeable portion of young adults with acute necrotizing encephalopathy have shown a poorer outcome, with dengue being an important underlying trigger in an endemic region.

**ABBREVIATION:** ANE = acute necrotizing encephalopathy

Acute necrotizing encephalopathy (ANE) is a parainfectious, pauciinflammatory disorder predominantly reported among children younger than 5 years of age. The diagnosis is based on the typical clinical presentation, imaging findings, and exclusion of other mimicking conditions.<sup>1,2</sup> Although the pathophysiology of ANE is not completely understood, it is considered to be immune-mediated after a viral infection.<sup>3-5</sup> A lack of inflammatory changes in ANE distinguishes it from other necrotizing encephalitides.

Hypercytokinemia, also known as “cytokine storm,”<sup>6,7</sup> is the most widely accepted theory that described the triggers for the development of ANE in susceptible hosts and is characterized by elevated serum interleukin (IL)-6, -10, -15, and -1 $\beta$ ; tumor necrosis factor- $\alpha$  (TNF- $\alpha$ ); and interferon- $\gamma$ .<sup>5-8</sup> Whereas neurotoxicity is associated with a higher concentration of IL-6, TNF- $\alpha$  is associated with endothelial damage involving the intracranial vessels.<sup>8</sup> Autopsy and histopathology of a previously reported patient showed coagulative necrosis accompanied by hemorrhages around the small vessels in the involved regions of the brain. Lymphocytic and neutrophilic infiltrates were not observed, which is suggestive

of a lack of cellular inflammatory response.<sup>9</sup> The lack of inflammatory cell infiltration might suggest a distant, spin-off effect because of uncontrolled inflammation secondary to the primary inciting event, commonly a viral infection. A missense mutation in the gene encoding the nuclear pore protein Ran binding protein 2 is found to increase an individual's susceptibility for ANE.<sup>10,11</sup> The mechanistic understanding between this mutation and the pathway leading to ANE is unknown; however, the mutation may affect energy production and lipid peroxidation within the cells along with altering the mechanism for viral entry, cytokine signaling, antigen presentation, immune response, and blood-brain barrier maintenance.<sup>10</sup>

Case reports have been published from around the world and those from East Asia in the late 1990s described symmetric brain lesions with bilateral thalamic involvement. Because most of the published literature involves the pediatric population, it is often labeled as ANE of childhood. The literature on older patients with ANE is sparse with only 30 cases published to date (PubMed and Google Scholar search without language restriction and age cutoff of 16 years). Hence, there are inadequate data to describe the pattern of brain parenchymal involvement among older patients and its possible correlation to final or long-term outcomes.

In this single-center retrospective study from a medical college hospital in South India, all patients (16 years of age and older) with clinical and radiologic findings suggestive of ANE were analyzed, and their clinical, imaging, laboratory findings, and outcomes were documented.

Received May 24, 2020; accepted after revision July 15.

From the Christian Medical College and Hospital, Tamil Nadu, India.

Please address correspondence to Dr. Harshad Arvind Vanjare, Dept. of Radiology, Christian Medical College and Hospital, Ida Scudder Rd, Vellore 632004, Tamil Nadu, India; e-mail: harshadcmc@cmcvellore.ac.in



Indicates article with supplemental on-line tables.



Indicates article with supplemental on-line photos.

<http://dx.doi.org/10.3174/ajnr.A6803>

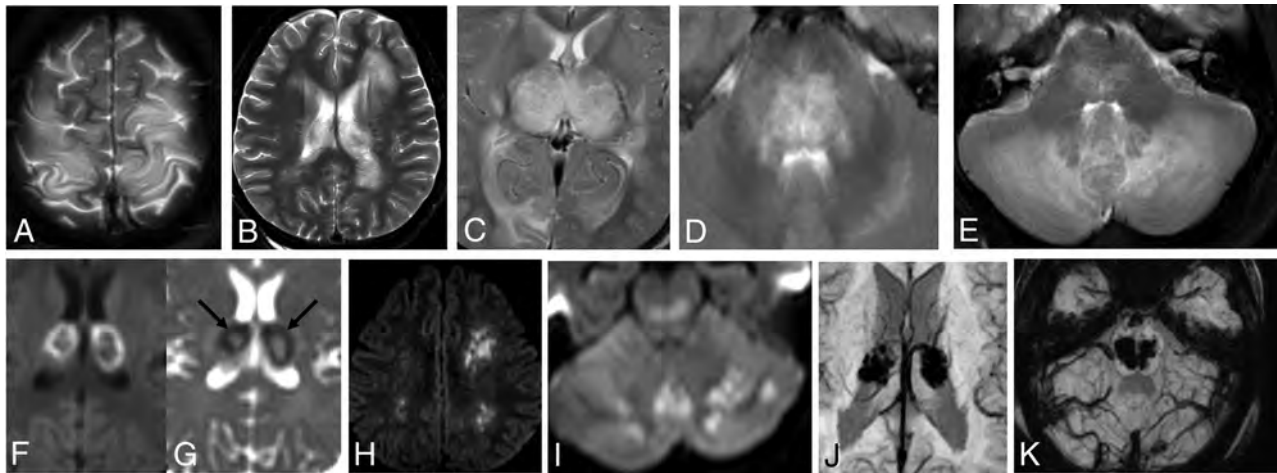


**FIGURE.** A–E, T2-weighted axial sections demonstrating the involvement of cortical gray matter, white matter, thalami, brain stem, and cerebellar hemispheres. F–I, DWI axial sections demonstrating diffusion restriction in thalami, cerebral, and cerebellar white matter. Trilaminar pattern on ADC (G) as a low signal ring (arrows) with central and peripheral hyperintensity. J and K, SWI demonstrating microhemorrhages in thalami and brain stem.

### CASE SERIES

The study was approved by the institutional review board. Patients were identified retrospectively by using the radiology database and hospital information system (from 2002 to 2019) based on the features proposed by Mizuguchi and coworkers,<sup>1,2</sup> which are as follows: 1) acute encephalopathy after a febrile viral disease and rapid deterioration in the level of consciousness; 2) CT or MR imaging findings for symmetric, multifocal brain lesions, including bilateral thalami; and 3) exclusion of other resembling diseases such as cerebral venous thrombosis, hypoxic-ischemic injury, and metabolic etiologies.

Patients younger than 16 years of age were excluded. Clinical and laboratory parameters were documented. A good outcome was defined as absent or mild to moderate neurologic deficits on follow-up, and a poor outcome was defined as severe neurologic deficits on follow-up or death during the hospital stay.

### Technical Information

MR imaging scans were performed on a 1.5T (Magnetom Avanto, Siemens) or a 3T (Intera Achieva, Philips Medical Systems) scanner, and the CT scan was performed on a 64-section scanner (Discovery 750 HD, GE Healthcare).

Ten patients with a mean age of 23.8 (SD, 5.9; median, 23.5; range, 17–32) years were included in the study. There were 8 men and 2 women. All the patients were of South Asian (Indian) descent with no premorbid illness or medical condition or family history of similar illness.

### Clinical and Laboratory Parameters

Patients presented with fever, altered sensorium, vomiting, and seizures, clinically raising the suspicion of encephalitis (On-line Table 1). The onset of symptoms was associated with the development of fever in all patients followed by other symptoms. The mean duration between the onset of fever and imaging was 3.6 days (SD, 1.07; median, 4 days; range, 2–5 days). On blood investigations, transaminitis was seen in 4 patients. CSF analysis showed elevated proteins in all 5 patients in whom the analysis

was performed. Other parameters assessed were liver function tests, including bleeding parameters and renal function. None of the patients were tested for elevated serum cytokine levels.

### Viral Infections and Medical Management

Of the 10 patients, 3 were positive for dengue and 1 for H1N1 influenza (On-line Table 2). The patients were managed conservatively with the use of antivirals, immunosuppression, and supportive care.

### Imaging Findings

Nine patients underwent MR imaging, and 1 had CT (On-line Table 3 and Figure). The brain lesions were seen as areas of T2-weighted hyperintensities associated with swelling with corresponding T1-weighted hypointensities on MR imaging scans, which were hypoattenuated on CT. Cerebral white matter involvement assessed on T2-weighted imaging was seen in 8 (89%) patients with involvement of subcortical white matter in 6 patients, deep white matter in 4 patients, and periventricular white matter in 3 patients. Cortical gray matter involvement was seen in 60%, brain stem involvement in 80%, and cerebellar hemisphere involvement in 100% of the patients. Thalamic involvement being a part of the diagnostic criteria was seen in all of the patients. Based on visual assessment, thalamic involvement was divided into <50%, >50% but not near-complete involvement, and near-complete involvement. All the patients had >50% involvement of the thalami. The basal ganglia involvement was not seen in any patient.

Of the 9 patients in whom an MR imaging scan was performed, diffusion restriction involving the white matter was seen in 44% of patients, gray matter involvement in 56%, brain stem involvement in 78%, and cerebellum involvement in 100% of patients. Trilaminar pattern of diffusion restriction, which is seen as a ring of low signal involving the thalamus on an apparent diffusion coefficient map with central and peripheral hyperintensity (Fig 1G), was observed in 100% of patients.

No significant postcontrast enhancement was seen in the 6 postcontrast MR imaging studies performed. Multiple foci of microhemorrhages, seen as blooming on a susceptibility-weighted



sequence involving the thalami, brain stem, and cerebellar hemispheres, were noted in all 9 MR imaging scans. Cavitation (defined as a cystic area on a T2-weighted sequence and hypointense area on a T1-weighted sequence or fluid density on CT scan) was identified in 1 case with bithalamic involvement (On-line Fig 1A).

### Outcome

Six patients with an average follow-up of 21 (SD, 29.6; median, 6; range, 1–76) months had good outcomes (On-line Table 4). Four patients had mild motor deficits, and 2 patients had developed mood changes with aggressive behavior. MR imaging was available in 2 patients at 5 and 31 months of follow-up (On-line Figs 1 and Fig 2); both showed residual gliotic changes in the previously involved parenchyma with resolution of diffusion restriction and edema. Four patients died during their hospital stay.

### DISCUSSION

ANE is a rare, albeit severe, parainfectious disorder predominantly seen in the pediatric age group and rarely reported in older patients. The clinical course in pediatric patients is divided into an initial prodromal stage, which is associated with fever, vomiting, and cough. This is followed by the acute encephalopathy stage associated with disturbance in consciousness and seizures, finally progressing to a prolonged recovery stage when few recover completely, with residual neurologic deficits in most of the survivors.<sup>8</sup>

Most of the patients described in the literature have a preceding viral infection that triggers an excessive immune response in susceptible hosts. Most of the published adult patients with ANE describe an influenza infection as the initial trigger. A recent case report has shown COVID-19 infection as an initial trigger for adult onset of ANE.<sup>12</sup> Dengue, as an inciting trigger for older patients with ANE, has not been described previously. Dengue was identified in 3 of our patients. In the pediatric population, ANE has been described with viral infections such as influenza, parainfluenza, herpesvirus 6 and 7, herpes simplex virus, measles, rubella, varicella, coxsackie A9, rotavirus, reovirus, and dengue.<sup>8,13</sup> Most of the data published on ANE are from the east Asian regions such as Japan, Korea, and Taiwan, where dengue infection is uncommon. Our case series therefore highlights the importance of dengue as a cause of ANE among young adults in endemic regions such as India.

Typical imaging findings in pediatric ANE include fairly symmetric abnormalities in bilateral thalami, cerebral white matter, brain stem, and cerebellar hemispheres.<sup>1–3,14–17</sup> The pediatric case series by Kim et al,<sup>18</sup> published in 2004 with 14 patients, showed the involvement of the internal capsule and deep white matter in 50% and 21%, respectively. Another case series published by Wong et al,<sup>19</sup> published in 2006 with 12 patients, showed a 67% involvement of the cerebral matter with no distinction made between subcortical, deep, and periventricular white matter. In our case series, the white matter was involved in 89% of patients, which is more frequent than that seen in the pediatric age group. On the other hand, our studies showed a 100% involvement of the cerebellum compared with 14% and 33% in the aforementioned pediatric ANE studies, respectively. Brain stem involvement was seen in 86% and 83% in the pediatric ANE case series, respectively, which is comparable to our case series with 80% involvement.

Parenchymal hemorrhage was seen in 36% and 42% in the pediatric ANE series; this rate was 90% in our series. This difference in the degree of parenchymal hemorrhage may be related to the use of the susceptibility-weighted sequence in all of our patients in whom hemorrhage was identified. There is a lack of published data describing diffusion restriction in different brain structures in ANE. In our patients, we found the involvement of posterior and central structures such as the cerebellum, brain stem, and thalami to be more common compared with the anterior structures such as the cerebral white matter and cortical gray matter.

Bithalamic involvement can be seen in multiple disorders such as West Nile encephalitis, Japanese encephalitis, Creutzfeldt-Jakob disease, Wernicke encephalopathy, acute disseminated encephalomyelitis, and thrombosis of the internal cerebral veins or straight sinus, among others.<sup>20</sup> Clinical presentation in patients with encephalitis can be very similar to that seen with ANE and can have significant thalamic involvement. However, a trilaminar pattern of diffusion restriction has not been described in patients with encephalitis. In Creutzfeldt-Jakob disease and Wernicke encephalopathy, the medial aspects of thalami are more involved. Acute disseminated encephalomyelitis is characterized by oval to round white matter demyelinating lesions, which may show an incomplete ring of enhancement, and thalami are not commonly involved, thereby distinguishing these conditions from ANE. Thrombosis of internal cerebral veins or the straight sinus can be identified by carefully examining T2-weighted coronal sections of the brain and postcontrast MR venograms.

Dengue is known to involve the brain. One study described the involvement of the thalami in one-fourth of the 35 patients presenting with dengue infection and neurologic symptoms.<sup>21</sup> Both encephalopathic and encephalitic presentation with bithalamic involvement in patients with dengue is described in the literature. The clinical distinction between these 2 is not possible. Encephalitis is often associated with CSF pleocytosis, which helps to distinguish it from encephalopathy, in which the CSF does not show an elevated cell count.

The presence of hemorrhage and cavitation are shown to correlate with poor outcomes in pediatric patients with ANE.<sup>19</sup> Similar data are not available for adult patients. In our series, microhemorrhages were seen on the susceptibility-weighted sequence in all 9 patients for whom MR imaging was performed with the involvement of central and posterior structures such as the thalami, brain stem tegmentum, and cerebellar hemispheres. Cavitation involving bilateral thalami was seen in 1 case with a good outcome.

Bilateral thalamic involvement is essential for the diagnosis of ANE; however, the degree of thalamic involvement and its correlation with the outcome has not been described in the literature. In our series, none of the patients had <50% of thalamic involvement. Three patients with >50% thalamic involvement (but less than near-complete involvement) were seen, all with good outcomes. Near-complete thalamic involvement was seen in the remaining 7; 4 had poor outcomes, and the other 3 fared well. Trilaminar pattern of diffusion restriction on the ADC sequence is considered to be specific for ANE<sup>8</sup> and was corroborated in all our patients with MR imaging, thus lending support to this imaging finding as an easy-to-identify imaging marker.

Brain stem lesion as a predictor for a poor outcome is controversial; however, 2 scoring systems have shown a correlation between brain stem lesions and poor outcome in pediatric patients.<sup>19,22</sup> In our case series, 80% of the patients had brain stem involvement (4 patients in the good outcome group and 4 patients in the poor outcome group).

Laboratory predictors for outcome have been inadequately assessed in adult patients. Normal or a mild increase in CSF protein in pediatric patients with ANE is associated with better clinical outcomes compared with those with elevated levels.<sup>18,23</sup> In our series, CSF analysis was available in 5 patients, all of whom had elevated levels of proteins and had good outcomes. This difference between the young adult and pediatric patients with ANE may be related to a more mature immune response with age.

There is no standardized protocol of management and treatment of ANE, so these are often tailored on a case-by-case basis and local expertise. Medical management mainly remains supportive with some studies showing benefits with the use of antivirals, immunoglobulins, and steroids.<sup>24,25</sup> The number of patients in our study were small with limited data on specifics of management to make any definitive observation. There is recent literature that shows the benefit of IL-6 blockade in the management of cytokine storm.<sup>26</sup> Similar intervention may benefit patients with ANE if the cytokine storm truly plays an important role in its pathogenesis. Sixty percent of patients in our series had good outcomes; however, these patients did not improve to their premorbid state and had residual motor deficits or mood changes. Despite medical advances, the poor outcome in ANE remains high with a 40% mortality rate seen in our case series.

## CONCLUSIONS

ANE in young adults is a rare immune-mediated disorder commonly involving the thalami, brain stem, and cerebellum. The characteristic trilaminar pattern of diffusion restriction on MR imaging, described in the literature, was seen in all of our patients. Coincidentally, in our study, we found that cerebellar involvement and parenchymal microhemorrhages were observed at a higher frequency than that which is reported in the literature for pediatric patients with ANE. The involvement of vital structures such as the thalami, brain stem, and cerebellum may explain the long-term deficits seen in survivors. Long-term sequelae include both motor deficits and mood disorders with treatment remaining largely supportive.

## ACKNOWLEDGMENT

The authors thank Dr. Carl Prem Trevor Colaco, Department of Radiology, Christian Medical College, Vellore, India, for English language support during manuscript preparation.

DISCLOSURES: Pavithra Mannam—UNRELATED: Employment: Christian Medical College and Hospital.

## REFERENCES

1. Mizuguchi M, Abe J, Mikkaichi K, et al. **Acute necrotizing encephalopathy of childhood: a new syndrome presenting with multifocal, symmetric brain lesions.** *J Neurol Neurosurg Psychiatry* 1995;58:555–61 CrossRef Medline
2. Mizuguchi M. **Acute necrotizing encephalopathy of childhood: a novel form of acute encephalopathy prevalent in Japan and Taiwan.** *Brain Dev* 1997;19:81–92 CrossRef Medline
3. Mizuguchi M, Yamanouchi H, Ichiyama T, et al. **Acute encephalopathy associated with influenza and other viral infections.** *Acta Neurol Scand Suppl* 2007;186:45–56 CrossRef Medline
4. Ito Y, Ichiyama T, Kimura H, et al. **Detection of influenza virus RNA by reverse transcription-PCR and proinflammatory cytokines in influenza-virus-associated encephalopathy.** *J Med Virol* 1999;58:420–25 CrossRef Medline
5. Ichiyama T, Endo S, Kaneko M, et al. **Serum cytokine concentrations of influenza-associated acute necrotizing encephalopathy.** *Pediatr Int* 2003;45:734–36 CrossRef Medline
6. Wang HS, Huang SC. **Acute necrotizing encephalopathy of childhood.** *Chang Gung Med J* 2001;24:1–10 Medline
7. Lim HY, Ho VPY, Lim TCC, et al. **Serial outcomes in acute necrotizing encephalopathy of childhood: a medium and long term study.** *Brain Dev* 2016;38:928–36 CrossRef Medline
8. Lin Y-Y, Lee K-Y, Ro L-S, et al. **Clinical and cytokine profile of adult acute necrotizing encephalopathy.** *Biomed J* 2019;42:178–86 CrossRef Medline
9. Kansagra SM, Gallentine WB. **Cytokine storm of acute necrotizing encephalopathy.** *Pediatr Neurol* 2011;45:400–02 CrossRef Medline
10. Wu X, Wu W, Pan W, et al. **Acute necrotizing encephalopathy: an underrecognized clinicoradiologic disorder.** *Mediators Inflamm* 2015;2015:e792578 CrossRef Medline
11. Ishii N, Mochizuki H, Moriguchi-Goto S, et al. **An autopsy case of elderly-onset acute necrotizing encephalopathy secondary to influenza.** *J Neurol Sci* 2015;354:129–30 CrossRef Medline
12. Neilson DE, Adams MD, Orr CMD, et al. **Infection-triggered familial or recurrent cases of acute necrotizing encephalopathy caused by mutations in a component of the nuclear pore, RANBP2.** *Am J Hum Genet* 2009;84:44–51 CrossRef Medline
13. Marco EJ, Anderson JE, Neilson DE, et al. **Acute necrotizing encephalopathy in 3 brothers.** *Pediatrics* 2010;125:e693–98 CrossRef Medline
14. Poyiadji N, Shahin G, Noujaim D, et al. **COVID-19-associated acute hemorrhagic necrotizing encephalopathy: CT and MRI features.** *Radiology* 2020;296:E119–20 CrossRef Medline
15. Abbas Q, Jafri SK, Ishaque S, et al. **Acute necrotizing encephalopathy of childhood secondary to dengue infection: a case report from Pakistan.** *J Pediatr Neurosci* 2017;12:165–67 CrossRef Medline
16. Toovey S. **Influenza-associated central nervous system dysfunction: a literature review.** *Travel Med Infect Dis* 2008;6:114–24 CrossRef Medline
17. Britton PN, Dale RC, Blyth CC, ACE study investigators and PAEDS network, et al. **Influenza-associated encephalitis/encephalopathy identified by the Australian Childhood Encephalitis Study 2013-2015.** *Pediatr Infect Dis J* 2017;36:1021–26 CrossRef Medline
18. Kim JH, Kim I-O, Lim MK, et al. **Acute necrotizing encephalopathy in Korean infants and children: imaging findings and diverse clinical outcome.** *Korean J Radiol* 2004;5:171–77 CrossRef Medline
19. Wong AM, Simon EM, Zimmerman RA, et al. **Acute necrotizing encephalopathy of childhood: correlation of MR findings and clinical outcome.** *AJNR Am J Neuroradiol* 2006;27:1919–23 Medline
20. Smith AB, Smirniotopoulos JG, Rushing EJ, et al. **Bilateral thalamic lesions.** *AJNR Am J Roentgenol* 2009;192:W53–62 CrossRef Medline

21. Vanjare HA, Mannam P, Mishra AK, et al. **Brain imaging in cases with positive serology for dengue with neurologic symptoms: a clinicoradiologic correlation.** *AJNR Am J Neuroradiol* 2018;39:699–703 CrossRef Medline
22. Yamamoto H, Okumura A, Natsume J, et al. **A severity score for acute necrotizing encephalopathy.** *Brain Dev* 2015;37:322–27 CrossRef Medline
23. Seo H-E, Hwang S-K, Choe BH, et al. **Clinical spectrum and prognostic factors of acute necrotizing encephalopathy in children.** *J Korean Med Sci* 2010;25:449–53 CrossRef Medline
24. Okumura A, Mizuguchi M, Kidokoro H, et al. **Outcome of acute necrotizing encephalopathy in relation to treatment with corticosteroids and gammaglobulin.** *Brain Dev* 2009;31:221–27 CrossRef Medline
25. Alsolami A, Shiley K. **Successful treatment of influenza-associated acute necrotizing encephalitis in an adult using high-dose oseltamivir and methylprednisolone: case report and literature review.** *Open Forum Infect Dis* 2017;4:ofx145
26. Tanaka T, Narazaki M, Kishimoto T. **Immunotherapeutic implications of IL-6 blockade for cytokine storm.** *Immunotherapy* 2016;8:959–70 CrossRef Medline



## Acute Necrotizing Encephalopathy: A Disease Meriting Greater Recognition

**A**cute necrotizing encephalopathy (ANE) is a rare subtype of acute infectious encephalopathy, first described by Mizuguchi,<sup>1</sup> a Japanese pediatric neurologist, in 1995. The clinical characteristics of ANE include febrile illness followed by altered consciousness and seizures. The pathologic features of the disease are necrosis and multiple petechiae in both the thalamus and tegmentum of the pons, as well as myelin pallor in the cerebral and cerebellar deep white matter. ANE typically develops in children younger than 5 years of age; only case reports have been published thus far in adults. In this issue of the *American Journal of Neuroradiology*, the authors report the clinical and radiologic findings of ANE in 10 adults and draw attention to several important aspects of the disease that should be recognized.<sup>2</sup>

The authors discuss the similarities and differences in MR imaging findings of ANE between children and adults. Thalamic involvement is a key radiologic finding for ANE diagnosis, regardless of patient age. A feature specific to ANE is the trilaminar pattern of restricted diffusion seen in the ADC map,<sup>3</sup> which was detected in all patients in this report. Whereas the core of the thalamic lesion shows high signal intensity, the adjacent pericore lesions show low signal intensity. The outer lesions also show high signal intensity on the ADC map. This characteristic neuroimaging pattern corresponds well with the pathologic findings reported previously.<sup>4</sup> Whereas the center of the thalamic lesion suggests hemorrhagic necrosis, the periphery of the core lesion suggests cytotoxic edema and the outside portions thalamic lesion vasogenic edema. Among the observed differences between ANE in adults and children, the authors report higher white matter (89%) and cerebellar (100%) involvement, in addition to parenchymal hemorrhage (90%), in adults. Our previous study of pediatric ANE found cerebellar lesions in only 23% of affected children.<sup>5</sup> The reason for the higher occurrence rate in adults than children is not considered in detail by the authors, but it may reflect differences in infectious agents, genetic background, immune response, and age-specific tissue vulnerability. However, in the study of Okumura et al,<sup>5</sup> there were no differences in clinical symptoms, laboratory data, or outcomes between children with ANE who had developed influenza and those who did not, suggesting that the pathogenetic mechanism of ANE is not dependent on an infectious agent. Further investigations are needed to

determine the reasons for the different MR imaging findings between children and adults with ANE.

Another interesting aspect of this study is the history of underlying infection because the authors identified dengue in 3 of the 10 patients. However, the study was retrospective and conducted in a single center (part of a medical school hospital in South India). Dengue is a mosquito-borne viral disease endemic in all tropical and subtropical countries, including South India. Although influenza virus is the most common pathogen in ANE, even in adults, other infectious agents, including human herpesvirus-6, herpes simplex virus, parvovirus B19, measles, rotavirus, *Mycoplasma* infection, and *Streptococcus pneumoniae* infection, can lead to the same pathologic condition that results in ANE in children. However, dengue virus belongs to the flaviviruses, which have rarely been reported as causal pathogens in ANE. We identified only 1 case report of ANE in which dengue was the antecedent infection; the patient was a 15-year-old girl in Pakistan.<sup>6</sup> Neurologic involvement resulting from dengue infection is uncommon, developing in only 4%–5% of patients. The neurologic manifestations include encephalopathy, acute disseminated encephalomyelitis, and dengue muscle dysfunction.<sup>7</sup> Vanjare et al<sup>8</sup> described the brain imaging patterns of patients with dengue and neurologic symptoms; a quarter of the patients had thalamic involvement. Another study reported a series of adult patients with dengue infection, as well as clinical and radiologic findings mimicking ANE.<sup>9</sup> The clinical and radiologic findings of these patients should be carefully evaluated to determine whether they meet the diagnostic criteria of ANE. Nevertheless, dengue should be suspected as the antecedent virus in patients with ANE residing in dengue-endemic regions.

As of August 2020, the COVID-19 pandemic continues largely unabated. Although affected patients typically present with fever, cough, and respiratory distress, accumulating evidence suggests that 30%–40% have neurologic complications, including stroke, encephalopathy, encephalitis, and meningitis.<sup>10,11</sup> Recent case reports have clearly demonstrated that Severe Acute Respiratory Syndrome coronavirus 2 (SARS-CoV-2) infection can also cause ANE, particularly in adults.<sup>12–14</sup> The neuroinvasive and neurotropic abilities of

SARS-CoV-2 are well established and have been attributed to the angiotensin-converting enzyme 2 receptor, expressed abundantly on venous endothelial cells and arterial smooth muscle cells in the brain. The virus directly accesses the brain via the nasal mucosa, lamina cribrosa, and olfactory bulb or via retrograde axonal transport. A proinflammatory and prothrombotic cascade develops in the wake of the virus-induced cytokine storm, a hyperinflammatory state that is also the central pathogenesis in patients with ANE, regardless of the causal agent. Both the brain vasculature and blood–brain barrier are affected, with edema and necrosis as secondary effects.

Immunosuppressive treatments, including methylprednisolone pulse therapy, and plasmapheresis may lead to favorable outcomes in some patients with ANE. A possible therapeutic target is the interleukin-6-STAT3 pathway, which has been shown to be responsive to tocilizumab, a monoclonal antibody against the interleukin-6 receptor.<sup>15</sup> Prompt diagnosis of ANE based on characteristic MR imaging findings is essential, but improved treatment strategies are required.

## REFERENCES

- Mizuguchi M, Abe J, Mikkaichi K, et al. **Acute necrotizing encephalopathy of childhood: a new syndrome presenting with multifocal, symmetric brain lesions.** *J Neurol Neurosurg Psychiatry* 1995;58:555–61 CrossRef Medline
- Vanjare HA, Selvi BT, Karuppusami R, et al. **Clinical and Radiological Findings of Acute Necrotizing Encephalopathy (ANE) in Young Adults.** *AJNR Am J Neuroradiol* 2020 [Epub ahead of print] CrossRef
- Albayram S, Bilgi Z, Selcuk H, et al. **Diffusion-weighted MR imaging findings of acute necrotizing encephalopathy.** *AJNR Am J Neuroradiol* 2004;25:792–97 Medline
- Mizuguchi M, Hayashi M, Nakano I, et al. **Concentric structure of thalamic lesions in acute necrotizing encephalopathy.** *Neuroradiology* 2002;44:489–93 CrossRef Medline
- Okumura A, Abe S, Kidokoro H, et al. **Acute necrotizing encephalopathy: a comparison between influenza and non-influenza cases.** *Microbiol Immunol* 2009;53:277–80 CrossRef Medline
- Abbas Q, Jafri S, Ishaque S, et al. **Acute necrotizing encephalopathy of childhood secondary to dengue infection: a case report from Pakistan.** *J Pediatr Neurosci* 2017;12:165–67 CrossRef Medline
- Carod-Artal FJ, Wichmann O, Farrar J, et al. **Neurological complications of dengue virus infection.** *Lancet Neurol* 2013;12:906–19 CrossRef Medline
- Vanjare HA, Mannam P, Mishra AK, et al. **Brain imaging in cases with positive serology for dengue with neurologic symptoms: a clinico-radiologic correlation.** *AJNR Am J Neuroradiol* 2018;39:699–703 CrossRef Medline
- Hegde V, Aziz Z, Kumar S, et al. **Dengue encephalitis with predominant cerebellar involvement: report of eight cases with MR and CT imaging features.** *Eur Radiol* 2015;25:719–25 CrossRef Medline
- Ellul MA, Benjamin L, Singh B, et al. **Neurological associations of COVID-19.** *Lancet Neurol* 2020 July 2 [Epub ahead of print] CrossRef Medline
- Paterson RW, Brown RL, Benjamin L, et al. **The emerging spectrum of COVID-19 neurology: clinical, radiological and laboratory findings.** *Brain* 2020 July 8 [Epub ahead of print] CrossRef Medline
- Dixon L, Varley J, Gontsarova A, et al. **COVID-19-related acute necrotizing encephalopathy with brain stem involvement in a patient with aplastic anemia.** *Neurol Neuroimmunol Neuroinflamm* 2020;7:e789 CrossRef Medline
- Virhammar J, Kumlien E, Fällmar D, et al. **Acute necrotizing encephalopathy with SARS-CoV-2 RNA confirmed in cerebrospinal fluid.** *Neurology* 2020 June 25 [Epub ahead of print] CrossRef Medline
- Poyiadji N, Shahin G, Noujaim D, et al. **COVID-19-associated acute hemorrhagic necrotizing encephalopathy: CT and MRI features.** *Radiology* 2020;296:E119–20 CrossRef
- Hirano T, Murakami M. **COVID-19: a new virus, but a familiar receptor and cytokine release syndrome.** *Immunity* 2020;52:731–73 CrossRef Medline

 H. Kidokoro

Department of Pediatrics, Nagoya University Graduate School of Medicine  
Nagoya, Japan

<http://dx.doi.org/10.3174/ajnr.A6821>

# Safety Profile of Infinity Deep Brain Stimulation Electrode Placement in a 1.5T Interventional MRI Suite: Consecutive Single-Institution Case Series

 N. Gravbrot,  M. Saranathan,  L.M. Nagae,  J. Becker, and  W.S. Kasoff

## ABSTRACT

**SUMMARY:** “Asleep” deep brain stimulation using general anesthesia and intraoperative MR imaging guidance is considered “off-label” use by current FDA guidelines but is widely used in neurosurgical practice, and excellent safety has been demonstrated using first-generation, omnidirectional electrodes. Safety data for second-generation, directional electrodes in the interventional MR imaging environment have not yet been published. Herein, we report 34 cases of asleep deep brain stimulation using second-generation, directional electrodes in an interventional MR imaging suite at a single institution. Procedural complications and imaging data are described. All patients underwent postoperative MR imaging with fully implanted (“internalized”) electrodes after scalp closure; 4 patients also underwent MR imaging with “externalized” electrodes before scalp closure. No MR imaging–related complications were observed, and procedural complication rates were comparable to prior series. This suggests that the use of second-generation, directional electrodes in the interventional MR imaging environment appears to be safe when following manufacturer-published imaging guidelines.

**ABBREVIATIONS:** DBS = deep brain stimulation; ET = essential tremor; GPi = globus pallidus internus; iMRI = interventional MRI; PD = Parkinson disease; SAR = specific absorption rate; STN = subthalamic nucleus; WMn = white matter-nulled; Vim = ventralis intermedius

Deep brain stimulation (DBS) is a well-established treatment for patients with movement disorders such as Parkinson disease (PD), essential tremor (ET), and dystonia. Its use is expected to increase after recent FDA approval for the treatment of medically refractory epilepsy, and DBS targets are under investigation for numerous other neurologic diseases.<sup>1</sup> DBS placement is typically performed in a standard operating room, with electrode placement guided by either physiologic mapping under local anesthesia (“awake DBS”) or intraoperative CT imaging under general anesthesia (“asleep DBS”). For postoperative imaging, existing DBS devices have “MR imaging-conditional” FDA labeling, meaning that MR imaging scans can be safely performed on patients with implanted systems under specific device and MR imaging conditions.

A newer method of asleep DBS placement is the use of intraprocedural MR imaging guidance, under sterile conditions and general anesthesia, within a diagnostic MR imaging suite. “Interventional MR imaging” (iMRI) DBS, like standard CT-based asleep DBS, has the advantages of greater patient comfort than awake surgery and real-time confirmation of electrode location. Large series of iMRI-

DBS using first-generation, omnidirectional DBS electrodes (eg, Medtronic Model 3387/3389) have been published, demonstrating an excellent safety profile.<sup>2–5</sup> However, despite the existing safety data and widespread acceptance into clinical practice, iMRI-DBS is still considered “off-label” use with respect to FDA approval of DBS electrodes. In addition, few published safety data exist regarding iMRI placement of second-generation, segmented (or “directional”) DBS electrodes, and the specific scenario of iMRI-DBS imaging performed with the electrodes in place but not yet secured under closed scalp incisions (“externalized” electrodes) is not addressed under MR imaging-conditional labeling, though these images are routinely obtained at some centers.

Given the discrepancy between practice and formal labeling, centers performing iMRI-DBS with segmented electrodes may therefore operate under restrictions for intraprocedural scanning, and institutional MR imaging safety committees have few data for guidance in these circumstances. There is consequently a need for postmarketing safety data on the use of iMRI for the placement of next-generation directional electrodes, as evidenced by the ongoing postmarket study by Abbott Medical Devices on the MR imaging safety of its Infinity DBS system (Abbott Neuromodulation).<sup>6</sup>

We present a single-institution study of 34 patients undergoing iMRI-DBS placement of Infinity segmented electrodes by using the ClearPoint system (MRI Interventions), including intraoperative imaging data and immediate perioperative safety outcomes.

Received April 28, 2020; accepted after revision June 15.

From the Departments of Neurosurgery (N.G., M.S., J.B., W.S.K.) and Medical Imaging (M.S., L.M.N., J.B.), University of Arizona School of Medicine, Tucson, Arizona.

Please address correspondence to Willard S. Kasoff, MD, M.P.H., 1501 N. Campbell Ave., Box 245070, Tucson, AZ 85724-5070; e-mail: wkasoff@email.arizona.edu  
<http://dx.doi.org/10.3174/ajnr.A6776>



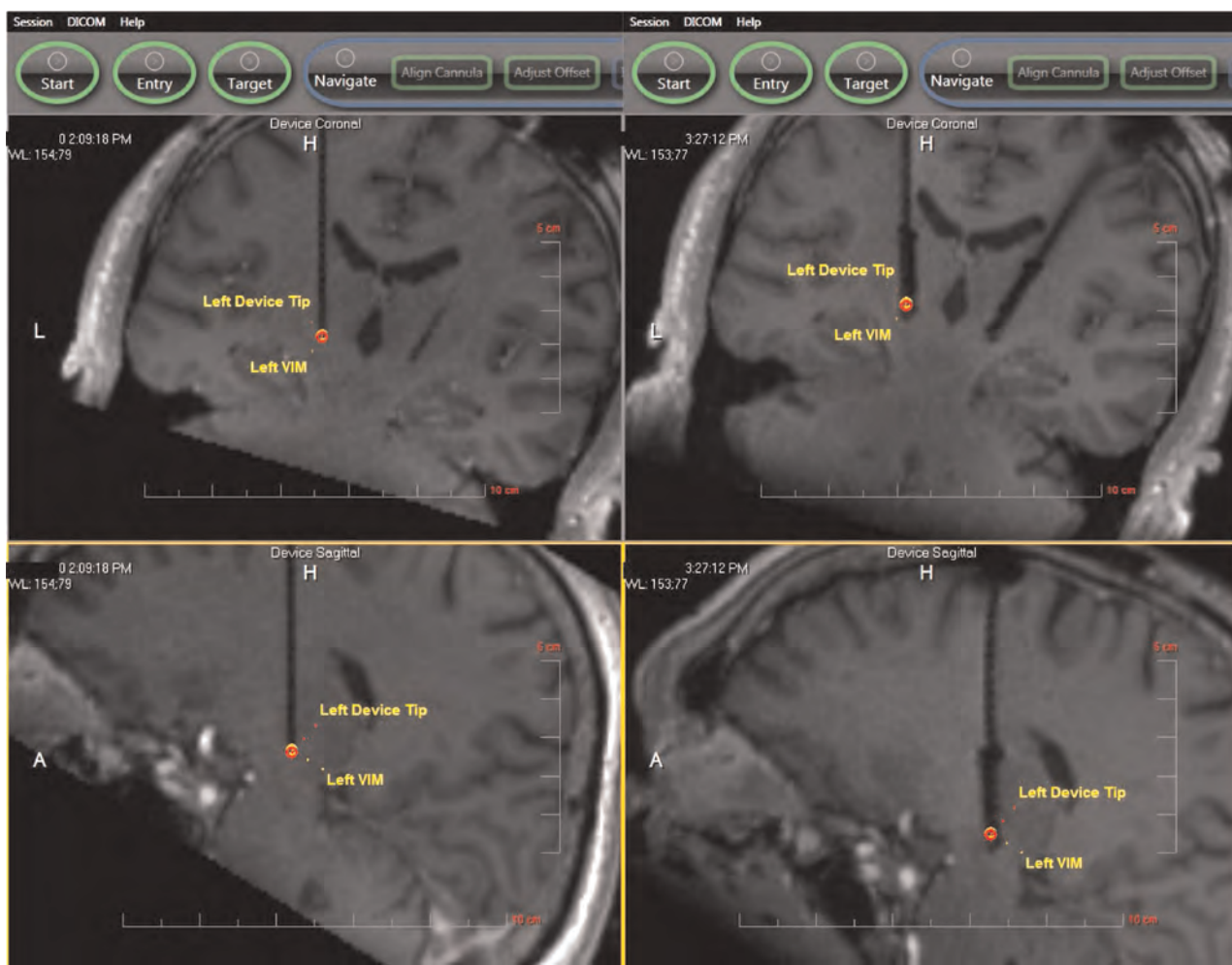


**FIG 1.** Sample iMRI before and after DBS placement. The left side of the figure shows intraoperative 3D T1 FLASH images of ceramic stylet placement in the left Vim (upper image, coronal; lower image, sagittal). The right side of the figure shows bilateral DBS electrode placement in the same patient. See “Surgical Procedure” in the Methods section for details.

## MATERIALS AND METHODS

### Data Collection

Following the Consensus Preferred Reporting Of CasE Series in Surgery (PROCESS) guidelines,<sup>7</sup> a single-surgeon, prospectively maintained database was retrospectively analyzed to identify all patients undergoing asleep, iMRI-guided placement of Infinity DBS electrodes using the ClearPoint system from September 1, 2017, to January 31, 2020. The research setting is an academic neurosurgical practice in Tucson, Arizona.

Clinical data were abstracted from the database and medical record review was conducted by the first (N.G.) and senior (W.S.K.) authors. MR imaging parameters were abstracted from intraoperative MR imaging protocols by the senior author and an experienced MR imaging physicist (M.S.). To identify complications, the official reports of intraoperative and postoperative imaging were reviewed, and each case was separately reviewed by an expert neuroradiologist (J.B.). For the purposes of this study, a complication was defined as any adverse event involving the intracranial electrodes within 30 days of surgery.

### Patient Selection for Surgery

Patients with medically refractory movement disorders were selected for DBS surgery after discussion at a multidisciplinary movement disorders conference consisting of, at minimum, the treating neurologist and neurosurgeon. Patients with PD and dystonia underwent preoperative neuropsychological screening; patients with ET did so at the treating neurologist’s discretion. Our institutional shift from the Activa DBS system (Medtronic) to the Infinity system occurred in September 2017.

### Surgical Procedure

The procedure for iMRI-DBS placement has been described in detail elsewhere.<sup>8</sup> In brief, after the induction of general anesthesia, the patient’s head is fixed to the MRI gantry with a custom 4-pin head holder (MRI Interventions). After sterile preparation and draping, the skull entry site is marked through the skin, the scalp is opened, and a skull-mounted miniframe (SmartFrame, MRI Interventions) is rigidly affixed using bone screws. MR imaging scans are obtained according to manufacturer specifications, the

**Table 1: MR imaging parameters**

Sequence Name	3D FSPGR	3D FSE	WMn MPRAGE	EPI	FLAIR
Sequence type	T1WI	T2WI	T1WI	DWI	T2WI
TR (ms)	14.0	3000	3500	4200	9000
TE (ms)	5.37	379	3.5	89	96
T1 (ms)	n/a	n/a	350	n/a	2500
Flip angle (deg)	20	Variable refocusing	10	90	120
Resolution (mm)	1.02 × 1.02	0.98 × 0.98	1.1 × 1.1	1.7 × 1.7	1.28 × 0.90
Section thickness (mm)	1.69	1.10	1.2	5.0	4.0
Matrix	320 × 320	232 × 256	204 × 224	130 × 130	179 × 256
Bandwidth (Hz/pix)	150	698	160	1480	201
Scan time (min)	1:59	5:00	6:44	1:13	2:24

**Note:**—FSPGR indicates fast-spoiled gradient-echo; n/a, not applicable.

**Table 2: Patient characteristics**

Id#	Sex	Age	Diagnosis	Side	Target
1	M	79	ET	R	Vim
2	M	74	ET	B	Vim
3	F	55	Dys	B	STN
4	M	62	ET	B	Vim
5	F	62	ET	B	Vim
6	M	69	ET	B	Vim
7	M	78	ET	B	Vim
8	F	67	PD	B	STN
9	M	64	ET	B	Vim
10	M	85	PD	B	STN
11	F	63	PD	B	GPI
12	F	61	PD	B	STN
13	M	69	ET	B	Vim
14	M	79	ET	L	Vim
15	M	76	PD	B	STN
16	M	80	PD	B	STN
17	M	71	PD	B	STN
18	F	73	PD	B	STN
19	F	79	PD	B	GPI
20	M	57	PD	B	STN/GPI
21	F	79	ET	B	Vim
22	M	65	ET	B	Vim
23	M	73	ET	B	Vim
24	M	70	ET	B	Vim
25	M	68	PD	R	STN
26	M	77	PD	L	STN
27	F	63	PD	R	STN
28	M	78	PD	B	GPI
29	M	63	Dys	B	GPI
30	F	66	PD	B	STN
31	M	62	PD	B	STN
32	F	71	PD	B	STN
33	M	75	PD	B	STN
34	M	63	ET	B	Vim

**Note:**—Dys indicates dystonia; R, right; L, left; B, bilateral.

target is selected by using intraoperative images, and the miniframe is iteratively adjusted until the cannula is aimed at target with less than 1-mm projected radial error. A ceramic stylet and peel-away sheath are then placed to target, and the actual error is measured. If stylet placement is acceptable (as determined by the surgeon, with 1.5-mm radial error being the usual cutoff), the stylet is replaced by the DBS electrode, and the peel-away sheath is removed. Postplacement images may be performed immediately after electrode placement, with the proximal ends of the electrodes extended within the bore of the scanner (“externalized”), after the

electrodes have been secured with silicone boots and coiled under the closed scalp incision (“internalized”), or both. Examples of iMRI are shown in Fig 1.

### **Intraoperative and Postoperative Imaging**

Surgeries were performed in a 1.5T, 70-cm bore MR imaging scanner (Aera; Siemens) using a vendor-supplied receive-only flexible coil (4 channels; 516 × 224 mm) outside of the sterile field. All imaging sequences performed after electrode placement used low-specific absorption rate (SAR)/B<sub>1+rms</sub> protocols (Table 1), keeping B<sub>1+rms</sub> below 2 μT and under 30 minutes of scan time, in accordance with the Infinity directions for use.<sup>9</sup> In all cases, after skin closure, volumetric T1 imaging was performed for electrode localization, and most patients underwent FLAIR and DWI sequences to rule out vasogenic and cytotoxic edema. In selected cases, volumetric T1 imaging and additional target-specific sequences (eg, T2 for subthalamic nucleus [STN], white-matter-nulled [WMn] MPRAGE, or proton attenuation for globus pallidus internus [GPI]) were performed with externalized electrodes to confirm placement before skin closure.

Postoperative CT scans were performed using the standard stereotactic protocol of 1-mm contiguous slices at zero gantry angle.

### **Data Analysis and Statistics**

Data were analyzed by using Excel (Microsoft); descriptive statistics are reported.

### **Safety Determination and Consent**

Before beginning the series, available MR imaging safety data (Papadaki and Thornton, unpublished data, 2016) for the Infinity electrodes were reviewed with our institutional MR Imaging Safety Committee, which granted permission to proceed by using manufacturer guidelines of low-SAR/B<sub>1+rms</sub> protocols after electrode placement. Standard surgical consent was obtained for all procedures, including the off-label nature of iMRI-guided DBS placement.

The University of Arizona Neuromodulation Clinical Data Base is maintained under the University of Arizona institutional review board #1906737419. No additional research informed consent was required because of the retrospective nature of the analysis. All research was performed according to the Declaration of Helsinki.

**Table 3: MR imaging sequences obtained per patient after DBS placement**

Id #	Before Closure	After Closure	Total # Scans	Scan Time (min)
1	-	T1, WMn, FLAIR	3	11.1
2	-	T1, T2, WMn, DWI	4	14.9
3	-	T1, T2, DWI	3	8.2
4	-	T1, T2, WMn, DWI	4	14.9
5	-	T1, T2, WMn, DWI	4	14.9
6	-	T1, T2, WMn, DWI	4	14.9
7	-	T1, T2, WMn, DWI	4	14.9
8	-	T1, T2, WMn, DWI	4	10.6
9	T1	T1, T2, WMn, DWI	5	12.6
10	-	T1, T2, DWI	3	8.2
11	-	T1, WMn, FLAIR, DWI	4	12.3
12	-	T1, T2, FLAIR, DWI	4	10.6
13	-	T1, WMn, FLAIR, DWI	4	12.3
14	-	T1, WMn, FLAIR, DWI	4	12.3
15	-	T1, T2, FLAIR, DWI	4	10.6
16	-	T1, T2, FLAIR, DWI	4	10.6
17	-	T1, T2, FLAIR, DWI	4	10.6
18	T1	T1, T2, FLAIR, DWI	5	12.6
19	-	T1, T2, FLAIR, DWI	4	10.6
20	T1, T2	T1, T2, WMn, FLAIR, DWI	7	24.3
21	-	T1, WMn, FLAIR, DWI	4	12.3
22	-	T1, FLAIR, DWI	3	5.6
23	-	T1, FLAIR, DWI	3	5.6
24	T1	T1, WMn, FLAIR, DWI	5	14.3
25	-	T1, FLAIR, DWI	3	5.6
26	-	T1, FLAIR, DWI	3	5.6
27	-	T1, T2, FLAIR, DWI	4	10.6
28	-	T1, FLAIR, DWI	3	5.6
29	-	T1, FLAIR, DWI	3	5.6
30	-	T1, FLAIR, DWI	3	5.6
31	-	T1, FLAIR, DWI	3	5.6
32	-	T1, T2, FLAIR, DWI	4	10.6
33	-	T1, FLAIR, DWI	3	5.6
34	-	T1, FLAIR, DWI	3	5.6

**Note:**—T1 indicates 3D T1 FLASH; T2, 3D T2 FSE; WMn, white-matter-nulled MPRAGE.

## RESULTS

### Patient and Electrode Characteristics

Thirty-four consecutive patients were identified. Patient characteristics, imaging data, and complications are summarized in Table 2. Median age was 69 years (range, 55–85 years). Twenty-three (68%) were male, likely reflecting our referral source from a local Veterans Administration hospital. Eighteen (53%) patients had PD, 14 (41%) ET, and 2 (6%) dystonia. There were 29 (85%) bilateral and 5 unilateral (2 left, 3 right) placements, for a total of 63 electrodes. Twenty-eight (44%) electrodes were placed in the STN, 26 (41%) in the nucleus ventralis intermedialis (Vim), and 9 (14%) in the GPi. Fifty-nine electrodes (94%) had 0.5-mm contact spacing (Infinity Model 6172), and 4 electrodes (6%) had 1.5-mm spacing (Infinity Model 6173). Surgical time was typically 5–6 hours.

### Stereotactic Accuracy

All electrodes were placed with a single pass. Accuracy (as measured at the tip of the ceramic stylet) was excellent, as previously published by using this technique. On the left, medial-lateral error was  $0.3 \pm 0.3$  mm, anteroposterior error was  $0.3 \pm 0.2$  mm, and radial error was  $0.5 \pm 0.3$  mm. On the right, medial-lateral error was  $0.3 \pm 0.3$  mm, anteroposterior error was  $0.3 \pm 0.3$  mm, and radial error was  $0.6 \pm 0.3$  mm.

### iMRI after Electrode Placement

Individual patient imaging is listed in Table 3. A total of 4 patients underwent imaging with externalized electrodes before skin closure. After electrode internalization and skin closure, all 34 patients underwent volumetric T1 imaging. DWI and FLAIR sequences were performed in 33 (97%) and 27 (74%) patients, respectively. Twenty-four (71%) patients underwent additional target-specific sequences. The median number of postplacement sequences was 4 (range, 3–7). Mean  $\pm$  SD total postplacement scan time was  $10.5 \pm 4.2$  minutes (range, 5.6–24.3). Variability in the number of postplacement sequences per patient is explained by the use of different target-specific sequences in some cases and in the standardization of our postplacement protocol partway through the series.

Imaging artifacts, although not a specific object of analysis in this study, were noted to be large, as is common with DBS electrodes under MR imaging. These were not used to determine stereotactic accuracy. Examples of electrode artifacts are shown in Fig 2.

### Complications

Intraoperative MR imaging showed intracerebral hemorrhage in 3 patients (9%). The first (patient 2) was a 6-mm

cortical intracerebral hemorrhage that appeared after burr-hole placement before the dura was opened. The second (patient 8) was minimal subcortical hemorrhage and edema that appeared between stylet placement and electrode placement. Both of these were asymptomatic and required no intervention. The third (patient 20) was a 3-cm subcortical intracerebral hemorrhage that occurred during dural opening and coagulation of a bleeding surface vessel before any device placement. This was evacuated during the procedure and was asymptomatic. In summary, all 3 intraprocedural hemorrhages were small, asymptomatic, and related to surgical access itself rather than any identifiable interaction between the DBS electrodes and the MR imaging field.

On FLAIR images, 1 patient (2.9%) had mild insertional vasogenic edema. DWI in all cases was negative for acute ischemic change.

In patients with MR imaging both before and after scalp closure ( $n=4$ ), there was no evidence of electrode migration between scans or local heating.

Thirty of 34 patients (88%) had a postoperative CT within 24 hours of electrode placement. In addition to the expected evolution of the MR imaging findings mentioned, 2 patients had new findings. In 1 patient (patient 28), a new 7-mm subdural hematoma was seen adjacent to a burr-hole. This was asymptomatic and



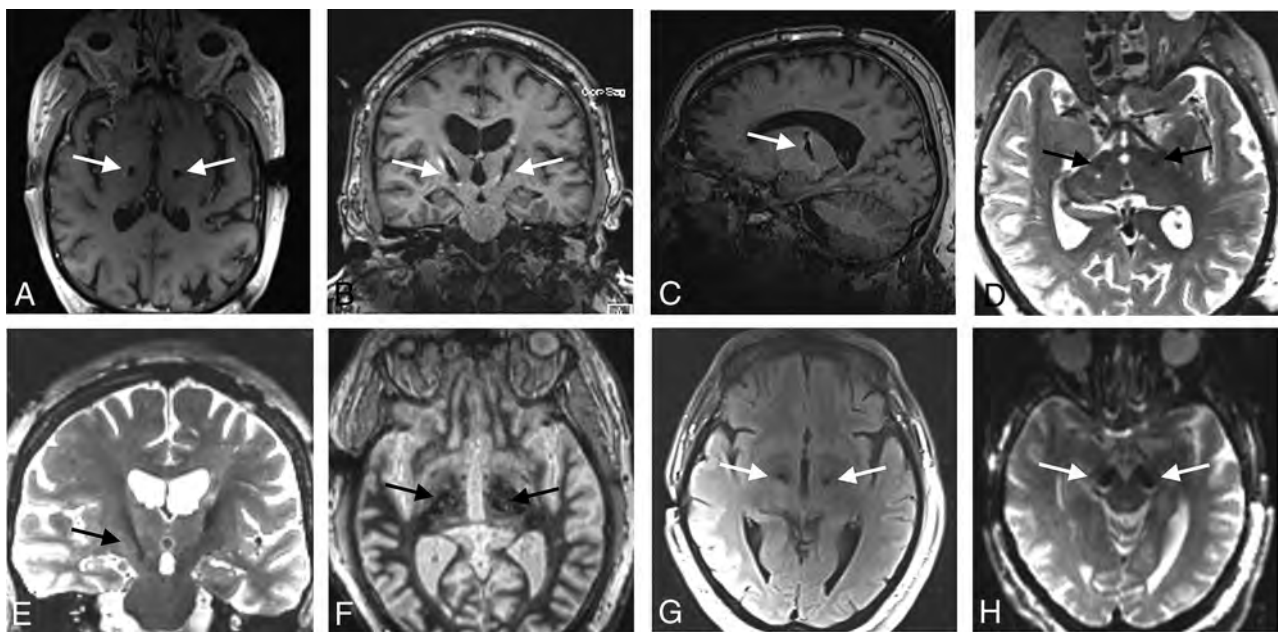


**FIG 2.** Examples of the MRI artifacts of implanted Infinity DBS electrodes. The largest artifacts were seen in T1 images (A–C) and the smallest artifacts on T2 images (D, E). Artifacts on WMn (F), FLAIR (G), and DWI (H) sequences are also shown. Arrows indicate electrodes.

required no intervention. A second patient (patient 30) developed mild subcortical edema around the left electrode. This also was asymptomatic and required no intervention.

During the 30 days after surgery, no patients complained of scalp heating or showed evidence of heat-related injuries or postoperative neurologic deficit. Electrode impedance at the time of pulse generator implantation (within 2 weeks after electrode placement) was normal in all cases.

There was 1 postoperative death: patient 8 died from a small-bowel obstruction at 5 days after surgery. There was 1 serious complication: patient 33 developed intracerebral infection, seizure, and hemiparesis, requiring electrode removal and surgical washout on postoperative day 9, after which he made a full recovery. There were 4 minor complications: patient 10 developed a urinary tract infection, patient 11 developed mild self-limited confusion, patient 28 had a superficial stitch abscess treated with oral antibiotics, and patient 32 had hyponatremia treated with fluid restriction.

## DISCUSSION

We present 34 consecutive cases of iMRI-DBS using Infinity electrodes. When using a low-SAR/ $B_{1+rms}$  protocol for imaging after electrode placement, no apparent iMRI-related complications, such as heating, lesioning, edema, electrode movement, or damage to the electrodes, occurred. This mirrors prior ClearPoint experience with Medtronic electrodes.<sup>2–5</sup>

We found no difficulty in adhering to manufacturer guidelines for electrode imaging with any postplacement sequences. T1-weighted sequences and EPI inherently have a low SAR because of small flip angles and large TR and were easily adapted by using the low-SAR radiofrequency option. Sequences with the highest SAR (T2 and FLAIR) because of the high flip angles were addressed adequately by using the low-SAR radiofrequency pulse

option and by increasing the TR and reducing the refocusing flip angle to 120 to obtain  $B_{1+rms}$  below  $2 \mu T$ .

Manufacturer guidelines now use  $B_{1+rms}$  limits instead of SAR. The advantage of using  $B_{1+rms}$  over SAR is that it is not patient-dependent. The protocol parameters affecting  $B_{1+rms}$ , such as TR and flip angles, were unchanged after optimization on the first patient, so there was no variability across patients. The only consequence of sequence adjustment from our standard institutional protocols was increased scan time because of longer TR; however, because the patients were anesthetized, motion artifacts were not an issue.<sup>10</sup>

There were 5 identifiable intraprocedural complications: 3 intracranial hemorrhages, 1 subdural hematoma, and 1 case of electrode-related edema, among 34 patients and 63 electrodes. None of these complications appeared to have any relationship to the iMRI environment or postplacement imaging of the electrodes but were all related to cranial access or ceramic stylet placement. Although our overall hemorrhage rate (11.7% per procedure, 6.3% per electrode) was higher than in previously published large iMRI series,<sup>5</sup> all hemorrhages were small, asymptomatic, and clinically insignificant. Postoperative complications were, similarly, all well-known surgical complications and showed no apparent relationship to the iMRI environment or postplacement iMRI scans.

In the time since we began iMRI-DBS using Infinity electrodes, Abbott has received FDA approval for MR imaging scanning of the internalized “leads-only” configuration.<sup>9</sup> However, we believe our results are still useful for several reasons. First, we additionally demonstrate safety of imaging with externalized electrodes. Second, postmarket safety data have not yet been published. Third, our patients are under anesthesia, providing reassurance that patient feedback is not necessary to ensure safe imaging. Fourth, we provide evidence for the safety of the iMRI-DBS approach using directional electrodes in general. The programming flexibility

permitted by directional electrodes combined with the accuracy of iMRI guidance allows a high degree of confidence in electrode placement even for targets with little immediate physiologic feedback, such as targets for psychiatric diseases, and may allow real-time biomarker assessment such as changes in functional MR imaging during electrode placement.<sup>11,12</sup>

Limitations of this study include the inability to report transient events such as scalp warming, motor activity, or paresthesias. These may emerge from the ongoing Abbott postmarket study,<sup>6</sup> which will be conducted in awake patients; however, transient sensorimotor effects would have no significance for patients undergoing iMRI-DBS under general anesthesia. Second, this study could be underpowered for low-frequency events. Finally, our results reflect the use of a single MR imaging scanner, though there would be no reason to suspect that the results would be different with other MR imaging models or manufacturers as long as manufacturer guidelines for  $B_{1+rms}$  and scan time are similarly followed.

## CONCLUSIONS

We present real-world data on the safety of Infinity DBS placement in an interventional MR imaging suite. When manufacturer guidelines for MR imaging safety by using fully implanted leads are followed, there appear to be no MR imaging-related safety issues with this technique. These data should be useful for other institutions considering iMRI-DBS placement using these devices.

## ACKNOWLEDGMENTS

The authors thank Janette Zingg and Sarah Cyr for assistance in collecting MR imaging parameters. The senior author is a site principal investigator for the Abbott Infinity postmarket MR imaging safety study,<sup>6</sup> for which no data are yet available and for which he receives no compensation. No patients reported here will be duplicated in the Abbott-sponsored study.












Disclosures: Jennifer Becker—UNRELATED: Consultancy: Nuvox Pharma and Siemens Syngo Via, Comments: Siemens-Consultancy, money paid to department, not related to this article, Nuvox-Consultancy work at AHA meeting 2019 Nuvox, not related to study, honorarium paid to me with travel expenses reimbursed\*; Payment for Lectures Including Service on Speakers Bureaus: Canon

(Vitrea), Comments: Lecture given on behalf of Canon, Phoenix 2020.\* \*Money paid to the institution.

## REFERENCES

1. Lee DJ, Lozano CS, Dallapiazza RF, et al. **Current and future directions of deep brain stimulation for neurological and psychiatric disorders.** *J Neurosurg* 2019;131:333–42 CrossRef Medline
2. Ostrem JL, Galifianakis NB, Markun LC, et al. **Clinical outcomes of PD patients having bilateral STN DBS using high-field interventional MR-imaging for lead placement.** *Clin Neurol Neurosurg* 2013;115:708–12 CrossRef Medline
3. Ostrem JL, Ziman N, Galifianakis NB, et al. **Clinical outcomes using ClearPoint interventional MRI for deep brain stimulation lead placement in Parkinson's disease.** *J Neurosurg* 2016;124:908–16 CrossRef Medline
4. Martin AJ, Larson PS, Ziman N, et al. **Deep brain stimulator implantation in a diagnostic MRI suite: infection history over a 10-year period.** *J Neurosurg* 2017;126:108–13 CrossRef Medline
5. Martin AJ, Starr PA, Ostrem JL, et al. **Hemorrhage detection and incidence during magnetic resonance-guided deep brain stimulator implantations.** *Stereotact Funct Neurosurg* 2017;95:307–14 CrossRef Medline
6. ClinicalTrials.gov. MRI study of Infinity DBS System. ClinicalTrials.gov Identifier: NCT03884231. <https://clinicaltrials.gov/ct2/show/NCT03884231>. Accessed April 17, 2020
7. Agha RA, Borrelli MR, Farwana R, PROCESS Group, et al. **The PROCESS 2018 statement: updating Consensus Preferred Reporting Of CasE Series in Surgery (PROCESS) guidelines.** *Int J Surg Lond Surg* 2018;60:279–82 CrossRef Medline
8. Starr PA, Markun LC, Larson PS, et al. **Interventional MRI-guided deep brain stimulation in pediatric dystonia: first experience with the ClearPoint system.** *J Neurosurg Pediatr* 2014;14:400–08 CrossRef Medline
9. St. Jude Medical. **MRI Procedure Information For St. Jude Medical™ MR Conditional Deep Brain Stimulation Systems.** St. Jude Medical; 2018
10. Faulkner W.  $B_{1+rms}$  as a condition of use, Signals 2016;5. [https://www.ismrm.org/smrt/E-Signals/2016FEBRUARY/eSig\\_5\\_1\\_hot\\_2.htm](https://www.ismrm.org/smrt/E-Signals/2016FEBRUARY/eSig_5_1_hot_2.htm). Accessed August 18, 2020
11. Hiss S, Hesselmann V, Hunsche S, et al. **Intraoperative functional magnetic resonance imaging for monitoring the effect of deep brain stimulation in patients with obsessive-compulsive disorder.** *Stereotact Funct Neurosurg* 2015;93:30–37 CrossRef Medline
12. In M-H, Cho S, Shu Y, et al. **Correction of metal-induced susceptibility artifacts for functional MRI during deep brain stimulation.** *NeuroImage* 2017;158:26–36 CrossRef Medline

# Characteristics of Large-Vessel Occlusion Associated with COVID-19 and Ischemic Stroke

 S. John,  P. Kesav,  V.A. Mifsud,  B. Piechowski-Jozwiak,  J. Dibu,  A. Bayrlee,  H. Elkambergy,  F. Roser,  M.S. Elhammady,  K. Zahra, and  S.I. Hussain



## ABSTRACT

**SUMMARY:** The mechanisms and phenotype of ischemic stroke associated with coronavirus disease 2019 (COVID-19) remain uncertain. A retrospective study was conducted in patients with COVID-19 presenting with ischemic stroke from March 1 to May 25, 2020, and cases with large-vessel occlusion were identified. To provide baseline institutional stroke data within and outside the COVID-19 pandemic, all consecutive ischemic stroke and TIA admissions (COVID and non-COVID) to the hospital during a 10-week period from March 1 to May 10, 2020, were collected and compared with data from the same time period in 2019. Among 20 patients with COVID-19 and acute ischemic stroke, 15 (75%) had large-vessel occlusion. These patients were young (mean age, 46.5 years), male (93%), without major burden of traditional cardiovascular risk factors, and had a severe stroke presentation. Large-vessel occlusions were observed in multiple vessels (40%), uncommonly affected vessels, and atypical locations with a large thrombus burden. Systemic thrombosis separate from large-vessel occlusion was not uncommon (26%). At short-term follow-up, stroke etiology remained undetermined in 46% of patients and functional outcome was poor. The above findings raise the possibility of stroke related to mechanisms induced by the COVID-19 infection itself, including a hypercoagulable state and/or endothelial damage. In addition, they document the severe presentation and poor outcomes of large-vessel occlusion in COVID-19 ischemic stroke.

**ABBREVIATIONS:** CCA = common carotid artery; COVID-19 = coronavirus disease 2019; LVO = large-vessel occlusion; SARS CoV-2 = Severe Acute Respiratory Syndrome coronavirus-2

Coronavirus disease 2019 (COVID-19) is an ongoing pandemic caused by infection with the Severe Acute Respiratory Syndrome coronavirus-2 (SARS CoV-2).<sup>1,2</sup> There are now multiple reports of COVID-19 affecting the central nervous system, ranging from meningitis/encephalitis to stroke.<sup>3-5</sup> In a single-center study of 214 hospitalized patients with COVID-19 from Wuhan, China, where the infection first occurred, up to 36.4% of patients had neurologic manifestation, including acute cerebrovascular disease with severe and nonsevere infection in 5.7% and 0.8% of these patients, respectively.<sup>3</sup> In addition, there are also reports of ischemic stroke being caused by large-vessel occlusion (LVO) in patients with COVID-19 without significant pre-

existing cardiovascular risk factors.<sup>6</sup> While the reasons for ischemic stroke in COVID-19 are unclear, hypotheses of an inflammatory cytokine storm–triggered hypercoagulable state, endothelial damage, and arrhythmias have been postulated.<sup>7,8</sup> However, as it stands, the mechanisms, phenotype, and optimal management of ischemic stroke associated with COVID-19 still remain uncertain.

There is an urgent need to identify associations and predictors of severity, morbidity, and mortality in patients with ischemic stroke and COVID-19, especially in the LVO subgroup, given that it is most disabling.

## MATERIALS AND METHODS

This is a single-center, retrospective, observational study. All consecutive patients who were admitted to the hospital with a diagnosis of COVID-19 from March 1 to May 25, 2020, were identified. These patients tested positive on SARS CoV-2 polymerase chain reaction testing via nasopharyngeal and oropharyngeal swabs or on sputum samples collected when intubated. Among the above cohort, all patients with ischemic stroke and LVO were identified.

To provide baseline institutional stroke data within and outside the COVID-19 pandemic, we collected all consecutive ischemic stroke and TIA admissions (COVID and non-COVID) to

Received June 15, 2020; accepted after revision July 24.

From the Department of Neurology (S.J., P.K., V.A.M., B.P.-J., S.I.H.), Neurological Institute; Neurointerventional Surgery (S.J., M.S.E., K.Z., S.I.H.), Neurological Institute; Neurocritical Care Unit (J.D., A.B., H.E.), Critical Care Institute; and Department of Neurosurgery, Neurological Institute (F.R., M.S.E.), Cleveland Clinic, Abu Dhabi, United Arab Emirates.

Please address correspondence to Seby John, MD, Neurointerventional Surgery, Neurological Institute, C-07-231, Cleveland Clinic Abu Dhabi, Al Maryah Island, Abu Dhabi, UAE; e-mail: johns5@clevelandclinicabudhabi.ae



Indicates open access to non-subscribers at [www.ajnr.org](http://www.ajnr.org)



Indicates article with supplemental on-line table.

<http://dx.doi.org/10.3174/ajnr.A6799>



the hospital during a 10-week period from March 1 to May 10, 2020, and compared then with the data from the same time period in 2019.

Retrospective data collection points included details regarding demographics, stroke risk factors, clinical presentation, stroke scales, imaging results and laboratory investigations, acute treatments including intravenous thrombolysis and endovascular thrombectomy, time metrics, stroke classification and etiology, ischemic stroke subtype classification based on the Trial of Org 10172 in Acute Stroke Treatment (TOAST),<sup>9</sup> clinical outcomes, and discharge disposition. Regarding the COVID-19 infection, additional information was collected including non-neurologic COVID-19 symptoms, chest imaging, and treatment details specific for COVID-19.

Institutional review board approval was obtained before pursuing this study.

### Statistical Methods

For baseline data, means and SDs were calculated for continuous variables, while categorical variables were expressed as counts and percentages. *P* values associated with comparisons on continuous variables, categorical variables, and count variables were calculated using independent-samples *t* tests, Fisher exact tests, and  $\chi^2$  tests, respectively. All statistical analyses were performed using Microsoft R Open 3.5.1 software (<https://mran.microsoft.com/>). The significance threshold was set at a 2-sided *P* value < .05.

### Findings

When we compared admissions during the 10-week period from March 1 to May 10 between 2019 and 2020, there was a significant increase in the number of ischemic strokes in 2020 (76 versus 103, *P* = .044), while TIA remained unchanged (33 versus 27, *P* = .439). LVO, including occlusion of the ICA, M1 and M2 segments of the MCA, and the basilar artery, was significantly higher in 2020 (20 [18.3%] versus 44 [33.8%], *P* = .008). When we compared time metrics between 2019 and 2020, presentation to the hospital from a mean last-known-well time (620.6 ± 743.7 versus 516.6 ± 556.86 minutes, *P* = .293) and mean door-to-needle times for intravenous thrombolysis (35.5 ± 12.7 versus 42.7 ± 14.8 minutes, *P* = .171) were similar in both years. However, door-to-groin puncture times for endovascular thrombectomy were significantly longer in 2020 (67.75 versus 104.30 minutes, *P* = .001).

From March 1 to May 25, six hundred seventy-three patients with COVID-19 were admitted to the hospital. Among these, 20 (2.97%) patients presented with acute ischemic stroke. Of these patients, 15 (75%) had documented LVO.

The On-line Table details the characteristics of patients with COVID-19 with ischemic stroke and LVO. The mean age at presentation was 46.5 years (range, 23–66 years), with 11 (73.3%) patients being 50 years of age or younger. This cohort was overwhelmingly male (14, 93.3%). Nine (60%) patients did not have any traditional cardiovascular risk factors for stroke. In the remaining patients, hypertension was present in 3 (20%); hyperlipidemia, in 1 (6.67%); diabetes mellitus, in 4 (26.67%); and coronary artery disease, in 1 (6.67%) patient. The maximum number of concurrent risk factors was 2, which 3 (20%) patients possessed. With regard to COVID-19 symptoms, 6 (40%) had fever, 5 (33.3%) had cough

or shortness of breath, and 6 (40%) were asymptomatic. Headache before stroke was present in 3 (20%) patients. Nine (60%) patients had pneumonia on chest x-ray or chest CT performed at or shortly after admission. Average C-reactive protein levels (closest to the time of stroke) and D-dimer levels (highest level) were 106.2 mg/L (range, 0.4–328.3 mg/L) and 2.34 mcg/mL fibrinogen equivalent units (range, 1.24–4 mcg/mL), respectively.

The mean NIHSS score at presentation was 21.5 (range, 0–38). A single patient with vertebral artery V4 segment occlusion with cerebellar strokes and gait ataxia had NIHSS = 0, but most patients had severe deficits at presentation. Twelve (80%) patients had anterior circulation stroke. On CTA of the head and neck, 7 patients (46.7%) had isolated occlusion of the MCA M1 segment. Two (13.3%) patients had tandem occlusion of the ICA and MCA, 2 (13.3%) patients had tandem occlusion of the common carotid artery (CCA), ICA, and MCA; and 1 (6.7%) patient had an occlusion in the M1 MCA but with concurrent subclavian artery thrombosis. Of the 3 (20%) patients with posterior circulation stroke, 1 (6.7%) had occlusion of the basilar artery and a separate posterior cerebral artery P2 segment occlusion. The other 2 (13.3%) patients had vertebral artery occlusion in the V4 segment and throughout its course soon after the origin, respectively. In total, multiple vessel occlusions were present in 6 (40%) patients, with large thrombus burden in these cases. Of note, there were 4 (26.7%) patients with other systemic thrombosis, including pulmonary embolus and vein thrombosis.

Figure 1 demonstrates patient 13 who had a large subocclusive thrombus at the ICA origin and tandem MCA occlusion. This patient did not have any underlying atherosclerotic disease in the ICA as demonstrated by postthrombectomy images, which showed a normal carotid bifurcation. Figure 2A, -B demonstrates patient 2 with discrete thrombus in the proximal ICA without underlying atherosclerotic disease followed by complete occlusion distally and tandem MCA occlusion. Figure 2 shows a large subocclusive thrombus in the CCA and complete occlusion of the proximal CCA, with a large thrombus burden in patients 6 (Fig 2C, D, and E) and 11 (Fig 2F, -G), respectively, with more distal complete occlusion of the ICA and MCA in both cases. Finally, Patient 12 (Fig 2H, -I) had a large subocclusive thrombus in the proximal subclavian artery and MCA occlusion. All cases demonstrated in Fig 2 did not have obvious features of underlying atherosclerotic disease. Figure 3 details patterns of infarcts with multiple infarcts in different vascular distributions.

Treatment with intravenous thrombolysis was administered in 3 (20%) patients, and 6 (40%) underwent mechanical thrombectomy, including 5 patients with isolated M1 occlusion and 1 with tandem cervical ICA and M1 occlusions. Successful recanalization of TICI score 2b–3 was achieved in 4 (66.7%), with a mean groin-to-recanalization time of 28.75 minutes (range, 17–53 minutes). In cases of successful recanalization, aspiration alone was used in three-quarters of cases, while combined stent retriever and aspiration were used in a single case. The 2 cases without recanalization were MCA occlusion from atherosclerotic disease. One patient underwent multiple thrombectomy and balloon angioplasty attempts without success, and the other had vessel rupture after a single pass of aspiration, which was the only complication in all thrombectomy cases. At discharge or 30 days



**FIG 1.** Patient 13. CTA of the head and neck reveals a large subocclusive clot at the right carotid bifurcation extending into the proximal ICA (A, arrow) and tandem right M1 MCA occlusion (B, arrow). The same was confirmed on DSA when the patient was taken for mechanical thrombectomy (C and D, arrow). Postthrombectomy DSA shows complete resolution of extracranial carotid thrombus with no underlying atherosclerotic disease (E, arrow) and recanalization of the MCA occlusion (F).

poststroke, 1 patient achieved an mRS score of 0–2, one achieved an mRS score of 3, and none died.

For the whole cohort, 7 (46.7%) patients had stroke of undetermined etiology; 4 (26.7%), from intracranial atherosclerotic disease; and 3 (20%), from a cardioembolic source. Only 3 (20%) patients achieved a good outcome of mRS 0–2 at discharge or 30 days poststroke, and 1 (6.7%) patient died in the hospital. Mortality was secondary to severe cerebral edema secondary to cardiac arrest.

## DISCUSSION

This retrospective study on COVID-19 and ischemic stroke has revealed multiple findings. There is a high rate of LVO in patients with ischemic stroke and COVID-19. In this series, 75% of patients with COVID-19 with ischemic stroke had LVO. Even if excluding the single patient with vertebral artery occlusion from possible dissection, the rate remains at 70%, which is considerably higher than that usually observed from historical controls. These patients were overwhelmingly male and young without a significant burden of traditional cardiovascular risk factors and had severe stroke presentation with or without systemic features related to COVID-19.

Traditionally the United Arab Emirates has had a younger age of onset for stroke with male predominance as a result of poorly controlled vascular risk factors among expatriate migrant male workers.<sup>10,11</sup> The mean age of patients in the 10-week study period presented above for 2019 and 2020 was approximately 58 years (33.4% of patients overall were 50 years of age or

younger) with up to 70% being male. Our comparison with historical controls confirms an even younger age of onset in patients with COVID-19 with ischemic stroke.

Unique patterns of LVO were observed in the patients with COVID-19 with ischemic stroke. Up to 40% of patients had >1 vessel with thrombosis or occlusion. In the anterior circulation, large thrombus burden was seen in uncommonly affected vessels and in atypical locations. These observations, along with the finding of separate systemic thrombosis in one-quarter of patients, suggest an association between a COVID-19-mediated hypercoagulable state and thromboembolism.<sup>12–15</sup> Further studies looking at inflammatory and hypercoagulable markers will need to be performed to establish the pathophysiology of COVID-19 in ischemic stroke.

There were 4 patients with LVO secondary to presumed intracranial atherosclerotic disease, including 3 with severe presentation from MCA occlusion. It is interesting that all 3 patients had pneumonia on chest imaging. Two of the 3 patients with M1 MCA occlusion secondary to intracranial atherosclerotic disease had only a deep basal ganglia infarct, despite having a large mismatch on perfusion imaging and nonrecanalization of the vessel. It is plausible that factors such as hypoxia or hypotension associated with COVID-19 pneumonia with or without acute respiratory distress syndrome may have resulted in acute decompensation of cerebrovascular autoregulation, which was previously preserved in the setting of chronic vascular occlusion or severe stenosis (Fig 4). Correction of hypoxia or hypotension may have prevented a larger territory infarct, assuming that collaterals were previously well-

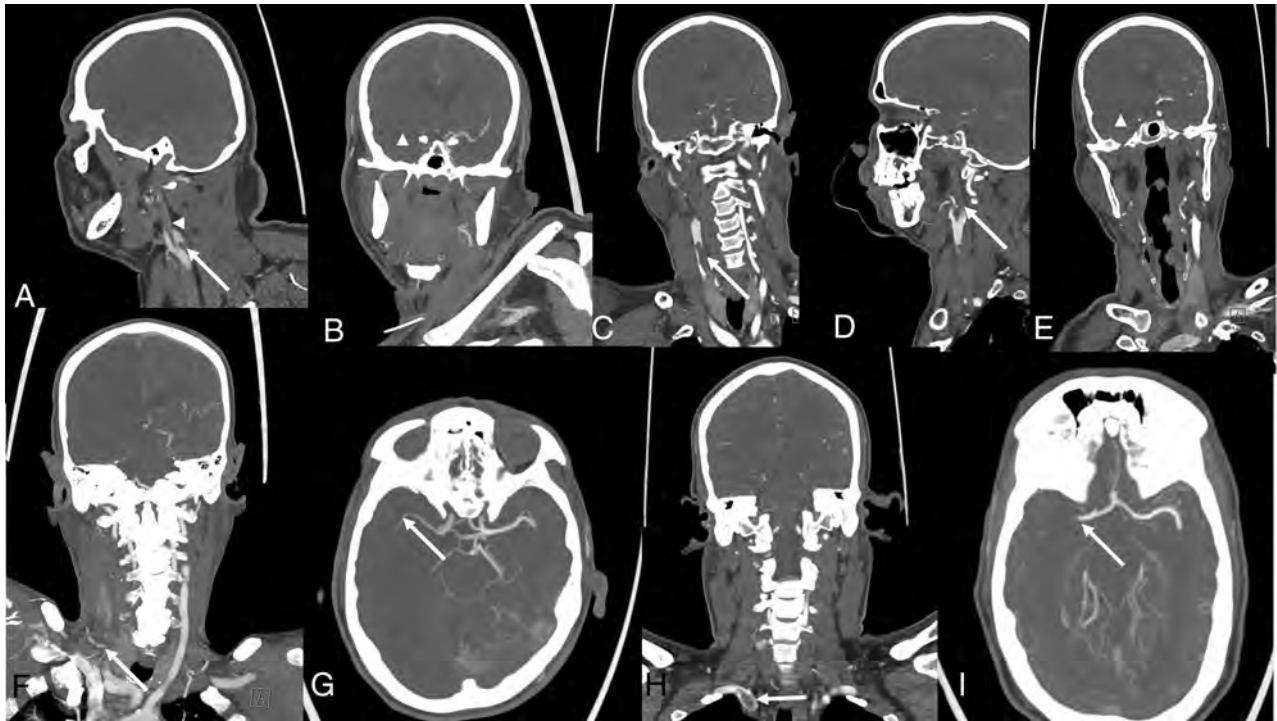


**FIG 2.** Patient 2. CTA of the head and neck reveals discrete thrombus in the proximal ICA without underlying atherosclerotic disease (A, arrow) followed by complete occlusion distally in the ICA (A, arrowhead) and tandem MCA occlusion (B, arrowhead). Patient 6. CTA reveals a large subocclusive thrombus in the right CCA (C, arrow) followed by complete occlusion of the ICA (D, arrow) and MCA (E, arrowhead). Patient 11. CTA reveals complete occlusion of proximal right CCA with a large thrombus burden (F, arrow) followed by complete occlusion of the right ICA and tandem M2 MCA occlusion (G, arrow). Patient 12. CTA reveals a large subocclusive thrombus in the proximal right subclavian artery (H, arrow) and tandem right M1 MCA occlusion (I, arrow).



**FIG 3.** Patterns of infarcts. Patient 9. CT of the head shows a large right MCA-distribution infarct (A, long arrow) secondary to right M1 MCA occlusion, but it also shows a smaller infarct in the left parietal lobe (A, short arrow). Patient 11. CT of the head shows a complete right hemispheric infarct (B, long arrow) but also small left parietal (B, short arrow) and right cerebellar (C, arrow) infarcts. Patient 14. Diffusion-weighted sequence on MR imaging shows scattered areas of infarcts in bilateral cerebellar hemispheres (D, arrows).

developed in these patients. Also, complete occlusion of underlying stenotic lesions causing LVO may have been an acute phenomenon due to in situ thrombosis secondary to a virus-induced hypercoagulable state, but this cannot be confirmed.

Despite only short-term follow-up data being available, close to one-half of patients had stroke of undetermined etiology. In the background of the cohort involving predominantly young

patients, without significant burden of cardiovascular risk factors, this finding again raises the possibility of stroke related to mechanisms induced by the COVID-19 infection itself. Although the cohort is small and only short-term follow-up is available, functional outcomes in these patients were poor, with only a minority of patients achieving a good outcome of mRS 0–2. This result could be related to multiple factors, the foremost of which is



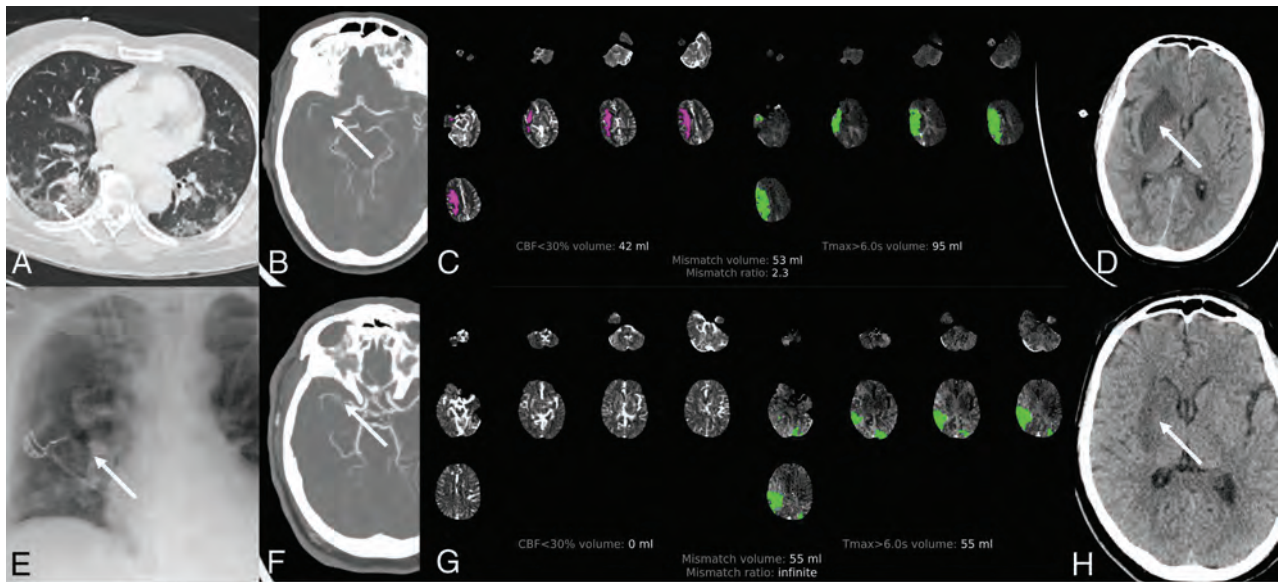


**FIG 4.** Patient 4. CT of the chest demonstrates diffuse lung parenchymal changes associated with viral pneumonia (A, arrow). CTA of the head shows right M1 MCA occlusion (B, arrow), and the CT perfusion maps show a large area of penumbral mismatch (C). However, follow-up CT of the head shows a smaller right basal ganglia final infarct (D, arrow). Patient 8. Chest x-ray shows multifocal infiltrates (E, arrow). CTA of the head shows right M1 MCA occlusion or critical stenosis (F, arrow), and CT perfusion maps show a large area of penumbral mismatch (G). Follow-up CT of the head shows a smaller right basal ganglia final infarct (H, arrow) despite nonrecanalization following endovascular thrombectomy.

because many patients were ineligible for thrombectomy at the time of presentation due to a large burden of established infarct or severe systemic disease. Historically, LVO subtype of stroke is the most disabling. The added insult of systemic disease from COVID-19 causing pneumonia and acute respiratory distress syndrome with consequent cerebral oxygenation and hemodynamic alterations may, in part, explain the poor outcomes. Patients with severe COVID-19 who require intubation and prolonged intensive care unit stays are prone to complications, including hypotension and cerebral hypoperfusion, stress cardiomyopathy and resultant decreased left ventricular ejection fraction, and atrial fibrillation with or without a rapid ventricular response. In addition, severe COVID-19 has been associated with a cytokine storm and hyperviscosity.<sup>16</sup> Progression to disseminated intravascular coagulation is more common in COVID-19, with 1 report documenting an incidence of 8.7% with associated 94% mortality.<sup>17</sup> Even in those patients who underwent thrombectomy and achieved successful recanalization, an mRS of 0–2 in 25% of patients was the best outcome achieved at short-term follow-up.

Our results are largely consistent with a few published small series of COVID-19 and ischemic stroke<sup>6,18,19</sup> with regard to younger age of onset along with less prevalence of traditional stroke risk factors among patients with COVID-19 with stroke. Oxley et al<sup>6</sup> published a case series of 5 young patients with COVID-19 and LVO, 3 (60%) of whom had vascular risk factors for stroke. In the case series of 32 patients in Yaghi et al,<sup>18</sup> 11 were 50 years of age or younger, of whom 45% had vascular risk factors. However, it is not clear how many of these patients had LVOs.

While there is the clear limitation of a small sample size and lack of follow-up, the above results serve at least to raise awareness of the severe presentation and outcomes of LVO in COVID-

19 ischemic stroke. Compared with many reports on drastic decreases in stroke admission, our institution recorded an increase in stroke admissions. This could be explained by other centers no longer taking care of such patients during the current pandemic and by a possible alteration in referral patterns because our institution continued to operate as a center of excellence for cerebrovascular care in addition to managing patients with COVID-19. In addition, the increase in the volume of patients with stroke cannot be generalized to imply an increase in the incidence of stroke during the pandemic. The increase in LVO in 2020 may possibly be related to the high incidence of LVO in COVID-19, but this again cannot be conclusively confirmed. With regard to our institutional stroke pathway workflow, there was no significant increase in door-to-needle times for intravenous thrombolysis for ischemic stroke during the pandemic. However, a significant delay in door-to-groin times for mechanical thrombectomy was observed. This can be explained by the institution of a protected code stroke in our institution based on recommendations by various societies and reflects the impact of the pandemic as a real-world experience.<sup>20</sup>

The study has limitations including its retrospective design, single-center setting, and small sample size. There could have been a referral bias of only more severe patients with COVID-19 and stroke being referred to our institution. However, this scenario is unlikely because larger facilities that became dedicated COVID-19 hospitals were mandated to transfer all patients with stroke, and smaller hospitals continued to transfer patients with stroke as per established transfer protocols similar to pre-COVID times. Alternatively, patients with stroke and COVID-19 and LVO could have been admitted to other centers during the study period. Only short-term follow-up of patients is available at the time of this writing.

## CONCLUSIONS

There is a high incidence of LVO in patients with COVID-19 presenting with ischemic stroke. These patients are young men, without significant burden of traditional cardiovascular risk factors and have severe stroke presentation with or without systemic features related to COVID-19. LVOs were observed in multiple vessels, uncommonly affected vessels, and atypical locations with a large thrombus burden. Systemic thrombosis separate from LVO was not uncommon. The etiology of the stroke remained undetermined in up to one-half of patients. The above findings raise the possibility of stroke related to mechanisms induced by the COVID-19 infection itself, including an induced hypercoagulable state and/or endothelial damage. Functional outcome was poor in this cohort at short-term follow-up.

## REFERENCES

1. Huang C, Wang Y, Li X, et al. **Clinical features of patients infected with 2019 novel coronavirus in Wuhan, China.** *Lancet* 2020;395:497–506 CrossRef Medline
2. Guan WJ, Ni ZY, Hu Y, et al; China Medical Treatment Expert Group for Covid-19. **Clinical characteristics of coronavirus disease 2019 in China.** *N Engl J Med* 2020;382:1708–20 CrossRef Medline
3. Mao L, Jin H, Wang M, et al. **Neurologic manifestations of hospitalized patients with coronavirus disease 2019 in Wuhan, China.** *JAMA Neurol* 2020;77:683 CrossRef Medline
4. Zhou Y, Li W, Wang D, et al. **Clinical time course of COVID-19, its neurological manifestation and some thoughts on its management.** *Stroke Vasc Neurol* 2020;5:177–79 CrossRef Medline
5. González-Pinto T, Luna-Rodríguez A, Moreno-Estébanez A, et al. **Emergency room neurology in times of COVID-19: malignant ischemic stroke and SARS-CoV2 infection.** *Eur J Neurol* 2020 April 30. [Epub ahead of print] CrossRef Medline
6. Oxley TJ, Mocco J, Majidi S, et al. **Large-vessel stroke as a presenting feature of Covid-19 in the young.** *N Engl J Med* 2020;382:e60 CrossRef Medline
7. Qin C, Zhou L, Hu Z, et al. **Dysregulation of immune response in patients with COVID-19 in Wuhan, China.** *Clin Infect Dis* 2020;71:762–68 CrossRef Medline
8. Zhang Y, Xiao M, Zhang S, et al. **Coagulopathy and antiphospholipid antibodies in patients with Covid-19.** *N Engl J Med* 2020;382:e38 CrossRef Medline
9. Adams HP Jr, Bendixen BH, Kappelle LJ, et al. **Classification of subtype of acute ischemic stroke: definitions for use in a multicenter clinical trial—TOAST: Trial of Org 10172 in Acute Stroke Treatment.** *Stroke* 1993;24:35–41 CrossRef Medline
10. Jozwiak BP, Kumar V, Hussain S, et al. **Cleveland Clinic Abu Dhabi stroke registry (CCADSR) young ischemic strokes: initial results.** *J Neurol Sciences* 2019;405:85 CrossRef
11. Khan M, Hashim H, Nisa Z, et al. **Thrombolysis for acute ischemic stroke: experience in Dubai, and comparison of Arab with non-Arab population.** *J Neurol Stroke* 2016;4:00156 CrossRef
12. Beyrouti R, Adams ME, Benjamin L, et al. **Characteristics of ischemic stroke associated with COVID-19.** *J Neurol Neurosurg Psychiatry* 2020;91:889–91 CrossRef Medline
13. Aggarwal G, Lippi G, Michael Henry B. **Cerebrovascular disease is associated with an increased disease severity in patients with coronavirus disease 2019 (COVID-19): a pooled analysis of published literature.** *Int J Stroke* 2020;15:385–89 CrossRef Medline
14. Avula A, Nalleballe K, Narula N, et al. **COVID 19 presenting as stroke.** *Brain Behav Immun* 2020;87:115–19 CrossRef Medline
15. Lodigiani C, Iapichino G, Carenzo L, et al; Humanitas COVID-19 Task Force. **Venous and arterial thromboembolic complications in COVID-19 patients admitted to an academic hospital in Milan, Italy.** *Thromb Res* 2020;191:9–14 CrossRef Medline
16. Chen G, Wu D, Guo W, et al. **Clinical and immunological features of severe and moderate coronavirus disease 2019.** *J Clin Invest* 2020;130:2620–29 CrossRef Medline
17. Tang N, Li D, Wang X, et al. **Abnormal coagulation parameters are associated with poor prognosis in patients with novel coronavirus pneumonia.** *J Thromb Haemost* 2020;18:844–47 CrossRef Medline
18. Yaghi S, Ishida K, Torres J, et al. **SARS2-CoV-2 and stroke in a New York healthcare system.** *Stroke* 2020;51:2002–11 CrossRef Medline
19. Sweid A, Hammoud B, Weinberg JH, et al. **Thrombotic neurovascular disease in COVID-19 patients.** *Neurosurgery* 2020 June 4. [Epub ahead of print] CrossRef Medline
20. Kerleroux B, Fabacher T, Bricout N, et al; SFNR, the ETIS registry, and the JENI-Research Collaborative. **Mechanical thrombectomy for acute ischemic stroke amid the COVID-19 outbreak: decreased activity, and increased care delays.** *Stroke* 2020;51:2012–17 CrossRef Medline

## The Forest and the Trees



**C**oronavirus disease 2019 (COVID-19) is a multisystem disease;<sup>1</sup> the brain is not spared, and neurologic presentations are increasingly reported. Neurologic symptoms, including headache, altered mental status, and anosmia, occur in many infected patients.<sup>2</sup> Pathologic findings range from white matter disease<sup>3</sup> to encephalitis,<sup>4</sup> with only small samples of pathologic specimens published to date.<sup>5</sup> Thrombosis is common in critically ill patients with COVID-19,<sup>6</sup> and vasculopathy has been described, clinically and pathologically.<sup>7</sup> Given this widespread vascular involvement, the impact of the pandemic on stroke has been a prominent concern.<sup>8</sup> Reports to date suggest large-vessel occlusion (LVO) stroke in unusual populations<sup>9</sup> and friable clot with an increased propensity for clot fragmentation during thrombectomy.<sup>10</sup>

In this issue of the *American Journal of Neuroradiology*, these considerations are further informed by an article by John et al,<sup>11</sup> from a large private medical center in the United Arab Emirates. The authors reviewed the experience of LVO care in patients positive for COVID-19 with stroke from March to May 2020, and compared this with a similar period in 2019. They found, in 2020, an increase in total stroke presentations and in LVOs (20 versus 44 patients,  $P=.008$ ), attributed to changes in referral pathways during the pandemic in the region. Despite increasing case frequency, longer door-to-groin puncture times were seen in 2020 (68 versus 104 minutes,  $P=.001$ ), caused by delays incurred by new safety protocols. A remarkably high rate of LVO in patients positive for COVID-19 with stroke was identified, 75% of COVID-19-associated stroke presentations in this series. Reperfusion was achieved in 67% of patients positive for COVID-19 with LVO undergoing thrombectomy, with excellent groin-to-reperfusion times. Who were these patients? Typically, younger (mean age of 46 years) with a preponderance of men (93%) who lacked traditional vascular risk factors (absent in 60% of the patients). Consistent with prior observations about prothrombotic tendencies, in this sample, a quarter of patients positive for COVID-19 with stroke had additional systemic thrombotic disease, and the burden of LVO clot and the multiplicity of vessels affected were notable. Forty percent of patients had more than a single intracranial arterial vessel affected by thrombosis or occlusion.

These results provide a snapshot of the potential impact of COVID-19 on stroke. The observational literature is growing. The study findings and similar reports<sup>9</sup> have strong pathophysiologic

plausibility. However, we must maintain appropriate caution. Beyond small sample sizes, there is the distinct risk of reporting bias in the literature available on COVID-19 and stroke. Reports of similar findings are lacking for other epicenters in China, Europe, and much of the most affected regions in the United States. This finding is surprising given the incidence reported in this and other positive samples. The additional variable of stroke geographies and stroke systems of care is also relevant. These results from Abu Dhabi compare technically very favorably with US or European centers, but stroke populations and systems of care are different, as the authors carefully highlight.

Despite these cautions, it seems likely that stroke presentations are affected directly by the virus. Perhaps this impact is as described in the available literature for particular subpopulations. What should we make of these and similar small series? These findings may have implications for prophylactic measures in patients severely affected by the virus, in whom coagulation abnormalities are widespread.<sup>12</sup> The role of therapeutic dosing of anticoagulation or antiplatelet therapy in patients with COVID-19 prophylactically remains controversial (though clearly deep venous thrombosis prophylaxis is widely indicated).<sup>13</sup> Venous cerebrovascular disease has also been reported,<sup>14</sup> for which anticoagulation clearly has a role, but whether addressing thrombotic risk in patients with COVID-19 impacts arterial stroke rates is unknown. It also seems likely that in patients who are positive for COVID-19 and have an LVO, our thrombectomy expectations must evolve. These patients pose a technical challenge with possibly reduced likelihood of recanalization and the need to treat potentially more than a single circulation. These are points of conjecture currently. Are findings specific to Severe Acute Respiratory Syndrome COVID-19 or should they be expected in any systemic viral illness of this severity, and are they only prominent because of the pandemic nature of this one? This, too, is uncertain.

To understand these questions better, we need large-dataset analysis, looking at incidence rates, therapies, and outcomes. For instance, the American Heart Association/American Stroke Association Get With The Guidelines stroke campaign (<https://www.heart.org/en/professional/quality-improvement/get-with-the-guidelines/get-with-the-guidelines-stroke>) collects data for hospitals treating stroke and will offer a window into this issue as data are progressively collated. This effort will be central to



our understanding of the broader impact of COVID-19 on stroke pathophysiology, as distinct from its effect in currently reported pockets of patients.

While we may rightly debate the pathophysiology of COVID-19 and stroke, there should be less debate about the impact of COVID-19 on stroke systems of care.<sup>15-17</sup> The identified decreases in overall stroke presentations are driven largely by a decrease in presentation of patients with milder strokes.<sup>18</sup> Severely affected patients with stroke still present for care, consistent with the findings of John, et al;<sup>11</sup> 75% of acute stroke presentations in their patients with COVID-19 had LVOs. John et al further reported systems approaches in the centralization of care that led to their increased stroke and LVO numbers. Localization of expertise has already been pursued in disease epicenters<sup>19</sup> and is acknowledged as effective in improving outcomes and using resources.<sup>20</sup> Although not the focus of the article by John et al, the response at a systems level bears special emphasis. We may experience limitations in our ability to impact stroke in the individual patient with COVID-19. Much remains unknown and may remain unknown. It is well within our power, however, to positively influence the impact of this disease on stroke systems of care.<sup>21</sup> This is the forest, not just the trees. Such system adaptations, when pursued thoughtfully and collaboratively, build a resilient stroke-care system to handle this pandemic, as well as other challenges in the future, despite the numerous uncertainties about stroke mechanisms.

## REFERENCES

1. Mahajan A, Hirsch JA. **Novel coronavirus: what neuroradiologists as citizens of the world need to know.** *AJNR Am J Neuroradiol* 2020;41:552–54 CrossRef Medline
2. Mao L, Jin, H, Wang, M, et al. **Neurological manifestations of hospitalized patients with COVID-19 in Wuhan, China: a retrospective case series study.** *JAMA Neurol* 2020 Apr 10. [Epub ahead of print] CrossRef Medline
3. Lang M, Buch K, Li MD, et al. **Leukoencephalopathy associated with severe COVID-19 infection: sequela of hypoxemia?** *AJNR Am J Neuroradiol* 2020 Jun 20. [Epub ahead of print] CrossRef Medline
4. Bernard-Valnet R, Pizzarotti B, Anichini A, et al. **Two patients with acute meningoencephalitis concomitant with SARS-CoV-2 infection.** *Eur J Neurol* 2020 Jun 20. [Epub ahead of print] CrossRef Medline
5. Solomon IH, Normandin E, Bhattacharyya S, et al. **Neuropathological features of Covid-19.** *N Engl J Med* 2020;383:989–92 CrossRef Medline
6. Klok FA, Kruip M, van der Meer NJ, et al. **Confirmation of the high cumulative incidence of thrombotic complications in critically ill ICU patients with COVID-19: an updated analysis.** *Thromb Res* 2020;191:148–50 CrossRef Medline
7. Varga Z, Flammer AJ, Steiger P, et al. **Endothelial cell infection and endotheliitis in COVID-19.** *Lancet* 2020;395:1417–18 CrossRef Medline
8. Spence JD, de Freitas GR, Pettigrew LC, et al. **Mechanisms of stroke in COVID-19.** *Cerebrovasc Dis* 2020 Jul 20. [Epub ahead of print] CrossRef Medline
9. Oxley TJ, Mocco J, Majidi S, et al. **Large-vessel stroke as a presenting feature of Covid-19 in the young.** *N Engl J Med* 2020;382:e60 CrossRef Medline
10. Wang A, Mandigo GK, Yim PD, et al. **Stroke and mechanical thrombectomy in patients with COVID-19: technical observations and patient characteristics.** *J Neurointerv Surg* 2020;12:648–53 CrossRef Medline
11. John S, Kesav P, Mifsud VA, et al. **Characteristics of large-vessel occlusion associated with COVID-19 and ischemic stroke.** *AJNR Am J Neuroradiol* 2020 Aug 27. [Epub ahead of print] CrossRef Medline
12. Bowles L, Platton S, Yartey N, et al. **Lupus anticoagulant and abnormal coagulation tests in patients with Covid-19.** *N Engl J Med* 2020;383:288–90 CrossRef Medline
13. Thachil J, Tang N, Gando S, et al. **ISTH interim guidance on recognition and management of coagulopathy in COVID-19.** *J Thromb Haemost* 2020;18:1023–26 CrossRef Medline
14. Cavalcanti DD, Raz E, Shapiro M, et al. **Cerebral venous thrombosis associated with COVID-19.** *AJNR Am J Neuroradiol* 2020;41:1370–76 CrossRef Medline
15. Rudilosso S, Laredo C, Vera V, et al. **Acute stroke care is at risk in the era of COVID-19: experience at a comprehensive stroke center in Barcelona.** *Stroke* 2020;51:1991–95 CrossRef Medline
16. Kansagra AP, Goyal MS, Hamilton S, et al. **Collateral effect of Covid-19 on stroke evaluation in the United States.** *N Engl J Med* 2020;383:400–01 CrossRef Medline
17. Montaner J, Barragan-Prieto A, Perez-Sanchez S, et al. **Break in the stroke chain of survival due to COVID-19.** *Stroke* 2020;51:2307–14 CrossRef Medline
18. Siegler JE, Heslin ME, Thau L, et al. **Falling stroke rates during COVID-19 pandemic at a comprehensive stroke center.** *J Stroke Cerebrovasc Dis* 2020;29:104953 CrossRef Medline
19. Stefanini GG, Azzolini E, Condorelli G. **Critical organizational issues for cardiologists in the COVID-19 outbreak: a frontline experience from Milan, Italy.** *Circulation* 2020;141:1597–99 CrossRef Medline
20. Vonlanthen R, Lodge P, Barkun JS, et al. **Toward a consensus on centralization in surgery.** *Ann Surg* 2018;268:712–24 CrossRef Medline
21. Leslie-Mazwi TM, Fargen KM, Levitt M, et al. **Preserving access: a review of stroke thrombectomy during the COVID-19 pandemic.** *AJNR Am J Neuroradiol* 2020;41:1136–41 CrossRef Medline

© T.M. Leslie-Mazwi


Departments of Neurosurgery and Neurology

© J.A. Hirsch

Department of Radiology  
Massachusetts General Hospital  
Boston, Massachusetts

<http://dx.doi.org/10.3174/ajnr.A6864>

# The Impact of COVID-19 on Emergent Large-Vessel Occlusion: Delayed Presentation Confirmed by ASPECTS

 D.J. Altschul,  N. Haranhalli,  C. Esenwa,  S.R. Unda,  R. de La Garza Ramos,  J. Dardick,  J. Fernandez-Torres,  A. Toma,  D. Labovitz,  N. Cheng,  S.K. Lee,  A. Brook, and  R. Zampolin



## ABSTRACT

**BACKGROUND AND PURPOSE:** Our hypothesis is that the COVID-19 pandemic led to delayed presentations for patients with acute ischemic stroke. This study evaluates the impact of the coronavirus disease 2019 pandemic on presentation, treatment, and outcomes of patients with emergent large-vessel occlusion using data from a large health system in the Bronx, New York.

**MATERIALS AND METHODS:** We performed a retrospective cohort study of 2 cohorts of consecutive patients with emergent large-vessel occlusion admitted to 3 Montefiore Health System hospitals in the Bronx from January 1 to February 17, 2020, (prepandemic) and March 1 to April 17, 2020 (pandemic). We abstracted data from the electronic health records on presenting biomarker profiles, admission and postprocedural NIHSS scores, time of symptom onset, time of hospital presentation, time of start of the thrombectomy procedure, time of revascularization, presenting ASPECTS, TIC1 recanalization score, mRS, functional outcomes, and mortality.

**RESULTS:** Of 179 patients admitted with ischemic stroke during the study periods, 80 had emergent large-vessel occlusion, of whom 36 were in the pandemic group. Patients in the pandemic group were younger (66 versus 72 years,  $P < .061$ ) and had lower ASPECTS (7 versus 9,  $P < .001$ ) and took longer to arrive at the hospital (361 versus 152 minutes,  $P < .004$ ) with no other major differences. There was a decreased rate of thrombolysis administration (22% versus 43%,  $P < .049$ ) and a decreased number of patients treated with mechanical thrombectomy (33% versus 61%,  $P < .013$ ).

**CONCLUSIONS:** The pandemic led to delays in patients arriving at hospitals, leading to decreased patients eligible for treatment, while in-hospital evaluation and treatment times remain unchanged.

**ABBREVIATIONS:** COVID-19 = coronavirus disease 2019; ELVO = emergent large-vessel occlusion

In March 2020, New York City became the epicenter of the coronavirus disease 2019 (COVID-19) pandemic, which disrupted regional systems of health care. The pandemic changed when and how patients presented for emergent evaluation. A recent study found a nearly 40% decrease in stroke-related imaging nationwide during the COVID-19 pandemic.<sup>1</sup> While delays in treatment of myocardial infarction systems of care have been reported, the effect of the COVID-19 pandemic on systems of emergent large-vessel occlusion (ELVO) stroke care is unreported.<sup>2</sup>

Mechanical thrombectomy has been proved safe and effective in treating ELVO, but its success in decreasing morbidity depends on the prehospital system as well as a streamlined in-house process of care.<sup>3</sup> Our current stroke triage process involves hospital prenotification, bypass of emergency department evaluation, direct advancement to CT scan assessment, and treatment before angi suite arrival.

The aim of this study was to evaluate the impact of the COVID-19 pandemic on ELVO systems of care, treatment, and outcomes. We describe all cases of ELVO treated in our institution (Montefiore Health System) during the COVID-19 pandemic and compare them with those treated before the pandemic. Our hypothesis is that the COVID-19 pandemic led to delays in patients presenting to hospitals. This delay may have led to worse outcomes during the pandemic.

## MATERIALS AND METHODS


### Study Design and Participants


The data that support the findings of the study are available from the corresponding author on reasonable request. This retrospec-

Received July 2, 2020; accepted after revision July 27.

From the Departments of Neurosurgery (D.J.A., N.H., S.R.U., R.d.L.G.R., J.F.-T., A.T.), Neurology (C.E.), and Radiology (D.L., N.C., S.K.L., A.B., R.Z.), Montefiore Medical Center/Albert Einstein College of Medicine, Bronx, New York; and Albert Einstein College of Medicine (J.D.), Bronx, New York.

Please address correspondence to David J. Altschul, MD, 3316 Rochambeau Ave, Bronx, NY 10467; e-mail: daltschu@montefiore.org; @DavidAltschulMD

 Indicates open access to non-subscribers at [www.ajnr.org](http://www.ajnr.org)

 Indicates article with supplemental on-line table.

<http://dx.doi.org/10.3174/ajnr.A6800>

ective cohort study included 2 cohorts of patients admitted to 3 of the hospitals in our health care network, including our comprehensive stroke center, which accepts transfers for complex cases from 8 community hospitals, from January 1 to February 17, 2020, (prepandemic) and March 1 to April 17, 2020, (pandemic). All patients diagnosed with ELVO were included. ELVO was defined as acute focal neurologic deficits with an associated occlusion of the internal carotid artery, M1 segment of the middle cerebral artery, M2 segment of the middle cerebral artery, or the basilar artery with radiologic confirmation by CTA. March 1 was the date chosen because it was the day of the first confirmed documented case in New York City. We also included patients with occlusions of the anterior cerebral artery, posterior cerebral artery, or vertebral artery and labeled them as “other” large-vessel occlusion. COVID-19 was confirmed by positive detection of Severe Acute Respiratory Syndrome coronavirus 2 RNA using real-time polymerase chain reaction assay testing performed within the hospital system or documented at an outside system before transfer. All patients presenting to our hospital during the pandemic period were tested for COVID-19 using real-time polymerase chain reaction assay testing.

This study was approved by the hospital institutional review board. Written informed consent was waived.

### Case Ascertainment and Study Variables

Cases were identified through neuroradiology logs or neurologic consultation for transfers. Data abstracted from the medical records included demographics, clinical variables, laboratory values, and neuroimaging findings (initial ASPECTS, stroke treatment time points, results as they pertain to mechanical thrombectomy, outcome variables [discharge mRS 0–2], in-hospital mortality). Fourteen patients with inpatient presentation were excluded from analysis.

### Statistical Analysis

We compared baseline characteristics between prepandemic and pandemic groups, performing parametric and nonparametric analyses with the *t* test,  $\chi^2$  test, and Mann-Whitney *U* test as appropriate. No imputation was made for missing data. Missing data are labeled in the footnotes of the On-line Table. Main outcomes, poor outcomes (discharge mRS 3–5), and in-hospital mortality) with a  $\chi^2$  test of  $P < .05$  were analyzed through univariate and multivariate logistic regression controlling for explanatory variables. Multivariate analysis was performed with factors with  $P < .05$  on univariate analysis controlling for explanatory variables with  $P < .25$  on univariate analysis.

## RESULTS

We found a total of 80 patients with ELVO during the entire study period, with 44 treated before and 36 during the COVID-19 pandemic. There was an 18% decrease in overall large-vessel occlusion volume during the pandemic. Pandemic patients were younger than those prepandemic (66 versus 72,  $P < .061$ ); however, this difference was not significant. There was no significant difference in comorbidities or race or ethnicity between the 2 groups. In the pandemic cohort, 38.7% tested positive for COVID-19 at admission.

Compared with the prepandemic cohort, pandemic patients with ELVO presented with a lower ASPECTS score (7 versus 9,  $P < .001$ ), despite no differences in occlusion location, and arrived at the hospital later (361 versus 152 minutes,  $P < .012$ ). There was a significantly lower rate of thrombolysis administration (22% pandemic versus 43% prepandemic,  $P = .049$ ) and a reduced proportion of patients treated with mechanical thrombectomy (33% versus 61%,  $P = .013$ ). There was no significant difference in poor functional outcomes as scored using the mRS grades 3–5 (88.2% versus 69.6%,  $P = .08$ ). There was no significant difference in mortality for patients with ELVO in prepandemic versus pandemic cohorts (15% versus 28.1%,  $P = .173$ ) (On-line Table).

## DISCUSSION

We aimed to evaluate the effect of the COVID-19 pandemic by comparing two 6-week epochs. We evaluated sociodemographic data, comorbidities, established treatment time parameters, established imaging parameters, neurologic outcomes, and mortality between the 2 groups.

Patient symptom-onset-to-hospital times more than doubled in the pandemic period, and patients presented with significantly lower ASPECTS scores. Because intravenous thrombolysis and mechanical thrombectomy have either strict time and/or neuroimaging criteria per current guidelines, delays to care have a cascading effect, as reflected in the significantly fewer pandemic patients undergoing these hyperacute stroke therapies.<sup>4</sup> In our 2 cohorts, there was no significant difference in race, ethnicity, vascular risk factors, or comorbidities (On-line Table). There was no significant difference in where (direct to a comprehensive stroke center versus a primary stroke center) patients presented between the 2 groups.

The reasons for delays in seeking care are multifactorial. A New York statewide shelter-in-place order and widespread media coverage of overwhelmed emergency health system resources likely helped mitigate the spread of COVID-19 but may have also unintentionally led to underuse of the emergency health system for other emergencies. This finding was not unique to New York City because similar delays were seen in other areas.<sup>5–7</sup> One possibility is that patients with less severe symptoms did not seek early care; however, we did not see a significant difference in presenting NIHSS scores between the 2 groups. Other studies used last-known-well times to predict a delay of onset; this data point is often subject to miscalculation and bias. This study is the first to confirm objectively using ASPECTS that patients had a higher degree of completed infarct when presenting to the hospital during the pandemic. While delays to presentation could be the main reason for the objective difference in ASPECTS at presentation, another possibility is that the multisystem inflammatory syndrome and hypercoagulable state associated with COVID-19 create a more severe stroke syndrome at presentation.<sup>8</sup>

Our hospital continued to treat patients regardless of their COVID status on the basis of our prepandemic standards of care. This approach did not impact our in-hospital triage and treatment times. The mortality rates were higher in the pandemic cohort; however, they did not reach clinical significance. Similar smaller reviews have suggested poor outcomes for patients with stroke who arrived during the pandemic.<sup>9</sup> Further multicenter studies are needed to confirm these findings.



The limitations of this study are its retrospective and single-center design and the sample size being small for the patients in the pandemic group.

## CONCLUSIONS











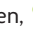










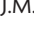
Acute stroke is an example of when the COVID-19 pandemic led to “collateral damage” for noninfected patients. Awareness of this impact is a crucial first step in mitigating unintended health consequences during a massive emergency response.

Disclosures: David J. Altschul—UNRELATED: Consultancy: Stryker/MicroVention; Grants/Grants Pending: National Institutes of Health, Comments: R01 Subaward. Allan Brook—RELATED: Consulting Fee or Honorarium: InNeuroCo.

## REFERENCES

1. Kansagra AP, Goyal MS, Hamilton S, et al. **Collateral effect of Covid-19 on stroke evaluation in the United States.** *N Engl J Med* 2020;383:400–01 CrossRef Medline
2. Tam CF, Cheung KS, Lam S, et al. **Impact of coronavirus disease 2019 (COVID-19) outbreak on ST-segment-elevation myocardial infarction care in Hong Kong, China.** *Circ Cardiovasc Qual Outcomes* 2020;13:e006631 CrossRef Medline
3. McTaggart RA, Yaghi S, Cutting SM, et al. **Association of a primary stroke center protocol for suspected stroke by large-vessel occlusion with efficiency of care and patient outcomes.** *JAMA Neurol* 2017;74:793–800 CrossRef
4. Powers WJ, Rabinstein AA, Ackerson T, et al. **Guidelines for the Early Management of Patients with Acute Ischemic Stroke: 2019 Update to the 2018 Guidelines for the Early Management of Acute Ischemic Stroke—A Guideline for Healthcare Professionals from the American Heart Association/American Stroke Association.** *Stroke* 2019;50:e344–418 CrossRef Medline
5. Teo KC, Leung WC, Wong YK, et al. **Delays in stroke onset to hospital arrival time during COVID-19.** *Stroke* 2020;51:2228–31 CrossRef Medline
6. Schirmer CM, Ringer AJ, Arthur AS, et al. **Delayed presentation of acute ischemic strokes during the COVID-19 crisis.** *J Neurointerv Surg* 2020;12:639–42 CrossRef Medline
7. Qin C, Zhou L, Hu Z, et al. **Clinical characteristics and outcomes of COVID-19 patients with a history of stroke in Wuhan, China.** *Stroke* 2020;51:2219–23 CrossRef Medline
8. Yaghi S, Ishida K, Torres J, et al. **SARS2-CoV-2 and stroke in a New York healthcare system.** *Stroke* 2020;51:2002–11 CrossRef Medline
9. Wang A, Mandigo GK, Yim PD, et al. **Stroke and mechanical thrombectomy in patients with COVID-19: technical observations and patient characteristics.** *J Neurointerv Surg* 2020;12:648–53 CrossRef Medline

# Considerations for Antiplatelet Management of Carotid Stenting in the Setting of Mechanical Thrombectomy: A Delphi Consensus Statement

 M. Goyal,  S. Yoshimura,  G. Milot,  J. Fiehler,  M. Jayaraman,  F. Dorn,  A. Taylor,  J. Liu,  F. Albuquerque,  M.E. Jensen,  R. Nogueira,  J.F. Fraser,  R. Chapot,  L. Thibault,  C. Majoie,  P. Yang,  N. Sakai,  D. Kallmes,  K. Orlov,  A. Arthur,  P. Brouwer, and  J.M. Ospel



## ABSTRACT

**BACKGROUND AND PURPOSE:** There are only few data and lack of consensus regarding antiplatelet management for carotid stent placement in the setting of endovascular stroke treatment. We aimed to develop a consensus-based algorithm for antiplatelet management in acute ischemic stroke patients undergoing endovascular treatment and simultaneous emergent carotid stent placement.

**MATERIALS AND METHODS:** We performed a literature search and a modified Delphi approach used Web-based questionnaires that were sent in several iterations to an international multidisciplinary panel of 19 neurointerventionalists from 7 countries. The first round included open-ended questions and formed the basis for subsequent rounds, in which closed-ended questions were used. Participants continuously received feedback on the results from previous rounds. Consensus was defined as agreement of  $\geq 70\%$  for binary questions and agreement of  $\geq 50\%$  for questions with  $>2$  answer options. The results of the Delphi process were then summarized in a draft manuscript that was circulated among the panel members for feedback.

**RESULTS:** A total of 5 Delphi rounds were performed. Panel members preferred a single intravenous aspirin bolus or, in jurisdictions in which intravenous aspirin is not available, a glycoprotein IIb/IIIa receptor inhibitor as intraprocedural antiplatelet regimen and a combination therapy of oral aspirin and a P2Y<sub>12</sub> inhibitor in the postprocedural period. There was no consensus on the role of platelet function testing in the postprocedural period.

**CONCLUSIONS:** More and better data on antiplatelet management for carotid stent placement in the setting of endovascular treatment are urgently needed. Panel members preferred intravenous aspirin or, alternatively, a glycoprotein IIb/IIIa receptor inhibitor as intraprocedural antiplatelet agent, followed by a dual oral regimen of aspirin and a P2Y<sub>12</sub> inhibitor in the postprocedural period.

**ABBREVIATIONS:** EVT = endovascular treatment; GPIIb/IIIa = glycoprotein IIb/IIIa

Currently, it is not clear whether and when carotid stent placement should be performed in patients with acute ischemic stroke with extracranial carotid stenosis, occlusion, or unstable

plaques undergoing endovascular treatment (EVT), but there is no doubt that carotid stent placement is necessary in some cases.<sup>1</sup> Numerous studies and review articles discuss the benefits and

Received June 1, 2020; accepted after revision July 17.

From the Departments of Clinical Neurosciences (M.G., J.M.O.) and Diagnostic Imaging (M.G.), University of Calgary, Calgary, Alberta, Canada; Department of Neurosurgery (S.Y.), Hyogo College of Medicine, Nishinomiya, Hyogo, Japan; Department of Neurosurgery (G.M.), Centre Hospitalier Universitaire de Québec, Québec City, Québec, Canada; Department of Diagnostic and Interventional Neuroradiology (J.F.), University Medical Center Hamburg-Eppendorf, Hamburg, Germany; Departments of Diagnostic Imaging, Neurology, and Neurosurgery (M.J.), Warren Alpert School of Medicine at Brown University, Providence, Rhode Island; Institute of Neuroradiology (F.D.), University of Munich, Ludwig-Maximilians-Universität, Munich, Germany; Groote Schuur Hospital (A.T.), University of Cape Town, Cape Town, South Africa; Department of Neurosurgery (J.L., P.Y.), Changhai Hospital Naval Medical University, Shanghai, China; Department of Neurosurgery (F.A.), Barrow Neurological Institute, Phoenix, Arizona; Departments of Neurological Surgery, Radiology, and Medical Imaging (M.E.J.), University of Virginia Health, Charlottesville, Virginia; Marcus Stroke & Neuroscience Center (R.N.), Grady Memorial Hospital, Atlanta, Georgia; Department of Neurology (R.N.), Emory University School of Medicine, Atlanta, Georgia; Departments of Neurosurgery (J.F.F.), Neurology, Radiology, and Neuroscience, University of Kentucky, Lexington, Kentucky; Department of Neuroradiology (R.C.), Alfred Krupp

Krankenhaus Essen, Essen, Germany; Member of the Scientific Committee (L.T.), World Federation of Interventional and Therapeutic Neuroradiology, Paris, France; Department of Radiology (C.M.), Academic Medical Center, Amsterdam, the Netherlands Department of Neurosurgery (N.S.), Kobe City Medical Center General Hospital, Kobe, Japan; Department of Radiology (D.K.), Mayo Clinic, Rochester, Minnesota; Meshalkin National Medical Research Center (K.O.), Novosibirsk, Russian Federation; Department of Neurosurgery (A.A.), Semmes-Murphey Clinic/University of Tennessee, Memphis, Tennessee; Department of Interventional Neuroradiology (P.B.), Karolinska Hospital, Stockholm, Sweden; University NeuroVascular Center (P.B.), University Medical Center, Haaglanden Medical Center, Leiden, the Netherlands; and Department of Neuroradiology (J.M.O.), University Hospital of Basel, Basel, Switzerland

Please address correspondence to Mayank Goyal, MD, Departments of Radiology and Clinical Neurosciences, Foothills Medical Centre, 1403 29th St NW, Calgary, AB, T2N2T9, University of Calgary, Calgary, AB, Canada; e-mail: mgoyal@ucalgary.ca; @mayank\_G0, @johanna\_ospel

 Indicates article with supplemental online appendix and table.

<http://dx.doi.org/10.3174/ajnr.A6888>

disadvantages of carotid stent placement in the setting of EVT,<sup>1-3</sup> and the need for dual-antiplatelet therapy is often cited as an argument to forego emergent stent placement. Some authors even argue that emergent carotid endarterectomy might be a better alternative because it does not require dual antiplatelet therapy.<sup>4</sup> There are only few data on antiplatelet management for carotid stenosis in the setting of conservative management,<sup>5</sup> and even less is known about periprocedural antiplatelet management for carotid stent placement during EVT.<sup>6</sup> There are no comprehensive studies that have compared the impact of different antiplatelet regimens on clinical outcomes and hemorrhagic events in patients who undergo EVT and simultaneous carotid stent placement.

Answering these questions is, however, of utmost importance because ischemic brain tissue is at higher risk of hemorrhage, and this risk may further increase with suboptimal antiplatelet management, especially if intravenous alteplase is administered concurrently.<sup>7,8</sup> The prevailing uncertainty regarding timing, dosage, and agents in antiplatelet therapy for emergent carotid stent placement might: 1) influence the decision about whether to place a carotid stent in a disadvantageous manner (ie, no carotid stent is placed in patients who could benefit from stent placement), and 2) compromise patient safety through increased thromboembolic or hemorrhagic complications in case a carotid stent is placed. In addition, the lack of standardization makes it difficult to perform unbiased retrospective studies. We used a modified Delphi approach to identify current challenges and unsolved questions in antiplatelet management for emergent carotid stent placement in the setting of EVT and attempted to propose a consensus-based algorithm for standardized antiplatelet management strategies until evidence-based guidelines become available. Of note, the question of whether and when carotid stent placement should be considered in a patient undergoing EVT was not the subject of this study.

## **MATERIALS AND METHODS**

### **Literature Search**

In preparation for the Delphi process, a MEDLINE literature search using the search terms “antiplatelet,” “emergent,” “acute,” “carotid stent placement,” “thrombectomy,” “endovascular,” and “stroke” was performed for the period from January 2010 to May 2020. Bibliographies of relevant publications were screened to identify additional studies. Together with the results from round 1 (open-ended questions), the identified articles provided the basis for the following, closed-ended survey questions.

### **Panel Members**

A panel of 19 neurointerventionalists (interventional neuroradiologists, vascular neurosurgeons, and vascular neurologists) from Europe, North America, Asia, and Africa with high clinical and academic expertise in endovascular stroke treatment was formed on the basis of personal and institutional academic and clinical collaborations, and care was taken to represent a broad spectrum of specialties and countries. Panel members were selected only if they had long-standing clinical experience and scientific interest in endovascular stroke treatment. A list of the panel members can be found in the Online Appendix. In addition, a pharmacology expert

(L.T.) with intraprocedural antiplatelet management experience in neurointervention was consulted and provided feedback.

### **Delphi Methodology**

The Delphi method was originally developed to predict the impact of technology on warfare during the cold war.<sup>9</sup> Delphi is a systematic and iterative forecasting method with interactive feedback loops that relies on a panel of individuals with high expertise in the area of interest. It is generally used when reliable data for a particular question of interest are not available. The panel undergoes a series of questionnaires with controlled-opinion feedback, whereby the ultimate goal is to reach a group consensus. The Delphi method has been successfully used in medicine to develop temporary treatment guidelines and to standardize patient care in areas with a relative paucity of data.<sup>10</sup> In this study, the Delphi technique was applied to identify challenges in antiplatelet management for carotid stent placement in the setting of EVT and to develop a proposed algorithm for such cases. Figure 1 outlines the principal steps of the Delphi approach as it was performed in this study.<sup>11</sup>

### **Data Collection and Analysis**

An anonymous online response system (Qualtrics.com) was used for all survey rounds. While the anonymization prevented us from performing stratified analysis, eg, by expert specialty or region of practice, we considered it necessary to blind the panel members as well as the data analysts to the results to avoid biases due to peer pressure. The 19 panel members responded independently from each other to subsequent iterations of questionnaires. The initial round contained exclusively open-ended questions. Answers from this round were thematically clustered and analyzed in an affinity diagram. The literature search results and the affinity diagram formed the basis for the following rounds, which consisted of closed-ended questions. An anonymized result summary from the previous round was fed back to the group during the next round, and group responses were assessed for consensus. One question was thereby asked a maximum of 2 times.

## **RESULTS**

### **Data Collection and Endorsement**

Response data were collected from March 31 to May 6, 2020. All 19 panel members completed a total of 5 survey rounds, in which they were asked to answer questions regarding antiplatelet management for carotid stent placement in the setting of EVT according to their personal experience and views, ie, their answers represented personal beliefs rather than established policies at their local institutions. The results were summarized in an initial document, which was circulated among the panel members for further discussion before finalizing the manuscript. The statement was endorsed by the World Federation of Interventional and Therapeutic Neuroradiology, the Japanese Society for Neuroendovascular Therapy, and the Chinese Neurosurgical Society.

### **Literature Search**

The literature search revealed wide practice variations in antiplatelet management for carotid stent placement in the setting of EVT. Numerous studies reported the safety and efficacy with



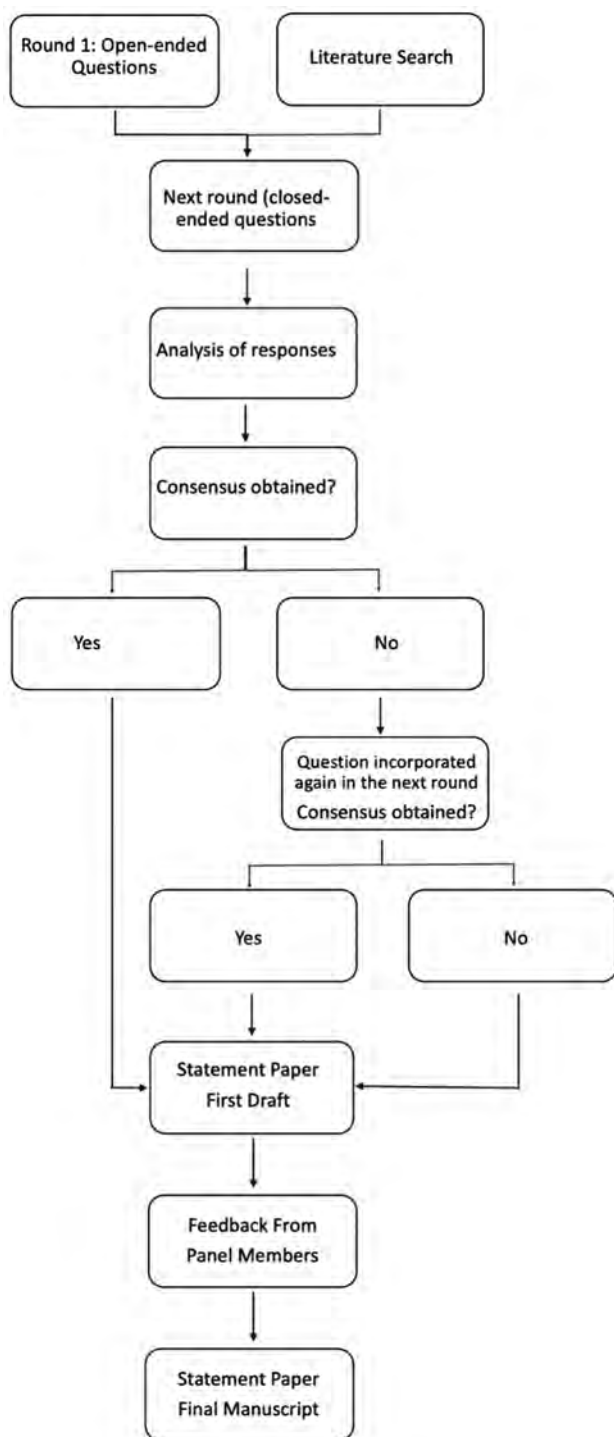


**FIG 1.** Delphi methodology as it was used in this article.

regard to clinical outcomes of the procedure itself, but the specific antiplatelet regimen used was reported in only very few studies. In those that did report it, antiplatelet protocols ranged from rather aggressive protocols with glycoprotein IIb/IIIa (GPIIb/IIIa) inhibitors and additional aspirin to no periprocedural antiplatelet therapy at all<sup>12</sup> (see Online Table for key publications). Most studies were retrospective in nature, and among those with

uniform antiplatelet regimens, most were small single-center series, while in larger multicenter studies, antiplatelet regimens were not reported or varied among patients.<sup>13</sup>

### **Delphi Consensus Results**

The panel achieved a consensus that antiplatelet management for carotid stent placement in the setting of EVT should follow a standard approach, irrespective of the baseline ASPECTS/ischemic “core” on perfusion imaging and the final reperfusion result (expanded TICI score), and that it should be independent of whether intravenous thrombolytics (alteplase, tenecteplase) are administered. They also believed that heparin, other than small doses in the infusion, should not be administered during the procedure.

Panel members did not achieve consensus on whether antiplatelet therapy should be initiated on the basis of noninvasive imaging findings (head and neck CTA) before the procedure if there is a perceived high likelihood of a carotid stent becoming necessary (eg, high-grade carotid stenosis). Thus, in the following, the results are reported separately for 2 scenarios: 1) patients in whom the likelihood of a carotid stent being needed seems high; therefore, the operator decides to initiate antiplatelet therapy before the procedure; and 2) patients in whom antiplatelet therapy has not been initiated before the start of the procedure but is initiated during the procedure.

### **Scenario 1: Initiation of Antiplatelet Therapy before the Procedure**

In case the likelihood of a carotid stent being placed is so high that the operator decides to initiate antiplatelet therapy before the EVT procedure, panel members agreed that aspirin should be used as a first-line agent (500 mg bolus) and is sufficient; a second periprocedural antiplatelet agent was not deemed necessary. In case intravenous aspirin is not available, most panel members favored GPIIb/IIIa inhibitors (see Table 1 for dose recommendations) or rectal aspirin as an alternative.

### **Scenario 2: Initiation of Antiplatelet Therapy during the Procedure**

If an operator decides to initiate antiplatelet therapy during the procedure because of carotid stent placement, the panel also preferred intravenous aspirin as a first-line agent (500 mg bolus) without any additional antiplatelet agents. In case intravenous aspirin is not available, GPIIb/IIIa inhibitors were deemed the most suitable alternative (see Table 1 for dose recommendations).

### **Postprocedural Antiplatelet Management**

Panel members agreed that the intraprocedural intravenous regimen can be converted to an oral regimen within 24 hours after the EVT procedure. Oral aspirin (70–100 mg, depending on the available dosages in individual jurisdictions) was the preferred first antiplatelet agent in the postprocedural period. P2Y12 inhibitors were the preferred second agent (see Table 2 for dose recommendations). It was believed that particularly in case of known clopidogrel resistance, it may be beneficial to choose another P2Y12 inhibitor. Regarding the usefulness and clinical impact of antiplatelet testing in the postprocedural period, no consensus was achieved. Figure 2 provides a short summary of the panel consensus.

**Table 1: Consensus recommendations for the dosage of GPIIb/IIIa receptor inhibitors<sup>a</sup>**

Agent	Tirofiban	Eptifibatide	Abciximab
Loading dose (IV or IA bolus)	12 mcg/kg for 30 min <sup>b</sup>	180 mcg/kg for 1–2 min	0.25 mg/kg
Maintenance dose (if necessary, IV infusion for 12–24 h)	0.1 mcg/kg/min	2 mcg/min	125 mcg/kg/min
Trade name	Aggrastat	Integrilin	ReoPro
Duration of antiplatelet effect	4–8 h	4 h	48 h

**Note:**—IA indicates intra-arterial.

<sup>a</sup> Dosages are suggestions based on the panel consensus and may vary according to local availability of dosages.

<sup>b</sup> 0.4 mcg/kg/min.

**Table 2: Consensus recommendations for dosing of oral P2Y<sub>12</sub> inhibitors in the postprocedural period<sup>a</sup>**

Agent	Clopidogrel	Ticagrelor	Prasugrel
Loading dose <sup>b</sup>	600 mg	180 mg	40–60 mg
Maintenance dose	75 mg daily	60–90 mg 2×/day	5–10 mg daily
Trade name	Plavix	Brilinta/Brilique	Effient
Onset of action	2 h	30 min	15–30 min

<sup>a</sup> Dosages are suggestions based on the panel consensus and may vary according to local availability of dosages.

<sup>b</sup> If deemed necessary.

## DISCUSSION

Panel members in this Delphi study reached to a consensus on a single-antiplatelet regimen with intravenous aspirin or alternatively an intravenous GPIIb/IIIa inhibitor as a first-line approach for carotid stent placement in the setting of EVT, irrespective of whether antiplatelet therapy is initiated prior to or during the procedure. The preferred oral antiplatelet regimen in the postprocedural period was a dual regimen with aspirin and a P2Y<sub>12</sub> inhibitor. No consensus was achieved on the role of platelet function testing.

Our literature search revealed a lack of high-level evidence for antiplatelet management for emergent carotid stent placement because most studies were small single-center series. Many publications did not report the antiplatelet regimen that was used at all, while in others, it was reported but not standardized. This leads to substantial uncertainty on the side of neurointerventionalists who have to decide whether to place a carotid stent during a thrombectomy procedure and might result in undertreatment, ie, a carotid stent is not placed though it is needed, or suboptimal antiplatelet regimens that increase the risk of either hemorrhagic or thromboembolic complications. Intravenous aspirin is a long-standing antiplatelet agent that has been used by neurointerventionalists in Europe for many years. It was the preferred agent for intraprocedural antiplatelet management in this study. However, intravenous aspirin is not available in North America and some other countries. In such cases, the panel believed that a GPIIb/IIIa inhibitor would constitute the best alternative. Panel members stated that they would use these antiplatelet regimens, irrespective of whether intravenous thrombolytics are administered, though the Antiplatelet therapy in combination with rtPA Thrombolysis in Ischemic Stroke (ARTIS) trial<sup>7</sup> and some other studies<sup>8</sup> have shown that the risk of bleeding in patients with acute ischemic stroke who receive intravenous alteplase is increased when antiplatelet therapy is initiated immediately. In the postprocedural period, the panel preferred an oral combination therapy with aspirin and a P2Y<sub>12</sub> inhibitor, which is very similar to the standard antiplatelet regimen after elective carotid stent placement.

Of note, this consensus is largely based on the panel members' experience rather than evidence, and there are large practice variations in antiplatelet management for emergent carotid stent placement.<sup>12,14</sup> Thus, the antiplatelet dosages on which the panel members agreed are also not in any way evidence-based and are largely extrapolated from existing literature on elective carotid stent placement and personal experience. The lack of consensus

regarding platelet function testing is most likely due to poor standardization of commercially available test kits and contradictory evidence regarding their utility in the setting of neurovascular procedures.<sup>15,16</sup> Panel members clearly emphasized the need for more and better, ideally prospective and multicentric, studies on the impact of antiplatelet regimens on hemorrhagic/thromboembolic events and outcomes in carotid stent placement during EVT, similar to the currently ongoing Multicenter Randomized CLinical trial of Endovascular treatment for Acute ischemic stroke in the Netherlands investigating the effect of periprocedural MEDication (MR CLEAN MED) trial (<https://www.mrclean-med.nl>), which evaluated the effect of heparin and/or antiplatelet agents in the setting of EVT (but without simultaneous carotid stent placement). They also pointed out the need for better standardization of and evidence for platelet function testing and the development of antithrombogenic surface coatings that could in the long run obviate the need for systemic antiplatelet therapy altogether.

## Limitations

The results of this Delphi consensus study are intended to identify challenges and unsolved questions in antiplatelet management for emergent carotid stent placement and to provide a possible antiplatelet management approach until sufficient data become available that allow evidence-based recommendations. This article does not intend, in any way, to replace such guidelines; on the contrary, its goal is to encourage investigators to initiate these urgently needed studies. It should also not be misinterpreted as advocating carotid stent placement in the setting of EVT; this question will hopefully be answered soon by randomized trials such as the Thrombectomy In TANdem occlusion (TITAN) trial (NCT03978988) (<https://clinicaltrials.gov/ct2/show/NCT03978988>), and it is not our intention to promote one antiplatelet agent over another.

Only a few countries being represented in the panel could have led to nongeneralizability of the results, eg, with regard to different geographic regions because region-specific access limitations to drugs could not be fully taken into account. This feature was, in

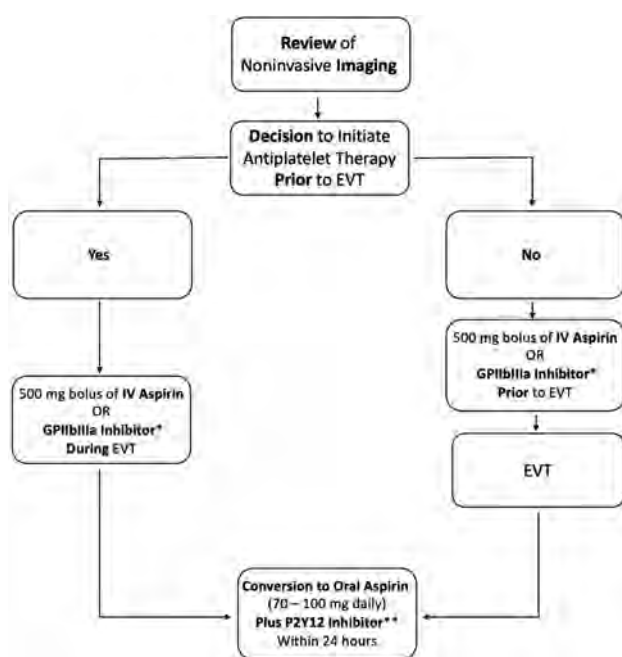


**FIG 2.** Summary of the results of the Delphi consensus panel. The asterisk means see Table 1 for dosages. Two asterisks mean see Table 2 for dosages.

part, related to the number of experts, which was rather small. We decided to stick to 15 experts, a number that is commonly used in the Delphi method because the chances of achieving group consensus decrease rapidly with larger group sizes. Last, antiplatelet agents and application forms are constantly refined and new ones are developed, and antithrombotic device surface coatings could soon find their way into clinical practice<sup>17,18</sup> so that the panel consensus might look different if this study were to be repeated in the future.

## CONCLUSIONS

More and better data on antiplatelet management for carotid stent placement in the setting of EVT are urgently needed. Expert panel members in this study preferred intravenous aspirin or, alternatively, a GPIIb/IIIa inhibitor as an intraprocedural antiplatelet agent, followed by a dual oral regimen of aspirin and a P2Y12 inhibitor in the postprocedural period.

**Disclosures:** Mayank Goyal—UNRELATED: Consultancy: Stryker, Medtronic, Mentice, MicroVention; Grants/Grants Pending: Cerenovus\*; Patents (Planned, Pending or Issued): GE Healthcare, Comments: licensing agreement for systems of stroke diagnosis. Shinichi Yoshimura—RELATED: Consulting Fee or Honorarium: Bayer, Sanofi, Otsuka Pharmaceutical, Stryker, Medtronic, Johnson & Johnson, Terumo, Medico's Hirata, Biomedical Solutions, Comments: lecture fee; UNRELATED: Payment for Lectures Including Service on Speakers Bureaus: Boehringer-Ingelheim, Daiichi Sankyo, Bristol-Meyers Squibb, Comments: lecture fee. Jens Fiehler—UNRELATED: Consultancy: Acandis, Cerenovus, Stryker, Medtronic, Penumbra; Grants/Grants Pending: Acandis, Cerenovus, Stryker, Medtronic, Route 92.\* Mahesh Jayaraman—UNRELATED: Payment for Lectures Including Service on Speakers Bureaus: Medtronic, Comments: speaking at ISC 2018 on Stroke Systems of Care. Franziska Dorn—UNRELATED: Consultancy: Balt, phenox, Cerus; Payment for Lectures Including Service on Speakers Bureaus: speakers honorarium for Cerenovus, Acandis. Allan Taylor—RELATED: Other: limited private practice; UNRELATED: Employment: Groote Schuur Hospital; Expert Testimony: defense and prosecuting attorneys. Raul Nogueira—Other Relationships: RGN reports, consulting fees for advisory roles with Anaconda, Biogen, Cerenovus, Genentech, Imperative Care, Medtronic, phenox,

Prolong Pharmaceuticals, Stryker Neurovascular; Stock/Stock Options: advisory roles with Astrocyte, Brainomix, Cerebrotech, Ceretrieve, Corindus Vascular Robotics, Vesalio, Viz-ai, and Perfuze. Justin F. Fraser—UNRELATED: Board Membership: Cerelux LLC, Comments: co-owner of company; Consultancy: Medtronic, Penumbra, Stream Biomedical, Comments: consultant fees; Grants/Grants Pending: American Heart Association and University of Kentucky, Comments: grant support\*; Stock/Stock Options: Fawkes Biotechnology, Comments: equity interest ownership. Rene Chapot—UNRELATED: Consultancy: MicroVention, Stryker\*; Payment for Development of Educational Presentations: Balt, MicroVention, Siemens.\* Charles Majoie—UNRELATED: Grants/Grants Pending: CVON/Dutch Heart Foundation, European Commission, Dutch Health Evaluation Program, TWIN Foundation, Stryker\*; Stock/Stock Options: NicoLab (modest), Comments: a company that focuses on the use of artificial intelligence for medical image analysis. David Kallmes—UNRELATED: Grants/Grants Pending: MicroVention, NeuroSigma, Medtronic, Comments: funding for pre-clinical research\*; Patents (Planned, Pending or Issued): Mayo Clinic, Comments: patent for protection device\*; Stock/Stock Options: Marblehead Medical LLC, Superior Medical Experts LLC. Patrick Brouwer—UNRELATED: Consultancy: Cerenovus. Nobuyuki Sakai—UNRELATED: Grants/Grants Pending: Daiichi Sankyo, NeuroVasc, Terumo\*; Payment for Lectures Including Service on Speakers Bureaus: Asahi-Intec, Biomedical Solutions. Adam Arthur—UNRELATED: Consultancy: Balt, Johnson & Johnson, Medtronic, MicroVention, Penumbra, Scientia, Siemens, Stryker\*; Grants/Grants Pending: Balt, Medtronic, MicroVention, Penumbra, Siemens\*; Stock/Stock Options: Azimuth, Bendit, Cerebrotech, EndoStream, Magneto, Marblehead Medical LLC, Neurogami, Serenity, Synchron, TRIAD MEDICAL, Vascular Simulations.\* \*Money paid to the institution.

## REFERENCES

- Naylor AR, Ricco JB, de Borst GJ, et al. **Editor's Choice: Management of Atherosclerotic Carotid and Vertebral Artery Disease—2017 Clinical Practice Guidelines of the European Society for Vascular Surgery (ESVS).** *Eur J Vasc Endovasc Surg* 2018;55:3–81 CrossRef Medline
- Poppe AY, Jacquin G, Roy D, et al. **Tandem carotid lesions in acute ischemic stroke: mechanisms, therapeutic challenges, and future directions.** *AJNR Am J Neuroradiol* 2020;41:1142–48 CrossRef Medline
- Eker OF, Buhlmann M, Dargazanli C, et al. **Endovascular treatment of atherosclerotic tandem occlusions in anterior circulation stroke: technical aspects and complications compared to isolated intracranial occlusions.** *Front Neurol* 2018;9:1046 CrossRef Medline
- Slawski DE, Jumaa MA, Salahuddin H, et al. **Emergent carotid endarterectomy versus stenting in acute stroke patients with tandem occlusion.** *J Vasc Surg* 2018;68:1047–53 CrossRef Medline
- Murphy SJ, Naylor AR, Ricco JB, et al. **Optimal antiplatelet therapy in moderate to severe asymptomatic and symptomatic carotid stenosis: a comprehensive review of the literature.** *Eur J Vasc Endovasc Surg* 2019;57:199–211 CrossRef Medline
- Heck DV, Brown MD. **Carotid stenting and intracranial thrombectomy for treatment of acute stroke due to tandem occlusions with aggressive antiplatelet therapy may be associated with a high incidence of intracranial hemorrhage.** *J Neurointerv Surg* 2015;7:170–75 CrossRef Medline
- Zinkstok SM, Roos YB; ARTIS investigators. **Early administration of aspirin in patients treated with alteplase for acute ischaemic stroke: a randomised controlled trial.** *Lancet* 2012;380:731–37 CrossRef Medline
- Diener HC, Foerch C, Riess H, et al. **Treatment of acute ischaemic stroke with thrombolysis or thrombectomy in patients receiving anti-thrombotic treatment.** *Lancet Neurol* 2013;12:677–88 CrossRef Medline
- Dayé C. **How to train your oracle: the Delphi method and its turbulent youth in operations research and the policy sciences.** *Soc Stud Sci* 2018;48:846–68 CrossRef Medline
- Steurer J. **The Delphi method: an efficient procedure to generate knowledge.** *Skeletal Radiol* 2011;40:959–61 CrossRef Medline
- Dalkey NH, Hemer O. **An experimental application of the Delphi method to the use of experts.** Santa Monica, California, 1962. [https://www.rand.org/content/dam/rand/pubs/research\\_memoranda/2009/RM727.1.pdf#:~:text=An%20Experimental%20Application%20of%20the%20Delphi%20Method%20to,RAND%2C%20designated%20internally%20as%20%22Project%20Delphi.%22%20Created%20Date. Accessed October 10, 2020](https://www.rand.org/content/dam/rand/pubs/research_memoranda/2009/RM727.1.pdf#:~:text=An%20Experimental%20Application%20of%20the%20Delphi%20Method%20to,RAND%2C%20designated%20internally%20as%20%22Project%20Delphi.%22%20Created%20Date. Accessed October 10, 2020)



12. Hwang SB, Kwak HS, Chung GH. **Forced suction thrombectomy after carotid stenting in patients with massive thrombus and acute extracranial internal carotid artery occlusion.** *J Neurointerv Surg* 2013;5:426–29 CrossRef Medline
13. Behme D, Mpotsaris A, Zeyen P, et al. **Emergency stenting of the extracranial internal carotid artery in combination with anterior circulation thrombectomy in acute ischemic stroke: a retrospective multicenter study.** *AJNR Am J Neuroradiol* 2015;36:2340–45 CrossRef Medline
14. Coffman S, Trott S, Alhajeri A, et al. **P-010 Practice variations in addressing acute tandem carotid occlusions in emergent large vessel occlusion strokes.** *Neurointerv Surg* 2017;9(Suppl 1):A26–27
15. Comin J, Kallmes DF. **Platelet-function testing in patients undergoing neurovascular procedures: caught between a rock and a hard place.** *AJNR Am J Neuroradiol* 2013;34:730–34 CrossRef Medline
16. Brinjikji W, Lanzino G, Cloft HJ, et al. **Platelet testing is associated with worse clinical outcomes for patients treated with the Pipeline embolization device.** *AJNR Am J Neuroradiol* 2015;36:2090–95 CrossRef Medline
17. Manning NW, Cheung A, Phillips TJ, et al. **Pipeline shield with single antiplatelet therapy in aneurysmal subarachnoid haemorrhage: multicentre experience.** *J Neurointerv Surg* 2019;11:694–98 CrossRef Medline
18. Perez MA, AlMatter M, Hellstern V, et al. **Use of the pCONus HPC as an adjunct to coil occlusion of acutely ruptured aneurysms: early clinical experience using single antiplatelet therapy.** *J Neurointerv Surg* 2020;12:862–68 CrossRef Medline

# Treatment of Ruptured Blister-Like Aneurysms with the FRED Flow Diverter: A Multicenter Experience

 M.A. Möhlenbruch,  F. Seker,  E. Özlük,  O. Kizilkilic,  E. Broussalis,  M. Killer-Oberpfalzer,  C.J. Griessenauer,  M. Bendszus, and  N. Kocer



## ABSTRACT

**BACKGROUND AND PURPOSE:** Treatment of ruptured blister-like aneurysms is technically challenging. This study aimed at analyzing the safety and efficacy of the Flow-Redirection Endoluminal Device (FRED) in the treatment of ruptured blister-like aneurysms.

**MATERIALS AND METHODS:** In a retrospective multicenter study, all patients treated with the FRED due to a ruptured intracranial blister-like aneurysm between January 2013 and May 2019 were analyzed. The primary end points for clinical safety were mRS 0–2 at 6 months after treatment and the absence of major ipsilateral stroke or death. The primary end points for efficacy were the absence of rebleeding after treatment and complete angiographic occlusion according to the O’Kelly-Marotta classification at 6 months after treatment.

**RESULTS:** In total, 30 patients with 30 ruptured blister-like aneurysms were treated. Immediate complete aneurysm obliteration (O’Kelly-Marotta classification D) with the FRED was achieved in 10 patients (33%). Of the 26 patients with follow-up, complete obliteration was achieved in 21 patients (80%) after 6 months and in 24 patients (92%) in the final follow-up (median, 22 months). Twenty-three patients (77%) achieved mRS 0–2 at 6 months. Major stroke or death occurred in 17%. Two patients died due to pneumonia, and 2 patients died due to infarction following cerebral vasospasm. There was no case of rebleeding after FRED implantation. There was 1 case of delayed asymptomatic stent occlusion.

**CONCLUSIONS:** Treatment of ruptured blister-like aneurysms with the FRED is safe and effective.

**ABBREVIATIONS:** OKM = O’Kelly-Marotta; FRED = Flow-Redirection Endoluminal Device; PED = Pipeline Embolization Device

**B**lister-like aneurysms are a subtype of intracranial aneurysm. It is assumed that blister-like aneurysms are a laceration of the arterial wall based on degeneration of the internal elastic lamina. This focal wall defect seems to be covered with normal adventitia and fibrinous tissue.<sup>1</sup> Blister-like aneurysms are characterized by a thin vessel wall and the absence of an aneurysm neck. There is no pseudolumen or organized thrombus. Blister-

like aneurysms typically arise at nonbranching segments of the supraclinoid internal carotid artery, but they can also arise at other locations such as the basilar artery.<sup>2–6</sup>

Surgical treatment and endovascular coiling of blister-like aneurysms are technically challenging.<sup>7</sup> The introduction of flow diverters, however, has allowed a safe and effective treatment option for blister-like aneurysms.<sup>8,9</sup> Several studies on the treatment of blister-like aneurysms with the Pipeline Embolization Device (PED; Medtronic) have shown good clinical and angiographic results.<sup>4,10–15</sup>

The aim of this retrospective multicenter study was to analyze the safety and efficacy of the Flow-Redirection Endoluminal Device (FRED; MicroVention) in the treatment of ruptured blister-like aneurysms.

## MATERIALS AND METHODS

### Patient Population

This retrospective multicenter study at 3 centers was approved by the local institutional review board at each participating center (Heidelberg/Germany, Istanbul/Turkey, Salzburg/Austria). Between January 2013 and September 2019, all patients with ruptured blister-


Received June 16, 2020; accepted after revision August 5.

From the Department of Neuroradiology (M.A.M., F.S., M.B.), Heidelberg University Hospital, Heidelberg, Germany; Department of Radiology (E.Ö.), Acibadem University Atakent International Hospital, Istanbul, Turkey; Division of Neuroradiology (O.K., N.K.), Department of Radiology, Cerrahpasa Medical Faculty, Istanbul University-Cerrahpasa, Istanbul, Turkey; Research Institute of Neurointervention (E.B., M.K.-O., C.J.G.), Paracelsus Medical University, Salzburg, Austria; and Department of Neurosurgery (C.J.G.), Geisinger, Danville, Pennsylvania.

M.A. Möhlenbruch and F. Seker contributed equally to this work.

Paper previously presented at: World Federation of Interventional and Therapeutic Neuroradiology Congress, October 21–24, 2019; Naples, Italy.

Please address correspondence to Naci Kocer, MD, Department of Radiology, Cerrahpasa School of Medicine, 34300 Cerrahpasa, Istanbul, Turkey; e-mail: nkocer@istanbul.edu.tr

 Indicates article with supplemental on-line table.

<http://dx.doi.org/10.3174/ajnr.A6849>

like aneurysms treated with the FRED as an off-label therapy were included. Blister-like aneurysms were defined according to Peschillo et al<sup>6</sup> as small, conical, wide-neck aneurysms located at a non-branching site of the circle of Willis. Data collection included demographics, clinical data, imaging data, aneurysm features, details of the aneurysm treatment, and clinical outcome.

### FRED

A detailed description of the FRED has been published previously. Briefly, the FRED is a braided self-expandable closed-cell flow diverter. The midsection, which encompasses 80% of its total length, has a dual-layer-design low-porosity inner mesh of higher pore attenuation (48 wires) and an outer stent with high porosity (16 wires). The inner mesh and the outer stent are attached by an interwoven double helix of tantalum strands. The FRED is currently available in 5 different diameters (3.5, 4.0, 4.5, 5.0, and 5.5 mm), recommended for vessel diameters from 3.0 to 5.5 mm, at working lengths from 7 to 56 mm.<sup>16-18</sup>

### Aneurysm Treatment

Endovascular treatment was performed with the patient under general anesthesia. All patients were treated with the FRED. FRED size was chosen according to the maximal diameter of the parent artery. FRED length covered the parent artery at least 3 mm proximal and distal to the blister-like aneurysm. Decisions for additional coiling (eg, due to aneurysm size) were at the discretion of the treating physician. Antiplatelet medication was given according to in-house protocols at each site.

### Imaging Data

Imaging was performed according to in-house protocols of each participating site. In general, patients were followed up at least once by DSA. Thereafter, aneurysms were followed up by DSA, flat panel CT angiography with intravenous contrast agent injection, or contrast-enhanced TOF-MRI. Local experienced neuro-interventionalists not involved in the aneurysm treatment reviewed the imaging data.

### Outcome Measures

End points for clinical safety were mRS 0–2 at 6 months after treatment and absence of major ipsilateral stroke or death. End points for efficacy were absence of rebleeding after treatment and complete angiographic occlusion according to the O'Kelly-Marotta classification (OKM) at 6 months after treatment.<sup>19</sup>

## RESULTS

### Study Subjects

In total, 30 patients with 30 ruptured blister-like aneurysms were included in this study. The mean age was 55.6 years, and 63.3% of the patients were female. Hunt and Hess grades and Fisher grades are shown in Table 1.

### Procedure

The median duration from onset to aneurysm treatment was 2 days. Treatment was delayed due to either delayed detection of the blister-like aneurysm and/or delayed referral of patients from other hospitals.

**Table 1: Baseline characteristics**

Characteristic	Value
Age (mean) (SD) (yr)	55.6 (12.9)
Female (No.) (%)	19 (63.3)
Hunt and Hess grade (No.) (%)	
1	13 (43.3)
2	4 (13.3)
3	5 (16.7)
4	6 (20.0)
5	2 (6.7)
Fisher grade (No.) (%)	
1	3 (10.0)
2	14 (46.7)
3	7 (23.3)
4	6 (20.0)
Extraventricular drain (No.) (%)	
Before aneurysm treatment	14 (46.7)
After aneurysm treatment	0 (0)
None	16 (53.3)

**Table 2: Aneurysm characteristics**

Characteristics	Value
Aneurysm rupture to treatment (No.) (%)	
0–1 day	13 (43.3)
2–7 days	8 (26.7)
>7 days	9 (30.0)
Aneurysm location (No.) (%)	
Internal carotid artery	19 (63.3)
Basilar artery	7 (23.3)
Vertebral artery	2 (6.7)
Anterior communicating artery	1 (3.3)
Posterior cerebral artery	1 (3.3)
Median aneurysm height (No.) (mm)	1.7
Median aneurysm diameter (No.) (mm)	2
Median diameter of parent vessel proximally (No.) (mm)	3.5
Median diameter parent vessel distally (No.) (mm)	3
Median diameter of FRED (No.) (mm)	4
Median length of FRED (No.) (mm)	13
Median No. of FREDs used	1
Aneurysms that were additionally coiled (No.) (%)	2 (6.7)

A ventricular drainage was placed in 14 patients (46.7%) before aneurysm treatment. No ventricular drainage was placed after flow diversion.

Aneurysm location was mostly the supraclinoid ICA (63.3%) and basilar artery (23.3%), with a median aneurysm size of 2 mm (Table 2). All aneurysms were initially treated with a single FRED flow diverter each. In 29 of 30 cases, the FRED was completely adherent to the wall of the parent artery immediately after deployment. In 1 case, the FRED opened; however, additional angioplasty was necessary to adhere the FRED completely to the vessel wall.

In 2 cases, the treating physician decided to place coils inside the blister-like aneurysm in addition to flow-diverter implantation because of the aneurysm size. The maximum aneurysm diameters in these 2 cases were 4 and 2 mm, respectively.

### Medication

Antiplatelet medication was given according to in-house protocols at each site. Preoperatively, dual-antiplatelet therapy with aspirin and clopidogrel was given in 8 patients (26.7%), and prasugrel was given in 4 patients (13.3%). Intraoperatively, 20



**Table 3: Aneurysm occlusion**

Occlusion Grading	End of the Procedure (n = 30)	At 6 Months (n = 26)	At 12 Months (n = 26)	Last Follow-Up <sup>a</sup> (n = 26)
OKM (No.) (%)				
D	10 (33.3)	21 (80.8)	22 (84.6)	24 (92.3)
C	4 (13.3)	3 (11.5)	3 (11.5)	2 (7.7)
B	16 (53.3)	2 (7.7)	1 (3.8)	0 (0)
A	0 (0)	0 (0)	0 (0)	0 (0)

<sup>a</sup> Median last follow-up was approximately 22 months (interquartile range, 12–37 months).

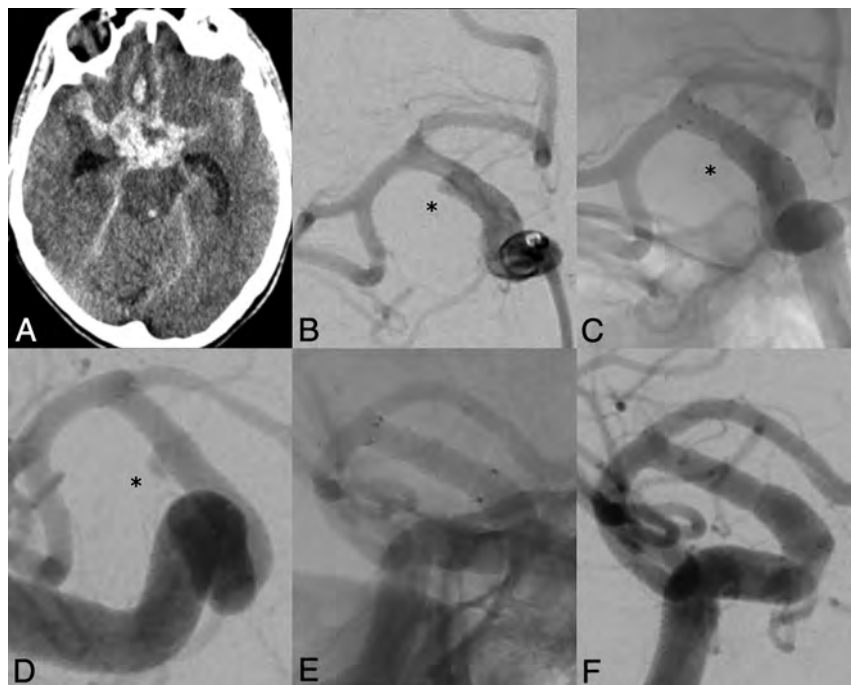


**FIGURE.** A, Nonenhanced head CT of a female patient in her 50s showing subarachnoid hemorrhage, Hunt and Hess grade 4, and Fisher grade 4. B, Angiography reveals a blister-like aneurysm of the right supraclinoid ICA with a maximum neck diameter of 3.3 mm. C, Angiographic result immediately after deployment of FRED 4.0 × 13 mm. D, Follow-up angiography at day 17 shows a residual aneurysm filling. E and F, Follow-up angiography at 3 months demonstrates complete aneurysm obliteration. mRS score at 3 months was 1.

patients (66.7%) received glycoprotein IIb/IIIa inhibitors, and 7 patients (23.3%) received heparin. Postoperatively, dual-antiplatelet therapy with aspirin and clopidogrel was given in 21 patients (70.0%); ticagrelor, in 5 patients (16.7%); and prasugrel, in 4 patients (13.3%). Patients continued antiplatelet therapy according to the standard of care in the respective hospital for at least 6 months.

### Safety

Twenty-three patients (76.7%) achieved mRS 0–2 after 6 months (Online Table). Two patients died due to pneumonia, and 2 patients died due to SAH-related delayed cerebral ischemia.

Procedure-related complications occurred in 4 cases: One patient with a basilar blister-like aneurysm had a major stroke after flow diversion. MR imaging revealed a left paramedian pontine infarction indicating a perforator stroke despite premedication of the patient with tirofiban and heparin before deployment of the FRED.

Another patient with a blister-like aneurysm of the ICA had a minor stroke due to distal cerebral emboli. Both patients received tirofiban during the procedure and were on dual-antiplatelet therapy after treatment. They were discharged with mRS 4, and both recovered to mRS 2 one year after treatment. In 1 case, there was partial thrombus formation within the FRED. However, this was not hemodynamically relevant, and the FRED was patent on follow-up images. The patient received tirofiban during the procedure and ticagrelor thereafter. There was 1 case of retroperitoneal hematoma requiring medical management.

In 1 patient, asymptomatic FRED occlusion occurred, which was diagnosed during a routine follow-up 19 months after aneurysm treatment. In this case, aspirin had been discontinued 12 months before.

There was no case of recurrent hemorrhage before or after flow diversion.

### Efficacy

Complete aneurysm obliteration (OKM D) at the end of the procedure was achieved in 10 patients (33.3%).

Follow-up imaging was not possible in 4 patients due to death as described above. Except for 1 patient who was followed up only once by flat panel CT with intravenous contrast agent injection, all patients underwent DSA at least once.

Follow-up imaging was available in 26 patients. Six months after aneurysm treatment, 21 patients (80.8%)

achieved complete obliteration (OKM D). A residual neck (OKM C) was visible in 3 patients (11.5%), and a residual aneurysm (OKM B) was visible in 2 patients (7.7%). In the final follow-up (median, 22 months), complete obliteration was observed in 24 patients (92.3%) (Table 3).

One patient required additional implantation of another FRED 10 days after the initial treatment due to aneurysm growth. Another patient required implantation of a second FRED 2 years after initial treatment because the blister-like aneurysm was not sufficiently obliterated. No complications occurred in either case, and the aneurysms were completely obliterated at follow-up imaging.

### DISCUSSION

The present retrospective study adds evidence that treatment of ruptured blister-like aneurysms with the FRED is safe and effective. Complete aneurysm obliteration with the FRED was achieved in 80% at 6 months and in 92% in the final follow-up.

Most important, there was no case of rebleeding after FRED implantation. About 77% achieved mRS 0–2 at 6 months. Major stroke or death occurred in 17%.

The results of the present study with the FRED are similar to those of Mokin et al,<sup>15</sup> who analyzed treatment of ruptured blister-like aneurysms with the PED. Mokin et al reported complete aneurysm obliteration in 87.5% on follow-up angiograms in patients treated with the PED. Furthermore, they reported that 68% of their patients achieved good clinical outcome at 3 months. The results of the present study suggest that the FRED and PED show similar safety and efficacy in the treatment of blister-like aneurysms. While the PED is a 48-strand braided mesh, the FRED is a dual-layer stent with an inner stent consisting of 48 wires and an additional outer stent with 16 wires serving as a scaffold for the inner stent. This design might potentially increase aneurysm obliteration after flow diversion with the FRED.<sup>18,20</sup> However, there are currently no data supporting this hypothesis.

For many years, treatment of blister-like aneurysms has been technically challenging for both clipping and coiling. Today, flow-diverter implantation allows the endovascular treatment of blister-like aneurysms just as in wide-neck and fusiform aneurysms.<sup>7,21</sup> The mesh design of flow diverters alters blood flow into the aneurysm and induces a thrombosis within the aneurysm (Figure).<sup>4</sup>

There are often concerns regarding stent or flow-diverter deployment in patients with aneurysmal SAH because it requires antiplatelet and/or anticoagulation treatment to avoid thrombosis.<sup>7</sup> Antiplatelet therapy, however, increases the risk of intracranial rebleeding. There was no rebleeding in any cases in this study, though. Mokin et al<sup>15</sup> reported that 1 of 49 patients had delayed aneurysmal rerupture. Mazur et al<sup>22</sup> and Nerva et al<sup>23</sup> each reported 1 case of delayed rebleeding after PED deployment in a patient with a ruptured blister-like aneurysm. There are, however, case studies by Ryan et al<sup>14</sup> ( $n=13$ ), Linfante et al<sup>12</sup> ( $n=10$ ), Capocci et al<sup>24</sup> ( $n=8$ ), Chalouhi et al,<sup>10</sup> ( $n=8$ ), Cerejo et al ( $n=8$ ),<sup>25</sup> Çinar et al ( $n=7$ ),<sup>26</sup> and Hu et al<sup>11</sup> ( $n=3$ ) reporting no rebleeding after flow-diverter implantation in patients with ruptured blister-like aneurysms. Ryan et al<sup>14</sup> ( $n=13$ ) reported 1 case of rebleeding, however, due to an unrecognized additional aneurysm. The data of the present study and previous studies show that the risk of rebleeding after flow-diverter implantation in blister-like aneurysms is low.

There was 1 case (3.3%) of delayed asymptomatic in-stent thrombosis in the present study. Thrombosis was diagnosed 19 months after aneurysm treatment during a routine follow-up. In this case, aspirin had been discontinued 12 months before. Thrombosis might have been prevented by a longer period of antiplatelet medication. Mokin et al<sup>15</sup> reported 2 cases of intraprocedural in-stent thrombosis, 2 cases of intraprocedural thrombosis in an M3 segment, 1 case of delayed asymptomatic in-stent stenosis, and 1 case of delayed asymptomatic in-stent thrombosis. These data suggest that the risk of thrombosis might be higher than that of rebleeding. Sufficient antiplatelet therapy is therefore mandatory.

This study has several limitations mostly due to its retrospective multicenter design with a potential selection and reporting bias. Aneurysm treatment and medication differed at each

participating site. Also imaging data and clinical outcome were not reviewed by a central core laboratory.

## CONCLUSIONS

This study adds evidence that treatment of blister-like aneurysms with the FRED is safe and effective. Outcome results are similar to those of the PED.

Disclosures: Markus A. Möhlenbruch—UNRELATED: Consultancy: Medtronic, MicroVention, Stryker\*; Grants/Grants Pending: Balt, Medtronic, MicroVention, Stryker\*; Payment for Lectures Including Service on Speakers Bureaus: Medtronic, MicroVention, Stryker.\* Christoph J. Griessenauer—UNRELATED: Consultancy: Stryker; Employment: Geisinger. Martin Bendszus—UNRELATED: Board Membership: Data and Safety Monitoring Board for Vascular Dynamics, Boehringer; Consultancy: Codman, Braun; Grants/Grants Pending: DFG, EU, Hopp Foundation, Novartis, Siemens, Stryker, Guerbet\*; Payment for Lectures Including Service on Speakers Bureaus: Novartis, Teva Pharmaceutical Industries, Codman, Guerbet, Merck, Grifols, Bayer. Naci Kocer—UNRELATED: Other: proctoring and consultant agreement with MicroVention. Monika Killer-Oberpalzer—RELATED: Grant: research grant from MicroVention/Terumo\*; \*Money paid to the institution.

## REFERENCES

- Ishikawa T, Nakamura N, Houkin K, et al. **Pathological consideration of a “blister-like” aneurysm at the superior wall of the internal carotid artery: case report.** *Neurosurgery* 1997;40:403–06 CrossRef Medline
- Abe M, Tabuchi K, Yokoyama H, et al. **Blood blister-like aneurysms of the internal carotid artery.** *J Neurosurg* 1998;89:419–24 CrossRef Medline
- Mizutani T, Miki Y, Kojima H, et al. **Proposed classification of non-atherosclerotic cerebral fusiform and dissecting aneurysms.** *Neurosurgery* 1999;45:253–59 CrossRef Medline
- Szmuda T, Sloniewski P, Waszak PM, et al. **Towards a new treatment paradigm for ruptured blood blister-like aneurysms of the internal carotid artery? A rapid systematic review.** *J Neurointerv Surg* 2016;8:488–94 CrossRef Medline
- Peschillo S, Miscusi M, Caporlingua A, et al. **Blister-like aneurysms in atypical locations: a single-center experience and comprehensive literature review.** *World Neurosurg* 2015;84:1070–79 CrossRef Medline
- Peschillo S, Cannizzaro D, Caporlingua A, et al. **A systematic review and meta-analysis of treatment and outcome of blister-like aneurysms.** *AJNR Am J Neuroradiol* 2016;37:856–61 CrossRef Medline
- Peitz GW, Sy CA, Grandhi R. **Endovascular treatment of blister aneurysms.** *Neurosurg Focus* 2017;42:E12 CrossRef Medline
- Rouchaud A, Brinjikji W, Cloft HJ, et al. **Endovascular treatment of ruptured blister-like aneurysms: a systematic review and meta-analysis with focus on deconstructive versus reconstructive and flow-diverter treatments.** *AJNR Am J Neuroradiol* 2015;36:2331–39 CrossRef Medline
- Zhu D, Yan Y, Zhao P, et al. **Safety and efficacy of flow diverter treatment for blood blister-like aneurysm: a systematic review and meta-analysis.** *World Neurosurg* 2018;118:e79–86 CrossRef Medline
- Chalouhi N, Zanaty M, Tjoumakaris S, et al. **Treatment of blister-like aneurysms with the Pipeline Embolization Device.** *Neurosurgery* 2014;74:527–32 CrossRef Medline
- Hu YC, Chugh C, Mehta H, et al. **Early angiographic occlusion of ruptured blister aneurysms of the internal carotid artery using the Pipeline Embolization Device as a primary treatment option.** *J Neurointerv Surg* 2014;6:740–43 CrossRef Medline
- Linfante I, Mayich M, Sonig A, et al. **Flow diversion with Pipeline Embolic Device as treatment of subarachnoid hemorrhage secondary to blister aneurysms: dual-center experience and review of the literature.** *J Neurointerv Surg* 2017;9:29–33 CrossRef Medline
- Yoon JW, Siddiqui AH, Dumont TM, et al. Endovascular Neurosurgery Research Group. **Feasibility and safety of Pipeline Embolization Device in patients with ruptured carotid blister aneurysms.** *Neurosurgery* 2014;75:419–29 CrossRef Medline

14. Ryan RW, Khan AS, Barco R, et al. **Pipeline Flow Diversion of ruptured blister aneurysms of the supraclinoid carotid artery using a single-device strategy.** *Neurosurg Focus* 2017;42:E11 CrossRef Medline
15. Mokin M, China A, Primiani CT, et al. **Treatment of blood blister aneurysms of the internal carotid artery with flow diversion.** *J Neurointerv Surg* 2018;10:1074–78 CrossRef Medline
16. Killer-Oberpfalzer M, Kocer N, Griessenauer CJ, et al. **European multicenter study for the evaluation of a dual-layer flow-diverting stent for treatment of wide-neck intracranial aneurysms: the European Flow-Redirection Intraluminal Device Study.** *AJNR Am J Neuroradiol* 2018;39:841–47 CrossRef Medline
17. Kocer N, Islak C, Kizilkilic O, et al. **Flow Redirection Endoluminal Device in treatment of cerebral aneurysms: initial experience with short-term follow-up results: clinical article.** *J Neurosurg* 2014;120:1158–71 CrossRef Medline
18. Möhlenbruch MA, Herweh C, Jestaedt L, et al. **The FRED Flow-Diverter Stent for intracranial aneurysms: clinical study to assess safety and efficacy.** *AJNR Am J Neuroradiol* 2015;36:1155–61 CrossRef Medline
19. O'Kelly CJ, Krings T, Fiorella D, et al. **A novel grading scale for the angiographic assessment of intracranial aneurysms treated using flow diverting stents.** *Interv Neuroradiol* 2010;16:133–37 CrossRef Medline
20. Griessenauer CJ, Thomas AJ, Enriquez-Marulanda A, et al. **Comparison of Pipeline Embolization Device and Flow Re-Direction Endoluminal Device flow diverters for internal carotid artery aneurysms: a propensity score-matched cohort study.** *Neurosurgery* 2019;85:E249–55 CrossRef Medline
21. Meling TR. **What are the treatment options for blister-like aneurysms?** *Neurosurg Rev* 2017;40:587–93 CrossRef Medline
22. Mazur MD, Taussky P, MacDonald JD, et al. **Rerupture of a blister aneurysm after treatment with a single flow-diverting stent.** *Neurosurgery* 2016;79:E634–38 CrossRef Medline
23. Nerva JD, Morton RP, Levitt MR, et al. **Pipeline Embolization Device as primary treatment for blister aneurysms and iatrogenic pseudoaneurysms of the internal carotid artery.** *J Neurointerv Surg* 2015;7:210–16 CrossRef Medline
24. Capocci R, Shotar E, Di Maria F, et al. **Delayed treatment ( $\geq 5$  days) by flow diversion of ruptured blister-like cerebral aneurysms.** *Clin Neuroradiol* 2020;30:287–96 CrossRef Medline
25. Cerejo R, Bain M, John S, et al. **Flow diverter treatment of cerebral blister aneurysms.** *Neuroradiology* 2017;59:1285–90 CrossRef Medline
26. Çinar C, Oran İ, Bozkaya H, et al. **Endovascular treatment of ruptured blister-like aneurysms with special reference to the flow-diverting strategy.** *Neuroradiology* 2013;55:441–47 CrossRef Medline



# Clinical Presentation and Imaging Findings of Patients with Dural Arteriovenous Fistulas with an Angiographic Pseudophlebitic Pattern

W. Brinjikji, H.J. Cloft, and G. Lanzino

## ABSTRACT

**BACKGROUND AND PURPOSE:** The pseudophlebitic pattern is an increasingly recognized angiographic manifestation of chronic venous congestion in the setting of a cranial dural arteriovenous fistula. We sought to study the clinical and radiologic manifestations of patients with the pseudophlebitic pattern.

**MATERIALS AND METHODS:** We retrospectively reviewed a cohort of patients with dural arteriovenous fistulas evaluated at our institution from 2008 to 2020. Angiograms were reviewed to classify dural arteriovenous fistulas and document the presence or absence of a pseudophlebitic pattern, defined as the presence of serpiginous and tortuous collateral, bridging, and cortical veins with an associated delay in circulation time of the normal brain. We then studied the association between the pseudophlebitic pattern and clinical presentation and MR imaging findings.

**RESULTS:** Two hundred one patients were included. Patients with a pseudophlebitic pattern had more hemorrhage (22.8% versus 8.4%,  $P = .005$ ), gait changes and ataxia (6.0% versus 0.0%,  $P = 0.002$ ), cognitive changes (6.9% versus 1.4%,  $P = .04$ ), and seizures (8.6% versus 2.1%,  $P = .03$ ). On MR imaging, the pseudophlebitic pattern was associated with higher rates of cerebral edema (70.9% versus 2.9%,  $P < .0001$ ), chronic hemosiderin deposition and microhemorrhage (17.3% versus 2.2%,  $P = .0002$ ), and dilated transmedullary veins (47.1% versus 0.0%,  $P < .0001$ ). When we considered only patients with malignant fistulas, there was no difference in hemorrhage at presentation between the 2 groups (22.6% versus 22.8%,  $P = .99$ ). Patients with a pseudophlebitic pattern did have higher rates of nonhemorrhagic neurologic deficits (24.1% versus 9.4%,  $P = .03$ ).

**CONCLUSIONS:** The pseudophlebitic pattern was associated with high rates of brain parenchymal changes and neurologic symptoms in this cohort of patients with dural arteriovenous fistulas.

**ABBREVIATION:** dAVF = dural arteriovenous fistula

It is well-known that the primary determinant of the natural history of a cranial dural arteriovenous fistula (dAVF) is the pattern of venous drainage as lesions that drain directly into leptomeningeal cortical veins have an annual risk of nonhemorrhagic deficit of 7% and an annual risk of intracranial hemorrhage of 8% compared with rates of close to 0% for lesions with antegrade venous drainage into the dural venous sinuses.<sup>1</sup> One factor that has not been examined as thoroughly as the presence of retrograde leptomeningeal venous drainage is the presence of a pseudophlebitic pattern on conventional angiography.<sup>2–4</sup> A pseudophlebitic pattern was first described in the setting of dAVFs by

Willinsky et al<sup>4</sup> to characterize the tortuous and engorged venous veins identified on the venous phase of the brain circulation (ie, not during the venous phase of the dAVF itself). These dilated serpiginous veins are the result of chronic and severe venous congestion and have been associated with high rates of nonhemorrhagic neurologic deficits as well as hemorrhage itself.

To better understand the significance of the pseudophlebitic pattern on conventional angiography, we performed a retrospective review of our institutional series of dAVFs. The aim of this study was to characterize the brain MR imaging findings, demographics, and clinical presentation of patients with dAVFs who have a pseudophlebitic pattern on conventional angiography.

Received June 15, 2020; accepted after revision August 5.

From the Departments of Radiology and Neurosurgery, Mayo Clinic, Rochester, Minnesota.

Please address correspondence to Waleed Brinjikji, MD, Mayo Clinic, Department of Radiology, 200 1st St SW, Rochester, MN 55905; e-mail: Brinjikji.waleed@mayo.edu; @wbrinjikji  
<http://dx.doi.org/10.3174/ajnr.A6811>

## MATERIALS AND METHODS

### Patient Population

Following institutional review board approval, we identified all patients with cranial dAVFs seen at our institution from 2008 to

2020 as part of a prospectively maintained data base. All included patients had a conventional cerebral angiogram for evaluation of their dural arteriovenous fistula and underwent clinical evaluation by a neurologist and neurosurgeon. Patients who did not consent to the use of their medical records for research were excluded from this study. Patients who did not undergo conventional angiography examining the bilateral internal carotid arteries and posterior circulation were excluded.

### Data Collection

All charts were reviewed to collect information on demographics (age and sex) and clinical presentation. For clinical presentation, we made note of the initial symptoms that the patient was manifesting at the time of diagnosis of the dural arteriovenous fistula. Clinical symptoms were categorized as the following: 1) hemorrhage, 2) incidental, 3) bruit/tinnitus, 4) ocular or visual, and 5) myelopathic symptoms, and 6) ataxia, 7) headache, 8) hydrocephalus, 9) seizures, and 10) other (including dementia and other cognitive defects).

### Review of Angiograms

Angiograms were reviewed by an endovascular neurosurgeon and interventional neuroradiologist. We collected the following data on angioarchitecture: 1) Borden classification, 2) Cognard classification, 3) fistula location, 4) presence of venous dilation, 5) presence of a venous varix, 6) presence of the pseudophlebitic pattern, and 7) draining vein stenosis. The presence of the pseudophlebitic pattern was based on the analysis of the venous drainage of the cerebellar or cerebral hemispheres and was defined by the presence of serpiginous and tortuous collateral, bridging, and cortical veins with an associated delay in circulation time. Venous dilation was defined as greater dilation of the cerebral veins than usual. Venous varix was defined as a venous dilation with a diameter more than twice as large as that of the veins proximal and distal to the varix. Fistula location was categorized as cavernous sinus, transverse sigmoid sinus, tentorial, anterior cranial fossa, middle cranial fossa, foramen magnum, hypoglossal/

jugular foramen, convexity, superior sagittal sinus, extensive, and multiple.<sup>4,5</sup> Tentorial dural arteriovenous fistulas were categorized according to a previously defined classification system.<sup>6</sup>

### Cross-Sectional Imaging Review

All patients with a brain MR imaging underwent review by a diagnostic and interventional neuroradiologist. In general, brain MRIs included T2, T2/FLAIR, sagittal T1, axial T1 postcontrast, and T2\*-weighted imaging (either gradient recalled-echo or SWI) and were performed at 1.5T or 3T. Images were reviewed for the presence of the following: 1) cerebral edema, 2) chronic hemosiderin or microhemorrhage on T2\* images, 3) venous infarction, 4) dilated transmedullary veins on SWI or postcontrast T1-weighted imaging, 5) sinus thrombosis, and 6) cortical venous reflux on 3D-TOF-MRA. All patients underwent imaging on a 1.5 or 3T scanner. A variety of scanners were used due to the long time-frame of this study.

### Statistical Analysis

Patients were divided into pseudophlebitic and nonpseudophlebitic groups. Baseline characteristics, clinical presentation, and angioarchitectural and cross-sectional imaging findings were compared across groups. A  $\chi^2$  test was used for categorical variables, and a Student *t* test was used to compare continuous variables. All statistical analyses were performed using JMP 14.0 (SAS Institute).

## RESULTS

### Patient Population

A total of 201 patients were included in this study. A pseudophlebitic pattern was seen in 58 patients (28.9%), and a nonpseudophlebitic pattern was seen in 143 patients (71.1%). The mean patient age was  $59.1 \pm 13.7$  years; 104 patients (51.7%) were men and 97 patients (48.3%) were women. The 3 most common presenting symptoms were tinnitus/bruit (86 patients, 42.8%), visual/ocular symptoms (37 patients, 18.4%), and hemorrhage (25 patients, 12.5%). These data are summarized in Table 1. Case examples are shown in Figs 1–3.

### Baseline Characteristics

Overall, there was no difference in mean age in the nonpseudophlebitic and pseudophlebitic groups ( $P = .32$ ). There was a higher proportion of men in the pseudophlebitic group than in the nonpseudophlebitic group (69.0% versus 44.8%,  $P = .002$ ). Regarding clinical presentation, patients with a pseudophlebitic pattern were more likely to present with hemorrhage (22.8% versus 8.4%,  $P = .005$ ), gait changes and ataxia (6.0% versus 0.0%,  $P = 0.002$ ), cognitive changes (6.9% versus 1.4%,  $P = .04$ ), and seizure (8.6% versus 2.1%,  $P = .03$ ). Patients in the nonpseudophlebitic group were more likely to present with tinnitus/bruit (53.9% versus 15.5%,  $P < .0001$ ).

**Table 1: Demographics and clinical presentation**

	Overall	Nonpseudophlebitic	Pseudophlebitic	P
No.	201	143 (71.1)	58 (28.9)	—
Mean age (SD) (yr)	59.1 (13.7)	60.5 (13.5)	58.4 (13.8)	.32
Sex				
Male (No.) (%)	104 (51.7)	64 (44.8)	40 (69.0)	
Female (No.) (%)	97 (48.3)	79 (55.2)	18 (31.0)	.002
Clinical presentation (No.) (%)				
Hemorrhage	25 (12.5)	12 (8.4)	13 (22.8)	.005
Incidental	22 (11.0)	18 (12.6)	4 (6.9)	.24
Headache	23 (11.4)	15 (10.5)	8 (13.8)	.51
Visual/ocular symptoms	37 (18.4)	29 (20.3)	8 (13.8)	.28
Tinnitus/bruit	86 (42.8)	77 (53.9)	9 (15.5)	<.0001
Cognitive changes	6 (3.0)	2 (1.4)	4 (6.9)	.04
Gait changes/ataxia	4 (2.0)	0 (0.0)	4 (6.0)	.002
Hydrocephalus	1 (0.5)	0 (0.0)	1 (1.7)	.11
Seizure	8 (4.0)	3 (2.1)	5 (8.6)	.03
Myelopathy	7 (3.5)	3 (2.1)	4 (6.0)	.12
Other	17 (8.5)	6 (4.2)	11 (18.9)	.0001

**Note:**—SD indicates standard deviation; yr, year; No., number; %, percentage.

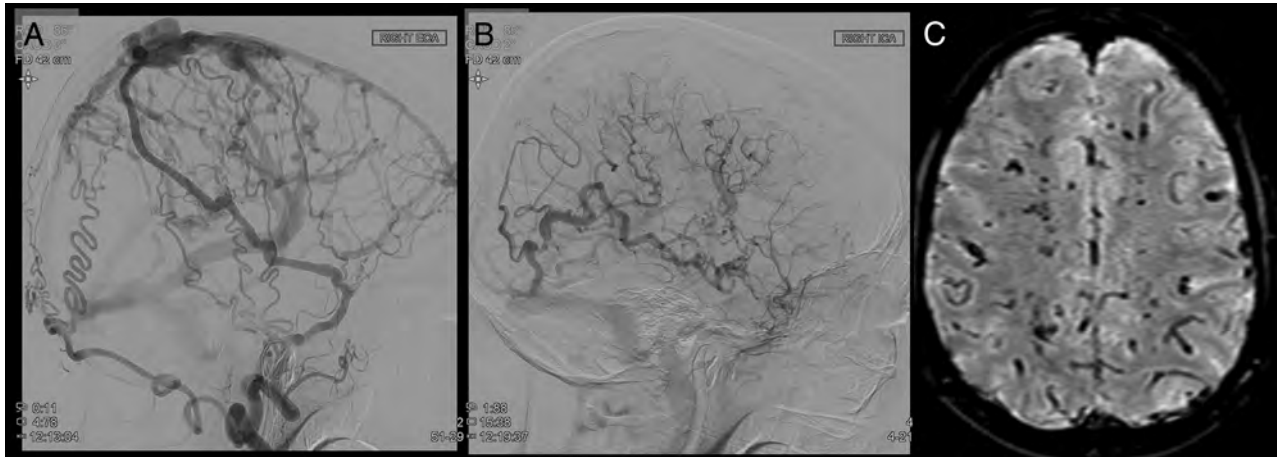


**FIG 1.** Pseudophlebitic pattern in a superior sagittal sinus fistula in a patient presenting with voice hoarseness. A, Right external carotid artery (ECA) injection shows the superior sagittal sinus fistula with reflux into the cortical veins. B, Right ICA cerebral angiogram shows dilated corkscrew veins in the right cerebral hemisphere during the parenchymal venous phase. There is stagnation of contrast due to the high venous pressure. C, SWI shows dilated T2-hypointense transmedullary veins reflective of venous hypertension.

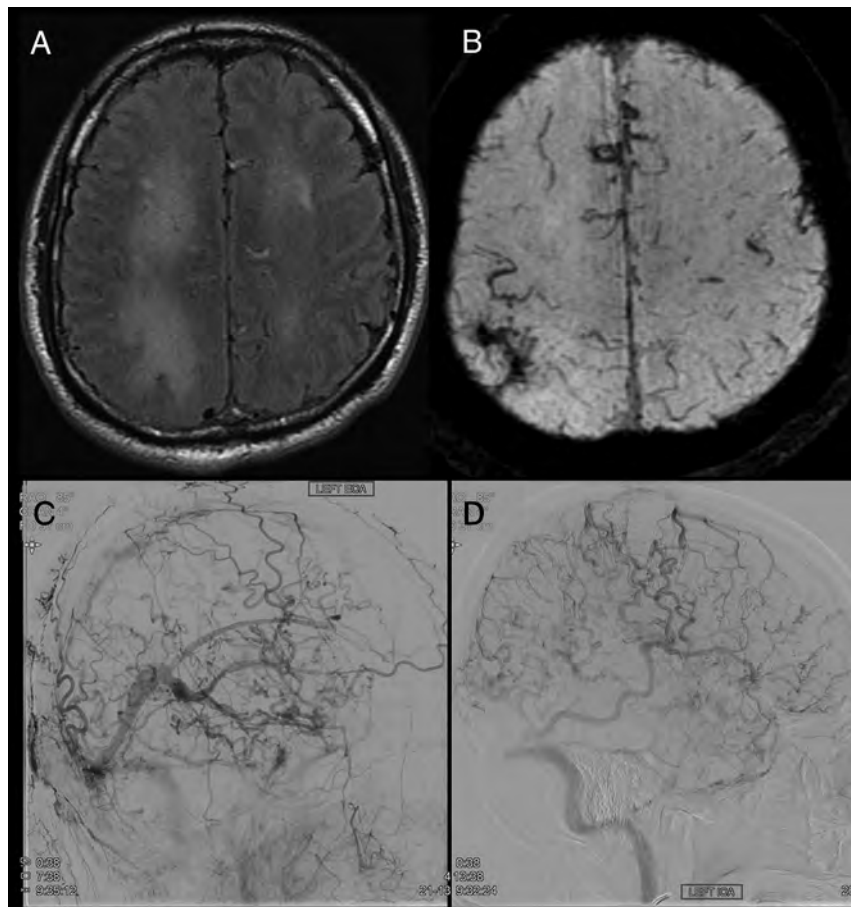


**FIG 2.** A pseudophlebitic pattern in a patient with an extensive dural arteriovenous fistula presenting with cognitive decline. A, FLAIR imaging shows parenchymal FLAIR signal in the bilateral cerebral hemispheres, right greater than left. B, SWI shows a chronic hemorrhagic in the right parietal lobe and some dilated transmedullary veins in the left hemisphere. C, Left external carotid artery (ECA) injection shows the superior sagittal sinus and torcular fistulas with reflux into the deep venous system and parenchymal veins. D, Left ICA injection shows dilated corkscrew parenchymal cerebral veins, which have some stagnation consistent with a pseudophlebitic pattern.

### Angiographic Findings and dAVF Characteristics

There was a significant difference in the location of fistulas between groups ( $P < .0001$ ). Patients with a nonpseudophlebitic pattern were more likely to have fistulas in the transverse-sigmoid sinuses (40.6% versus 8.6%,  $P < .0001$ ) and cavernous sinus (16.1% versus 6.9%,  $P < .0001$ ). Meanwhile, patients with a pseudophlebitic pattern were more likely to have the fistulas located in the tentorium (51.7% versus 16.8%,  $P < .0001$ ) and superior sagittal sinus (8.6% versus 0.7%,  $P = .003$ ).

Patients with a pseudophlebitic pattern were also more likely to have malignant fistulas with Borden II/III rates of 100.0% compared with 43.3% in the nonpseudophlebitic group ( $P < .0001$ ). Dilation of the draining vein was more common in the pseudophlebitic group (72.4% versus 23.8%,  $P < .0001$ ) as was the presence of a venous varix (63.8% versus 14.0%,  $P < .0001$ ) and draining vein stenosis (44.8% versus 15.4%,  $P < .0001$ ). These data are summarized in Table 2.

### MR Imaging Findings

A total of 191 patients had a preoperative MR imaging (136 in the nonpseudophlebitic group and 55 in the pseudophlebitic group). Cerebral edema was found in 70.9% of the pseudophlebitic group compared with 2.9% of the



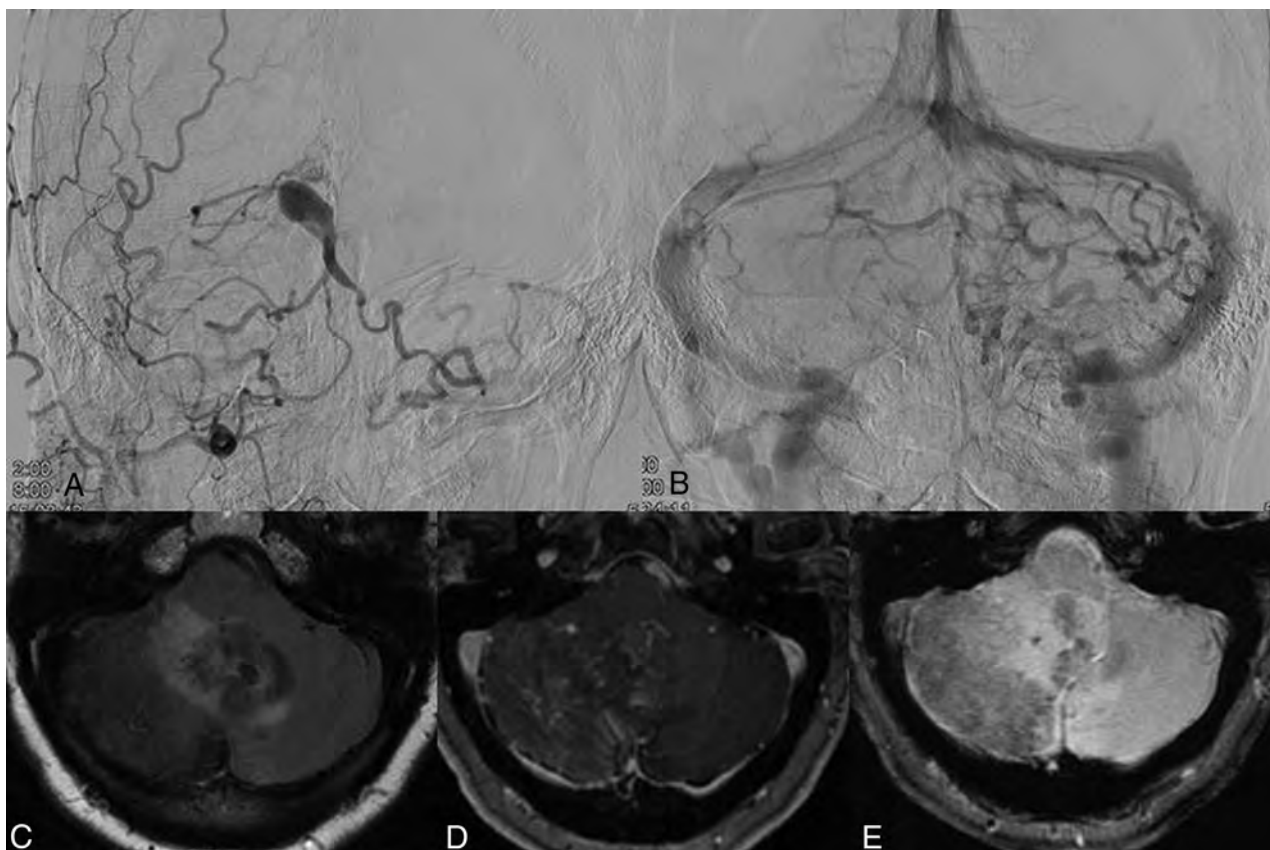


**FIG 3.** Pseudophlebitic pattern in a patient with a tentorial dural arteriovenous fistula presenting with ataxia. *A*, Right external carotid artery angiogram shows a tentorial dural arteriovenous fistula with reflux into the bilateral cerebellar hemispheres. *B*, Parenchymal venous phase of a left vertebral artery injection shows a pseudophlebitic pattern of the cerebellar parenchymal veins. *C*, FLAIR MR imaging shows edema in the bilateral cerebellar hemispheres and vermis. *D*, Postcontrast MR imaging shows dilated transmedullary veins in the right cerebellar hemisphere and vermis. *E*, Gradient recalled-echo MR imaging shows chronic hemosiderin deposition in the right cerebellar hemisphere.

nonpseudophlebitic group ( $P < .0001$ ). Chronic hemosiderin deposition and microhemorrhage were found in 17.3% of the pseudophlebitic group compared with 2.2% of the nonpseudophlebitic group ( $P = .0002$ ). Dilated transmedullary veins on SWI or contrast-enhanced T1-weighted images were found in 47.1% of the pseudophlebitic group compared with 0.0% of the nonpseudophlebitic group ( $P < .0001$ ). These data are summarized in Table 3.

#### **Impact of Pseudophlebitic Pattern on Malignant Fistulas**

To determine whether the pseudophlebitic pattern was independently associated with a higher rate of neurologic symptoms and MR imaging findings, we performed a subgroup analysis of patients with malignant fistulas (ie, Borden II/III or cortical venous reflux for cavernous sinus fistulas). A total of 110 patients had malignant fistulas (53 nonpseudophlebitic and 57 pseudophlebitic). There was no difference in hemorrhage at presentation between the 2 groups (22.6% versus 22.8%,  $P = .99$ ). Patients with a pseudophlebitic pattern did have higher rates of nonhemorrhagic neurologic deficits (24.1% versus 9.4%,  $P = .03$ ). Regarding imaging findings, among patients with malignant fistulas, cerebral edema was more prevalent in patients with a pseudophlebitic pattern (70.9% versus 7.6%,  $P < .0001$ ) as was chronic hemosiderin deposition (17.3% versus 3.9%,  $P = .03$ ) and dilated transmedullary veins (47.1% versus 0.0%,  $P < .0001$ ).

#### **DISCUSSION**

Our study examining the association between the pseudophlebitic pattern on global angiography and clinical symptoms and imaging findings demonstrated a number of interesting findings. First, the presence of a pseudophlebitic pattern was associated with a significantly higher rate of hemorrhage and other nonhemorrhagic neurologic deficits such as cognitive changes, gait dysfunction, and seizure. Regarding fistula classification, we found that the locations most commonly associated with the presence of a pseudophlebitic pattern were tentorial fistulas (>50%) and superior sagittal sinus fistulas (nearly 10%). As expected, a pseudophlebitic pattern was seen exclusively in malignant fistulas as defined by the Borden and Cognard classification scales. A number of cross-sectional MR imaging findings were found to be independently associated with the presence of a pseudophlebitic pattern, including cerebral edema, chronic hemosiderin deposition, and dilated transmedullary veins. These findings are important because they highlight the pseudophlebitic pattern being a reliable prognostic marker for a symptomatic and malignant fistula.

The pseudophlebitic pattern was first described in the setting of cranial dural arteriovenous fistulas by Willinsky et al.<sup>4</sup> In their series of 122 patients, a pseudophlebitic pattern was seen in 51 patients, (42%) most of whom presented with hemorrhage or nonhemorrhagic neurologic deficits. Similar to our study, Willinsky et al found

**Table 2: Angiographic findings**

	Overall	Nonpseudophlebitic	Pseudophlebitic	P
Fistula location				
Transverse sigmoid	63 (31.3)	58 (40.6)	5 (8.6)	<.0001
Cavernous sinus	27 (13.4)	23 (16.1)	4 (6.9)	
Tentorial	54 (26.9)	24 (16.8)	30 (51.7)	
Foramen magnum	7 (3.5)	4 (2.8)	3 (5.2)	
Superior sagittal sinus	6 (3.0)	1 (0.7)	5 (8.6)	
Anterior cranial fossa	5 (2.5)	5 (3.5)	0 (0.0)	
Extensive	1 (0.5)	1 (0.7)	0 (0.0)	
Multiple	9 (4.5)	4 (2.8)	5 (8.6)	
Hypoglossal/jugular foramen	16 (8.0)	13 (9.1)	3 (5.2)	
Convexity	7 (3.5)	5 (3.5)	2 (3.5)	
Middle cranial fossa	2 (1.0)	1 (0.7)	1 (1.7)	
Other	4 (2.0)	4 (2.8)	0 (0.0)	
Tentorial location				
Superior petrosal sinus	8 (14.6)	3 (12.5)	5 (16.1)	.49
Straight sinus	1 (1.8)	0 (0.0)	1 (3.2)	
Galenic	11 (20.0)	4 (16.7)	7 (22.6)	
Tentorial sinus	25 (45.5)	14 (58.3)	11 (35.5)	
Torcular	10 (18.2)	3 (12.5)	7 (22.6)	
Borden classification (non-cavernous sinus)				
I	68 (33.8)	68 (56.7)	0 (0.0)	<.0001
II	27	13 (10.8)	14 (25.9)	
III	79	39 (32.5)	40 (74.1)	
Cognard classification (non-cavernous sinus)				
I	52	52 (43.3)	0 (0.0)	<.0001
Ila	16	16 (13.3)	0 (0.0)	
Ilb	6	5 (4.2)	1 (1.9)	
Ila+b	22	7 (5.8)	15 (27.8)	
III	22	17 (14.2)	5 (9.3)	
IV	52	22 (18.3)	30 (55.6)	
V	4	1 (0.8)	3 (5.6)	
Venous dilation	76 (37.8)	34 (23.8)	42 (72.4)	<.0001
Venous varix	57 (28.4)	20 (14.0)	37 (63.8)	<.0001
Draining vein stenosis	48 (23.9)	22 (15.4)	26 (44.8)	<.0001

**Table 3: Cross-sectional imaging findings**

	Overall	Nonpseudophlebitic	Pseudophlebitic	P
Cerebral edema	43 (22.5)	4 (2.9)	39 (70.9)	<.0001
Chronic hemosiderin deposition/microhemorrhage	12 (6.4)	3 (2.2)	9 (17.3)	.0002
Venous infarct	2 (1.1)	1 (0.7)	1 (1.9)	.49
Dilated transmedullary veins on SWI or CE T1	24 (12.9)	0 (0.0)	24 (47.1)	<.0001
Sinus thrombosis	14 (7.4)	8 (5.9)	6 (11.1)	.21
Cortical venous reflux on 3D-TOF	68 (38.9)	32 (24.6)	46 (80.0)	<.0001

**Note:**—CE indicates contrast-enhanced.

that most of the lesions associated with a pseudophlebitic pattern were associated with tentorial or superior sagittal sinus fistulas. Fifty-two patients in their series also had brain MRIs, of whom 20% had cerebral edema, and 90% of those with cerebral edema had a pseudophlebitic pattern. Our study adds to this study in that we report more extensively on the MR imaging findings of 191 patients, 95% of the patients included in this study.

Our study highlights additional imaging findings that are unique to those with a pseudophlebitic pattern. First, we found that the prevalence of cerebral edema among patients with a pseudophlebitic pattern was 71%, significantly higher than the 20% reported in previous studies.<sup>4</sup> This prevalence is likely a function of improved imaging techniques (ie, increased use of

FLAIR, routine 1.5T and 3T MR imaging, and so forth). Cerebral edema in these patients is likely a reflection of diffuse venous congestion (congestive edema) resulting in fluid retention in the interstitial tissues. We found that 17% of patients had chronic hemosiderin deposition or microhemorrhage on T2\*-weighted imaging, which is likely a function of tiny perivenular microhemorrhages in the setting of severe venous hypertension. Dilated transmedullary veins on SWI or contrast-enhanced T1 imaging were found in nearly 50% of patients with a pseudophlebitic pattern, a unique association, likely a function of rerouting of normal cerebral venous drainage via transmedullary venous pathways.<sup>7</sup> We did not find any association between venous sinus narrowing or thrombosis and the presence of a pseudophlebitic

pattern. This finding is likely because in most cases of dural venous sinus thrombosis-associated dAVFs, the lesions are located in the transverse and sigmoid sinuses and there are multiple venous egress pathways available for the draining cortical veins. Tentorial and ethmoidal dAVFs are less likely to be associated with venous sinus thrombosis or stenosis.

The pseudophlebitic pattern was not independently associated with hemorrhage but was independently associated with the presence of nonhemorrhagic neurologic deficits. Previous studies have suggested that the pseudophlebitic pattern is a risk factor for hemorrhage, but they did not stratify lesions by the presence or absence of retrograde leptomeningeal venous drainage.<sup>4</sup> When we examined patients who had retrograde leptomeningeal venous drainage, we found that the rate of hemorrhage was similar between those who did and did not have a pseudophlebitic pattern. This finding suggests that the primary driver of hemorrhage is the venous pathology along the draining vein rather than the venous congestion in the affected territory. However, the fact that nonhemorrhagic neurologic deficits such as seizure and cognitive decline are more common among those with a pseudophlebitic pattern suggests that the chronic venous congestion resulting from the normal brain not being able to properly drain in the setting of leptomeningeal venous drainage is the primary driver of these particular symptoms.<sup>3,8-10</sup> This feature has been suggested by prior reports on the characteristics of dAVFs associated with cognitive decline, which have suggested that nearly all of these patients have evidence of medullary venous hypertension with reflux or congestion of the transmedullary veins on conventional imaging and angiography.<sup>11</sup> Given the strong association between the pseudophlebitic pattern and nonhemorrhagic neurologic deficits in our study, we think that the presence of this pattern should encourage the neurointerventionalist or neurosurgeon to be more aggressive in treating and curing the fistula to prevent the downstream effects of chronic venous congestion.

One additional interesting finding from our study was the location of most lesions associated with the pseudophlebitic pattern. Most of these lesions were more or less midline in location (ie, tentorial or superior sagittal sinus). Tentorial dAVFs involving the midline tentorial sinuses, the torcula, or the vein of Galen cause significant venous hypertension in the vein of Galen–straight sinus–torcula draining pathway. Thus, in such cases, the primary means by which the deep venous system drains into the dural venous sinuses is under high pressure, resulting in high pressure in the parenchymal veins draining into the deep venous system and a pseudophlebitic congestive pattern. The same is true for superior sagittal sinus fistulas because the cortical veins experience markedly elevated venous pressure resulting in congestion of the parenchymal veins and an associated pseudophlebitic pattern. This feature would be less common in laterally located lesions (ie, transverse sigmoid junction fistulas) because there may be more avenues for venous egress for the parenchymal veins.

Regarding sex, we found that male sex was associated with a pseudophlebitic pattern on angiography. A number of large clinical case series have found that male sex is associated with a more aggressive angioarchitecture of cranial dural arteriovenous fistulas; however, the reason for this association is unclear.<sup>4,12,13</sup> In

their review of >300 cranial and spinal arteriovenous fistulas, Geibprassert et al noticed that fistulas associated with more benign locations and angioarchitecture had a female predominance while those in locations associated with more malignant angioarchitecture were much more common in men.<sup>13</sup> These findings point to a difference in the etiology of cranial dural arteriovenous fistulas by location. We hypothesize that women are more likely to have the more benign fistulas in the cavernous sinus and transverse sigmoid region due to their propensity to have dural venous sinus thromboses, while men are more likely to have aggressive tentorial or anterior ethmoidal fistulas due to higher rates of trauma.

### Limitations

Our study has limitations. This patient population is from a 12-year time span. During the time period, there have been significant advancements in neuroimaging with increased use of susceptibility-weighted imaging over gradient recalled-echo and higher-resolution FLAIR sequences, which could increase the sensitivity for detecting microhemorrhages and edema, respectively. In addition, imaging was performed across a variety of scanners with 1.5T and 3T field strengths, so there was not 100% uniformity in the imaging protocols. All cross-sectional imaging interpretation was performed by a single neuroradiologist. Last, we did not include multiphase imaging in our study (ie, Time Resolved Imaging of Contrast Kinetics). It is possible that this could have a role in understanding the presence of a pseudophlebitic pattern before conventional angiography.

### CONCLUSIONS

Our study of 201 cranial dural arteriovenous fistulas, 191 of which had MR imaging, found that the pseudophlebitic pattern was associated with more aggressive dural arteriovenous fistulas. When we examined patients with retrograde leptomeningeal venous drainage, the pseudophlebitic pattern was independently associated with nonhemorrhagic neurologic deficits, but not hemorrhage. MR imaging findings most commonly associated with the pseudophlebitic pattern were cerebral edema, dilated transmedullary veins on postcontrast or T2\*-weighted imaging, and chronic hemosiderin deposition/microhemorrhage. These findings can help in the risk stratification of dural arteriovenous fistulas.

Disclosures: Giuseppe Lanzino—UNRELATED: Board Membership: Superior Medical Editing, Nested Knowledge.

### REFERENCES

1. Reynolds MR, Lanzino G, Zipfel GJ. **Intracranial dural arteriovenous fistulae.** *Stroke* 2017;48:1424–31 CrossRef Medline
2. Biondi A, Casasco A, Houdart E, et al. **Evolution of angiographic signs of venous hypertension and clinical signs of intracranial hypertension in intracranial dural arteriovenous fistulas** [in French]. *J Neuroradiol* 1999;26:49–58 Medline
3. Cognard C, Casasco A, Toevi M, et al. **Dural arteriovenous fistulas as a cause of intracranial hypertension due to impairment of cranial venous outflow.** *J Neurol Neurosurg Psychiatry* 1998;65:308–16 CrossRef Medline
4. Willinsky R, Goyal M, terBrugge K, et al. **Tortuous, engorged pial veins in intracranial dural arteriovenous fistulas: correlations with**



- presentation, location, and MR findings in 122 patients. *AJNR Am J Neuroradiol* 1999;20:1031–36 Medline
5. Osada T, Krings T. **Intracranial dural arteriovenous fistulas with pial arterial supply.** *Neurosurgery* 2019;84:104–15 CrossRef Medline
  6. Lawton MT, Sanchez-Mejia RO, Pham D, et al. **Tentorial dural arteriovenous fistulae: operative strategies and microsurgical results for six types.** *Neurosurgery* 2008;62:110–24; discussion 24–25 CrossRef Medline
  7. Nakagawa I, Taoka T, Wada T, et al. **The use of susceptibility-weighted imaging as an indicator of retrograde leptomeningeal venous drainage and venous congestion with dural arteriovenous fistula: diagnosis and follow-up after treatment.** *Neurosurgery* 2013;72:47–54; discussion 55 CrossRef Medline
  8. Iwama T, Hashimoto N, Takagi Y, et al. **Hemodynamic and metabolic disturbances in patients with intracranial dural arteriovenous fistulas: positron emission tomography evaluation before and after treatment.** *J Neurosurg* 1997;86:806–11 CrossRef Medline
  9. Kanemaru K, Kinouchi H, Yoshioka H, et al. **Cerebral hemodynamic disturbance in dural arteriovenous fistula with retrograde leptomeningeal venous drainage: a prospective study using (123) I-iodoamphetamine single photon emission computed tomography.** *J Neurosurg* 2015;123:110–17 CrossRef Medline
  10. Kwon BJ, Han MH, Kang HS, et al. **MR imaging findings of intracranial dural arteriovenous fistulas: relations with venous drainage patterns.** *AJNR Am J Neuroradiol* 2005;26:2500–07 Medline
  11. Brito A, Tsang AC, Hilditch C, et al. **Epidemiology of dural arteriovenous fistula in Japan: analysis of Japanese Registry of Neuroendovascular Therapy (JR-NET2).** *Neurol Med Chir (Tokyo)* 2019;121:e543–53 Medline
  12. Brito A, Tsang AC, Hilditch C, et al. **Intracranial dural arteriovenous fistula as a reversible cause of dementia: case series and literature review.** *World Neurosurg* 2014;54(Suppl 2):63–71 CrossRef Medline
  13. Geibprasert S, Pereira V, Krings T, et al. **Dural arteriovenous shunts: a new classification of craniospinal epidural venous anatomical bases and clinical correlations.** *Stroke* 2008;10:2783–94 CrossRef Medline

# Endovascular Cerebral Venous Sinus Imaging with Optical Coherence Tomography

C.R. Pasarikovski, J.C. Ku, J. Keith, J. Ramjist, Y. Dobashi, S.M. Priola, L. da Costa, and V.X.D. Yang



## ABSTRACT

**BACKGROUND AND PURPOSE:** Imaging of the cerebral venous sinuses has evolved Substantially during the past 2 decades, and most recently intravascular sinus imaging with sonography has shed light on the pathophysiology of sinus thrombosis and intracranial hypertension. Optical coherence tomography is the highest resolution intravascular imaging technique available but has not been previously used in cerebral sinus imaging. The purpose of this study was to develop a preclinical animal model of endovascular optical coherence tomography cerebral venous sinus imaging and compare optical coherence tomography findings with histology.

**MATERIALS AND METHODS:** Four consecutive Yorkshire swine were selected. The superior sagittal sinus was first catheterized with a microwire, and the optical coherence tomography catheter was delivered via a monorail technique into the sinus. Luminal blood was cleared with a single arterial injection. After structural and Doppler optical coherence tomography imaging, a craniotomy was performed and the sinus and adjacent dura/veins were resected. Bland-Altman analysis was performed to compare optical coherence tomography and histology.

**RESULTS:** Technically successful optical coherence tomography images were obtained in 3 of 4 swine. The luminal environment and visualization of dural arteries and draining cortical veins were characterized. The average maximum diameters of the sinus, dural arteries, and cortical veins were 3.14 mm, 135  $\mu$ m, and 260  $\mu$ m, respectively. Bland-Altman analysis demonstrated good agreement between histology and optical coherence tomography images.

**CONCLUSIONS:** Endovascular optical coherence tomography imaging was feasible in this preclinical animal study. Adoption of this imaging technique in the human cerebral venous sinus could aid in the diagnosis, treatment, and understanding of the pathophysiology of various diseases of the sinus. Human safety and feasibility studies are needed.

**ABBREVIATIONS:** CVS = cerebral venous sinuses; dOCT = Doppler OCT; IIH = idiopathic intracranial hypertension; IVUS = intravascular ultrasound; OCT = optical coherence tomography

The cerebral venous sinuses (CVS) are rigid structures located between the periosteal and meningeal layers of the dura mater.<sup>1</sup> The sinuses act as reservoirs for collecting venous blood from both the deep and superficial venous systems of the brain and are lined with endothelium and elastic lamina.<sup>2</sup> They lack the

smooth-muscle layers found in most blood vessels and have no valves.<sup>3</sup> Diseases of the CVS include dural arteriovenous fistulas, cerebral venous sinus thrombosis, and idiopathic intracranial hypertension (IIH).

Imaging of the CVS has evolved considerably during the past 2 decades. CTV and MRV, with either 2D-TOF or contrast-enhanced MRV, are the current imaging modalities of choice for the diagnosis of cerebral venous sinus thrombosis or venous sinus stenosis in IIH.<sup>4</sup> However, large studies comparing the sensitivity and specificity of MRV for determining the degree of stenosis with DSA, which is the presumed criterion standard for cerebral venous imaging, are lacking. Boddu et al<sup>5</sup> showed that contrast-enhanced MRV significantly overestimated the size of sinus stenosis in patients with IIH compared with intravascular ultrasound (IVUS), concluding that contrast-enhanced MRV would be a poor technique for stent-size selection. Similarly, the accuracy of DSA has been questioned owing to the limitations of 2D

Received April 14, 2020; accepted after revision July 28.

From the Division of Neurosurgery (C.R.P., J.C.K.), Department of Surgery, University of Toronto, Toronto, Ontario, Canada; Department of Anatomic Pathology (J.K.), Sunnybrook Health Sciences Center, Toronto, Ontario, Canada; Division of Neurosurgery (J.R., Y.D., L.D.C., V.X.D.Y.), Sunnybrook Hospital, University of Toronto, Toronto, Ontario, Canada; Division of Neurosurgery (S.M.P.), Department of Surgery, Health Sciences North, Sudbury, Ontario, Canada; and Hurvitz Brain Sciences Research Program (V.X.D.Y.), Sunnybrook Research Institute, Sunnybrook Health Sciences Centre, University of Toronto, Toronto, Ontario, Canada.

Please address correspondence to Christopher R. Pasarikovski, MD, Surgeon-Scientist Training Program, Division of Neurosurgery, University of Toronto, 399 Bathurst St, WW 4-427 Toronto, ON M5T 2S8 Canada; e-mail: chris.pasarikovski@mail.utoronto.ca

<http://dx.doi.org/10.3174/ajnr.A6909>

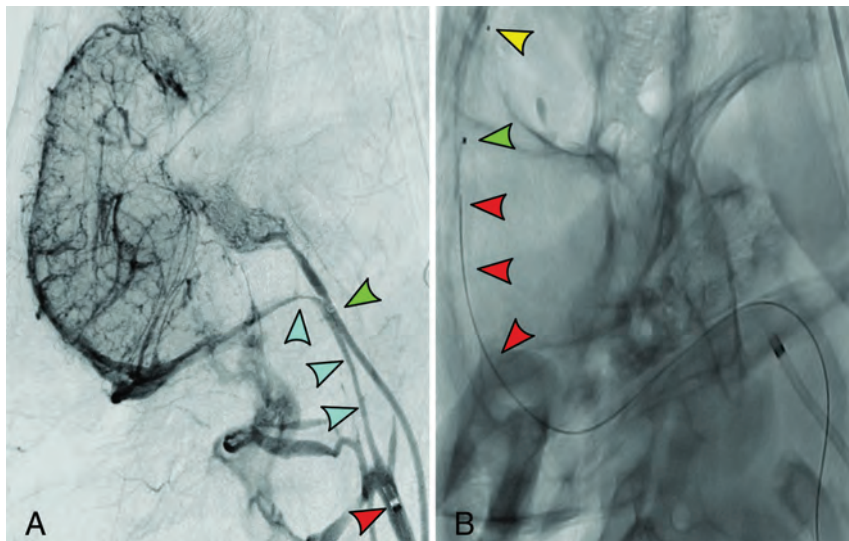


**FIG 1.** Swine cerebral venous sinus. A, Combined arterial and venous diagnostic angiography injections in a lateral view via a guide catheter tip in the ascending pharyngeal artery (green arrow) and the internal jugular vein (red arrow), revealing the connection between the internal jugular vein and sigmoid sinus (blue arrows). B, OCT catheter in the superior sagittal sinus. The distal catheter marker (yellow arrow), lens marker (green arrow), and optical fiber (red arrows) are visible in the superior sagittal sinus.

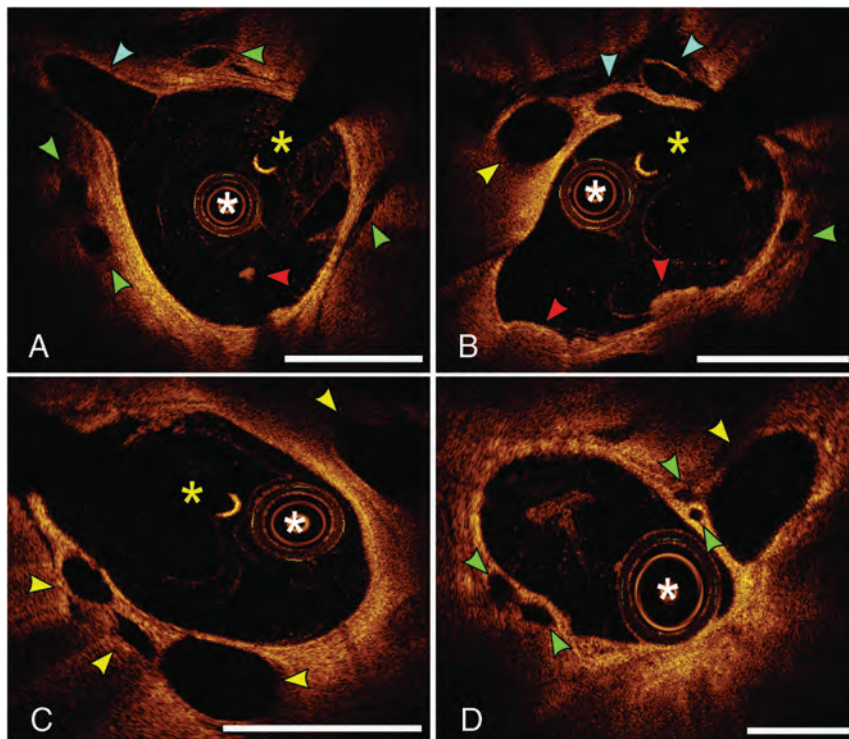


**FIG 2.** Cross-sectional OCT imaging within the superior sagittal sinus. Large draining cortical veins can be observed entering the sinus (light blue arrow) with multiple adjacent dural arteries visible (green arrows), along with adjacent cortical veins outside the sinus lumen (yellow arrows). Small red thrombi (red arrows) are also visible in certain sections, either free-floating or attached to the sinus wall. The white asterisk is the OCT lens, and the yellow asterisk is the artifact from the wire. White bars = 2 mm.

planar imaging. Karmon et al<sup>6</sup> compared DSA with IVUS and reported that angiography was less sensitive in describing the luminal environment, frequently missing luminal thrombus, valves in the internal jugular vein, flaps, and septations.

Endovascular optical coherence tomography (OCT) is the highest resolution intravascular imaging technique available, using near-infrared light with a wavelength of approximately 1300 nm, and excellent spatial resolution of 10  $\mu$ m is achievable.<sup>7</sup> In comparison, IVUS has a spatial resolution of 100  $\mu$ m (approximately 10 times less resolution), and 3T MR vessel wall imaging has a voxel size of 2.0  $\times$  0.4  $\times$  0.4 mm. With near-histologic resolution, OCT has been described as an optical biopsy technique.<sup>8</sup>

We hypothesized that endovascular OCT would enable superior characterization of the cerebral sinus luminal environment and would visualize draining cortical veins and dural arteries. To our knowledge, endovascular OCT imaging of the human CVS has not been undertaken. The purpose of this research was to develop a proof of concept animal endovascular OCT cerebral venous sinus imaging model and compare OCT imaging with histology. Doppler OCT images were also acquired.

## MATERIALS AND METHODS

All experiments were conducted according to the policies and standards established by the authors' institutional animal research ethics board (Sunnybrook Health Sciences Center Research Ethics Board). Four consecutive Yorkshire swine weighing 40–45 kg were used for sinus imaging. There was no pre-screening imaging of venous anatomy for any animal. All procedures were performed with the animal under a general anesthetic with continuous hemodynamic monitoring. The animals were fed standard diets at our facility for 2 weeks before the procedure.

Ultrasound-guided right femoral punctures were performed, and a 6F sheath was inserted into the right



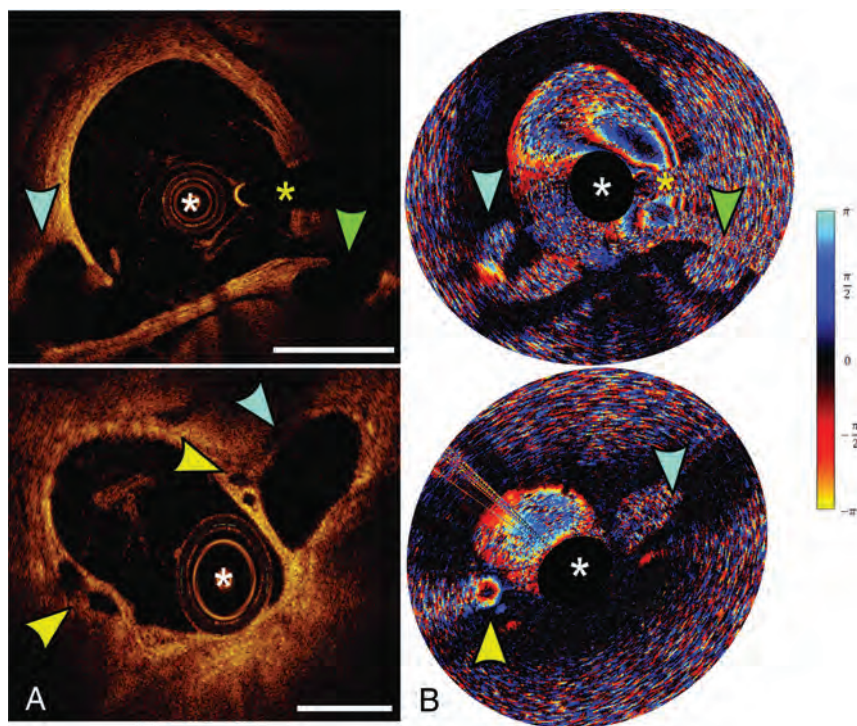


**FIG 3.** Corresponding structural and Doppler OCT imaging. A, Two separate structural images reveal large draining cortical veins (light blue and green arrows) along with dural arteries (yellow arrows) and their corresponding Doppler imaging with a phase-shift color map demonstrating flow in the sinus and dural arteries (B). The white asterisk is the OCT lens, and the yellow asterisk is the artifact from the wire. White bars = 2mm.

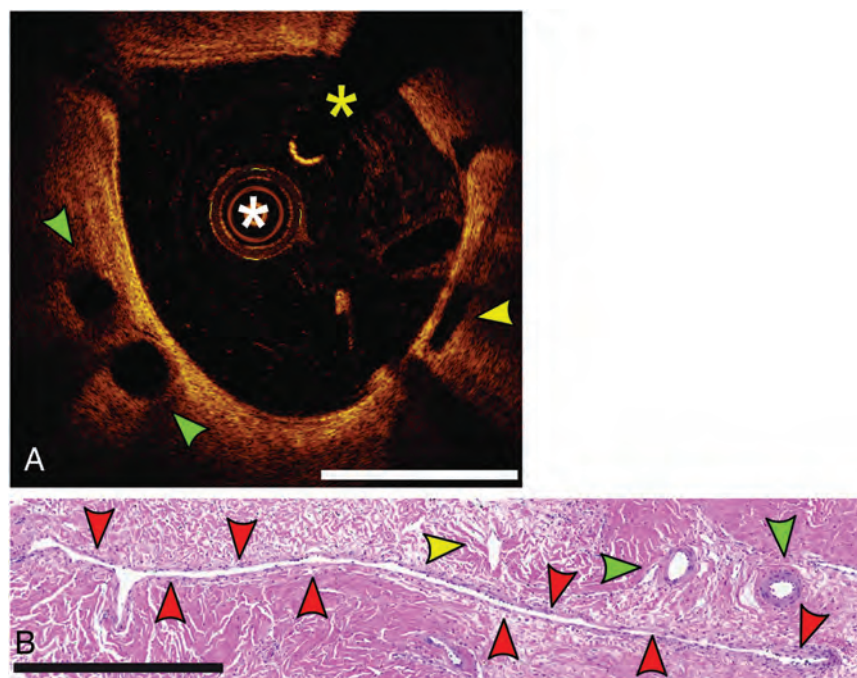


**FIG 4.** OCT imaging and corresponding histologic cross-section. A, OCT shows 2 dural arteries (green arrows) and a dural venule (yellow arrow). B, Histologic cross-section with H&E staining. The sinus is collapsed, and the lumen is outlined with red arrows, along with adjacent arterioles (green arrows) and a venule (yellow arrow). The white asterisk is the artifact from the wire. White bars = 2 mm. Black scale bar = 500  $\mu$ m.

common femoral artery, and another, into the right femoral vein. First, a 6F Envoy guide catheter (Codman & Shurtleff) was used in conjunction with a 150-cm Glidewire (Terumo) to select the right ascending pharyngeal artery. The guide catheter was positioned before the rete mirabile. The C-Arm (Philips Healthcare) was then positioned in a true lateral view, and cerebral angiography was performed to visualize the sinus.

Next, a second 6F Envoy was positioned in the right internal jugular vein. Combined arterial pump injections from the ascending pharyngeal artery and venous hand injection, timed to the late venous phase of the arterial pump injection, were performed to visualize the internal jugular and sigmoid junction (Fig 1A). A Transend micro-guidewire (Stryker) was navigated into the superior sagittal sinus via the sigmoid and transverse sinuses under a roadmap technique.

### Optical Coherence Tomography Imaging

The Dragonfly OCT catheter (Abbott) was used for image acquisition. The following steps were sequentially followed for image acquisition: 1) Load an automated injection pump with 150-mL mixture of 50:50 contrast and saline. The pump is connected to the Envoy catheter in the ascending pharyngeal artery. This is used to clear the blood within the sinus lumen during OCT image acquisition. 2) Mount the OCT catheter on the Transend micro-guidewire and advance the device in a monorail fashion into the superior sagittal sinus, 3) position the OCT catheter so that the optical lens radiopaque marker is in the anterior third of the sinus (Fig 1B), 4) inject 3 mL per second for 8 seconds total (24 mL total) via the pump, and 5) enable manual OCT pullback mode and initiate the pullback manually once the lumen begins to clear. The OCT catheter performs the motorized automated pullback of 54 mm total. The OCT imaging frequency is 100 frames per second, with a total of 540 cross-sectional images generated per pullback.

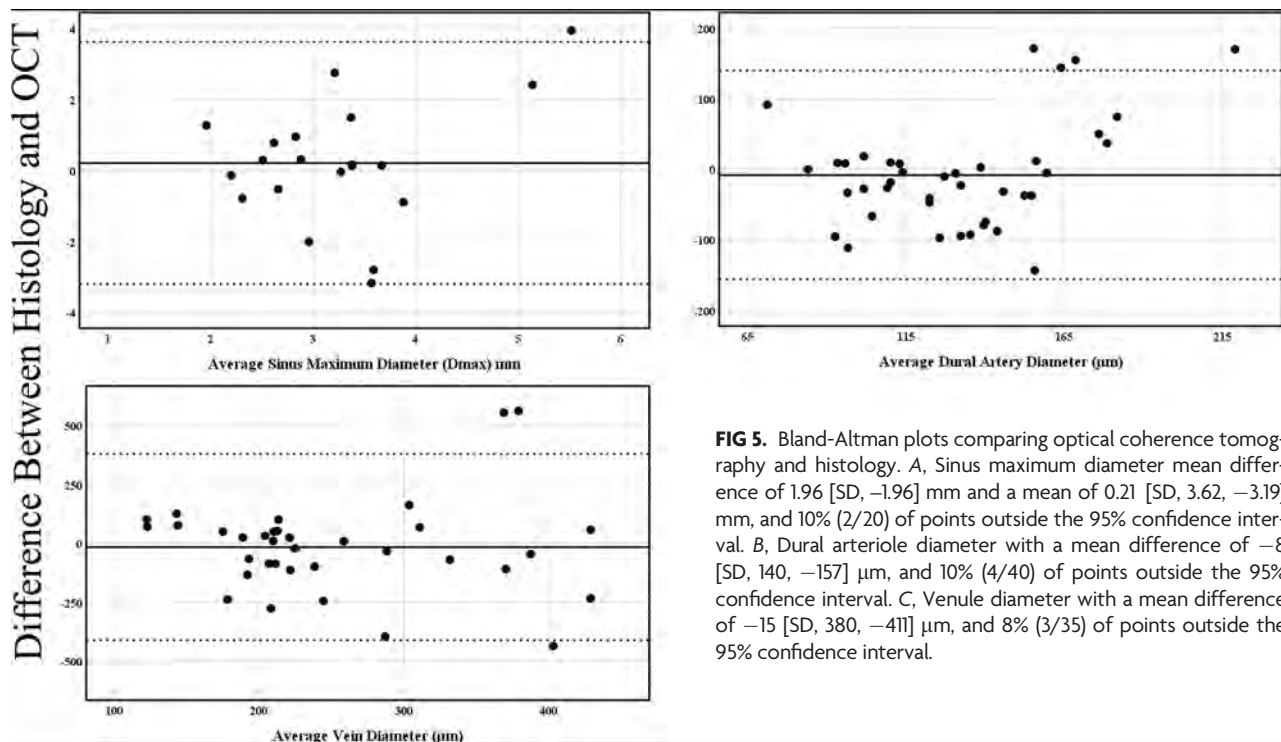


**FIG 5.** Bland-Altman plots comparing optical coherence tomography and histology. A, Sinus maximum diameter mean difference of 1.96 [SD, -1.96] mm and a mean of 0.21 [SD, 3.62, -3.19] mm, and 10% (2/20) of points outside the 95% confidence interval. B, Dural arteriole diameter with a mean difference of -8 [SD, 140, -157]  $\mu$ m, and 10% (4/40) of points outside the 95% confidence interval. C, Venule diameter with a mean difference of -15 [SD, 380, -411]  $\mu$ m, and 8% (3/35) of points outside the 95% confidence interval.

The technique for Doppler OCT (dOCT) image acquisition has been previously described by Vuong et al.<sup>9</sup> Briefly, a split spectrum dOCT technique was used to reduce phase noise without incorporating external bulk optical devices. During the image acquisition, an arterial injection of 2 mL per second for 10 seconds (20 mL total) was performed. Both OCT and dOCT images were reviewed independently by 2 physicians with extensive experience in analyzing OCT images (C.R.P. and V.X.D.Y.).

### Pathology

After OCT imaging and the sacrifice of the animal, craniotomy was performed as well as resection of the superior sagittal sinus beyond the torcula into the bilateral transverse sinuses, with 2-cm margins of the adjacent dura along with preservation of draining cortical veins. The resected specimen segments were fixed in 10% neutral buffered formalin. Then the sinuses were sectioned coronally into 5-mm segments and submitted in total from anterior to posterior in tissue blocks for embedding in paraffin. One level through each of these tissue blocks was created, and 5- $\mu$ m-thick tissue sections were mounted on glass slides and stained with H&E. H&E-stained slides from each block of the sampled sinus were scanned by an Aperio AT Turbo slide scanner (Leica Biosystems), and the resulting digital histology images were examined using the Aperio eSlide Manager (<https://www.leicabiosystems.com/digital-pathology/manage/aperio-eslide-manager/>) by an experienced neuropathologist (J.K.).

For each digital histology image, the maximum diameter of the observed lumen of the superior sagittal sinus and/or transverse sinuses was measured digitally in micrometers, and the location and luminal diameter of the adjacent arterioles and venules were also recorded in micrometers. Digital photomicrographs were obtained, with and without the annotated dimensions, and the digital

photomicrographs were compared with the images obtained by structural OCT. For statistical analysis, Bland-Altman plots were generated using the mean difference between histology and OCT scores and a 1.96 SD with respect to the various luminal characteristics.

### RESULTS

Cerebral venous sinus access was successful in all animals, and successful OCT and dOCT images were acquired in 3 of 4 swine. In swine 2, access was gained into the superior sagittal sinus with the 0.014-inch microwire; however, the OCT catheter could not traverse a suspected venous valve at the junction of the internal jugular vein and the sigmoid sinus; therefore, no OCT or dOCT images were obtained. In the remaining 3 swine, technically successful images were acquired. For image acquisitions to be defined as successful, they had to meet all the following criteria: 1) navigation of the OCT catheter to the appropriate location within the sinus, 2) clearing of luminal blood with minimal artifacts from red blood cells, 3) capturing circumferential OCT images of the entire sinus lumen along the entire region of interest, 4) identifying normal anatomic structures when present, and 5) identifying luminal lesions and vessel wall lesions when present.

The luminal environment could be characterized without ambiguity (Fig 2). The luminal diameter could readily be calculated, along with visualization of dural arteries and draining cortical veins (Fig 3). When present, luminal thrombus, likely secondary to microguidewire manipulation, could be observed and characterized as red or white thrombus.

The average maximum diameter of the sinus was 3.14 mm (95% CI, 5.11–1.17 mm). The average diameter of adjacent dural arteries was 135  $\mu$ m (95% CI, 211–60  $\mu$ m). The average venule diameter was 260  $\mu$ m (95% CI, 520–1  $\mu$ m). Bland-Altman analysis



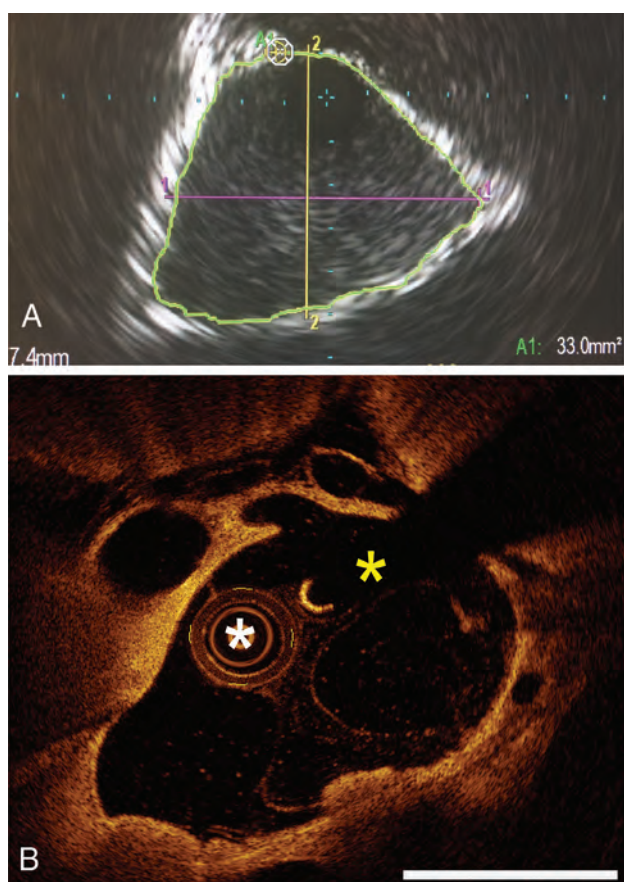


**FIG 6.** IVUS and OCT. A, IVUS of human superior sagittal sinus to determine the maximal diameter and circumference (A), and swine structural OCT imaging of the superior sagittal sinus (B). Although direct anatomic comparison cannot be made, OCT can clearly provide improved visualization of the sinus lumen and adjacent vessels. The *white asterisk* is the OCT lens, and the *yellow asterisk* is the artifact from the wire. *White bars* = 2 mm. Adapted with permission from Boddu et al.<sup>5</sup>

demonstrated good agreement between histology (Fig 4) and OCT images across Dmax and arterial/venule diameter measurements (Fig 5). For Dmax, a mean difference with 1.96 and  $-1.96$  SD (mean, [SD]) of 0.21 mm [3.62,  $-3.19$ ] was observed, with 10% (2/20) of points outside the 95% confidence interval (Figure 5). For dural arteriole diameter, a mean difference of  $-8$   $\mu$ m [140,  $-157$ ] was observed, with 10% (4/40) of points outside the 95% confidence interval (Fig 5). For venule diameter, a mean difference of  $-15$   $\mu$ m [380,  $-411$ ] was observed, with 8% (3/35) of points outside the 95% confidence interval (Fig 5).

## DISCUSSION

The goal of this study was to test the hypothesis that endovascular optical coherence tomography can characterize the cerebral venous sinus luminal environment and visualize draining cortical veins and dural arteries with near-histologic accuracy. In this pre-clinical swine study, OCT imaging was found to be technically feasible, with luminal blood clearing through a single arterial injection, and accurate compared with histology findings.

The first described use of intravascular imaging of the cerebral venous sinuses was by Tsumoto et al,<sup>10</sup> in 2003. They described IVUS imaging in a patient with sigmoid sinus

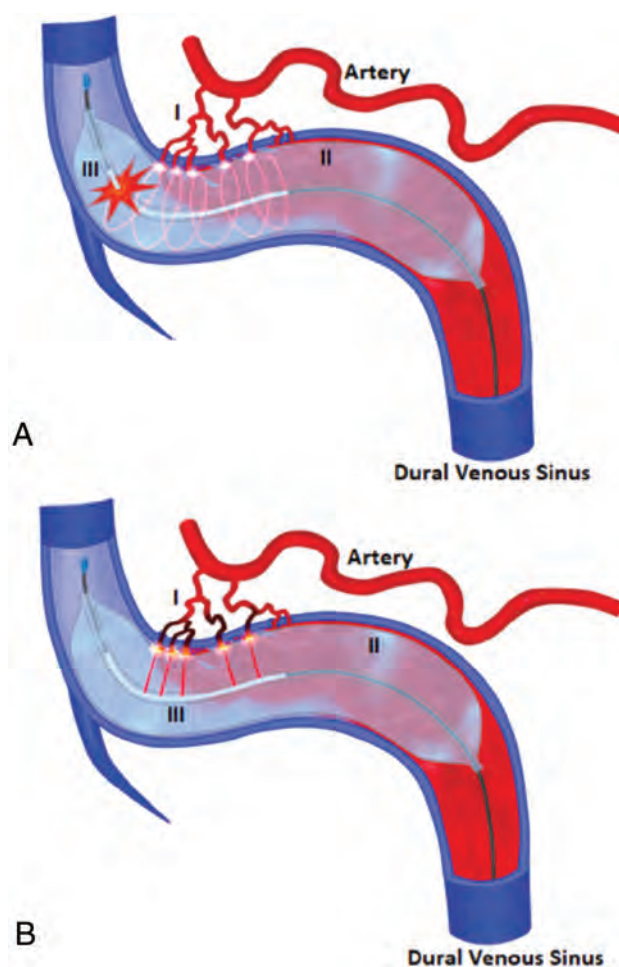


**FIG 7.** A dural arteriovenous fistula imaged and treated using novel OCT technology. A, The OCT device is navigated into the dural venous sinus and through a transparent dual-lumen balloon (II), optical imaging is undertaken (III) to identify the exact spatial position of arterial feeders (I) into the dural venous sinus. B, Laser ablation of the arterial feeders (I) is accomplished under image guidance through the saline-filled balloon. The arterial feeders (I) previously identified now undergo image-guided laser ablation (III) through the transparent dual lumen balloon (II). Adapted from Pasarikovski et al.<sup>21</sup>

restenosis after stent placement for venous hypertension and identified intimal proliferation over the stent causing the stenosis. Radvany et al<sup>11</sup> demonstrated, for the first time using IVUS, that transverse sinus stenosis in 2 patients with IIH was the result of intraluminal abnormalities (echogenic material within the sinus) and not extrinsic compression from raised intracranial pressure. Several authors have since described the use of IVUS as a diagnostic tool and treatment adjunct for patients with IIH, particularly highlighting the inability of CTV/MRV or even DSA to differentiate thrombus and structural stenosis and to select proper stent sizes.<sup>12-14</sup>

To our knowledge, cerebral venous sinus imaging with OCT has not been previously reported in humans or in preclinical animal studies. Gounis et al,<sup>15</sup> in 2018, described the use of optical coherence tomography in neurointerventional surgery. Current arterial applications of OCT include the following: visualizing stent-vessel interactions during carotid stent placement and flow diversion for aneurysmal embolization, characterizing intracranial



atherosclerotic disease, and after endovascular thrombectomy, assessing residual thrombus.<sup>16-20</sup>

Optical coherence tomography has approximately 10 times the spatial resolution of IVUS, producing much higher quality images and enabling improved visualization of the lumen, venous sinus wall, draining cortical veins, and dural arteries (Fig 6). This improved visualization has great potential with respect to aiding in the diagnosis and treatment of patients with cerebral venous pathology. Abnormalities such as sinus septations and luminal thrombus can be visualized readily. The potential applications of endovascular OCT in treating diseases of the CVS is boundless. For example, it is hypothesized that the near-histologic accuracy of OCT in detecting and characterizing dural arteries could be used for image-guided ablation of arterial feeders in a dural arteriovenous fistula (Fig 7).

In this swine model, clearing blood within the sinus lumen for OCT acquisition was achieved with an arterial injection. The authors could not place a large-gauge catheter ( $\geq 5F$ ) in the swine sinus (distal internal jugular or sigmoid) to try to clear luminal blood directly because the swine sinus diameter is small. On the other hand, it is likely that in human imaging, the sinus blood can be cleared with an intravenous injection through a guide catheter positioned in the sinus.

There are several limitations to this study. First, OCT was tested in swine, whereas human CVS are larger with the possibility of increased tortuosity; therefore, difficult navigation of the OCT catheter is possible in certain patients. Second, the safety of OCT in human imaging needs to be further studied. Although the OCT catheter is delivered via a monorail technique over a 0.014-inch wire, venous perforation is possible via the stiff catheter tip.

## CONCLUSIONS

Endovascular optical coherence tomography imaging was technically feasible in this preclinical swine study. Adoption of this imaging technique in the human cerebral venous sinus could aid in the diagnosis, treatment, and understanding of the pathophysiology of dural arteriovenous fistulas, cerebral venous sinus thrombosis, and ITH. Human safety and feasibility studies are needed.

Disclosures: Joel Ramjist—RELATED: Grant: Canadian Foundation for Innovation, Comments: The grant paid for the establishment of biophotonics research equipment in neurosurgical practice, grant title: "Biophotonics Experimental Operating Room."\* Yuta Dobashi—UNRELATED: Employment: University of Toronto. \*Money paid to the institution.

## REFERENCES

- Mack J, Squier W, Eastman JT. **Anatomy and development of the meninges: implications for subdural collections and CSF circulation.** *Pediatr Radiol* 2009;39:200–10 CrossRef Medline
- Vignes JR, Dagain A, Guerin J, et al. **A hypothesis of cerebral venous system regulation based on a study of the junction between the cortical bridging veins and the superior sagittal sinus: laboratory investigation.** *J Neurosurg* 2007;107:1205–10 CrossRef Medline
- Adeeb N, Mortazavi MM, Tubbs RS, et al. **The cranial dura mater: a review of its history, embryology, and anatomy.** *Childs Nerv Syst* 2012;28:827–37 CrossRef Medline
- Saposnik G, Barinagarrementeria F, Brown RD Jr, et al; American Heart Association Stroke Council and the Council on Epidemiology and Prevention. **Diagnosis and management of cerebral venous thrombosis: a statement for healthcare professionals from the American Heart Association/American Stroke Association.** *Stroke* 2011;42:1158–92 CrossRef Medline
- Boddu SR, Gobin P, Oliveira C, et al. **Anatomic measurements of cerebral venous sinuses in idiopathic intracranial hypertension patients.** *PLoS One* 2018;13:e0196275 CrossRef Medline
- Karmon Y, Zivadinov R, Weinstock-Guttman B, et al. **Comparison of intravascular ultrasound with conventional venography for detection of extracranial venous abnormalities indicative of chronic cerebrospinal venous insufficiency.** *J Vasc Interv Radiol* 2013;24:1487–98 CrossRef Medline
- Tearney GJ, Regar E, Akasaka T, et al; International Working Group for Intravascular Optical Coherence Tomography (IWG-IVOCT). **Consensus standards for acquisition, measurement, and reporting of intravascular optical coherence tomography studies: a report from the International Working Group for Intravascular Optical Coherence Tomography Standardization and Validation.** *J Am Coll Cardiol* 2012;59:1058–72 CrossRef Medline
- Tearney GJ, Brezinski ME, Bouma BE, et al. **In vivo endoscopic optical biopsy with optical coherence tomography.** *Science* 1997;276:2037–39 CrossRef Medline
- Vuong B, Genis H, Wong R, et al. **Evaluation of flow velocities after carotid artery stenting through split spectrum Doppler optical coherence tomography and computational fluid dynamics modeling.** *Biomed Opt Express* 2014;5:4405–16 CrossRef Medline
- Tsumoto T, Miyamoto T, Shimizu M, et al. **Restenosis of the sigmoid sinus after stenting for treatment of intracranial venous hypertension: case report.** *Neuroradiology* 2003;45:911–15 CrossRef Medline
- Radvany MG, Gomez J, Gailloud P. **Intravascular ultrasound of the transverse sinus in two patients with pseudotumor cerebri: technical note.** *J Neurointerv Surg* 2011;3:379–82 CrossRef Medline
- Mokin M, Kan P, Abl A, et al. **Intravascular ultrasound in the evaluation and management of cerebral venous disease.** *World Neurosurg* 2013;80:55.e7–13 CrossRef Medline
- Buell TJ, Raper DM, Pomeranec IJ, et al. **Transient resolution of venous sinus stenosis after high-volume lumbar puncture in a patient with idiopathic intracranial hypertension.** *J Neurosurg* 2018;129:153–56 CrossRef Medline
- Yan F, Rajah G, Ding Y, et al. **Safety and efficacy of intravascular ultrasound as an adjunct to stenting for cerebral venous sinus stenosis-induced idiopathic intracranial hypertension: a pilot study.** *J Neurosurg* 2019 Mar. [Epub ahead of print] CrossRef Medline
- Gounis MJ, Ughi GJ, Marosfoi M, et al. **Intravascular optical coherence tomography for neurointerventional surgery.** *Stroke* 2018 Nov 29. [Epub ahead of print] CrossRef Medline
- Griessenauer CJ, Gupta R, Shi S, et al. **Collar sign in incompletely occluded aneurysms after Pipeline embolization: evaluation with angiography and optical coherence tomography.** *AJNR Am J Neuroradiol* 2017;38:323–26 CrossRef Medline
- Dohad S, Zhu A, Krishnan S, et al. **Optical coherence tomography guided carotid artery stent procedure: technique and potential applications.** *Catheter Cardiovasc Interv*. 2018;91:521–30 CrossRef Medline
- Pasarikovski CR, da Costa L, Pereira VM, et al. **Optical coherence tomography-guided flow diversion for aneurysmal treatment.** *Neurol Clin Pract* 2020;10:e30–32 CrossRef Medline
- Pasarikovski CR, Ramjist J, da Costa L, et al. **Optical coherence tomography imaging after endovascular thrombectomy for basilar artery occlusion: report of 3 cases.** *J Neurosurg* 2020;133:1141–46 CrossRef Medline
- Xu X, Li M, Liu R, et al. **Optical coherence tomography evaluation of vertebrobasilar artery stenosis: case series and literature review.** *J Neurointerv Surg* 2020;12:809–13 CrossRef Medline
- Pasarikovski CR, Cardinell J, Yang VX. **Perspective review on applications of optics in cerebral endovascular neurosurgery.** *J Biomed Opt* 2019;24:1–7 CrossRef Medline

# Patients Requiring Conversion to General Anesthesia during Endovascular Therapy Have Worse Outcomes: A Post Hoc Analysis of Data from the SAGA Collaboration

C.Z. Simonsen, S. Schönenberger, P.L. Hendén, A.J. Yoo, L. Uhlmann, A. Rentzos, J. Bösel, J. Valentin, and M. Rasmussen

## ABSTRACT

**BACKGROUND AND PURPOSE:** Endovascular therapy for acute ischemic stroke is often performed with the patient under conscious sedation. Emergent conversion from conscious sedation to general anesthesia is sometimes necessary. The aim of this study was to assess the functional outcome in converted patients compared with patients who remained in conscious sedation and to identify predictors associated with the risk of conversion.

**MATERIALS AND METHODS:** Data from 368 patients, included in 3 trials randomizing between conscious sedation and general anesthesia before endovascular therapy (SIESTA, ANSTROKE, and GOLIATH) constituted the study cohort. Twenty-one (11%) of 185 patients randomized to conscious sedation were emergently converted to general anesthesia.

**RESULTS:** Absence of hyperlipidemia seemed to be the strongest predictor of conversion to general anesthesia, albeit a weak predictor (area under curve = 0.62). Sex, hypertension, diabetes, smoking status, atrial fibrillation, blood pressure, size of the infarct, and level and side of the occlusion were not significantly associated with conversion to general anesthesia. Neither age (mean age,  $71.3 \pm 13.8$  years for conscious sedation versus  $71.6 \pm 12.3$  years for converters,  $P = .58$ ) nor severity of stroke (mean NIHSS score,  $17 \pm 4$  versus  $18 \pm 4$ , respectively,  $P = .27$ ) were significantly different between converters and those who tolerated conscious sedation. The converters had significantly worse outcome with a common odds ratio of 2.67 ( $P = .015$ ) for a shift toward a higher mRS score compared with the patients remaining in the conscious sedation group.

**CONCLUSIONS:** Patients undergoing conversion had significantly worse outcome compared with patients remaining in conscious sedation. No factor was identified that predicted conversion from conscious sedation to general anesthesia.

**ABBREVIATIONS:** AUC = area under the curve; CS = conscious sedation; EVT = endovascular therapy; GA = general anesthesia; MABP = mean arterial blood pressure; SAGA = SIESTA, ANSTROKE, and GOLIATH

Five studies published in 2015 proved the efficacy of endovascular therapy (EVT) for acute ischemic stroke caused by a large-vessel occlusion.<sup>1</sup> However, numerous questions remain regarding how to best deliver this treatment, including evaluation of the optimal thrombectomy technique,<sup>2</sup> the most effective method of patient

triage,<sup>3</sup> or whether EVT should be performed with the patient under either general anesthesia (GA) or conscious sedation (CS).

Observational studies have suggested that EVT with the patient under CS is associated with better neurologic outcome and lower mortality compared with GA.<sup>4</sup> However, 3 randomized trials reported similar outcomes between CS and GA.<sup>5-7</sup> Proposed benefits of CS include stable hemodynamics, clinical monitoring, and a potentially shorter procedure. The disadvantages are an unprotected airway and patient movement, which sometimes may require emergent conversion to GA. Patients who need conversion might be sicker (larger strokes, more medical complications), but the conversion procedure itself may also have a potentially deleterious influence on outcome due to the emergent anesthetic induction, associated hypotension, and added time delay before reperfusion.

Although most patients can be treated under the less complex CS, it is of interest to identify factors that can predict the risk of conversion and hence the requirement for GA. We undertook a detailed analysis of the patients who were converted from CS to

Received May 20, 2020; accepted after revision August 5.

From the Departments of Neurology (C.Z.S.) and Anesthesia (M.R.), Section of Neuroanesthesia, Aarhus University Hospital, Aarhus, Denmark; Department of Neurology (S.S.), Heidelberg University Hospital, Heidelberg, Germany; Departments of Anesthesiology and Intensive Care Medicine (P.L.H.), and Radiology (A.R.), Sahlgrenska Academy, University of Gothenburg, Sahlgrenska University Hospital, Gothenburg, Sweden; Division of Neurointervention (A.J.Y.), Texas Stroke Institute, Dallas-Fort Worth, Texas; Institute of Medical Biometry and Informatics (L.U.), University of Heidelberg, Heidelberg, Germany; Department of Neurology (J.B.), Klinikum Kassel, Kassel, Germany; and Department of Clinical Medicine, (J.V.), Danish Center for Clinical Health Services Research, Aalborg University and Aalborg University Hospital, North Denmark Region, Denmark.

C.Z. Simonsen, S. Schönenberger, and P.L. Hendén contributed equally to this work.

Please address correspondence to Claus Z. Simonsen, MD, PhD, Department of Neurology, Aarhus University Hospital, Aarhus, Denmark; e-mail: clasim@rm.dk  
<http://dx.doi.org/10.3174/ajnr.A6823>

**Table 1: Reasons for conversion among the 21 patients who were randomized to conscious sedation but converted to general anesthesia**

Reason for conversion (No.)	SIESTA	ANSTROKE	GOLIATH	Total
Severe agitation	7	2	3	12
Respiratory insufficiency/loss of airway	3	1	1	5
Direct puncture of the internal carotid artery	0	4	0	4

GA in our individual patient data base from the 3 randomized trials to examine the outcome of the converted patients compared with patients who remained in CS. We also aimed to identify possible predictors associated with a need for GA with EVT.

## MATERIALS AND METHODS

Access to original study data resulted from the cross-institutional SIESTA (Sedation versus Intubation for Endovascular Stroke Treatment), ANSTROKE (Sedation Versus General Anesthesia for Endovascular Therapy in Acute Stroke—Impact on Neurological Outcome), and GOLIATH (General Or Local Anaesthesia in Intra Arterial Therapy) Association (SAGA).<sup>5–7</sup> The study database contains individual patient-level data concerning demographics, comorbidities, imaging and time metrics, anesthesia, and functional outcome for all patients included in the 3 trials. All recruited patients or their legal representatives had provided informed consent according to each trial protocol, and all trials had been approved by their respective local ethics committees. The decision for EVT was based on local treatment protocols. The 3 studies included patients with acute ischemic stroke caused by an occlusion in the anterior circulation that was eligible for EVT. The patients had to be 18 years of age or older and have an NIHSS score of  $\geq 10$ . Patients in the Anesthesia During Stroke (ANSTROKE) trial had to have a premorbid mRS of 0–3,<sup>6</sup> while in the General or Local Anesthesia in Intra Arterial Therapy (GOLIATH) trial,<sup>7</sup> the premorbid mRS had to be 0–2. GOLIATH also excluded patients with an infarct volume of  $> 70$  mL.

### Population

The study population consists of all patients from the SAGA data originally randomized to CS.

### Outcome

The outcome event is defined as conversion from CS to GA during EVT for any of the given reasons. The shift in the 90-day mRS score in the converted group was compared with the scores of the patients who remained in the CS group.

### Possible Predictors

Common baseline and demographic factors for stroke were collected for all the patients: sex, age, hypertension, diabetes, hyperlipidemia, smoking status (Sedation vs Intubation for Endovascular Stroke Treatment [SIESTA] and GOLIATH: current smoker; ANSTROKE: current and previous smoker), atrial fibrillation, premorbid mRS score, NIHSS score on admission, ASPECTS, occlusion site, IV thrombolysis given, and mean arterial blood pressure (MABP) as well as systolic blood pressure at the start of EVT.

## Statistical Analysis

We compared converters (CS to GA) with patients who remained in CS on all possible predictors. We used the Student *t* test for variables of SDs or frequencies and percentages when appropriate. In addition, we conducted ordered logistic regression analysis on

the mRS at 90 days, comparing converters with nonconverters with a random effects on study identification. We estimated the group mean of mRS at 90-day follow-up for the 3 groups: the “converters,” the patients who stayed in the CS group, and the GA group and compared relevant variables that might have affected outcome (time to groin puncture, minimum MABP, and proportion of successful reperfusion). Results were presented with 95% confidence intervals. In addition, we generated Grotta bars of the mRS score at 90-day follow-up stratified by the same groups.

Second, we conducted forward selection stepwise logistic regression without data splitting on the above-defined outcome with all possible predictors as input variables. Each variable was selected on the basis of the lowest *P* value, and selection was based on a 3-fold cross validation. The optimistic incremental area under the curve (AUC) was estimated at each step, ie, without data split, as well as an incremental AUC based on the 3-fold cross-validation. In addition, we estimated the receiver operating characteristic curve for the final model, which was used to assess the predicted probabilities of conversion. Moreover, we estimated the AUC of a univariable logistic regression analysis of all selected potential predictors on the basis of a 3-fold cross-validation.

All analyses were conducted using STATA 15 (Release 15, 2017; StataCorp). A *P* value  $< .05$  was considered statistically significant.

## RESULTS

The SIESTA study excluded 42 patients due to severe agitation and 7 due to vomiting/loss of airway before randomization.<sup>5</sup> After randomization, 10 patients converted from CS to GA. (In the original article, 11 patients converted, but the patient who was converted due to puncturing of the carotid artery was only converted for the last few minutes of the procedure and was not counted as a converter in this analysis). ANSTROKE excluded 59 patients for medical reasons before randomization and 7 patients converted to GA after randomization. GOLIATH excluded 7 patients who were intubated before arrival at the EVT center, and 18 patients were excluded due to MR imaging contraindications, but only 3 of these were due to excessive movement or vomiting. Four patients were converted to GA after randomization. Conversion reasons are outlined in Table 1.

Of 185 patients randomized to CS, 21 (11%) required conversion to GA. For the univariable analyses of associations, we found statistically significant differences for hyperlipidemia and premorbid mRS (Table 2). The absence of hyperlipidemia and a premorbid mRS of 0 were associated with a higher risk of conversion to GA.

Patients who converted from CS to GA scored significantly higher on the mRS at 90-day follow-up with an odds ratio of 2.67 ( $P = .015$ ) for a shift toward a higher score compared with the patients who remained in the CS group. Mean scores are presented



**Table 2: Among the 185 patients allocated to conscious sedation (CS), the 21 converters are compared to the 164 who were treated under CS**

	CS as Treated (n = 164)	Converted to GA (n = 21)	P Value
Hypertension	96 (59%)	12 (57%)	1.00
Diabetes	28 (17%)	5 (24%)	.54
Hyperlipidemia	72 (44%)	3 (14%)	.009
Smoker	38 (24%)	3 (14%)	.42
Atrial fibrillation	71 (44%)	10 (48%)	.82
Sex (male)	85 (52%)	10 (48%)	.82
Pre-mRS ( $\geq 1$ )	51 (31%)	2 (10%)	.042
ASPECTS ( $< 6$ )	22 (14%)	1 (5%)	.48
Left side affected	79 (48%)	12 (57%)	.49
IV thrombolysis given	49 (30%)	4 (19%)	.44
Occlusion type, ICA (neck)	12 (7%)	0 (0%)	.36
ICA-T	28 (17%)	4 (19%)	
M1	83 (51%)	13 (62%)	
M2	18 (11%)	0 (0%)	
Tandem	23 (14%)	4 (19%)	
Age (mean) (SD) (yr)	71 (14)	72 (12)	.58
NIHSS score on admission (mean) (SD)	17.3 (3.8)	17.8 (4.4)	.27
Systolic blood pressure start EVT (mmHg), mean (SD)	165 (28)	161 (25)	.55
MABP at start of EVT (mmHg), mean (SD)	113 (19)	111 (16)	.62

**Note:**—ICA-T indicates ICA bifurcation; Pre, premorbid.

**Table 3: Group mean of mRS at 90-day follow-up, time to groin puncture, and minimum MABP for the 3 groups—the converters, the patients who stayed in the CS group, and the GA group**

	Converted from CS to GA (n = 21)	Stayed in CS (n = 164)	GA Group (n = 183)
Mean mRS (95% CI)	4.3 (3.7–4.9)	3.1 (2.8–3.4)	2.8 (2.5–3.1)
Mean rate of successful reperfusion (mTICI 2b–3) (95% CI)	71.4 (47.8–88.7)	76.2 (69.0–82.5)	85.2 (79.3–90.0)
Mean arrival at angi suite to groin puncture (95% CI) (min)	25.1 (16.3–34.0)	17.7 (15.7–19.8)	24.0 (21.9–26.2)
Mean groin puncture to reperfusion (95% CI) (min)	90.2 (68.8–111.6)	67.2 (59.1–75.3)	63.1 (55.7–70.4)
Mean onset to reperfusion (95% CI) (min)	276 (241–312)	258 (241–275)	273 (256–290)
Minimum MABP during EVT (95% CI) (mm Hg)	68.7 (62.8–74.6)	87.8 (85.7–89.9)	76.0 (74.0–78.0)

**Note:**—mTICI indicates modified TICI.

in Table 3, and outcomes are shown in Fig 1. The time of conversion was not registered, but many patients were probably converted after groin puncture, which is indicated by the longer procedural time in the converter group. However, there was no significant difference in the delay from onset to reperfusion (276 minutes [range, 241–312 minutes] for the converters versus 258 minutes [range, 241–275 minutes] for the CS group). The minimum MABP was significantly lower in the converter group compared with the CS group (68.7 mm Hg [range, 62.8–74.6 mm Hg] versus 87.8 mm Hg [range, 85.7–89.9 mm Hg], respectively). The mean mRS score and rate of reperfusion were statistically favorable for the GA group compared with both of the remaining groups (Table 3).

Three variables were selected in the stepwise regression analysis, for which hyperlipidemia had the highest predictive value. Incremental AUCs of the selection process are shown in Table 4, and the receiver operating characteristic curve of the final model is shown in Fig 2.

The cross-validated AUC for hyperlipidemia was 0.62 (95% CI, 0.50–0.73).

## DISCUSSION

We performed an analysis of patients who converted from CS to GA in the SIESTA, ANSTROKE, and GOLIATH studies and had 2 main findings: First, patients who underwent emergent conversion from CS to GA had a significantly worse outcome than patients who had EVT under CS. Second, none of the tested variables were predictive of the risk of conversion (hence, the necessity for GA) except for the absence of hyperlipidemia. Indicators for the necessity of GA are generally considered to be stroke severity<sup>8</sup> and laterality, with left-sided strokes more prone to need GA.<sup>9</sup>

Only the absence of hyperlipidemia was considered a predictor of conversion from CS to GA because the univariable AUC of the remaining potential predictors was  $< 0.6$ . We believe that this is a chance finding. Also, the result should be interpreted with some caution because of the low event rate of the outcome. Other studies have not been able to confirm our findings, with 2 studies finding a near-significant higher frequency of hyperlipidemia in the CS arm,<sup>4,10</sup> and another study finding a near-significant higher rate of hypercholesterolemia in the GA arm.<sup>11</sup>

The insignificance of our findings was further confirmed with a poor predictive power because the stepwise

regression model conducted with data splitting was not able to display any predictive ability. Even the optimistic model, for which the AUC was calculated on the basis of the training set, barely showed a predictive ability above poor.

One large observational study looking at comorbidities among patients subjected to either CS or GA has not reported differences.<sup>12</sup> A general finding in observational studies is that patients undergoing GA had higher NIHSS scores.<sup>13–15</sup> The study by Campbell et al<sup>4</sup> based on patients in the HERMES (Highly Effective Reperfusion evaluated in Multiple Endovascular Stroke Trials) collaboration found a median NIHSS score in the CS group of 17 versus 18 in the GA group, which was nearly significant, and a significantly lower ASPECTS (ie, bigger strokes) in the GA arm. This study found a higher prevalence of diabetes in the CS arm. (Another observational study found a higher frequency of diabetes in the GA arm.<sup>13</sup>) Age has, in some studies, been older in the GA group,<sup>11</sup> but in others, it was older in the

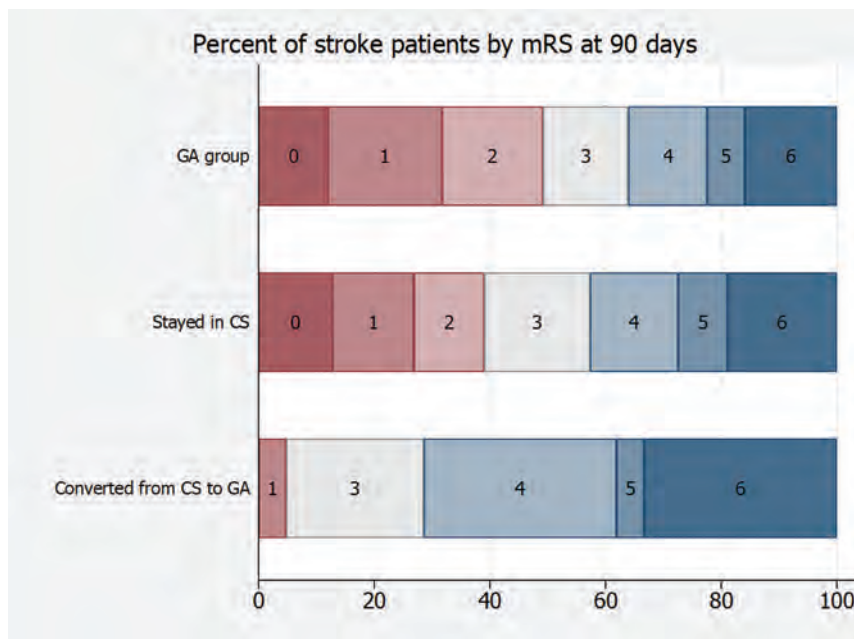


**FIG 1.** Grotta bars of the mRS score at 90 days by the 3 groups: the converters and the patients who stayed in the CS group and the GA group. The number in each bar indicates the mRS score. The odds ratio for a shift to a higher (worse) group was 2.67 for the converted group compared with the CS group.

**Table 4: Incremental predictive value of the 4 best predictors of conversion from conscious sedation to general anesthesia<sup>a</sup>**

	Incremental AUC (without Data Split)	Incremental AUC (Cross-Validated)	Univariable AUC (Cross-Validated)
Hyperlipidemia (95% CI)	0.65 (0.56–0.73)	0.62 (0.50–0.73)	0.62 (0.50–0.73)
Diabetes (95% CI)	0.68 (0.58–0.78)	0.66 (0.54–0.78)	0.49 (0.36–0.61)
Pre-mRS (95% CI)	0.69 (0.60–0.79)	0.67 (0.55–0.79)	0.57 (0.45–0.69)
Age (95% CI) <sup>b</sup>	0.73 (0.62–0.83)	0.62 (0.50–0.74)	0.38 (0.26–0.50)

**Note:**—Pre indicates premonitory.

<sup>a</sup> Analysis was conducted without data splitting. Each AUC reflects the predictive power of the model consisting of the corresponding variable as well as all above variables.

<sup>b</sup> Not included in the final model.

CS group.<sup>4</sup> Generally, the retrospective studies had large unbalanced patient groups, making identification of the role of differentiating characteristics very difficult.

We compared the converters with those in the CS group because this was the allocation from which the converters originated and hence the logical comparator. Because this was a randomized study, the GA group would, by chance, have a similar number of unstable patients, but they were not detected because they were intubated up front.

We found that the patients undergoing conversion had a significantly worse outcome compared with the patients remaining in the CS arm despite similar age and NIHSS and ASPECTS scores. We examined whether this could be explained by differences in time delay, reperfusion rates, or blood pressure drop associated with acute conversion. Reperfusion rates did not differ significantly between the converters and the CS group as shown in Table 3. Procedural time was longer for the converters, probably due to the

conversion procedure, but there was no significant difference on the overall time from stroke onset to reperfusion, and this delay is unlikely to affect the outcome as shown in the meta-analysis.<sup>16</sup>

These findings argue for the conclusion that patients who need GA for medical reasons or because of excessive movement simply are at higher risk of a worse outcome. The combination of longer procedural time and lower MABP caused by the emergent conversion may have added to the poor outcome. The worse outcomes associated with GA in the observational studies are likely secondary to confounding by indication. This was also seen in the Interventional Management of Stroke (IMS-3) study.<sup>15</sup> The strength of our analysis is that it is based on randomization.

In contrast to our findings, a recent study reported that conversion from local anesthesia/CS to GA was not associated with worse outcome. However, outcome in this study was very poor, with a median mRS score of 5 in both the converters and the GA and CS groups.<sup>17</sup>

In the SAGA individual patient data meta-analysis, the GA group proved to have a better outcome compared with the CS group.<sup>16</sup> Due to the lack of predictor variables for conversion to GA in this study, it is impossible to perform a subgroup analysis to compare how the converters would have done with a primary GA versus primary CS strategy. Accordingly, it should be assumed that this subgroup

should have better outcomes with primary GA, like the entire population. An alternative possibility is that this subgroup may help to explain why patients with primary GA did better overall. In either case, a reasonable implication is to perform primary GA on everyone to avoid hurting the approximately 10% of patients that would require conversion under a primary CS approach, provided that GA can be rapidly administered with attention to blood pressure control as in the SAGA trials.

The limitation of our study is that patients who were not able to undergo CS were excluded before randomization in the contributing trials. Another limitation is the relatively small number of patients in the group that required conversion to GA, reflecting the tolerance of most EVT patients for undergoing treatment under CS. However, the findings in the present study, particularly with respect to NIHSS and ASPECTS, may be because sicker patients who required GA were removed before randomization (ie, not eligible for both CS and GA) in the randomized trials.

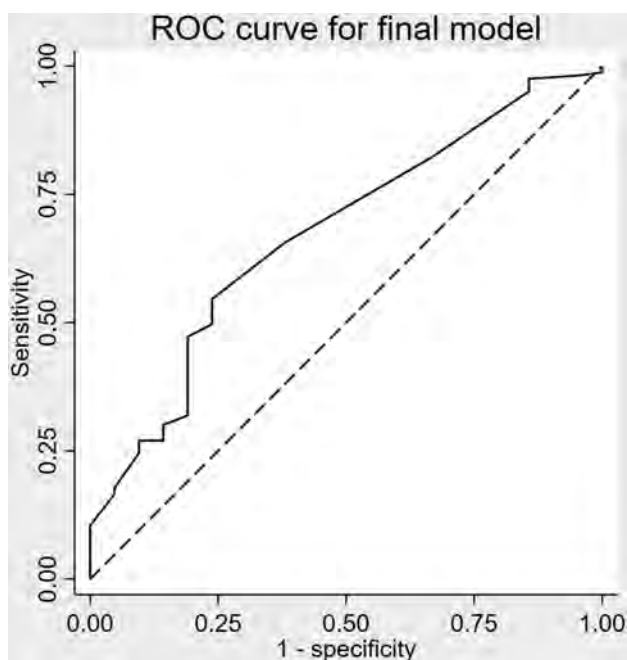


**FIG 2.** Receiver operating characteristic (ROC) curve of the final model of the forward selection stepwise regression.

Indicators will probably only be identified if all patients are randomized irrespective of their clinical presentation (airway, agitation, level of consciousness, and so forth), which is ethically challenging.

## CONCLUSIONS

In this meta-analysis of randomized anesthesia trials, there are no clear factors that predict the risk of conversion to GA for a patient who seems amenable to EVT under CS. However, if a patient needs conversion to GA, the outcome is worse. These findings potentially support the use of primary GA in all patients before EVT, provided that it can be rapidly administered.

**Disclosures:** Claus Z. Simonsen—*RELATED: Grant:* Novo Nordisk Foundation.\* Pia Löwhagen Henden—*UNRELATED: Employment:* Sahlgrenska University Hospital, clinical work as an MD. Albert J. Yoo—*UNRELATED: Consultancy:* Cerenovus, Penumbra, Genentech; *Grants/Grants Pending:* Medtronic, Cerenovus, Penumbra, Stryker, Genentech\*; *Other:* Inera Therapeutics, *Comments:* equity interest. Julian Bösel—*UNRELATED: Grants/Grants Pending:* Patient-Centered Outcomes Research Institute, *Comments:* participation in Patient-Centered Outcomes Research Institute, Award for SETPOINT2; *Payment for Lectures Including Service on Speakers Bureaus:* Medtronic, Boehringer Ingelheim, ZOLL Medical Corporation, *Comments:* speakers honoraria and travel support; *Royalties:* Thieme, *Comments:* book on neurocritical care, several book chapters; *Travel/Accommodations/Meeting Expenses Unrelated to Activities Listed:* Medtronic, Boehringer Ingelheim, ZOLL Medical Corporation. Mads Rasmussen—*RELATED: Grant:* Health Research Foundation of Central Denmark Region. \*Money paid to the institution.

## REFERENCES

- Goyal M, Menon BK, van Zwam WH, et al; HERMES collaborators. Endovascular thrombectomy after large-vessel ischaemic stroke: a meta-analysis of individual patient data from five randomised trials. *Lancet* 2016;387:1723–31 CrossRef Medline
- Lapergue B, Blanc R, Gory B, et al; ASTER Trial Investigators. Effect of endovascular contact aspiration vs stent retriever on revascularization in patients with acute ischemic stroke and large vessel occlusion: the ASTER randomized clinical trial. *JAMA* 2017;318:443–52 CrossRef Medline
- Carrera D, Gorchs M, Querol M, et al; Catalan Stroke Code and Reperfusion Consortium (Cat-SCR). Revalidation of the race scale after its regional implementation in Catalonia: a triage tool for large vessel occlusion. *J Neurointerv Surg* 2019;11:751–56 CrossRef Medline
- Campbell BC, van Zwam WH, Goyal M, et al; HERMES collaborators. Effect of general anaesthesia on functional outcome in patients with anterior circulation ischaemic stroke having endovascular thrombectomy versus standard care: a meta-analysis of individual patient data. *Lancet. Neurol* 2018;17:47–53 CrossRef Medline
- Schonenberger S, Uhlmann L, Hacke W, et al. Effect of conscious sedation vs general anesthesia on early neurological improvement among patients with ischemic stroke undergoing endovascular thrombectomy: a randomized clinical trial. *JAMA* 2016;316:1986–96 CrossRef Medline
- Lowhagen Henden P, Rentzos A, Karlsson JE, et al. General anesthesia versus conscious sedation for endovascular treatment of acute ischemic stroke: the ANSTROKE trial (anesthesia during stroke). *Stroke* 2017;48:1601–07 CrossRef Medline
- Simonsen CZ, Yoo AJ, Sorensen LH, et al. Effect of general anesthesia and conscious sedation during endovascular therapy on infarct growth and clinical outcomes in acute ischemic stroke: a randomized clinical trial. *JAMA Neurol* 2018;75:470–77 CrossRef Medline
- Brinjikji W, Murad MH, Rabinstein AA, et al. Conscious sedation versus general anesthesia during endovascular acute ischemic stroke treatment: a systematic review and meta-analysis. *AJNR Am J Neuroradiol* 2015;36:525–29 CrossRef Medline
- Steinberg JA, Somal J, Brandel MG, et al. Site of occlusion may influence decision to perform thrombectomy under general anesthesia or conscious sedation. *Neurosurg Anesthesiol* 2019 Sept 17. [Epub ahead of print] CrossRef Medline
- John S, Thebo U, Gomes J, et al. Intra-arterial therapy for acute ischemic stroke under general anesthesia versus monitored anesthesia care. *Cerebrovasc Dis* 2014;38:262–67 CrossRef Medline
- van den Berg LA, Koelman DL, Berkhemer OA, et al; Participating centers. Type of anesthesia and differences in clinical outcome after intra-arterial treatment for ischemic stroke. *Stroke* 2015;46:1257–62 CrossRef Medline
- Bekelis K, Missios S, MacKenzie TA, et al. Anesthesia technique and outcomes of mechanical thrombectomy in patients with acute ischemic stroke. *Stroke* 2017;48:361–66 CrossRef Medline
- Davis MJ, Menon BK, Baghirzada LB, et al; Calgary Stroke Program. Anesthetic management and outcome in patients during endovascular therapy for acute stroke. *Anesthesiology* 2012;116:396–405 CrossRef Medline
- Abou-Chebl A, Zaidat OO, Castonguay AC, et al. North American Solitaire Stent-Retriever Acute Stroke Registry: choice of anesthesia and outcomes. *Stroke* 2014;45:1396–1401 CrossRef Medline
- Abou-Chebl A, Yeatts SD, Yan B, et al. Impact of general anesthesia on safety and outcomes in the endovascular arm of Interventional Management of Stroke (IMS) III trial. *Stroke* 2015;46:2142–48 CrossRef Medline
- Schonenberger S, Henden PL, Simonsen CZ, et al. Association of general anesthesia vs procedural sedation with functional outcome among patients with acute ischemic stroke undergoing thrombectomy: a systematic review and meta-analysis. *JAMA* 2019;322:1283–93 CrossRef Medline
- Flottmann F, Leischner H, Broocks G, et al. Emergency conversion to general anesthesia is a tolerable risk in patients undergoing mechanical thrombectomy. *AJNR Am J Neuroradiol* 2020;41:122–27 CrossRef Medline



# Interrater Reliability in the Measurement of Flow Characteristics on Color-Coded Quantitative DSA of Brain AVMs

K.H. Narsinh, K. Mueller, J. Nelson, J. Massachi, D.C. Murph, A.Z. Copelan, S.W. Hetts, V.V. Halbach, R.T. Higashida, A.A. Abl, M.R. Amans, C.F. Dowd, H. Kim, and D.L. Cooke



## ABSTRACT

**BACKGROUND AND PURPOSE:** Hemodynamic features of brain AVMs may portend increased hemorrhage risk. Previous studies have suggested that MTT is shorter in ruptured AVMs as assessed on quantitative color-coded parametric DSA. This study assesses the interrater reliability of MTT measurements obtained using quantitative color-coded DSA.

**MATERIALS AND METHODS:** Thirty-five color-coded parametric DSA images of 34 brain AVMs were analyzed by 4 neuroradiologists with experience in interventional neuroradiology. Hemodynamic features assessed included MTT of the AVM and TTP of the dominant feeding artery and draining vein. Agreement among the 4 raters was assessed using the intraclass correlation coefficient.

**RESULTS:** The interrater reliability among the 4 raters was poor (intraclass correlation coefficient = 0.218; 95% CI, 0.062–0.414; *P* value = .002) as it related to MTT assessment. When the analysis was limited to cases in which the raters selected the same image to analyze and selected the same primary feeding artery and the same primary draining vein, interrater reliability improved to fair (intraclass correlation coefficient = 0.564; 95% CI, 0.367–0.717; *P* < .001).

**CONCLUSIONS:** Interrater reliability in deriving color-coded parametric DSA measurements such as MTT is poor so minor differences among raters may result in a large variance in MTT and TTP results, partly due to the sensitivity and 2D nature of the technique. Reliability can be improved by defining a standard projection, feeding artery, and draining vein for analysis.

**ABBREVIATIONS:** AUC = area under the curve; bAVM = brain AVM; cDSA = color-coded parametric quantitative DSA; ICC = intraclass correlation coefficient; IQR = interquartile range; PCA = posterior cerebral artery; SCA = superior cerebellar artery

Brain AVMs (bAVMs) are uncommon high-flow vascular malformations that often present with intracranial hemorrhage, seizure, or headache in young adults.<sup>1–3</sup> Increasingly, bAVMs are discovered incidentally during brain imaging performed for other reasons.<sup>4</sup> However, management of bAVMs is challenging due to the risk of disability or death associated with hemorrhage, seizure, or infarct during the course of any of the common management strategies, which generally include observation, microsurgical resection, endovascular embolization, stereotactic radiosurgery, or

a combination thereof.<sup>5</sup> For example, in A Randomized Trial of Unruptured Brain AVMs (ARUBA), stroke or death occurred in 30.7% of patients in the interventional arm and 10.1% of patients in the medical management arm during a mean follow-up of 33.3 months.<sup>6</sup> To better risk-stratify patients who would be best served by intervention versus medical management, improved imaging biomarkers are needed to determine which patients with unruptured bAVMs have a high risk of rupture and whether the administered treatments are effective in reducing this risk.

DSA remains the standard method for morphologic and hemodynamic characterization of bAVMs during endovascular interventions, as well as before and after radiosurgical or microsurgical treatment. Angioarchitectural features of bAVM morphology that portend an increased risk of hemorrhage include the presence of nidus or prenidus aneurysms, exclusive deep venous drainage, a single draining vein, venous outflow stenosis, or small nidus size.<sup>7–9</sup> However, clinical and angioarchitectural features alone incompletely estimate hemorrhagic risk.<sup>10–13</sup> For example, the R<sub>2</sub>eD AVM score has recently been proposed as a predictive tool to aid in hemorrhagic risk stratification, incorporating both clinical and angioarchitectural features.<sup>14</sup> Specifically,

Received May 9, 2020; accepted after revision August 5.

From the Department of Radiology and Biomedical Imaging (K.H.N., J.M., D.C.M., A.Z.C., S.W.H., V.V.H., R.T.H., M.R.A., C.F.D., D.L.C.), Center for Cerebrovascular Research (J.N., H.K.), Department of Anesthesiology, and Department of Neurological Surgery (A.A.A.), University of California San Francisco, San Francisco, California; and Siemens Medical Solutions (K.M.), Malvern, Pennsylvania.

This work was supported by National Institutes of Health National Institute of Neurological Disorders and Stroke R01grant NS099628 and NIH NINDS U54 NS065705.

Please address correspondence to Daniel L. Cooke, MD, UCSF Department of Radiology & Biomedical Imaging, 505 Parnassus Ave, L-349, San Francisco, CA, 94143; e-mail: Daniel.Cooke@ucsf.edu

Indicates open access to non-subscribers at www.ajnr.org

<http://dx.doi.org/10.3174/ajnr.A6846>

the score is based on race, exclusive deep location, AVM size, exclusive deep venous drainage, and monoarterial feeding. However, the area under the curve (AUC) of the receiver operating characteristic of the R<sub>2</sub>ED AVM score is 0.685,<sup>14</sup> which may be characterized as “poor” or “fair” compared with other medical tests. Therefore, although the R<sub>2</sub>ED AVM score is an important advance in validating a hemorrhagic risk-prediction model, the incorporation of hemodynamic or genetic features may improve model performance and further validate its use. Specifically, hemodynamic risk factors such as a lower ratio of draining vein to feeding artery TTP,<sup>11,15</sup> shorter MTT or TTP of the nidus,<sup>11,16</sup> and lower mean total AVM flow,<sup>12</sup> could be helpful in supplementing hemorrhagic risk assessment,<sup>13</sup> but they cannot be easily measured during angiography.

Color-coded parametric quantitative DSA (cDSA) has been suggested as a surrogate marker of hemodynamics and a potential metric of hemorrhage risk<sup>11,13,17</sup> and treatment effectiveness<sup>18</sup> in bAVMs. cDSA converts a stack of 2D DSA images into a single composite parametric image that is color-coded according to the TTP opacification of contrast in each pixel.<sup>19</sup> However, the reproducibility of these surrogate cDSA measurements of hemodynamics has not been assessed. In this study, we sought to assess the degree of interrater reliability in cDSA measurements among 4 neuroradiologists reviewing 35 cDSA images from 34 AVMs.

## MATERIALS AND METHODS

### Patients

Thirty-four consecutive patients with ruptured and unruptured bAVMs who were referred for cerebral angiography between June 2017 and December 2018 were included in the study. All patients provided written informed consent.

### Angiography and Data Postprocessing

Using standard neuroangiographic techniques, we acquired DSA series on an Artis Q biplane angiography system (Siemens). A 5F catheter was advanced into the internal carotid or vertebral artery, and iodinated contrast was power-injected at a rate of 5–8 mL/s for a total of 7–11 mL, at a rate of 7.5 frames/s, depending on the feeding and draining vessels identified. All images from the angiographic study were reviewed by the study coordinator, and for each participant, an image with an appropriate projection to visualize the feeding and draining vessels separate from the nidus was designated for review by the raters.

Flow analysis software (syngo iFlow; Siemens) was used to create cDSA images. The diameter of a circular ROI was less than the caliber of a selected vessel, as independently drawn by each rater. In each case, ROIs of the same size were placed on the primary feeding artery and primary draining vein. ROIs were placed as close to the AVM nidus as possible with care to minimize overlap with other feeding arteries or draining veins. For each manually placed ROI, a time-versus-intensity graph was produced and exported by the software with calculated parameters of the following: 1) ROI peak time: time that the contrast intensity of a selected ROI reaches peak value; 2) ROI arrival time: time of arrival of contrast material; 3) MTT: average contrast material transit time through the target, measured as the time between the venous ROI peak and the arterial ROI peak; and 4) TTP: time elapsing from the first appearance of contrast material in the ROI

to the peak contrast concentration in the ROI, that is, TTP = ROI peak time – ROI arrival time. Additionally, the AUC of the time-density graph was calculated as a surrogate marker of the total volume of blood passing through the ROI during the measured time period.

### Raters

Four neuroradiologists (holding Certificates of Added Qualification in neuroradiology from the American Board of Radiology) specializing in interventional neuroradiology interpreted all cDSAs of bAVMs. Two interventional neuroradiology fellows participated, who were in their first and second years of their interventional neuroradiology fellowships and who had completed a diagnostic neuroradiology fellowship and at least 7 years of postgraduate training. Two interventional neuroradiology faculty participated, who had 8 and 35 years of interventional neuroradiology experience. Each rater was given short tutorials on drawing ROIs and a protocol instruction sheet to consult during their reads.

The tutorial and instruction sheet specified the goal of the task and the keystrokes required to open the prespecified images (selected by the study coordinator as described above), place ROIs, and store the quantitative data output. Raters were instructed to provide a qualitative assessment of the AVM flow rate (mild, moderate, or fast) relative to physiologic flow before beginning the postprocessing phase. Raters were then instructed to manually draw a circular ROI on the prespecified image and manually place it on the feeding artery as close to the nidus as possible while avoiding overlapping vasculature. After the initial ROI was placed, raters would make a copy of the circle (to ensure that the 2 were identical) and place it on the draining vein as close to the nidus as possible. Raters were permitted to consult with other neuroradiologists not involved in the study during interpretation.

### Statistical Analysis

The intraclass correlation coefficient (ICC) was calculated to measure agreement of MTT among the 4 raters reviewing 35 AVM images from 34 different AVMs. The ICC calculations assumed a 2-way random-effects model (random raters and cases) with absolute agreement among raters. ICC calculations were also run on multiple subsets of the data on the basis of the following conditions: excluding instances when a rater did not use the prespecified image to review, excluding instances when a rater did not select the consensus feeding and draining vessels, and excluding highly influential outliers that exceeded the threshold of 4 SDs from the mean. Data analysis was conducted with STATA 15.1 (Release 15; StataCorp, 2017). ICC values were calculated using the user-created module KAPPAETC.<sup>20</sup>

## RESULTS

Thirty-five AVM images from 34 AVMs were evaluated (Table 1). The median patient age was 43.5 years (interquartile range [IQR] = 28.8–59.0 years), and 14 (41%) were women. Sixteen (47%) AVMs were ruptured at diagnosis, 27 (79%) were lobar, and 17 of 34 (50%) had deep venous drainage. The median AVM size was 2.15 cm (IQR = 1.4–3.8 cm).

The 35 images were each reviewed by the 4 raters (for a total of 140 reviews). In 135 (96%) instances, the correct image (the

**Table 1: Patient and AVM characteristics**

Characteristic	Summary
Count	34
Patient age (median) (IQR) (yr)	43.5 (28.8–59.0)
Female (No.) (%)	14 (41)
AVM size (median) (IQR) (cm)	2.2 (1.4–3.8)
Ruptured prior imaging (No.) (%)	16 (47)
Lobar location (No.) (%)	27 (79)
Deep venous drainage (No./total) (%)	17/34 (50)

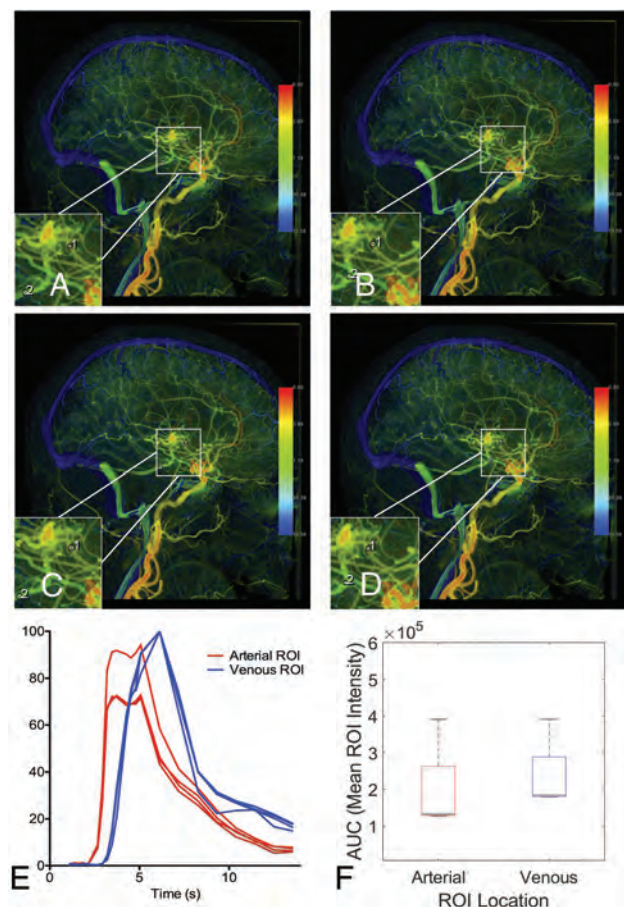


**FIG 1.** cDSA with low variance among raters in MTT results. Right internal carotid arteriogram in a lateral projection shows a right frontal operculum AVM supplied by 2 anterior cortical branches of the MCA, with dominant venous drainage into the vein of Labbe. All 4 raters (A–D) chose the same image to interpret and placed ROIs on the primary feeding artery and primary draining vein, in almost the same location. E, Time-density curves for the 4 raters are largely consistent, with the exception of a slightly larger arterial ROI by rater 3 (C) encompassing an adjacent overlapping vessel, which results in a larger AUC for the arterial ROI (F). The peaks of the time-density curves are consistent, however, yielding reproducible results (median MTT of 1.73 seconds with IQR = 1.06–2.4).

image prespecified in the protocol sheet provided to the raters) was reviewed. When the correct image was reviewed, there were 116 (86%) instances in which the consensus feeding artery was selected and 115 (85%) instances in which the consensus draining vein was selected. In 100 (74%) instances, both the consensus feeding and draining vessels were selected. The median MTT was 0.93 seconds (IQR = 0.54–1.20 seconds), with a minimum value

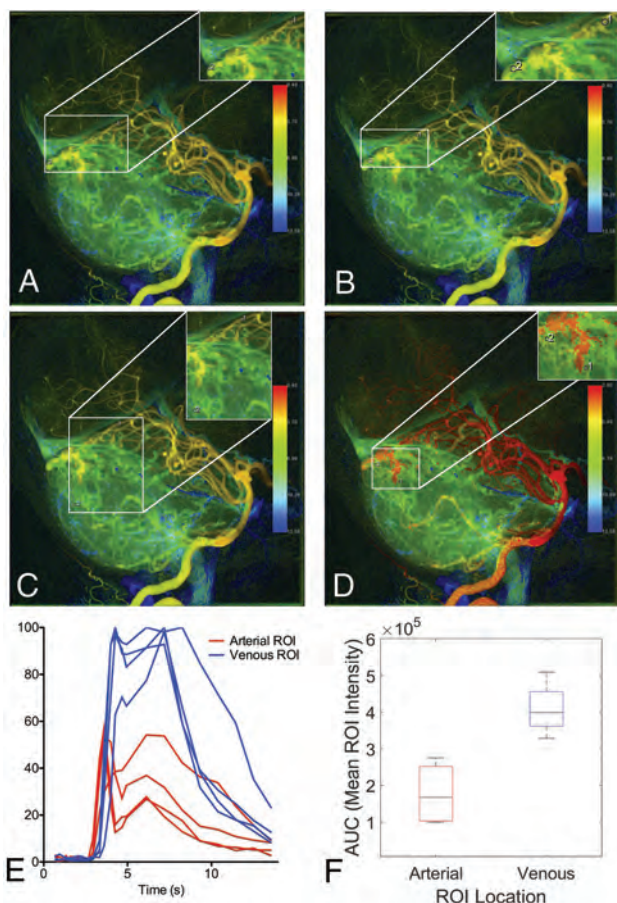
of –0.94 seconds (the only negative value) and a maximum of 7.06 seconds. Negative results for MTT do not have a physically interpretable meaning, due to overlapping vessels in the 2D projection resulting in an arterial ROI TTP greater than the venous ROI TTP.

Figure 1 demonstrates how the same cDSA image was interpreted by the 4 raters with the same vessels selected for analysis and low variance in cDSA results. On the lateral projection of a right internal carotid arteriogram, a right frontal operculum AVM is identified, supplied by 2 anterior cortical branches of the MCA, with dominant venous drainage into the vein of Labbe and minor venous drainage into the thalamostriate vein (not well-seen on cDSA). All 4 raters chose the correct image to interpret and chose the same feeding and draining vessels to analyze (ie, placed the ROIs on the same primary feeding artery and primary draining vein, though the ROI size slightly varied among raters). As a result, cDSA measurements were similar among raters, with a median MTT of 1.73 seconds (IQR = 1.06–2.4 seconds).

Figure 2 demonstrates how the same cDSA image was interpreted by the 4 raters with high variance in results. On the lateral projection of a left vertebral arteriogram, an AVM in the dorsal vermis of the cerebellum is identified, with arterial supply from the left superior cerebellar artery (SCA) and left PICA and venous drainage into the vermician and tentorial veins. Both rater 1 (upper left) and rater 2 (upper right) placed ROIs on the same vessels (the SCA and tentorial vein) at nearly the same location, yet the MTT for rater 1 was 3.6 seconds, while the MTT for rater 2 was 0.7 seconds. The venous time-density curve for rater 1 has a larger second peak, which increased the calculated venous TTP. Rater 3 (lower left) selected an inferior vermician vein rather than a tentorial vein for the venous ROI placement. Rater 4 (lower right) selected the left PICA rather than the SCA for the arterial ROI placement. This case illustrates how raters differed in their assignment of the feeding and draining vessels, leading to cDSA measurements that were not reproducible, with a median MTT of 2.13 seconds (IQR = 0.50–4.66 seconds).

Figure 3 demonstrates how the same cDSA image was interpreted by the 4 raters with different vessels selected for analysis but low variance in the cDSA results. On the lateral projection of a right vertebral arteriogram, a right occipital lobe AVM is identified, supplied by calcarine and parieto-occipital branches of the right posterior cerebral artery (PCA). Dominant venous drainage is into 2 internal occipital veins superior to the nidus, with minor drainage into a tentorial vein inferiorly. The tentorial venous egress overlaps the calcarine branch of the PCA feeding the AVM. All raters selected the calcarine branch of the PCA as the dominant arterial feeder but placed the ROI either proximal or distal to the overlapping tentorial venous egress. Three raters selected the more superior of the internal occipital veins as the primary draining vein, while 1 rater selected the smaller, more inferior of the internal occipital veins as the primary draining vein. For this participant, the median normalized linear distance between paired ROIs was 0.56 (IQR = 0.41–0.85). As a result, the slopes and AUC of the arterial and venous time-density curves vary among raters. Nevertheless, the TTP measurements were similar among raters, with a median MTT of 0.53 seconds (IQR = 0.53–0.8 seconds).





**FIG 2.** cDSA with high variance among raters in MTT results. Left vertebral arteriogram in a lateral projection shows a cerebellar AVM with arterial supply from the left SCA and left PICA and venous drainage into vermian and tentorial veins. A and B, Raters 1 and 2 placed ROIs on the same vessels, the SCA and tentorial vein, at nearly the same location, yet the MTT for rater 1 (A) is 3.6 seconds, while the MTT for rater 2 is 0.7 seconds. The venous time-density curve for rater 1 (A) has a larger second peak, which increased the calculated venous TTP. Rater 1 (A) placed the ROI on a draining vein where it overlaps with a normal draining vein, and the second peak is a manifestation of the normal venous phase of the angiogram. C, Rater 3 selected an inferior vermian vein rather than a tentorial vein for venous ROI placement. D, Rater 4 selected the left PICA rather than the SCA for arterial ROI placement. Differences in ROI placement result in different time-density curves (E) and calculated AUCs (F).

Figure 4 is a scatterplot comparing MTT values of 2 of the 4 raters. The raters often disagreed on the feeding and draining vessels, placing ROIs on different feeding arteries and draining veins, and rarely used the wrong image for analysis (despite instructions to use a specified image).

We calculated that the ICC of the MTT among the 4 raters was 0.218 (95% CI, 0.062–0.414;  $P$  value = .002; Table 2). When excluding instances when raters assessed the incorrect image, the ICC increased to 0.243 (95% CI, 0.083–0.446;  $P$  = .001). When we only considered ratings that chose the consensus feeding and draining vessels, the ICC increased to 0.564 (95% CI, 0.347–0.717;  $P$  < .001). Results for the sensitivity analyses excluding outliers are presented in Table 2. Raters also made qualitative

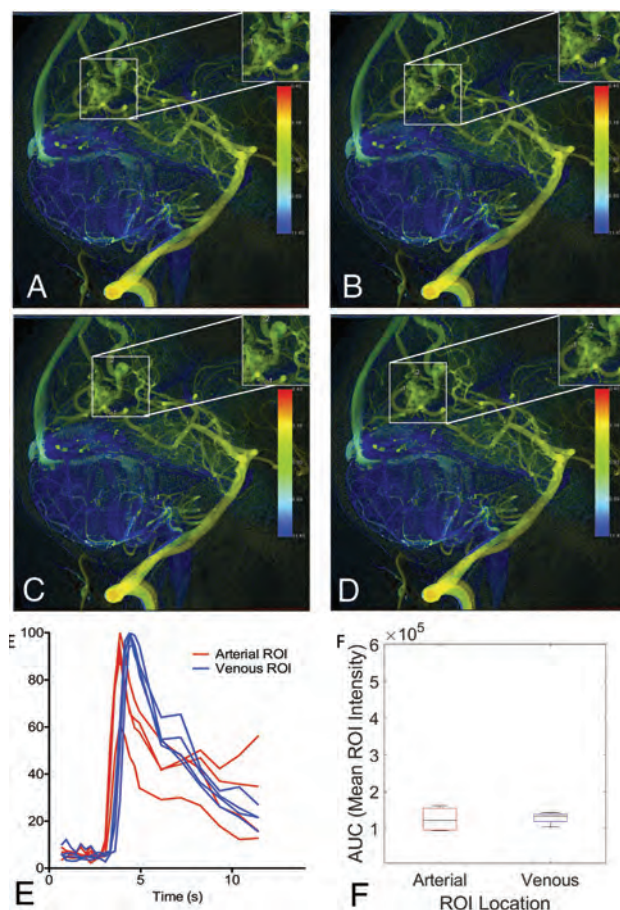


**FIG 3.** cDSA with variation among raters in vessels selected for analysis. Left vertebral arteriogram in a lateral projection shows a right occipital lobe AVM supplied by the calcarine and parieto-occipital branches of the right PCA, with dominant drainage into 2 internal occipital veins superior to the nidus and minor drainage into a tentorial vein inferiorly. A, Rater 1 placed the arterial ROI on the calcarine branch of the PCA distal to the overlapping minor venous egress and placed the venous ROI on the more superior internal occipital vein. B, Rater 2 placed the arterial ROI on the calcarine branch of the PCA proximal to the overlapping minor venous egress and placed the venous ROI on the more superior internal occipital vein. C, Rater 3 placed the arterial ROI on the calcarine branch of the PCA proximal to the overlapping minor venous egress and placed the venous ROI on the more superior internal occipital vein, though distal relative to rater 2. D, Rater 4 placed the arterial ROI on the calcarine branch of the PCA distal to the overlapping minor venous egress, similar to rater 1. Rater 4 also placed the venous ROI on the more inferior internal occipital vein, unlike the other raters. Despite differences in the vessels selected for analysis, time-density curves (E) and AUCs (F) were largely reproducible because the ROIs were placed so close to the nidus by all raters.

assessments of flow (mild, moderate, or fast), which were in fair agreement ( $\kappa$  = 0.33; 95% CI, 0.17–0.49;  $P$  < .001).

We next sought to demonstrate how variability in ROI placement affects hemodynamic metrics. We selected 2 representative AVMs with a clearly identifiable feeding artery and draining vein and then placed 4 ROIs along the primary feeding artery and 4 ROIs along the primary draining vein to generate time-density curves and peak times.

Figure 5 shows cDSA of a right internal carotid arteriogram in a lateral projection demonstrating a right frontal lobe AVM supplied by a frontopolar branch of the anterior cerebral artery with venous drainage into a frontal cortical vein that empties into the superior sagittal sinus. Arterial ROIs 1 and 3 include overlapping vessels that opacify in the normal arterial phase, resulting in longer peak times than arterial ROIs 2 and 4. Venous ROI 2 includes an overlapping artery that opacifies in the normal arterial phase, resulting in a shorter peak time than venous ROIs 1, 3, and 4.

Figure 6 show cDSA of a left internal carotid arteriogram in lateral projection, demonstrating a left parietal lobe AVM supplied by an enlarged callosomarginal branch of the left anterior cerebral artery, with venous drainage into a dilated left internal cerebral vein. Arterial ROI 1 is placed closest to the nidus, resulting in the largest peak time. Arterial ROI 3 is placed on a segment of the callosomarginal artery that courses laterally into the sulcus (labeled by an asterisk in lower left inset of Fig 5A), resulting in slightly increased contrast density within that ROI because of the in-plane course of that vessel segment and a smaller peak time (Fig 5D). Venous ROI 1 results in the largest AUC because it is placed closest to the nidus (Fig 6C), but the peak times are identical among venous ROIs 1, 2, and 4. However, venous ROI 3 results in a shorter peak time (Fig 6D) because of accumulation of contrast in that segment after ribbonlike streaming of contrast mixing with unopacified blood around the curve containing venous ROIs 1 and 2.<sup>21</sup>

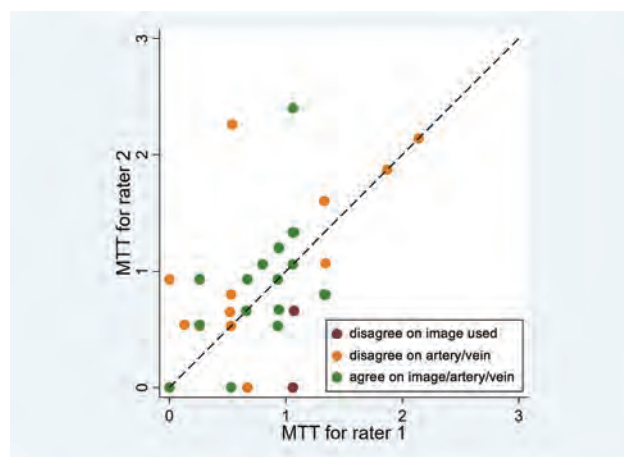


**FIG 4.** Interrater agreement between 2 representative raters. The calculated MTTs for raters 1 and 2 were compared (horizontal axis = rater 1, vertical axis = rater 2). A dashed diagonal line represents perfect agreement between the 2 raters. When the same image, feeding artery, and draining vein are used for analysis, agreement improves. Similar interrater agreement was observed in other pair-wise comparisons of raters.

## DISCUSSION

bAVMs are high-flow vascular malformations typified by transit of blood from arteries to veins through a nidus without a normal intervening capillary bed. The nidus typically has lower vascular resistance than normal capillaries; therefore, bAVMs are subject to a rapid rate of blood flow. These abnormal hemodynamics affect the molecular and structural composition of blood vessels in ways that are still being elucidated. For instance, in bulk RNA sequencing experiments comparing bAVMs with high and low flow, activation of Wnt signaling has been found as a feature of low-flow bAVMs.<sup>22</sup> In vitro and murine in vivo models have found that connexin 37 expression is differentially regulated by shear stress, and that reduced expression of connexin 37 allows enlargement of capillaries and their conversion into arteriovenous shunts.<sup>23</sup> Increased flow and resulting wall shear stress have also been implicated as factors associated with the growth of aneurysms,<sup>24–26</sup> likely due to increased inflammation in the aneurysm wall.<sup>27</sup> In addition to effects on the arteries, increased flow and pressure in the draining veins are associated with venous intimal hyperplasia that contributes to increased wall thickness and venous outflow stenosis, a known risk factor for bAVM hemorrhage.<sup>12,28</sup>

Hemodynamic features are an important component of bAVM assessment in that one may gain insight into underlying pathobiology, individual hemorrhagic risk, and patient treatment goals. However, hemodynamic features of bAVMs are difficult to study because of complicated flow patterns through the nidus and the need for minimal invasiveness in assessing blood vessels at risk of rupture. Studies of bAVM hemodynamics have investigated the use of transcranial sonography, MRA, and DSA. An early study of transcranial sonography found no significant association with hemorrhage risk,<sup>29</sup> but this technique has largely been supplanted by MRA due to its superior spatial coverage. The supposition that the increased flow rate in bAVMs contributes to prenidus and perinidal aneurysm formation is supported by the results of Shakur et al,<sup>30</sup> who, using phase-contrast MRA, demonstrated increased wall shear stress in arterial afferents harboring aneurysms compared with arterial afferents that did not. On the other hand, Illies et al<sup>31</sup> found that hemodynamic parameters on time-resolved MRA showed no association to known anatomic or angioarchitectural features of increased hemorrhage risk, including associated aneurysms. Rather, they found that MTT was increased in bAVMs that had previously ruptured, which did not seem to change or normalize with time, suggesting a permanent alteration in hemodynamics after rupture.

Catheter-based cerebral angiography remains the standard reference test for bAVMs because of its superior temporal and spatial resolution, allowing confident diagnosis typified by identification of an early draining vein relative to normal brain

**Table 2: Intraclass correlation coefficients**

Reviews Included	Primary Analysis				Sensitivity Analysis Excluding Outliers			
	No.	ICC	95% CI	P Value	No.	ICC	95% CI	P Value
All	140	0.218	(0.062–0.414)	.002	138	0.463	(0.294–0.641)	<.001
Consensus images only	135	0.243	(0.083–0.446)	.001	133	0.478	(0.307–0.655)	<.001
Consensus image, feeding artery, and draining vein	100	0.564	(0.347–0.717)	<.001	100	0.564	(0.347–0.717)	<.001

**Note:**—No. indicates total number of reviews included across all raters



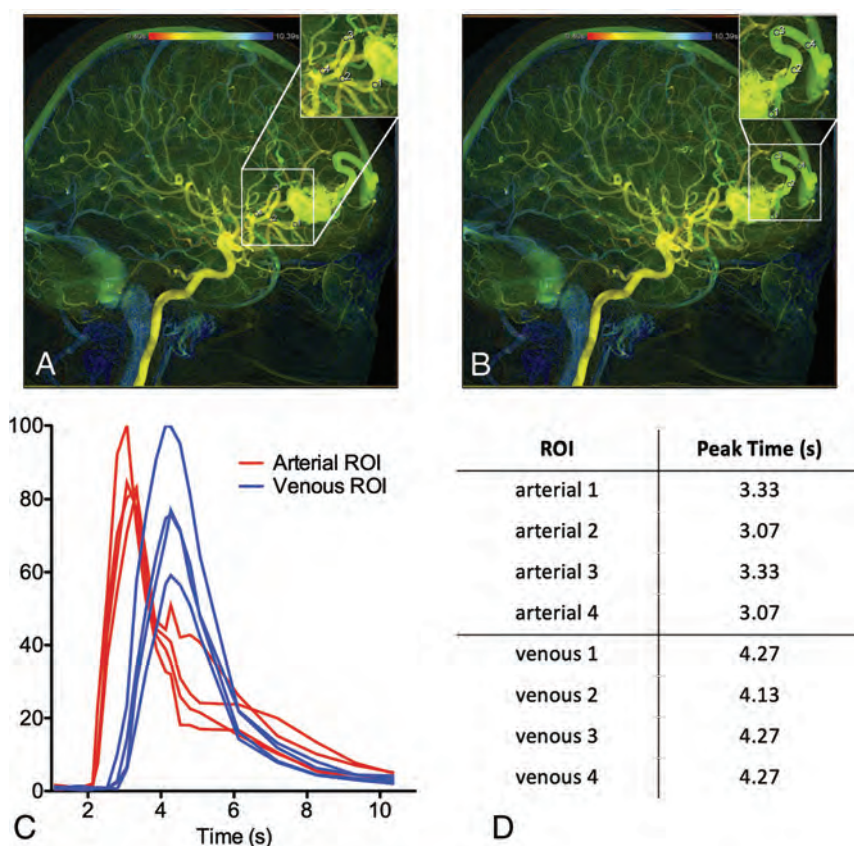


**FIG 5.** Variations in ROI placement can alter time-density curves and calculated peak times due to overlapping vessels. A right internal carotid arteriogram in a lateral projection demonstrates a right frontal lobe AVM supplied by the frontopolar branch of the right anterior cerebral artery with venous drainage into a frontal cortical vein, which drains into the superior sagittal sinus. A, Four arterial ROIs were placed along the course of the arterial feeder with varying proximity to the nidus. B, Four venous ROIs were placed along the course of the draining vein with varying proximity to the nidus. C, The resulting time-density curves are not reproducible. D, The resulting peak times are not reproducible.

parenchyma, even if the nidus is small, and evaluation for angio-graphic features that inform hemorrhage risk and treatment risk. Thus, DSA is routinely performed to diagnose and assess angioarchitectural risk factors of bAVMs such as the presence of nidus or prenidus aneurysms, exclusive deep venous drainage, a single draining vein, venous outflow stenosis, or small nidus size.<sup>7-9</sup> Hemodynamic metrics may augment hemorrhagic risk stratification models that are currently based on clinical and angioarchitectural features alone.<sup>11,16,17</sup>

cDSA can be obtained on the angiographic dataset using post-processing software without additional contrast administration or an ionizing radiation dose. cDSA has been used by multiple groups to study hemodynamic parameters that may predict the natural history and/or treatment response of a particular AVM.<sup>11,16-18,32-34</sup> However, the reproducibility of such measurements and operator-dependence have not been evaluated. While angioarchitectural features have standardized terminology,<sup>35</sup> no such standardization has yet been adopted for cDSA measurements.

Herein, we evaluated the interrater reliability among 4 neuro-radiologists of cDSA measurements obtained during DSA of bAVMs. Among our group of raters, considerable variability was

seen in the images and vessels used for cDSA analysis. Although reproducibility was fair in instances in which the same image and vessels were selected for analysis, ROI placement along the length of the vessel (ie, proximal to distal) varied among raters, leading to variability in results. Interrater reliability was poor overall but improved to fair in the subset of measurements in which raters agreed on the same image, feeding artery, and draining vein to analyze. Even when a consensus image, feeding artery, and draining vein were selected for analysis, differences in placement of the ROI (from proximal to distal) varied the impact of overlapping vessels on the resulting time-density curves and hence altered the derived metrics. When all raters placed ROIs close to the nidus without overlapping other vessels, results became more reproducible, though the finite temporal resolution of cDSA may preclude meaningful comparison of such results among patients. These results enjoin caution in the widespread application of cDSA without strict supervision of image analysis because measurements varied considerably among physicians in the current study, and variation among institutions has not yet been assessed. By comparison, inter- and intraobserver variability in the assessment of angioarchitectural features at high risk of hemorrhage, such as feeding

artery aneurysms or intranidal aneurysms, is also poor.<sup>36</sup>

A 4D rotational flat panel CT could allow one to better select vessels for hemodynamic measurements in 3D, thereby avoiding the challenge of overlapping vessel anatomy in the 2D projection space and possibly improving reproducibility.<sup>37,38</sup> Such techniques require a separate rotational flat panel conebeam CT acquisition and are not based on the conventional 2D planar DSA images that serve as the current workhorse method for evaluating AVM angioarchitecture. When measuring hemodynamics using cDSA of 2D planar data, other groups have chosen to place ROIs at locations less susceptible to variation (eg, the cavernous internal artery or jugular bulb), which may improve reproducibility. However, if ROIs are placed at the skull base, a more general assessment of global hemispheric flow is obtained. Arteriovenous shunting of contrast due to the AVM is averaged with physiologic cerebral perfusion, a feature that may reduce noise in the calculation of MTT or other hemodynamic measures but may also reduce the magnitude of any meaningful hemodynamic change, thereby limiting the sensitivity of the method. In the future, reproducibility may be improved using postprocessing software with semiautomated ROI selection based on vessel-diameter



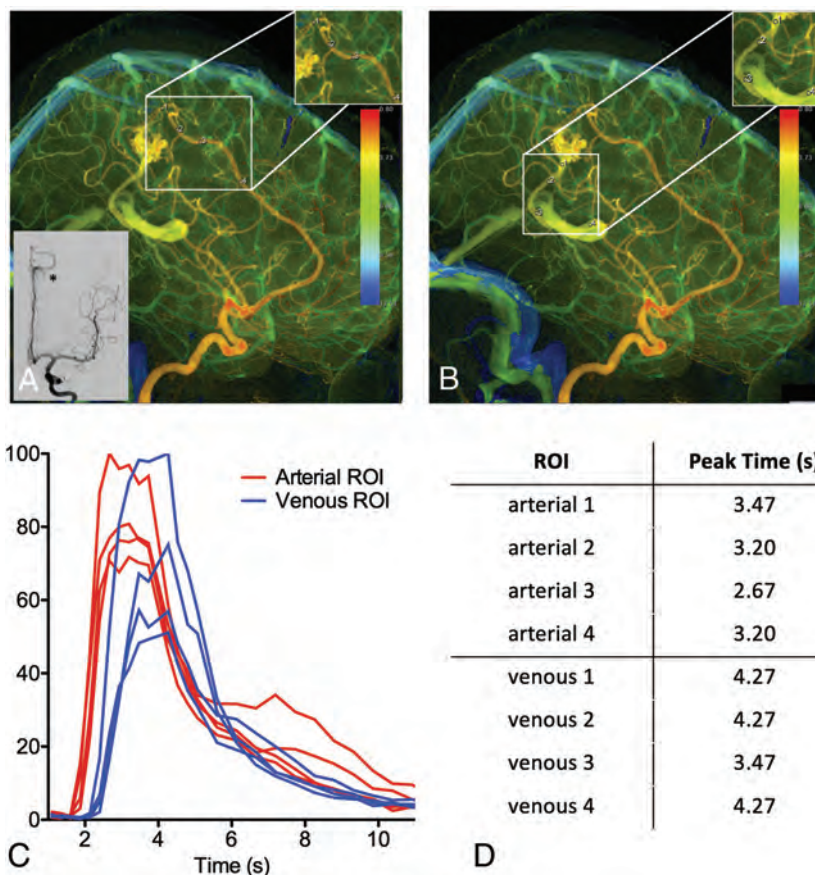


**FIG 6.** Variation in ROI placement can alter time-density curves and calculated peak times due to the in-plane vessel course and contrast mixing. Left internal carotid arteriogram in a lateral projection demonstrates a left parietal lobe AVM supplied by the left anterior cerebral artery with venous drainage into a dilated left internal cerebral vein. A, Four arterial ROIs were placed along the course of the left anterior cerebral artery feeder with varying proximity to the nidus. B, Four venous ROIs were placed along the course of the draining vein that empties into the left internal cerebral vein with varying proximity to the nidus. C, The resulting time-density curves are not reproducible. D, The resulting peak times are not reproducible.

thresholds. Automation in ROI placement based on computed juxtanal arterial and venous diameters and avoidance of overlapping vessels would eliminate subjective assessments of primary afferent and efferent features.

## CONCLUSIONS

Interrater reliability of cDSA measurements was poor overall but could be improved when raters agreed on the same image, primary draining artery, and primary draining vein to analyze. Caution should be used in interpretation of hemodynamic measures derived from cDSA because results may vary among physicians without strict supervision of image analysis.

Disclosures: Jeffrey Nelson—RELATED: Grant: National Institutes of Health.\* Kerstin Mueller—RELATED: Other: employed by Siemens; UNRELATED: Employment: Siemens. Steven W. Hetts—UNRELATED: Grants/Grants Pending: Siemens, Comments: research contracts for X-ray angiography systems\*. Christopher F. Dowd—UNRELATED: Other: Stryker, Comments: I serve as Chief Adjudicator of the Angio Core Lab for the EVOLVE flow-diverter clinical trial (department salary support).\* Helen Kim—RELATED: Grant: National Institutes of Health, Comments: R01NS034949.\* Money paid to institution.

## REFERENCES

1. Brown RD, Wiebers DO, Torner JC, et al. Frequency of intracranial hemorrhage as a presenting symptom and subtype analysis: a population-based study of intracranial vascular malformations in Olmsted County, Minnesota. *J Neurosurg* 1996;85:29–32 CrossRef Medline
2. Brown RD, Wiebers DO, Forbes G, et al. The natural history of unruptured intracranial arteriovenous malformations. *J Neurosurg* 1988;68:352–57 CrossRef Medline
3. Graf CJ, Perret GE, Torner JC. Bleeding from cerebral arteriovenous malformations as part of their natural history. *J Neurosurg* 1983;58:331–37 CrossRef Medline
4. Morris Z, Whiteley WN, Longstreth WT, et al. Incidental findings on brain magnetic resonance imaging: systematic review and meta-analysis. *BMJ* 2009;339:b3016 CrossRef Medline
5. Derdeyn CP, Zipfel GJ, Albuquerque FC, et al; American Heart Association Stroke Council. Management of Brain Arteriovenous Malformations: A Scientific Statement for Healthcare Professionals From the American Heart Association/American Stroke Association. *Stroke* 2017;48:e200–24 CrossRef Medline
6. Mohr JP, Parides MK, Stapf C, et al; International ARUBA investigators. Medical management with or without interventional therapy for unruptured brain arteriovenous malformations (ARUBA): a multicentre, non-blinded, randomised trial. *Lancet* 2014;383:614–21 CrossRef Medline
7. Alexander MD, Cooke DL, Nelson J, et al. Association between venous angioarchitectural features of sporadic brain arteriovenous malformations and intracranial hemorrhage. *AJNR Am J Neuroradiol* 2015;36:949–52 CrossRef Medline
8. Sahlein DH, Mora P, Bekske T, et al. Features predictive of brain arteriovenous malformation hemorrhage. *Stroke* 2014;45:1964–70 CrossRef Medline
9. Stein K-P, Wanke I, Forsting M, et al. Associated aneurysms in supratentorial arteriovenous malformations: impact of aneurysm size on haemorrhage. *Cerebrovasc Dis* 2015;39:122–29 CrossRef Medline
10. Shakur SF, Liesse K, Amin-Hanjani S, et al. Relationship of cerebral arteriovenous malformation hemodynamics to clinical presentation, angioarchitectural features, and hemorrhage. *Neurosurgery* 2016;63:136–40 CrossRef Medline
11. Chen X, Cooke DL, Saloner D, et al. Higher flow is present in unruptured arteriovenous malformations with silent intrasubcortical microhemorrhages. *Stroke* 2017;48:2881–84 CrossRef Medline
12. Shakur SF, Hussein AE, Amin-Hanjani S, et al. Cerebral arteriovenous malformation flow is associated with venous intimal hyperplasia. *Stroke* 2017;48:1088–91 CrossRef Medline
13. Norris JS, Valiante TA, Wallace MC, et al. A simple relationship between radiological arteriovenous malformation hemodynamics and clinical presentation: a prospective, blinded analysis of 31 cases. *J Neurosurg* 1999;90:673–79 CrossRef Medline

14. Feghali J, Yang W, Xu R, et al. **R2eD AVM score.** *Stroke* 2019;50:1703–10 CrossRef Medline
15. Raoult H, Bannier E, Maurel P, et al. **Hemodynamic quantification in brain arteriovenous malformations with time-resolved spin-labeled magnetic resonance angiography.** *Stroke* 2014;45:2461–64 CrossRef Medline
16. Lin TM, Yang HC, Lee CC, et al. **Stasis index from hemodynamic analysis using quantitative DSA correlates with hemorrhage of supratentorial arteriovenous malformation: a cross-sectional study.** *J Neurosurg* 2019 April 26. [Eub ahead of print] CrossRef Medline
17. Burkhardt JK, Chen X, Winkler EA, et al. **Delayed venous drainage in ruptured arteriovenous malformations based on quantitative color-coded digital subtraction angiography.** *World Neurosurg* 2017;104:619–27 CrossRef Medline
18. Rivera R, Sordo JG, Echeverria D, et al. **Quantitative evaluation of arteriovenous malformation hemodynamic changes after endovascular treatment using parametric color coding: a case series study.** *Interv Neuroradiol* 2017;23:650–55 CrossRef Medline
19. Strother CM, Bender F, Deuerling-Zheng Y, et al. **Parametric color coding of digital subtraction angiography.** *AJNR Am J Neuroradiol* 2010;31:919–24 CrossRef Medline
20. Klein DK. **KAPPAETC: Stata Module to Evaluate Interrater Agreement.** Boston College Department of Economics. 2019. <https://econpapers.repec.org/software/bocbocode/s458283.htm>. Accessed October 03, 2020.
21. Ruedinger KL, Harvey EC, Schafer S, et al. **Optimizing the quality of 4D-DSA temporal information.** *AJNR Am J Neuroradiol* 2019;40:2124–29 CrossRef Medline
22. Huo R, Fu W, Li H, et al. **RNA sequencing reveals the activation of Wnt signaling in low flow rate brain arteriovenous malformations.** *J Am Heart Assoc* 2019;8:e012746 CrossRef Medline
23. Peacock HM, Tabibian A, Criem N, et al. **Impaired SMAD1/5 mechanotransduction and Cx37 (connexin 37) expression enable pathological vessel enlargement and shunting.** *Arterioscler Thromb Vasc Biol* 2020;40:e87–104 CrossRef Medline
24. Cebal JR, Mut F, Weir J, et al. **Association of hemodynamic characteristics and cerebral aneurysm rupture.** *AJNR Am J Neuroradiol* 2011;32:264–70 CrossRef Medline
25. Sforza DM, Kono K, Tateshima S, et al. **Hemodynamics in growing and stable cerebral aneurysms.** *J Neurointerv Surg* 2016;8:407–12 CrossRef Medline
26. Varble N, Rajabzadeh-Oghaz H, Wang J, et al. **Differences in morphologic and hemodynamic characteristics for “PHASES-based” intracranial aneurysm locations.** *AJNR Am J Neuroradiol* 2017;38:2105–10 CrossRef Medline
27. Cebal J, Ollikainen E, Chung BJ, et al. **Flow conditions in the intracranial aneurysm lumen are associated with inflammation and degenerative changes of the aneurysm wall.** *AJNR Am J Neuroradiol* 2017;38:119–26 CrossRef Medline
28. Viñuela F, Nombela L, Roach MR, et al. **Stenotic and occlusive disease of the venous drainage system of deep brain AVM's.** *J Neurosurg* 1985;63:180–84 CrossRef Medline
29. Kader A, Young WL, Pile-Spellman J, et al. **The influence of hemodynamic and anatomic factors on hemorrhage from cerebral arteriovenous malformations.** *Neurosurgery* 1994;34:801–08 CrossRef Medline
30. Shakur SF, Amin-Hanjani S, Mostafa H, et al. **Hemodynamic characteristics of cerebral arteriovenous malformation feeder vessels with and without aneurysms.** *Stroke* 2015;46:1997–99 CrossRef Medline
31. Illies T, Forkert ND, Saering D, et al. **Persistent hemodynamic changes in ruptured brain arteriovenous malformations.** *Stroke* 2012;43:2910–15 CrossRef Medline
32. Todaka T, Hamada JJ, Kai Y, et al. **Analysis of mean transit time of contrast medium in ruptured and unruptured arteriovenous malformations.** *Stroke* 2003;34:2410–14 CrossRef Medline
33. Shellikeri S, Bai H, Setser RM, et al. **Association of intracranial arteriovenous malformation embolization with more rapid rate of perfusion in the peri-nidal region on color-coded quantitative digital subtraction angiography.** *J Neurointerv Surg* 2020;12:902–05 CrossRef Medline
34. Ma GM, Dmytriw AA, Patel PA, et al. **Quantitative color-coded digital subtraction neuroangiography for pediatric arteriovenous shunting lesions.** *Childs Nerv Syst* 2019;35:2399–403 CrossRef Medline
35. Atkinson RP, Awad IA, Batjer HH, et al; Joint Writing Group of the Technology Assessment Committee American Society of Interventional and Therapeutic Neuroradiology; Joint Section on Cerebrovascular Neurosurgery a Section of the American Association of Neurological Surgeons and Congress of Neurological Surgeons; Section of Stroke and the Section of Interventional Neurology of the American Academy of Neurology. **Reporting terminology for brain arteriovenous malformation clinical and radiographic features for use in clinical trials.** *Stroke* 2001;32:1430–42 CrossRef Medline
36. Iancu-Gontard D, Weill A, Guilbert F, et al. **Inter- and intraobserver variability in the assessment of brain arteriovenous malformation angioarchitecture and endovascular treatment results.** *AJNR Am J Neuroradiol* 2007;28:524–27 Medline
37. Lin EY, Lee RC, Guo WY, et al. **Three-dimensional quantitative color-coding analysis of hepatic arterial flow change during chemoembolization of hepatocellular carcinoma.** *J Vasc Interv Radiol* 2018;29:1362–68 CrossRef Medline
38. Meijs M, Pegge S, A H, Murayama K, et al. **Color-mapping of 4D-CTA for the detection of cranial arteriovenous shunts.** *AJNR Am J Neuroradiol* 2019;40:1498–1504 CrossRef Medline

# Selection of Patients for Treatment of Brain Arteriovenous Malformations by the Transvenous Approach: Relationship with Venous Anatomy and Risk of Hemorrhagic Complications

J.M.B. De Sousa, C. Iosif, L.Z. Sganzerla, A.N. Rafie, V. Borodetsky, A. Rouchaud, S. Saleme, and C. Mounayer

## ABSTRACT

**BACKGROUND AND PURPOSE:** Intracranial hemorrhage represents a severe complication of brain arteriovenous malformation treatment. The aim of this cohort was to report the rate of hemorrhagic complications after transvenous endovascular embolization and analyze the potential angioarchitectural risk factors as well as clinical outcomes.

**MATERIALS AND METHODS:** During an 11-year period, 57 patients underwent transvenous endovascular embolization. All cases of hemorrhagic complications were identified. We analyzed the following variables: sex, age, hemorrhagic presentation, Spetzler-Martin grade, size of the AVM before the transvenous treatment, number of venous collectors, pattern of drainage, presence of dilated veins, and technical aspects. Univariate and multivariate multiple regression analyses were performed to evaluate the potential risk factors for procedure-related hemorrhagic complications.

**RESULTS:** Hemorrhagic complications (either intraprocedural or periprocedural) unrelated to a perforation due to microneavigation occurred in 8 (14.0%) procedures. Significant ( $mRS > 2$ ) and persistent neurologic deficits were present in 2 (3.5%) patients at 6-month control. Larger nidi, especially  $> 3$  cm ( $P = .03$ ), and a larger number of venous collectors have shown a statistically significant correlation with hemorrhagic complications. Only the number of venous collectors was identified as an independent predictor of hemorrhagic complications in the multivariate analysis (OR, 8.7; 95% confidence interval, 2.2–58.2) ( $P = .006$ ).

**CONCLUSIONS:** Larger nidus sizes and an increased number of venous collectors may increase the risk of hemorrhagic complications when implementing transvenous endovascular treatment of AVMs. The technique is effective and promising, especially with small nidi and single venous collectors.

**ABBREVIATIONS:** bAVM = brain arteriovenous malformation; HC = hemorrhagic complications; TVE = transvenous endovascular embolization

Endovascular treatment for brain arteriovenous malformations (bAVMs) was traditionally focused on targeting the nidus through an intra-arterial approach, whether as a means of curative treatment or targeted embolization as an adjunctive or emergency treatment. In an attempt to target parts of the nidus that lie in the deep brain areas or that are supplied by very thin or perforating arterial branches, transvenous endovascular embolization (TVE) has emerged and is becoming a new tool to target otherwise incurable brain AVMs.<sup>1–3</sup>

Even though TVE has several advantages, including a very high rate of angiographic cure up to 92.6%<sup>3</sup> and a means of

curing otherwise incurable bAVMs,<sup>4,5</sup> it still needs to be used very selectively, to reduce hemorrhagic complications (HC).

Nevertheless, the technique is not exempt from intraprocedural or periprocedural complications. Hemorrhagic complications represent the most important and challenging procedure-related issues with this technique, which may lead to poor clinical outcomes.<sup>6–9</sup>

A greater understanding of the frequency and risk factors for HC may optimize patient selection for TVE. The aim of this study was to estimate the rates of intraprocedural and periprocedural hemorrhage after TVE for bAVMs, to assess the morbidity and mortality associated with bleeding, and to analyze the angioarchitectural risk factors linked with such complications.

## MATERIALS AND METHODS

### Study Design and Participants

The institutional review board and ethics committee of our institution had approved the current study protocol. All subjects (or

Received June 10, 2020; accepted after revision August 4.

From the Department of Interventional Neuroradiology, Hôpital Dupuytren, Centre Régional Hospitalier Universitaire de Limoges, Limoges, France.

Please address correspondence to Jorge Murilo Barbosa De Sousa, MD, MSc, Department of Interventional Neuroradiology, Hôpital Dupuytren, Centre Régional Hospitalier Universitaire de Limoges, 2 Ave Martin Luther-King, 87042 Limoges Cedex, France; e-mail: jorgemurilobos@gmail.com  
<http://dx.doi.org/10.3174/ajnr.A6810>



legal guardians) signed an informed consent form. This cohort study was performed in accordance with the Code of Medical Ethics of the World Medical Association (Declaration of Helsinki, 2014).

We reviewed a prospectively collected data base of 192 patients with bAVMs who underwent endovascular treatment at our institution between January 2008 and July 2019. A total of 57 patients underwent TVE.

We assessed demographics, medical history, imaging results, postoperative examinations, and clinical follow-up among all patients. All HC were prospectively evaluated, and the location of the hemorrhage, its temporal relationship with TVE, clinical outcomes, mRS score, and imaging outcomes at discharge and after 6 months were recorded in a quantified fashion in a prospectively maintained data base.

The recorded anatomic data included the largest diameter of the nidus before any intervention, the diameter of the nidus immediately before TVE, the location of the nidus (cortical or deep), and the number of venous collectors. Three senior interventional neuroradiologists retrospectively evaluated whether draining veins were dilated or nondilated. The evaluator were also blinded to the outcome and a vein being dilated when it had at least twice the diameter of the corresponding contralateral vein. Additionally, we classified the nidi of bAVMs into 2 groups: those that were 0–3 cm in diameter and those of >3 cm in diameter.

In addition to adult patients, children and adolescents with bAVMs treated by TVE were included.

Patients diagnosed with vein of Galen malformations and dural arteriovenous fistulas were excluded.

### Outcome Assessments

In all cases, the goal of TVE was curative embolization of the bAVMs. Arterial embolization usually preceded the intervention, whenever possible, to reduce the size of nidus. However, for this series, we present only the clinical outcomes and complications of TVE.

Patients were examined by a senior neuroradiologist and a senior anesthesiologist. A CT scan was obtained immediately after each TVE session. As part of our protocol, cranial MR imaging was performed for all patients 24 hours before and after embolization.

The mRS score was used preoperatively and at follow-up assessment in a prospective fashion. The parameters assessed were the following: the overall frequency of HC (related and unrelated to endovascular access), the rate of obliteration at 6 months after treatment with TVE, and the existence of permanent neurologic deficits at 6 months. An adverse event was defined as a new neurologic deficit that occurred within 6 months of embolization. Angioarchitectural analyses considered only HC unrelated to endovascular access to avoid selection bias.

Follow-up angiograms were obtained at 6 months postembolization. Embolization was considered curative when obliteration of the nidus with no evidence of early venous drainage was demonstrated on an angiogram.

Follow-up data considered all patients, including those with incomplete endovascular therapy.

### Treatment

Endovascular management was proposed for ruptured bAVMs as well as for unruptured bAVMs with high-risk angiographic

findings, such as intranidal aneurysms and high-flow shunts and those presenting with symptoms suggestive of vascular flow steal phenomena.

TVE was performed as either a single TVE session or combined transarterial embolization and TVE. Ideally, the selection criteria for TVE included a nidus diameter of <3 cm and a single draining vein. In cases with unfavorable anatomy for arterial embolization, including supply by tiny perforating arteries, “en passage” feeders, or no obvious arterial pedicle, a single TVE was performed. In cases in which partial arterial embolization was feasible, to reduce the nidus size, the embolization was initiated by the arterial side and was resumed by venous side embolization, to obtain complete occlusion of the nidus.

The complete technical description of TVE has been published elsewhere.<sup>3,5</sup> All procedures were performed with the patient under heparinization. In TVE, a microcatheter was always placed into an arterial feeder, and a superselective angiogram was performed to obtain better visualization of the nidus, without overlapping vascular structures. This maneuver facilitated an optimal position of the venous microcatheter.

A microcatheter was placed as close as possible to the nidus (venous side), and ethylene-vinyl alcohol copolymer was slowly injected. On completion of the procedure, the microcatheter was cut at the level of the jugular sheath at all times. Arterial blood pressure was maintained at a maximum of 120 × 80 mm Hg after endovascular treatment or 20 mm Hg lower than baseline tension in patients with previous hypertension. No further anticoagulant therapy was administered. After embolization, patients were kept in the intensive care unit for 48 hours.

To allow a continuous injection and a faster penetration of ethylene-vinyl alcohol copolymer in the nidus and minimize backflow inside the vein, we used coils on the venous side for veins of ≥5 mm in diameter, with low packing density and no glue. In these cases, a second microcatheter for coils was placed proximal to the tip of the first microcatheter.

### Statistical Analysis

Statistical analysis was performed using R statistical and computing software, Version 3.6.1. (<http://www.r-project.org/>) and Excel for Mac, 2019 (Microsoft). Descriptive analysis was conducted to characterize the sample. Any missing data were described. Quantitative variables were expressed as the mean ± SD, and qualitative variables were expressed as frequency and percentage values. The normality of the data distribution was assessed using a Q-Q plot.

The Student *t* test was used to compare continuous variables when normality was determined. In cases of rejection, the Mann-Whitney test was used. The Fisher exact test was used to compare qualitative data and frequency of occurrence. A statistical significance level of 5% was used for all analyses.

Multiple linear regression analysis was conducted to identify the independent predictors among the clinical-anatomic-demographic data for the HC. For this analysis, all variables were initially considered. The selection process was performed using a stepwise algorithm. The strength of the relationship between HC and their correlates was interpreted using odds ratios with 95% confidence intervals. A *P* value < .05 in the final model was

considered statistically significant. In addition, calibration of the model was established using the Hosmer–Lemeshow goodness of fit test, as well as a calibration curve. The discriminative ability of the model was assessed by receiver operating characteristic curve analysis.

## RESULTS

A total of 57 consecutive patients undergoing treatment for bAVMs by TVE were included. Clinical-demographic and anatomic variables are summarized in Table 1.

In 17 (29.8%) patients, TVE was used exclusively, and in 40 patients (70.2%), it was used in combination with the arterial approach (either during the same session or in previous sessions). The drainage vein was coiled in 17 (29.8%) patients. An arterial balloon, aimed at obstructing and controlling flow at the nidus and facilitating the progression of embolic liquid through the vein, was used in 14 (24.5%) patients.

**Table 1: Clinical-demographic and anatomic variables of patients undergoing TVE for bAVMs**

Variables	Patients (n = 57)
Sex (No.) (%)	
Male	29 (50.9%)
Female	28 (49.1%)
Age (mean) (range) (yr)	38.05 ± 18.1 (9–78)
Previous rupture (No.) (%)	38 (66.6%)
bAVM location (No.) (%)	
Cortical (lobar or cerebellum)	41 (72%)
Deep (brain stem, thalamus, or basal ganglia)	16 (28.0%)
Nidus diameter (original size) (mean) (cm)	2.91 ± 1.26
Nidus diameter before treatment by TVE (mean) (cm)	2.44 ± 0.99
Dilated vein (No.) (%)	
Evaluator 1	24 (42.1%)
Evaluator 2	28 (49.1%)
Evaluator 3	36 (63.1%)
Pattern of venous drainage (No.) (%)	
Superficial	25 (43.9%)
Deep	28 (49.1%)
Superficial and deep	4 (7.0%)
Venous collector (No.) (%)	
1	37 (64.9%)
2	18 (31.6%)
3	2 (3.5%)
Spetzler–Martin grade	
I	5 (8.8%)
II	18 (31.6%)
III	23 (40.4%)
IV	10 (17.5%)
V	1 (1.7%)

**Table 2: Functional outcome status of patients with hemorrhagic complications**

Patient	mRS before Treatment	mRS before Discharge	6-Month Follow-Up mRS
1	0	0	0
2	0	1	NA
3	0	0	0
4	1	4	3
5	0	3	2
6	1	2	1
7	0	4	4
8	0	2	1

Note:— NA indicates not available.

A control angiogram was obtained in all patients. The anatomic cure rate was documented in 52 (91.2%) bAVMs. We noticed total occlusion in 100% of the cases with Spetzler–Martin grades I, II, and III.

Only 1 patient missed follow-up (mRS score at 6 months) by moving to a different county. Specifically in this case, angiographic control was performed within 1 month.

## Outcomes and Hemorrhagic Complications

We recorded 10 (17.5%) overall hemorrhagic complications. One of these patients had subarachnoid hemorrhage due to intracranial dissection during arterial access in the combined approach. Another patient had perforation of the draining cortical vein during microneavigation. These 2 patients had no clinical consequences and were excluded from analysis of the HC.

Thus, we analyzed a total of 8 (14.0%) HC with TVE, which was either intraprocedural or periprocedural. Three patients (5.2%) had intraprocedural HC; 3 patients (5.2%) had HC within 24 hours of

the procedure; 1 patient (1.7%), within 48 hours; and 1 patient (1.7%), within 96 hours. No patient showed a hemorrhagic complication after this period.

Only 2 (3.5%) patients had unfavorable outcomes (mRS score at 6 months of >2) at the 6-month follow-up (Table 2). Procedure-related mortality was 0%.

Concerning the neuroimaging findings, of the 8 patients (14.0%), 3 (5.2%) had perinidal hematoma exclusively; 3 (5.2%) had a hematoma with an intraventricular hemorrhage; 1 patient (1.7%) had cortical subarachnoid hemorrhage; and 1 patient (1.7%) had intraventricular hemorrhage. During the follow-up period, no recurrence was noted among the treated patients.

## Univariate and Multivariate Analyses

Tables 3, 4, and 5 show the univariate and multivariate analyses performed to identify the independent predictors among the clinical, anatomic, demographic, and technical aspects of TVE data for the patients with HC. In univariate analysis, we found a statistically significant correlation between HC and the number of venous collectors, nidus diameter before any intervention, and nidus diameter immediately before treatment by TVE. No other significant associations were observed.

In the multiple linear regression analysis (Table 5), only the number of

**Table 3: Univariate analysis showing the association between findings on HC and the clinical-anatomic-demographic variables of patients treated by TVE**

Variable	Were There HC?		P
	No (n = 49)	Yes (n = 8)	
Spetzler-Martin grading system			1.0 <sup>a</sup>
I, II, and III	39 (68.5%)	7	
IV and V	10 (17.5%)	1	
Previous rupture			1.0 <sup>a</sup>
No	16	3	
Yes	33	5	
Sex			.70 <sup>a</sup>
Female	25	3	
Male	24	5	
Mean age on admission (SD) (yr)	37.1 (18.6)	46.8 (13.6)	.16 <sup>b</sup>
No. of venous collectors (mean) (SD)	1.2 (0.45)	2.0 (0.75)	.003 <sup>c</sup>
Presence of dilated draining vein (No.) (%)			.06 <sup>a</sup>
Evaluator 1 = 24/57	18 (31.5%)	6 (10.5%)	
Presence of dilated draining vein (No.) (%)			.14 <sup>a</sup>
Evaluator 2 = 28/57	22 (38.5%)	6 (10.5%)	
Presence of dilated draining vein (No.) (%)			.69 <sup>a</sup>
Evaluator 3 = 36/57	30 (52.6%)	6 (10.5%)	
Pattern of venous drainage			.48 <sup>a</sup>
Superficial	21	4	
Deep	25	3	
Superficial and deep	3	1	
Nidus diameter before any intervention (mean) (SD) (cm)	2.74 (1.19)	3.88 (1.40)	.01 <sup>b</sup>
Nidus diameter before TVE (mean) (SD) (cm)	2.28 (0.92)	3.37 (1.00)	.003 <sup>b</sup>
Nidus diameter before TVE (2 groups)			.03 <sup>a</sup>
0–3 cm	38	3	
>3 cm	11	5	
AVM location			.09 <sup>a</sup>
Cortical (lobar or cerebellum)	33	8	
Deep (brain stem, thalamus, or basal ganglia)	16	0	

<sup>a</sup> Fisher exact test.<sup>b</sup> Student t test.<sup>c</sup> Mann-Whitney test.**Table 4: Univariate analysis showing the association between hemorrhagic complications and the technical variables of patients treated by TVE**

Variable	Were There Hemorrhagic Complications?		P
	No (n = 49)	Yes (n = 8)	
Arterial balloon			.39 <sup>a</sup>
Yes	11	3	
No	38	5	
No. of embolization sessions, (mean) (SD)	1.8 (1.2)	1.8 (0.99)	.50 <sup>b</sup>
Coiled vein			1.0 <sup>a</sup>
Yes	15	2	
No	34	6	
Total occlusion (angiographic cure)			1.0 <sup>a</sup>
Yes	44	8	
No	5	0	

<sup>a</sup> Fisher exact test.<sup>b</sup> Mann-Whitney test.**Table 5: Multivariate logistic model with hemorrhagic complications as the binary end point<sup>a</sup>**

Variable	OR	95% CI	P Value
No. of venous collectors (unitary increase)	8.72	2.2–58.2	.006 <sup>b</sup>

<sup>a</sup> Hosmer-Lemeshow goodness-of-fit test:  $\chi^2 = 6.6$ ,  $df = 8$ , and  $P$  value = .57.<sup>b</sup> Significant at  $P$ -value < .05.

venous collectors still showed an association with HC ( $P = .006$ ). The exponential coefficient of the number of venous collectors was 8.72, which represented the odds ratio. This means that the existence of 1 more venous collector could increase the risk of HC by approximately 8.7 times (95% confidence interval, 2.2–58.2).

The Hosmer-Lemeshow goodness of fit test, which was not statistically significant ( $P = .57$ ), indicated that the predicted probability was in high concordance with the observed probability. The area under the receiver operating characteristic curve was 0.768. The numeric value of the cutoff point for the predicted probability was 0.041 (cutoff for probability = 4.1%). The sensitivity and specificity were 75.0% and 71.4%, respectively. The negative and positive predictive values were 70.0% and 5.4%, respectively.

## DISCUSSION

To the best of our knowledge, this is the first publication with a specific focus on periprocedural HC in TVE of bAVMs. The angiographic cure rate using TVE in the present study has remained roughly the same since our recent publications.<sup>3,5</sup> These studies reflected cure rates above 90%, further reinforcing the effectiveness of this therapeutic technique for bAVMs.

In the study presented herein, hemorrhagic complications were observed in 14.0% of cases; nevertheless, unfavorable clinical outcomes (mRS score at 6 months of >2) at 6 months were low (3.5%). Fifty-nine percent of bAVMs (34 patients) in our series were Spetzler-Martin grade III or higher, thus yielding a higher risk of complications with all potential therapeutic alternatives. High Spetzler-Martin grades represent a challenge for all invasive therapeutic approaches. In neurosurgery, high Spetzler-Martin grades ( $\geq$ III) and deep brain localizations<sup>10</sup> are related to high complication rates.<sup>11–14</sup>

Schaller et al<sup>15</sup> reported a series of 150 patients undergoing microsurgery: the morbidity rate was 15.3%, with permanent new deficits in 10.6%. Another publication showed early neurologic deterioration after microsurgery in



39.2% of the 288 patients, among whom 12.2% had permanent deficits.<sup>16</sup>

A literature review by Chen et al<sup>17</sup> of 13 publications focused on TVE for bAVM (most of which were case reports) yielded an overall complication rate of 4.3%. However, most of the 69 patients evaluated in that literature review were from our department.<sup>3</sup>

In another study of 408 patients treated by endovascular means with an arterial access, the rate of HC was 92 of 827 procedures (11.1%); 48 complications (5.8%) were unrelated to arterial perforation.<sup>18</sup> In a meta-analysis that included a total of 98 publications and 8009 patients, periprocedural hemorrhage was observed after 2.6% of the transarterial embolization procedures for bAVMs,<sup>7</sup> though cure rates with an arterial approach are lower than TVE.<sup>19</sup>

Given the high rate of angiographic cure in TVE embolization, a better understanding of HC may facilitate improved patient selection. Thus, we chose to perform univariate and multivariate analyses of only HC that were unrelated to access perforation.

In our univariate analysis, patients with larger nidi (either before any intervention or immediately before performance of TVE) had a significantly higher number of HC. In our view, larger bAVMs (>3 cm) are more likely to have HC for the following reasons: a larger nidus has a higher likelihood of a small hidden nidal remnant due to the superposition of the embolic agent and the subtraction process, which may fail to demonstrate a small remnant at the end of the procedure. Although all 8 patients had angiographic exclusion, ie, the absence of early venous drainage, in cases with a large nidus, the existence of a large cast of embolic liquid overlapping the nidal remnant is more probable.

Another potential factor is because there is greater difficulty in achieving complete distal occlusion of all arterial pedicles in cases with large nidi. Another possible reason, and not yet fully understood, is the phenomenon referred to as “delayed postoperative hemorrhage.”<sup>20</sup> After embolization sessions, although the patients in the present study followed a strict blood pressure control protocol in an intensive care unit, we could not guarantee whether some of these patients experienced delayed postoperative hemorrhage. This is a condition of impaired cerebral vasoreactivity of the perinidal tissues, leading to edema and, in some cases, hemorrhage after exclusion of the artery-vein shunt.<sup>21,22</sup>

These results emphasize the necessity, whenever possible, of an initial arterial approach, to reduce the size of the nidus. This is common practice in our department, especially for bAVMs of >3 cm. Otherwise, TVE seems appropriate when bAVM remnants are not safely accessible by other therapeutic means.

Another variable that showed statistical significance with HC in the present study was the number of venous collectors in both univariate and multivariate analyses. The risk of HC increased by 8.7-fold for each additional venous collector unit ( $P = .0061$ ). Indeed, these results challenge the initial theory of the creators of the TVE technique, which was demonstrated by Massoud and Hademenos<sup>23</sup> in animals. Those researchers stated that “these veins would act, in effect, as a safety valve to decompress the nidus in the event that the cumulative intranidal pressure becomes too high (eg, by an excessive retrograde injection pressure in the face of insufficient arterial hypotension).”<sup>23</sup>

Our hypothesis is that in the presence of >1 venous collector, retrograde injection may induce inadvertent occlusion of the other drainage veins before complete occlusion of the nidus. This can then lead to increased intranidal pressure, rupture, and HC. This result has been well-demonstrated by Baharvahdat et al<sup>18</sup> in a work on arterial embolization of HC, in which early venous occlusion was significantly correlated with HC.

In addition to the reasons already mentioned, other hypotheses about non-access-related perforation HC include progressive venous congestion due to a slow flow and thrombosis and inflammatory reactions or mural necrosis induced by the embolic liquid.<sup>6,9,18,24</sup>

For TVE, our years of practice have shown that the best option for microcatheter removal is to cut it at the level of venous puncture, thereby avoiding unnecessary traction of fragile veins and an embolic material cast.<sup>3,5</sup> Nevertheless, we cannot conclude that alternative techniques may lead to HC because in all such cases, cutting of the venous microcatheter was routinely performed.

When we compared our clinical outcomes with those of other bAVM embolization studies, only 3.5% of our patients had poor outcomes (mRS score at 6 months of >2) and no procedure-related deaths were observed. In other studies of the arterial approach, we observed persistent symptoms after embolization, ranging from 3.8% to 14%.<sup>6,25,26</sup> We believe that immediately after the procedure, neuroimaging is essential to evaluate all outcomes, in addition to intensive care and neurosurgical decompression when necessary.<sup>24,27</sup>

Nevertheless, our study provides adequate data to support the use of TVE in patients with bAVMs as an alternative in challenging cases or those with nidus remnants from previous therapeutic maneuvers. When deciding the appropriate treatment of bAVMs (ruptured or high-risk bAVMs), the ideal selection for TVE technique would be:

- Cases with single venous collector
- Nidi of <3 cm
- Deep-seated bAVMs.

In nidi of >3 cm or bAVMs with >1 venous collector, TVE may be reasonable with prior arterial embolization. In addition, our study shows that dilated drainage veins should not deter the use of this treatment technique.

There are limitations to our study. First, the groups under evaluation were relatively small, precluding subset analysis, eg, of the technical aspects (Table 5), or showing no evidence of statistical significance. Second, although our data had been collected prospectively, data analysis was conducted retrospectively. The angiographic follow-up period was relatively short, and a longer duration would have promoted greater confidence in assessing anatomic obliteration. Furthermore, our study has other limitations that are common to cohort studies.

## CONCLUSIONS

TVE seems to be a relatively safe and effective alternative for challenging bAVMs or bAVM remnants, especially when rapid cure is needed. In the presented study, a single venous collector, nidi <3 cm, and deeply seated bAVMs seemed to yield fewer hemorrhagic complications when TVE is used. Even though larger

studies are needed, these factors should be considered in the patient selection for this technique and should be further investigated.

## ACKNOWLEDGMENTS

We thank Angelo da Silva Cabral for assistance in statistical analysis of the study data.

## REFERENCES

1. Choudhri O, Ivan ME, Lawton MT. **Transvenous approach to intracranial arteriovenous malformations: challenging the axioms of arteriovenous malformation therapy?** *Neurosurgery* 2015;77:644–51 CrossRef Medline
2. Mendes GA, Iosif C, Silveira EP, et al. **Transvenous embolization in pediatric plexiform arteriovenous malformations.** *Neurosurgery* 2016;78:458–65 CrossRef Medline
3. Mendes GA, Kalani MY, Iosif C, et al. **Transvenous curative embolization of cerebral arteriovenous malformations: a prospective cohort study.** *Neurosurgery* 2018;83:957–64 CrossRef Medline
4. Consoli A, Renieri L, Nappini S, et al. **Endovascular treatment of deep hemorrhagic brain arteriovenous malformations with transvenous Onyx embolization.** *AJNR Am J Neuroradiol* 2013;34:1805–11 CrossRef Medline
5. Iosif C, Mendes GA, Saleme S, et al. **Endovascular transvenous cure for ruptured brain arteriovenous malformations in complex cases with high Spetzler-Martin grades.** *J Neurosurg* 2015;122:1229–38 CrossRef Medline
6. Haw CS, Terbrugge K, Willinsky R, et al. **Complications of embolization of arteriovenous malformations of the brain.** *J Neurosurg* 2006;104:226–32 CrossRef Medline
7. Subat YW, Dasenbrock HH, Gross BA, et al. **Periprocedural intracranial hemorrhage after embolization of cerebral arteriovenous malformations: a meta-analysis.** *J Neurosurg* 2019 Sep 13. [Epub ahead of print] CrossRef Medline
8. Ledezma CJ, Hoh BL, Carter BS, et al. **Complications of cerebral arteriovenous malformation embolization: multivariate analysis of predictive factors.** *Neurosurgery* 2006;58:602–11; discussion 602–11 CrossRef
9. Saatci I, Geyik S, Yavuz K, et al. **Endovascular treatment of brain arteriovenous malformations with prolonged intranidal Onyx injection technique: long-term results in 350 consecutive patients with completed endovascular treatment course—clinical article.** *J Neurosurg* 2011;115:78–88 CrossRef Medline
10. Potts MB, Jahangiri A, Jen M, et al; UCSF Brain AVM Study Project. **Deep arteriovenous malformations in the basal ganglia, thalamus, and insula: multimodality management, patient selection, and results.** *World Neurosurg* 2014;82:386–94 CrossRef Medline
11. Pan J, He H, Feng L, et al. **Angioarchitectural characteristics associated with complications of embolization in supratentorial brain arteriovenous malformation.** *AJNR Am J Neuroradiol* 2014;35:354–59 CrossRef Medline
12. Heros RC. **Brain resection for exposure of deep extracerebral and paraventricular lesions.** *Surg Neurol* 1990;34:188–95 CrossRef Medline
13. Lawton MT, Hamilton MG, Spetzler RF. **Multimodality treatment of deep arteriovenous malformations: thalamus, basal ganglia, and brain stem.** *Neurosurgery* 1995;37:29–36 CrossRef Medline
14. Liu KD, Lee LS. **Microsurgical treatment of deep arteriovenous malformations: basal ganglia and thalamus.** *Zhonghua Yi Xue Za Zhi (Taipei)* 2001;64:23–30 Medline
15. Schaller C, Schramm J, Haun D. **Significance of factors contributing to surgical complications and to late outcome after elective surgery of cerebral arteriovenous malformations.** *J Neurology Neurosurgery Psychiatry* 1998;65:547–54 CrossRef Medline
16. Schramm J, Schaller K, Esche J, et al. **Microsurgery for cerebral arteriovenous malformations: subgroup outcomes in a consecutive series of 288 cases.** *J Neurosurg* 2017;126:1056–63 CrossRef Medline
17. Chen CJ, Norat P, Ding D, et al. **Transvenous embolization of brain arteriovenous malformations: a review of techniques, indications, and outcomes.** *Neurosurg Focus* 2018;45:E13–17 CrossRef
18. Baharvahdat H, Blanc R, Termechi R, et al. **Hemorrhagic complications after endovascular treatment of cerebral arteriovenous malformations.** *AJNR Am J Neuroradiol* 2014;35:978–83 CrossRef Medline
19. Elsenousi A, Aletich VA, Alaraj A. **Neurological outcomes and cure rates of embolization of brain arteriovenous malformations with n-butyl cyanoacrylate or Onyx: a meta-analysis.** *J Neurointerv Surg* 2016;8:265–72 CrossRef Medline
20. Morgan MK, Wiedmann MK, Assaad NN, et al. **Deliberate employment of postoperative hypotension for brain arteriovenous malformation surgery and the incidence of delayed postoperative hemorrhage: a prospective cohort study.** *J Neurosurg* 2017;127:1025–40 CrossRef Medline
21. Niini T, Laakso A, Tanskanen P, et al. **Perioperative treatment of brain arteriovenous malformations between 2006 and 2014: the Helsinki Protocol.** *Neurocrit Care* 2019;31:346–56 CrossRef Medline
22. Rangel-Castilla L, Spetzler RF, Nakaji P. **Normal perfusion pressure breakthrough theory: a reappraisal after 35 years.** *Neurosurg Rev* 2015;38:399–405 CrossRef Medline
23. Massoud TF, Hademenos GJ. **Transvenous retrograde nidus sclerotherapy under controlled hypotension (TRENSh): a newly proposed treatment for brain arteriovenous malformations—Concepts and rationale.** *Neurosurgery* 1999;45:351–65 CrossRef Medline
24. Cronqvist M, Wirestam R, Ramgren B, et al. **Endovascular treatment of intracerebral arteriovenous malformations: procedural safety, complications, and results evaluated by MR imaging, including diffusion and perfusion imaging.** *AJNR Am J Neuroradiol* 2006;27:162–76 Medline
25. Hartmann A, Pile-Spellman J, Stapf C, et al. **Risk of endovascular treatment of brain arteriovenous malformations.** *Stroke* 2002;33:1816–20 CrossRef Medline
26. Meisel HJ, Mansmann U, Alvarez H, et al. **Effect of partial targeted N-butyl-cyano-acrylate embolization in brain AVM.** *Acta Neurochir (Wien)* 2002;144:879–88; discussion 888 CrossRef Medline
27. Cronqvist M, Ramgren B, Geijer B, et al. **Diffusion- and perfusion-weighted MRI in therapeutic neurointerventional procedures.** *Neuroradiology* 2001;43:662–71 CrossRef Medline

# Can a Stent Retriever Damage the JET 7 Reperfusion Catheter?

J. Pearly Ti, L. Yeo, and G. Anil



## ABSTRACT

**SUMMARY:** We encountered 2 separate instances of damage to JET 7 reperfusion catheters when they were used in conjunction with a stent retriever during mechanical thrombectomy. On both occasions, after 1 or 2 passes with a stent retriever, we found that the distal end of the catheter was frayed and it ballooned up on flushing with saline. This mechanical failure could potentially lead to serious complications; hence, it should be shared with fellow neurointerventionalists.

**ABBREVIATION:** DAC = distal access catheters

In endovascular treatment for acute ischemic stroke with large-vessel occlusion, stent retriever thrombectomy has been the default standard of care.<sup>1</sup> The Cost and Medical Care of Patients With Advanced Serious Illness in Singapore trial proved that aspiration with large-bore distal access catheters (DACs) using a direct aspiration first-pass technique (ADAPT) is equally effective and safe.<sup>2</sup> However, both techniques (ie, aspiration and stent retrievers) are often used together.<sup>3</sup> Most interesting, even in the COMPASS trial, stent retrievers were used in 21% of patients in the aspiration-first group and DACs were used in most of the stent retriever first-line group.<sup>2</sup> For all practical purposes, a DAC used in stroke thrombectomy is expected to be compatible for use with stent retrievers. However, we encountered 2 separate cases of unexpected damage to JET 7 Reperfusion Catheters with XTRA FLEX technology (Penumbra) when they were used in conjunction with a stent retriever. Below are the brief reports of the 2 cases.

## Incident 1

An 82-year-old woman presented with acute left hemiparesis and an NIHSS score of 20. Her right ICA was occluded from the distal cervical segment to the ICA termination. Intravenous rtPA was

administered, and the patient was taken for mechanical thrombectomy under sedation and local anesthesia. An angiogram performed with a Neuron MAX 6F 088 (Penumbra) long sheath in the distal common carotid artery showed no antegrade flow beyond the mid-cervical ICA (On-line Fig 1). Aspiration thrombectomy was attempted using a JET 7 catheter introduced through the Neuron MAX over a Velocity delivery microcatheter (Penumbra) and a Transend 0.014-inch microwire (Boston Scientific). After 2 passes and extraction of a large volume of thrombus, the petrous and cavernous parts of the ICA were now patent, but the supraclinoid ICA was still occluded (On-line Fig 2). At this stage, to address excessive patient movement, sedation was converted to general anesthesia. Next, the distal ICA occlusion was crossed with the Velocity microcatheter, and a 4 × 20 mm Trevo ProVue (Stryker) stent retriever was deployed from the right M1 into the supraclinoid ICA. The microcatheter was gently removed, while allowing the JET 7 to close over the proximal few millimeters of the stent retriever with continuous aspiration (using the ENGINE aspiration pump [Penumbra]) until there was no back flow. After 3 minutes of stent dwell time, the whole assembly (ie, the stent retriever partially corks at the distal end of the aspiration catheter and the aspiration catheter itself) was withdrawn with continuous suction on the JET 7 as well as the Neuron MAX (On-line Fig 3). Two passes with this technique cleared most of the clots from the supraclinoid ICA with a small residual clot at the proximal M1-ICA termination.

At this stage, while preparing the aspiration catheter, we noted that its distal end, approximately 15 mm proximal to its tip, was frayed. On connecting the catheter to the pressurized saline flush, the tip of the JET 7 started to balloon (Fig 1). This damaged JET 7 was replaced with an ACE68 aspiration catheter (Penumbra), and by means of the same technique, the procedure was completed to achieve TICI 3 reperfusion (On-line Fig 4). The total

Received June 4, 2020; accepted after revision July 21.

From the Department of Neuroradiology (J.P.T.), National Neuroscience Institute, Singapore; Division of Neurology (L.Y.) and Division of Interventional Radiology (G.A.), Department of Diagnostic Imaging, National University Hospital, Singapore; and Departments of Medicine (L.Y.) and Radiology (G.A.), Yong Loo Lin School of Medicine, National University of Singapore, Singapore.

Please address correspondence to Anil Gopinathan, MBBS, MD, FRCR (UK), FAMS, Division of Interventional Radiology, National University Hospital, 5 Lower Kent Ridge Rd, 119074 Singapore; e-mail: ivyanil10@gmail.com



Indicates article with supplemental on-line photos.

<http://dx.doi.org/10.3174/ajnr.A6804>





**FIG 1.** The JET 7 catheter used in the thrombectomy for patient 1 shows ballooning of its distal end with separation of the reinforcing braids from the surrounding polymer.

procedure time was 50 minutes, and the time from ictus to recanalization was 7 hours. A postprocedural CT scan on day 4 did not show any hemorrhagic changes or new infarcts. However, there was no significant clinical improvement in the neurologic deficits at the 3-month follow-up with a modified Rankin Score (mRS) of 4, starting from a baseline of 3.

### Incident 2

An 88-year-old woman presented with right M1 MCA occlusion and an NIHSS score of 12. Because she was outside the time window for intravenous thrombolysis, she was directly transferred to the angiosuite for mechanical thrombectomy. With the intention of using the direct aspiration first-pass technique, a JET 7 catheter was advanced over a 3MAX (Penumbra) and Transend 0.014-inch microcatheter-wire assembly, through a 6F Neuron MAX. However, it could not be navigated past the ledge of the ophthalmic artery origin. Hence, the procedure was converted to stent retriever thrombectomy. A 6 × 30 mm Solitaire-2 stent retriever (Medtronic) was deployed across the occlusion and allowed to integrate with the clot for 4 minutes. The Solitaire and the microcatheter were retrieved through the JET 7 with continuous suction using the ENGINE aspiration system. While we withdrew the stent retriever, the JET 7 spontaneously advanced beyond the ophthalmic segment of the ICA and wedged at the right M1-clot interface. Therefore, the operator decided to completely retrieve the Solitaire-microcatheter combination and left the JET 7 catheter in situ. The aspiration was continued for a further 3 minutes during which the aspiration tubing demonstrated slow continuous movement of blood toward the canister before removal of the JET 7. A subsequent angiogram showed TICI 3 reperfusion. When the JET 7 was flushed to check for clots *ex vivo*, we noted a similar ballooning (Fig 2) of the distal aspect of the catheter as described in case 1.

### DISCUSSION

In this report, we have described 2 instances of unforeseen damage to the JET 7 reperfusion catheter encountered during



**FIG 2.** The damaged distal segment of the JET 7 thrombectomy catheter used in patient 2 has ballooned on flushing.

thrombectomy. These procedures were performed by 2 different operators at different institutions. Between the two, the operators have >15 years of experience in neurointervention and have performed >250 thrombectomies using various generations of Penumbra aspiration catheters with stent retrievers. The thrombectomy techniques used in these 2 cases are comparable with the steps described in published literature; the first one was like the stent retriever–assisted vacuum-locked extraction technique, and the conventional Solumbra technique was used in the second case. In the Solumbra technique, a stent retriever is placed across the clot, while a DAC is advanced to the clot face. Subsequently, the stent retriever is pulled back into the DAC, while negative pressure within the aspiration catheter is preserved with pump aspiration or a negative-pressure syringe. Meanwhile, in the stent retriever–assisted vacuum-locked extraction technique, the stent retriever is deployed with its proximal segment within the clot and the distal segment beyond it. Next, the DAC under suction is advanced to the clot face with gentle traction on the stent wire until a wedged position with the proximal end of the stent is achieved. This wedged stent retriever–DAC assembly is pulled out as a single unit with suction applied on the guide catheter.<sup>4</sup> At the time of these incidents, the JET 7 catheter with XTRA FLEX technology had been newly introduced into our practice. The 2 events happened 3 weeks apart. One of authors (G.A.) had used the JET 7 uneventfully with first-pass TICI 3 reperfusion on 3 previous occasions. Similarly, the second operator (J.P.T.) had also used the JET 7 twice for aspiration thrombectomy with good angiographic outcomes and no adverse events.

The exact mechanism of the damage to the catheter in these cases is not clearly understood. Pulling an unsheathed stent through the aspiration catheter could potentially harm its integrity due to the friction between the two. However, in the first case, even this mechanism is not plausible because the stent retriever was pushed out of the distal end of the catheter after removing both the catheter and stent together as a single assembly, ie, without pulling it through the JET 7. We did not encounter similar incidents with use

of the earlier generations of Penumbra aspiration catheters. However, in the last 5 years, there is an ongoing race to manufacture wider bore aspiration catheters with better flexibility and trackability, without increasing their outer diameters. Intuitively, this pursuit could entail a certain degree of compromise on their strength. Operators need to be cognizant of such trade-offs between the stoutness of a catheter against its flexibility and softness, while choosing them off the shelf. In the 2 cases reported here, the distal end of the catheter, beyond the site of ballooning, could have fragmented and embolized or been retained within the patient. Following this experience, after each pass, we closely examine these aspiration catheters for their integrity before re-introducing them into the cerebral circulation.

Disclosures: Anil Gopinathan—UNRELATED: Consultancy: Stryker, Medtronic, Penumbra\*; Payment for Lectures Including Service on Speakers Bureaus: Penumbra, Medtronic, Stryker.\* \*Money paid to the institution.

### Note

Since this report was submitted, Penumbra has issued a safety alert about this problem.<sup>5</sup> It states that the safety and efficacy of the use of revascularization devices from other manufactures

with JET 7 catheter (XTRA FLEX technology) is unknown. They also advise against injection of contrast media through this catheter.

### REFERENCES

1. Powers W, Rabinstein AA, Ackerson T, et al. **Guidelines for the Early Management of Patients with Acute Ischemic Stroke: 2019 Update to the 2018 Guidelines for the Early Management of Acute Ischemic Stroke—A Guideline for Healthcare Professionals from the American Heart Association/American Stroke Association.** *Stroke* 2019;50:e344–418 CrossRef Medline
2. Turk AQ, Siddiqui A, Fifi JT, et al. **COMPASS trial aspiration thrombectomy versus stent retriever thrombectomy as first-line approach for large vessel occlusion (COMPASS): a multicentre, randomised, open label, blinded outcome, non-inferiority trial.** *Lancet* 2019;393:998–1008 CrossRef Medline
3. Brehm A, Maus V, Tsogkas I, et al. **Stent-retriever assisted vacuum-locked extraction (SAVE) versus a Direct Aspiration First Pass Technique (ADAPT) for acute stroke: data from the real-world.** *BMC Neurol* 2019;19:65 CrossRef Medline
4. Maus V, Behme D, Kabbasch C, et al. **Maximizing first-pass complete reperfusion with SAVE.** *Clin Neuroradiol* 2018;28:327–38 CrossRef Medline
5. <https://www.snisonline.org/wp-content/uploads/2020/08/Penumbra-JET-7.pdf>

# MRI-Based Assessment of the Pharyngeal Constrictor Muscle as a Predictor of Surgical Margin after Transoral Robotic Surgery in HPV-Positive Tonsillar Cancer

Y.J. Kim, W.-J. Jeong, Y.J. Bae, H. Kim, B.S. Choi, Y.H. Jung, S.H. Baik, L. Sunwoo, and J.H. Kim



## ABSTRACT

**BACKGROUND AND PURPOSE:** Transoral robotic surgery is an emerging strategy for treating human papillomavirus–positive cancers, but the role of MR imaging in predicting the surgical outcome has not been established. We aimed to identify preoperative MR imaging characteristics that predispose the outcome of transoral robotic surgery toward an insecure (positive or close) surgical margin in human papillomavirus–positive tonsillar squamous cell carcinoma.

**MATERIALS AND METHODS:** Between December 2012 and May 2019, sixty-nine patients underwent transoral robotic surgery at our institution. Among these, 29 who were diagnosed with human papillomavirus–positive tonsillar squamous cell carcinoma, did not receive neoadjuvant treatment, underwent preoperative 3T MR imaging, and had postoperative pathologic reports and were included in this retrospective study. Two neuroradiologists evaluated the preoperative MR imaging scans to determine the tumor spread through the pharyngeal constrictor muscle using a 5-point scale: 1, normal constrictor; 2, bulging constrictor; 3, thinning constrictor; 4, obscured constrictor; and 5, tumor protrusion into the parapharyngeal fat. The risk of an insecure surgical margin (involved or <1 mm) according to the MR imaging scores was predicted using logistic regression with the Firth correction.

**RESULTS:** The interobserver agreement for the MR imaging scores was excellent ( $\kappa = 0.955$ ,  $P < .001$ ). A score of  $\geq 4$  could predict an insecure margin with 87.5% sensitivity and 92.3% specificity (area under the curve = 0.899) and was the only significant factor associated with an insecure margin in the multivariable analysis (OR, 6.59; 95% CI, 3.11–22.28;  $P < .001$ ).

**CONCLUSIONS:** The pre-transoral robotic surgery MR imaging scoring system for the pharyngeal constrictor muscle is a promising predictor of the surgical margin in human papillomavirus–positive tonsillar squamous cell carcinoma.

**ABBREVIATIONS:** AUC = area under the curve; cN = clinical node; cT = clinical tumor; HPV = human papillomavirus; pN = pathologic node; pT = pathologic tumor; ROC = receiver operating characteristic; SCC = squamous cell carcinoma; TORS = transoral robotic surgery

Oropharyngeal squamous cell carcinoma (SCC) is a head and neck cancer with increasing prevalence as a consequence of rising human papillomavirus (HPV) infections.<sup>1,2</sup> HPV-positive oropharyngeal SCC is known for its excellent prognosis with substantially improved survival compared with HPV-negative SCC.<sup>3–5</sup> Surgery, radiation, and chemotherapy are the main treatment methods for oropharyngeal SCC and can be used alone or in combination depending on the cancer stage.<sup>6</sup>

The treatment protocol for HPV-positive SCC has shifted toward a “deintensification” approach to maintain favorable oncologic outcomes while minimizing treatment-related morbidity.<sup>7–9</sup> Long-term adverse effects from radiation or chemotherapy and high morbidity from traditional surgery through external mandibulotomy can reduce the quality of life, particularly in young patients who have to live with the consequences for far longer.<sup>10–13</sup> Recently, transoral robotic surgery (TORS) has emerged as a first-line treatment, particularly for early-stage HPV-positive oropharyngeal SCC.<sup>14,15</sup> While avoiding functional deficits from the traditional external approaches, TORS can reduce the need for adjuvant

Received January 28, 2020; accepted after revision July 29.

From the Departments of Radiology (Y.J.K., Y.J.B., B.S.C., S.H.B., L.S., J.H.K.), Otolaryngology–Head and Neck Surgery (W.-J.J., Y.H.J.), and Pathology (H.K.), Seoul National University Bundang Hospital, Seongnam, Republic of Korea.

Yong Ju Kim and Woo-Jin Jeong contributed equally to this article.

This work was supported by the National Research Foundation of Korea grant funded by the Korea government (No. 2019R1A1063771) and grant No. 09-2019-003 from the Seoul National University Bundang Hospital Research Fund.

Paper previously presented at: American Society of Head and Neck Radiology 53rd Annual Meeting, where it won the first-place scientific exhibit award, October 2–6, 2019; Phoenix, Arizona.

Please address correspondence to Yun Jung Bae, MD, PhD, Department of Radiology, Seoul National University Bundang Hospital, 82, Gumi-ro 173beon-gil, Bundang-gu, Seongnam, 13620, Republic of Korea; e-mail: bae729@gmail.com

Indicates open access to non-subscribers at [www.ajnr.org](http://www.ajnr.org)

Indicates article with supplemental on-line appendix and tables.

Indicates article with supplemental on-line photo.

<http://dx.doi.org/10.3174/ajnr.A6806>



therapy after surgery or can use surgery as a single-technique therapy while preserving oncologic outcomes, particularly when the negative margin is achieved by TORS.<sup>2,3,5,16-18</sup>

Despite these advantages, there is still a risk of obtaining an insecure surgical margin (ie, positive margin involvement by the tumor or a close margin of <1 mm between the tumor and the margin) in TORS, which necessitates adjuvant therapies, even in early T1 and T2 tumors.<sup>3,19</sup> Because oncologic outcomes in such cases are similar to those with chemoradiation alone,<sup>3</sup> it is important to preselect patients who are expected to have an insecure surgical margin to avoid unnecessary dual treatment. However, no published study has evaluated the preoperative MR imaging characteristics that can predict the surgical margin after TORS. It has been noted that tumor invasion through the pharyngeal constrictor muscle confirmed in a surgical field will likely have a positive margin related to locoregional recurrence, but data supporting an imaging-based predictor are still lacking.<sup>2,5,20</sup>

In our study, we aimed to identify preoperative MR imaging characteristics, particularly with regard to pharyngeal constrictor muscle involvement by the tumor in early stage cancers, that predispose the outcome of TORS toward an insecure surgical margin in HPV-positive tonsillar SCC.

## MATERIALS AND METHODS

### Study Subjects

This retrospective study was approved by our institutional review board (B-1906-544-101), and the requirement for written informed consent was waived. Between December 2012 and May 2019 at our institution, a nationwide third-referral hospital, we included 36 subjects who met the following criteria: 1) diagnosed with HPV-positive tonsillar SCC, 2) had preoperative 3T MR imaging available, and 3) had postoperative pathologic reports available. Among them, 6 who received neoadjuvant therapy and 1 who did not have a postoperative pathologic report available were excluded from the analysis.

Clinical records were examined for demographic characteristics and staging, and treatment data were obtained from electronic medical records. The clinical primary tumor (cT) and nodal (cN) categories were staged according to the 8th edition of the *American Joint Committee on Cancer (AJCC) Cancer Staging Manual*.<sup>21</sup> All included subjects underwent TORS using the da Vinci surgical robotic system (Intuitive Surgical) performed by 2 head and neck surgeons (W-J.J. and Y.H.J. with 10 and 15 years' experience in head and neck surgery, respectively). Adjuvant treatment was considered when the cancer-free margin was insufficient. Follow-up surveillance was initially performed 3 months after the operation and every 3–6 months after the initial follow-up using CT or MR imaging and/or PET/CT to assess locoregional recurrence. The treatment option for each patient was decided at a weekly multidisciplinary tumor board including otorhinolaryngology–head and neck surgeons, oncologists, radiologists, and pathologists, following the 2018 *National Comprehensive Cancer Network (NCCN) Clinical Practice Guidelines in Oncology* for oropharyngeal cancer.<sup>22</sup>

### Image Acquisition

MR images were acquired using a 3T MR imaging unit (Ingenia; Philips Healthcare) with a 32-channel sensitivity

encoding head coil. Axial TSE T2WI was performed with and without fat suppression using the multipoint Dixon technique. The imaging parameters were as follows: TR, 3300 ms; TE, 80 ms; FOV, 180 × 220 mm<sup>2</sup>; acquisition matrix, 440 × 440; section thickness, 3 mm; no section gap; NEX, 1. Other parameters for the full MR imaging sequences are described in the On-line Appendix.

### Image Analysis

The cT category according to the 8th edition of the *AJCC Cancer Staging Manual* for the primary tumor was verified by 1 board-certified neuroradiologist (Y.J.B. with 10 years' experience in neurology and head and neck imaging) on the basis of MR imaging.

On axial T2WI, tumor spread through the pharyngeal constrictor muscle was independently determined by 2 board-certified neuroradiologists (Y.J.B. and B.S.C. with 20 years' experience in neurology and head and neck imaging) who were blinded to the clinical and histopathologic information. The following 5-point scale scoring system was used for the assessment of the status of the pharyngeal constrictor muscle: 1, normal constrictor; 2, bulging constrictor; 3, thinning constrictor; 4, obscured constrictor; 5, tumor protrusion into the parapharyngeal fat (Fig 1). After an independent reading, the final MR imaging score was designated by 2 readers in consensus and used for further analysis.

### Histopathologic Review

According to the 8th edition of the *AJCC Cancer Staging Manual*,<sup>21</sup> the pathologic tumor (pT) and the nodal (pN) statuses were staged by 1 pathologist (H.K.) who specialized in head and neck pathology with 11 years' experience. First, in pathologic specimens, the histologic pharyngeal constrictor muscle invasion by the tumor was evaluated and determined as negative or positive. Next, the status of the surgical margin was determined using the excised superior constrictor muscle as the deep margin. If the surgical margin involved the tumor, it was defined as a positive margin. A close margin was defined as a distance between the surgical margin and the tumor of <1 mm. Positive and close margins were designated as insecure surgical margins. A negative margin was defined as a distance between the surgical margin and the tumor of ≥1 mm.

### Statistical Analysis

Continuous variables are expressed as the median and range. Clinico-histopathologic findings according to the final surgical margin status were compared using the Fisher exact test and the Mann-Whitney *U* test. Interobserver agreement of MR imaging scores between the 2 readers was tested by Cohen  $\kappa$  coefficient statistics: >0.75, excellent agreement; 0.40–0.75, fair-to-good agreement; and <0.40, poor agreement.<sup>23</sup> The relationship between the MR imaging score and the histologic pharyngeal constrictor muscle invasion by the tumor was tested using the Linear-By-Linear Association test and the Spearman correlation. Diagnostic performances predicting an insecure surgical margin using MR imaging scores were evaluated using receiver operating characteristic (ROC) curve analysis. Area under the curve (AUC) values from each ROC curve analysis were compared using the DeLong test.<sup>24</sup> We further used the univariable and multivariable

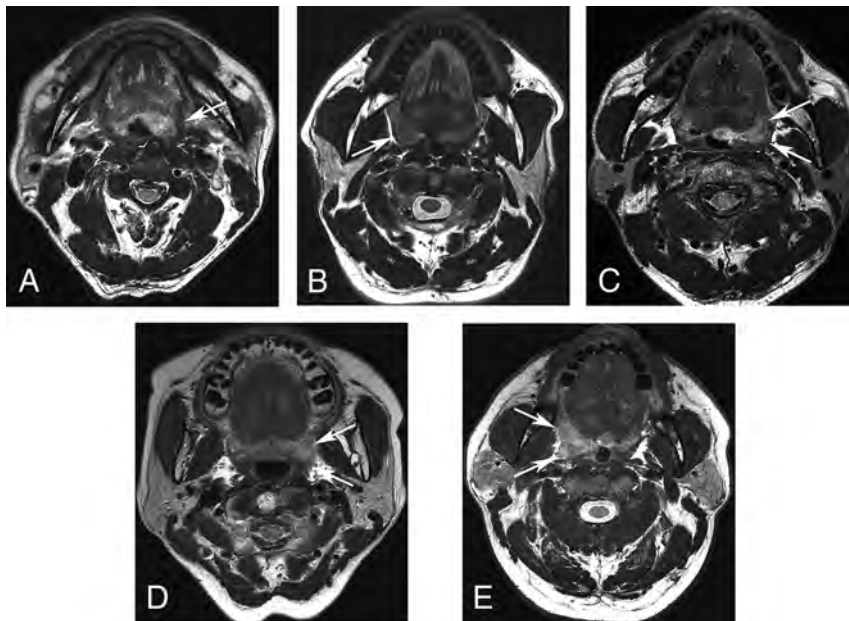


**FIG 1.** Representative 5-point scale preoperative MR imaging scores for tumor spread through the pharyngeal constrictor muscle. A, Axial T2WI of a 79-year-old man with left-tonsillar SCC revealing a normal constrictor muscle (arrow) (score 1). B, Axial T2WI of a 59-year-old man with right-tonsillar SCC revealing the bulging contour of the constrictor muscle due to the tumor, but normal thickness (arrow) (score 2). C, Axial T2WI of a 66-year-old man with left-tonsillar SCC reveals thinning of the constrictor muscle due to the tumor (score 3). Note that the thickness of the left constrictor muscle is reduced compared with the right side (arrows). D, Axial T2WI of a 69-year-old man with left tonsillar SCC revealing the obscured margin of the constrictor muscle by the tumor (score 4). Note that the normal contour of the constrictor muscle is not visualized (arrows). E, Axial T2WI of a 54-year-old man with right-tonsillar SCC revealing definite protrusion of the tumor into the parapharyngeal fat (arrows) (score 5).

logistic regression with a Firth correction<sup>25</sup> for risk evaluation of MR imaging scores for the pharyngeal constrictor muscle status to predict an insecure surgical margin after TORS. *P* values < .05 were considered statistically significant. Statistical analyses were performed using SPSS software (Version 17.0; IBM), MedCalc 17.9 (MedCalc Software), and SAS (Version 9.3; SAS Institute).

## RESULTS

### Clinico-Histopathologic Findings According to the Surgical Margin

According to the inclusion and exclusion criteria, 29 patients (26 men, 3 women; age range, 38–80 years; mean age, 61.6 years) were included for further analysis. Baseline patient characteristics are presented in Table 1. The cT categories were primarily T2 (*n* = 23), followed by T1 (*n* = 5), and T4 (*n* = 1). Twenty-seven patients underwent TORS with nodal dissection, and 2 patients underwent TORS alone without nodal dissection. The histopathologic results revealed a positive surgical margin in 7 patients, including 1 patient with cT4 who did not undergo neoadjuvant therapy, and a close surgical margin in 9 patients, for a total of 16 patients with an insecure surgical margin. After TORS, 18 patients underwent adjuvant chemoradiation (*n* = 10) or radiation only (*n* = 8), including 11 patients with an insecure surgical margin. Thirteen patients, including 8 with an insecure surgical margin, had lymphovascular

invasion, and 2 patients with an insecure surgical margin had perineural invasion in the surgical specimen. There were no differences in the clinico-histopathologic findings according to the surgical margin status (Table 1). On-line Table 1 summarizes the patient information regarding the tumor stage, MR imaging and pathologic findings, and adjuvant therapy.

### Interobserver Agreement of MR Imaging Scores for Pharyngeal Constrictor Muscle Involvement

The interobserver agreement between the 2 readers was excellent ( $\kappa$  = 0.955; *P* < .001). The final MR imaging scores were 1 in 5 patients, 2 in 4 patients, 3 in 5 patients, 4 in 9 patients, and 5 in 6 patients.

### Correlation between the Preoperative MR Imaging Score and Histologic Pharyngeal Constrictor Muscle Invasion

There was a significant difference in the state of histologic pharyngeal constrictor muscle invasion by the tumor according to the MR imaging scores (On-line Table 2). Patients with higher MR imaging scores showed a trend toward a positive histologic pharyngeal constrictor muscle invasion by the tumor (Spearman correlation coefficient, 0.601; *P* = .001).

### Prediction of the Surgical Margin Using the Preoperative MR Imaging Scores

In the ROC analysis, MR imaging scores of  $\geq 4$  (AUC = 0.899; 95% CI, 0.730–0.979) and  $\geq 3$  (AUC = 0.846; 95% CI, 0.664–0.952) enabled good prediction of an insecure surgical margin (Fig 2). However, there was no difference in the diagnostic performance between the 2 thresholds (*P* = .477). Optimal cutoff scores with AUCs, sensitivities, and specificities are provided in Table 2.

The results of the univariable analysis of the clinico-histopathologic factors and the MR imaging scores affecting the surgical margin status are presented in Table 3. The MR imaging scores were the most significant predictive factors of an insecure margin (*P* < .05). In the multivariable analysis of the variables with *P* values < .15 in the univariable analysis (ie, cT, pT, and MR imaging score), an MR imaging score of  $\geq 4$  was the only significant predictive factor of an insecure surgical margin (Table 4).

### Patient Follow-Up

The mean follow-up period from the time of surgery was  $28.9 \pm 19.4$  months. During the follow-up period, 4 patients with a close surgical margin after TORS exhibited locoregional recurrence on surveillance imaging, and 2 patients were confirmed to have locoregional recurrence using biopsy (On-line Figure). Among

**Table 1: Clinico-histopathologic findings according to the surgical margin status**

	Insecure Margin (n = 16)	Negative Margin (n = 13)	P Value
Age (median, range) (yr)	63, 45–80	60, 38–78	.345
Sex (female:male)	0:16	3:10	.078
cT category (No., %)			.164
cT1	1, 6.3%	4, 30.8%	
cT2	14, 87.5%	9, 69.2%	
cT3	0, 0%	0, 0%	
cT4	1, 6.3%	0, 0%	
cN category (No., %)			.422
cN0	1, 6.3%	2, 15.4%	
cN1	15, 93.8%	11, 84.6%	
pT category (No., %)			.202
pT1	2, 12.5%	5, 38.5%	
pT2	13, 81.3%	8, 61.5%	
pT3	0, 0%	0, 0%	
pT4	1, 6.3%	0, 0%	
pN category (No., %)			.625
pNx	1, 6.3%	1, 7.7%	
pN0	1, 6.3%	1, 6.3%	
pN1	12, 75.0%	10, 76.9%	
pN2	2, 12.5%	1, 7.7%	
Histopathologic differentiation (No., %)			.310
Well	2, 12.5%	0, 0%	
Moderate	5, 31.3%	8, 61.5%	
Poor	4, 25.0%	2, 15.4%	
Not applicable <sup>a</sup>	5, 31.3%	3, 23.1%	
Positive LVI (No., %)	8, 50.0%	5, 38.5%	.705
Positive perineural invasion (No., %)	2, 12.5%	0, 0%	.359
Treatment technique (No., %)			.485
TORS alone	5, 31.3%	6, 46.2%	
TORS+adjuvant radiation	4, 25.0%	4, 30.8%	
TORS+adjuvant chemoradiation	7, 43.8%	3, 23.1%	

Note—LVI indicates lymphovascular invasion.

<sup>a</sup>No pathologic statement of the histopathologic differentiation.

them, the preoperative MR imaging score was 5 for 2 patients, 4 for 1 patient, and 3 for 1 patient. The other clinico-histopathologic findings of these patients are summarized in On-line Table 3.

## DISCUSSION

In this study, we adopted the MR imaging–based scoring system for assessing the involvement of the pharyngeal constrictor muscle in HPV-positive tonsillar SCC and evaluated the predictive value of the MR imaging score for the surgical margin status after TORS. Patients with higher MR imaging scores showed a trend toward positive histologic pharyngeal constrictor muscle invasion by the tumor. An MR imaging score of  $\geq 4$  (obscured pharyngeal constrictor muscle by the tumor or parapharyngeal tumor extension) was the single most significant predictive factor of an insecure surgical margin after TORS with an OR of 6.59. Patients with a higher MR imaging score tended to exhibit locoregional recurrence during follow-up, despite the low preoperative cT category of the tumor.

Assessing the anatomic landmarks of the superior pharyngeal constrictor muscle and the parapharyngeal fat is important in the preoperative evaluation of HPV-positive tonsillar SCC before TORS. Tonsillar SCC invading the pharyngeal constrictor muscle

on a surgical field is known to increase a risk of locoregional recurrence,<sup>26</sup> and tumor invasion of the parapharyngeal fat is likely to leave an insecure surgical margin.<sup>5</sup> These structures can be directly visualized on MR imaging, which is an excellent imaging tool for the head and neck with superb soft-tissue contrast and high spatial resolution. In this regard, we hypothesized that preoperative MR imaging could predict the surgical margin status by scoring the degree of constrictor and parapharyngeal space invasion by the initial tumor. This hypothesis was supported by our results, which indicated that the 5-scale MR imaging scoring system could effectively predict insecure surgical margins after TORS.

Our results identified 14 patients who were diagnosed with early cT2 or cT1 cancers but had MR imaging scores of  $\geq 4$  (On-line Table 1). These 14 patients underwent TORS as a first-line surgical treatment, but 9 had insecure surgical margins necessitating adjuvant therapy according to the NCCN guidelines. On the basis of this observation, it can be inferred that if we can predict insecure margins before TORS, particularly in patients with early-stage cancer (ie, cT1 or cT2), we can preselect the patients who can receive radiation or chemoradiation instead of surgery as a

first-line treatment, despite the low clinical T-stage. Therefore, the preoperative MR imaging scoring system may have a significant clinical impact on treatment selection for patients with HPV-positive tonsillar SCC by predicting the surgical margin.

Our study results have important implications for patients who are candidates for TORS. First, MR imaging scores of 4 and 5 not only were related to the histologic pharyngeal muscle invasion by the tumor but also indicated a high probability of obtaining a positive or close margin. It is known that the invasion of the superior constrictor muscle itself should not lead to a positive margin if the surgery is performed correctly and the muscle is excised as the deep margin. However, our findings suggest that tonsillar SCC seemingly invading the constrictor muscle on MR imaging may include microscopic parapharyngeal fat invasion, and the preoperative work-up cannot guarantee tumor-free parapharyngeal fat.

Second, the selection of candidates for TORS as a first-line treatment has predominantly been based on clinical T-staging to date.<sup>2,5,27–30</sup> However, because the status of the constrictor muscle or parapharyngeal fat in HPV-positive tonsillar SCC is not currently applied in the AJCC staging<sup>21</sup> or NCCN guidelines,<sup>22</sup> there is risk of selecting improper patients for surgery who are predicted to have an insecure margin. We hope that our study result can be a



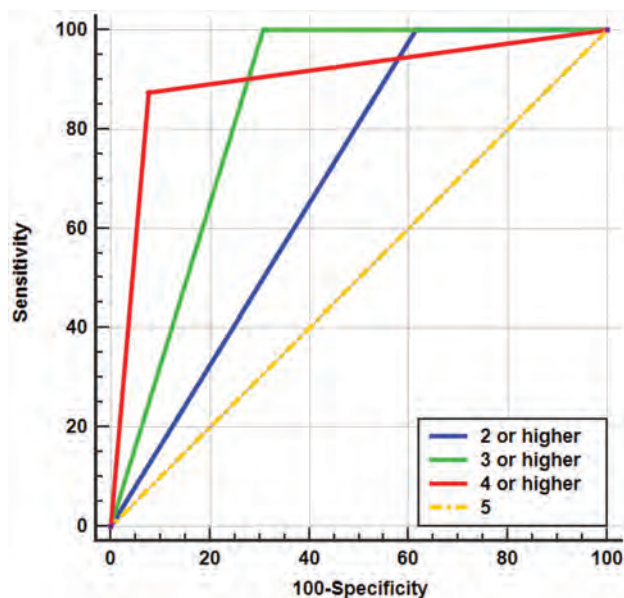


**FIG 2.** ROC curves for diagnosing an insecure surgical margin according to MR imaging scores for the pharyngeal constrictor muscle involvement. The ROC curve of the MR imaging score of  $\geq 4$  (red) has the highest AUC value of 0.899, followed by the MR imaging score of  $\geq 3$  (green, AUC value of 0.846), MR imaging score of  $\geq 2$  (blue, AUC value of 0.692), and MR imaging score of 5 (orange, AUC value of 0.500).

**Table 2: Diagnostic performance of the MR imaging score for predicting an insecure surgical margin**

Cutoff Value	AUC (95% CI)	Sensitivity (%) (95% CI)	Specificity (%) (95% CI)
$\geq 2$	0.692 (0.494–0.849)	100.0 (79.4–100.0)	38.5 (13.9–68.4)
$\geq 3$	0.846 (0.664–0.952)	100.0 (79.4–100.0)	69.2 (38.6–90.9)
$\geq 4$	0.899 (0.730–0.979)	87.5 (61.7–98.4)	92.3 (64.0–99.8)
5	0.500 (0.310–0.690)	0.0 (0.0–24.7)	100.0 (79.4–100.0)

**Table 3: Univariable analysis of predictors of an insecure surgical margin**

Factors	Contrast	OR	95% CI	P Value
cT category	cT1 vs cT2	4.58	0.701–51.21	.115
	cT1 vs cT4	9.0	0.303–1669.30	.208
cN category	cN0 vs cN1	2.25	0.262–27.08	.56
pT category	pT1 vs pT2	3.49	0.666–23.32	.141
	pT1 vs pT4	6.6	0.255–1118.92	.259
pN category	pN0 vs pNx	1.0	0.034–29.19	1.0
	pN0 vs pN1	1.09	0.079–14.88	.946
	pN0 vs pN2	5.0	0.148–965.12	.378
Histopathologic differentiation	Well vs moderate	0.13	0.001–2.00	.153
	Well vs poor	0.36	0.002–7.44	.533
LVI	Positive vs negative	1.31	0.296–6.094	.724
Perineural invasion	Positive vs negative	2.61	0.128–394.57	.543
Treatment technique	TORS only vs TORS+adjuvant radiation	0.78	0.124–4.61	.78
	TORS only vs TORS+adjuvant chemoradiation	2.14	0.415–12.46	.366
MR imaging score	1 vs 2–5	21.35	2.03–2930.98	.007 <sup>a</sup>
	1–2 vs 3–5	69.67	6.68–9652.57	<.0001 <sup>a</sup>
	1–3 vs 4–5	48.33	7.131–634.53	<.0001 <sup>a</sup>
	1–4 vs 5	3.99	0.653–43.33	.14

<sup>a</sup> P values < .05.

motive for future prospective clinical trials to verify the interrelation between the MR imaging score and clinical staging.

Third, during the follow-up period, 4 patients with early cancer (On-line Table 3) had locoregional recurrence. Despite the low clinical and pathologic staging, the initial MR imaging score for the pharyngeal constrictor of these patients was  $\geq 3$ , and the final surgical margin was close. We speculate that the preoperative MR imaging score could be associated with locoregional recurrence. However, the number of patients with locoregional recurrence was small, and the follow-up duration was rather short. Future prospective studies that can determine the statistical significance of the relationship between disease-free survival and the MR imaging score are warranted.

Our study had some limitations. First, most of the study subjects were retrospectively analyzed and thus inherently had low pre-TORS clinical and pathologic T-categories of c/pT1 and c/pT2. In addition, the treatment-related factors such as the presence or absence of the types of adjuvant treatment were variable among the patients. However, despite the heterogeneity of the clinical data, we performed the univariable and multivariable logistic regression analyses with Firth correction to overcome this limitation, and they revealed that the MR imaging score for pharyngeal constrictor muscle invasion was a significant predictor of a surgical margin, even after the consideration of the cT and pT categories. Second, the sample size was small, and the mean follow-up period of 28.9 months was too short to firmly establish the role of MR imaging scores in predicting locoregional recurrence.

Future prospective studies are warranted on a larger scale, such as a multicenter study, which can determine the relationship between the preoperative MR imaging score and clinical outcome. Third, although parapharyngeal tumor extension is a relative contraindication for TORS,<sup>5</sup> we

**Table 4: Multivariable analysis of predictors of an insecure surgical margin**

Factors	Contrast	OR	95% CI	P Values
cT category	cT1 vs cT2	3.35	0.177–1013.92	1.0
pT category	pT1 vs pT2	0.60	0.012–9.453	1.0
MR imaging score	1–3 vs 4–5	6.59	3.11–22.28	<.001 <sup>a</sup>

<sup>a</sup> P value < .05.

included 6 patients who had MR imaging scores of 5 but received TORS as a first-line treatment. However, the tumor protrusion on MR imaging was not substantial in these patients; thus, we believed that parapharyngeal tumor excision could be performed as reported in a previous article.<sup>31</sup>

Fourth, there were false-negative and false-positive cases of histologic pharyngeal constrictor muscle invasion when determined by the MR imaging scores of 4 and 5. There was also 1 patient with an MR imaging score of 5, but with a negative surgical margin. We assumed that the reason for the false-negative cases was the microscopic tumor invasion, which could not be detected on MR imaging under its current resolution. In addition, the false-positive cases were probably due to the pushing margin, which means the tumor compressed and pushed the constrictor muscle toward the parapharyngeal fat but preserved the lateral fascia of the superior pharyngeal constrictor muscle near the pterygomandibular raphe. Future advancement in the MR imaging resolution may assist in reducing the false-negative and false-positive cases. Lastly, TORS was performed by 2 surgeons who might have had varied surgical techniques. However, both were highly experienced and equally skilled surgeons. Therefore, we can ensure that the difference in the surgical technique between the 2 surgeons had little influence on the result of the surgical margin.

## CONCLUSIONS

The MR imaging–based scoring system is an effective tool for assessing pharyngeal constrictor muscle involvement in HPV-positive tonsillar SCC. An MR imaging score of  $\geq 4$  was the single most significant predictive factor of an insecure surgical margin after TORS, independent of the clinical and pathologic staging. Therefore, the preoperative MR imaging scoring system for the pharyngeal constrictor muscle is a promising predictor of the final surgical margin, thereby assisting in the appropriate selection of TORS treatment of HPV-positive tonsillar SCC, even in early T2 tumors.

## ACKNOWLEDGMENTS

We thank the Medical Research Collaborating Center at Seoul National University Bundang Hospital for assisting with statistical analyses and Editage (www.editage.co.kr) for English language editing.

## REFERENCES

1. Chaturvedi AK, Engels EA, Pfeiffer RM, et al. Human papillomavirus and rising oropharyngeal cancer incidence in the United States. *J Clin Oncol* 2011;29:4294–301 CrossRef Medline
2. Morisod B, Venara V, II, Alzuphar S, et al. Minimizing adjuvant treatment after transoral robotic surgery through surgical margin revision and exclusion of radiographic extracapsular extension: a prospective observational cohort study. *Head Neck* 2017;39:965–73 CrossRef Medline
3. Persky MJ, Albergotti WG, Rath TJ, et al. Positive margins by oropharyngeal subsite in transoral robotic surgery for T1/T2 squamous cell carcinoma. *Otolaryngol Head Neck Surg* 2018;158:660–66 CrossRef Medline
4. Ang KK, Sturgis EM. Human papillomavirus as a marker of the natural history and response to therapy of head and neck squamous cell carcinoma. *Semin Radiat Oncol* 2012;22:128–42 CrossRef Medline
5. Baskin RM, Boyce BJ, Amdur R, et al. Transoral robotic surgery for oropharyngeal cancer: patient selection and special considerations. *Cancer Manag Res* 2018;10:839–46 CrossRef Medline
6. Park YM, Jung CM, Cha D, et al. A new clinical trial of neoadjuvant chemotherapy combined with transoral robotic surgery and customized adjuvant therapy for patients with T3 or T4 oropharyngeal cancer. *Ann Surg Oncol* 2017;24:3424–29 CrossRef Medline
7. Mirghani H, Blanchard P. Treatment de-escalation for HPV-driven oropharyngeal cancer: where do we stand? *Clin Transl Radiat Oncol* 2018;8:4–11 CrossRef Medline
8. Masterson L, Moualel D, Liu ZW, et al. De-escalation treatment protocols for human papillomavirus-associated oropharyngeal squamous cell carcinoma: a systematic review and meta-analysis of current clinical trials. *Eur J Cancer* 2014;50:2636–48 CrossRef Medline
9. Chen AM, Felix C, Wang PC, et al. Reduced-dose radiotherapy for human papillomavirus-associated squamous-cell carcinoma of the oropharynx: a single-arm, Phase 2 study. *Lancet Oncol* 2017;18:803–11 CrossRef Medline
10. Mallen-St Clair J, Alani M, Wang MB, et al. Human papillomavirus in oropharyngeal cancer: the changing face of a disease. *Biochim Biophys Acta* 2016;1866:141–50 CrossRef Medline
11. Eisbruch A, Schwartz M, Rasch C, et al. Dysphagia and aspiration after chemoradiotherapy for head-and-neck cancer: which anatomic structures are affected and can they be spared by IMRT? *Int J Radiat Oncol Biol Phys* 2004;60:1425–39 CrossRef Medline
12. Rieger JM, Zalmanowitz JG, Wolfaardt JF. Functional outcomes after organ preservation treatment in head and neck cancer: a critical review of the literature. *Int J Oral Maxillofac Surg* 2006;35:581–87 CrossRef Medline
13. Machtay M, Moughan J, Trotti A, et al. Factors associated with severe late toxicity after concurrent chemoradiation for locally advanced head and neck cancer: an RTOG analysis. *J Clin Oncol* 2008;26:3582–89 CrossRef Medline
14. Bhayani MK, Holsinger FC, Lai SY. A shifting paradigm for patients with head and neck cancer: transoral robotic surgery (TORS). *Oncology (Williston Park)* 2010;24:1010–15 Medline
15. Mydlarz WK, Chan JY, Richmon JD. The role of surgery for HPV-associated head and neck cancer. *Oral Oncol* 2015;51:305–13 CrossRef Medline
16. Duek I, Billan S, Amit M, et al. Transoral robotic surgery in the HPV era. *Rambam Maimonides Med J* 2014;5:e0010 CrossRef Medline
17. Holsinger FC, McWhorter AJ, Ménard M, et al. Transoral lateral oropharyngectomy for squamous cell carcinoma of the tonsillar region. I: technique, complications, and functional results. *Arch Otolaryngol Head Neck Surg* 2005;131:583–91 CrossRef Medline
18. Moore EJ, Janus J, Kasperbauer J. Transoral robotic surgery of the oropharynx: clinical and anatomic considerations. *Clin Anat* 2012;25:135–41 CrossRef Medline
19. Chen MM, Roman SA, Kraus DH, et al. Transoral robotic surgery: a population-level analysis. *Otolaryngol Head Neck Surg* 2014;150:968–75 CrossRef Medline
20. An Y, Park HS, Kelly JR, et al. The prognostic value of extranodal extension in human papillomavirus-associated oropharyngeal squamous cell carcinoma. *Cancer* 2017;123:2762–72 CrossRef Medline
21. Zhan KY, Eskander A, Kang SY, et al. Appraisal of the AJCC 8th edition pathologic staging modifications for HPV-positive

- oropharyngeal cancer, a study of the National Cancer Data Base. *Oral Oncol* 2017;73:152–59 CrossRef Medline
22. NCCN Clinical Practice Guideline Sin Oncology. 2018 Version I.2018. <https://www.firshospital.cn/upload/doc/201911/21175519.pdf>. Accessed May 13, 2018
23. Fleiss J, Levin B, Paik MC. *Statistical Methods for Rates and Proportions*. 2nd ed. John Wiley; 1981:38–46
24. DeLong ER, DeLong DM, Clarke-Pearson DL. Comparing the areas under two or more correlated receiver operating characteristic curves: a nonparametric approach. *Biometrics* 1988;44:837–45 CrossRef Medline
25. Heinze G, Schemper M. A solution to the problem of monotone likelihood in Cox regression. *Biometrics* 2001;57:114–19 CrossRef Medline
26. Cracchiolo JR, Roman BR, Kutler DI, et al. Adoption of transoral robotic surgery compared with other surgical modalities for treatment of oropharyngeal squamous cell carcinoma. *J Surg Oncol* 2016;114:405–11 CrossRef Medline
27. Moore EJ, Van Abel KM, Price DL, et al. Transoral robotic surgery for oropharyngeal carcinoma: surgical margins and oncologic outcomes. *Head Neck* 2018;40:747–55 CrossRef Medline
28. Funk RK, Moore EJ, Garcia JJ, et al. Risk factors for locoregional relapse after transoral robotic surgery for human papillomavirus-related oropharyngeal squamous cell carcinoma. *Head Neck* 2016;38(Suppl 1):E1674–79 CrossRef Medline
29. Cracchiolo JR, Baxi SS, Morris LG, et al. Increase in primary surgical treatment of T1 and T2 oropharyngeal squamous cell carcinoma and rates of adverse pathologic features: National Cancer Data Base. *Cancer* 2016;122:1523–32 CrossRef Medline
30. Weinstein GS, O'Malley BW Jr, Rinaldo A, et al. Understanding contraindications for transoral robotic surgery (TORS) for oropharyngeal cancer. *Eur Arch Otorhinolaryngol* 2015;272:1551–52 CrossRef Medline
31. Chan JY, Tsang RK, Eisele DW, et al. Transoral robotic surgery of the parapharyngeal space: a case series and systematic review. *Head Neck* 2015;37:293–98 CrossRef Medline



# Radioanatomic Characteristics of the Posteromedial Intraconal Space: Implications for Endoscopic Resection of Orbital Lesions

 A. Jafari,  A.E. Lehmann,  N. Wolkow,  A.F. Juliano,  B.S. Bleier, and  K.L. Reinshagen



## ABSTRACT

**BACKGROUND AND PURPOSE:** Imaging is essential in the diagnostic work-up of patients with orbital lesions. The position of an orbital lesion relative to the inferomedial muscular trunk of the ophthalmic artery determines endoscopic resectability, anticipated technical difficulty, and patient morbidity. Although the inferomedial muscular trunk is not readily identifiable on preoperative imaging, we hypothesize that it is spatially approximate to the location where the ophthalmic artery crosses the optic nerve. Our aim was to determine whether the ophthalmic artery–optic nerve crosspoint anatomically approximates the inferomedial muscular trunk in a cadaver study and can be appreciated on imaging of known posteromedial orbital lesions.

**MATERIALS AND METHODS:** Dissection was performed on 17 fresh-frozen cadaver orbits to assess the relationship between the inferomedial muscular trunk and ophthalmic artery–optic nerve crosspoint. Retrospective review of imaging in 9 patients with posteromedial orbital lesions assessed posteromedial orbital compartment characteristics and the ability to locate the ophthalmic artery–optic nerve crosspoint.

**RESULTS:** In our cadaver study, the mean distance between the ophthalmic artery–optic nerve crosspoint and the inferomedial muscular trunk was  $1.21 \pm 0.64$  mm. Retrospectively, the ophthalmic artery–optic nerve crosspoint was identifiable in 9/9 patients, whereas the inferomedial muscular trunk was not identifiable in any patient. Total or partial effacement of the posteromedial intraconal fat triangle was observed in 9/9 patients.

**CONCLUSIONS:** This study of neurovascular relationships within the posteromedial orbit demonstrates that the ophthalmic artery–optic nerve crosspoint closely approximates the inferomedial muscular trunk and can be seen in patients with posteromedial orbital lesions. Posteromedial intraconal fat effacement may help to localize these lesions. These findings may facilitate multidisciplinary communication and help predict lesion resectability and patient outcomes.

**ABBREVIATIONS:** CECT = contrast-enhanced CT; IMT = inferomedial muscular trunk of the ophthalmic artery; NECT = non-contrast-enhanced CT; OA = ophthalmic artery; ON = optic nerve

**R**adiologic characteristics of orbital lesions as well as their locations relative to critical neurovascular structures are essential to determine the surgical approach for resection and to anticipate outcomes.<sup>1–3</sup> A keen understanding of orbital anatomy is required to determine whether an orbital lesion is amenable to endoscopic

resection and which structures are at risk. However, certain orbital structures that are essential to surgical planning and that determine surgical complexity are not readily discernable on imaging.

For example, the inferomedial muscular trunk (IMT) of the ophthalmic artery (OA) defines the anterior and posterior medial compartments of the orbit when considering an endoscopic resection.<sup>2,3</sup> Injury of the IMT may result in bleeding and ischemia of the medial and inferior rectus muscles, which can cause retrobulbar hemorrhage, difficult/incomplete resection, or diplopia.<sup>3</sup> Thus, lesions located posterior to the IMT tend to be more difficult to resect and have a greater risk of poorer patient outcomes.<sup>3</sup> Thus, the position of a lesion relative to the IMT is an important component of the validated Cavernous Hemangioma Exclusively Endonasal Resection orbital staging system.<sup>3</sup>

Although the IMT is a key landmark for operative planning and surgical dissection, it has a relatively small caliber (approximately

Received April 27, 2020; accepted after revision July 29.

From the Departments of Otolaryngology–Head & Neck Surgery (A.J., A.E.L., B.S.B.), Ophthalmology (N.W.), and Radiology (A.F.J., K.L.R.), Massachusetts Eye and Ear, Harvard Medical School, Boston, Massachusetts; and Department of Otolaryngology–Head & Neck Surgery (A.J.), University of Washington, Seattle, Washington.

Paper previously presented at: Annual Meeting of the American Rhinologic Society, September 11–12, 2020; Virtual.

Please address correspondence to Aria Jafari, MD, Division of Rhinology and Endoscopic Skull Base Surgery, Department of Otolaryngology–Head & Neck Surgery, University of Washington, Box 356515, Health Sciences Building, Suite BB1165, Seattle, WA 98195; e-mail: ajafari@uw.edu



Indicates article with supplemental on-line table.

<http://dx.doi.org/10.3174/ajnr.A6822>

0.7 mm)<sup>4</sup> and is, thus, challenging to identify on preoperative imaging. Prior anatomic studies have described the IMT taking off from the inferior aspect of the OA near its second bend.<sup>5</sup> The location of this bend is thought to spatially approximate the location where the OA crosses the optic nerve (ON) at the medial aspect of the nerve (the OA-ON crosspoint). Although the IMT is not reliably seen on imaging, the OA-ON crosspoint is a radiologically salient finding.<sup>4,5</sup> However, the precise anatomic relationship of the OA-ON crosspoint and the IMT has not yet been investigated.

Reporting the OA-ON crosspoint may enhance multidisciplinary communication between neuroradiologists and orbital surgeons. The aim of this study was to determine the following: 1) whether the OA-ON crosspoint anatomically approximates the IMT in a cadaver study, and 2) whether this radiologic landmark (the OA-ON crosspoint) could be appreciated on imaging of known orbital lesions. We posit that this is a readily identifiable radiologic landmark in cases of orbital lesions.

## MATERIALS AND METHODS

This study consisted of 2 parts: The first part was an anatomic evaluation using cadaveric specimens to determine the neurovascular relationships between the OA and ON, including the OA-ON crosspoint. The second part of the study assessed whether this OA-ON crosspoint could be identified on preoperative imaging in a retrospective case series of posteromedial orbital lesions. The study was approved by the Institutional Review Board of Partners HealthCare, Protocol No. 2019P003408.

### Anatomic Evaluation

Anatomic dissection was performed on 9 fresh-frozen cadaver head specimens (8 without latex injection and 1 with latex injection). One orbit was not included because this specimen had a prior enucleation. Two included specimens (totaling 4 orbits) had their corneas donated and were thus missing the anterior segments of their globes. A total of 17 orbits were dissected. Three specimens were male and 6 were female. The mean age at death was  $63.2 \pm 16.5$  years (range, 39–86 years).

For each specimen, a bicoronal incision was performed extending from the zygomatic roots through the periosteum and down to cranial bone. A soft-tissue flap was elevated anteriorly to the level of the supraorbital ridges, and the frontal bone was exposed. A bifrontal craniotomy was planned, and a bone flap was created using a high-powered drill. After elevation of the bone flap from the dura, a durotomy was performed, and the frontal lobe contents were removed. The dura and remaining intracranial contents were then dissected off the cribriform plate in an anterior-to-posterior fashion to expose the orbital roofs bilaterally. An osteotomy was created in the orbital roof, and rongeurs were used to remove the bone of the orbital roof and expose the periorbita. The periorbita was then incised, and the orbital contents were visualized. This portion of the dissection was performed by 2 otolaryngologists (A.J. and A.E.L.).

Once the periorbita was opened, the frontal nerve, levator palpebrae superioris, and superior rectus muscles were transected anteriorly and reflected posteriorly. Orbital fat was removed to reveal the ON and the OA. The branches of the OA were dissected free of orbital fat and followed to their targets. In all

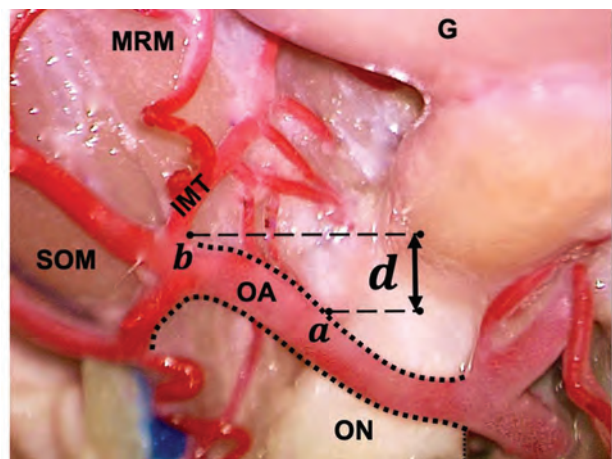


**FIG 1.** Dorsal view of the right orbit and its contents, with the medial rectus muscle (MRM) and superior oblique muscle (SOM) reflected laterally. G indicates globe; a, OA-ON crosspoint; b, branch point of IMT; d, distance (in millimeters) from the OA-ON crosspoint and the IMT branch point.

specimens, the OA emerged from the optic canal lateral to the ON. The OA then crossed above the ON, coursing along the medial aspect of the ON in the posteromedial intraconal space. In all specimens, the IMT emerged from the inferior aspect of the OA and was identified medial to the ON, with its branches heading toward the medial and inferior rectus muscles. This portion of the dissection was performed by an ophthalmologist (N.W.).

Quantitative measurements were then obtained. The OA was traced to the point at which the vessel crossed the medial aspect of the ON, and this crosspoint was marked. The distance between this crosspoint and the point of origin of the IMT from the OA was measured using calipers, and digital still images illustrating the surgical relationships were captured (see Fig 1 for illustration of these points and orientation of distance measurement). All 3 investigators involved in the dissections participated in obtaining the distance measurements for all orbits (A.J., A.E.L., and N.W.).

### Radiographic Evaluation

We reviewed 9 consecutive patients with posterior intraconal orbital pathology who had undergone both MR and CT orbital imaging. Seven of 9 patients underwent 3T MR imaging at our institution, while 2 patients had outside 1.5T MRIs reviewed. Seven of 9 patients underwent CT at our institution, while 2 patients had outside CT studies reviewed. All MRIs were performed at our institution on the same 3T Achieva scanner with an 8-channel head coil (Philips Healthcare). Eight of 9 patients had intravenous gadolinium-based contrast, while 1 patient could not receive MR imaging contrast due to prior anaphylaxis. All MRIs performed included 2- to 3-mm section thickness, precontrast axial  $\pm$  coronal T1WI, and postcontrast axial  $\pm$  coronal T1WI of the orbits with or without fat suppression. At 3T, T1WI was performed with TE = 10–12 ms, TR = 510–710 ms, number of excitations = 1–2, flip angle = 90°, axial FOV = 140  $\times$  140 mm, coronal FOV = 150  $\times$  150 mm, axial bandwidth = 163–170 Hz, coronal bandwidth = 246–300 Hz, acquired pixel size in the axial plane = 0.43  $\times$  0.43 mm, acquired pixel size in the coronal plane = 0.47  $\times$  0.47 mm, scan time

(minute:second) = axial (2–3 mm): 4 minutes and 21 seconds and coronal (3 mm): 4 minutes and 11 seconds. Outside 1.5T T1WI was performed with TE = 10–17 ms, TR = 492–635 ms, number of excitations = 1–3, flip angle = 90°.

All MR images evaluated were 2D. All CTs were performed on 64-section multidetector units. Of those performed at our institution, all were performed on the same Discovery 750HD scanner (GE Healthcare). All CTs were performed with 120 kV and had a range of 60–258 mA. Three of 9 patients underwent contrast-enhanced CT (CECT), while the remainder (6/9) underwent non-contrast-enhanced CT (NECT). CT images were reviewed in 2- to 3-mm section-thickness axial and coronal reformats in a soft-tissue window. The images were reviewed independently by 2 attending neuroradiologists (A.F.J. and K.L.R., with 12 and 4 years' experience, respectively), who determined, by consensus, the visibility of the OA-ON crosspoint on CT and MR imaging. The OA-ON crosspoint was assessed with axial 2D-T1WI spin-echo sequences and, if available, axial or coronal 2D-T1WI fat-suppressed postcontrast images.

Because posteromedial orbital lesions are considered more difficult to resect than their anteromedial counterparts, we also assessed whether orbital fat effacement in the posteromedial intraconal triangle was a radiologic characteristic in this series of posteromedial orbital lesions. The effacement of orbital fat within the posteromedial intraconal triangle, defined anteriorly by a coronally oriented line through the OA-ON crosspoint, laterally by the long axis of the medial rectus, medially by the ON, and posteriorly by the orbital apex, was determined on precontrast T1WI or CT images. The degree of orbital fat effacement was determined subjectively as follows: At the level of the mass, no visible fat was described as completely effaced, and >50% degree of fat effacement was described as near-total or partial fat effacement. The neuroradiologists were blinded to the results of the cadaveric dissection and intraoperative findings.

## RESULTS

### Anatomic Neurovascular Relationships

In our cadaver study, the OA was encountered lateral to the ON after exiting the optic canal in all (17/17) orbits. The course of the OA then proceeded from lateral to medial. The OA traversed above the ON in all (17/17) orbits. The point at which the OA crossed the medial aspect of the ON (point a) and the IMT (point b) was able to be identified in all (17/17) specimens, as seen in Fig 1. The IMT was located proximal to the OA-ON crosspoint in 1 orbit. The mean distance between these 2 landmarks (point a to b) was determined to be  $1.31 \pm 0.75$  mm on the left,  $1.11 \pm 0.55$  mm on the right ( $P = .53$ ), and  $1.21 \pm 0.64$  mm for all orbits combined. Any discrepancy in measurements was resolved by consensus by investigators (A.J., A.E.L., N.W.).

### Radiologic Characteristics

In our retrospective case series of patients with orbital apex lesions, 3 patients were men and 6 were women. The mean age was  $48.9 \pm 22.2$  years. Dates of imaging were from November 2012 to September 2019. Most lesions were orbital venous malformations, previously referred to as cavernous hemangiomas (5/9, 55.6%), and the remainder were rhabdomyosarcoma, meningioma, squamous cell carcinoma, and schwannoma (1 each). The OA was visualized

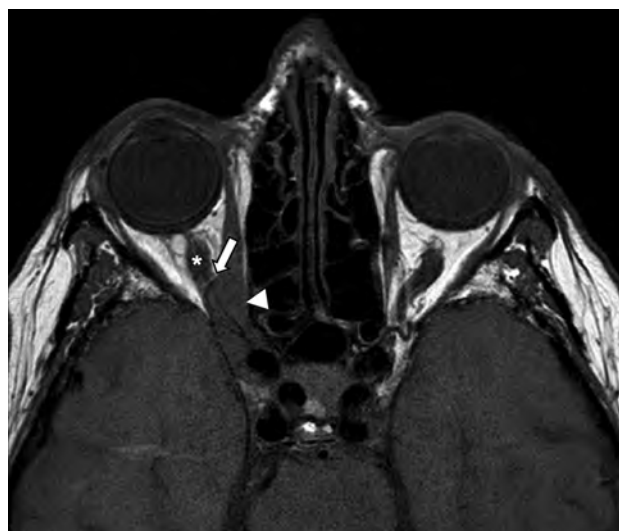


**FIG 2.** Axial T1-weighted MR image in a 75-year-old woman with squamous cell carcinoma (white arrowhead) in the posterior intraconal right orbit. The OA (white arrow) is seen crossing the medial margin of the ON (asterisk).

lateral to the ON after exiting the optic canal, traversing from lateral to medial in all (9/9) orbits. Additional details are shown in the Online Table. The point at which the OA crossed the medial aspect of the ON (the OA-ON crosspoint) could be identified on imaging for all (9/9) patients (Figs 2–5). The OA-ON crosspoint was visible on non-fat-suppressed T1WI in all (9/9) patients. While 8 of 9 patients had fat-suppressed, postcontrast T1WI of the orbits, the OA-ON crosspoint was only visible in 2 of 8 patients in these fat-suppressed sequences. Of the 6 patients who underwent NECT, the OA-ON crosspoint could be seen in 6 patients (100%) (Fig 3A–C). Of the 3 patients who underwent CECT, the OA-ON crosspoint could be seen in 2 patients (66.7%) (Fig 4). The IMT could not be identified in any (0/9) of the imaging studies. The posteromedial intraconal fat triangle characteristics were recorded and classified into categories based on the degree of effacement by the lesion. Near-total or partial effacement was observed in 3 of 9 (33.3%) patients (Fig 3), and total effacement was observed in 6 of 9 (67.7%) patients (Fig 5).

## DISCUSSION

Diagnostic imaging and interpretation are essential in the work-up of patients with orbital lesions, especially because the physical examination may be unremarkable early in the disease.<sup>1</sup> The precise location of an orbital lesion within the orbit and its position relative to the IMT of the OA determine endoscopic resectability, anticipated technical difficulty, and patient morbidity.<sup>2,3,6</sup> This feature is most likely relevant for solitary lesions with well-circumscribed, pushing borders as opposed to infiltrative lesions in which the IMT may be engulfed by the lesion. However, despite its significance during orbital lesion surgery, the IMT is not readily identifiable on preoperative diagnostic imaging.

The purpose of this study was to integrate neurovascular associations, radiologic findings, and surgical anatomy to describe the posteromedial orbit, a highly complex and technically challenging space. Our results demonstrate that the OA-ON crosspoint is a



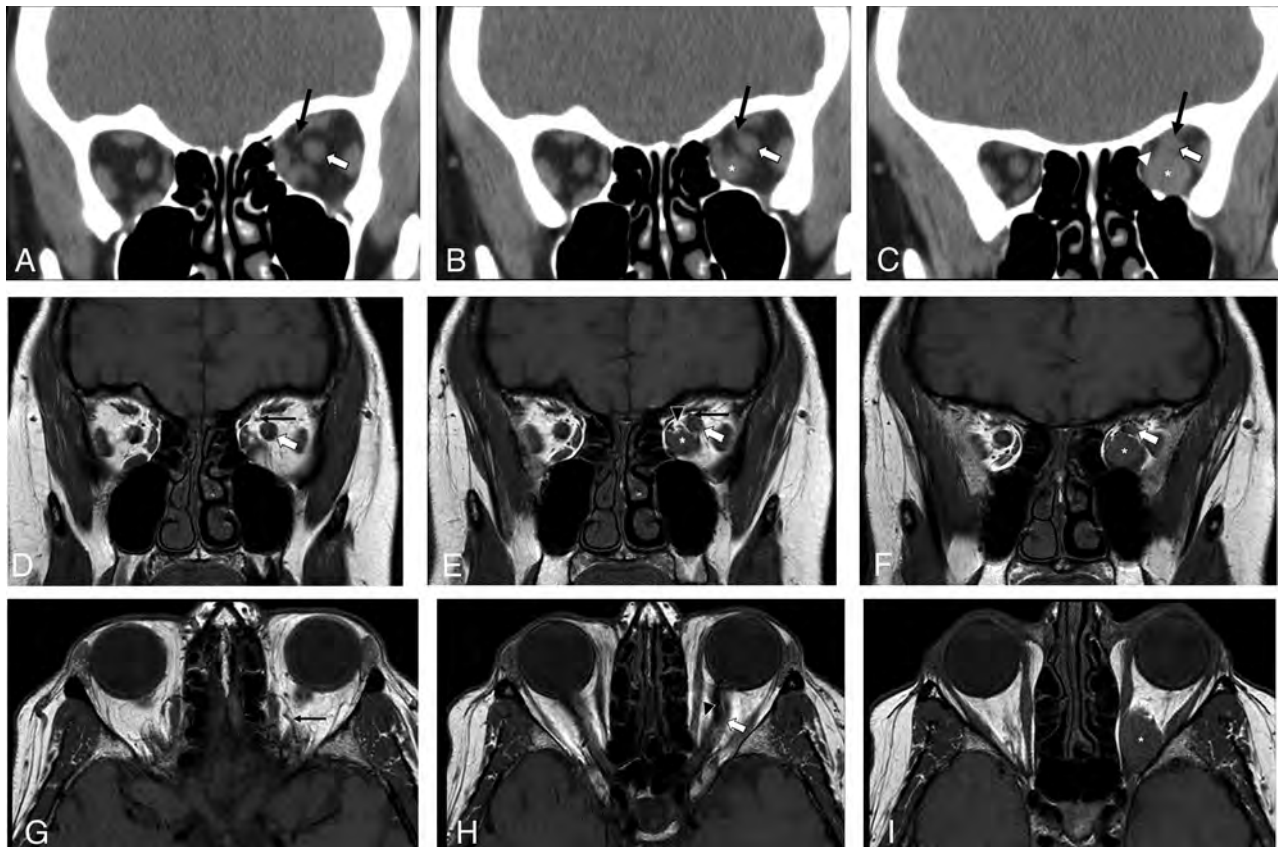


**FIG 3.** Orbital imaging in a 69-year-old woman with a venous malformation in the posterior intraconal left orbit (*asterisk*). Coronal NECT images (A–C, anterior to posterior) show the OA (*black arrow*) crossing the medial margin of the ON (*white arrow*, B). There is incomplete effacement of the fat at the level of the lesion within the posteromedial intraconal space on CT (*white arrowhead*). Coronal T1-weighted (D–F, anterior to posterior) and axial T1-weighted MR images (G–I, superior to inferior) of the orbits show the OA (*black arrow*) coursing above the ON (*white arrow*). The OA is seen crossing the medial margin of the ON (E). There is incomplete effacement of the posteromedial intraconal fat on MR imaging at the level of the lesion (*black arrowhead*).

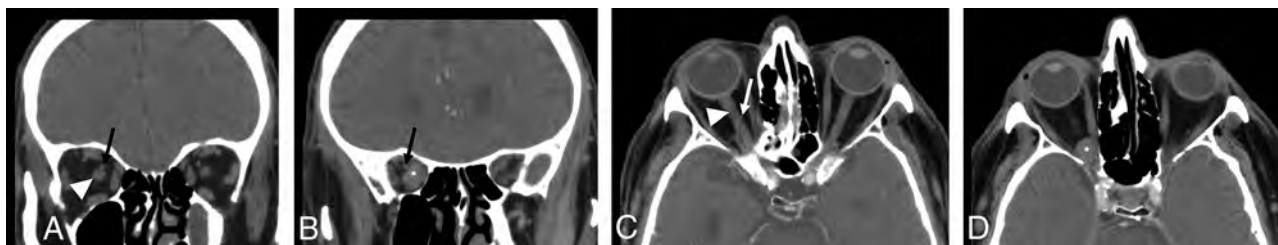


**FIG 4.** CECT of the orbits in a 74-year-old man with a venous malformation in the posterior intraconal right orbit. Coronal images (A and B, anterior to posterior) demonstrate the OA (*black arrow*) crossing the medial margin of the ON (*white arrowhead*, A) anterior to the lesion (*asterisk*). Axial images (C and D, superior to inferior) also demonstrate the OA (*white arrow*) crossing the medial margin of the ON (*white arrowhead*, C) anterior to the lesion (*asterisk*, D). Effacement of the fat in the posteromedial intraconal space is demonstrated at the level of the lesion (D).

radiologically consistent finding on our retrospective imaging review, and it closely approximates the location of the origin of the IMT from the OA (mean distance,  $1.21 \pm 0.64$  mm) on our cadaveric study. In addition, we found that effacement of the posteromedial intraconal fat triangle on imaging was seen in our select patient sample with pathology within this space. These radioanatomic findings offer additional tools for effective reporting because endoscopic orbital surgery is used in an increasingly broad array of orbital pathologies.

Findings from previous anatomic dissections of neurovascular structures detail the close association of the OA and ON within the posterior orbit and support the findings demonstrated in this study.<sup>4–6</sup> In the optic canal and the posterior orbit, the OA is adherent to the ON through connective tissue attachments to the ON dural sheath.<sup>5</sup> This adherence extends throughout the optic canal and into the posterior orbit as the OA crosses the ON from lateral to medial.<sup>5</sup> After the OA crosses the medial margin of the ON, the OA turns anteriorly, gives off the IMT, and is then no



**FIG 5.** Axial T1-weighted precontrast (A and B, superior to inferior) and coronal T1-weighted postcontrast (C and D, anterior to posterior) images of the orbits in a 39-year-old woman with a venous malformation in the posterior intraconal left orbit. The OA (black arrowhead) can be seen crossing the medial margin of the ON (white arrow, A and C) anterior to the lesion (asterisk). There is full effacement of the posterior intraconal fat at the level of the lesion (B and D).

longer adherent to the ON.<sup>4,5</sup> The reliability of the OA-ON crosspoint demonstrated in the present study, along with the known adherence of the OA to the ON in this location, supports the utility of the OA-ON crosspoint in cases of orbital pathology, even when mass effect may distort other soft-tissue landmarks.

Identification of the OA-ON crosspoint (a radiologically distinct structure) as an approximation of the IMT (a radiologically indistinct structure) allows more accurate preoperative staging of orbital lesions, which, in turn, optimizes surgical planning and patient counseling.<sup>2,3,7</sup> Lesions located posterior to the IMT may require a more complex operation, including binocular access, a 2-surgeon approach, and vascularized reconstruction. Lesions in this location may also carry a greater risk for postoperative visual and cosmetic morbidity.<sup>3</sup> Our study supports the complementary use of orbital MR imaging in the preoperative setting to best visualize the OA-ON crosspoint. While CT is more readily available and often used in intraoperative guidance, the OA-ON crosspoint was not visualized in 1 patient with CECT. In this patient, the OA was similar in density to the avidly enhancing rhabdomyosarcoma and was not definitively visualized at the medial margin of the ON. The OA may be more visible on MR imaging because the OA in our patients was seen as a dark flow void on precontrast T1WI and thus was more visible against the lesion background and adjacent optic nerve, whereas it typically has a similar density to the surrounding lesion or optic nerve on CT. In addition, the OA-ON crosspoint was best visualized on non-fat-suppressed spin-echo T1WI, likely due to the contrast between the dark flow void of the OA against intraconal orbital fat. This effect is likely due to the black-blood effect seen with spin-echo T1WI and would be expected to be spoiled using a gradient-echo T1WI. This black-blood effect has been effective in vessel wall imaging.<sup>8,9</sup>

In our population with lesions in the posterior intraconal space, we found that lesions that were posterior to the IMT demonstrated partial or complete effacement of the posteromedial fat triangle, which could be a useful additional sign, particularly if the OA-ON crosspoint cannot be visualized. This behavior of fat relative to critical structures is also seen in parapharyngeal space lesions, in which poststyloid lesions demonstrate anterolateral displacement of the prestyloid fat and effacement of the fat around the great vessels.<sup>10</sup> Because the orbital lesions are similarly space-occupying, we suspect that the effacement seen within the posteromedial orbital compartment reflects similar displacement within the orbit.

This study has limitations. The relatively small sample size of cadaver specimens may have limited our ability to capture anatomic variability inherent in orbital vasculature. For example, in a small subset of patients, the OA may run under the ON, a relationship not seen in our dissections.<sup>4,5</sup> Furthermore, distance measurements may have been affected by postmortem changes and the inherent compliance of the structures within the mobile orbital fat. In addition, due to the retrospective nature of this study, the MR imaging and CT techniques used varied slightly among patients because outside images were included in our analysis. A prospective study with larger patient numbers to confirm these findings and determine the most efficient imaging strategy for these patients would be helpful. As a result of the retrospective nature of this study, the origin of the

IMT in relationship to the OA-ON crosspoint was not confirmed intraoperatively in these patients, a further limitation, which would benefit from further prospective studies. In addition, future studies could include the use of high-resolution microscopy coil MR imaging for further characterization of the intraconal orbital anatomy.<sup>11</sup> Last, further studies are needed to determine whether the identification of the OA-ON crosspoint is linked with decreased morbidity and improved patient outcomes in clinical practice.

## CONCLUSIONS

This study of neurovascular relationships within the posteromedial orbit demonstrates that the OA-ON crosspoint (a radiologically distinct structure) closely approximates the IMT (a radiologically indistinct structure), which is a critical structure for operative planning and surgical dissection of orbital lesions. Partial and complete posteromedial intraconal fat effacement was seen in our patient population with posterior intraconal space lesions. Together, these radiologic findings may facilitate multidisciplinary communication between neuroradiologists and orbital surgeons and help predict lesion resectability and patient outcomes.

Disclosures: Natalie Wolkow—UNRELATED: Consultancy: Pykus Therapeutics, Comments: consulting services on a subject not related to the above work. Benjamin S. Bleier—UNRELATED: Consultancy: Olympus, Karl Storz SE & Co, Medtronic, Sinopsis, Baxter Healthcare, 3D Matrix; Grants/Grants Pending: 1 R01 NS108968-01 National Institutes of Health/National Institute of Neurological Disorders and Stroke (Principal Investigator), paid to the institution; Royalties: Thieme, paid to the individual. Amy F. Juliano—UNRELATED: Employment: Massachusetts Eye and Ear, Comments: This is my regular full-time job as a practicing clinical radiologist.

## REFERENCES

1. Bilaniuk LT. **Orbital vascular lesions: role of imaging.** *Radiol Clin North Am* 1999;37:169–83.xi CrossRef Medline
2. Bleier BS, Healy DY, Chhabra N, et al. **Compartmental endoscopic surgical anatomy of the medial intraconal orbital space.** *Int Forum Allergy Rhinol* 2014;4:587–91 CrossRef Medline
3. El Rassi E, Adappa ND, Battaglia P, et al. **Development of the international orbital Cavernous Hemangioma Exclusively Endonasal Resection (CHEER) staging system.** *Int Forum Allergy Rhinol* 2019;9:804–12 CrossRef Medline
4. Erdogmus S, Govsa F. **Arterial vascularization of the extraocular muscles on its importance for orbital approaches.** *J Craniofac Surg* 2007;18:1125–32 CrossRef Medline
5. Hayreh SS. **Orbital vascular anatomy.** *Eye (Lond)* 2006;20:1130–44 CrossRef Medline
6. Li L, London NR Jr, Silva S, et al. **Transnasal prelacrimal approach to the inferior intraconal space: a feasibility study.** *Int Forum Allergy Rhinol* 2019;9:1063–68 CrossRef Medline
7. Maxfield AZ, Brook CD, Miyake MM, et al. **Compartmental endoscopic surgical anatomy of the inferior intraconal orbital space.** *J Neurol Surg B Skull Base* 2018;79:189–92 CrossRef Medline
8. Mandell DM, Mossa-Basha M, Qiao Y, et al; Vessel Wall Imaging Study Group of the American Society of Neuroradiology. **Intracranial vessel wall MRI: principles and expert consensus recommendations of the American Society of Neuroradiology.** *AJNR Am J Neuroradiol* 2017;38:218–29 CrossRef Medline
9. Mohammed-Brahim N, Clavel G, Charbonneau F, et al. **Three Tesla 3D high-resolution vessel wall MRI of the orbit may differentiate arteritic from nonarteritic anterior ischemic optic neuropathy.** *Invest Radiol* 2019;54:712–18 CrossRef Medline
10. Stambuk HE, Patel SG. **Imaging of the parapharyngeal space.** *Otolaryngol Clin North Am* 2008;41:77–101 CrossRef Medline
11. Dobbs NW, Budak MJ, White RD, et al. **MR-Eye: high-resolution microscopy coil MRI for the assessment of the orbit and periorbital structures, Part 1: technique and anatomy.** *AJNR Am J Neuroradiol* 2020;41:947–50 CrossRef Medline



# Gadolinium-Enhanced 3D T1-Weighted Black-Blood MR Imaging for the Detection of Acute Optic Neuritis

I. Riederer, N. Sollmann, M. Mühlau, C. Zimmer, and J.S. Kirschke



## ABSTRACT

**BACKGROUND AND PURPOSE:** A 3D T1-weighted black-blood sequence was recently shown to improve the detection of contrast-enhancing lesions in the brain in patients with MS compared with a 3D T1-weighted MPRAGE sequence. We compared a contrast-enhanced 3D T1-weighted black-blood sequence with a dedicated orbital contrast-enhanced T1-weighted Dixon sequence in patients with acute optic neuritis.

**MATERIALS AND METHODS:** MR imaging data (3T) of 51 patients showing symptoms of acute optic neuritis were analyzed retrospectively, including whole-brain contrast-enhanced 3D T1-weighted black-blood and dedicated orbital coronal 2D or 3D contrast-enhanced T1-weighted Dixon sequences. Two neuroradiologists assessed the images for overall image quality, artifacts, diagnostic confidence, and visual contrast enhancement. Furthermore, the standardized contrast-to-noise ratio was calculated. The final diagnosis of acute optic neuritis was established on the basis of clinical presentation, visually evoked potentials, and optical coherence tomography.

**RESULTS:** Thirty of 51 patients were diagnosed with acute optic neuritis. Of those, 21 showed contrast-enhancing lesions in the optic nerves, similarly detectable on contrast-enhanced T1-weighted Dixon and contrast-enhanced T1-weighted black-blood images. Thus, the accuracy for each sequence was identical, with a resulting sensitivity of 70% and specificity of 90% or 100% (depending on the reader). Overall image quality, diagnostic confidence, visual contrast enhancement, and artifacts were rated similarly in contrast-enhanced 3D T1-weighted black-blood and dedicated orbital contrast-enhanced T1-weighted Dixon sequences. There was no significant difference ( $P = .27$ ) in the mean standardized contrast-to-noise ratio between contrast-enhanced T1-weighted black-blood ( $1.76 \pm 1.07$ ) and contrast-enhanced T1-weighted Dixon ( $2.29 \pm 2.49$ ) sequences.

**CONCLUSIONS:** Contrast-enhanced 3D T1-weighted black-blood imaging is comparable in accuracy and qualitative/quantitative features with dedicated orbital contrast-enhanced T1-weighted Dixon imaging for the detection of acute optic neuritis. Therefore, when used, it has the potential to considerably shorten total patient imaging time.

**ABBREVIATIONS:** BB = black-blood; DIR = double inversion recovery; FS = fat-suppressed; OCT = optical coherence tomography; ON = optic neuritis; VEP = visually evoked potentials

Acute optic neuritis (ON) may result in visual disturbances, pain during eye movement, and dyschromatopsia. Acute ON can occur as an isolated syndrome or can be associated with MS. In particular, patients with ON show a high risk of conversion to definite MS (34%–75%),<sup>1,2</sup> and a high percentage of patients with MS develop ON during the course of the disease (70%).<sup>3–5</sup> Although discussed and recommended by the Magnetic Resonance Imaging in

MS (MAGNIMS; <https://www.magnims.eu/>) consensus guidelines on MS criteria in MR imaging,<sup>6</sup> ON has not yet been included in the criterion of dissemination in space in the McDonald criteria (2017) for the diagnosis of MS.<sup>7</sup> Nevertheless, the importance of the involvement of the optic nerve was emphasized by the International Panel on MS Diagnosis, and further research on this issue was encouraged.<sup>6</sup>

Acute ON is traditionally diagnosed clinically by visually evoked potentials (VEP) and optical coherence tomography (OCT) and can

Received February 7, 2020; accepted after revision July 29.

From the Departments of Neuroradiology (I.R., N.S., C.Z., J.S.K.) and Neurology (M.M.), and Neuroimaging Center TUM-NIC, Klinikum rechts der Isar (M.M. and N.S.), School of Medicine, Technical University of Munich, Munich, Germany.

Paper previously presented, in part, at: Annual Meeting of the European Society for Neuroradiology, September 19–20, Oslo, Norway, and Annual Meeting of the German Society for Neuroradiology, October 9–10, Frankfurt, Germany, as oral presentations, and Annual Meeting of the European Committee for Treatment and Research in Multiple Sclerosis, September 11–13, 2019, Stockholm, Sweden as a poster.

Please address correspondence to Isabelle Riederer, MD, Department of Diagnostic and Interventional Neuroradiology, Klinikum rechts der Isar, School of Medicine, Technical University of Munich, Ismaninger Str 22, 81675 Munich, Germany; e-mail: [isabelle.riederer@tum.de](mailto:isabelle.riederer@tum.de)

Indicates open access to non-subscribers at [www.ajnr.org](http://dx.doi.org/10.3174/ajnr.A6807)  
<http://dx.doi.org/10.3174/ajnr.A6807>

be diagnosed through MR imaging. The recommended MR imaging protocol for ON consists of coronal fat-suppressed (FS) T2WI.<sup>8</sup> Recent studies have demonstrated that double inversion recovery (DIR) images can be used for the detection of ON with high sensitivity and specificity.<sup>9,10</sup> Additionally, it has been shown that DIR images reveal acute and chronic optic nerve lesions with higher sensitivity compared with VEP.<sup>11</sup> Coronal T1-weighted images before and after contrast administration are recommended for the detection of acute ON.<sup>8</sup> Contrast enhancement can be detected in up to 94% of the patients with acute ON, but results vary depending on study inclusion criteria and sequences used.<sup>8,12</sup> Recently, a study showed that 3D T1-weighted TSE black-blood (BB) images improve the detection rate of contrast-enhancing lesions in the brain in patients with MS<sup>13</sup> or intracranial metastases<sup>14-17</sup> compared with a conventional 3D T1-weighted MPRAGE sequence.

Originally, T1-weighted BB sequences had been designed to detect inflammatory changes of the vascular wall of the heart or blood vessels by distinct suppression of the blood signal.<sup>18,19</sup> For this purpose, T1-weighted BB imaging was based on the DIR technique and initially restricted to 2D acquisition mode with only a small FOV coverage. Recently, a new type of T1-weighted BB TSE sequence was introduced with variable flip angle refocusing pulses, thus allowing 3D imaging with high isotropic resolution.<sup>17,20</sup> This new T1-weighted BB sequence combines a highly sensitive depiction of contrast enhancement with fast imaging and high spatial resolution and is thus gaining popularity in routine MR imaging for different purposes. As a TSE-based approach, this sequence has fewer artifacts compared with gradient-echo-based sequences. The benefits of reduced artifacts, particularly at the skull base and the sensitive depiction of contrast enhancement may render T1-weighted BB imaging well-suited for orbital imaging. In fact, a recent study showed that T1-weighted BB imaging is able to detect arteritic posterior ciliary artery involvement in patients with arteritic anterior ischemic optic neuropathy.<sup>21</sup> However, T1-weighted BB imaging has not yet been assessed for acute ON.

Here, we hypothesize that contrast-enhanced 3D T1-weighted BB imaging is superior to dedicated orbital FS contrast-enhanced T1WI for detecting acute ON.

## MATERIALS AND METHODS

### Patients

Data were analyzed retrospectively with approval of the local ethics committee. The patient group consisted of 51 consecutive patients (31 women, 20 men; mean age,  $35 \pm 11$  years; age range,

18–66 years) showing symptoms of acute ON (such as visual disturbances or pain during eye movement) who had undergone MR imaging between April 2018 and January 2020. All MR imaging data included dedicated orbital Dixon sequences and 3D T1-weighted BB. None of them had to be excluded due to motion artifacts. Final diagnoses were established by the treating neurologists considering history, symptoms, response to steroid treatment, MR imaging findings, and paraclinical tests such as VEP or OCT.

### MR Imaging Acquisition

MR imaging was performed on a 3T scanner (Ingenia; Philips Healthcare) using a 32-channel array head coil. MR imaging included 3D FLAIR, 3D DIR, coronal FS 2D T2-weighted sequences (T2 Dixon or T2 spectral presaturation with inversion recovery), contrast-enhanced 3D T1-weighted MPRAGE, and contrast-enhanced 3D T1-weighted BB sequences of the whole brain in all patients, as well as coronal FS contrast-enhanced 2D T1-weighted Dixon ( $n = 43$ ) or contrast-enhanced 3D T1-weighted Dixon ( $n = 8$ ) sequences covering the orbit. The acquisition parameters of T1-weighted BB and T1-weighted Dixon sequences are shown in Table 1.

Due to the small number of 3D T1-weighted Dixon images ( $n = 8$ ), we pooled 2D and 3D T1-weighted Dixon images for the analysis. On average, contrast-enhanced T1-weighted Dixon was acquired about 5 minutes later than contrast-enhanced T1-weighted BB (T1-weighted BB was performed at a mean of  $13:25 \pm 4:45$  (min:sec) and contrast-enhanced T1-weighted BB,  $8:11 \pm 4:07$  (min:sec) after the intravenous administration of gadolinium).

### MR Imaging Analysis

Imaging data were independently assessed by 2 neuroradiologists (blinded to the diagnosis and side of the affected optic nerve) on a standard PACS workstation. The images were read twice, first by assessing contrast-enhanced T1-weighted BB and excluding contrast-enhanced T1-weighted Dixon images and second by assessing contrast-enhanced T1-weighted Dixon and excluding contrast-enhanced T1-weighted BB with an interval of 2 weeks between both reads to avoid memory bias.

During each reading process, DIR and FS T2-weighted images could be consulted simultaneously. In case of 3D images, 1-mm-section-thickness reconstructions were performed in 3D in orientations perpendicular to and along the optic nerves, with sagittal reconstructions being generated in an oblique direction per side.

**Table 1: Acquisition parameters of the T1-weighted sequences**

Sequence	T1-Weighted BB	T1-Weighted Dixon	T1-Weighted Dixon
Sequence type	TSE	TFE	TSE
Acquisition mode	3D	3D	2D
Acquisition plane	Sagittal	Axial	Coronal
Acquired voxel size (mm <sup>3</sup> )	$0.90 \times 0.89 \times 0.90$	$0.90 \times 0.99 \times 0.90$	$0.60 \times 0.72 \times 2.5$
Acquisition matrix	$280 \times 281$	$132 \times 157$	$200 \times 210$
FOV (mm)	240	154	151
TR (ms)	700	6.2	500
TE (ms)	35	0	9.8
Acquisition time (min)	1:36	3:11	2:00
Average delay after IV administration of gadolinium (min:sec)	8:42	12:46	13:36

Both readers individually counted contrast-enhancing lesions in the optic nerves and assessed the images on a 5-point Likert scale for overall image quality in the orbit (1, nondiagnostic; 2, poor; 3, average; 4, good; or 5, excellent), artifacts (1, severe; 2, pronounced; 3, moderate; 4, mild; or 5, none), and diagnostic confidence (1, unlikely; 2, vague; 3, likely; 4, high; or 5, very high). Moreover, a 4-point Likert scale was considered for visual contrast enhancement of the optic nerves, if any (1, none; 2, minimal; 3, moderate; or 4, strong). Afterward, a consensus read was performed in patients with discrepant numbers of contrast-enhancing lesions. A contrast-enhancing lesion was defined as a circumscribed hyperintense signal within the optic nerve depicted after gadolinium administration on T1-weighted images.

In addition, 1 neuroradiologist categorized the localization of lesions into the following sections of the optic nerve: intraorbital, extraorbital intracranial, and extraorbital intracranial (chiasmatic) segments. Furthermore, a standardized contrast-to-noise ratio (sCNR) was measured. Because it is difficult to compare contrast-to-noise ratios between different sequences, we defined a “standardized” contrast-to-noise ratio as previously described<sup>22,23</sup> by respecting the dependency of the contrast-to-noise ratio on voxel size and acquisition time of the sequences according to the following formula:

$$sCNR = (S_{\text{lesion}} - S_{\text{optic nerve}}) / (SD_{\text{optic nerve}} \times V_{\text{voxel}} \times \sqrt{t_{\text{acq}}})$$
 where  $S_{\text{lesion}}$  represents the mean signal in an ROI (2–5 mm<sup>2</sup>) in a contrast-enhancing lesion in the optic nerve, and  $S_{\text{optic nerve}}$  represents the signal of an ROI in the contralateral optic nerve in a corresponding normal-appearing location.  $SD_{\text{optic nerve}}$  is the SD in a region in the nonaffected optic nerve,  $V_{\text{voxel}}$  is the voxel size, and  $t_{\text{acq}}$  represents the acquisition time of the sequence in seconds.

### Statistical Analyses

Statistical analyses were performed using SPSS 25 (SPSS Statistics for Windows; IBM). Wilcoxon signed-rank tests were performed to compare overall image quality, artifacts, diagnostic confidence,

and visual contrast enhancement between both sequences for each reader separately. Concordance between both raters was assessed using the intraclass correlation coefficient. Furthermore, the standardized contrast-to-noise ratio was compared using a 2-sided Student *t* test for paired samples. A value of  $P < .05$  was considered statistically significant. Sensitivity and specificity were calculated and compared between sequences.

## RESULTS

The diagnosis of acute ON was established by the treating neurologists for 30 of the 51 patients. Of these 30 patients with the final diagnosis of ON, 7 were known to have MS, ON was a first manifestation of MS in 9 patients, ON was a clinically isolated syndrome in 12 patients, and a neuromyelitis optica spectrum disorder was seen in the remaining 2 cases. VEP were available for 18 patients, with 14 exhibiting a pathologic pattern. Furthermore, OCT was available for 19 patients, with 5 showing a pattern of acute ON and 6 showing a pattern of atrophy.

Two discrepant lesion counts were found between readers (reader one, 21 lesions; reader two, 23 lesions), with reader 2 counting 2 artifacts as contrast-enhancing lesions in both sequences. In the consensus reading of both neuroradiologists, 21 patients showed at least 1 contrast-enhancing lesion in the optic nerve (unilateral,  $n = 20$ ; bilateral,  $n = 1$ ). In the case of bilateral contrast-enhancing lesions, analyses of only 1 optic nerve (with the longer lesion) were included in the statistics.

One patient showed signal alterations in DIR, FS T2WI, and FLAIR sequences but no contrast enhancement. Nine patients showed a T2-/DIR-hyperintense signal in the contralateral optic nerve without contrast enhancement and without recent clinical symptoms. The contrast-enhancing lesions were intraorbital ( $n = 13$ ), extraorbital intracranial ( $n = 4$ ), extraorbital intracranial ( $n = 1$ ), or intra- and extraorbital ( $n = 3$ ). None of the contrast-enhancing lesions detected in contrast-enhanced T1-weighted Dixon sequences were missed in contrast-enhanced T1-weighted BB sequences and vice versa. All contrast-enhancing lesions in T1-weighted images had a corresponding T2-/DIR-hyperintense signal. Eight patients with diagnoses of acute ON but no contrast-enhancing lesions also showed no signal alterations of the optic nerves in other sequences (DIR, FS T2WI, or FLAIR). VEP showed a normal pattern for 3 patients, and OCT findings were normal for 4 of these 9 patients without contrast-enhancing lesions. Contingency data with more information about diagnostics, sensitivity, and specificity are provided in Tables 2 and 3. Sensitivity (reader 1 and 2: 70%) and specificity (reader 1, 100%; and reader 2, 90%) were identical for both sequences regarding the final diagnoses.

Final diagnoses for the 21 patients not diagnosed with acute ON included other eye diseases not involving the optic nerve ( $n = 4$ ) or psychosomatic disorders ( $n = 3$ ), or remained unclear ( $n = 14$ ); none of these patients' optic nerves showed a contrast-enhancing lesion or a signal alteration in DIR or FS T2WI. Furthermore, none of these patients showed a pathologic pattern in VEP (available in 19/21 patients). OCT was available in 12/21 patients and showed a normal pattern in 11 patients; in 1 patient, it revealed a bilateral global atrophy of the peripapillary retinal

**Table 2: Sensitivity and specificity**

Final Diagnosis “Acute ON” <sup>a</sup>	CE + (Reader 1/ Reader 2)	CE – (Reader 1/ Reader 2)
ON+	21/21	9/9
ON–	0/2	21/19

**Note:**—CE + indicates contrast enhancement; CE –, no contrast enhancement; ON+, optic neuritis; ON–, no optic neuritis.

<sup>a</sup>Reader 1: sensitivity, 21/30 = 70%; specificity, 21/21 = 100%; reader 2: sensitivity, 21/30 = 70%; specificity, 19/21 = 90%.

**Table 3: Contingency table of all available diagnostics and the correlation of their results to contrast-enhancing lesions in MR imaging**

		Diagnosis		ON		Other Diagnoses	
				CE+	CE–	CE+	CE–
Diagnostics (availability)	VEP (37/51)	+		11	3	0	0
		–		1	3	0	19
OCT (31/51)		+ (Acute)		3	2	0	0
		+ (Chronic)		4	2	0	1
		–		4	4	0	11

**Note:**—CE+ indicates contrast enhancement; CE–, no contrast enhancement; +, pathological; –, normal.



**Table 4: Results of the qualitative image evaluation<sup>a</sup>**

Assessment	T1-Weighted BB (Mean) (95% CI)	T1-Weighted Dixon (Mean) (95% CI)	P (Intrareader Comparison)
Overall image quality			
Reader 1	4.33 ± 0.71 (4.05–4.50)	4.45 ± 0.58 (4.25–4.58)	.36
Reader 2	4.22 ± 0.64 (3.98–4.36)	4.06 ± 0.58 (3.86–4.19)	.07
Mean	4.27 ± 0.68 (4.05–4.41)	4.25 ± 0.61 (4.13–4.40)	.81
Artifacts			
Reader 1	4.25 ± 0.69 (3.98–4.41)	4.57 ± 0.57 (4.36–4.71)	.01 <sup>b</sup>
Reader 2	4.25 ± 0.72 (3.97–4.42)	4.16 ± 0.76 (3.86–4.30)	.20
Mean	4.25 ± 0.70 (4.03–4.39)	4.36 ± 0.70 (4.17–4.49)	0.17
Diagnostic confidence			
Reader 1	4.22 ± 1.00 (3.70–4.43)	4.24 ± 0.74 (3.96–4.39)	.90
Reader 2	4.41 ± 0.80 (4.08–4.59)	3.96 ± 0.94 (3.55–4.14)	< 0.001 <sup>b</sup>
Mean	4.31 ± 0.91 (3.98–4.49)	4.10 ± 0.85 (3.86–4.24)	.04
Visual contrast enhancement			
Reader 1	1.92 ± 1.23 (1.35–1.89)	1.92 ± 1.21 (1.36–1.89)	1.00
Reader 2	1.84 ± 1.08 (1.36–1.84)	1.71 ± 0.90 (1.36–1.73)	.007 <sup>b</sup>
Mean	1.88 ± 1.15 (1.36–1.87)	1.81 ± 1.07 (1.35–1.82)	0.11

<sup>a</sup> The results are listed separately per reader (reader 1 + reader 2) and as mean values between the readers, given as mean values with SDs and 95% confidence intervals.

<sup>b</sup> Significant differences between T1-weighted BB and T1-weighted Dixon ( $P < .05$ ).

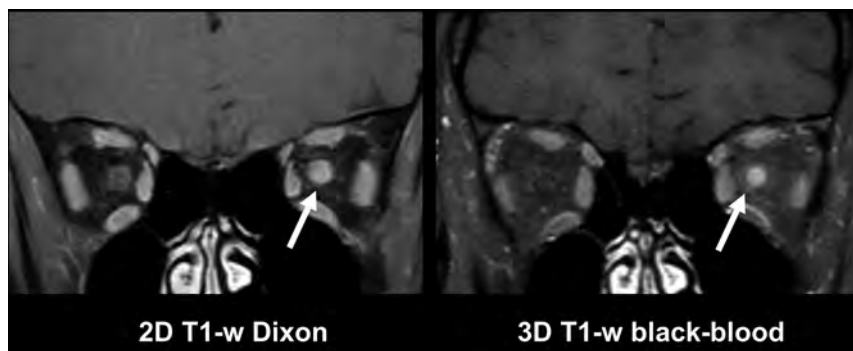


**FIG 1.** MR imaging of a 34-year-old female patient with symptoms of acute optic neuritis of the left eye with loss of vision and pain during eye movement for 3 days. Images of a contrast-enhanced 2D T1-weighted Dixon sequence with coronal orientation (*left*) and a contrast-enhanced 3D T1-weighted BB sequence with coronal reconstruction (*right*) are shown. Note a contrast-enhancing lesion in the left optic nerve in the intraorbital section with similarly high contrast in both sequences (*arrows*).

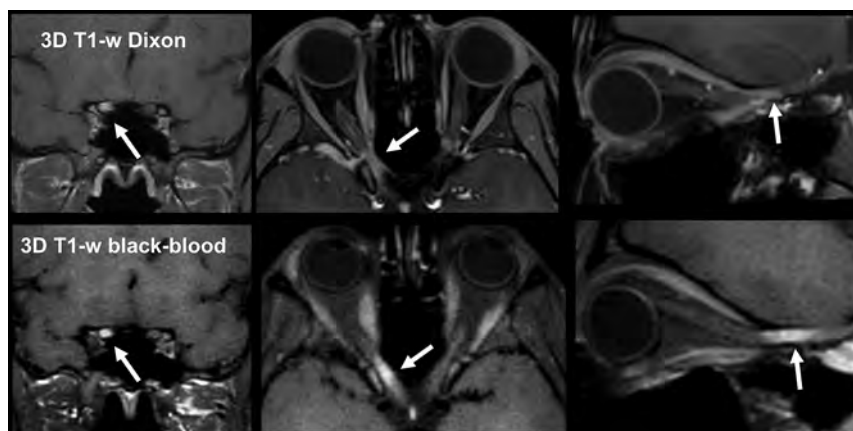


**FIG 2.** MR imaging of a 27-year-old female patient with symptoms of acute optic neuritis of the right eye with retrobulbar pain and loss of vision for 4 days. Images of a contrast-enhanced 3D T1-weighted Dixon sequence are shown in the *upper row*, and contrast-enhanced 3D T1-weighted BB images, in the *lower row* with coronal, axial, and sagittal reconstructions. Note the enhancing lesion in the right optic nerve in the extraorbital section (*arrows*) with improved contrast depiction in the contrast-enhanced 3D T1-weighted BB sequence compared with the contrast-enhanced 3D T1-weighted Dixon imaging.

nerve fiber layer and the macula, which was thought to be associated with another ocular disease.

The results of the qualitative image evaluation are listed in Table 4. Overall image quality, artifacts, diagnostic confidence, and visual contrast enhancement were rated by both readers similarly for T1-weighted BB and T1-weighted Dixon sequences, with a slight tendency toward better quality on T1-weighted BB sequences. The intraclass correlation coefficient was excellent and slightly higher when assessing T1-weighted BB compared with T1-weighted Dixon (0.923 versus 0.872).

There was no significant difference ( $P = .27$ ) between the standardized contrast-to-noise ratio of T1-weighted BB ( $1.76 \pm 1.07$ ) and T1-weighted Dixon ( $2.29 \pm 2.49$ ). Examples of 2 patients are shown in Figs 1 and 2.

## DISCUSSION

In this study, a contrast-enhanced 3D T1-weighted BB sequence successfully detected active contrast-enhancing lesions in the optic nerves in patients with ON. In particular, whole-brain contrast-enhanced 3D T1-weighted BB images showed high accuracy and qualitative/quantitative characteristics similar to those of dedicated orbital contrast-enhanced T1-weighted Dixon sequences, with the advantage of shorter scan times. This finding is comparable with those of previous studies investigating

different pathologies in the brain.<sup>13,15,16,24</sup> Thus, the advantage of a fast 3D acquisition with sensitive contrast depiction of 3D T1-weighted BB sequences also holds true in anatomically more complex regions such as the orbits and, in particular, the optic canal.

The results of our study are also in accordance with initial outcomes of the study of Sommer et al,<sup>13</sup> describing the possibility of the assessment of the orbit using a T1-weighted modified volumetric isotropic turbo spin-echo acquisition to diagnose ON. However, they did not show any qualitative or quantitative data analysis.

Contrary to other studies<sup>8,12</sup> that reported contrast enhancement of the optic nerve in acute ON in up to 94% of the cases, only 70% (21 of 30 patients) of the patients with acute ON showed contrast enhancement in our study. The contrast enhancement of the optic nerve in case of acute ON might depend on the severity of the inflammation or dimension of the affected optic nerve. Additionally, the high percentage of contrast enhancement in the above-mentioned study<sup>12</sup> might depend on its strict inclusion and exclusion criteria (the study included patients within 20 days of visual loss, and patients were excluded if they had a history of ON of the affected eye and when vision did not return to normal). In our experience, the percentage of 70% contrast enhancement is closer to our referral clinical experience than the higher numbers of more selective studies. Furthermore, we included 1 patient who had already received high doses of IV prednisolone therapy before MR imaging; this patient showed a pathologic pattern in VEP but no contrast enhancement on MR imaging.

Recently, 1 study<sup>25</sup> showed a potentially important role of a postcontrast FS FLAIR sequence demonstrating perioptic leptomeningeal contrast enhancement that might reflect an inflammatory process preceding or accompanying ON. We did not observe leptomeningeal enhancement on postcontrast T1-weighted BB sequences, but a dedicated study comparing postcontrast FLAIR sequences with postcontrast T1-weighted BB imaging for perioptic contrast enhancement might be of interest and clinical relevance.

One important advantage of 3D T1-weighted BB imaging is the short scan time. Because the acquisition of our whole-brain 3D T1-weighted BB sequence takes only 1:30 (min:sec) at a 0.9-mm isotropic resolution and seems to lead to a higher detection rate of contrast-enhancing MS lesions in the brain,<sup>13</sup> it might replace standard T1-weighted sequences such as MPRAGE and, importantly, dedicated sequences for the optic nerves, thus contributing to scan efficiency.

We are aware of several limitations of our study, including the relatively small sample size and retrospective study design. Furthermore, the readers could not be blinded to the type of sequences because they have characteristic appearances. In addition, the postcontrast T1-weighted sequences of this study were performed with different delays after intravenous administration of gadolinium-based contrast agents; on average, T1-weighted Dixon was performed 5 minutes later than contrast-enhanced T1-weighted BB. It is known that the sensitivity of postcontrast images increases with the length of delay after administration of a gadolinium-based contrast agent.<sup>26</sup> Therefore, this difference might contribute to a bias but should not alter the main findings of this study in general.

## CONCLUSIONS

Whole-brain contrast-enhanced 3D T1-weighted BB images of the optic nerves showed high accuracy and qualitative/quantitative

characteristics similar to those of dedicated orbital contrast-enhanced T1-weighted Dixon images to diagnose acute ON. Thus, if contrast-enhanced 3D T1-weighted BB images are routinely acquired for the detection of contrast-enhancing MS lesions in the brain, potentially, additional dedicated orbital sequences may not be needed, allowing shorter standard MR imaging protocols.

## ACKNOWLEDGMENTS

The authors would like to thank Mrs Marianne Schoenbach-Engmann for proofreading the manuscript.

Disclosures: Mark Mühlau—RELATED: Grant: research fund, Comments: German Federal Ministry for Education and Research, German Competence Network Multiple Sclerosis, grant No. 01G11604A.\* Claus Zimmer—RELATED: C. Zimmer disclosed no relevant relationships regarding activities related to the present article. UNRELATED: He has served on scientific advisory boards for Philips and Bayer Schering, serves as co-editor on the Advisory Board of *Clinical Neuroradiology*, has received speaker honoraria from Bayer Schering and Philips Healthcare; the institution has received research support and investigator fees for clinical studies from Biogen Idec, Quintiles Transnational, Merck Sharp & Dohme, Boehringer Ingelheim, Inventive Health Clinical UK Ltd, AdvanceCor Biotechnologie, BrainsGate, Pfizer, Bayer Schering, Novartis, Roche, Servier, Penumbra, WCT GmbH, Syngis, SSS International Clinical Research, PPD Germany GmbH, Worldwide Clinical Trials Ltd, phenox, Covidien, Actelion, Medivation, Medtronic, Harrison Clinical Research, Concentric, PharmTrace, Reverse Medical Corp, Premier Research Germany Ltd, Surpass Medical Ltd, GlaxoSmithKline, AXON Neuroscience, Bristol-Myers Squibb, Genentech, Acandis, Eisai, NeuroRx, Italfarmaco, BioClinica, MIAC Analytics, and IXICO.\* No patents issued and pending. Jan S. Kirschke—UNRELATED: Grants/Grants Pending: Deutsche Forschungsgemeinschaft, European Research Council, Nvidia Corporation\*; Payment for Lectures Including Service on Speakers Bureaus: Philips Healthcare.\*Money paid to the institution.

## REFERENCES

1. Francis DA, Compston DA, Batchelor JR, et al. **A reassessment of the risk of multiple sclerosis developing in patients with optic neuritis after extended follow-up.** *J Neurol Neurosurg Psychiatry* 1987;50:758–65 CrossRef Medline
2. Rizzo JF 3rd, Lessell S. **Risk of developing multiple sclerosis after uncomplicated optic neuritis: a long-term prospective study.** *Neurology* 1988;38:185–90 CrossRef Medline
3. Hickman SJ, Dalton CM, Miller DH, et al. **Management of acute optic neuritis.** *Lancet* 2002;360:1953–62 CrossRef Medline
4. Toosy AT, Mason DF, Miller DH. **Optic neuritis.** *Lancet Neurol* 2014;13:83–99 CrossRef Medline
5. Wikstrom J, Poser S, Ritter G. **Optic neuritis as an initial symptom in multiple sclerosis.** *Acta Neurol Scand* 1980;61:178–85 CrossRef Medline
6. Filippi M, Rocca MA, Ciccarelli O, et al; MAGNIMS Study Group. **MRI criteria for the diagnosis of multiple sclerosis: MAGNIMS consensus guidelines.** *Lancet Neurol* 2016;15:292–303 CrossRef Medline
7. Thompson AJ, Banwell BL, Barkhof F, et al. **Diagnosis of multiple sclerosis: 2017 revisions of the McDonald criteria.** *Lancet Neurol* 2018;17:162–73 CrossRef Medline
8. Petzold A, Wattjes MP, Costello F, et al. **The investigation of acute optic neuritis: a review and proposed protocol.** *Nat Rev Neurol* 2014;10:447–58 CrossRef Medline
9. Hadjhoum N, Hodel J, Defoort-Dhellemmes S, et al. **Length of optic nerve double inversion recovery hypersignal is associated with retinal axonal loss.** *Mult Scler* 2016;22:649–58 CrossRef Medline
10. Hodel J, Outteryck O, Bocher AL, et al. **Comparison of 3D double inversion recovery and 2D STIR FLAIR MR sequences for the imaging of optic neuritis: pilot study.** *Eur Radiol* 2014;24:3069–75 CrossRef Medline
11. Riederer I, Mühlau M, Hoshi MM, et al. **Detecting optic nerve lesions in clinically isolated syndrome and multiple sclerosis: double-inversion recovery magnetic resonance imaging in comparison**

- with visually evoked potentials. *J Neurol* 2019;266:148–56 CrossRef Medline
12. Kupersmith MJ, Alban T, Zeiffer B, et al. **Contrast-enhanced MRI in acute optic neuritis: relationship to visual performance.** *Brain* 2002;125:812–22 CrossRef Medline
  13. Sommer NN, Saam T, Coppenrath E, et al. **Multiple sclerosis: improved detection of active cerebral lesions with 3-dimensional T1 black-blood magnetic resonance imaging compared with conventional 3-dimensional T1 GRE imaging.** *Invest Radiol* 2018;53:13–19 CrossRef Medline
  14. Park J, Kim J, Yoo E, et al. **Detection of small metastatic brain tumors: comparison of 3D contrast-enhanced whole-brain black-blood imaging and MP-RAGE imaging.** *Invest Radiol* 2012;47:136–41 CrossRef Medline
  15. Yoneyama M, Nakamura M, Tabuchi T, et al. **Whole-brain black-blood imaging with magnetization-transfer prepared spin echo-like contrast: a novel sequence for contrast-enhanced brain metastasis screening at 3T.** *Radiol Phys Technol* 2013;6:431–36 CrossRef Medline
  16. Kammer NN, Coppenrath E, Treitl KM, et al. **Comparison of contrast-enhanced modified T1-weighted 3D TSE black-blood and 3D MP-RAGE sequences for the detection of cerebral metastases and brain tumours.** *Eur Radiol* 2016;26:1818–25 CrossRef Medline
  17. Treitl KM, Treitl M, Kooijman-Kurfuerst H, et al. **Three-dimensional black-blood T1-weighted turbo spin-echo techniques for the diagnosis of deep vein thrombosis in comparison with contrast enhanced magnetic resonance imaging: a pilot study.** *Invest Radiol* 2015;50:401–08 CrossRef Medline
  18. Edelman RR, Chien D, Kim D. **Fast selective black-blood MR imaging.** *Radiology* 1991;181:655–60 CrossRef Medline
  19. Edelman RR, Mattle HP, Wallner B, et al. **Extracranial carotid arteries: evaluation with “black-blood” MR angiography.** *Radiology* 1990;177:45–50 CrossRef Medline
  20. Treitl KM, Maurus S, Sommer NN, et al. **3D-black-blood 3T-MRI for the diagnosis of thoracic large vessel vasculitis: a feasibility study.** *Eur Radiol* 2017;27:2119–28 CrossRef Medline
  21. Sommer NN, Treitl KM, Coppenrath E, et al. **Three-dimensional high-resolution black-blood magnetic resonance imaging for detection of arteritic anterior ischemic optic neuropathy in patients with giant cell arteritis.** *Invest Radiol* 2018;53:698–704 CrossRef Medline
  22. Riederer I, Karampinos DC, Settles M, et al. **Double inversion recovery sequence of the cervical spinal cord in multiple sclerosis and related inflammatory diseases.** *AJNR Am J Neuroradiol* 2015;36:219–25 CrossRef Medline
  23. Edelstein WA, Glover GH, Hardy CJ, et al. **The intrinsic signal-to-noise ratio in NMR imaging.** *Magn Reson Med* 1986;3:604–18 CrossRef Medline
  24. Park J, Kim EY. **Contrast-enhanced, three-dimensional, whole-brain, black-blood imaging: application to small brain metastases.** *Magn Reson Med* 2010;63:553–61 CrossRef Medline
  25. Pino-Lopez L, Wenz H, Bohme J, et al. **Contrast-enhanced fat-suppressed FLAIR for the characterization of leptomeningeal inflammation in optic neuritis.** *Mult Scler* 2019;25:792–800 CrossRef Medline
  26. Uysal E, Erturk SM, Yildirim H, et al. **Sensitivity of immediate and delayed gadolinium enhanced MRI after injection of 0.5 M and 1.0 M gadolinium chelates for detecting multiple sclerosis lesions.** *AJR Am J Roentgenol* 2007;188:697–702 CrossRef Medline



# Quantitative T1 $\rho$ MRI of the Head and Neck Discriminates Carcinoma and Benign Hyperplasia in the Nasopharynx

Q.Y.H. Ai, W. Chen, T.Y. So, W.K.J. Lam, B. Jiang, D.M.C. Poon, S. Qamar, F.K.F. Mo, T. Blu, Q. Chan, B.B.Y. Ma, E.P. Hui, K.C.A. Chan, and A.D. King



## ABSTRACT

**BACKGROUND AND PURPOSE:** T1 $\rho$  imaging is a new quantitative MR imaging pulse sequence with the potential to discriminate between malignant and benign tissue. In this study, we evaluated the capability of T1 $\rho$  imaging to characterize tissue by applying T1 $\rho$  imaging to malignant and benign tissue in the nasopharynx and to normal tissue in the head and neck.

**MATERIALS AND METHODS:** Participants with undifferentiated nasopharyngeal carcinoma and benign hyperplasia of the nasopharynx prospectively underwent T1 $\rho$  imaging. T1 $\rho$  measurements obtained from the histogram analysis for nasopharyngeal carcinoma in 43 participants were compared with those for benign hyperplasia and for normal tissue (brain, muscle, and parotid glands) in 41 participants using the Mann-Whitney *U* test. The area under the curve of significant T1 $\rho$  measurements was calculated and compared using receiver operating characteristic analysis and the Delong test, respectively. A *P* < .05 indicated statistical significance.

**RESULTS:** There were significant differences in T1 $\rho$  measurements between nasopharyngeal carcinoma and benign hyperplasia and between nasopharyngeal carcinoma and normal tissue (all, *P* < .05). Compared with benign hyperplasia, nasopharyngeal carcinoma showed a lower T1 $\rho$  mean (62.14 versus 65.45  $\times$  ms), SD (12.60 versus 17.73  $\times$  ms), and skewness (0.61 versus 0.76) (all *P* < .05), but no difference in kurtosis (*P* = .18). The T1 $\rho$  SD showed the highest area under the curve of 0.95 compared with the T1 $\rho$  mean (area under the curve = 0.72) and T1 $\rho$  skewness (area under the curve = 0.72) for discriminating nasopharyngeal carcinoma and benign hyperplasia (all, *P* < .05).

**CONCLUSIONS:** Quantitative T1 $\rho$  imaging has the potential to discriminate malignant from benign and normal tissue in the head and neck.

**ABBREVIATIONS:** AHP = adiabatic half passage; AUC = area under the curve; NPC = nasopharyngeal carcinoma; rAHP = reverse adiabatic half passage; TSL = time of spin-lock; PSNR = peak signal-to-noise ratio

The spin-lattice relaxation time in the rotating frame known as T1 $\rho$  is sensitive to biologic processes associated with alterations in the macromolecular content of tissue. Quantitative T1 $\rho$  imaging has been used to study normal tissue and nonmalignant diseases in cartilage, discs, and ligaments,<sup>1-3</sup> brain,<sup>4-7</sup> liver,<sup>8,9</sup> heart,<sup>10</sup> muscles,<sup>11</sup> and parotid glands.<sup>11-13</sup> However, T1 $\rho$  imaging also has the potential to characterize benign and malignant processes, but only a few studies have preliminarily evaluated T1 $\rho$  for human cancer

imaging. These studies showed differences of T1 $\rho$  values between high- and low-grade gliomas<sup>14</sup> and between benign and malignant tissue in the brain,<sup>15,16</sup> breast,<sup>17</sup> and prostate.<sup>18</sup>

We are interested in quantitative MR imaging sequences that can be used to discriminate nasopharyngeal carcinoma (NPC) from benign hyperplasia in the nasopharynx because these entities may overlap on anatomic MR imaging sequences.<sup>19,20</sup> Our hypothesis is that the T1 $\rho$  value of malignancy is different from that of benign tissue and can be used to discriminate these 2 entities. In this preliminary study, we also applied T1 $\rho$  imaging to a

Received January 16, 2020; accepted after revision August 7.

From the Department of Imaging and Interventional Radiology (Q.Y.H.A., W.C., T.Y.S., B.J., S.Q., A.D.K.), Li Ka Shing Institute of Health Sciences (W.K.J.L., D.M.C.P., B.B.Y.M., E.P.H., K.C.A.C.), Department of Clinical Oncology (D.M.C.P., F.K.F.M., B.B.Y.M., E.P.H.), State Key Laboratory in Oncology in South China, Sir Y.K. Pao Centre for Cancer, The Chinese University of Hong Kong, Prince of Wales Hospital, Hong Kong, SAR; State Key Laboratory of Translational Oncology (W.K.J.L., D.M.C.P., F.K.F.M., B.B.Y.M., E.P.H., K.C.A.C.) and Department of Electrical Engineering (T.B.), The Chinese University of Hong Kong, Hong Kong, SAR; Department of Chemical Pathology (W.K.J.L., K.C.A.C.), State Key Laboratory in Oncology in South China, Li Ka Shing Institute of Health Sciences, The Chinese University of Hong Kong, Shatin, New Territories, Hong Kong, SAR; and Philips Healthcare (Q.C.), Hong Kong, SAR; and

Paper previously presented, in part, at: European Society Head and Neck Society Refresh, October 3–5, 2019; Sicily, Italy.

Please address correspondence to Weitian Chen, PhD, Department of Imaging and Interventional Radiology, Faculty of Medicine, The Chinese University of Hong Kong, Prince of Wales Hospital, 30-32 Ngan Shing St, Shatin, New Territories, Hong Kong, SAR; e-mail: wtchen@cuhk.edu.hk

Indicates article with supplemental on-line tables.

<http://dx.doi.org/10.3174/ajnr.A6828>

range of normal tissue in the head and neck (brain, pterygoid muscle, and parotid gland) to compare the T1 $\rho$  values of normal tissue with those of NPC.

## MATERIALS AND METHODS

### Participants

This prospective study was performed with local institutional board approval. Written informed consent was obtained from ethnically Chinese participants who underwent MR imaging between September 2018 and August 2019 in the Prince of Wales Hospital, Hong Kong, SAR.

Participants with NPC had newly diagnosed biopsy-proved undifferentiated carcinoma and a primary tumor of >5 mm. The primary tumor was staged according to the 8th edition of the *AJCC Cancer Staging Manual*.<sup>21</sup> Participants with benign hyperplasia had been referred for MR imaging for suspected NPC because of persistently raised plasma Epstein-Barr virus DNA and benign hyperplasia of >5 mm on MR imaging without evidence of NPC on MR imaging, endoscopic examination, and clinical follow-up at a minimum of 6 months.

### MR Imaging Acquisition

MR imaging was performed with an Achieva TX 3T scanner (Philips Healthcare). T1 $\rho$  imaging was performed using an adiabatic continuous wave constant amplitude spin-lock approach,<sup>22</sup> followed by a single-shot turbo spin-echo acquisition. Fat signal was suppressed using spectral attenuated inversion recovery. The spin-lock radiofrequency pulse cluster consisted of a constant amplitude spin-lock radiofrequency pulse sandwiched by an adiabatic half passage (AHP) and a reverse adiabatic half passage (rAHP). Hyperbolic secant pulses were used as the AHP and rAHP with the B<sub>1</sub> amplitude of the AHP and rAHP set equal to that of the spin-lock radiofrequency pulse.<sup>22,23</sup> Details of the pulse sequence are reported previously,<sup>24</sup> but in summary, the imaging parameters were the following: TR/TE, 2500/15 ms; FOV, 230 × 216 mm; resolution, 1.2 × 1.2 mm; section thickness, 4 mm; number of slices, 9; sensitivity encoding factor, 2; AHP and rAHP duration, 25 ms; maximum amplitude of frequency waveform modulation of the AHP and rAHP, 400 Hz; coefficient factor  $\beta$  for AHP and rAHP, 4; frequency of spin-lock, 400 Hz; and time of spin-lock (TSL), 0, 10, 30, 55, and 90 ms. The total T1 $\rho$  imaging scan time was 1 minute 50 seconds.

Anatomic MR imaging consisted of a minimum of the following: 1) an axial fat-suppressed T2-weighted turbo spin-echo sequence (TR/TE, 4000/80 ms; FOV, 230 × 230 mm; section thickness, 4 mm; echo-train length, 15–17; sensitivity encoding factor, 1; number of signals acquired, 2); and 2) an axial T1-weighted turbo spin-echo sequence (TR/TE, 500/10 ms; FOV, 230 × 230 mm; section thickness, 4 mm; echo-train length, 4; sensitivity encoding factor, 1; number of signals acquired, 2). The patients with NPC were also scanned using a T1-weighted turbo spin-echo sequence following a bolus injection of 0.1 mmol of gadoteric acid (Dotarem; Guerbet) per kilogram of body weight.

### Imaging Analysis

T1 $\rho$  images were reconstructed at a matrix size of 288 × 288. These images were used for T1 $\rho$  quantification using an in-house Matlab (MathWorks) program. The images were smoothed by a

sliding 2 × 2 window throughout the image before quantification. At each pixel, the image intensity was fitted to the relaxation model  $y = A \times \exp\left(-\frac{TSL}{T1\rho}\right) + B$  to calculate the T1 $\rho$  value, where  $A$  and  $B$  are 2 unknown constants. We used a variant of the dichotomy method<sup>25</sup> to fit the data to this relaxation model to quantify T1 $\rho$  values. For on-resonance spin-lock, the  $B$  term is positive. This condition was incorporated into the fitting algorithm to improve fitting accuracy. The peak signal-to-noise ratio (PSNR) was calculated to evaluate the goodness of fit. The definition of PSNR is

$$PSNR = 10 \times \log_{10} \left( \frac{N \times \max_i (y_i - \bar{y})^2}{\sum_{i=1}^N (y_i - \hat{y}_i)^2} \right),$$

where  $y_i$ ,  $\bar{y}$ ,  $N$ , and  $\hat{y}_i$  are the raw data, their mean, their number, and their fitted values, respectively. Criteria were set to exclude pixels with obvious errors or possible unreliable fitting results. A pixel was excluded from final analysis if it had a PSNR of < 30 or an extreme T1 $\rho$  value (<15 ms or >200 ms).

The walls and/or adenoid of benign hyperplasia (Fig 1A) and the primary NPC (Fig 1B) were contoured manually, excluding obvious necrotic, cystic, or hemorrhagic areas, with reference to the corresponding anatomic images (Fig 1C, -D). The normal brain (cerebellum), muscle (lateral pterygoid muscle), and parotid gland were also manually contoured in 41 participants with benign hyperplasia. Contouring was performed by a researcher with 5 years' experience in MR imaging of NPC and repeated after an interval of 2 weeks (observer 1) and by a diagnostic radiologist with 1-year postfellowship experience in head and neck imaging (observer 2). The mean, SD, skewness, and kurtosis were calculated from the histogram of the T1 $\rho$  map (Fig 1E, -F).

### Statistical Analysis

T1 $\rho$  measurements of NPC were compared with those of benign hyperplasia in the nasopharynx and with those of normal tissue using the Mann-Whitney  $U$  test. Subgroup analysis was performed to assess the differences in T1 $\rho$  measurements between stage T1 NPC and stage T2–4 NPC using the Mann-Whitney  $U$  test. Receiver operating characteristic curve analysis and area under the curve (AUC) calculations of statistically significant T1 $\rho$  measurements were used to identify the optimal thresholds for discriminating NPC and benign hyperplasia by maximizing the sensitivity plus specificity; the statistically significant of these optimal thresholds was re-evaluated with the  $\chi^2$  test. The sensitivity, specificity, positive predictive value, negative predictive value, and accuracy of the optimal thresholds were calculated, and the AUCs were compared using the Delong test.<sup>26</sup> Differences in the T1 $\rho$  measurements of normal brain and muscle and the parotid gland were compared using the analysis of variance test, and for statistically significant differences, the Fisher least significant difference test was then used for post hoc multiple comparisons. These analyses used the average values of the measurements obtained from the 2 observers.

Intraclass correlation coefficients with 95% confidence intervals were calculated to assess the intra- and interobserver agreement for T1 $\rho$  measurements. Intraclass correlation coefficients of  $\leq 0.20$ , 0.21–0.40, 0.41–0.60, 0.61–0.80, and 0.81–1.00 indicated slight, fair, moderate, substantial, and almost perfect agreement, respectively.<sup>27</sup> All of the statistical tests were 2-sided, and a  $P$  value

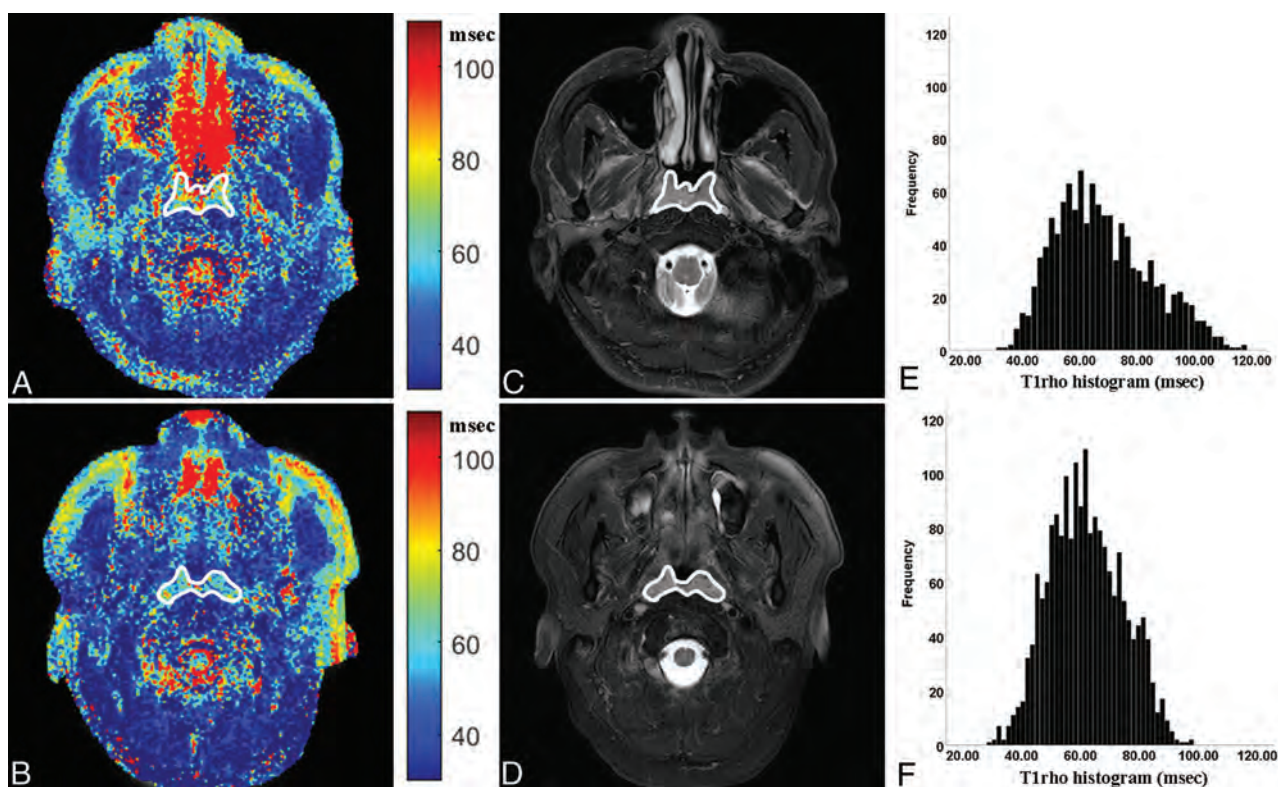


**FIG 1.** The T1rho maps (A and B) and histograms (C and D) of a participant with benign hyperplasia (A and C) and a participant with NPC (B and D), respectively. Compared with participant with benign hyperplasia, the participant with NPC had a lower T1rho mean (70.92 versus 61.96 ms), T1rho SD (16.75 versus 13.30 ms), and T1rho skewness (0.62 versus 0.47).

**Table 1: Characteristics of 43 participants with NPC and 41 participants with benign hyperplasia in the nasopharynx**

Clinical Characteristics	Patients with NPC (n = 43)	Patients with Benign Hyperplasia (n = 41)
Age (yr)		
Median	53 (33–83) <sup>a</sup>	54 (41–66) <sup>a</sup>
Mean ± SD	54.5 ± 10.5	53.6 ± 6.9
Sex		
Men	31	41
Women	12	0
Primary tumor invasion		
Deep invasion absent (stage T1)	14	NA
Deep invasion present (stages T2–4)	29	NA

**Note:**—NA indicates not applicable.

<sup>a</sup> Data in parentheses indicate the range.

< .05 was considered a statistically significant difference. Analyses were performed using MedCalc statistical software (Version 14.8.1; MedCalc Software) and SPSS (Version 25.0; IBM).

## RESULTS

### Participants

Forty-three participants with NPC and 41 participants with benign hyperplasia were recruited for analysis. The characteristics of each group are shown in Table 1. NPCs were staged to T1, T2, T3, and T4 in 14, 12, 12, and 5 participants, respectively. Participants with benign hyperplasia showed no evidence of NPC at follow-up (median, 15.0 months; range, 7.5–19.4 months).

### T1ρ Imaging in Normal Tissue, NPC, and Benign Hyperplasia in the Head and Neck

T1ρ measurements of NPC, benign hyperplasia, and normal tissue (brain, muscle, and parotid gland) are shown in On-line Table 1. Compared with benign hyperplasia, the T1ρ mean, SD, and skewness of NPC were lower (all,  $P < .01$ ) (On-line Table 1 and Fig 2A–C), but there was no difference in kurtosis ( $P = .18$ ) (On-line Table 1 and Fig 2D). T1ρ maps with the contours and histograms of a participant with benign hyperplasia and

NPC are shown in Fig 1. There were no differences in T1ρ mean, SD, skewness, and kurtosis between stage T1 and T2–T4 NPCs (all,  $P > .05$ ) (Table 2). Compared with normal tissue, the T1ρ means of NPC were lower than those of brain and higher than those of muscle and the parotid gland (all,  $P < .001$ ), and the T1ρ SD of NPC was higher than all 3 normal tissues (all  $P < .001$ ) (On-line Table 1). For the normal tissues, differences in T1ρ measurements between any of the 2 normal tissues were statistically significant (all,  $P < .05$ ).

The intra- and interobserver agreement for T1ρ measurements is shown in On-line Table 2. The highest intra- and interobserver agreement was found for the T1ρ mean (intraclass correlation coefficients = 0.99 and 0.99, respectively) and for the



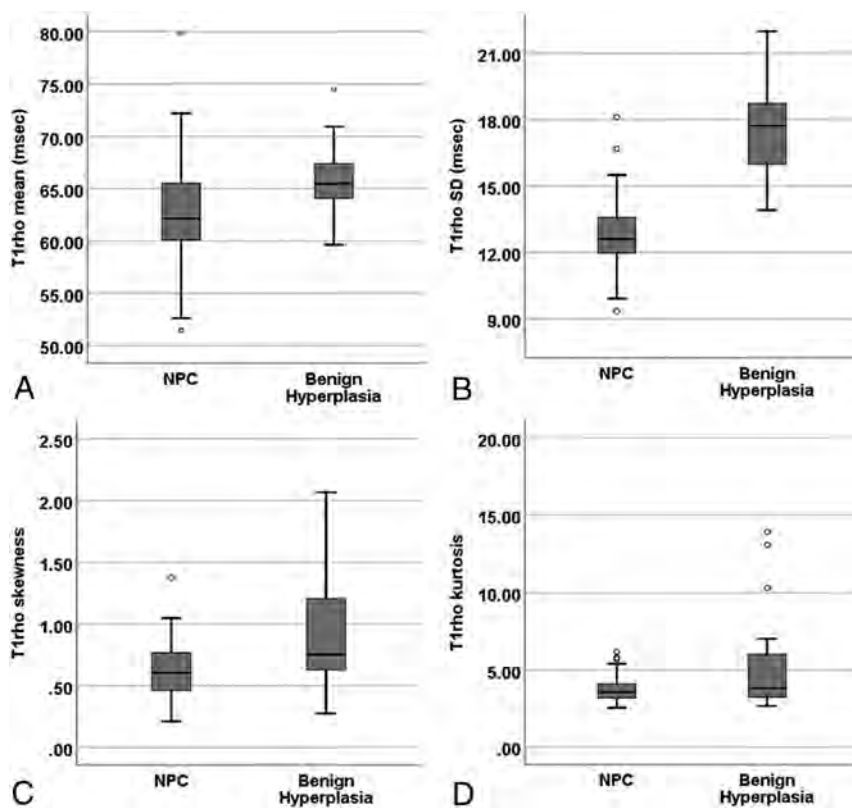


**FIG 2.** Boxplots of the T1rho mean (A), T1rho SD (B), T1rho skewness (C), and T1rho kurtosis (D) in participants with benign hyperplasia and NPC. Boundaries of boxes closest to and furthest from 0 ms indicate the 25th and 75th percentiles, respectively. The line within each box indicates median values. Error bars indicate the smallest and largest values within 1.5 box lengths of the 25th and 75th percentiles. Individual points indicate outliers. Compared with participants with benign hyperplasia, participants with NPC had a lower T1rho mean (A), T1rho SD (B), and T1rho skewness (C) (all,  $P < .01$ ). There were no differences between the 2 groups for T1rho kurtosis (D) ( $P = .18$ ).

**Table 2: T1ρ measurements in stage T1 and T2–4 NPC<sup>a</sup>**

T1rho Measurements	Stage T1 NPCs (n = 14)	Stage T2–4 NPCs (n = 29)	P Value
Mean (ms)	61.94 (59.18–64.51)	62.14 (60.23–66.56)	.31
SD (ms)	12.48 (11.75–14.21)	12.62 (11.91–13.88)	.92
Skewness	0.59 (0.39–0.78)	0.61 (0.48–0.77)	.57
Kurtosis	3.10 (2.89–3.92)	3.38 (3.02–4.16)	.08

<sup>a</sup>Data are median values; data in parentheses are interquartile range. P values < .05 indicate statistical significance.

**Table 3: Diagnostic performance of T1ρ imaging for detecting malignancy of NPC from nasopharyngeal benign hyperplasia<sup>a</sup>**

	T1rho Mean	T1rho SD	T1rho Skewness
AUC	0.72 (0.60–0.81)	0.95 (0.88–0.99)	0.72 (0.61–0.81)
P value	.001	.001	.001
Threshold	≤62.70 × ms	≤14.50 × ms	≤0.57
Sensitivity (%)	58.1	88.4	48.8
Specificity (%)	90.2	95.1	90.2
PPV (%)	86.2	95.0	84.0
NPV (%)	67.3	88.6	62.7
Accuracy (%)	73.8	91.7	69.0

**Note:**—PPV indicates positive predictive value; NPV, negative predictive value

<sup>a</sup>Unless otherwise indicated, data in parentheses are 95% confidence intervals. P values < .05 indicate statistical significance.

T1ρ SD (intraclass correlation coefficients = 0.98 and 0.96, respectively).

### Diagnostic Performance of T1ρ Measurements for Discriminating NPC and Benign Hyperplasia

The AUC, optimal threshold, and diagnostic performance of statistically significant T1ρ measurements for discriminating between NPC and benign hyperplasia are shown in Table 3. The T1ρ SD showed the highest AUC of 0.95 compared with the T1ρ mean (AUC = 0.72) and T1ρ skewness (AUC = 0.72) (all,  $P < .001$ , Table 3 and Fig 3). The T1ρ SD of ≤14.50 ms achieves a sensitivity of 88.4%, specificity of 95.1%, positive predictive value of 95.0%, negative predictive value of 88.6%, and accuracy of 91.7% for discriminating NPC from benign hyperplasia.

### DISCUSSION

In this preliminary study, we evaluated the capability of this new quantitative T1ρ MR imaging sequence for head and neck cancer imaging to discriminate malignant tissue, specifically NPC from benign tissue in the nasopharynx and from surrounding normal tissue. In keeping with a previous study published in 1998,<sup>11</sup> the T1ρ mean varied between different normal tissues, being higher in brain, followed by in the parotid gland and muscle. Compared with these normal tissues, the T1ρ mean of NPC was lower than that of the brain but higher than that of the parotid gland and muscle. Moreover, the T1ρ mean of NPC was statistically significantly lower than that of the benign hyperplasia. Factors in the head and neck that influence T1ρ values are unclear, but previous phantom and in vivo musculoskeletal studies have reported that the T1ρ value is negatively associated with the macromolecule content and positively associated with water content.<sup>28–30</sup> Therefore, the overexpression of macromolecular proteins could be contributing to the low T1ρ mean values in NPC, while higher water content in the inflammation could be contributing to the high mean T1ρ values in benign hyperplasia.

We further analyzed measurements other than the T1ρ mean from the

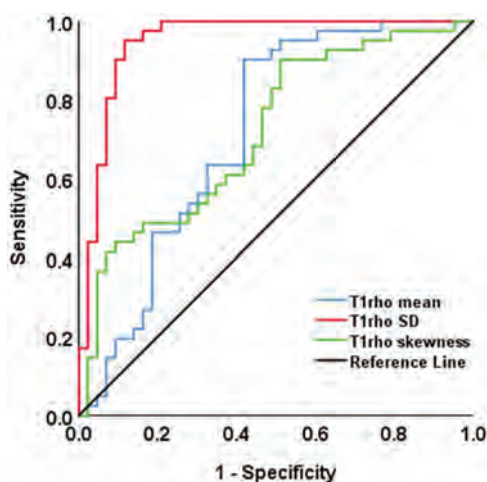


**FIG 3.** The receiver operating characteristic curves of T1rho mean (blue curve), T1rho SD (red curve), and T1rho skewness (green curve) for discriminating NPC and benign hyperplasia in the nasopharynx. The T1rho SD showed the highest AUC of 0.95 compared with the T1rho mean (AUC = 0.72) and T1rho skewness (AUC = 0.72) ( $P < .05$ ) for distinguishing NPC from benign hyperplasia.

T1 $\rho$  histogram and found that T1 $\rho$  SD and skewness were lower in NPC than in benign hyperplasia, with low values indicating NPC but higher values being unable to discriminate these 2 entities. Of all these measurements, the SD achieved the highest AUC. The lower T1 $\rho$  SD in NPC compared with benign hyperplasia suggests that this cancer is less heterogeneous than inflammation. The use of the optimal T1 $\rho$  SD showed a high positive predictive value, suggesting that the potential role of T1 $\rho$  imaging could be to minimize false-positive findings and hence reduce the number of patients referred unnecessarily for further examinations. The intraclass correlation coefficients were high for all T1 $\rho$  measurements with the exception of kurtosis, which had a low intraclass correlation coefficient and was the only T1 $\rho$  measurement that did not show a difference between the 2 groups.

A potential future role for T1 $\rho$  imaging in the nasopharynx is for MR imaging screening of NPC. MR imaging detects 10%–17% more NPCs than an endoscopic examination,<sup>31–33</sup> but discrimination of early-stage NPCs is confined to the nasopharynx (stage T1), and benign hyperplasia can be problematic on anatomic-based MR imaging sequences when the cancer involves both sides of the nasopharynx symmetrically.<sup>19,20,34</sup> The results of the current study are encouraging because we found differences in T1 $\rho$  measurements between NPC and benign hyperplasia. Furthermore, there were no differences in the T1 $\rho$  values of stage T1 and T2–4 NPCs, so it is probable that these results could be applied to a screening population with early-stage disease. However, future studies are needed to validate the findings, evaluate optimal thresholds, and determine whether T1 $\rho$  imaging can improve on the diagnostic performance of anatomic MR imaging sequences in NPC detection.

One advantage of using T1 $\rho$  imaging in MR imaging screening is that it does not require extra hardware or an intravenous injection of contrast. These advantages also apply to diffusion-weighted imaging, which is another functional MR imaging sequence that has shown promise in the discrimination of malignant and benign tissue

in the head and neck.<sup>35–37</sup> However, susceptibility artifacts can limit the application of diffusion-weighted imaging.<sup>35</sup> This image distortion can be mitigated by a fast spin-echo acquisition, but this results in significant loss of signal-to-noise-ratio efficiency compared with an echo-planar imaging acquisition, often leading to a longer scan time. On the other hand, there is less image distortion from  $B_0$  field inhomogeneities in T1 $\rho$  imaging. This is achieved using an adiabatic continuous wave constant amplitude spin-lock to ensure that all spins are well-locked along the effective spin-lock field, even in the presence of  $B_1$  radiofrequency and  $B_0$  field inhomogeneities.<sup>22,23</sup>

This study had several limitations. First, it did not correlate T1 $\rho$  imaging with biologic characteristics, so the underlying biologic factors contributing to the T1 $\rho$  values in the head and neck remain unclear. Second, most participants with NPC referred to MR imaging for staging had already undergone a nasopharyngeal biopsy. This scenario is unavoidable, but to minimize the potential influence of a biopsy on the T1 $\rho$  measurement, any foci of hemorrhage were excluded when contouring the primary tumor. Third, while obvious cysts can be excluded from the contoured region, very small cysts of 1–2 mm, which are more commonly seen in benign hyperplasia, cannot be excluded from the analysis. Fourth, this study did not analyze the reproducibility of T1 $\rho$  imaging in the head and neck, but previous studies have reported high reproducibility of T1 $\rho$  imaging in other tissue.<sup>38,39</sup> Furthermore, with an adiabatic continuous wave constant amplitude spin-lock, the spins are locked at a tilted angle from the transverse plane during the spin-lock, which results in T1 contamination of the T1 $\rho$  measurements.<sup>23</sup> The level of T1 contamination depends on the  $B_0$  field inhomogeneities and the  $B_1$  amplitude of the spin-lock radiofrequency pulse or the frequency of the spin-lock. In our previous study,<sup>23</sup> we reported that the maximum error of T1 $\rho$  quantification due to this effect is within 4% at a frequency of spin-lock of 500 Hz and a maximum  $B_0$  field inhomogeneity of 100 Hz, but the maximum error at this site is unknown.

## CONCLUSIONS

There are quantitative differences in the T1 $\rho$  measurements of normal, malignant, and benign tissue in the head and neck. T1 $\rho$  imaging, therefore, has the potential to be used to identify malignant tumors. This is a new area for cancer research, and further studies are needed to validate these findings.

**Disclosures:** Weitian Chen—UNRELATED: Employment: The Chinese University of Hong Kong; Grants/Grants Pending: The Chinese University of Hong Kong\*; Patents (Planned, Pending or Issued): a pending US patent and a pending Chinese patent; W. Chen and B. Jiang: System and Method for Continuous Wave Constant Amplitude On-Resonance and Off-resonance Spin-Lock for Magnetic Resonance Imaging, US 15/663,254, US patent, pending; CN 201710649663.X, pending; Comments: no money received; OTHER RELATIONSHIPS: I am a shareholder of the company Illuminatio Medical Technology limited. Wai Kei Jacky Lam—UNRELATED: Patents (Planned, Pending or Issued): patent on clinical applications of circulating DNA\*; Stock/Stock Options: Grail. Queenie Chan—UNRELATED: Employment: Queenie Chan is an employee of Philips Healthcare, but she had no control over inclusion of any data or information that might have presented a conflict of interest. There are no actual or potential conflicts of interest to declare in relation to this article. Edwin P. Hui—UNRELATED: Consultancy: Merck Sharp & Dohme, Comments: Advisory Board; Payment for Lectures Including Service on Speakers Bureaus: Merck Sharp & Dohme, Merck Serono, Comments: speakers honoraria. K. C. Allen Chan—RELATED: Consulting Fee or Honorarium: Grail; UNRELATED: Board Membership: Take2, DRA; Consultancy: Grail; Grants/Grants Pending: Grail, Cirina\*;



Patents (Planned, Pending or Issued): I am an inventor of over 70 patents; parts of the portfolio have been licensed to Illumina, Grail, Xcelom, DRA; Royalties: Grail, Sequenom, Illumina, Take2, Xcelom; Stock/Stock Options: Grail, DRA, Take2; Travel/Accommodations/Meeting Expenses Unrelated to Activities Listed: Bio-Rad Laboratories. \*Money paid to the institution.

## REFERENCES

- Regatte RR, Akella SV, Wheaton AJ, et al. **3D-T1 $\rho$ -relaxation mapping of articular cartilage: in vivo assessment of early degenerative changes in symptomatic osteoarthritic subjects.** *Acad Radiol* 2004;11:741–49 CrossRef Medline
- Wang YX, Zhao F, Griffith JF, et al. **T1 $\rho$  and T2 relaxation times for lumbar disc degeneration: an in vivo comparative study at 3.0-Tesla MRI.** *Eur Radiol* 2013;23:228–34 CrossRef Medline
- Li X, Kuo D, Theologis A, et al. **Cartilage in anterior cruciate ligament-reconstructed knees: MR imaging T1  $\rho$  and T2: initial experience with 1-year follow-up.** *Radiology* 2011;258:505–14 CrossRef Medline
- Haris M, Singh A, Cai K, et al. **T1 $\rho$  (T1 $\rho$ ) MR imaging in Alzheimer' disease and Parkinson's disease with and without dementia.** *J Neurol* 2011;258:380–05 CrossRef Medline
- Magnotta VA, Heo HY, Dlouhy BJ, et al. **Detecting activity-evoked pH changes in human brain.** *Proc Natl Acad Sci U S A* 2012;109:8270–73 CrossRef Medline
- Haris M, McArdle E, Fenty M, et al. **Early marker for Alzheimer's disease: hippocampus T1 $\rho$  (T1 $\rho$ ) estimation.** *J Magn Reson Imaging* 2009;29:1008–12 CrossRef Medline
- Nestrasil I, Michaeli S, Liimatainen T, et al. **T1 $\rho$  and T2 $\rho$  MRI in the evaluation of Parkinson's disease.** *J Neurol* 2010;257:964–68 CrossRef Medline
- Wang YX, Yuan J, Chu ES, et al. **T1 $\rho$  MR imaging is sensitive to evaluate liver fibrosis: an experimental study in a rat biliary duct ligation model.** *Radiology* 2011;259:712–19 CrossRef Medline
- Allkemper T, Sagmeister F, Cicinnati V, et al. **Evaluation of fibrotic liver disease with whole-liver t1 $\rho$  MR imaging: a feasibility study at 1.5 T.** *Radiology* 2014;271:408–15 CrossRef Medline
- Muthupillai R, Flamm SD, Wilson JM, et al. **Acute myocardial infarction: tissue characterization with T1  $\rho$ -weighted MR imaging: initial experience.** *Radiology* 2004;232:606–10 CrossRef Medline
- Markkola AT, Aronen HJ, Ramadan UA, et al. **Determination of T1 $\rho$  values for head and neck tissue at 0.1 T: a comparison to T1 and T2 relaxation times.** *Magn Reson Imaging* 1998;16:377–83 CrossRef Medline
- Zhou N, Chu C, Dou X, et al. **Early changes of irradiated parotid glands evaluated by T1 $\rho$ -weighted imaging: a pilot study.** *J Comput Assist Tomogr* 2017;41:472–76 CrossRef Medline
- Chu C, Zhou N, Zhang H, et al. **Use of T1 $\rho$  MR imaging in Sjögren's syndrome with normal appearing parotid glands: initial findings.** *J Magn Reson Imaging* 2017;45:1005–12 CrossRef Medline
- Cao M, Ding W, Han X, et al. **Brain T1 $\rho$  mapping for grading and IDH1 gene mutation detection of gliomas: a preliminary study.** *J Neurooncol* 2019;141:245–52 CrossRef Medline
- Aronen HJ, Abo Ramadan U, Peltonen TK, et al. **3D spin-lock imaging of human gliomas.** *Magn Reson Imaging* 1999;17:1001–10 CrossRef Medline
- Villanueva-Meyer JE, Barajas RF, Mabray MC, et al. **Differentiation of brain tumor-related edema based on 3D T1 $\rho$  imaging.** *Eur J Radiol* 2017;91:88–92 CrossRef Medline
- Santyr GE, Henkelman RM, Bronskill MJ. **Spin locking for magnetic resonance imaging with application to human breast.** *Magn Reson Med* 1989;12:25–37 CrossRef Medline
- Jambor I, Pesola M, Taimen P, et al. **Rotating frame relaxation imaging of prostate cancer: repeatability, cancer detection, and Gleason score prediction.** *Magn Reson Med* 2016;75:337–44 CrossRef Medline
- King AD, Wong LY, Law BK, et al. **MR imaging criteria for the detection of nasopharyngeal carcinoma: discrimination of early-stage primary tumors from benign hyperplasia.** *AJNR Am J Neuroradiol* 2018;39:515–23 CrossRef Medline
- Wang ML, Wei XE, Yu MM, et al. **Value of contrast-enhanced MRI in the differentiation between nasopharyngeal lymphoid hyperplasia and T1 stage nasopharyngeal carcinoma.** *Radiology Med* 2017;122:743–51 CrossRef Medline
- Amin MB, American Joint Committee on Cancer *AJCC Cancer Staging Manual*. 8th ed. Springer-Verlag; 2017
- Jiang B, Chen W. **On-resonance and off-resonance continuous wave constant amplitude spin-lock and T1 $\rho$  quantification in the presence of B1 and B0 inhomogeneities.** *NMR Biomed* 2018;31:1–17 CrossRef Medline
- Chen W. **Artifacts correction for T1 $\rho$  imaging with constant amplitude spin-lock.** *J Magn Reson* 2017;274:13–23 CrossRef Medline
- Chen W, Chan Q, Wang YX. **Breath-hold black blood quantitative T1 $\rho$  imaging of liver using single shot fast spin echo acquisition.** *Quant Imaging Med Surg* 2016;6:168–77 CrossRef Medline
- Wilde DJ. *Optimum Seeking Methods*. Prentice Hall; 1964
- Delong ER, Delong DN, Clarke-Pearson DL. **Comparing the areas under two or more correlated receiver operating characteristic curves: a nonparametric approach.** *Biometrics* 1988;44:837–45 Medline
- Kundel HL, Polansky M. **Measurement of observer agreement.** *Radiology* 2003;228:303–08 CrossRef Medline
- Ali SO, Fessas P, Kaggie JD, et al. **Evaluation of the sensitivity of R1  $\rho$  MRI to pH and macromolecular density.** *Magn Reson Imaging* 2019;58:156–61 CrossRef Medline
- Hatcher CC, Collins AT, Kim SY, et al. **Relationship between T1 $\rho$  magnetic resonance imaging, synovial fluid biomarkers, and the biochemical and biomechanical properties of cartilage.** *J Biomech* 2017;55:18–26 CrossRef Medline
- Paul CP, Smit TH, Graaf MD, et al. **Quantitative MRI in early intervertebral disc degeneration: T1 $\rho$  correlates better than T2 and ADC with biomechanics, histology and matrix content.** *PLoS One* 2018;13:e0191442 CrossRef Medline
- King AD, Vlantis AC, Bhatia KS, et al. **Primary nasopharyngeal carcinoma: diagnostic accuracy of MR imaging versus that of endoscopy and endoscopic biopsy.** *Radiology* 2011;258:531–37 CrossRef Medline
- King AD, Vlantis AC, Yuen TW, et al. **Detection of nasopharyngeal carcinoma by MR imaging: diagnostic accuracy of MRI compared with endoscopy and endoscopic biopsy based on long-term follow-up.** *AJNR Am J Neuroradiol* 2015;36:2380–85 CrossRef Medline
- King AD, Woo JK, Ai QY, et al. **Complementary roles of MRI and endoscopic examination in the early detection of nasopharyngeal carcinoma.** *Ann Oncol* 2019;30:977–82 CrossRef Medline
- King AD, Woo JK, Ai QY, et al. **Early detection of cancer: Evaluation of MR imaging grading systems in patients with suspected nasopharyngeal carcinoma.** *AJNR Am J Neuroradiol* 2020;41:515–20 CrossRef Medline
- Thoeny HC, De Keyser F, King AD. **Diffusion-weighted MR imaging in the head and neck.** *Radiology* 2012;263:19–32 CrossRef Medline
- Noij DP, Martens RM, Marcus JT, et al. **Intravoxel incoherent motion magnetic resonance imaging in head and neck cancer: a systematic review of the diagnostic and prognostic value.** *Oral Oncol* 2017;68:81–91 CrossRef Medline
- Ai QY, King AD, Chan JSM, et al. **Distinguishing early-stage nasopharyngeal carcinoma from benign hyperplasia using intravoxel incoherent motion diffusion-weighted MRI.** *Eur Radiol* 2019;29:5627–34 CrossRef Medline
- Wang YX, Deng M, Lo GG, et al. **Breath-hold black-blood T1 $\rho$  mapping improves liver T1 $\rho$  quantification in healthy volunteers.** *Acta radiol* 2018;59:257–65 CrossRef Medline
- Nemeth A, Di Marco L, Boutitie F, et al. **Reproducibility of in vivo magnetic resonance imaging T1  $\rho$  and T2 relaxation time measurements of hip cartilage at 3.0T in healthy volunteers.** *J Magn Reson Imaging* 2018;47:1022–33 CrossRef Medline



# Design of 3D-Printed Nasopharyngeal Swabs for Children is Enabled by Radiologic Imaging

 Z. Starosolski,  P. Admane,  J. Dunn,  B. Kaziny,  T.A.G.M. Huisman, and  A. Annapragada



## ABSTRACT

**SUMMARY:** 3D-printed nasopharyngeal swabs for COVID-19 molecular diagnostic testing address the national shortage of swabs. Swab designs for adult use were placed in the public domain in March 2020. Swabs for pediatric use, however, need to be smaller and more flexible to navigate delicate pediatric nasopharyngeal cavities. We describe a novel use of maxillofacial CT scans to aid in the design of pediatric nasopharyngeal swabs.

**ABBREVIATIONS:** COVID-19 = coronavirus disease 2019; RT-PCR = real-time polymerase chain reaction

Coronavirus disease 2019 (COVID-19) is a worldwide pandemic and has resulted in shortages of medical supplies, including nasopharyngeal swabs used in diagnostic tests. 3D printing provides a novel solution, and designs for 3D-printed nasopharyngeal swabs are freely distributed via a GitHub repository.<sup>1</sup> The effort, however, has focused on swabs for use in adult patients. These adult swabs are too inflexible and too large for safe pediatric use, particularly in children younger than 3 years of age. At our hospital (Texas Children's Hospital), a large pediatric tertiary-care center, a 3D-printed swab that replicated the dimensions of a commercial pediatric swab (COPAN Flock Technologies; Puritan Diagnostics) was evaluated by one of our pediatric emergency physicians. However, the 3D-printed swab was not sufficiently flexible and would risk damaging the nasal passages of the child. Simply reducing the diameter of the flexible shaft was deemed inadvisable because the use of the swab involves twisting in both directions after insertion and a thinner shaft would risk breakage in situ. We, therefore, set out to design and produce novel 3D-printed swabs for use in infants and young children.

## MATERIALS AND METHODS

The institutional review board approved all clinical data use. Examination of maxillofacial CT scans of patients 1–3 years of age suggested that primary deflection of the swab in the sagittal plane would be sufficient to navigate from the external nares to the posterior nasopharynx. We, therefore, designed elliptical cross-section swabs (Fig 1) and verified that sagittal shaft deflection was adequate. We then made 3D prints of the nasopharyngeal passage itself, and physically tested the ability of individual swab prototypes to navigate the passage. We noted that less flexible designs would get trapped in the crenulations of the nasopharyngeal passage and might require multiple attempts to reach the posterior nasopharynx, thus lengthening the time required to reach the sampling location and possibly injuring the delicate pediatric anatomy. On the assumption that increased navigation time and resistance correlated with patient discomfort, we chose the navigation time and a qualitative assessment of resistance as measures of patient discomfort, ultimately selecting the design with the shortest navigation time and the lowest resistance score for clinical use.

Maxillofacial CT datasets of 5 patients, 11 to 34 months of age and unremarkable for pathologies involving the maxillofacial region, were randomly selected from our data base. Images were processed in 3D Slicer (Version 4.10; <http://www.slicer.org>) to create Standard Triangle Language files for printing. Nasopharyngeal passages were printed on a Form2 printer using Elastic Resin (Formlabs). Swab designs were made in Fusion 360 (AUTODESK) and printed on a Form2 printer using Surgical Guide Resin (Formlabs).


We tested 5 swabs designs: 2 commercial mini-swabs, Flocked 1, PURITAN Diagnostics and Flocked 2, COPAN Flock Technologies; and 3 in-house-printed, all of which had a flexible shaft length of approximately 50 mm, a handle of 78 mm, and a transition zone of

Received July 6, 2020; accepted after revision July 22.

From the Edward B. Singleton Department of Radiology (Z.S., T.A.G.M.H., A.A.), Texas Children's Hospital, Houston, Texas; Department of Radiology (P.A.), Baylor College of Medicine, Houston, Texas; and Departments of Pediatrics (B.K.), and Medical Microbiology and Virology (J.D.), Texas Children's Hospital, Houston, Texas.

This work was partially funded by a grant from the Soicher Family Foundation to A.A.

Please address correspondence to Ananth Annapragada, PhD, Edward B. Singleton Department of Radiology, Texas Children's Hospital, 1102 Bates St Suite 850, Feigin Center, Houston, TX 77030; e-mail: [avannapr@texaschildrens.org](mailto:avannapr@texaschildrens.org)

 Indicates open access to non-subscribers at [www.ajnr.org](http://www.ajnr.org)

<http://dx.doi.org/10.3174/ajnr.A6794>



**FIG 1.** A, Sagittal section of a maxillofacial CT scan of a 22-month-old patient. Shown in red is the trajectory of a virtually inserted swab reaching the posterior nasopharynx. The white box shows the portion of the anatomy chosen to print the nasopharyngeal passage. B, A commercial flocked pediatric swab (COPAN Flock Technologies swab) reaching the posterior nasopharynx within the 3D-printed nasopharyngeal passage. C, Design of the elliptical-section 3D-printed pediatric swab (Design ES).

**Tabularized dimensions for 2 commercial and 3 in-house printed swab designs<sup>a</sup>**

Swab	a	b	c	d	e	f	g	h	i	j	k	l
Flocked 1	2.3	7.0	0	2.3	2.5	2.5	1.2	1.2	7.0	44	8.3	94
Flocked 2	2.7	7.4	0	2.7	2.5	2.5	0.9	0.9	7.4	66	24.5	53
Design E	2.7	8.5	0	1.9	3.5	5.0	0.8	1.2	8.5	50.8	14.3	78.4
Design I	2.7	8.5	0	2.6	5.0	5.0	1.2	1.2	8.5	50.8	14.3	78.4
Design ES	2.7	8.5	1.8	1.9	3.5	5.0	0.8	1.2	10.4	49	14.3	78.4

<sup>a</sup> Dimensions are in millimeters. Columns represents dimensions as in Fig 1C.

14 mm, as shown in Fig 1, and varied in the flexible shaft cross-section: Design E, 1.2 mm × 0.8 mm; Design I, 1.2 mm; and Design ES, 1.2 mm × 0.8 mm, with an additional slanted posterior edge of the brush. The Table shows dimensions (in millimeters) for each of the swab types tested. Navigation of each swab from the external nares to the posterior nasopharynx was done by 1 individual, the order of testing of the individual swabs and anatomic models was randomized, and each test was repeated 3 times. The time to complete navigation was timed by an observer using a hand-held stopwatch, while the resistance on insertion was classified using a 3-level resistance score (1, easy insertion: no resistance; 2, medium: mild resistance; and 3, hard: resistance requiring extra force). All statistical calculations were performed in Matlab R19a (MathWorks).

The quality of specimen recovery from Design ES nasopharyngeal swabs was determined by performing a crossover collection study with the commercial swabs (Puritan Diagnostics) and prototype NB swabs in 2 healthy adult volunteers, a 26-year-old man and a 28-year-old woman. Both nostrils of the volunteers were sampled by each swab in successive order. The swabs were placed into a MicroTest M4RT viral transport containing 3 mL of media (Remel). Nucleic acid was extracted using 200 µL from each viral transport on the eMAG system (bioMérieux) and eluted into 50 µL of buffer. Real-time polymerase chain reaction (RT-PCR) was performed on each eluate using the Centers for Disease Control's 2019–Novel Coronavirus (2019-nCoV) Emergency Use Authorization assay,<sup>2</sup> which includes 2 targets in the Severe Acute Respiratory

Syndrome coronavirus 2 nucleocapsid region and 1 target in the human RNase P gene to assess the cellular quality of the sample.

## RESULTS

Two commercial flocked mini-swabs (from Puritan Diagnostics and COPAN Flock Technologies) and 3 in-house printed swab designs were tested. All

in-house swabs were successfully navigated to the posterior nasopharynx in all 5 nasopharyngeal passage models, while 1 commercial swab (COPAN Flock Technologies) was incapable of insertion into anatomic model 1 (Fig 2). On the basis of the shortest navigation time and the lowest resistance score (Fig 2C), Design ES was chosen as the preferred design for clinical testing. Preliminary clinical testing in 2 adult volunteers demonstrated recovery of cellular material from Design ES swabs to be within a concentration of 0.3 log of that from the currently used nasopharyngeal swabs.

## DISCUSSION

Pediatric nasopharyngeal swabs (mini-swabs) are a thinner, smaller, more flexible version of those used for adults and are in even shorter supply during the COVID-19 pandemic than the adult swabs.

3D-printed swabs are fundamentally different from existing commercial swab designs in the form of the swab tip: While commercial swabs have flocked fibrous tips, 3D-printed swabs have solid tips with hemispheric nubs. However, both in vitro and in vivo testing have shown them to be practically identical in sample transfer for viral assay by RT-PCR both in our own labs and in other labs.<sup>3,4</sup> Of note, at the time of this writing, the pediatric swabs printed using Design ES have now been used in our hospital in >1000 patients with no reported problems.

This brief report has several limitations. Only 5 nasopharyngeal prints of patients in a limited age range (1–3 years) were

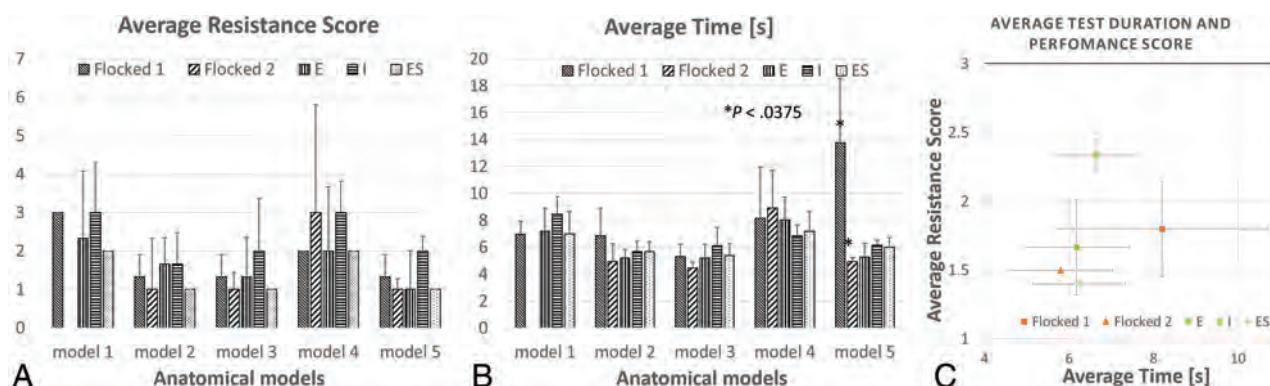


**FIG 2.** Results comparison based on 3 repetitions and 5 anatomic models. A, Average performance score (a lower value of the performance is better). B, Average time of the procedure in seconds. The Flocked 2 swab was not able to complete the testing procedure due to very narrow nasal passages of model 1. The asterisk indicates the significant difference calculated by multiple ANOVA statistical tests. Error bars represent SDs. C, Graph showing the relation of time and performance test results for each of the tested swabs. Locations closer to the graph origin indicate faster and smoother test performance.

used for the testing. A broader range of ages and a larger number of patients would make this study more rigorous. The insertion tests were performed by 1 individual, a technologist with intimate knowledge of the nasopharyngeal anatomy. Testing by a medical professional who would routinely use such swabs in daily practice may change the results. Clinical validation was only performed on 2 adult volunteers and not on a larger number of pediatric subjects. All of these, however, are compromises we made for this emergency development.

Radiology departments have adopted 3D printers recently to provide prints for surgical planning and patient education and are uniquely positioned to produce 3D-printed nasopharyngeal swabs during this pandemic. Additionally, they have unique access to volumetric imaging data to optimize and test swab designs. The methods described in this report demonstrate an effective collaboration between members of clinical and research departments in accelerating development and enabling creative patient-centric solutions.

**Disclosures:** Zbigniew Starosolski—UNRELATED: Patents (Planned, Pending or Issued): Texas Children's Hospital, Comments: submitted invention disclosure form to Texas Children's Hospital for a patent titled "Design of Pediatric 3D Printed Nasopharyngeal Swab on June 16, 2020; Stock/Stock Options: Alzeca Biosciences stock. Prasad Admane—RELATED: Grant: Baylor College of Medicine, Comments: Soicher Family Foundation\*; RELATED: Patents (Planned,







Pending or Issued): Texas Children's Hospital, Comments: submitted invention disclosure form to Texas Children's Hospital for a patent titled "Design of Pediatric 3D Printed Nasopharyngeal Swab on June 16, 2020. Ananth Annapragada—RELATED: Grant: Soicher Family Foundation, Comments: to support work on bioprinting\*; UNRELATED: Board Membership: Alzeca Biosciences; Consultancy: Alzeca Biosciences; Grants/Grants Pending: National Institutes of Health, Comments: I have several grants pending at National Institutes of Health\*; Patents (Planned, Pending or Issued): numerous US and foreign patent applications, Comments: The full list can be obtained at <https://patentscope.wipo.int/search/en/advancedSearch.jsf> using search terms: IN: Ananth AND IN: Annapragada\*; Royalties: University of Texas, Comments: royalties on patents licensed by the University of Texas to third parties; Stock/Stock Options: Sensulin, Alzeca Biosciences, Comments: I am a significant stockholder in Sensulin and Alzeca Biosciences; Other: Abbott Laboratories, Comments: I am a significant stockholder. \*Money paid to the institution.

## REFERENCES

1. Covidswab. <http://github.com/rarnaout/Covideswab>. Accessed April 1, 2020
2. Centers for Disease Control and Prevention. CDC 2019-Novel Coronavirus (2019-nCoV) Real-Time RT-PCR. U.S. Food and Drug Administration emergency use authorization instructions for use. <https://www.fda.gov/media/134922/download>. Accessed July 17, 2020
3. Corman VM, Landt O, Kaiser M, et al. Detection of 2019 novel coronavirus (2019-nCoV) by real-time RT-PCR. *Euro Surveill* 2020;25:2000045 CrossRef Medline
4. Mullis KB, Faloona FA. Specific synthesis of DNA in vitro via a polymerase-catalyzed chain reaction. *Methods Enzymol* 1987;155:335–50 CrossRef Medline



# Vessel Wall Enhancement and Focal Cerebral Arteriopathy in a Pediatric Patient with Acute Infarct and COVID-19 Infection

 E. Gulko,  P. Overby,  S. Ali,  H. Mehta,  F. Al-Mufti, and  W. Gomes



## ABSTRACT

**SUMMARY:** Herein, we report the findings of intracranial arterial wall enhancement, consistent with focal cerebral arteriopathy–inflammatory type, in a child presenting with acute infarct in the setting of coronavirus disease 2019 (COVID-19) infection. To our knowledge, this report provides the first description of vessel wall imaging findings in COVID-19-associated acute stroke.

**ABBREVIATIONS:** COVID-19 = coronavirus disease 2019; FCA = focal cerebral arteriopathy; SARS-CoV-2 = Severe Acute Respiratory Syndrome coronavirus 2; VWI = vessel wall imaging

Severe Acute Respiratory Syndrome coronavirus 2 (SARS-CoV-2) has resulted in the world-wide pandemic of coronavirus disease 2019 (COVID-19) illnesses, including Severe Acute Respiratory Syndrome and a multitude of neurologic manifestations.<sup>1</sup> There is emerging evidence for the role of the cerebrovascular system in neurologic manifestations of COVID-19 infection, and patients with COVID-19 infection may be at greater risk for thromboembolic disease.<sup>2</sup> Recent studies have demonstrated that patients can develop intracranial hemorrhages, acute strokes,<sup>3</sup> and large-vessel arterial occlusions.<sup>4</sup> The pathomechanisms that underlie COVID-19-associated cerebrovascular disease remain unclear. While growing numbers of case reports and studies have highlighted COVID-19-associated neurologic disease in adults, there are few reports of COVID-19-associated neurologic disease in children. A recent case report demonstrated stenosis of the left middle cerebral artery, which was attributed to focal cerebral arteriopathy (FCA), in a pediatric patient with COVID-19 and acute stroke.<sup>5</sup> Herein, we describe the second documented case of COVID-19-associated FCA and acute stroke in a pediatric patient. Additionally, we provide the presumptive first description of MR imaging vessel wall imaging (VWI) findings in a patient with COVID-19-related stroke.

A 13-year-old right-handed girl presented with fluctuating-but-persistent headache, speech difficulty, and right upper and

lower extremity weakness for 4 days. Two months before presentation, she and other family members experienced fever, myalgias, and anosmia, which subsequently resolved. One month before admission, she and other family members tested positive for SARS-CoV-2 qualitative antibodies. Antibody testing for the patient was performed with the ADVIA Centaur SARS-CoV-2 Total Assay (Siemens). The child had no other medical history. There was no family history of thrombophilia.


The initial exam was normal for temperature, blood pressure, and heart rate. Her speech was dysfluent with word-finding difficulties. She had mild-to-moderate extensor weakness in the right arm and leg. Initial head CT showed a left frontal hypodensity (not shown) concerning for ischemic infarct. Consequently, the patient was transferred to our tertiary referral center. At our facility, results of testing for SARS-CoV-2 RNA by real-time reverse transcription polymerase chain reaction with a nasopharyngeal swab specimen were positive.

MR imaging of the brain demonstrated small regions of restricted diffusion and FLAIR hyperintensity, with the left frontal, parietal, and temporal lobes consistent with acute-subacute infarcts in the left middle cerebral artery vascular territory (Fig 1). Noncontrast MRA of the head was performed with a time-of-flight sequence. Vessel wall imaging was performed with and without intravenous gadolinium contrast with 3D volume isotropic turbo spin-echo acquisition T1 and black-blood sequences on a 3T MR imaging instrument. MRA of the head demonstrated focal moderate stenosis within the M1 segment of the left middle cerebral artery (Fig 1). Vessel wall imaging targeted to the left middle cerebral artery M1 segment demonstrated wall thickening and marked, concentric contrast enhancement (Fig 2) at the site of stenosis. These imaging features, in conjunction with the clinical presentation, were consistent with focal cerebral arteriopathy of childhood-inflammatory type.<sup>6</sup>

Received June 19, 2020; accepted after revision July 16.

From the Department of Radiology, Division of Neuroradiology (E.G., S.A., H.M., W.G.), Department of Pediatrics (P.O.), and Department of Neurology (F.A.-M.), Westchester Medical Center, Valhalla, New York.

Please address correspondence to Edwin Gulko, MD, Division of Neuroradiology, Department of Radiology, Westchester Medical Center, 100 Woods Rd, Valhalla New York, 10595; e-mail: Edwin.Gulko@wmchealth.org

 Indicates open access to non-subscribers at [www.ajnr.org](http://www.ajnr.org)

<http://dx.doi.org/10.3174/ajnr.A6778>

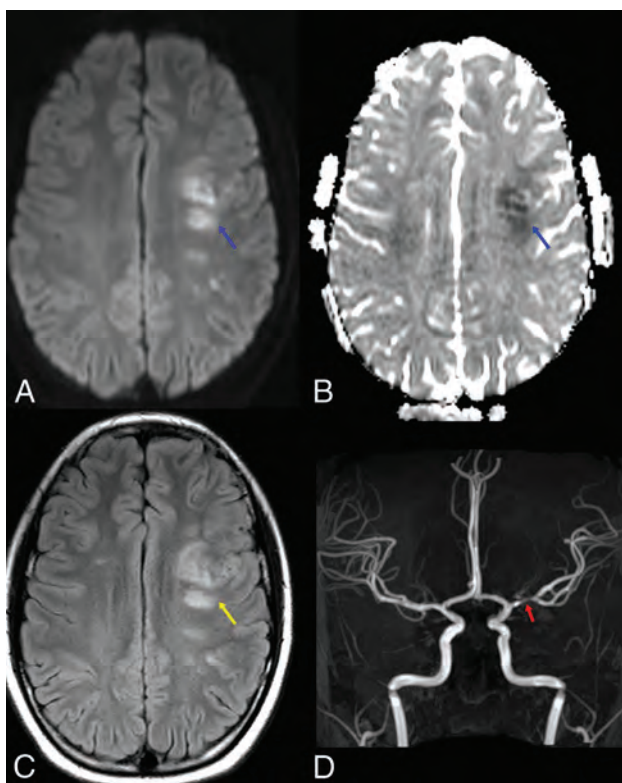


**FIG 1.** COVID-19-associated left MCA vascular territory acute infarcts in a pediatric patient. Axial diffusion (A), ADC map (B), and FLAIR (C) images demonstrate foci of restricted diffusion (*blue arrows*) and cytotoxic edema (*yellow arrow*) within the left middle cerebral artery vascular territory, consistent with acute infarcts. Anterior projection from a TOF-MRA of the head (D) demonstrates a focal segment of moderate stenosis within the left M1 middle cerebral artery (*red arrow*).

Additional work-up for the patient was unrevealing. The echocardiogram findings were within normal limits. The lumbar puncture result was within normal limits. Multiple viral polymerase chain reaction tests, including herpes simplex virus and varicella zoster virus, were negative from the spinal fluid, as were bacterial cultures. Thrombophilia evaluation had normal findings. Other inflammatory markers, typically elevated in COVID-19-associated pediatric multisystem inflammatory syndrome, were normal. Clinically, the patient improved, and the neurologic examination was unremarkable at the time of discharge. A follow-up MR imaging examination has not yet been performed at the completion of this article.

Large-vessel cerebral arteriopathy is the most common cause of arterial ischemic stroke in a previously healthy child.<sup>7</sup> The Vascular Effects of Infection in Pediatric Stroke study<sup>6</sup> found that the most common arteriopathies in children presenting with acute arterial ischemic stroke included Moyamoya disease, arterial dissection, and FCA-inflammatory type. An updated definition of FCA by Wintermark et al<sup>6</sup> includes unifocal and unilateral stenosis/irregularity of the distal internal carotid artery and/or its proximal branches. FCA-inflammatory type describes FCA that is presumed to be inflammatory (a focal vasculitis) and can be diagnosed by marked concentric vessel wall enhancement on VWI.<sup>6</sup> FCA, dissection type, in contrast, refers to intracranial arterial dissection, typically associated with a history of trauma.

VWI is capable of distinguishing among disease entities involving the intracranial arterial system.<sup>8</sup> CNS vasculitis typically demonstrates vessel wall thickening on VWI, with homogeneous and concentric contrast enhancement,<sup>8</sup> and infectious pathogens such as varicella zoster have been shown to cause concentric vessel wall enhancement.<sup>9</sup> Other forms of arteriopathy can also result in vessel wall enhancement, including arterial dissection,

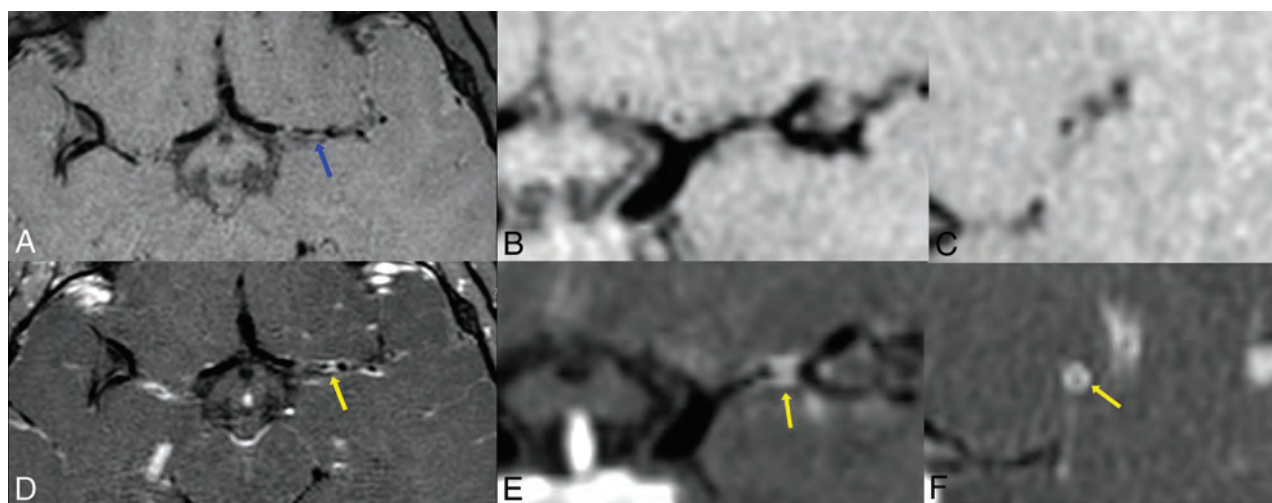


**FIG 2.** Vessel wall enhancement within the M1 left MCA. Vessel wall imaging targeted to the left middle cerebral artery with axial pre- (A) and postcontrast (D) 3D T1 volume isotropic turbo spin-echo acquisition sequences, with reformatted coronal images (B and E, respectively). Pre- (C) and postcontrast (F) reformatted sagittal images en face to the M1 left middle cerebral artery at the level of the *blue* and *yellow* arrows, respectively. There is wall thickening (*blue arrow*) and marked concentric contrast enhancement of the M1 left middle cerebral artery at the segment of stenosis (*yellow arrows*). The imaging findings, in conjunction with the clinical history, were consistent with FCA-inflammatory type.

cardioembolism, and drug-induced vasospasm.<sup>10,11</sup> However, in our patient, no clinical or laboratory findings were present to support these other possibilities.

Existing evidence in the adult population supports thromboembolism as a common cause of stroke in patients with COVID-19,<sup>2</sup> possibly secondary to “cytokine storms,” which can lead to vascular endothelial damage.<sup>12,13</sup> It is currently unknown whether the pathophysiology of COVID-19-associated acute infarcts in the pediatric population is similar to that described in adults. A recent report by Mirzaee et al<sup>5</sup> described a case of presumed focal cerebral arteriopathy in a pediatric patient with COVID-19, but VWI was not performed. We similarly observed evidence of focal cerebral arteriopathy on MRA but were able to corroborate the diagnosis of FCA-inflammatory type with VWI. Taken together, our results and those of Mirzaee et al suggest FCA as a mechanism of SARS-CoV-2-related acute ischemic stroke in children. It is currently unclear whether FCA is also a significant cause of ischemic infarction in adults with COVID-19.

To our knowledge, this report provides the first description of vessel wall imaging findings in a patient with COVID-19 with acute ischemic stroke. We believe that VWI may facilitate the specific diagnosis of focal cerebral arteriopathy in children (and perhaps adults) with COVID-19. Of note, steroid therapy may improve the outcome in focal cerebral arteriopathy;<sup>14</sup> recognition of focal cerebral arteriopathy on imaging may, therefore, contribute to the choice of a therapeutic regimen in COVID-19-related infarction. We, therefore, suggest that clinicians and neuroradiologists consider using vessel wall imaging to aid in the evaluation of patients with COVID-19 and acute stroke.

Disclosures: Philip Overby—UNRELATED: Expert Testimony: legal medical reviews. Fawaz Al-Mufti—UNRELATED: Employment: Westchester Medical Center at New York Medical College.

## REFERENCES

1. Helms J, Kremer S, Merdji H, et al. **Neurologic features in severe SARS-CoV-2 infection.** *N Engl J Med* 2020;382:2268–70 CrossRef Medline
2. Bikdeli B, Madhavan MV, Jimenez D, et al; the IUA, Supported by the ESC Working Group on Pulmonary Circulation and Right Ventricular Function. **COVID-19 and thrombotic or thromboembolic disease: implications for prevention, antithrombotic therapy, and follow-up.** *J Am Coll Cardiol* 2020;75:2950–73 CrossRef Medline
3. Radmanesh A, Raz E, Zan E, et al. **Brain imaging utilization and findings in COVID-19: a single academic center experience in the epicenter of disease in the United States.** *AJNR Am J Neuroradiol* 2020;41:1179–83 CrossRef Medline
4. Oxley TJ, Mocco J, Majidi S, et al. **Large-vessel stroke as a presenting feature of Covid-19 in the young.** *N Engl J Med* 2020;382:e60 CrossRef Medline
5. Mirzaee SM, Gonçalves FG, Mohammadifard M, et al. **Focal cerebral arteriopathy in a COVID-19 pediatric patient.** *Radiology* 2020 June 2. [Epub ahead of print] CrossRef Medline
6. Wintermark M, Hills NK, DeVeber GA, et al; the VIPS Investigators. **Clinical and imaging characteristics of arteriopathy subtypes in children with arterial ischemic stroke: results of the VIPS study.** *AJNR Am J Neuroradiol* 2017;38:2172–79 CrossRef Medline
7. Fullerton HJ, Elkind MS, Barkovich AJ, et al. **The vascular effects of infection in pediatric stroke (VIPS) study.** *J Child Neurol* 2011;26:1101–10 CrossRef Medline
8. Mandell DM, Mossa-Basha M, Qiao Y, et al; Vessel Wall Imaging Study Group of the American Society of Neuroradiology. **Intracranial vessel wall MRI: principles and expert consensus recommendations of the American Society of Neuroradiology.** *AJNR Am J Neuroradiol* 2017;38:218–29 CrossRef Medline
9. Cheng-Ching E, Jones S, Hui FK, et al. **High-resolution MRI vessel wall imaging in varicella zoster virus vasculopathy.** *J Neurol Sci* 2015;351:168–73 CrossRef Medline
10. Stence NV, Pabst LL, Hollatz AL, et al. **Predicting progression of intracranial arteriopathies in childhood stroke with vessel wall imaging.** *Stroke* 2017;48:2274–77 CrossRef Medline
11. Dlamini N, Yau I, Muthusami P, et al. **Arterial wall imaging in pediatric stroke.** *Stroke* 2018;49:891–98 CrossRef Medline
12. Ye Q, Wang B, Mao J. **The pathogenesis and treatment of the “cytokine storm” in COVID-19.** *J Infect* 2020;80:607–13 CrossRef Medline
13. Mehta P, McAuley DF, Brown M, et al; HLH Across Speciality Collaboration, UK. **COVID-19: consider cytokine storm syndromes and immunosuppression.** *Lancet* 2020;395:1033–34 CrossRef Medline
14. Steinlin M, Bigi S, Stojanovski B, et al; Swiss NeuroPediatric Stroke Registry. **Focal cerebral arteriopathy: do steroids improve outcome?** *Stroke* 2017;48:2375–82 CrossRef Medline



# Variations of Intracranial Dural Venous Sinus Diameters from Birth to 20 Years of Age: An MRV-Based Study

A.S. Larson, G. Lanzino, and W. Brinjikji



## ABSTRACT

**BACKGROUND AND PURPOSE:** The role of the dural venous sinus system in cerebrovascular pathology and the understanding of normal developmental patterns and sizes of the dural venous sinus system continue to expand. The purpose of this study was to review MR venograms to elucidate developmental patterns and diameters of the major dural venous sinuses from 0 to 20 years of age.

**MATERIALS AND METHODS:** All available MR venograms of patients 0–20 years of age who presented to our institution were retrospectively reviewed. Patient age at the time of image acquisition was noted, and measurements were taken of the diameters of the major dural venous sinuses. The presence of embryonic sinuses including the persistent falcine sinus and the occipital sinus was noted. Dominance patterns of the transverse sinus system were determined. Mean diameters of each sinus were plotted as a function of age. The prevalence of persistent prenatal sinuses and transverse sinus–dominance patterns was compared across ages.

**RESULTS:** A total of 429 MR venograms from 429 patients were reviewed. All dural venous sinuses demonstrated a maximal growth rate from 0 to 7 years of age and reached maximal diameters around 5–10 years of age. The prevalence of falcine sinuses and occipital sinuses trended downward across increasing age categories ( $P = .09$  and  $<.0001$ , respectively).

**CONCLUSIONS:** Dural venous sinuses demonstrate maximal growth between 0 and 7 years of age and reach adult size around 5–10 years of age. Involution of the prenatal sinuses continues to take place after birth into childhood but is largely absent in early adulthood.

**ABBREVIATIONS:** DVS = dural venous sinus; SSS = superior sagittal sinus; VOG = vein of Galen

Evidence continues to accumulate supporting the idea that the dural venous sinus (DVS) system is a plastic, active player in cerebrovascular pathology rather than a fixed and immutable entity.<sup>1,2</sup> As the role that the DVS system plays in cerebrovascular disease continues to expand, an understanding of the normal developmental patterns of the DVS system becomes increasingly important. The fixed anatomy of the DVS system and the prevalence of certain anatomic variations are relatively well-understood.<sup>3,4</sup> The developmental patterns of individual components of the DVS system from birth into adulthood, however, remain relatively unknown. This study consisted of the following 4 objectives: 1) to

elucidate the growth patterns of each dural venous sinus from birth to 20 years of age, 2) to compare the mean size of each dural venous sinus among ages, 3) to compare the prevalence of persistent prenatal sinuses among ages, and 4) to determine the prevalence of transverse sinus–dominance patterns among ages.

## MATERIALS AND METHODS

### Patients

This was a cross-sectional retrospective study of MRVs obtained at a single institution. Institutional review board approval was obtained before the initiation of this study. All included patients provided written informed consent for involvement in research activities at our institution. MR venography was chosen as the imaging technique over CT venography because younger populations at our institution preferentially undergo MRV over CTV to mitigate radiation exposure; therefore, a larger population of patients 20 years of age and younger had available MRV imaging studies. MR venogram studies of the cerebral venous system that were obtained between 2017 and 2019 were reviewed. These

Received May 24, 2020; accepted after revision August 5.

From the Departments of Radiology (A.S.L., G.L., W.B.) and Neurosurgery (G.L., W.B.), Mayo Clinic, Rochester, Minnesota.

Please address correspondence to Anthony Larson, BS, Department of Radiology, Mayo Clinic, 200 First St SW, Rochester, MN 55905; e-mail: lars4689@umn.edu; @TonyLarsonBS



Indicates article with supplemental on-line table.

<http://dx.doi.org/10.3174/ajnr.A6816>

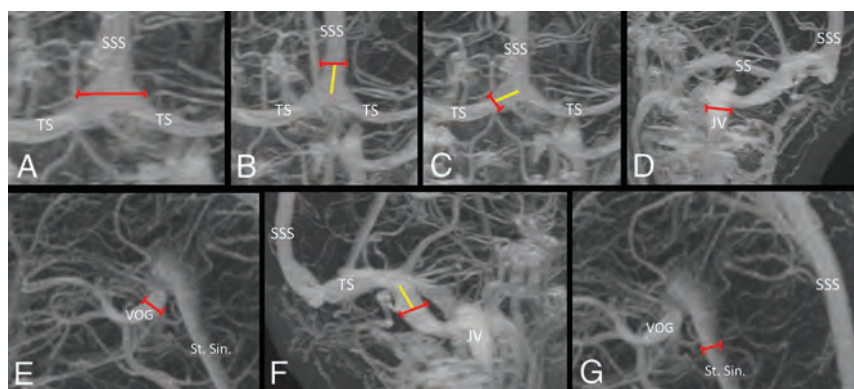


**FIG 1.** Measurement strategy for determining the diameter of components of dural venous sinuses. A, The maximal diameter of torcula is obtained. Superior sagittal sinus (B) and bilateral transverse sinuses (C) are measured (red line) 1 cm away from the center of the torcula (yellow line). D, The maximal diameter of the internal jugular vein is measured at the skull base. E, The maximal diameter of the vein of Galen is obtained. F, The sigmoid sinuses are measured (red line) 1 cm distal to the transverse sigmoid junction (yellow line). G, The maximal diameter of the straight sinus is obtained. JV indicates jugular vein; SS, sigmoid sinus; St. Sin., straight sinus; TS, transverse sinus; SSS, superior sagittal sinus; VOG, vein of Galen.



**FIG 2.** Examples of various transverse venous sinus anatomy patterns. A, Codominance between the right (solid arrow) and left (dashed arrow) transverse sinuses. B, Right-side-dominant (solid white arrow) transverse sinus compared with the left (dashed white arrow), with an occipital sinus noted (black arrow). C, Left-side-atretic transverse sinus (dashed arrow) with flow through the right (solid white arrow).

included both contrast-enhanced and non-contrast-enhanced venograms. The indications for obtaining an MRV included headache, migraine, ruling out venous sinus thrombosis, seizures, coagulation defects, papilledema, postconcussive syndrome, or a history of malignancy. In patients with multiple MR venograms, only the earliest study was included. Studies were excluded if the patient was found to have 1 of following vascular anomalies: an arteriovenous malformation involving a draining vein into a dural venous sinus, a dural arteriovenous fistula, dural venous sinus thrombosis, vein of Galen (VOG) malformation, or any kind of external compression of the venous sinuses. Data extracted from each MRV study included the diameter of the specific components of the DVS system, the presence of any persistent prenatal sinus including the persistent falcine sinus or occipital sinus, and the dominance patterns of the transverse venous system. Patient age at the time of MRV imaging was obtained. We used the following age categories: younger than 1, 1–5, 6–10, 11–15, and 16–20 years of age.

### Venogram Parameters

Gadolinium bolus MRV examinations were performed on multiple 3T scanners (Discovery M750; GE Healthcare) throughout our institution using a 64-channel coil. Images were obtained in

the sagittal plane. We used the following scan parameters: TR = 3.83 ms, TE = 1.39 ms, section thickness = 0.65 mm, skip = 20%, FOV = 240 mm.

### Measurements of the Dural Venous Sinus System

All measurements were made by a single author. All measurements were obtained on a 3D MR venogram with or without contrast. Measurements were obtained of the diameter of the following DVS components: superior sagittal sinus (SSS), straight sinus, VOG, torcular Heterophili, bilateral transverse sinuses, bilateral sigmoid sinuses, and bilateral internal jugular veins. The SSS and transverse sinuses were measured 1 cm from the middle of the torcula as performed previously.<sup>5</sup> The maximum diameters of the straight sinus, VOG, and torcula were measured. Because the diameters of the straight sinus and VOG could be relatively small in some cases (particularly in younger patients), the maximum diameter of each was measured on each study for consistency and ease of measurement across studies. The diameters of the sigmoid sinuses were measured 1 cm distal to the transverse-sigmoid junction, and the diameter of the internal jugular vein was measured at the base of the skull.<sup>5</sup>

The anatomy of the transverse sinus system was classified as codominant, right-side-dominant, left-side-dominant, right-side-atretic, or left-side-atretic. All measurements were performed in QREADS imaging software (Mayo Clinic). Figure 1 is an example of the measurement process, and Fig 2 shows sample patterns of transverse sinus anatomy.

### Validation of Venous Sinus Measurements

To validate measurements made on 3D MR venograms, we selected 20 patients with available 2D MR venograms and obtained measurements of each DVS component measured on 3D images. Patients were selected from each age category to represent the age distributions of the overall population included in the study. The SSS was measured in the axial plane approximately 1 cm from the torcula. The torcula and internal jugular veins were, likewise, measured in the axial plane. The largest dimensions of the straight sinus and VOG were measured in the coronal plane. The bilateral transverse sinuses were measured in the sagittal plane 1 cm from the torcula. The sigmoid sinuses were measured in the axial plane approximately 1 cm from the transverse-sigmoid junction. Mean values of each DVS component as measured on 2D MR venograms were calculated and compared with the mean values as measured on the 3D MR venograms of the 20 patients included.

## Statistical Analysis

Means and SDs were calculated for continuous variables. Student's 2-tailed *t* test was used to determine significance between mean diameter values in the imaging-validation analysis. Percentages were calculated for binary/categorical variables. The  $\chi^2$  test was used to determine the significance among categorical variables. To compare the diameters of individual venous sinuses by age, we plotted measurements against age and applied a trivariate fit to the graph. Any *P* value < .05 was considered statistically significant. All calculations took place in Excel (Microsoft) and SPSS Statistics for Windows (Version 25.0; IBM).

## RESULTS

### Patients and Baseline Information

In total, 488 venograms from 477 patients were reviewed. Three patients had 3 MR venograms included, and 5 patients had 2 venograms included. Fifty-five imaging studies were excluded for

the following reasons: AVM draining into a dural venous sinus (*n* = 6), venous sinus compression (*n* = 1), dural arteriovenous fistula (*n* = 3), venous sinus thrombosis (*n* = 43), and VOG malformation (*n* = 2). Three patients had multiple venograms: Two patients had 2 venograms, and 1 patient had 3. After exclusion, we included 429 venograms from 429 patients. Patient and baseline information are further summarized in Table 1.

### Venous Sinus Diameter by Age

The following data are summarized in Table 2. Regarding the transverse sinuses, the largest mean dimension for the right transverse sinus was found in the 6- to 10-year age category ( $8.1 \pm 2.0$  mm), whereas the largest mean dimension for the left transverse sinus was found in 6–10 and 11–15 age categories ( $6.4 \pm 2.5$  mm and  $6.4 \pm 2.4$  mm, respectively). The torcula ranged from  $8.4 \pm 4.1$  mm in the younger than 1-year category to  $17.4 \pm 4.1$  mm in the 16–20 age category. The SSS ranged from  $4.0 \pm 1.5$  mm in the younger than 1-year category to  $8.8 \pm 1.6$  mm in the 6- to 10-year category. The straight sinus ranged from  $3.9 \pm 1.1$  mm in the younger than 1-year category to  $5.4 \pm 2.7$  mm in the 1- to 5-year age category. The VOG ranged from  $3.2 \pm 0.8$  mm in younger than 1-year category to  $4.9 \pm 1.0$  mm in the 11- to 15-year age category. Regarding the right and left sigmoid sinuses, the maximum size was observed in the 11–15 category ( $10.1 \pm 2.4$  mm) and the 16–20 age category ( $9.0 \pm 2.1$  mm), respectively. Regarding the internal jugular veins, the maximum mean diameter was observed in the 16–20 age category on both right and left sides ( $10.0 \pm 2.2$  and  $8.1 \pm 2.1$  mm, respectively).

To determine at which specific age the sinuses of the DVS system reached maximal diameter, we plotted the diameter of

each sinus as a function of age. The plots are shown in Figs 3 and 4. The SSS, torcula, straight sinus, and VOG all reached maximal diameter by 7–10 years of age. Both the right and left transverse venous sinuses reached maximal size around 5–7 years of age. The left sigmoid sinus reached maximal diameter around 7–10 years of age, while the right sigmoid sinus reached maximal size around 12.5 years of age. The right and left internal jugular veins reached maximal size around 7–10 years of age.

**Table 1: Baseline demographics**

Demographics	
Total MR venograms Included	429
Total patients included	429
No. of MR venograms with IV contrast (%)	327 (76.2)
Age categories (No.) (%) (yr)	
0	25 (5.8)
1–5	24 (5.6)
6–10	21 (4.9)
11–15	70 (16.3)
16–20	289 (67.4)
Mean age (SD) (yr)	15.1 (5.9)
Male (No.) (%)	129 (30.0)

**Table 2: Variations in size measurements of cerebral venous system components by age<sup>a</sup>**

	Age Category (Years)				
	<1	1–5	6–10	11–15	16–20
No.	25	24	21	70	289
Right transverse sinus diameter (mm)	3.7 (2.1)	5.4 (2.8)	8.1 (2.0)	7.1 (2.2)	7.6 (2.1)
Left transverse sinus diameter (mm)	3.1 (2.2)	5.9 (3.1)	6.4 (2.5)	6.4 (2.4)	6.1 (2.0)
Torcula	8.4 (4.1)	13.3 (4.5)	15.4 (3.4)	16.5 (4.1)	17.4 (4.1)
Superior sagittal sinus	4.0 (1.5)	7.4 (2.5)	8.8 (1.6)	8.6 (1.9)	8.7 (1.6)
Straight sinus	3.9 (1.1)	5.4 (2.7)	5.2 (1.6)	5.2 (1.5)	4.8 (1.3)
Vein of Galen	3.2 (0.8)	4.4 (1.1)	4.8 (0.9)	4.9 (1.0)	4.8 (1.0)
Right sigmoid sinus	5.0 (2.1)	6.7 (1.4)	8.6 (2.4)	10.1 (2.4)	10.0 (1.9)
Left sigmoid sinus	4.0 (2.0)	7.3 (2.8)	8.0 (2.2)	8.8 (2.5)	9.0 (2.1)
Right internal jugular vein	4.4 (1.5)	6.8 (1.4)	9.0 (2.2)	9.9 (2.2)	10.0 (2.2)
Left internal jugular vein	3.9 (1.4)	6.8 (2.8)	7.4 (1.7)	7.8 (2.2)	8.1 (2.1)

<sup>a</sup> Data are mean diameters (SD).

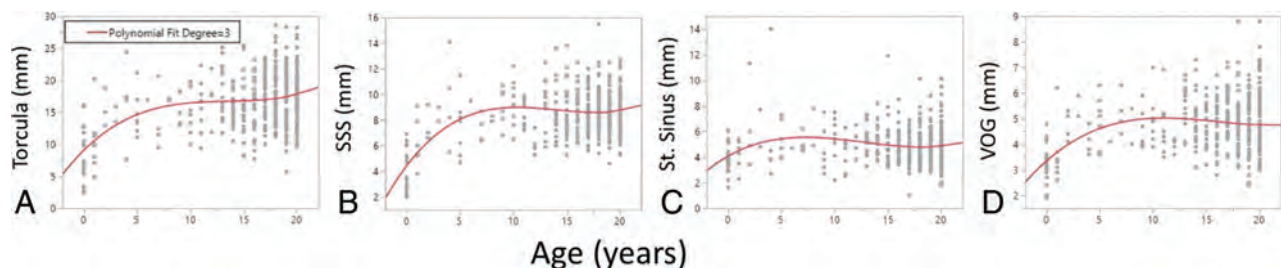


**FIG 3.** Variations in venous size by age in the torcula (A), superior sagittal sinus (B), straight sinus (C), and vein of Galen (D). SSS indicates superior sagittal sinus; St. Sinus, straight sinus; VOG, vein of Galen.



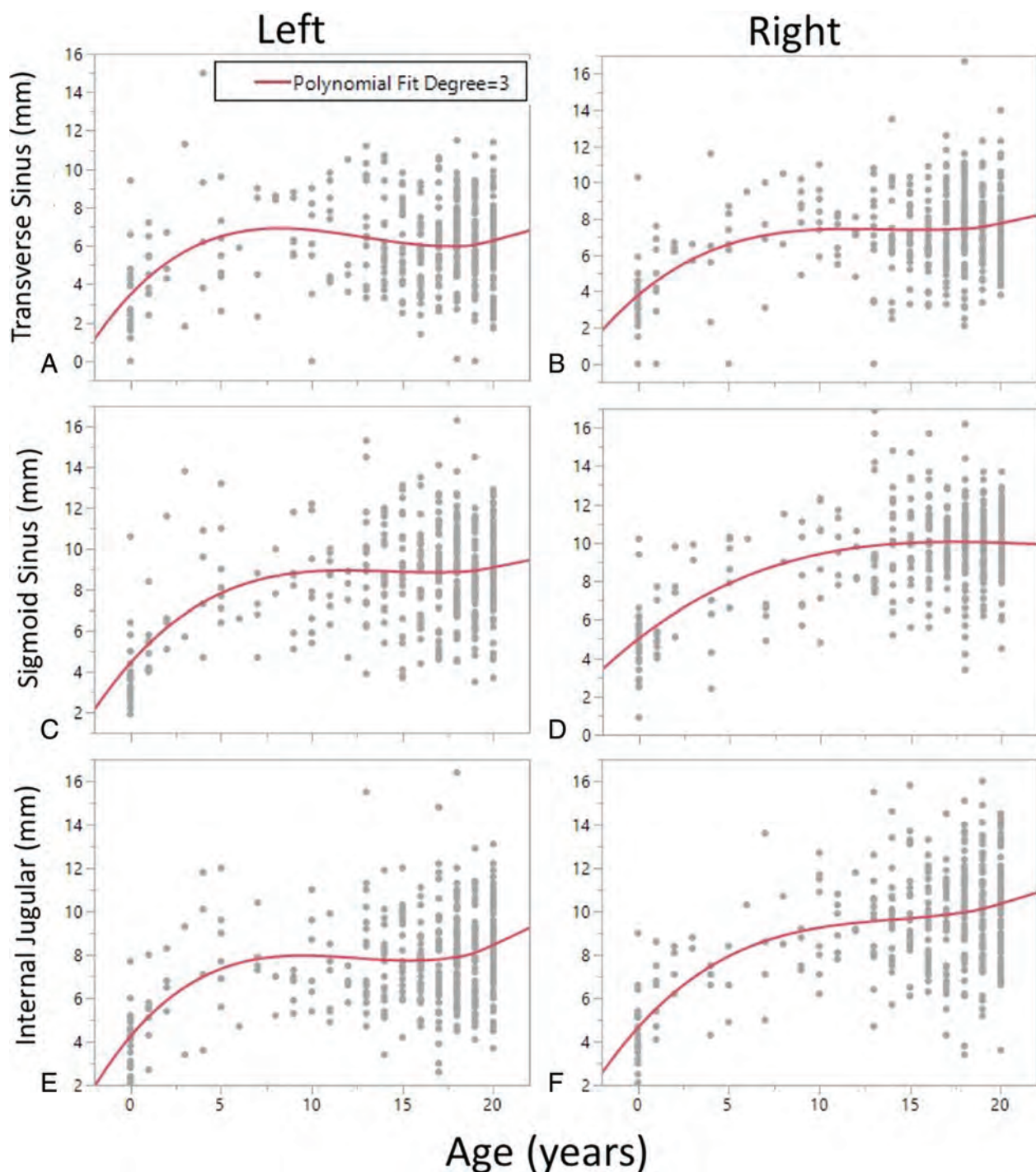


**FIG 4.** Variations in venous sinus size by age in the left (A) and right (B) transverse venous sinuses, left (C) and right (D) sigmoid sinuses, and left (E) and right (F) internal jugular veins.

#### Validation of Venous Sinus Measurements

The age distribution of patients included in the validation analysis was as follows: One patient (5%) was younger than 1 year of age, 1 patient (5%) was between 1 and 5 years of age, 1 patient (5%) was between 6 and 10 years of age, 3 patients (15%) were between 11 and 15 years of age, and 14 patients (70%) were between 16 and 20 years of age. For all components of the DVS system, there were no differences between the mean values of the measurements made on 2D MR venograms compared with

the mean values of measurements made on 3D MR venograms. These data are summarized in the On-line Table.

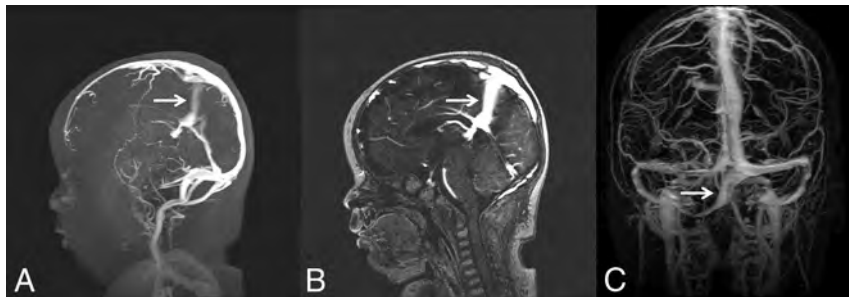
#### Persistent Prenatal Sinuses by Age Category

The following data are summarized in Table 3. A persistent fal-cine sinus was observed in 8.0% of the younger than 1-year age category. This percentage trended downward to 1.4% of the 16- to 20-year age category, yet the difference between groups did not reach statistical significance ( $P = .09$ ). A similar downward trend

**Table 3: Persistence of postnatal sinuses by age**

	Age Category (Years)					P Value
	<1	1–5	6–10	11–15	16–20	
No.	25	24	21	70	289	—
Persistent falcine sinus (No.) (%)	2 (8.0)	2 (8.3)	1 (4.8)	2 (2.9)	4 (1.4)	.09
Occipital sinus (No.) (%)	6 (24.0)	6 (25.0)	1 (4.8)	6 (8.7)	8 (2.8)	<.0001

**Note:**— indicates that no *P*-value was calculated.

**FIG 5.** Examples of embryonic sinuses. Persistent falcine sinus in a 2-month-old infant seen on 3D-MRV (A) and a sagittal section of 2D-MRV (B, arrows). C, Occipital sinus (arrow).**Table 4: Transverse venous sinus anatomy patterns by age**

	Age Category (Years)					P Value
	<1	1–5	6–10	11–15	16–20	
No. patients in each age category	25	24	21	70	289	—
Codominant (No. of patients) (% of age group)	12 (48.0)	12 (50.0)	8 (38.1)	37 (52.9)	177 (61.2)	.14
Right-dominant	8 (32.0)	4 (16.7)	9 (42.9)	22 (31.4)	76 (26.3)	.18
Left-dominant	3 (12.0)	6 (25.0)	3 (14.3)	9 (12.9)	23 (8.0)	
Right-atretic	1 (4.0)	1 (4.2)	0 (0.0)	1 (1.4)	3 (1.0)	.81
Left-atretic	1 (4.0)	1 (4.2)	1 (4.8)	1 (1.4)	10 (3.4)	

**Note:**— indicates that no *P*-value was calculated.

was noted with the occipital sinus, which was present in 24.0% of the younger than 1-year population and trended downward to 2.8% of the 16- to 20-years of age category ( $P < .0001$ ). A sample MRV of a persistent falcine sinus and occipital sinus is demonstrated in Fig 5.

#### Transverse Sinus Anatomy Patterns by Age Category

Regarding the anatomic makeup of the transverse sinus system, codominance was observed most commonly in all age categories except the 6- to 10-year category, in which right-sided transverse sinus dominance was most commonly observed. Right-sided dominance was more commonly seen than left-sided dominance in all age categories except ages 1–5. There was no difference in the prevalence of codominance across age categories ( $P = .14$ ). There was no difference in the prevalence of left-versus-right-sided dominance across age categories ( $P = .18$ ). This was also true when comparing left-versus-right-sided atresia ( $P = .81$ ). These data are summarized in Table 4.

## DISCUSSION

Our study of 429 MR venograms demonstrates the patterns of development of the major sinuses of the DVS system from birth to

20 years of age. Three important findings are evident: First, dural venous sinuses, in general, demonstrated maximal growth between 0 and 7 years of age, and most sinuses reached adult size around 7–10 years of age. This finding emphasizes the postnatal plasticity of the DVS system. Second, a higher prevalence of the persistent pre-natal sinuses was found in younger age categories compared with older categories, implying that involution of these sinuses continues to take place after birth into childhood but largely ceases in early adulthood. Finally, we found no difference in patterns of transverse venous sinus drainage across age categories, suggesting that transverse venous sinus dominance patterns are maintained into early adulthood.

The main finding from our study is that postnatal growth of the DVS system continues until 10 years of age after which diameters remain stable. These findings track closely with the rates of head circumference growth as well as growth of the intracranial arteries across time.<sup>6</sup> There are important clinical implications to understanding the rate of change of the cerebral venous system across time. For example, with the growing use of venous sinus stent placement for treatment of idiopathic intracranial hypertension in adults, there have been

several reports in the literature describing venous sinus stent placement to treat pediatric patients.<sup>7–9</sup> An understanding of normal age-related venous sinus diameters would be important for device sizing and treatment planning in these patients. There are also growing reports on mechanical endovascular recanalization of venous sinus thrombosis in the pediatric population, and again, having an understanding of the normal venous sinus diameters would be important for sizing of thrombectomy devices.<sup>10,11</sup>

Our data suggest a gradual involution of the occipital and persistent falcine sinuses from birth to 20 years of age. The occipital sinus originates from the torcular plexus and is discernable as early as the third gestational month.<sup>12,13</sup> Secondary to increased hemodynamic burden within the developing posterior fossa, the occipital sinus demonstrates a rapid expansion in the fourth and fifth gestational months, followed by diminution in the sixth and seventh months.<sup>12,13</sup> The presence of an occipital sinus in post-natal life is, therefore, less commonly observed. Similar to the pattern observed in the current study, Widjaja and Griffiths<sup>5</sup> found an occipital sinus in 9 of 50 patients (18%), most of whom were younger than of 2 years of age, and none were found in those older than 9 years of age. Additionally, Mizutani et al<sup>14</sup> found that 6 of 13 infants (46.2%) had an occipital sinus, compared with

only 3 of 35 adults (8.6%), suggesting that persistent occipital sinuses largely regress by adulthood.

Persistent falcine sinuses are exceptionally rare and are typically present in the context of absent, hypoplastic, or occluded venous outflow tracts.<sup>15,16</sup> This observation implies that alterations in cerebral venous flow dynamics may result in recanalization of the falcine sinus. In the current study, we observed a trend in which the prevalence of the persistent falcine sinus decreased across age categories; this trend may suggest that venous outflow dynamics normalize with increasing age, thereby prompting involution of the falcine sinus. One separate study found no difference in the prevalence of persistent falcine sinuses between infants and adults.<sup>14</sup> This finding is likely due to small sample sizes, however, given that persistent falcine sinuses have an exceptionally low prevalence overall. The findings of the current study relating to the prevalence of the falcine and occipital sinuses demonstrate the dynamic nature of the DVS system in younger age categories.

Prenatal formation of the transverse venous sinuses is characterized by rapid expansion in the fourth fetal month, which is followed by contraction to a relatively stable diameter at 7–8 months of fetal life.<sup>12,13,17</sup> Much variation exists within the anatomic patterns of the transverse venous system. Although many individuals have a codominant transverse venous system, a large proportion of the population exhibits unilateral dominance, typically on the right, suggesting that a single transverse sinus is sufficient in providing outflow for the superficial venous system.<sup>13,18</sup> Nevertheless, changes in transverse sinus dimensions to compensate for altered flow mechanics may occur.<sup>19</sup> Our data here demonstrate that transverse sinus patterns do not change as a result of increasing age, suggesting that the in utero establishment of a transverse sinus–dominance pattern is sufficient for maintaining adequate venous drainage from birth into adulthood. Our study may be limited in the conclusions that may be drawn in this regard; however, the transverse sinuses were found to be codominant in every age group other than the 6- to 10-year-old patients, suggesting that the dural venous sinuses are still developing in younger children and that 1 transverse sinus becomes unilaterally dominant by 6–10 years of age. If this scenario were the case, however, this pattern of transverse sinus dominance would be prevalent in adulthood as well. Given that this pattern was not found to be prevalent, this issue suggests a potential sampling error in our study. Further study is, therefore, warranted to more fully elucidate developmental patterns of the transverse sinus system.

Fetal development of the cerebral DVS system is highly complex and begins early in fetal development.<sup>5,13</sup> The findings from our study highlight the incredibly dynamic nature of the dural venous sinus system with rapid growth of some sinuses and regression of others in postnatal life and into early childhood. The dynamic character of the cerebral venous system and its role in the pathogenesis of various intracranial vascular malformations has only recently been acknowledged.<sup>2</sup> For example, several reports of de novo formation of vascular malformations with venous components imply active pathogenetic involvement of the venous system.<sup>20–22</sup> Our understanding of the role of the venous system in various pathologic states continues to evolve.

Important limitations of this report must be considered. Our study population was heavily skewed toward those 16–20 years of

age; therefore, the prevalence of embryonic sinuses may be underestimated in the younger age categories. Our study is prone to selection bias for 2 reasons: All those who had MRV studies had a clinical indication for imaging, and the patient population was obtained from a single quaternary referral center.

Most important, a minority of studies ( $n = 23.8$ ) were not performed with contrast, possibly resulting in suboptimal measurements. Our measurements were made on 3D MR venograms, which may make it difficult to ascertain the true diameter of a 2D structure (ie, the diameter of the lumen of a given venous sinus). Ideally, measurements would be made on a 2D image on which the image section is perpendicular to the long axis of the vessel. However, our validation analysis found no differences between measurements made on 3D and 2D; therefore, our measurement protocol was sufficient for the purposes of this study. Future studies should adopt stringent quality control measures with regard to the technical aspects of each study because various physiologic and imaging-based parameters may potentially affect the measured diameter of each DVS system component. Future studies should also consist of multiple measurements made by multiple authors for validation purposes.

## CONCLUSIONS

We studied 429 MR venograms to demonstrate patterns of development of the DVS system from birth to 20 years of age. In general, dural venous sinuses demonstrated maximal growth between 0 and 7 years of age, which demonstrates postnatal plasticity of the cerebral venous system. Involution of persistent prenatal sinuses continues to take place after birth into childhood but largely ceases in early adulthood. Transverse venous sinus dominance patterns are likely maintained throughout the aging process.

Disclosures: Giuseppe Lanzino—UNRELATED: Board Membership: Superior Medical Editing, Nested Knowledge.

## REFERENCES

1. Mullan S, Mojtahedi S, Johnson DL, et al. **Embryological basis of some aspects of cerebral vascular fistulas and malformations.** *J Neurosurg* 1996;85:1–8 CrossRef Medline
2. Aboian MS, Daniels DJ, Rammos SK, et al. **The putative role of the venous system in the genesis of vascular malformations.** *Neurosurg Focus* 2009;27:E9 CrossRef Medline
3. Bisaria KK. **Anatomic variations of venous sinuses in the region of the torcular Herophili.** *J Neurosurg* 1985;62:90–95 CrossRef Medline
4. Cure JK, Van Tassel P, Smith MT. **Normal and variant anatomy of the dural venous sinuses.** *Semin Ultrasound CT MR* 1994;15:499–519 CrossRef Medline
5. Widjaja E, Griffiths PD. **Intracranial MR venography in children: normal anatomy and variations.** *AJNR Am J Neuroradiol* 2004;25:1557–62 Medline
6. Vaughan J, Taylor M, Leach JL, et al. **Abstract TMP113: non-invasive estimate of intracranial arterial luminal diameter in children.** *Stroke* 2020;51(Suppl 1):ATMP113
7. Tibussek D, Distelmaier F, von Kries R, et al. **Pseudotumor cerebri in childhood and adolescence: results of a Germany-wide ESPED-survey.** *Klin Padiatr* 2013;225:81–85 CrossRef Medline
8. Buell TJ, Starke RM, Ding D, et al. **Venous sinus stenting using transcranial access for the treatment of idiopathic intracranial hypertension in a pediatric patient.** *J Neurosci Rural Pract* 2017;8:672–75 CrossRef Medline



9. Rajpal S, Niemann DB, Turk AS. **Transverse venous sinus stent placement as treatment for benign intracranial hypertension in a young male: case report and review of the literature.** *J Neurosurg* 2005;102:342–46 CrossRef Medline
10. Csakanyi Z, Rosdy B, Kollar K, et al. **Timely recanalization of lateral sinus thrombosis in children: should we consider hypoplasia of contralateral sinuses in treatment planning?** *Eur Arch Otorhinolaryngol* 2013;270:1991–98 CrossRef Medline
11. Omoto K, Nakagawa I, Park HS, et al. **Successful emergent endovascular mechanical thrombectomy for pediatric and young adult cerebral venous sinus thrombosis in coma.** *World Neurosurg* 2019;122:203–08 CrossRef Medline
12. Okudera T, Huang YP, Ohta T, et al. **Development of posterior fossa dural sinuses, emissary veins, and jugular bulb: morphological and radiologic study.** *AJNR Am J Neuroradiol* 1994;15:1871–83 Medline
13. Tubbs RS. *Anatomy, Imaging and Surgery of the Intracranial Dural Venous Sinuses: E-Book.* Elsevier Health Sciences; 2019
14. Mizutani K, Miwa T, Akiyama T, et al. **Fate of the three embryonic dural sinuses in infants: the primitive tentorial sinus, occipital sinus, and falcine sinus.** *Neuroradiology* 2018;60:325–33 CrossRef Medline
15. Raybaud CA, Strother CM, Hald JK. **Aneurysms of the vein of Galen: embryonic considerations and anatomical features relating to the pathogenesis of the malformation.** *Neuroradiology* 1989;31:109–28 CrossRef Medline
16. Manoj KS, Krishnamoorthy T, Thomas B, et al. **An incidental persistent falcine sinus with dominant straight sinus and hypoplastic distal superior sagittal sinus.** *Pediatr Radiol* 2006;36:65–67 CrossRef Medline
17. Kopuz C, Aydin ME, Kale A, et al. **The termination of superior sagittal sinus and drainage patterns of the lateral, occipital at confluens sinuum in newborns: clinical and embryological implications.** *Surg Radiol Anat* 2010;32:827–33 CrossRef Medline
18. Durgun B, Ilgt ET, Cizmeli MO, et al. **Evaluation by angiography of the lateral dominance of the drainage of the dural venous sinuses.** *Surg Radiol Anat* 1993;15:125–30 CrossRef Medline
19. Nicholson P, Lenck S, Kucharczyk W, et al. **Dynamic nature of intracranial venous sinuses in idiopathic intracranial hypertension.** *Interv Neuroradiol* 2020;26:118–20 CrossRef Medline
20. Perrini P, Lanzino G. **The association of venous developmental anomalies and cavernous malformations: pathophysiological, diagnostic, and surgical considerations.** *Neurosurg Focus* 2006;21:e5 CrossRef Medline
21. Campeau NG, Lane JI. **De novo development of a lesion with the appearance of a cavernous malformation adjacent to an existing developmental venous anomaly.** *AJNR Am J Neuroradiol* 2005;26:156–59 Medline
22. Brinjikji W, El-Masri AE, Wald JT, et al. **Prevalence of cerebral cavernous malformations associated with developmental venous anomalies increases with age.** *Childs Nerv Syst* 2017;33:1539–43 CrossRef Medline

# Risk Factors for Early Brain AVM Rupture: Cohort Study of Pediatric and Adult Patients

 L. Garzelli,  E. Shotar,  T. Blauwblomme,  N. Sourour,  Q. Alias,  S. Stricker,  B. Mathon,  M. Kossorotoff,  F. Gariel,  N. Boddaert,  F. Brunelle,  P. Meyer,  O. Naggara,  F. Clarençon, and  G. Boulouis

## ABSTRACT

**BACKGROUND AND PURPOSE:** Whether architectural characteristics of ruptured brain AVMs vary across the life span is unknown. We aimed to identify angioarchitectural features associated with brain AVMs ruptured early in life.

**MATERIALS AND METHODS:** Patients with ruptured brain AVMs referred to 2 distinct academic centers between 2000 and 2018 were pooled and retrospectively analyzed. Imaging was retrospectively reviewed for angioarchitectural characteristics, including nidus size, location, Spetzler-Martin grade, venous drainage, and arterial or nidal aneurysm. Angioarchitecture variations across age groups were analyzed using uni- and multivariable models; then cohorts were pooled and analyzed using Kaplan-Meier and Cox models to determine factors associated with earlier rupture.

**RESULTS:** Among 320 included patients, 122 children (mean age,  $9.8 \pm 3.8$  years) and 198 adults (mean age,  $43.3 \pm 15.7$  years) were analyzed. Pediatric brain AVMs were more frequently deeply located (56.3% versus 21.2%,  $P < .001$ ), with a larger nidus (24.2 versus 18.9 mm,  $P = .002$ ), were less frequently nidal (15.9% versus 23.5%,  $P = .03$ ) and arterial aneurysms (2.7% versus 17.9%,  $P < .001$ ), and had similar drainage patterns or Spetzler-Martin grades. In the fully adjusted Cox model, supratentorial, deep brain AVM locations (adjusted relative risk, 1.19; 95% CI, 1.01–1.41;  $P = .03$  and adjusted relative risk, 1.43; 95% CI, 1.22–1.67;  $P < .001$ , respectively) and exclusively deep venous drainage (adjusted relative risk, 1.46, 95% CI, 1.21–1.76;  $P < .001$ ) were associated with earlier rupture, whereas arterial or nidal aneurysms were associated with rupture later in life.

**CONCLUSIONS:** The angioarchitecture of ruptured brain AVMs significantly varies across the life span. These distinct features may help to guide treatment decisions for patients with unruptured AVMs.

**ABBREVIATION:** HR = hazard ratio

The most devastating complication of brain AVMs is their rupture, leading to intracranial hemorrhage,<sup>1</sup> responsible for

considerable morbidity and mortality. The management of patients with unruptured brain AVMs relies on the evaluation of the risk-benefit balance between invasive treatment and follow-up. The optimal approach is yet to be determined in pediatric patients,<sup>2</sup> in whom decisions are made more complex by the potential long life span and cumulative risk of rupture. Previous data have shown that brain AVM angioarchitecture evolves across time.<sup>3,4</sup> On the basis of the common model of “wear and tear,” brain AVMs are believed to rupture in sectors with more severe arterial and venous vasculopathies and increased frailty features, more frequently seen in adults than during childhood. Nonetheless, intracranial hemorrhage remains the most common revelation in children, and brain AVMs represent the leading etiology of intracranial hemorrhage in the pediatric group; thus, the identification of individual biomarkers associated with impending or higher risk of rupture is of crucial importance to guide therapeutic management. Several angioarchitectural brain AVM characteristics (deep location, exclusive deep venous drainage, associated aneurysms, or venous ectasia)<sup>5–7</sup> have

Received June 19, 2020; accepted after revision August 6.

From the Department of Neuroradiology (L.G., O.N., G.B.), Sainte-Anne University Hospital, Institut National de la Santé et de la Recherche Médicale Unité Mixte de Recherche 1266, Paris, France; Departments of Neuroradiology (L.G., F.C.) and Neurosurgery (B.M.), Sorbonne University, Paris, France; Departments of Neuroradiology (E.S., N.S., F.C.) and Neurosurgery (B.M.), Pitié-Salpêtrière University Hospital, Public Assistance–Paris Hospitals, Paris, France; Department of Pediatric Neurosurgery (T.B., S.S.), French Center for Pediatric Stroke, Department of Pediatric Imaging (Q.A., N.B., F.B., O.N., G.B.), Department of Pediatric Neurology (M.K.), French Center for Pediatric Stroke, and Department of Anesthesiology (P.M.), Necker-Enfants Malades University Hospital, Public Assistance–Paris Hospitals, Paris, France; Université de Paris (T.B., N.B., F.B., O.N., G.B.), Paris, France; Brain and Spine Institute (B.M.), Institut National de la Santé et de la Recherche Médicale, Unité Mixte de Recherche 1127; Centre National de la Recherche Scientifique, Unité Mixte de Recherche 7225, Paris, France; and Department of Neuroimaging (F.G.), Pellegrin Hospital, University Hospital of Bordeaux, Bordeaux, France.

Paper previously presented at: French Days of Radiology, October 11–14, 2019; Paris, France.

Please address correspondence to Gregoire Boulouis, MD, Pediatric Radiology, Necker Enfants Malades, 149 rue de Sévres, 75006 Paris, France; e-mail: gregoireboulouis@gmail.com; @gboulouis  
<http://dx.doi.org/10.3174/ajnr.A6824>

been identified as being more prevalent in ruptured than in unruptured brain AVMs, but these data are derived mostly from adult samples and remain scarce in pediatric populations.<sup>1,8</sup> Furthermore, such findings do not formally allow identifying characteristics associated with earlier rupture, due to the great risk of recognition biases (eg, the higher prevalence of a biomarker in the ruptured population does not indicate that this biomarker is responsible for a rupture earlier in life).

In this retrospective multicentric cohort of children and adult patients with first brain AVM rupture, we aimed to determine brain AVM angioarchitectural characteristics associated with rupture early in life.

## MATERIALS AND METHODS

### Pediatric Cohort

Pediatric patients with nontraumatic intracranial hemorrhage referred to a pediatric quaternary care center (Necker-Enfants Malades University Hospital), the coordinating center for the French Pediatric Stroke Network, are prospectively collected into an inception retrospective (2003–2008) and prospective (2008–ongoing) registry, described in detail elsewhere.<sup>9,10</sup> This registry was retrospectively queried to identify children with first ruptured brain AVMs. Patients meeting the following criteria were retrospectively screened for inclusion: 1) 28 days to 18 years of age at the time of symptom onset; 2) having nontraumatic intracerebral, intraparenchymal, or intraventricular hemorrhage; and 3) having a ruptured brain AVM.

### Adult Cohort

Records of adult patients with brain AVMs referred to a distinct tertiary care center (Pitié-Salpêtrière University Hospital) between January 1, 2003, and February 1, 2018, as described in detail elsewhere,<sup>11</sup> were retrospectively reviewed. Adult patients with ruptured brain AVMs, naive to any previous targeted treatment, were retrospectively screened for inclusion.

### Data Acquisition

Clinical, demographic, and imaging data (brain 1.5T MR imaging, brain CT, cerebral conventional angiography) were retrospectively assessed. Data included age at presentation, sex, admission Glasgow Coma Scale score, hemorrhage location and volume (AxBxC/2 method<sup>12</sup>), as well as brain AVM angioarchitectural features (nidus size; maximal 2D diameter; location; Spetzler-Martin grade;<sup>13</sup> venous drainage pattern as deep, superficial, or mixed; and nidal or arterial aneurysm). Per guidelines, we assessed the presence of deep venous drainage if the internal cerebral veins, basal veins, or precentral cerebral vein participated in the nidus venous drainage.<sup>14</sup> All data were acquired in consensus by a distinct pair of interventional neuroradiologists (1 senior and 1 junior) in each cohort.

### Ethics

All aspects of the study were in accordance with the General Data Protection Regulation and actual French law and ethics in health-related research. Institutional review board approval was obtained under the reference of Comité de Protection des Personnes Ile de France 3, 18062012. As in all observational studies with retrospective analysis of routinely acquired data, written informed consent

was waived, and patients or children's parents could oppose the use of their health-related data. The article was prepared in accordance with the Strengthening of Reporting of Observational Studies in Epidemiology statement.<sup>15</sup>

### Statistics

Continuous variables were expressed as mean  $\pm$  SD or median (interquartile range) as appropriate. Categorical variables were expressed as absolute numbers with percentages. We compared variable differences between the adult and pediatric cohort (using 18 years of age as a cutoff) univariable analyses with the *t* test, Mann-Whitney *U* test,  $\chi^2$  test, and multivariate analysis of variance as appropriate. Variables associated with the pediatric cohort in univariable analyses at  $P < .1$  were entered into a multivariable nominal logistic regression model; then, a backward elimination was used to eliminate nonsignificant variables. Considering age at presentation as a continuous variable, used as the time to rupture, we performed survival analyses. Data were not censored because birth was the chosen initiation of time to the event and intracranial hemorrhage presentation was the event. We first ran Kaplan-Meier analyses with significance testing with the log-rank test to determine univariate predictors of early rupture. Then we conducted univariable Cox proportional hazards analysis to calculate the unadjusted hazard ratio (HR) for the risk of rupture. Variables with  $P < .1$  in univariable Cox analysis were included in multivariable Cox proportional hazards models to determine adjusted HRs of early rupture. Two-sided *P* values  $< .05$  were considered statistically significant. All statistical analyses were performed using JMP Pro 14.0 (SAS Institute).

## RESULTS

### Patient Population and Baseline Characteristics

A total of 122 children (mean,  $9.8 \pm 3.8$  years of age) and 198 adult patients (mean,  $43.3 \pm 15.7$  years of age) were included in the analysis. There was no difference regarding the female proportion (45.9% versus 42.9%,  $P = .62$ ) or baseline Glasgow Coma Scale score between children and adults, respectively ( $11.6 \pm 3.9$  versus  $12.4 \pm 3.7$ ,  $P = .09$ ) (Table 1). Age distribution at rupture is presented in Fig 1.

Hemorrhages were most commonly supratentorial, with no difference among cohorts (76.7% versus 72.7%,  $P = .45$ ). Intracranial hemorrhage volumes were significantly larger in adults than in children ( $19.8 \pm 16.7$  versus  $38.6 \pm 35.5$  mL,  $P < .001$ ).

### AVM Characteristics

**Pediatric-to-Adult Comparisons.** In univariate analyses, brain AVMs in the pediatric group were more frequently deeply located (56.3% versus 21.2%,  $P < .001$ ) and larger ( $24.2 \pm 14.3$  versus  $18.9 \pm 14.3$  mm,  $P = .002$ ) with less frequent nidal (15.9% versus 23.5%,  $P = .03$ ) and prenidid arterial aneurysms (2.7% versus 17.9%,  $P < .001$ ). There was no significant difference in venous drainage patterns, Spetzler-Martin grade, and nidus location.

After we adjusted for sex, nidus size, pre- or nidal arterial aneurysm presence, and supratentorial location, the nidus size (adjusted OR, 0.95 per millimeter increase; 95% CI, 0.93–0.97;  $P < .001$ ), prenidid aneurysms (adjusted OR, 28.9; 95% CI, 5.6–148;  $P < .001$ ), and nidal aneurysms (adjusted OR, 2.6; 95% CI, 1.1–5.3;  $P = .006$ ) showed a significant association with rupture



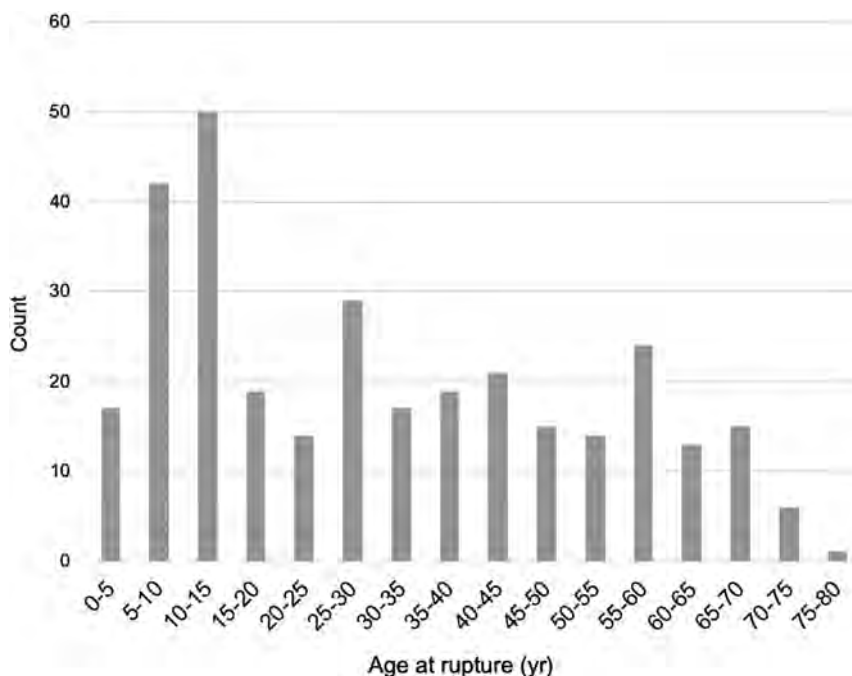
**Table 1: Baseline clinical and imaging characteristics<sup>a</sup>**

Variable	Pediatric (n = 122)	Adult (n = 198)	All (n = 320)	P Value
Clinical presentation				
Age (yr)	9.8 ± 3.8	43.3 ± 15.7	30.8 ± 20.6	<.001
Female sex	56 (45.9%)	85 (42.9%)	141 (44.1%)	.62
GCS at baseline	11.6 ± 3.9	12.4 ± 3.7	12.1 ± 3.8	.09
GCS score <9	33 (28%)	38 (21.2%)	71 (23.9%)	.09
Imaging presentation				
Hemorrhage location				.45
Supratentorial	92 (76.7%)	128 (72.7%)	220 (74.3%)	
Infratentorial	16 (13.3%)	33 (18.8%)	49 (16.6%)	
Other (SAH/IVH)	12 (10%)	15 (8.5%)	27 (9.1%)	
Hemorrhage volume (mL) <sup>b</sup>	19.8 ± 16.7	38.6 ± 35.5	30.6 ± 30.4	<.001
AVM characteristics				
Deep location	67 (56.3%)	42 (21.2%)	109 (34.4%)	<.001
Supratentorial location	103 (86.6%)	153 (77.3%)	256 (80.8%)	.052
Nidus max. diameter	24.2 ± 14.3	18.9 ± 14.3	20.9 ± 14.5	.002
Spetzler-Martin grade				.7
I	24 (20.9%)	49 (26.6%)	73 (24.4%)	
II	50 (43.5%)	75 (40.8%)	125 (41.8%)	
III	27 (23.5%)	44 (23.9%)	71 (23.7%)	
IV	10 (8.7%)	11 (6%)	21 (7%)	
V	4 (3.5%)	5 (2.7%)	9 (3%)	
AVM-related aneurysms				
Nidal aneurysm	18 (15.9%)	42 (23.5%)	60 (20.5%)	.03
Prenidal arterial aneurysm	3 (2.7%)	32 (17.9%)	35 (12%)	<.001
AVM venous drainage				
Exclusively deep	35 (29.7%)	46 (25.8%)	81 (27.4%)	.87
Any deep drainage	58 (49.2%)	86 (48%)	144 (48.5%)	.85

**Note:**—IVH indicates intraventricular hemorrhage; GCS, Glasgow Coma Scale; max., maximum.

<sup>a</sup> Data are presented as absolute count (percentage) and mean ± SD as appropriate.

<sup>b</sup> For 114 and 155 patients with intraparenchymal hemorrhages.

**FIG 1.** Age distribution at rupture in the study sample.

during adulthood. When we forced adjustment for the venous drainage pattern in the same model, deep venous drainage appeared as a risk factor for rupture during childhood (adjusted OR, 0.55; 95% CI, 0.30–0.99;  $P = .04$ ).

## Birth-to-Rupture Survival Analyses.

In univariate survival analysis, AVM supratentorial location, deep location, and exclusively deep venous drainage were associated with earlier rupture (log-rank,  $P < .05$  for all), whereas nidal or prenidil arterial aneurysms were associated with later rupture (log-rank,  $P < .001$ ) (Fig 2). There was no rupture-free survival difference based on the presence of any deep venous drainage (log-rank,  $P = .61$ ).

Similar predictors were found in univariable Cox regression, and the fully adjusted proportional model found AVM supratentorial and deep locations (HR, 1.19; 95% CI, 1.01–1.41;  $P = .03$  and HR, 1.43; 95% CI, 1.22–1.67;  $P < .001$ , respectively) and the absence of an aneurysm (HR, 0.62; 95% CI, 0.46–0.83;  $P < .001$ ) to be associated with earlier rupture (Table 2).

In the above-mentioned model, when we removed deep location to avoid confounding on the venous pattern, an exclusive deep venous drainage became a strong predictor of earlier rupture (adjusted relative risk, 1.46; 95% CI, 1.21–1.76;  $P < .001$ ).

## DISCUSSION

We found that supratentorial and deep locations and exclusive deep venous drainage were more frequently seen in pediatric than in adult ruptured brain AVMs and that these features were associated more generally with rupture earlier in life. We also found that nidal or afferent arterial aneurysms were more prevalent in brain AVMs that rupture later in the life span.

These results contribute to the evidence that various morphologic brain AVM characteristics are associated with brain AVM rupture at initial diagnosis. By inference, variables such as AVM size, deep venous drainage pattern, and associated arterial aneurysms have been considered “risk factors” for brain AVM hemorrhage in general.<sup>4,5,16–18</sup> Here, we extend knowledge by characterizing patterns associated with rupture

across the life span, that is, factors that influence or are seen at earlier or later rupture.

Age group is long known to strongly influence the presentation of brain AVMs,<sup>2</sup> and it has been shown that brain AVMs in

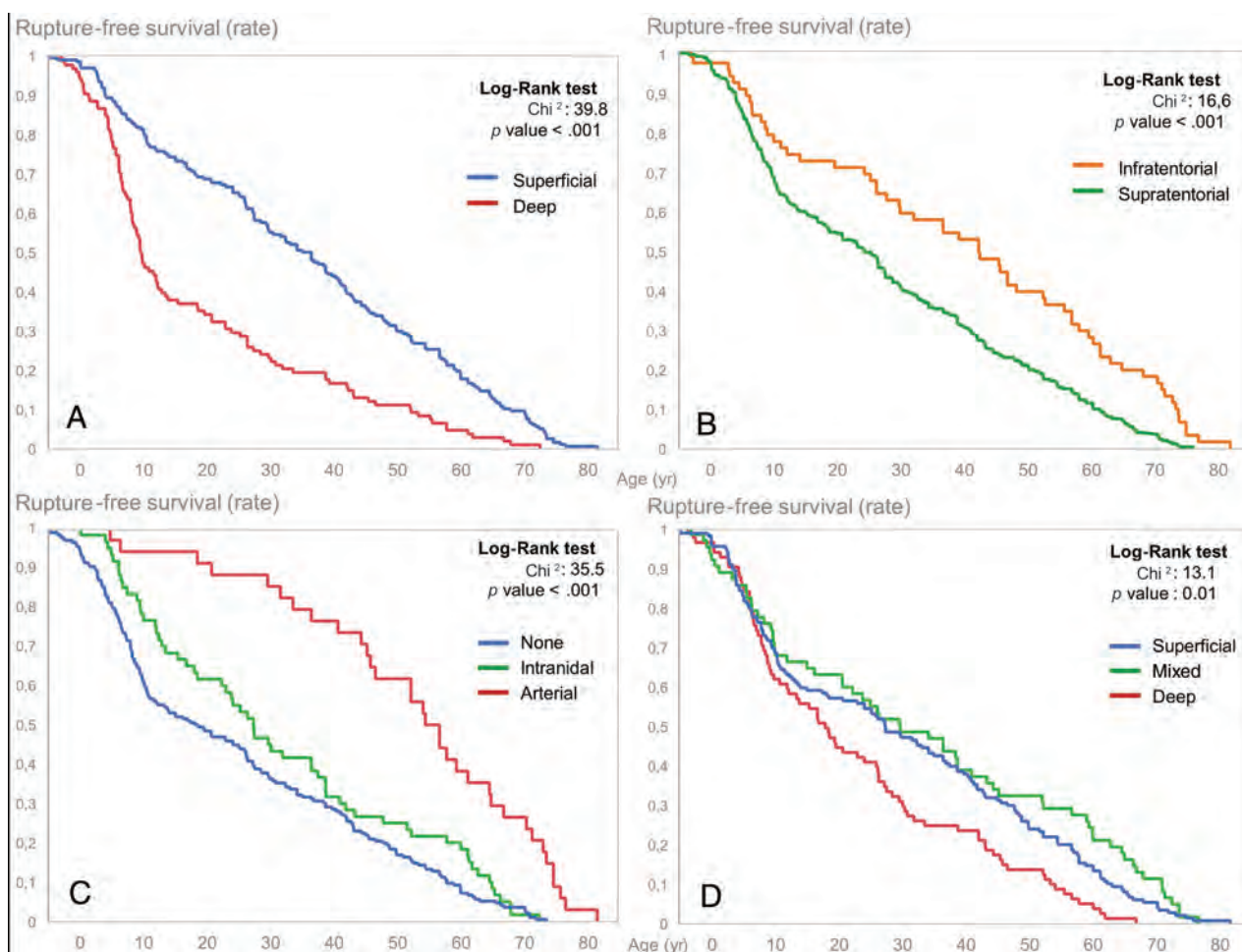


**FIG 2.** Rupture-free survival according to brain AVM characteristics, Kaplan-Meier survival curves, delay until rupture (age in years), and brain AVM location (A and B), aneurysm presence (C), and venous drainage pattern (D).

**Table 2: Uni- and multivariable proportional hazards for time to rupture**

Variable	Univariable <sup>a</sup>			Multivariable <sup>b</sup>		
	RR	95% CI	P Value	aRR	95% CI	P Value
Brain AVM supratentorial location	1.46	1.21–1.76	<.001	1.19	1.01–1.41	.03
Brain AVM deep location	1.46	1.29–1.65	<.001	1.43	1.22–1.67	<.001
Nidus size	1	1–1.01	.36			
Pretrident arterial aneurysm	0.5	0.37–0.65	<.001	0.62	0.46–0.83	<.001
Intracranial aneurysm	1.25	1–1.55	.27			
Any deep venous drainage	1.03	0.92–1.16	.61			
Exclusively deep venous drainage	1.39	1.16–1.67	.002	1.12	0.9–1.4	.43

**Note:**—RR indicates relative risk; aRR, adjusted relative risk.

<sup>a</sup> Confidence intervals are profile-likelihood.

<sup>b</sup> Confidence intervals are Wald.

children disproportionately present with intracranial hemorrhage compared with adults. This finding has led to the common belief that children are at higher risk for brain AVM rupture. Yet, the higher rates of hemorrhages in children with brain AVMs is debated because they may result from confounding by presentation. In other words, the higher rate of hemorrhage in children may only result from children having fewer reasons to undergo brain imaging and have a fortuitous (or near-fortuitous, for instance in headaches) discovery of their brain AVM, in turn

raising the proportion of brain AVMs discovered after a rupture. This has been shown to be true even after correcting for a potential informative censoring (ie, the higher rate of preventive treatment in nonhemorrhagic pediatric brain AVMs).<sup>2</sup> Other authors, alternatively, believe that the difference in hemorrhagic rates may be the result of biologic differences leading to more aggressive/frail brain AVMs that rupture early in children.

Among angioarchitectural characteristics of brain AVMs reported to be associated with rupture at presentation,<sup>1,6,8,18–21</sup>

smaller nidus size was long considered a major rupture risk factor in brain AVM natural history.<sup>22-24</sup> This could be interpreted as a contradiction to our finding because early rupture was associated with larger nidus size. However, in the absence of a control group comprising patients with unruptured brain AVMs, we cannot conclude about the absolute or relative risk of rupture but only infer from survival models that among patients who will experience a rupture, larger brain AVMs are likely to rupture earlier. Furthermore, larger nidi are more likely to become symptomatic in the absence of bleeding than smaller ones, with a higher risk for causing epilepsy or headaches, conditions for which children may be less likely to get brain imaging than adults; this feature may, in turn, explain the over-representation of smaller brain AVMs in previously reported samples of ruptured (versus unruptured) lesions. Furthermore, larger AVMs may uniquely express a hemodynamic or biologic feature that promotes early rupture, but the particular feature may be expressed at a low frequency, yielding to the alternate hypothesis that the risk of rupture may be generally lower for large AVMs, but when larger AVMs rupture, it happens earlier in life.

Recognition bias from previously published works may also explain our finding that supratentorial (rather than infratentorial) location was associated with earlier rupture, challenging the results of Ellis et al<sup>6</sup> and Oulasvirta et al,<sup>8</sup> who observed the opposite. These seemingly contradictory results likely reflect infratentorial brain AVMs only coming to clinical attention after a rupture, while supratentorial lesions may present with other symptoms. Our results, in that sense, add key additional data by establishing that among brain AVMs that first present with hemorrhage, both supratentorial location and larger AVMs are associated with earlier rupture.

We found arterial and intranidal aneurysms to be associated with rupture later in life. In previous studies, Hetts et al<sup>1</sup> and Stapf et al<sup>25</sup> found that aneurysms were significantly associated with later AVM diagnosis, and several converging reports indicate that arterial and nidus aneurysms are more common in older individuals and disproportionately more so in late hemorrhagic presentations.<sup>1,2,6,26</sup> These data as well as our results indicate that these frailty features develop later in life, possibly due to chronic hemodynamic stress,<sup>27</sup> mandate life-long follow-up to detect their appearance, and potentially indicate impending or higher risk of bleeding.<sup>18</sup> Our results in that sense reinforce the assertion that aneurysms (whether arterial or nidus) are manifestations of wear and tear of AVMs forming through a cumulative damage processes and are, therefore, expected to be acquired across time and be expressed more frequently in older patients with AVMs.

The main limitations include the retrospective nature of our study and our results being derived from 2 distinct populations, when it is known that brain AVM characteristics may be heterogeneous across settings.<sup>28</sup> We believe this feature to be a very unlikely source of confusion, given the geographic proximity of both including centers (3 kilometers) and the potential population pool differing only in age.

## CONCLUSIONS

In this large sample of pediatric and adult patients with ruptured brain AVMs, we demonstrated significantly different architectural

features according to age at rupture and showed that earlier rupture was associated with deep, supratentorial brain AVMs with exclusively deep venous drainage, whereas aneurysms (nidus or arterial) were associated with later rupture. Whether these differences reflect biases versus biologic differences in the natural history of brain AVMs along the life span deserves further study.

Disclosures: Nader Sourour—UNRELATED: Consultancy: Medtronic, Balt, MicroVention. Frederic Clarençon—UNRELATED: Board Membership: ArteDrone; Payment for Lectures Including Service on Speakers Bureaus: Penumbra, Stryker, Balt, MicroVention.

## REFERENCES

1. Hetts SW, Cooke DL, Nelson J, et al. **Influence of patient age on angioarchitecture of brain arteriovenous malformations.** *AJNR Am J Neuroradiol* 2014;35:1376–80 CrossRef Medline
2. Fullerton HJ, Achrol AS, Johnston SC, et al; UCSF BAVM Study Project. **Long-term hemorrhage risk in children versus adults with brain arteriovenous malformations.** *Stroke* 2005;36:2099–2104 CrossRef Ref
3. Sure U, Butz N, Schlegel J, et al. **Endothelial proliferation, neoangiogenesis, and potential de novo generation of cerebrovascular malformations.** *J Neurosurg* 2001;94:972–77 CrossRef Medline
4. Redekop G, TerBrugge K, Montanera W, et al. **Arterial aneurysms associated with cerebral arteriovenous malformations: classification, incidence, and risk of hemorrhage.** *J Neurosurg* 1998;89:539–46 CrossRef
5. Gross BA, Du R. **Natural history of cerebral arteriovenous malformations: a meta-analysis.** *J Neurosurg* 2013;118:437–43 CrossRef Medline
6. Ellis MJ, Armstrong D, Vachhrajani S, et al. **Angioarchitectural features associated with hemorrhagic presentation in pediatric cerebral arteriovenous malformations.** *J Neurointerv Surg* 2013;5:191–95 CrossRef Medline
7. Kim H, Al-Shahi Salman R, McCulloch CE, et al; MARS Coinvestigators. **Untreated brain arteriovenous malformation: patient-level meta-analysis of hemorrhage predictors.** *Neurology* 2014;83:590–97 CrossRef Medline
8. Oulasvirta E, Koroknay-Pal P, Hafez A, et al. **Characteristics and long-term outcome of 127 children with cerebral arteriovenous malformations.** *Neurosurgery* 2019;84:151–59 CrossRef Medline
9. Guédon A, Blauwblomme T, Boulouis G, et al. **Predictors of outcome in patients with pediatric intracerebral hemorrhage: development and validation of a modified score.** *Radiology* 2018;286:651–58 CrossRef
10. Blauwblomme T, Bourgeois M, Meyer P, et al. **Long-term outcome of 106 consecutive pediatric ruptured brain arteriovenous malformations after combined treatment.** *Stroke* 2014;45:1664–71 CrossRef
11. Shotar E, Amouyal C, Jacquens A, et al. **S100B serum elevation predicts in-hospital mortality after brain arteriovenous malformation rupture.** *Stroke* 2019;50:1250–53 CrossRef Medline
12. Kothari RU, Brott T, Broderick JP, et al. **The ABCs of measuring intracerebral hemorrhage volumes.** *Stroke* 1996;27:1304–05 CrossRef Medline
13. Spetzler RF, Martin NA. **A proposed grading system for arteriovenous malformations.** *J Neurosurg* 1986;65:476–83 CrossRef Medline
14. Atkinson RP, Awad IA, Batjer HH, et al; Joint Writing Group of the Technology Assessment Committee American Society of Interventional and Therapeutic Neuroradiology; Joint Section on Cerebrovascular Neurosurgery a Section of the American Association of Neurological Surgeons and Congress of Neurological Surgeons; Section of Stroke and the Section of Interventional Neurology of the American Academy of Neurology. **Reporting terminology for brain arteriovenous malformation clinical and radiographic features for use in clinical trials.** *Stroke* 2001;32:1430–42 CrossRef Medline
15. von Elm E, Altman DG, Egger M, et al; STROBE Initiative. **The Strengthening the Reporting of Observational Studies in Epidemiology (STROBE) Statement: guidelines for reporting observational studies.** *Int J Surg* 2014;12:1495–99 CrossRef Medline



16. Shotar E, Pistocchi S, Haffaf I, et al. **Early rebleeding after brain arteriovenous malformation rupture, clinical impact and predictive factors: a monocentric retrospective cohort study.** *Cerebrovasc Dis* 2017;44:304–12 CrossRef Medline
17. Nataf F, Meder JF, Roux FX, et al. **Angioarchitecture associated with haemorrhage in cerebral arteriovenous malformations: a prognostic statistical model.** *Neuroradiology* 1997;39:52–58 CrossRef Medline
18. Stapf C, Mast H, Sciacca RR, et al. **Predictors of hemorrhage in patients with untreated brain arteriovenous malformation.** *Neurology* 2006;66:1350–55 CrossRef Medline
19. Yamada S, Takagi Y, Nozaki K, et al. **Risk factors for subsequent hemorrhage in patients with cerebral arteriovenous malformations.** *J Neurosurg* 2007;107:965–72 CrossRef Medline
20. Langer DJ, Lasner TM, Hurst RW, et al. **Hypertension, small size, and deep venous drainage are associated with risk of hemorrhagic presentation of cerebral arteriovenous malformations.** *Neurosurgery* 1998;42:481–86; discussion 487–89 Medline
21. Spetzler RF, Hargraves RW, McCormick PW, et al. **Relationship of perfusion pressure and size to risk of hemorrhage from arteriovenous malformations.** *J Neurosurg* 1992;76:918–23 CrossRef Medline
22. Ai X, Ye Z, Xu J, et al. **The factors associated with hemorrhagic presentation in children with untreated brain arteriovenous malformation: a meta-analysis.** *J Neurosurg Pediatr* 2019;23:343–54 CrossRef
23. Anderson RC, McDowell MM, Kellner CP, et al. **Arteriovenous malformation-associated aneurysms in the pediatric population.** *J Neurosurg Pediatr* 2012;9:11–16 CrossRef Medline
24. Hoffman C, Riina HA, Stieg P, et al. **Associated aneurysms in pediatric arteriovenous malformations and the implications for treatment.** *Neurosurgery* 2011;69:315–22 CrossRef Medline
25. Stapf C, Khaw AV, Sciacca RR, et al. **Effect of age on clinical and morphological characteristics in patients with brain arteriovenous malformation.** *Stroke* 2003;34:2664–69 CrossRef Medline
26. Turjman F, Massoud TF, Vinuela F, et al. **Correlation of the angioarchitectural features of cerebral arteriovenous malformations with clinical presentation of hemorrhage.** *Neurosurgery* 1995;37:856–60; discussion 860–62 CrossRef Medline
27. Shakur SF, Amin-Hanjani S, Mostafa H, et al. **Hemodynamic characteristics of cerebral arteriovenous malformation feeder vessels with and without aneurysms.** *Stroke* 2015;46:1997–99 CrossRef Medline
28. Halim AX, Singh V, Johnston SC, et al; UCSF BAVM Study Project: Brain Arteriovenous Malformation. **Characteristics of brain arteriovenous malformations with coexisting aneurysms: a comparison of two referral centers.** *Stroke* 2002;33:675–79 CrossRef Medline

# Longitudinal Assessment of Neuroradiologic Features in Wolfram Syndrome

A. Samara, H.M. Lugar, T. Hershey, and J.S. Shimony



## ABSTRACT

**BACKGROUND AND PURPOSE:** Wolfram syndrome is a rare genetic disease with characteristic brain involvement. We reviewed the brain MR images of patients with Wolfram syndrome to determine the frequency and characteristics of common neuroradiologic findings.

**MATERIALS AND METHODS:** We retrospectively reviewed the imaging data of patients with genetically-confirmed Wolfram syndrome who had been recruited to the Washington University Wolfram Syndrome Research Clinic. These patients were evaluated between 2010 and 2019 with annual MRIs, along with other measures. MR images were assessed for clinical neuroradiologic signs at each individual's first and last follow-up visits to characterize the frequency, rate of progression, and clinical correlations of these signs.

**RESULTS:** We included 30 patients (13 males/17 females; average age at first visit, 14 years; average age at last visit, 19 years). The median duration of follow-up was 5 years (range, 2–9 years). The most common findings were an absent or diminished posterior pituitary bright spot (first, 53%; last, 70%), T1/T2 pons signal abnormalities (first, 53%; last, 67%), optic nerve atrophy (first, 30%; last, 80%), white matter T2 hyperintensities (first, 27%; last, 35%), and cerebellar atrophy (first, 23%; last, 70%).

**CONCLUSIONS:** Patients with Wolfram syndrome present characteristic neuroradiologic findings that involve the posterior pituitary gland, optic nerves, white matter, brain stem, and cerebellum. These abnormal findings appear at an early age and tend to increase in frequency with time. However, the neurologic significance and neuropathologic mechanisms of each sign require more investigation. Neuroradiologists should be aware of the pattern of these features in Wolfram syndrome.

**ABBREVIATIONS:** DI = diabetes insipidus; PPBS = posterior pituitary bright spot

Wolfram syndrome is a rare genetic multisystem disease characterized by juvenile-onset diabetes mellitus, progressive optic atrophy, sensorineural hearing loss, and diabetes insipidus (DI). Two clinical variants of Wolfram syndrome result from *wolframin ER transmembrane glycoprotein* (*WFS1*) and *CDGSH iron sulfur domain 2* (*CISD2*) (*WFS2*) mutations.<sup>1,2</sup> The pathophysiology

of Wolfram syndrome is attributed to multiple etiologies, including increased endoplasmic reticulum stress, calcium homeostasis disturbances, and primary or downstream mitochondrial dysfunction.<sup>3–5</sup> Previous studies have shown that Wolfram syndrome is associated with structural brain changes and multiple neurologic symptoms, eg, bladder dysfunction, gait and balance abnormalities, and loss of smell and taste sensations.<sup>6–9</sup> The pathophysiologic mechanisms underlying these neurologic manifestations are an area of active research.

Convergent evidence derived from histopathologic and quantitative neuroimaging studies indicates that Wolfram syndrome-related structural brain changes comprise a combination of early developmental hypomyelination and late neurodegeneration.<sup>10–12</sup> Neuroradiologic findings previously reported in Wolfram syndrome include marked brain stem and cerebellar atrophy, optic nerve and optic tract atrophy, and an absent posterior pituitary bright spot on T1-weighted MR images.<sup>13–15</sup> However, this work has been limited by small cohorts of patients with advanced disease, did not include longitudinal follow-up,<sup>13,14</sup> and was typically conducted before the age of genetic testing for Wolfram syndrome.<sup>15</sup> To better define the range and progress of neuroradiologic signs in

Received June 26, 2020; accepted after revision August 6.

From the Departments of Psychiatry (A.S., H.M.L.) and Neurology (T.H.) and Mallinckrodt Institute of Radiology (T.H., J.S.S.), Washington University School of Medicine, St. Louis, Missouri.

The research reported in this publication was supported by National Institute on Drug Abuse grant Nos. 5T32DA007261–27, HD070855 (T. Hershey, Principal Investigator), U54 HD087011 (Intellectual and Developmental Disabilities Research Center at Washington University), UL1 RR024992 (Clinical and Translational Science Awards), DK020579 (Diabetes Research Center); the George Decker and Julio V. Santiago Pediatric Diabetes Research Fund; the Snow Foundation; the American Diabetes Association; Mallinckrodt Institute of Radiology; and the McDonnell Center for Systems Neuroscience.

Please address correspondence to Tamara Hershey, PhD, Mallinckrodt Institute of Radiology, Washington University School of Medicine, 4525 Scott Ave, St. Louis, MO 63110; e-mail: tammy@wustl.edu

Indicates open access to non-subscribers at www.ajnr.org

<http://dx.doi.org/10.3174/ajnr.A6831>

Wolfram syndrome, we evaluated the evolution of clinical neuro-radiologic findings across time in a genetically-confirmed group of children, adolescents, and young adults with Wolfram syndrome.

## MATERIALS AND METHODS

### Study Population

Data from participants in the Washington University Wolfram Syndrome Research Clinic were evaluated. Patients were enrolled between January 2010 and December 2019. Inclusion criteria were genetically-confirmed Wolfram syndrome (*WFS1* mutations on both alleles that are known or suspected to be pathogenic), participant's awareness of the diagnosis, age younger than 30 years at the time of enrollment, and the ability to travel to St. Louis for the annual research clinic visits. We have previously reported aspects of the clinical and imaging data from subsets of this cohort.<sup>7,8,10,11,16-18</sup>

### MR Imaging Review

A single 3T Tim Trio scanner (Siemens) was used in 2010–2018, and a single 3T Magnetom Prisma scanner (Siemens) was used for 2019. Each scanning session included 3D T1-weighted sequences. For the Tim Trio, the T1-weighted MPRAGE sequence was used (sagittal acquisition: TR = 2400 ms, TE = 3.16 ms, TI = 1000 ms, voxel resolution = 1 × 1 × 1 mm, time = 8 minutes and 9 seconds).

**Table 1: The demographic and clinical characteristics in patients with Wolfram syndrome at first and last follow-up visits<sup>a</sup>**

	First Visit (n = 30)	Last Visit (n = 30)
Age (yr)	14 ± 6	19 ± 6
Duration of disease (yr)	3 ± 3	8 ± 4
Diabetes mellitus	29 (97)	30 (100)
Vision impairment	28 (93)	28 (93)
Hearing loss	20 (67)	23 (77)
Diabetes insipidus	15 (50)	19 (63)
Bladder dysfunction	13 (43)	26 (86)

<sup>a</sup> For the age and duration of disease, means and SDs are reported. For comorbid conditions, numbers and percentages are reported.

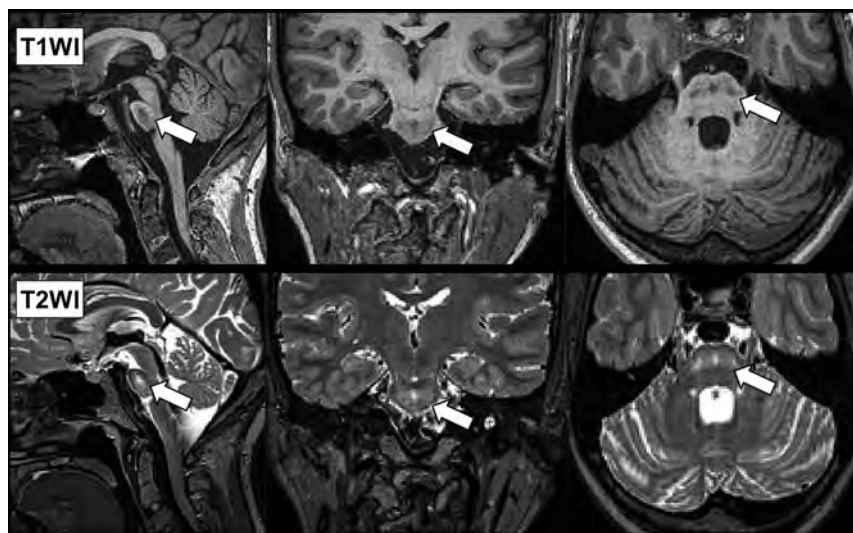


**FIG 1.** Sagittal, coronal, and axial MR images show pons signal abnormalities as T1 hypointensity and T2 hyperintensity in a patient with Wolfram syndrome (white arrows). Brain stem atrophy is also evident on this MR image.

On the Magnetom Prisma scanner, the MPRAGE sequence was slightly different (TR = 2500 ms, TE1 = 1.81 ms, TE2 = 3.6 ms, TE3 = 5.39 and 7.18 ms, TI = 1000 ms, voxel resolution = 0.8 × 0.8 × 0.8 mm, maximum acquisition time = 8 minutes and 22 seconds). FLAIR was acquired on the Tim Trio scanner before 2019. The FLAIR sequence had the following parameters: transverse acquisition—TR = 9190 ms, TE = 98 ms, TI = 2500 ms, flip angle = 150°, voxel resolution = 0.9 × 0.9 × 3 mm, time = 3 minutes and 59 seconds. Resting-state blood oxygen level–dependent and diffusion-weighted scans were also acquired but are not reported in this publication.

On the basis of prior studies,<sup>13–15,19</sup> we focused our review on 6 neuroradiologic signs: 1) a negative posterior pituitary bright spot (PPBS) seen on T1-weighted images, midline sagittal view; 2) T1/T2 pons signal abnormalities, defined as T1 hypointensity and T2 hyperintensity on midline sagittal views; 3) optic nerve atrophy and optic chiasm thinning evaluated on coronal sections at the level of optic chiasm; 4) white matter T2 hyperintensity on FLAIR images; 5) cerebellar atrophy; and 6) brain stem atrophy.

One neuroimaging researcher with 3 years of experience (A.S.) and a board-certified neuroradiologist with >20 years of experience (J.S.S.) reviewed MRIs at each individual's first and last visit between 2010 and 2019. Because T2-weighted or FLAIR images were not collected in 2019, scans from the most recent visit before 2019 were used instead.

Each neuroradiologic sign was described categorically: “yes” if present, “no” if not present for all except the PPBS sign. The PPBS sign was categorized as “present,” “diminished,” or “absent,” and the last 2 assignments were combined to indicate a negative PPBS sign. When the 2 readings were different, the final decision for which reading would be used in the analysis was made through consensus.

### Statistical Analysis

Statistical analyses were conducted using R statistical and computing software (Version 3.6.3; <http://www.r-project.org/>). For the 6 most common findings, interrater reliability ( $\kappa$ ) was calculated<sup>20</sup> and categorized as poor (<0.21), fair (0.21–0.40), moderate (0.41–0.60), substantial (0.61–0.80), or almost perfect (>0.80).<sup>21</sup>

$\chi^2$  tests were used to compare the frequency distributions between the first and last visits, and Mann–Whitney *U* tests were used to compare the median number of neuroradiologic signs at first and last visits. The Spearman's  $\rho$  was used to determine whether age and the total number of neuroradiologic signs were linearly associated. The significance level was set at a  $P < .05$ .

## RESULTS

### Patient Characteristics

MRIs from 30 patients (13 males/17 females) with at least 2 MR imaging sessions were evaluated. Scans were



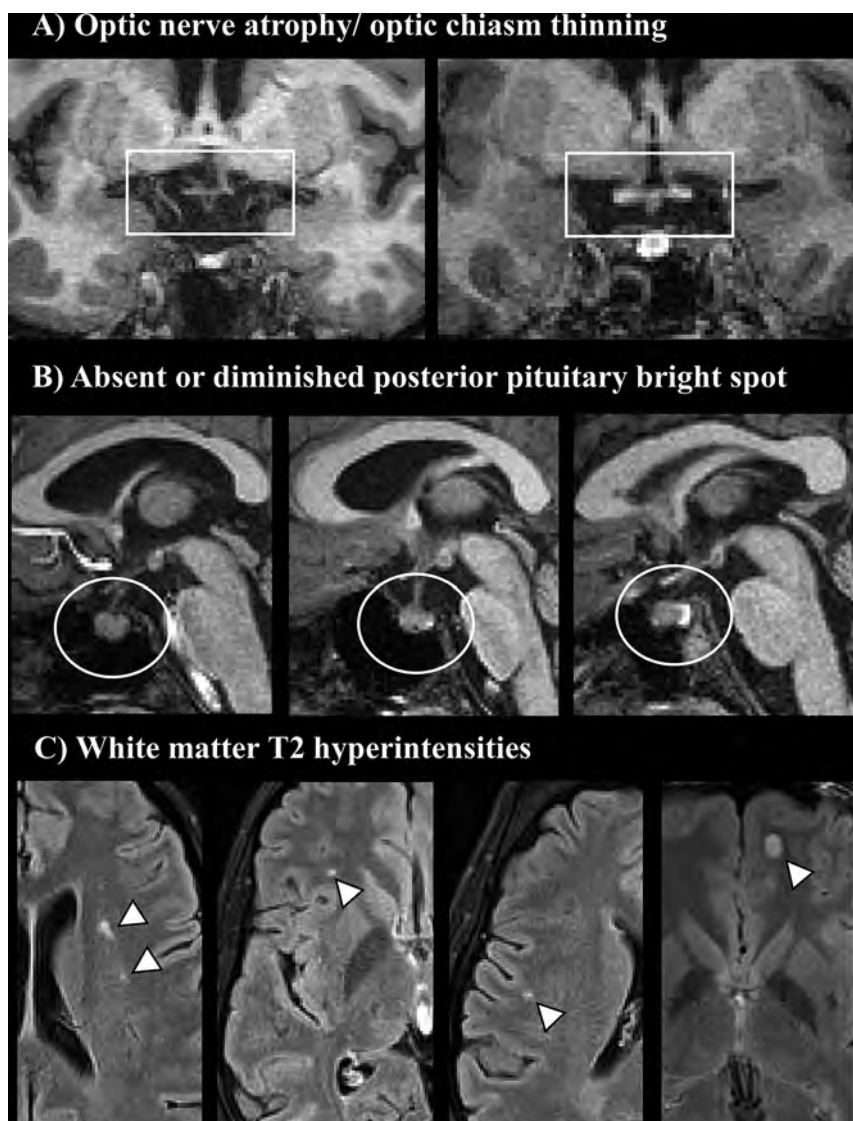


**FIG 2.** Examples of neuroradiologic findings in patients with Wolfram syndrome. A, Thinning of the optic chiasm (*white box*) as seen in coronal T1-weighted images (*left*, patient with Wolfram syndrome; *right*, healthy control). B, Abnormal PPBS signal (*white circles*) in midline sagittal T1-weighted images (*from left to right*, absent, diminished, and physiologic signal). C, White matter hyperintensities in FLAIR MR imaging (*white arrowheads*).

between 2 and 9 years apart (median, 5 years). Demographics and clinical features at each session are in found in Table 1.

### Neuroradiologic Findings

Interrater reliability ranged between fair and almost perfect: optic nerve atrophy ( $\kappa = 0.8$ ), negative PPBS ( $\kappa = 0.79$ ), cerebellar atrophy ( $\kappa = 0.83$ ), pons signal change ( $\kappa = 0.42$ ), white matter hyperintensity ( $\kappa = 0.58$ ), and brain stem atrophy ( $\kappa = 0.37$ ). See Figs 1–3 for examples of neuroradiologic signs and Table 2 for the frequency of these signs in patients at first and last scanning. Because of the low interrater reliability in evaluating brain stem atrophy, we excluded this sign from subsequent statistical analyses. However, a

previous quantitative analysis of brain stem atrophy in a subset of our cohort revealed a 27% difference in volume compared with controls and a mean estimated annual percentage rate of change of  $-0.85\%$ .<sup>10,18</sup>

At the first visit, the most common neuroradiologic findings were a negative PPBS sign and T1/T2 pons signal abnormalities, followed by optic nerve atrophy, white matter T2 hyperintensities, and cerebellar atrophy. In all cases, the signs observed in the first visit were either stable or increased on follow-up scans. Optic nerve and cerebellar atrophy showed the most progression across time with a 160%–200% increase in prevalence between the first and last visits ( $P < .001$  for both). On the other hand, white matter T2 hyperintensities seemed to be a relatively stable sign, with only a 25% increase in prevalence between the first and last visits ( $P = .51$ ). Overall, patients had a median of 2 and 3 neuroradiologic signs at the first and the last visits, respectively (paired Wilcoxon test,  $P < .001$ ). About 80% of patients had at least 1 neuroradiologic sign at the first visit, and 100% had at least 1 sign at the last visit (Fig 4A). Longer duration of follow-up was associated with a greater increase in the number of neuroradiologic signs (Spearman's  $\rho = 0.47$ ,  $P = .008$ ).

### Relationship between Neuroradiologic Findings and Clinical Variables

Older age was associated with a higher number of neuroradiologic signs at both visits (Spearman's  $\rho$ : first = 0.53, last = 0.55,  $P < .01$ ; Fig 4B). The median number of signs was not different

between males and females at both follow-up visits (Mann-Whitney  $U$  test: first,  $P = 0.79$ ; last,  $P = 0.77$ , respectively). There were no differences in sex ratios for each sign.

The positive/negative PPBS sign was not associated with the presence/absence of DI ( $\chi^2$ ; first:  $P = .27$ ; last:  $P = .32$ ). The sensitivity and specificity of the PPBS sign in predicting the DI diagnosis was 75% and 60% for the first visit and 79% and 45% for the last visit. The absence of the PPBS sign was not predictive of a future DI diagnosis during the follow-up period. Finally, there was no difference in mean best-corrected visual acuity (Logarithm of the Minimum Angle of Resolution) between normal-appearing and radiologically identified optic

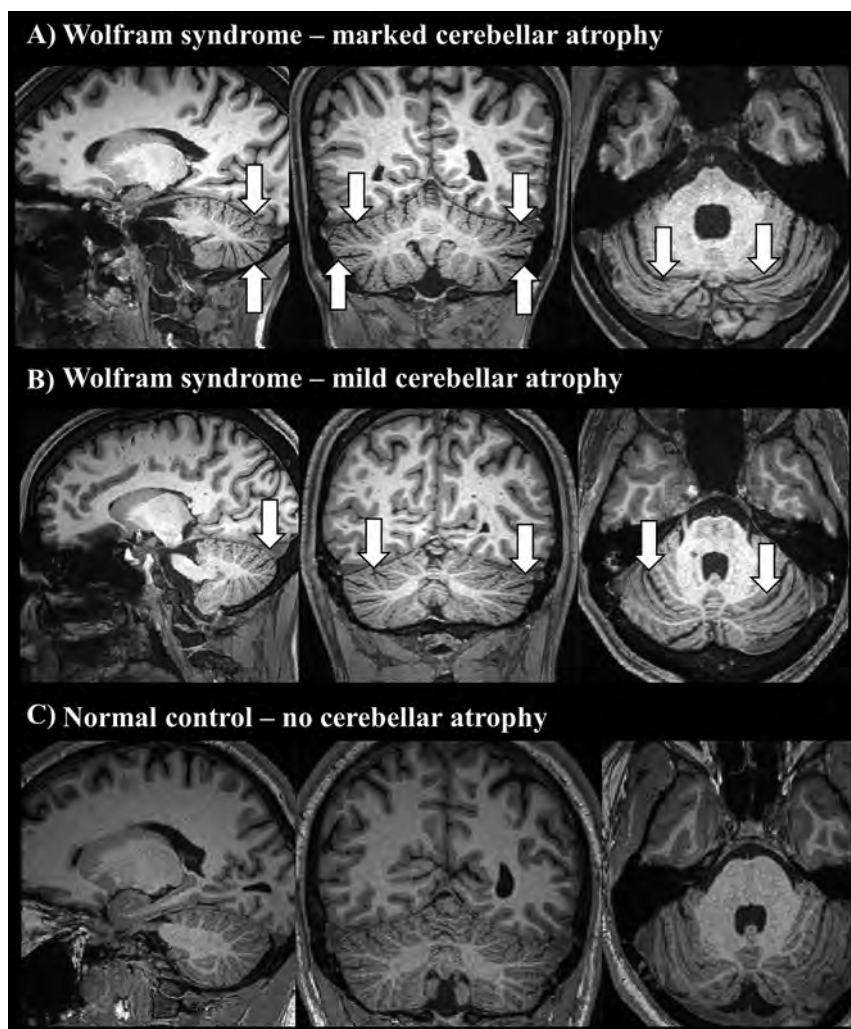


**FIG 3.** Marked (A) and mild (B) cerebellar atrophy in patients with Wolfram syndrome, as shown in sagittal, coronal, and axial T1-weighted MR images (white arrows), compared with a healthy control (C).

**Table 2: Neuroradiologic findings in brain MR images in patients with Wolfram syndrome<sup>a</sup>**

Radiologic Sign	First Visit (n = 30)	Last Visit (n = 30)
Negative PPBS sign <sup>b</sup>	16 (53)	21 (70)
T1/T2 pons signal abnormalities	16 (53)	20 (67)
Optic nerve atrophy	9 (30)	24 (80) <sup>c</sup>
White matter T2 hyperintensities <sup>d</sup>	8 (27)	10 (33)
Cerebellum atrophy	7 (23)	21 (70) <sup>c</sup>

<sup>a</sup> Numbers and percentages are reported.

<sup>b</sup> Absent and diminished PPBS sign.

<sup>c</sup> P value < .01 ( $\chi^2$  test).

<sup>d</sup> FLAIR images were not available to evaluate white matter T2 hyperintensity for 1 scan, and T2-weighted images were used instead.

nerve atrophy (Mann-Whitney *U* test; first: *P* = .09, and last: *P* = .48).

## DISCUSSION

We describe the neuroradiology findings in a cohort of patients with well-characterized and genetically-confirmed Wolfram

syndrome with longitudinal follow-up. The most common findings were a negative PPBS sign, T1/T2 pons signal abnormalities, optic nerve atrophy, white matter T2 hyperintensities, and cerebellar atrophy. The prevalence of these findings was higher in older patients and increased with time within individuals, suggesting that the accumulation of these signs reflects the evolution of neurodegenerative processes in this disease.

Overall, the most common neuroradiologic sign noticed in our cohort was a negative PPBS sign. Typically, the PPBS appears as a region of T1-weighted hyperintensity in the posterior portion of the sella turcica. The nature of this signal has been controversial, and the exact substance responsible for the T1-shortening is not known.<sup>22</sup> Changes in the appearance of the PPBS have been linked to the functional state of the pituitary gland, the neurosecretory granules containing the antidiuretic hormone (vasopressin), and the phospholipid component of the vesicles.<sup>23,24</sup> A negative PPBS sign is observed in scans of healthy individuals in about 4% of the adult population<sup>25</sup> but is more prevalent in most cases of primary and secondary central DI.<sup>26</sup> One study has also shown that a preoperative negative PPBS sign was a predictor for postoperative DI development in cases of pituitary adenoma.<sup>27</sup> The PPBS sign was also previously described in a case report of Wolfram syndrome.<sup>28</sup> In our cohort, although the negative PPBS sign was twice as prevalent in the DI group compared with the non-DI group, the presence of this sign was not a significant predictor of the diagnosis because half of the individuals without DI also showed this sign.

The T1/T2 pons signal abnormalities observed in our cohort are rarely mentioned in the Wolfram syndrome imaging literature. Only 1 case report described similar pons signal changes in a patient with Wolfram syndrome.<sup>19</sup> The location of the pontine signal change appears to overlap with the pontine nuclei and pontocerebellar white matter fibers.<sup>29</sup> Because of its unique appearance and location in an area susceptible to imaging artifacts, this sign might have been previously missed and so under-reported in the literature. On the other hand, visual inspection of brain stem atrophy seems unreliable and less sensitive than quantitative analyses.

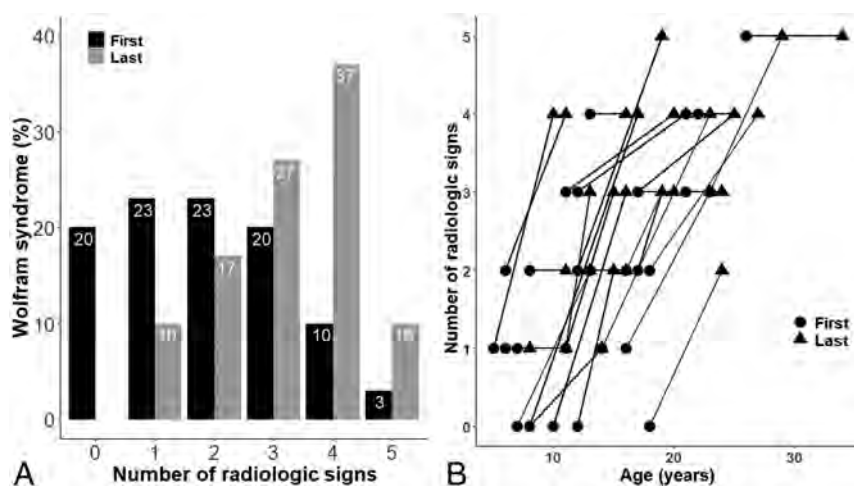


**FIG 4.** A, Frequency of neuroradiologic signs in patients with Wolfram syndrome at first and last visits. B, The relationship between age and the number of neuroradiologic signs. A line connecting a circle-shaped point (first visit) and a triangle-shaped point (last visit) represents each patient.

However, quantitative evaluation of brain stem atrophy would require advanced segmentation software not available in all clinical settings.<sup>8,11</sup> T1/T2 pons signal abnormalities may be more easily captured by visual inspection and appeared concurrently or sometimes preceded the development of brain stem atrophy detectable visually. Most interesting, although we did not include brain stem atrophy in the statistical analyses due to low interrater agreement, the cerebellum and brain stem atrophy observed in our cohort co-occurred at a high rate. Embryologically, these structures form together and are tightly linked.<sup>30</sup> In patients with Wolfram syndrome, postmortem histologic examination of both the brain stem and cerebellum showed evidence of neuronal loss and gliosis in most brain stem nuclei.<sup>31–33</sup> In the same studies, the cerebellum showed microscopic evidence of variable neuronal loss in the dentate nuclei and variable reduction of Purkinje cells of the cerebellum.<sup>31–33</sup>

The visual system is severely affected in Wolfram syndrome, as shown by previous histologic and neuroimaging studies.<sup>8,10,11,31–33</sup> The optic nerves and optic chiasm were grossly atrophic with a prominent perioptic CSF space. The optic nerve atrophy in Wolfram syndrome may be related to retinal dysfunction and degeneration.<sup>34</sup> This finding was evident as early as the first decade of life in our cohort. Histologic examination also reflects this dramatic change with multiple studies reporting optic nerve axonal degeneration associated with marked loss of myelinated axons and gliosis.<sup>31–33</sup> Furthermore, previous work from our group has also shown that this damage is progressive, involves both pregeniculate and postgeniculate regions of the visual pathway, and correlates with the decline in visual function.<sup>35</sup> Although the degree of visual system structure-function relationships is better evaluated via quantitative analyses, visual inspection of clinical scans captured the progressive nature of the visual pathway damage.

The presence of white matter lesions in Wolfram syndrome has been previously reported.<sup>36</sup> The white matter hyperintensities appeared as small round or oval lesions mainly in the frontal and parietal white matter with no confluent lesions. The frequency of this finding exceeds what might be considered incidental clinically

insignificant T2 hyperintensities.<sup>37</sup> The radiologic appearance of these white matter T2 signal hyperintensities suggests possible demyelination, gliosis, or an inflammatory process. Previous histopathologic studies showed patchy demyelination and axonal degeneration in several white matter tracts in Wolfram syndrome, eg, the optic radiation and the pontocerebellar and corticopontine tracts.<sup>31–33</sup> In prior work by our group, we evaluated white matter microstructure in Wolfram syndrome using diffusion tensor imaging.<sup>8,10,11</sup> These quantitative analyses revealed that patients with Wolfram syndrome had widespread lower fractional anisotropy (reflecting decreased integrity of axon bundles) and higher radial diffusivity (reflecting impaired myelination) compared with age-equivalent controls.

Given that this finding was observed as early as 10 years of age in our cohort and was also relatively stable across time, it may be a neurodevelopmental process that occurs in the early stages of the disease.<sup>8,12</sup>

Finally, previous studies have reported some neuroradiologic features in patients with Wolfram syndrome that we did not observe in our cohort. These include cortical malformations, diffuse white matter leukoencephalopathy,<sup>38</sup> and high signal on proton-density and T2-weighted images in the substantia nigra.<sup>39</sup>

## CONCLUSIONS

Our study describes the primary neuroradiologic features observed on MR imaging in Wolfram syndrome. The most common findings involved the posterior pituitary gland, optic nerve and optic chiasm, cerebral white matter, brain stem, and cerebellum. One strength of our study is that it includes a large cohort of patients with genetically-confirmed Wolfram syndrome with longitudinal follow-up from an early age. We also showed the rate of progression of these findings and their relation to demographic variables. However, our study was also limited by the lack of an explicit control group and the different sequences used for both the first and last visits.

Neuroradiologists should be aware of these findings when reading MR imaging studies of patients with Wolfram syndrome. Future research could pursue the diagnostic and prognostic value of these signs when combined with quantitative neuroimaging data and the pathophysiologic processes underlying these signs.

## ACKNOWLEDGMENTS

We thank all of the participants at the Washington University Wolfram Research Clinic and their families for their time and effort and the Washington University Wolfram Research Clinic study staff for their dedication. We also thank the former and current Washington University Wolfram Study Group members for their advice and support.



Disclosures: Amjad Samara—*RELATED: Grant:* National Institute on Drug Abuse. *Comments:* Amjad Samara is a postdoctoral scholar supported by the National Institute on Drug Abuse grant No. 5T32DA007261–27. Heather M. Lugar—*RELATED: Grant:* I receive payment via grants from the National Institutes of Health; *UNRELATED: Employment:* I receive payment via grants from National Institutes of Health; *Grants/Grants Pending:* I receive payment via grants from the National Institutes of Health. Tamara Hershey—*RELATED: Grant:* National Institutes of Health\*; *Support for Travel to Meetings for the Study or Other Purposes:* National Institutes of Health\*; *UNRELATED: Employment:* Washington University School of Medicine; *Grants/Grants Pending:* National Institutes of Health.\* \*Money paid to the institution.

## REFERENCES

- Amr S, Heisey C, Zhang M, et al. **A homozygous mutation in a novel zinc-finger protein, ERIS, is responsible for Wolfram syndrome 2.** *Am J Hum Genet* 2007;81:673–83 CrossRef Medline
- Inoue H, Tanizawa Y, Wasson J, et al. **A gene encoding a transmembrane protein is mutated in patients with diabetes mellitus and optic atrophy (Wolfram syndrome).** *Nat Genet* 1998;20:143–48 CrossRef Medline
- Cagalinac M, Liiv M, Hodurova Z, et al. **Role of mitochondrial dynamics in neuronal development: mechanism for Wolfram syndrome.** *PLoS Biol* 2016;14:e1002511 CrossRef Medline
- Takei D, Ishihara H, Yamaguchi S, et al. **WFS1 protein modulates the free Ca(2+) concentration in the endoplasmic reticulum.** *FEBS Lett* 2006;580:5635–40 CrossRef Medline
- Delprat B, Maurice T, Delettre C. **Wolfram syndrome: MAMs' connection?** *Cell Death Dis* 2018;9:364 CrossRef Medline
- Alfaro R, Doty T, Narayanan A, et al. **Taste and smell function in Wolfram syndrome.** *Orphanet J Rare Dis* 2020;15:57 CrossRef Medline
- Rove KO, Vricella GJ, Hershey T, et al. **Lower urinary tract dysfunction and associated pons volume in patients with Wolfram syndrome.** *J Urol* 2018;200:1107–13 CrossRef Medline
- Pickett KA, Duncan RP, Paciorkowski AR, et al; Washington University Wolfram Study Group. **Balance impairment in individuals with Wolfram syndrome.** *Gait Posture* 2012;36:619–24 CrossRef Medline
- Pickett KA, Duncan RP, Hoekel J, et al; Washington University Wolfram Study Group. **Early presentation of gait impairment in Wolfram syndrome.** *Orphanet J Rare Dis* 2012;7:92 CrossRef Medline
- Lugar HM, Koller JM, Rutlin J, et al. **Evidence for altered neurodevelopment and neurodegeneration in Wolfram syndrome using longitudinal morphometry.** *Sci Rep* 2019;9:6010 CrossRef Medline
- Lugar HM, Koller JM, Rutlin J, et al; Washington University Wolfram Syndrome Research Study Group. **Neuroimaging evidence of deficient axon myelination in Wolfram syndrome.** *Sci Rep* 2016;6:21167 CrossRef Medline
- Samara A, Rahn R, Neyman O, et al. **Developmental hypomyelination in Wolfram syndrome: new insights from neuroimaging and gene expression analyses.** *Orphanet J Rare Dis* 2019;14:279 CrossRef Medline
- Gocmen R, Guler E. **Teaching NeuroImages: MRI of brain findings of Wolfram (DIDMOAD) syndrome.** *Neurology* 2014;83:e213–14 CrossRef Medline
- Ito S, Sakakibara R, Hattori T. **Wolfram syndrome presenting marked brain MR imaging abnormalities with few neurologic abnormalities.** *AJNR Am J Neuroradiol* 2007;28:305–06 Medline
- Scolding NJ, Kellar-Wood HF, Shaw C, et al. **Wolfram syndrome: hereditary diabetes mellitus with brainstem and optic atrophy.** *Ann Neurol* 1996;39:352–60 CrossRef Medline
- Bischoff AN, Reiersen AM, Buttlair A, et al; Washington University Wolfram Syndrome Research Group. **Selective cognitive and psychiatric manifestations in Wolfram syndrome.** *Orphanet J Rare Dis* 2015;10:66 CrossRef Medline
- Marshall BA, Permutt MA, Paciorkowski AR, et al; Washington University Wolfram Study Group. **Phenotypic characteristics of early Wolfram syndrome.** *Orphanet J Rare Dis* 2013;8:64 CrossRef Medline
- Hershey T, Lugar HM, Shimony JS, et al; Washington University Wolfram Study Group. **Early brain vulnerability in Wolfram syndrome.** *PLoS One* 2012;7:e40604 CrossRef Medline
- Harsha KJ, Parameswaran K. **Wolfram (DIDMOAD) syndrome with ventral central pontine hyperintensity without brainstem atrophy.** *Neurol India* 2016;64:1310–12 CrossRef Medline
- Cohen J. **A coefficient of agreement for nominal scales.** *Educational and Psychological Measurement* 1960;20:37–46 CrossRef
- Landis JR, Koch GG. **The measurement of observer agreement for categorical data.** *Biometrics* 1977;33:159–74 Medline
- Bonneville F, Cattin F, Marsot-Dupuch K, et al. **T1 signal hyperintensity in the sellar region: spectrum of findings.** *Radiographics* 2006;26:93–113 CrossRef Medline
- Fujisawa I, Asato R, Kawata M, et al. **Hyperintense signal of the posterior pituitary on T1-weighted MR images: an experimental study.** *J Comput Assist Tomogr* 1989;13:371–77 CrossRef Medline
- Kucharczyk W, Lenkinski RE, Kucharczyk J, et al. **The effect of phospholipid vesicles on the NMR relaxation of water: an explanation for the MR appearance of the neurohypophysis?** *AJNR Am J Neuroradiol* 1990;11:693–700 Medline
- Klyn V, Dekeyser S, Van Eetvelde R, et al. **Presence of the posterior pituitary bright spot sign on MRI in the general population: a comparison between 1.5 and 3T MRI and between 2D-T1 spin-echo- and 3D-T1 gradient-echo sequences.** *Pituitary* 2018;21:379–83 CrossRef Medline
- Fujisawa I, Nishimura K, Asato R, et al. **Posterior lobe of the pituitary in diabetes insipidus: MR findings.** *J Comput Assist Tomogr* 1987;11:221–25 CrossRef Medline
- Wang S, Lin K, Xiao D, et al. **The relationship between posterior pituitary bright spot on magnetic resonance imaging (MRI) and postoperative diabetes insipidus for pituitary adenoma patients.** *Med Sci Monit* 2018;24:6579–86 CrossRef Medline
- Elli FM, Ghirardello S, Giavoli C, et al. **A new structural rearrangement associated to Wolfram syndrome in a child with a partial phenotype.** *Gene* 2012;509:168–72 CrossRef Medline
- Shepherd TM, Ades-Aron B, Bruno M, et al. **Direct in vivo MRI discrimination of brain stem nuclei and pathways.** *AJNR Am J Neuroradiol* 2020;41:777–84 CrossRef Medline
- Doherty D, Millen KJ, Barkovich AJ. **Midbrain and hindbrain malformations: advances in clinical diagnosis, imaging, and genetics.** *Lancet Neurol* 2013;12:381–93 CrossRef Medline
- Genis D, Davalos A, Molins A, et al. **Wolfram syndrome: a neuropathological study.** *Acta Neuropathol* 1997;93:426–29 CrossRef Medline
- Shannon P, Becker L, Deck J. **Evidence of widespread axonal pathology in Wolfram syndrome.** *Acta Neuropathol* 1999;98:304–08 CrossRef Medline
- Hilson JB, Merchant SN, Adams JC, et al. **Wolfram syndrome: a clinicopathologic correlation.** *Acta Neuropathol* 2009;118:415–28 CrossRef Medline
- Scaramuzzi M, Kumar P, Peachey N, et al. **Evidence of retinal degeneration in Wolfram syndrome.** *Ophthalmic Genet* 2019;40:34–38 CrossRef Medline
- Hoekel J, Narayanan A, Rutlin J, et al. **Visual pathway function and structure in Wolfram syndrome: patient age, variation and progression.** *BMJ Open Ophthalmol* 2018;3:e000081 CrossRef Medline
- Pakdemirli E, Karabulut N, Bir LS, et al. **Cranial magnetic resonance imaging of Wolfram (DIDMOAD) syndrome.** *Australas Radiol* 2005;49:189–91 CrossRef Medline
- Zhuang FJ, Chen Y, He WB, et al. **Prevalence of white matter hyperintensities increases with age.** *Neural Regen Res* 2018;13:2141–46 CrossRef Medline
- Chausseuot A, Bannwarth S, Rouzier C, et al. **Neurologic features and genotype-phenotype correlation in Wolfram syndrome.** *Ann Neurol* 2011;69:501–08 CrossRef Medline
- Galluzzi P, Filosomi G, Vallone IM, et al. **MRI of Wolfram syndrome (DIDMOAD).** *Neuroradiology* 1999;41:729–31 CrossRef Medline

# Neonatal Developmental Venous Anomalies: Clinicoradiologic Characterization and Follow-Up

A.F. Geraldo, S.S. Messina, D. Tortora, A. Parodi, M. Malova, G. Morana, C. Gandolfo, A. D'Amico, E. Herkert, P. Govaert, L.A. Ramenghi, A. Rossi, and M. Severino



## ABSTRACT

**BACKGROUND AND PURPOSE:** Although developmental venous anomalies have been frequently studied in adults and occasionally in children, data regarding these entities are scarce in neonates. We aimed to characterize clinical and neuroimaging features of neonatal developmental venous anomalies and to evaluate any association between MR imaging abnormalities in their drainage territory and corresponding angioarchitectural features.

**MATERIALS AND METHODS:** We reviewed parenchymal abnormalities and angioarchitectural features of 41 neonates with developmental venous anomalies (20 males; mean corrected age, 39.9 weeks) selected through a radiology report text search from 2135 neonates who underwent brain MR imaging between 2008 and 2019. Fetal and longitudinal MR images were also reviewed. Neurologic outcomes were collected. Statistics were performed using  $\chi^2$ , Fisher exact, Mann-Whitney *U*, or *t* tests corrected for multiple comparisons.

**RESULTS:** Developmental venous anomalies were detected in 1.9% of neonatal scans. These were complicated by parenchymal/ventricular abnormalities in 15/41 cases (36.6%), improving at last follow-up in 8/10 (80%), with normal neurologic outcome in 9/14 (64.2%). Multiple collectors ( $P = .008$ ) and larger collector caliber ( $P < .001$ ) were significantly more frequent in complicated developmental venous anomalies. At a patient level, multiplicity ( $P = .002$ ) was significantly associated with the presence of  $\geq 1$  complicated developmental venous anomaly. Retrospective fetal detection was possible in 3/11 subjects (27.2%).

**CONCLUSIONS:** One-third of neonatal developmental venous anomalies may be complicated by parenchymal abnormalities, especially with multiple and larger collectors. Neuroimaging and neurologic outcomes were favorable in most cases, suggesting a benign, self-limited nature of these vascular anomalies. A congenital origin could be confirmed in one-quarter of cases with available fetal MR imaging.

**ABBREVIATIONS:** CCM = cerebral cavernous malformation; c-DVA = complicated developmental venous anomaly; cUS = cerebral ultrasound; CVMS = cerebrofacial venous metamerism syndrome; DVA = developmental venous anomaly; u-DVA = uncomplicated developmental venous anomaly

Developmental venous anomalies (DVAs) are the most frequently diagnosed intracranial vascular malformations, often encountered as incidental neuroimaging findings.<sup>1,2</sup> On MR imaging, DVAs are recognized on postcontrast T1WI as radially oriented veins with a “caput medusae” pattern converging into 1 (or rarely more) dilated venous collector.<sup>3,4</sup> These features may be also detected on precontrast MR images,<sup>3-5</sup> especially if T2\*-weighted sequences such as high-resolution SWI are included in

the protocol.<sup>5</sup> In addition, DVAs may be occasionally recognized in utero using fetal MR imaging.<sup>6</sup>

DVAs are usually considered benign anatomic variants.<sup>7</sup> However, they represent areas of venous fragility that can become symptomatic through diverse pathomechanisms.<sup>8,9</sup> Indeed, DVA-associated brain abnormalities are frequently depicted, including-

Paper previously presented, in part, as an oral communication at: Italian Congress of Pediatric Neuroradiology, October 11–13, 2018; Brescia, Italy.

All procedures performed in the studies involving human participants were in accordance with the ethical standards of 1964 Helsinki Declaration and its later amendments or comparable ethical standards. Informed consent was waived by the institutional research committee.

Please address correspondence to Andrea Rossi, MD, Neuroradiology Unit, IRCCS Istituto Giannina Gaslini, Via Gaslini 5, Genova 16148 Italy; e-mail: andrea.rossi@gaslini.org; @AndreaRossi\_NRX; @MSavinaSeverino

Indicates open access to non-subscribers at www.ajnr.org

Indicates article with supplemental on-line appendix and table.

Indicates article with supplemental on-line photos.

<http://dx.doi.org/10.3174/ajnr.A6829>

Received April 15, 2020; accepted after revision August 6.

From the Neuroradiology Unit (A.F.G.), Centro Hospitalar de Vila Nova de Gaia/Espinho, Vila Nova de Gaia, Portugal; Neuroradiology Unit (A.F.G., D.T., G.M., A.R., M.S.), Neonatal Intensive Care Unit (A.P., M.M., L.A.R.), and Interventional Unit (C.G.), IRCCS Istituto Giannina Gaslini, Genova, Italy; Radiology Unit (S.S.M.), Casa di Cura Regina Pacis, Palermo, Italy; Dipartimento di Scienze Biomediche Avanzate (A.D.), Università Federico II, Napoli, Italy; and Division of Neonatology (E.H., P.G.), Department of Paediatrics, Erasmus University Medical Centre, Rotterdam, the Netherlands.

This work was supported by funds from “Ricerca Corrente Disordini Neurologici e Muscolari (Linea 5)” of the Italian Ministry of Health and the Compagnia di San Paolo (ROL 20573).

but-not limited-to sporadic cerebral cavernous malformations (CCMs).<sup>8-16</sup> Moreover, a higher prevalence of DVAs has been described in patients with different pathologies and/or genetic conditions.<sup>17-21</sup>

Although DVAs are widely described and characterized in adults, they remain under-reported in the pediatric population. Indeed, there are noticeably fewer studies focusing exclusively on DVAs in this age group, especially in the neonatal period.<sup>17,18,21-24</sup> In particular, the largest case series of neonatal DVAs described so far included 14 neonates, mostly detected using ultrasound during routine scanning for other reasons,<sup>22</sup> with limited information on the prevalence and perinatal characteristics of these vascular abnormalities, including complications and longitudinal evolution. Moreover, additional data on neonatal and fetal DVAs would be of great interest because there is an ongoing debate regarding their congenital or postnatal etiology.<sup>25</sup>

In this study, we aimed to describe the pre- and postnatal appearance of DVAs and associated brain anomalies in a relatively large single-center group of neonates, providing information on their imaging and clinical follow-up. In addition, we tested a possible association between parenchymal and ventricular abnormalities in the drainage territory of neonatal DVAs and their angioarchitectural features.

## MATERIALS AND METHODS

### Population

After institutional review board approval, 1 pediatric neuroradiologist (M.S.) searched in the radiology information system of a tertiary pediatric institution (IRCCS Istituto Giannina Gaslini, Genoa, Italy) for reports of brain MR imaging studies performed in subjects up to 28 days of corrected age containing the term “developmental venous anomaly,” during a 12-year period (January 2008 to December 2019). During this period, 2135 neonates underwent brain MR imaging. All procedures performed in the studies involving human participants were in accordance with the ethical standards of 1964 Helsinki Declaration and its later amendments or comparable ethical standards. Informed consent was waived by the institutional research committee.

### MR Imaging Technique and Image Analysis

Neonates were scanned on 1.5T or 3T MR imaging units with different imaging protocols, all including at least T1WI, T2WI, DWI, and T2\*WI (either gradient recalled-echo or SWI) sequences. Gadolinium-based contrast agents were injected only if clinically indicated. Neonates were fed before the MR imaging examination to achieve spontaneous sleep, with mild oral midazolam sedation (0.1 mg/kg) in case of head movements, and were breathing spontaneously during the examination.

Brain MR imaging studies were reviewed by 2 pediatric neuroradiologists (M.S. and A.F.G. with 10 and 5 years of experience, respectively), who confirmed the diagnosis and evaluated the presence of DVA-related mechanical compression of adjacent structures, draining vein thrombosis, and/or parenchymal abnormalities within the drainage territory. The latter included any of the following: increased T2 signal of surrounding WM, foci of restricted diffusion, hemorrhage, CCM,<sup>26</sup> malformations of cortical development, or calcifications (defined as focal areas of hyperintensity on SWI phase images in right-handed MR imaging systems or hyperdensity

on head CT scans). Microhemorrhages were distinguished from type IV CCMs on the basis of their evolution on imaging. Indeed, vessels of CCMs have a tendency to leak and bleed, thus frequently increasing or stabilizing in size with time, while microhemorrhages typically present a regular evolution of hemoglobin degradation with a faster reduction in size and/or complete regression.

Subjects with  $\geq 1$  associated abnormality were considered to have complicated DVAs (c-DVA group), and the remainder, uncomplicated DVAs (u-DVA group).

Additionally, we registered the number of DVAs per patient as well as the corresponding angioarchitecture features:<sup>3,11</sup> direction of drainage, number of collector veins, and mean collector caliber (defined as the caliber of the collector vein in case of a single collector or the mean of all collector calibers in case of multiple collectors, measured on axial T2\*WI). Multiple collectors were defined as  $\geq 2$  draining veins. Fetal MR imaging, neonatal cerebral ultrasound (cUS), DSA, and follow-up MR imaging were reviewed when available.

Imaging findings at last MR imaging follow-up were classified as interval improvement, progression, stability, or mixed evolution.

Discrepancies were resolved by a third pediatric neuroradiologist (A.R. with 25 years of experience).

### Clinical Data

Data on sex, pregnancy history, gestational age at birth, cause of prematurity, type of delivery, Apgar scores, corrected age at first MR imaging, and imaging indications were obtained from the electronic clinical records. For neonates with c-DVAs, additional data including treatment, age at last clinical assessment, and neurologic outcome (graded as normal, mild, moderate, or severe impairment) were also registered.

### Statistical Analysis

Quantitative data were presented as median and interquartile range, and categorical data, as frequencies and percentages. Fisher exact,  $\chi^2$ , and independent samples Student *t* tests were used to compare clinical characteristics between patient groups with c-DVAs and u-DVAs. Fisher exact,  $\chi^2$ , and Mann-Whitney *U* tests were used to compare angioarchitectural characteristics and associated parenchymal/ventricular abnormalities between individual complicated and uncomplicated DVAs. All results were corrected for multiple-comparison testing using the Bonferroni correction method. Statistical significance was reached if the *P* value was  $< 0.05/k$ , where *k* indicates the number of tests, resulting in thresholds for statistical significance of  $P < .0045$  and  $.0083$  for patient and DVA levels of comparison, respectively. Statistical analyses were performed using SPSS Statistics software, Version 24.0 (IBM).

## RESULTS

### Neonatal Imaging Features

Forty-one neonates with DVAs were retrieved by a report search and confirmed by image review (20 males; mean corrected age at first MR imaging, 39.9 weeks; range, 33–44 weeks), corresponding to a real-world MR imaging DVA detection of 1.9% (41/2135) in a tertiary pediatric center. Neonates were preterm in 46.3% of cases ( $n = 19$ ). Brain MR imaging was obtained on a 3T scanner in 22 cases (53.7%). SWI and postcontrast T1WI were acquired in 38 (92.7%) and 7 cases (17.1%), respectively.



**Table 1: Location and angioarchitecture characteristics of developmental venous anomalies**

	Total (n = 58)	Complicated DVA (n = 21) (36.2%)	Uncomplicated DVA (n = 37) (63.2%)	P Value <sup>a</sup>
Location (%)				.44
Frontal	24 (41.4)	9 (42.9)	15 (40.5)	
Parieto-occipital	16 (27.7)	6 (28.6)	10 (27)	
Temporal	8 (13.8)	3 (14.3)	5 (13.5)	
Basal ganglia/thalami	5 (8.6)	0 (0)	5 (13.5)	
Brain stem	2 (3.4)	1 (4.8)	1 (2.7)	
Cerebellum	3 (5.2)	2 (9.5)	1 (2.7)	
Infratentorial (%)	5 (8.6)	3 (14.3)	2 (5.4)	.34
Right side (%)	33 (56.9)	13 (61.9)	20 (54.1)	.59
Multiple collectors (%)	9 (15.5)	7 (33.3)	2 (5.4)	.008 <sup>b</sup>
Main collector caliber (median) (IQR) (mm)	1.6 (1.18–2.10)	2.1 (1.95–2.30)	1.2 (1–1.6)	<.001 <sup>b</sup>
Drainage (%)				.70
Deep	31 (53.4)	11 (52.4)	20 (54.1)	
Superficial	19 (32.8)	6 (28.6)	13 (35.1)	
Both	8 (13.8)	4 (19)	4 (10.8)	

**Note:**—IQR indicates interquartile range.

<sup>a</sup> P values for group comparisons were determined by  $\chi^2$  or Fisher exact tests for categoric variables or by Mann-Whitney *U* tests for continuous variables, as appropriate.

<sup>b</sup> Value statistically significant (statistical significance was set at  $P < .0083$  after Bonferroni correction for multiple comparisons).

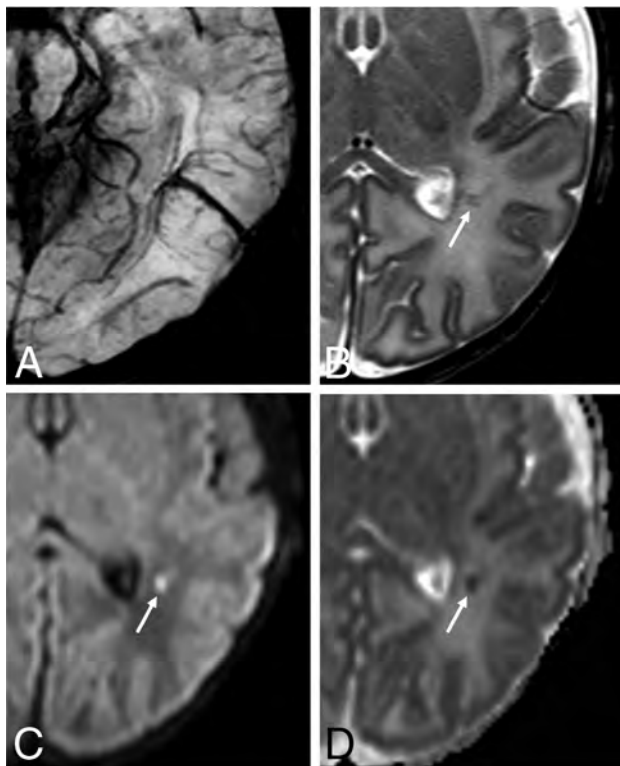


**FIG 1.** Neonatal developmental venous anomaly complicated by focal areas of venous ischemia. A, Axial SWI shows a left parietal developmental venous anomaly with superficial drainage. B, Axial T2WI reveals small linear hypointense lesions in the surrounding WM (arrow), with corresponding hyperintensity on  $b = 1000$  image (C, arrow) and low ADC values on the ADC map (D, arrow).

Fifteen patients (36.6%) had at least 1 DVA (range, 1–6) associated with parenchymal abnormalities and/or CSF obstruction (c-DVA group) (Table 1 and Figs 1–3). Two of these neonates

were affected by cerebrofacial venous metamerism syndrome (CVMS). The On-line Table summarizes clinico-radiologic associations. In particular, at-term birth ( $P = .02$ ), higher gestational age ( $P = .05$ ), and imaging indications other than “preterm screening” ( $P = .005$ ) were significantly more frequent in the c-DVA group but did not reach statistical significance after adjusting for multiple comparisons. Moreover, multiple DVAs as well as additional craniofacial vascular lesions were also more common in patients with c-DVAs ( $P = .002$  and  $P = .02$ , respectively), but only multiplicity remained significant after multiple-comparison correction. Neonatal seizures likely attributable to a symptomatic DVA were detected in 2/15 patients with c-DVAs. One additional patient with a c-DVA developed probable DVA-related seizures at 11 months. A direct causal relationship

between the DVA and neonatal seizures was not identified in 2 patients with u-DVA presenting with this symptom.

Overall, 58 DVAs were identified, comprising multiple DVAs in 9 cases. DVA location and angioarchitecture features are presented in Table 1. Multiple collectors and larger collector calibers were significantly more frequent in complicated DVAs ( $P = .008$  and  $P < .001$ , respectively), even after adjusting for multiple comparisons.

DSA was performed in 4 patients with c-DVAs. No signs of arteriovenous shunting through the DVA with or without an associated classic nidus were identified, while a subject with CVMS had an intraorbital AVF.

#### **Fetal MR Imaging and Postnatal cUS**

Fetal MR imaging was performed in 11 patients (26.8%), of whom 6 belonged to the c-DVA group (21 examinations in total, 1–4 studies per patient, acquired between 20 and 38 gestational weeks). Retrospective analysis of single-shot FSE,  $b = 0$ , and/or T2\*WI identified a DVA and/or an abnormally enlarged draining pathway in 3 fetuses (27.3%). In another case, a DVA-associated cerebellar hemorrhage was detected but precluded the identification of the subjacent DVA. Of the remaining 7 fetuses in whom the DVA was not visible, 3 presented with craniofacial vascular lesions.

Postnatal cUS was available in 36 neonates: In 3 cases, the DVA was suspected before the MR imaging examination due to the presence of a parenchymal linear hyperechogenic focus.

#### **Management and Clinico-radiologic Outcome of Neonates with c-DVAs**

Of 15 neonates with c-DVAs, 13 were conservatively managed, with a wait-and-see approach in 10 cases, anticoagulation treatment in 2, and antiepileptic drugs in 1. Endoscopic third ventriculostomy was performed in 1 neonate with DVA-related obstructive

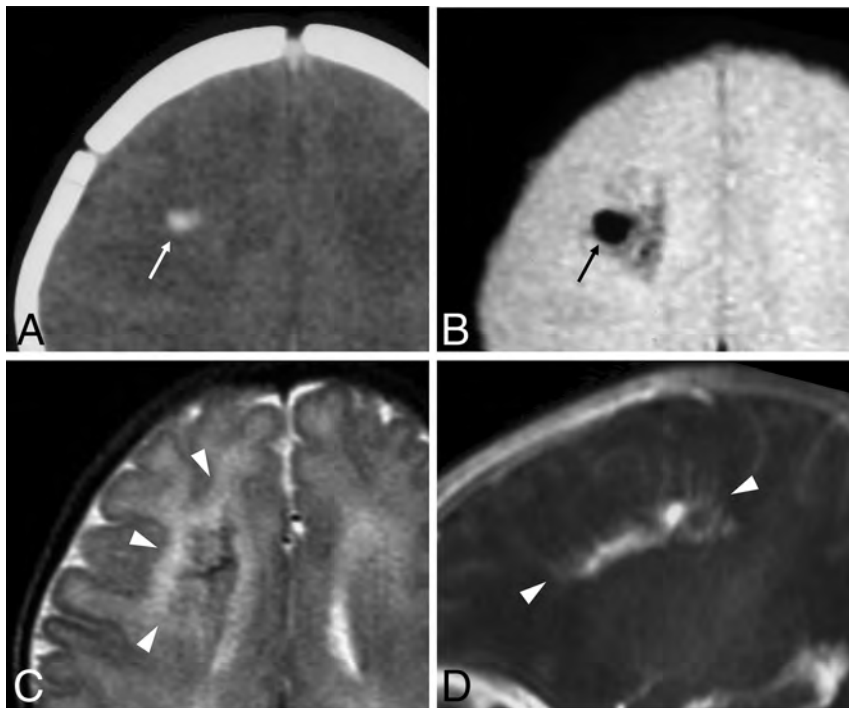


**FIG 2.** Neonatal developmental venous anomaly complicated by focal hemorrhage and diffuse WM signal abnormalities likely related to venous congestion. *A*, Unenhanced head CT scan demonstrates a focal area of spontaneous hyperdensity (white arrow) in the right frontal region, suggestive of recent hemorrhage. Corresponding axial gradient-echo T2\*-weighted image (*B*) and T2WI (*C*) show a blooming artifact (black arrow) in the region corresponding to the hemorrhage, which subsequently regressed (not shown), and diffuse hyperintensity of the surrounding WM (arrowheads), in keeping with venous congestion. *D*, Sagittal contrast-enhanced T1WI reveals a large developmental venous anomaly characterized by several radially-oriented dilated veins with a caput medusae morphology and deep venous drainage (arrowheads).

hydrocephalus. Multiple interventional procedures were performed in the child with CVMS and an AVF.

Table 2 reports the clinicoradiologic outcome of subjects with c-DVAs. Longitudinal MR imaging was available in 10/15 patients (median follow-up, 39.1 months; range, 2–97 months; age at last follow-up, 2.5 months–8.2 years). Eight patients (80%) showed imaging signs of improvement, while stability ( $n = 1$ ) or mixed evolution ( $n = 1$ ) was detected in the remaining cases.

Follow-up neurologic evaluation was available in 14 neonates with c-DVAs (median follow-up, 27.5 months; range, 11–97 months), and findings were judged normal in 9 cases (64.2%), while minor or moderate psychomotor impairment was detected in 4 (28.5%) and 1 (7.1%) patient, respectively.

A brief description of a few illustrative cases of neonatal c-DVA is presented in the On-line Appendix.

## DISCUSSION

In this study, we identified 41 neonates with DVAs, for a total of 58 DVAs, from a population of 2135 neonates undergoing brain MR imaging for diverse clinical reasons and with different imaging techniques, corresponding to a real-world detection in a tertiary pediatric center of 1.9%. These findings are similar to a recent retrospective study by Brinjikji et al,<sup>25</sup> describing a prevalence of

1.5% in the 0- to 12-month age group. Most interesting, both percentages are lower than those reported in studies including older children, adults, or mixed populations (5%–10%).<sup>4,23,25</sup> Because the pathogenesis of DVAs remains controversial, including their cause and timing of development, some authors have attributed these age-related prevalence differences to a postnatal origin.<sup>25</sup> However, caution is advised due to methodologic discrepancies among studies in terms of selection criteria and imaging protocols. In addition, DVAs may potentially be more difficult to detect in neonates due to small head size, incomplete myelination, short imaging protocols, and motion artifacts. On the other hand, statistically significant associations between DVAs and both primary brain tumors and multiple sclerosis have been previously described.<sup>18,20</sup> Because these disorders are frequent MR imaging indications in adults but very uncommon in the neonatal setting and infancy, the clinical indication itself may act as a confounder in the relationship between age and DVAs. Prospective neuroimaging studies in the healthy population at different ages using standardized imaging protocols are needed to better understand the

relationship between age and DVAs. Of note, we retrospectively identified DVAs and/or related enlarged drainage pathways in 27.2% of cases with available fetal MR imaging, confirming a congenital origin of these vascular abnormalities in those patients.<sup>6,27</sup> Conversely, we did not identify new DVAs in follow-up studies, but we considered this a limited population; thus, we cannot exclude some DVAs actually developing de novo postnatally.

In our cohort, greater than one-third of neonates presented with at least 1 type of vascular complication directly linked to DVAs. Similarly, Horsch et al<sup>22</sup> found a high percentage (42.9%) of abnormalities surrounding neonatal DVAs, while variable frequencies have been described in studies including adults and/or older children.<sup>10–13,15</sup> Of note, initial differences regarding the corrected age at first MR imaging, prematurity, and imaging indications between neonates with cDVAs and u-DVAs likely represent a detection bias related to the neuroimaging screening program of preterm neonates with birth weights of <1500 g performed in our institution or even by chance, because these values did not reach statistical significance after multiple-comparison correction.

In detail, associated WM signal abnormalities were present in 17.1% of our neonates and were even more frequent in the series published by Horsch et al<sup>22</sup> (21.4%). Previous studies have suggested that DVA-related WM changes present a bimodal distribution, peaking in younger children and older adults.<sup>11,12</sup> However,

the underlying mechanisms of these signal changes remain poorly understood. In younger children, delayed myelination in the draining territory of the DVA has been proposed as a potential explanation.<sup>12</sup> Alternatively, these signal alterations may represent venous congestion edema in the DVA territory due to an imbalance of the

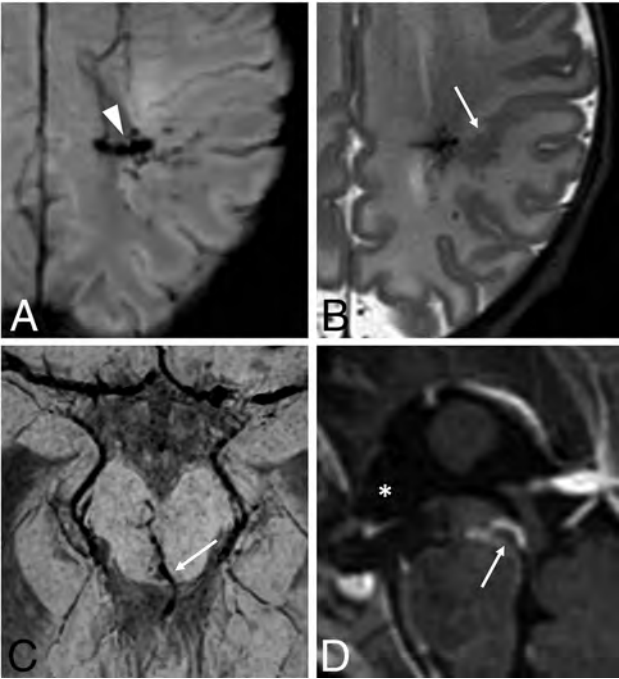


**FIG 3.** Neonatal developmental venous anomalies associated with focal polymicrogyria (A and B) and supratentorial hydrocephalus (C and D) in 2 different patients. Axial SWI (A) and T2WI (B) depict a developmental venous anomaly with deep venous drainage (arrowhead) and an adjacent area of cortical abnormality consistent with focal polymicrogyria (arrow). Axial SWI (C) and sagittal postgadolinium T1WI (D) demonstrate a mesencephalic developmental venous anomaly with the venous collector (arrows) causing focal compression of the inferior third of the cerebral aqueduct and consequent dilation of the anterior recesses of the third ventricle (asterisk), in keeping with supratentorial obstructive hydrocephalus (see also On-line Fig 8).

in- and outflow of blood in the DVA system, raising the pressure in the DVA.<sup>8</sup> Of note, the latter mechanisms can also explain the relatively high frequency of associated hemorrhages and/or ischemic changes identified in our sample (19.5% and 9.8% of cases, respectively). In the general population, the risk of DVA-related hemorrhage is considered to be low (<1%/year) and is usually attributed to adjacent CCM bleeding.<sup>2</sup> However, we detected CCMs in only a small percentage of cases (4.9%), in keeping with the theory that nonfamilial CCMs are acquired lesions related to DVAs through the process of hemorrhagic angiogenic proliferation.<sup>28,29</sup>

Taken together, our findings suggest that in the neonatal period, there is a higher risk of flow-related complications in DVAs, potentially leading to venous hypertension and associated venous congestion, hemorrhage, and/or infarction. Putative neonatal risk factors of hemodynamic decompensation include mechanical distortion during vaginal birth and immaturity of the venous, immune, and hemostatic systems as well as hypercoagulability, which may be potentiated by maternal factors or inflammation.<sup>30-32</sup> Finally, angioarchitectural factors yet unexplored in the neonatal setting, including angulation and stenosis of draining veins or tortuosity of medullary veins, could contribute to the development of ischemic or hemorrhagic complications.<sup>10,33</sup>

Most interesting, the presence of multiple DVAs (ie, multiplicity) was significantly more common in neonates with c-DVAs, even after multiple-comparisons correction, suggesting that more severe and widespread venous pathology may correspond to a more fragile venous outflow system and/or a higher propensity for thrombotic DVA events. Of note, 2 of these neonates presented with clinical-neuroradiologic features consistent with CVMS, a rare craniofacial vascular malformation disorder characterized by a wide spectrum of slow-flow vascular lesions distributed along  $\geq 1$  of the 3 craniofacial metameres, further supporting this theory.<sup>19</sup> Remarkably, 1 neonate also presented with a superior orbital fissure AVF, suggesting that this complex disorder may actually be a continuum potentially affecting  $> 1$  vessel type.

Our study also revealed focal polymicrogyria in the draining region of a DVA in 2 neonates (4.9%). DVAs or other venous drainage abnormalities or both have already been described adjacent to dysplastic cortical areas using

conventional and ultra-high-field MR imaging.<sup>34-37</sup> Because polymicrogyria is frequently associated with in utero disruptive events, coexistence of these 2 lesions suggests a causative effect of the DVA in the formation of this cortical malformation or, more probably, a shared pathomechanism related to early failure, abnormal development, or intrauterine occlusion of normal cerebral vessels.<sup>34,35,38</sup> Finally, in 1 neonate, we observed obstructive hydrocephalus related to another type of DVA complication, ie, mechanical compression of the cerebral aqueduct.<sup>8</sup> As in our patient, CSF diversion techniques usually lead to a good outcome in these rare cases.<sup>39</sup>

**Table 2: Neuroimaging abnormalities associated with developmental venous anomalies**

MRI Abnormalities	Neonatal Period <sup>a</sup> (n = 15)	Last Follow-Up <sup>a</sup> (n = 10)
WM T2 signal abnormalities	7	Reduced 2/5 Stable 1/5 Complete regression, 2/5
Restricted diffusion foci	4	Total regression, 2/2
Hemorrhagic foci	8	Gliosis with or without hemosiderin deposits, 3/3
Multiple CCM	2 <sup>b</sup>	Stable, 1/2 Growth, 1/2
PMG	2	Stable, 2/2
Calcifications	2	Stable, 2/2
Triventricular hydrocephalus	1	Resolution, 1/1 <sup>c</sup>
Draining venous varix thrombosis	1	Recanalization, 1/1

**Note:**—PMG indicates polymicrogyria.

<sup>a</sup> Some patients presented with  $\geq 1$  DVA-related complication.

<sup>b</sup> Includes 1 neonate with cerebrofacial venous metamerism syndrome.

<sup>c</sup> Postendoscopic third ventriculostomy.



As previously described, in our neonatal cohort, DVAs were more commonly located supratentorially and in the frontal lobe (41.4%).<sup>10,32</sup> Other common locations included the parieto-occipital (27.7%) and temporal (13.8%) lobes, while the basal ganglia and thalamus were involved in only 8.6% of cases. Of note, different from a previous neonatal case series, in our series, we identified infratentorial DVAs in 8.4% of cases, thus confirming a potential selection bias related to the use of cUS to depict posterior fossa DVAs.<sup>22</sup>

Regarding angioarchitecture features, we noticed a higher prevalence of multiple DVA collectors, which, together with larger caliber collectors, were significantly associated with DVA-related parenchymal abnormalities. These features may be related to the DVA size and, ultimately, to the volume of parenchyma under hemodynamic stress, ie, with reduced venous drainage capacity. Larger collectors may also be theoretically more prone to abnormal venous flow, with increased stasis and thrombosis. However, other studies performed in adults did not show statistically significant differences between parenchymal abnormalities and collecting vein diameters;<sup>11</sup> therefore, the relationship between these neuroimaging features requires more detailed study. Similarly, in the present study, posterior fossa location was not a risk factor for complicated DVAs. Methodologic issues in terms of populations of interest and types of complication may justify this variability,<sup>16,23,32</sup> and further studies are needed to also address this topic.

Serial imaging of a subgroup of neonates with c-DVAs revealed that DVAs and adjacent MR imaging abnormalities frequently present a dynamic evolution during the early years of life. These findings are in line with previous studies and probably reflect progressive brain and vascular maturation during early infancy.<sup>22,40</sup> Indeed, neuroimaging follow-up demonstrated overall improvement in most cases of c-DVAs. More specifically, WM abnormalities were reduced in size or even completely resolved. Furthermore, ischemic and hemorrhagic foci also tended to subside without signs of intracranial re-hemorrhage. Of note, clinical outcomes of patients with c-DVAs was concordant with their favorable MR imaging evolution, with normal neurologic examination findings in most cases. Good clinical and neurologic outcomes were also reported by Horsch et al<sup>22</sup> and are probably related to intrinsic brain plasticity as well as normalization of potential risk factors present in the neonatal phase.

### Limitations

This study has some limitations. First, case selection was based on a retrospective single-center search of radiology reports. Therefore, although DVAs are routinely described in our institution by all staff members, the true DVA prevalence might be underestimated. Similarly, a relevant number of neonates was scanned on a 1.5T system, and gadolinium-based contrast media were only occasionally used, potentially leading to lower DVA detection.<sup>34</sup> However, SWI was performed in almost all neonates (92.7%) and has a high diagnostic sensitivity for DVAs in children, especially when sedation is achieved without propofol and sevoflurane.<sup>4</sup> Second, this study was performed in a tertiary pediatric institution, leading to potential selection bias toward inclusion of more severe DVA cases and limiting generalizability

toward a different setting. Moreover, DVA collectors were measured on axial T2\*WI, and this sequence can be influenced by the level of blood oxygenation and the magnetic field strength. However, none of the neonates were examined under general anesthesia, and complicated DVAs were actually less frequent in the group of subjects scanned using a 3T magnet. Therefore, if there were any bias related to the examination technique in terms of DVA collector size and MR imaging complications, it would actually exert its influence toward the null hypothesis. Finally, longitudinal data were missing in some patients, and clinical evaluation at follow-up was obtained from clinical records, though formal neurologic evaluation was performed in all assessed cases.

### CONCLUSIONS

Real-world DVA detection in this population of neonates with clinically-indicated brain MR imaging reached 1.9%, which is lower than percentages of studies including older children and adults and might be an underestimation of the true prevalence. Of all neonates with detected DVAs, around one-third presented with DVA-related complications. The latter group had a significant tendency toward multiplicity and additional vascular malformations but usually had favorable neuroimaging findings and neurologic evolution at follow-up. DVAs could be retrospectively diagnosed in utero in one-quarter of neonates with fetal MR imaging, confirming, at least in these cases, a congenital origin.

Disclosures: Ana F. Geraldo—UNRELATED: Grants/Grants Pending: European Society of Neuroradiology, Comments: annual research grant. Alessandro Parodi—UNRELATED: Consultancy: Shire Human Genetic Therapies, Comments: 2018–2019 collaboration in the ROPP-2008-01 clinical trial (assessment of cranial ultrasound images of enrolled subjects). Paul Govaert—UNRELATED: Payment for Development of Educational Presentations: book, Mac Keith Press London. Mariasavina Severino—RELATED: Grant: "Ricerca Corrente Disordini Neurologici e Muscolari (Linea 5)" of Italian Ministry of Health, Compagnia di San Paolo (ROL 20573)\*; UNRELATED: Employment: neuroradiology consultant, Scientific Institute for Research, Hospitalization and Healthcare Istituto Giannina Gaslini. \*Money paid to the institution.

### REFERENCES

1. Malova M, Rossi A, Severino M, et al. **Incidental findings on routine brain MRI scans in preterm infants.** *Arch Dis Child Fetal Neonatal Ed* 2017;102:F73–78 CrossRef Medline
2. Hon JM, Bhattacharya JJ, Counsell CE, et al; SIVMS Collaborators. **The presentation and clinical course of intracranial developmental venous anomalies in adults: a systematic review and prospective, population-based study.** *Stroke* 2009;40:1980–85 CrossRef Medline
3. Lee C, Pennington MA, Kenney CM, et al. **MR evaluation of developmental venous anomalies: medullary venous anatomy of venous angiomas.** *AJNR Am J Neuroradiol* 1996;17:61–70 Medline
4. Gökçe E, Acu B, Beyhan M, et al. **Magnetic resonance imaging findings of developmental venous anomalies.** *Clin Neuroradiol* 2014;24:135–43 CrossRef Medline
5. Young A, Poretti A, Bosemani T, et al. **Sensitivity of susceptibility-weighted imaging in detecting developmental venous anomalies and associated cavernomas and microhemorrhages in children.** *Neuroradiology* 2017;59:797–802 CrossRef Medline
6. Geraldo AF, Melo M, Monteiro D, et al. **Developmental venous anomaly depicted incidentally in fetal MRI and confirmed in post-natal MRI.** *Neuroradiology* 2018;60:993–94 CrossRef Medline
7. Lasjaunias P, Burrows P, Planet C. **Developmental venous anomalies (DVA): the so-called venous angioma.** *Neurosurg Rev* 1986;9:233–42 CrossRef Medline

8. Pereira VM, Geibprasert S, Krings T, et al. **Pathomechanisms of symptomatic developmental venous anomalies.** *Stroke* 2008;39:3201–15 CrossRef Medline
9. Rinaldo L, Lanzino G, Flemming KD, et al. **Symptomatic developmental venous anomalies.** *Acta Neurochir (Wien)* 2020;162:1115–25 CrossRef Medline
10. San Millán Ruiz D, Delavelle J, Yilmaz H, et al. **Parenchymal abnormalities associated with developmental venous anomalies.** *Neuroradiology* 2007;49:987–95 CrossRef Medline
11. Santucci GM, Leach JL, Ying J, et al. **Brain parenchymal signal abnormalities associated with developmental venous anomalies: detailed MR imaging assessment.** *AJNR Am J Neuroradiol* 2008;29:1317–23 CrossRef Medline
12. Linscott LL, Leach JL, Zhang B, et al. **Brain parenchymal signal abnormalities associated with developmental venous anomalies in children and young adults.** *AJNR Am J Neuroradiol* 2014;35:1600–07 CrossRef Medline
13. Takasugi M, Fujii S, Shinohara Y, et al. **Parenchymal hypointense foci associated with developmental venous anomalies: evaluation by phase-sensitive MR imaging at 3T.** *AJNR Am J Neuroradiol* 2013;34:1940–44 CrossRef Medline
14. Sharma A, Zipfel GJ, Hildebolt C, et al. **Hemodynamic effects of developmental venous anomalies with and without cavernous malformations.** *AJNR Am J Neuroradiol* 2013;34:1746–51 CrossRef Medline
15. Umino M, Maeda M, Matsushima N, et al. **High-signal-intensity abnormalities evaluated by 3D fluid-attenuated inversion recovery imaging within the drainage territory of developmental venous anomalies identified by susceptibility-weighted imaging at 3 T.** *Jpn J Radiol* 2014;32:397–404 CrossRef Medline
16. Zhang S, Ma L, Wu C, et al. **A rupture risk analysis of cerebral cavernous malformation associated with developmental venous anomaly using susceptibility-weighted imaging.** *Neuroradiology* 2020;62:39–47 CrossRef Medline
17. Jones BV, Linscott L, Koberlein G, et al. **Increased prevalence of developmental venous anomalies in children with intracranial neoplasms.** *AJNR Am J Neuroradiol* 2015;36:1782–85 CrossRef Medline
18. Roux A, Edjlali M, Porelli S, et al. **Developmental venous anomaly in adult patients with diffuse glioma: a clinically relevant coexistence?** *Neurology* 2019;92:e55–62 CrossRef Medline
19. Brinjikji W, Nicholson P, Hilditch CA, et al. **Cerebrofacial venous metamerism syndrome: spectrum of imaging findings.** *Neuroradiology* 2020;62:417–25 CrossRef Medline
20. Halicioglu S, Turkoglu SA. **Role of developmental venous anomalies in etiopathogenesis of demyelinating diseases.** *Int J Neurosci* 2019;129:245–51 CrossRef Medline
21. Shiran SI, Ben-Sira L, Elhasid R, et al. **Multiple brain developmental venous anomalies as a marker for constitutional mismatch repair deficiency syndrome.** *AJNR Am J Neuroradiol* 2018;39:1943–46 CrossRef Medline
22. Horsch S, Govaert P, Cowan FM, et al. **Developmental venous anomaly in the newborn brain.** *Neuroradiology* 2014;56:579–88 CrossRef Medline
23. Silva AH, Wijesinghe H, Lo WB, et al. **Paediatric developmental venous anomalies (DVAs): how often do they bleed and where?** *Childs Nerv Syst* 2020;36:1435–43 CrossRef Medline
24. Linscott LL, Leach JL, Jones BV, et al. **Developmental venous anomalies of the brain in children: imaging spectrum and update.** *Pediatr Radiol* 2016;46:394–406 CrossRef Medline
25. Brinjikji W, El-Masri AE, Wald JT, et al. **Prevalence of developmental venous anomalies increases with age.** *Stroke* 2017;48:1997–99 CrossRef Medline
26. Zabramski JM, Wascher TM, Spetzler RF, et al. **The natural history of familial cavernous malformations: results of an ongoing study.** *J Neurosurg* 1994;80:422–32 CrossRef Medline
27. Okudera T, Huang YP, Fukusumi A, et al. **Micro-angiographical studies of the medullary venous system of the cerebral hemisphere.** *Neuropathology* 1999;19:93–118 CrossRef Medline
28. Dammann P, Wrede K, Zhu Y, et al. **Correlation of the venous angioarchitecture of multiple cerebral cavernous malformations with familial or sporadic disease: a susceptibility-weighted imaging study with 7-Tesla MRI.** *J Neurosurg* 2017;126:570–77 CrossRef Medline
29. Brinjikji W, El-Masri AE, Wald JT, et al. **Prevalence of cerebral cavernous malformations associated with developmental venous anomalies increases with age.** *Childs Nerv Syst* 2017;33:1539–43 CrossRef Medline
30. Yang JY, Chan AK, Callen DJ, et al. **Neonatal cerebral sinovenous thrombosis: shifting the evidence for a diagnostic plan and treatment strategy.** *Pediatrics* 2010;126:e693–e700 CrossRef Medline
31. Ami O, Maran JC, Gabor P, et al. **Three-dimensional magnetic resonance imaging of fetal head molding and brain shape changes during the second stage of labor.** *PLoS One* 2019;14:e0215721 CrossRef Medline
32. Kumar S, Lanzino G, Brinjikji W, et al. **Infratentorial developmental venous abnormalities and inflammation increase odds of sporadic cavernous malformation.** *J Stroke Cerebrovasc Dis* 2019;28:1662–67 CrossRef Medline
33. Hong YJ, Chung TS, Suh SH, et al. **The angioarchitectural factors of the cerebral developmental venous anomaly: can they be the causes of concurrent sporadic cavernous malformation?** *Neuroradiology* 2010;52:883–91 CrossRef Medline
34. Thompson JE, Castillo M, Thomas D, et al. **Radiologic-pathologic correlation polymicrogyria.** *AJNR Am J Neuroradiol* 1997;18:307–12 Medline
35. Cagneaux M, Paoli V, Blanchard G, et al. **Pre- and postnatal imaging of early cerebral damage in Sturge-Weber syndrome.** *Pediatr Radiol* 2013;43:1536–39 CrossRef Medline
36. De Ciantis A, Barkovich AJ, Cosottini M, et al. **Ultra-high-field MR imaging in polymicrogyria and epilepsy.** *AJNR Am J Neuroradiol* 2015;36:309–16 CrossRef Medline
37. Mankad K, Biswas A, Espagnet MCR, et al. **Venous pathologies in paediatric neuroradiology: from foetal to adolescent life.** *Neuroradiology* 2020;62:15–37 CrossRef Medline
38. Stutterd CA, Leventer RJ. **Polymicrogyria: a common and heterogeneous malformation of cortical development.** *Am J Med Genet C Semin Med Genet* 2014;166C:227–39 CrossRef Medline
39. Higa N, Dwiutomo R, Oyoshi T, et al. **A case of developing obstructive hydrocephalus following aqueductal stenosis caused by developmental venous anomalies.** *Childs Nerv Syst* 2020;36:1549–55 CrossRef Medline
40. Howard T, Abruzzo T, Jones B, et al. **Postnatal evolution of a developmental venous anomaly.** *J Pediatr Neuroradiol* 2015;01:305–11 CrossRef

# Perinatal Arterial Ischemic Stroke in Fetal Vascular Malperfusion: A Case Series and Literature Review

A.F. Geraldo, A. Parodi, M. Bertamino, F. Buffelli, S. Uccella, D. Tortora, P. Moretti, L. Ramenghi, E. Fulcheri, A. Rossi, and M. Severino



## ABSTRACT

**SUMMARY:** Fetal vascular malperfusion includes a continuum of placental histologic abnormalities increasingly associated with perinatal brain injury, namely arterial ischemic stroke. Here, we describe the clinical-neuroimaging features of 5 neonates with arterial ischemic stroke and histologically proved fetal vascular malperfusion. All infarcts involved the anterior territories and were multiple in 2 patients. In 2 neonates, there were additional signs of marked dural sinus congestion, thrombosis, or both. A mixed pattern of chronic hypoxic-ischemic encephalopathy and acute infarcts was noted in 1 patient at birth. Systemic cardiac or thrombotic complications were present in 2 patients. These peculiar clinical-radiologic patterns may suggest fetal vascular malperfusion and should raise the suspicion of this rare, underdiagnosed condition carrying important implications in patient management, medico-legal actions, and future pregnancy counseling.

**ABBREVIATIONS:** FVM = fetal vascular malperfusion; PAIS = perinatal arterial ischemic stroke

Perinatal stroke is a group of cerebrovascular diseases occurring between 20 weeks of fetal life and 28 postnatal days caused by focal disruption of normal (arterial or venous) cerebral blood flow.<sup>1,2</sup> Many patients are diagnosed several months after birth and therefore classified as having “presumed” perinatal stroke.<sup>1,2</sup>

Perinatal arterial ischemic stroke (PAIS) and presumed PAIS are the most frequent subtypes of perinatal stroke,<sup>2,3</sup> with an overall incidence up to 1 per 1600 live births.<sup>4</sup> They represent an important cause of cerebral palsy and are frequently associated with epilepsy and abnormal cognitive, neurosensory, and behavioral outcomes.<sup>2,5</sup> The pathomechanisms of PAIS and presumed PAIS are very likely similar but remain elusive, with multiple maternal, fetal, and placental risk factors proposed.<sup>2,6</sup> Of these, placental abnormalities are the least investigated.<sup>6</sup> Indeed, scant data about the placenta have been presented in the largest multicenter PAIS studies published so far.<sup>7</sup>

Fetal vascular malperfusion (FVM), previously known as fetal thrombotic vasculopathy,<sup>8</sup> is an umbrella term introduced in 2015 by the Amsterdam International Consensus group of pathologists, encompassing a spectrum of histologic placental abnormalities, frequently at different stages compatible with reduced or absent perfusion in any location of the fetoplacental vasculature, such as occlusive thrombi, mainly in large-stem vessels, accompanied by downstream changes, including organization, septation, red cell extravasation, endothelial destruction, loss of vascularity (avascular villi), and ultimately fibrosis.<sup>9</sup> According to the location or extension of placental abnormalities, it can be further classified into low- or high-grade FVM.<sup>9</sup> The exact pathogenesis of FVM is still not clear. However, venous stasis, endothelial or vessel wall damage, and hypercoagulability are potentially involved (Virchow triad).<sup>9,10</sup> Importantly, there is increasing evidence that FVM plays an important role in neonatal mortality, morbidity, and outcome, including brain injury.<sup>11-14</sup> In particular, the

Received May 7, 2020; accepted after revision July 17.

From the Units of Neuroradiology (A.F.G., D.T., A.R., M.S.), Neonatal Intensive Care (A.P., L.R.), Physical Medicine and Rehabilitation (M.B., P.M.), Gynaecologic and Fetal-Perinatal Pathology (F.B., E.F.), and Child Neuropsychiatry (S.U.), IRCCS Istituto Giannina Gaslini, Genoa, Italy; Diagnostic Neuroradiology Unit (A.F.G.), Imaging Department, Centro Hospitalar Vila Nova de Gaia/Espinho, Portugal; and Departments of Neurosciences, Rehabilitation, Ophthalmology, Genetics, Maternal and Child Health (DINOEMI) (L.R.), Surgical Sciences and Integrated Diagnostics, Pathology Division of Anatomic Pathology (E.F.), and Health Sciences (DISSAL) (A.R.), University of Genoa, Genoa, Italy; and

This work was supported by funds of Compagnia San Paolo (Reaserch Grant to MDR; SIME 2017-0621, ROL 20573), the “Associazione per la Lotta all’Ictus Cerebrale” (ALICe) and “Ricerca Corrente 2020 (linea 5)” of the Italian Ministry of Health, assigned to Rehabilitation Unit of IRCCS Giannina Gaslini. These sponsors had no involvement in any of the study steps: design, data collection, analysis, and interpretation, writing of the report, and following submission.

Ethics approval: All procedures performed in studies involving human participants were in accordance with ethical standards of the institutional and/or national research committee and with the 1964 Helsinki declaration and its later amendments or comparable ethical standards.

Informed consent was waived due to retrospective nature of the study.

Please address correspondence to Marta Bertamino, MD, PhD, Physical Therapy and Rehabilitation Unit, IRCCS Istituto Giannina Gaslini, Genoa, Italy; e-mail: MartaBertamino@gaslini.org; @MBertamino

Indicates open access to non-subscribers at [www.ajnr.org](http://www.ajnr.org)

Indicates article with supplemental on-line tables.

Indicates article with supplemental on-line photos.

<http://dx.doi.org/10.3174/ajnr.A6857>



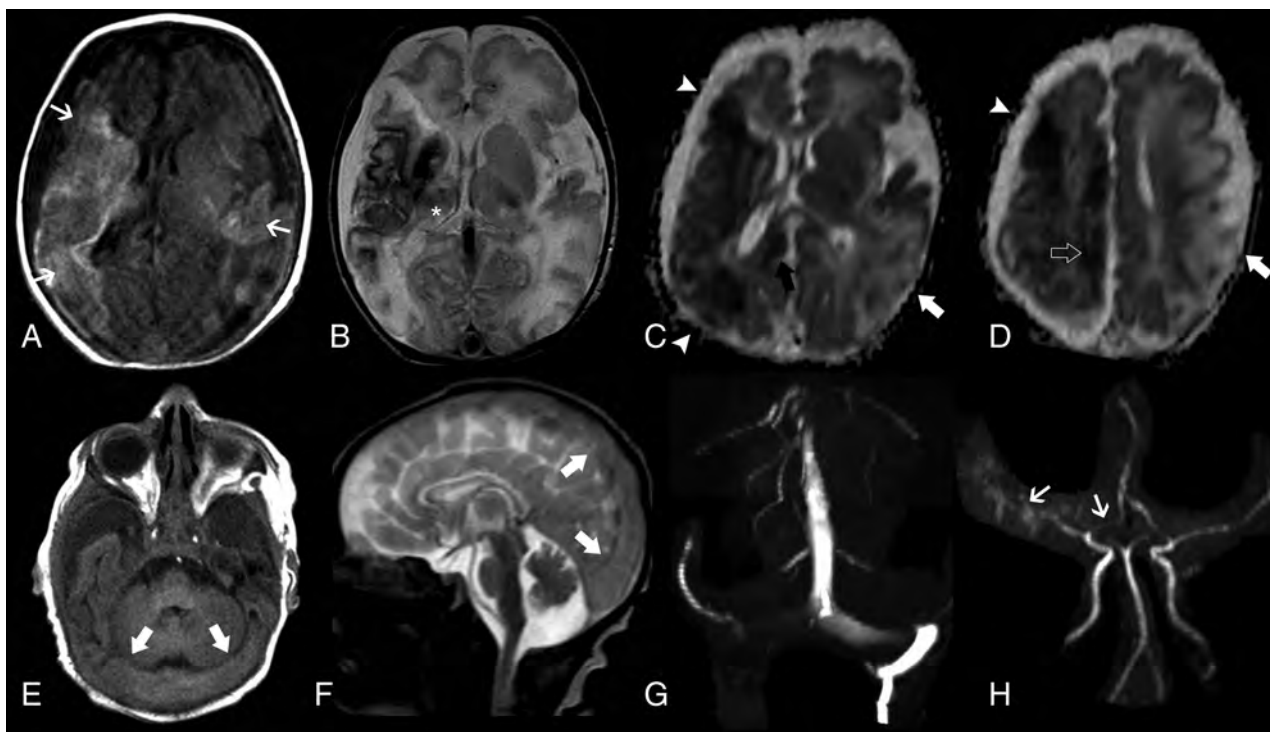


**FIG 1.** Brain MR imaging of patient 1 performed on day 1. Axial T1-weighted image (A), T2-weighted image (B), and ADC maps (C and D) demonstrate acute ischemic infarcts in the territory of the right MCA (arrowhead) and right anterior cerebral artery (ACA) (open arrow) associated with mild diffuse atrophy of this cerebral hemisphere as well as a late subacute infarct in the territory of the left MCA (arrow). In addition, there are signs of early secondary network injury of the right thalamus (asterisk) and splenium of the corpus callosum (black arrow) as well as subcortical and deep white matter injury and laminar cortical necrosis (small arrows). Axial T1-weighted image (E) and sagittal T2-weighted image (F) depict marked distension of the transverse and superior sagittal sinuses (arrows) with signs of slowing of the venous blood flow, confirmed on the coronal view of MRV (G). MRA (H) shows reduced visualization of the right MCA and ACA branches compared with the contralateral side (small arrows).

association between FVM and perinatal arterial and venous stroke is increasingly acknowledged.<sup>10,11,13-17</sup> On the other hand, FVM remains an underrecognized cause of PAIS because the onset of clinical manifestations is usually around 12–72 hours after birth or even months later in presumed PAIS, thus limiting the availability of placental tissue for histologic examination.<sup>2,18,19</sup> Moreover, reports focusing on imaging data of patients with PAIS in the context of proved FVM are still limited, especially within the radiology literature.<sup>11,13,15-18</sup> Nevertheless, failure to recognize this etiology may have important implications in patient management, as well as in medicolegal actions and future pregnancy counseling.<sup>19</sup> Therefore, it is crucial to increase awareness of FVM-related PAIS in the neuroradiology community and to highlight the importance of knowing the results of placenta examination when reporting these cases.

Here, we describe the neuroradiological features of 5 neonates with PAIS and histologically proved FVM and their correlation with histopathologic and clinical findings as well as neurologic outcome.

### CASE SERIES

Regional review board approval was obtained for this single-center series (N.096/2019), waiving parental written informed consent. Five patients with PAIS and histologically proved FVM were identified from the institutional database of pediatric patients treated for stroke at the Gaslini Children's Hospital between 2012 and 2019. All patients were initially investigated by cranial sonography followed

by brain MR imaging in 4 patients (range: 1 day–2.3 months). Longitudinal brain MR imaging were obtained in 3 neonates (range: 14 days–2.4 years). In total, 11 brain MR imaging and 2 head CT studies were available for review. Images were analyzed in consensus by 2 pediatric neuroradiologists (M.S. and A.F.G., 10 and 5 years' experience, respectively). FVM histologic features were reviewed by 2 pathologists (E.F. and F.B., 30 and 5 years' experience, respectively) and classified into high or low grade.<sup>9</sup> Clinical data at diagnosis and follow-up (range: 15 days–5 years) were obtained from electronic charts.

On-line Table 1 lists clinical and placental features and the outcomes of our cohort. Neuroimaging features are summarized in On-line Table 2. Parents were nonconsanguineous, and family history was unremarkable in all patients. All neonates were male and born by cesarean section (4/5 urgent procedures). Two neonates were born from dichorionic diamniotic twin pregnancies. Three pregnancies were complicated by threatened preterm labor, preterm premature rupture of membranes, and preeclampsia. Mean gestational age at birth was 34.2 weeks (range: 30–39 weeks). Intrauterine growth restriction was diagnosed in 3/5 patients. Mean birth weight was 1843 g (range: 910–3280 g), length was 42 cm (range: 35–51 cm), and head circumference was 30 cm (range: 26–34 cm). PAIS was symptomatic at birth in 3/5 neonates (clonic seizures and apneas) and was incidentally discovered in 2/5 neonates. In all patients, coagulopathies and congenital cardiac malformations were not detected. Associated clinical findings included a large

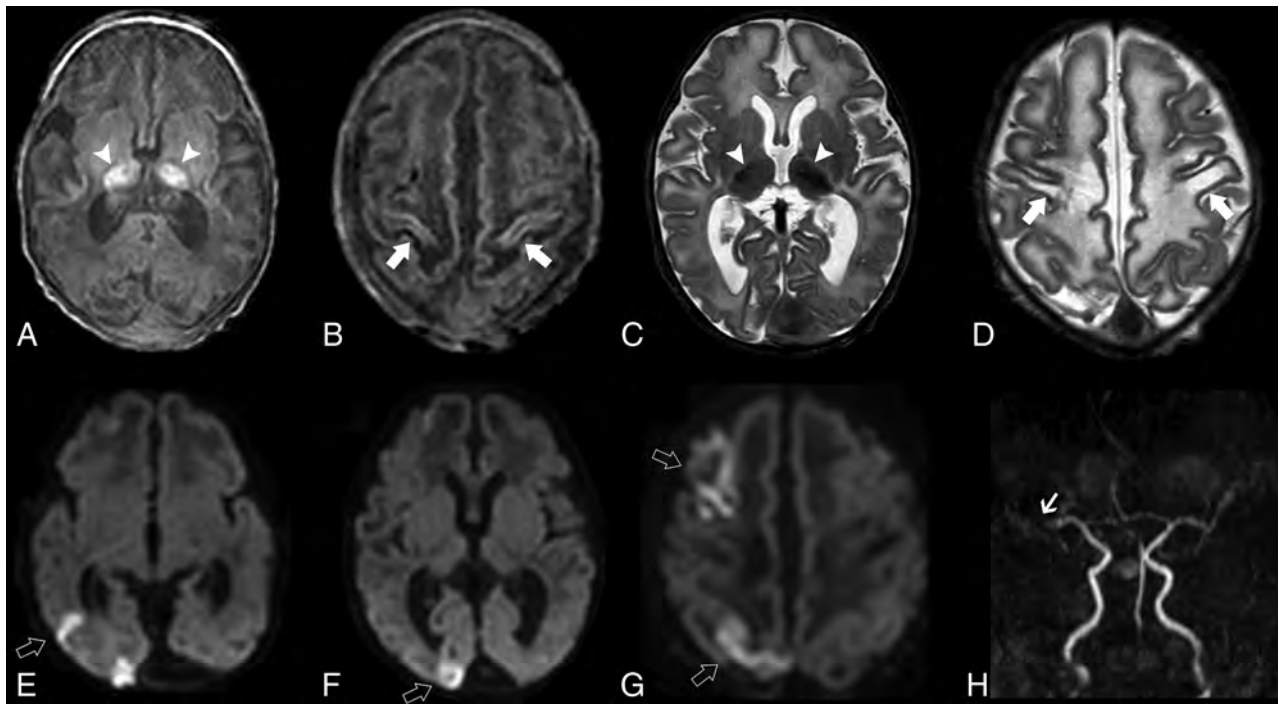


**FIG 2.** Brain MR imaging of patient 2 performed on day 1. Axial T1-weighted image (A and B), T2-weighted (C and D) and diffusion-weighted (E–G) images show bilateral atrophy and abnormal T1 and T2 signal intensity of the thalami (*arrowheads*) and perirhinal regions (*arrows*) in the context of hypoxic-ischemic lesions. Also note multiple areas of acute ischemic infarct distributed in the right MCA territory and watershed region (*open arrows*). MRA (H) demonstrates reduced flow-related signal of the right MCA branches (*small arrow*).

deep skin ulcer related to distal thromboembolism ( $n = 1$ , On-line Fig 1), transient myocardial ischemia ( $n = 1$ ), respiratory distress syndrome of prematurity ( $n = 3$ ), and necrotizing enterocolitis ( $n = 1$ ).

Cranial sonography findings were abnormal in 4/5 patients, showing unilateral or bilateral WM hyperechogenicity ( $n = 3$ ) and a focal irregular cavitation in the parietal subcortical WM ( $n = 1$ , On-line Fig 2).

On imaging, PAISs were multiple in 2/5 patients and involved the anterior circulation in all patients (MCA in 4 neonates, with additional anterior cerebral artery involvement in 1 patient), mostly with a superficial involvement (4/5 patients, On-line Fig 3). In 2/5 patients, PAIS was detected in different phases (acute, subacute, or chronic) at birth (Figs 1 and 2). Signs of early corticobasal diaschisis were noted in 3/4 patients, and early Wallerian degeneration of the corticospinal tract was present in 2/4 patients (Fig 3). Concomitant dural sinus congestion, thrombosis, or both was depicted in 2/5 patients, 1 of whom also displayed signs of chronic hypoxic-ischemic encephalopathy at birth (Figs 1, 2 and On-line Fig 4). MRA at diagnosis was available in 2 patients, showing reduced flow-signal in the involved arteries. Follow-up brain MR imaging and MRA studies demonstrated chronic evolutions of PAIS, without new arterial infarcts, in 2/3 patients. In 1 patient, we observed the phenomenon of DWI reversal of the cortical ischemic lesions, in keeping with spontaneous blood flow restoration in the affected distal MCA branches.<sup>20</sup> Resolution of dural sinus congestion and thrombosis was noted in 2/2 patients (On-line Figs 4 and 5).

Histologic examination of the placenta revealed long-standing high-grade FVM in different evolutionary stages in all affected patients (Fig 4). In both dichorionic diamniotic twin pregnancies, FVM was detected in the chorionic disk of each twin with brain injury, but no signs of FVM were found in the chorionic disk of the unaffected co-twin. The placentas of the co-twins presented minor signs of long-standing hypoxic damage and asynchronous patchy ischemic lesions in 1 patient and focal congestion with recent intravillous hemorrhages in the other. Signs of maternal vascular malperfusion were present in 4/5 patients. Umbilical cord abnormalities were present in all affected patients: nuchal cord ( $n = 2$ ), hypercoiled ( $n = 1$ ), hypocoiled ( $n = 1$ ), and false knots with torsion ( $n = 1$ ). No signs of inflammation of the umbilical cord, membranes, or amniochorial vessels were depicted in any of the patients.

The preterm neonate who developed necrotizing enterocolitis died at 15 days of life. Mean age at last clinical follow-up of the remaining patients was 28 months (range: 6–60). Moderate to severe developmental delay was diagnosed in 3 children, associated with microcephaly in 2 patients. Motor deficits were present in 3/5 children; 1 developed drug-resistant epilepsy, required noninvasive respiratory support and enteral artificial nutrition through gastrostomy at 9 months of age, and died at 10 months after a respiratory infection. Both co-twins of the 2 affected patients were born with appropriate birth weight, length, and head circumference for gestational age and presented with normal psychomotor development at last follow-up (24 and 36 months, respectively).

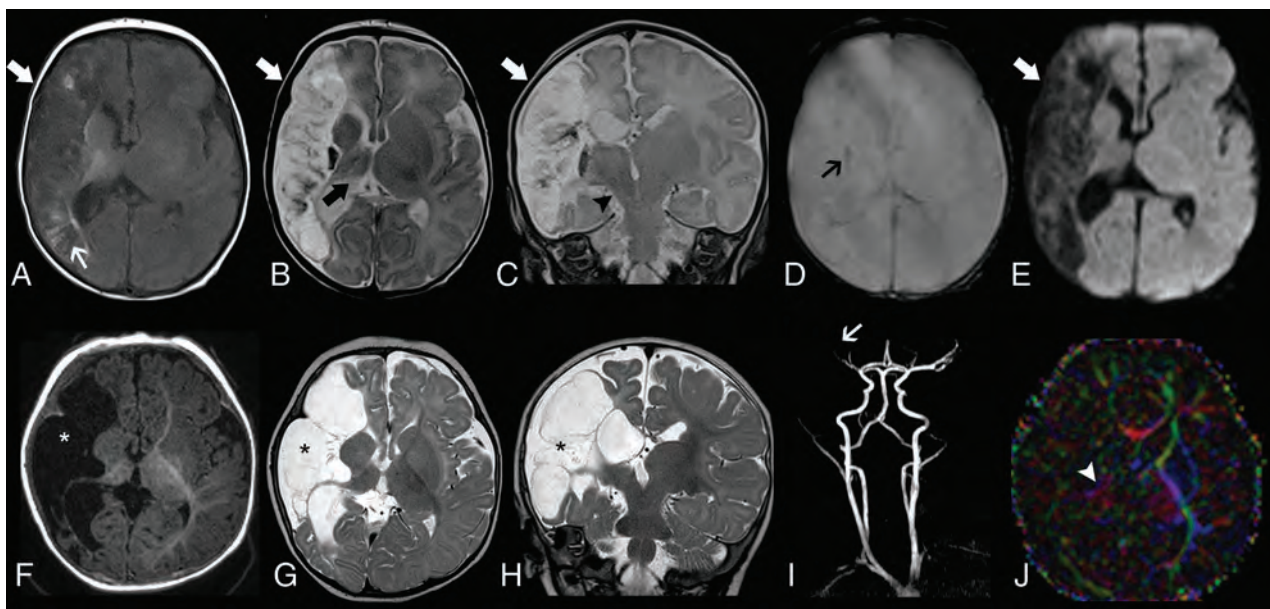


**FIG 3.** Longitudinal neuroimaging evaluation of patient 5. Initial brain MR imaging obtained at 18 days of life, including axial T1-weighted image (A), axial (B) and coronal (C) T2-weighted images, axial T2\* image (D) and diffusion-weighted image (E), demonstrate a large ischemic infarct in the superficial and deep territory of the right MCA in the late subacute or early chronic phase (arrows). There are associated areas of cortical laminar necrosis (thin white arrow) and a focus of hemorrhagic transformation (thin black arrow). Also note signs of ipsilateral thalamic diaschisis (thick black arrow) and Wallerian degeneration of the corticospinal tract (arrowhead). Follow-up brain MR imaging performed at 6 months (F–J). Axial T1-weighted image (A) and axial (B) and coronal (C) T2-weighted images depict progressive cystic encephalomalacia and atrophy in the infarcted area with ex vacuo enlargement of the adjacent CSF spaces (asterisks). MRA reveals reduced visibility of right MCA branches (arrow). Axial directionally encoded color fractional anisotropy (FA) map at the level of the basal ganglia shows markedly reduced FA of the posterior limb of the right internal capsule (arrowhead).

## DISCUSSION

Data on neuroimaging features of neonatal stroke associated with thrombotic or inflammatory placental disorders are very rare.<sup>15,17</sup> In the largest study, which was by Bernson-Leung et al,<sup>17</sup> collecting 46 children with neonatal arterial or venous ischemic stroke from 3 academic medical centers, 13/28 (46.4%) PAISs and 10/18 (55.5%) venous strokes were linked to FVM. Regarding the imaging pattern, PAIS mostly involved the left hemisphere in the MCA territory and was frequently multiple or superficial, but the right hemisphere or perforator territories were affected only in a minority of patients.<sup>15,17</sup> Similarly, we found that the anterior territories were always involved with sparing of the posterior circulation. In addition, multiple recurrent infarcts and/or small corticosubcortical infarcts were prevalent, suggesting a thromboembolic phenomenon occurring at different phases as the most plausible pathomechanism linking FVM to PAIS. Indeed, because the rate of thrombophilia is similar in placentas with and without FVM,<sup>12,13</sup> the main hypothesis is the spread of FVM-related thromboemboli into the venous fetal circulation, in turn reaching the aorta and then the intracranial vessels through a patent foramen ovale and a right-to-left direction of blood flow in the fetal ductus arteriosus.<sup>21,22</sup> Predominant involvement of the MCA territory is also described in most studies including patients with PAIS of mixed or unknown cause,<sup>3,7,23</sup> though multiple infarcts are usually less frequent (<20%–30%).<sup>23</sup> Interestingly, some of the recurrent infarcts seen in our cohort appeared to be chronic with cortical T1 hyperintensity indicative of laminar necrosis despite having been detected in neonates on day 1; such observation favors an intrauterine onset, as expected to occur in FVM.

Reduced flow signal involving distal arterial branches ipsilateral to the ischemic strokes was present in 2 patients in this series. Intracranial arterial abnormalities have been reported in a subset of neonates with PAIS of variable causes,<sup>24–26</sup> likely reflecting reduced arterial blood supply to the infarcted territory and/or persistently occluded or near-occluded vessels in the context of a proximal thromboembolism.<sup>24,25</sup> We did not identify large-vessel occlusions in any of our patients, but these have only been exceptionally described in FVM-related PAIS,<sup>19,21</sup> probably caused by rapid vessel recanalization in neonates and/or more distal embolization.<sup>19,27</sup>

Interestingly, 2 of our neonates presented additional features related to severe venous congestion and/or thrombosis involving the superior sagittal and transverse sinuses. The co-occurrence of both arterial and venous complications in the setting of FVM has not been reported before but is theoretically plausible because FVM has been described in association with both PAIS and isolated neonatal cerebral sinovenous thrombosis.<sup>5,17</sup> In particular, this peculiar combination might be caused by common risk factors underlying FVM, activating coagulation and inflammatory pathways in both the arterial and venous system<sup>28</sup> or by secondary marked reduction of venous flow in the dural sinuses caused by diffuse fetoplacental venous stasis.<sup>17</sup> On the other hand, additional risk factors previously described in the literature for neonatal dural sinovenous thrombosis<sup>29,30</sup> and not necessarily related to FVM, such as emergent cesarean section, might have contributed to venous complications in the present patients. Therefore, future studies on larger series are needed to elucidate the role of FVM in perinatal venous stroke and to estimate the exact prevalence of both arterial and venous abnormalities in neonates with documented FVM.



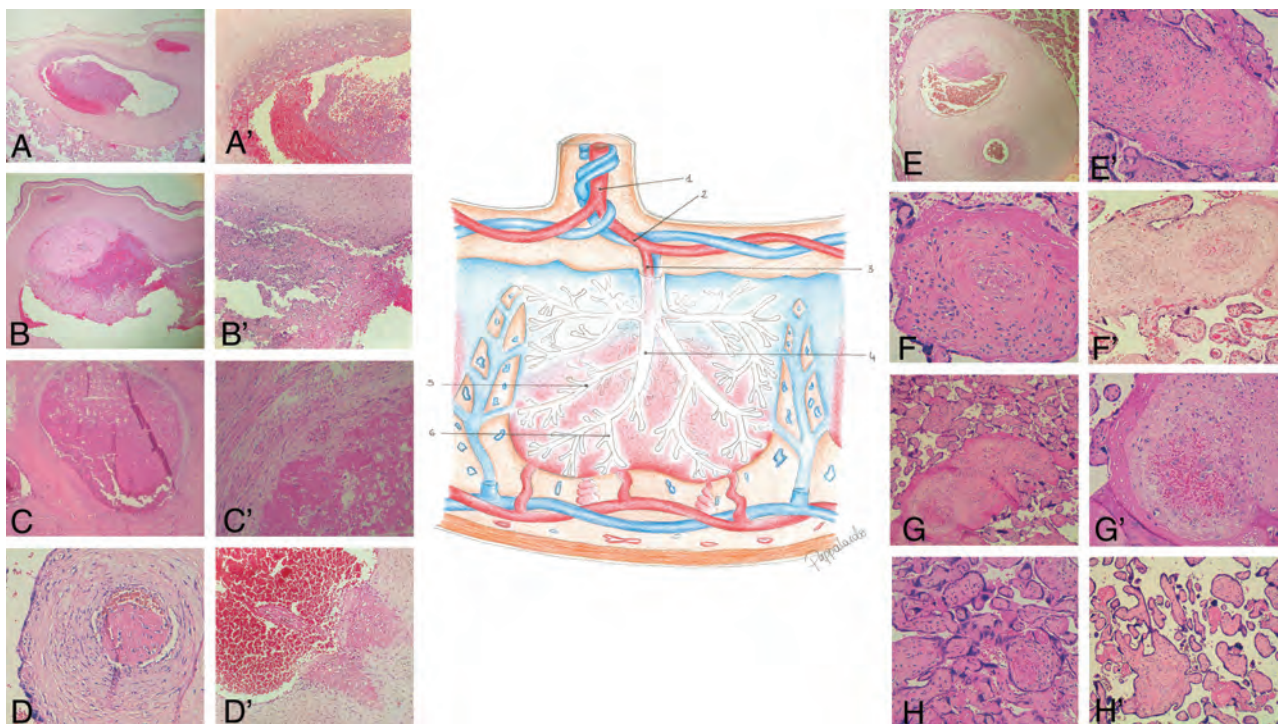


**FIG 4.** Schematic representation of the placental fetal vascularization and histologic features of fetal vascular malperfusion. 1. Vessel of umbilical cord. 2. Amniotome vessels (A, A', B, B'). 3. First-order stem vessels (C, C'). 4. Second-order stem vessels (D, D'). 5. Third-order stem vessels (E, E', F). 6. Fourth-order stem vessels (F', G, G', H). A. Amniotome vessel with dilated lumen occupied by a floating thrombus adhering to the wall by means of coagulation (patient 5). A'. Detail of the previous figure: evidence of wall damage in the form of a necrotic fibrinoid band (patient 5). B. Amniotome vessel with dilated lumen in which a thrombus in various phases of evolution adheres to the wall; the thrombus has a fibrous nucleus, at the margins of which a recent coagulation and a fibrous thrombus in a medium stage of evolution are observed (patient 5). B'. Detail of B: granulocytic infiltrate of the wall indicating vasculitis as the cause of thrombosis (patient 5). C. First-order stem vessel totally occupied by a long-standing thrombus adherent to the wall (patient 1). C'. Detail of C, a segment of the destructured wall shows evolving lesions after adhesion of the thrombus (patient 1). D. Second-order stem vessel with a thrombotic formation occluding the lumen without adhering to the wall (patient 3). D'. Second-order stem vessel with wall lesion and initial detachment of a floating thrombus into the bloodstream. E. Third-order stem vessel displaying wall damage and initial adhesion of a fibrinoid thrombus. E'. Third-order stem vessel with the lumen completely occluded by a long-standing thrombotic formation hampering the recognition of vessel wall structure (patient 1). F. Third-order stem vessel with a long-standing partly recanalized occlusive thrombus (patient 1). F'. Fourth-order stem vessel: occluded lumen with revascularization; adjacent to this, a totally occluded vessel whose wall structure is no longer recognizable (patient 4). G. Fourth-order stem vessel displaying initial recanalization and endothelial proliferation promoting endoluminal neoangiogenesis (patient 1). G'. Detail of G showing the intermixing of nonagglutinated erythrocytes and incomplete neo-formed vessels (patient 1). H. Fourth-order stem vessel: the lumen is occupied by a long-standing thrombotic formation but displays recanalization; villi undergoing ischemic necrosis caused by perfusion block (patient 1). H'. Group of villi undergoing ischemic necrosis; long-standing lesion integrates the picture of so-called avascularized villi (patient 3).

Another peculiar finding in our series was the concurrence of clinical and imaging signs of chronic hypoxic-ischemic encephalopathy and multiple acute infarcts in 1 neonate at birth. Although it is accepted that FVM is a risk factor for both hypoxic-ischemic encephalopathy and PAIS<sup>31,32</sup> and both neonatal hypoxic-ischemic encephalopathy and PAIS involve hypoxia-ischemia, patients with a mixed pattern on neuroimaging have not been described in the setting of proven FVM to the best of our knowledge. Such combination, although rare, may be a potential alerting sign of FVM in neonates with PAIS. In addition, as documented in our series and previously described in the literature, the presence of intrauterine growth retardation, thromboembolism in multiple organs, or cardiac complications in neonates with PAIS are also associated with FVM and should raise suspicion of this underestimated condition.<sup>12,19,33</sup>

Previous studies reported an extremely low rate of recurrence of stroke after PAIS even in the context of FVM,<sup>10</sup> supporting the

concept that risk factors associated with both FVM and PAIS completely subside outside the perinatal period in most patients. Similarly, we did not detect additional infarcts on follow-up studies nor the appearance of clinical manifestations related to new arterial ischemic strokes. Independent of the subjacent etiology, PAIS frequently results in epilepsy, cerebral palsy, and cognitive deficits.<sup>2,5</sup> In our cohort, 1 preterm neonate died during the neonatal period because of severe necrotizing colitis. Adverse neurologic outcomes were detected in most of the other patients, representing a higher proportion than that described in most series of PAIS.<sup>22</sup> However, these data should be considered with caution because they might be related to selection bias caused by nonsystematic evaluation of placenta histology.

High-grade FVM is associated with a higher risk of brain injury.<sup>16</sup> Indeed, all our patients were classified as having high-grade FVM, showing occlusive thrombi, mainly in large-stem vessels, accompanied by downstream changes, including organization,

separation, red cell extravasation, endothelial destruction, loss of vascularity and, ultimately, fibrosis. These changes are similar to those seen in intrauterine fetal demise but are focal rather than diffuse and, especially, in different stages of evolution.<sup>9</sup> However, no differences in terms of severity and extension of FVM-related lesions were noted among patients with severe or mild imaging patterns in our series. This is in agreement with prior literature showing no stringent correlation between MR imaging and histologic data.<sup>10</sup>

Although the likelihood of FVM and PAIS is thought to be increased by endothelial damage caused by fetal inflammatory response,<sup>9</sup> these lesions were not detected in the present series. On the other hand, as documented in almost all our patients, FVM is frequently associated with other placental abnormalities, such as maternal vascular malperfusion.<sup>10,34</sup> Interestingly, we had 2 cases of twin dichorionic diamniotic pregnancies, but no co-twin had a stroke or evidence of FVM features in the corresponding placenta, as previously demonstrated.<sup>17</sup> Of note, umbilical cord abnormalities (ie, potentially obstructing anatomic lesions and/or clinical conditions) are considered major risk factors of FVM, probably through promotion of venous obstruction, congestion, and stasis.<sup>10,11</sup> Accordingly, 4 neonates presented cord abnormalities associated with FVM, including entanglements, hypercoiling, and/or torsion. Unfortunately, placentas are generally discarded soon after delivery, but the clinical presentation of PAIS is often mild and nonspecific, and the diagnosis is most often made a few days or even months after birth, as in the present series.<sup>2,6</sup> These are major limitations in the diagnosis of FVM in PAIS, and the extent to which different FVM histologic patterns and umbilical cord anomalies may impact on the type of PAIS or brain injury at birth remains an intriguing issue awaiting further exploration.

In conclusion, we confirm the prevalent involvement of the anterior circulation in FVM-related PAISs that were frequently multiple, asynchronous, and distributed superficially, thus suggesting an embolic origin. Moreover, we describe for the first time the co-occurrence of imaging signs of hypoxic-ischemic lesions and/or dural sinus congestion or thrombosis in these neonates, and the association of these features with FVM is worth further investigation. Together with clinical manifestations such as intrauterine growth retardation, thromboembolism in other organs, and cardiac complications, these MR imaging features may raise the suspicion of a subjacent FVM, a rare but likely underdiagnosed condition. Larger prospective studies including placental examination in all neonates are needed to clarify the pathomechanisms of FVM-related PAIS and the correlation between clinical, imaging, and histologic findings.

## ACKNOWLEDGMENTS

We are grateful to the associations Associazione per la Lotta all'Ictus Cerebrale (ALICE) and FightTheStroke for their support of our study. We also thank Doctor Simona Pappalardo for the drawing of Fig 4.

Disclosures: Ana Geraldo—UNRELATED: Grants/Grants Pending: ESNR, Comments: Annual Research Fellowship in diagnostic neuroradiology, paid to individual. Alessandro Parodi—RELATED: Grant: Compagnia di San Paolo (ROL 20573), Associazione per la Lotta all'Ictus Cerebrale (ALICE) and Ricerca Corrente Disordini Neurologici e Muscolari (Linea 5) of Italian Ministry of Health\*; UNRELATED:

Consultancy: Shire HGT, Comments: Consultancy for assessment of cranial ultrasound examinations from ROPP-2008-01 Study. Marta Bertamino—RELATED: Grant: Compagnia di San Paolo (ROL 20573), ALICE and Ricerca Corrente Disordini Neurologici e Muscolari (Linea 5) of Italian Ministry of Health\*. Compagnia di San Paolo (ROL 20573), the ALICE and Ricerca Corrente Disordini Neurologici e Muscolari (Linea 5) of Italian Ministry of Health\*. Sara Uccella—RELATED: Grant: Compagnia di San Paolo (ROL 20573), ALICE and Ricerca Corrente Disordini Neurologici e Muscolari (Linea 5) of Italian Ministry of Health\*. Paolo Moretti—RELATED: Grant: Compagnia di San Paolo (ROL 20573); the ALICE and Ricerca Corrente Disordini Neurologici e Muscolari (Linea 5) of Italian Ministry of Health\*. Mariasavina Severino—RELATED: Grant: Compagnia di San Paolo (ROL 20573), ALICE and Ricerca Corrente Disordini Neurologici e Muscolari (Linea 5) of Italian Ministry of Health, Comments: These sponsors had no involvement in any of the study steps: design, data collection, analysis, and interpretation, writing of the report, and following submission\*; UNRELATED: Employment: Neuroradiology consultant, IRCCS Istituto Giannina Gaslini. Luca Ramenghi—RELATED: Grant: Compagnia di San Paolo (ROL 20573), ALICE and Ricerca Corrente Disordini Neurologici e Muscolari (Linea 5) of Italian Ministry of Health\*; UNRELATED: Employment: IRCCS Gaslini, Department of Neurosciences, Rehabilitation, Ophthalmology, Genetics, and Maternal and Children's Sciences, University of Genoa, Genoa, Italy, Comments: Chief of Mother-Baby Department. \*Money paid to the institution.

## REFERENCES

1. Raju TNK, Nelson KB, Ferriero D, et al. **Ischemic perinatal stroke: summary of a workshop sponsored by the National Institute of Child Health and Human Development and the National Institute of Neurological Disorders and Stroke.** *Pediatrics* 2007;120:609–16 CrossRef Medline
2. Dunbar M, Kirton A. **Perinatal stroke: mechanisms, management, and outcomes of early cerebrovascular brain injury.** *Lancet Child Adolesc Health* 2018;2:666–76 CrossRef Medline
3. Wagenaar N, Martinez-Biarge M, van der Aa NE, et al. **Neurodevelopment after perinatal arterial ischemic stroke.** *Pediatrics* 2018;142:e20174164 CrossRef Medline
4. Laugesaar R, Kolk A, Tomberg T, et al. **Acutely and retrospectively diagnosed perinatal stroke: a population-based study.** *Stroke* 2007;38:2234–40 CrossRef Medline
5. Kirton A, deVeber G. **Life after perinatal stroke.** *Stroke* 2013;44:3265–71 CrossRef Medline
6. Mineyko A, Kirton A. **The black box of perinatal ischemic stroke pathogenesis.** *J Child Neurol* 2011;26:1154–62 CrossRef Medline
7. Kirton A, Armstrong-Wells J, Chang T, et al. **Symptomatic neonatal arterial ischemic stroke: the International Pediatric Stroke Study.** *Pediatrics* 2011;128:e1402–10 CrossRef Medline
8. Redline RW, Pappin A. **Fetal thrombotic vasculopathy: the clinical significance of extensive avascular villi.** *Hum Pathol* 1995;26:80–85 CrossRef Medline
9. Khong TY, Mooney EE, Ariel I, et al. **Sampling and definitions of placental lesions: Amsterdam Placental Workshop Group Consensus Statement.** *Arch Pathol Lab Med* 2016;140:698–713 CrossRef Medline
10. Redline RW, Ravishanker S. **Fetal vascular malperfusion, an update.** *APMIS* 2018;126:561–69 CrossRef Medline
11. Redline RW. **Severe fetal placental vascular lesions in term infants with neurologic impairment.** *Am J Obstet Gynecol* 2005;192:452–57 CrossRef Medline
12. Saleemuiddin A, Tantbirojn P, Sirois K, et al. **Obstetric and perinatal complications in placentas with fetal thrombotic vasculopathy.** *Pediatr Dev Pathol* 2010;13:459–64 CrossRef Medline
13. Roescher AM, Timmer A, Erwich JJHM, et al. **Placental pathology, perinatal death, neonatal outcome, and neurological development: a systematic review.** *PLoS One* 2014;9:e89419 CrossRef Medline
14. Kraus FT, Acheen VI. **Fetal thrombotic vasculopathy in the placenta: cerebral thrombi and infarcts, coagulopathies, and cerebral palsy.** *Hum Pathol* 1999;30:759–69 CrossRef Medline
15. Elbers J, Viero S, MacGregor D, et al. **Placental pathology in neonatal stroke.** *Pediatrics* 2011;127:e722–29 CrossRef Medline
16. Chisholm KM, Heerema-McKenney A. **Fetal thrombotic vasculopathy.** *Am J Surg Pathol* 2015;39:274–80 CrossRef Medline

17. Bernson-Leung ME, Boyd TK, Meserve EE, et al. **Placental pathology in neonatal stroke: a retrospective case-control study.** *J Pediatr* 2018;195:39–47.e5 CrossRef Medline
18. Fluss J, Garcia-Tarodo S, Granier M, et al. **Perinatal arterial ischemic stroke related to carotid artery occlusion.** *Eur J Paediatr Neurol* 2016;20:639–48 CrossRef Medline
19. Heider A. **Fetal vascular malperfusion.** *Arch Pathol Lab Med* 2017;141:1484–89 CrossRef Medline
20. Nagaraja N, Forder JR, Warach S, et al. **Reversible diffusion-weighted imaging lesions in acute ischemic stroke: a systematic review.** *Neurology* 2020;94:571–87 CrossRef Medline
21. Cheong JLY, Cowan FM. **Neonatal arterial ischaemic stroke: obstetric issues.** *Semin Fetal Neonatal Med* 2009;14:267–71 CrossRef Medline
22. Chabrier S, Saliba E, Nguyen The Tich S, et al. **Obstetrical and neonatal characteristics vary with birthweight in a cohort of 100 term newborns with symptomatic arterial ischemic stroke.** *Eur J Paediatr Neurol* 2010;14:206–13 CrossRef Medline
23. Husson B, Hertz-Pannier L, Renaud C, et al. **Motor outcomes after neonatal arterial ischemic stroke related to early MRI data in a prospective study.** *Pediatrics* 2010;126:e912 CrossRef Medline
24. Husson B, Hertz-Pannier L, Adamsbaum C, et al. **MR angiography findings in infants with neonatal arterial ischemic stroke in the middle cerebral artery territory: a prospective study using circle of Willis MR angiography.** *Eur J Radiol* 2016;85:1329–35 CrossRef Medline
25. Siddiq I, Armstrong D, Surmava A-M, et al. **Utility of neurovascular imaging in acute neonatal arterial ischemic stroke.** *J Pediatr* 2017;188:110–14 CrossRef
26. Wintermark M, Hills NK, DeVeber GA, et al. **Clinical and imaging characteristics of arteriopathy subtypes in children with arterial ischemic stroke: results of the VIPS study.** *AJNR Am J Neuroradiol* 2017;38:2172–79 CrossRef Medline
27. van der Aa NE, Porsius ED, Hendrikse J, et al. **Changes in carotid blood flow after unilateral perinatal arterial ischemic stroke.** *Pediatr Res* 2012;72:50–56 CrossRef Medline
28. Prandoni P. **Venous and arterial thrombosis: is there a link?** *Adv Exp Med Biol* 2017;906:273–83 CrossRef Medline
29. Rutherford MA, Ramenghi LA, Cowan FM. **Neonatal stroke.** *Arch Dis Child Fetal Neonatal Ed* 2013;98:F180 CrossRef Medline
30. Ramenghi LA, Cardiello V, Rossi A. **Neonatal cerebral sinovenous thrombosis.** *Handb Clin Neurol* 2019;162:267–80 CrossRef Medline
31. Mir IN, Johnson-Welch SF, Nelson DB, et al. **Placental pathology is associated with severity of neonatal encephalopathy and adverse developmental outcomes following hypothermia.** *Am J Obstet Gynecol* 2015;213:849.e1-7–849.e7 CrossRef Medline
32. Vik T, Redline R, Nelson KB, et al. **The placenta in neonatal encephalopathy: a case-control study.** *J Pediatr* 2018;202:77–85.e3 CrossRef Medline
33. Gluck O, Schreiber L, Marciano A, et al. **Pregnancy outcome and placental pathology in small for gestational age neonates in relation to the severity of their growth restriction.** *J Matern Fetal Neonatal Med* 2019;32:1468–73 CrossRef
34. Zur RL, Kingdom JC, Parks WT, et al. **The placental basis of fetal growth restriction.** *Obstet Gynecol Clin North Am* 2020;47:81–98 CrossRef Medline



## Ocular MR Imaging as a Substitute for Ultrasound during the COVID-19 Pandemic



**T**he novel coronavirus disease 2019 (COVID-19) pandemic is a public health emergency of international concern, bringing a multitude of new challenges in caring for patients. There is considerable variability in the prevalence of the virus as well as the availability of personal protective equipment (PPE) worldwide.

Ultrasonography examinations involve close, often prolonged (>10 minutes) physical contact with patients and confer a high risk of viral transmission by respiratory droplets. This is particularly the case for ocular ultrasound, with the practitioner positioned directly above the patient's head in close proximity to the upper respiratory tract and nasopharynx.<sup>1</sup> Furthermore, Severe Acute Respiratory Syndrome coronavirus 2 (SARS-CoV-2) viral RNA has been detected in ocular swab samples in patients with conjunctivitis and in ocular fluids in the early incubation period before the onset of characteristic respiratory symptoms. Therefore, ocular fluids may not only be the point of virus entry but also a source of contagion to other patients and eye care professionals.<sup>2</sup>

Strict protective measures by each ultrasonography operator are necessary when performing an examination on patients positive for COVID-19. The American Institute of Ultrasound in Medicine advises that all patients be considered as possibly infected with COVID-19 for the purposes of protecting personnel.<sup>3</sup> Radiologic and ophthalmologic societies recommend that all examinations be strictly limited to an absolute minimum. Given the limited supply of PPE, health care professionals are at high risk of contamination, including those in ophthalmology, previously considered a low-risk subspecialty.<sup>4</sup>

In response to the COVID-19 pandemic, we, as an institution, have devised a high-resolution MR imaging protocol as a substitute for ocular ultrasonography in the setting of ophthalmologic emergencies. This is an initiative by the radiology department in collaboration with our ophthalmology colleagues, as a risk-mitigation strategy to protect staff while maintaining optimum patient care.<sup>1</sup> Local institutional review board authorization was granted.

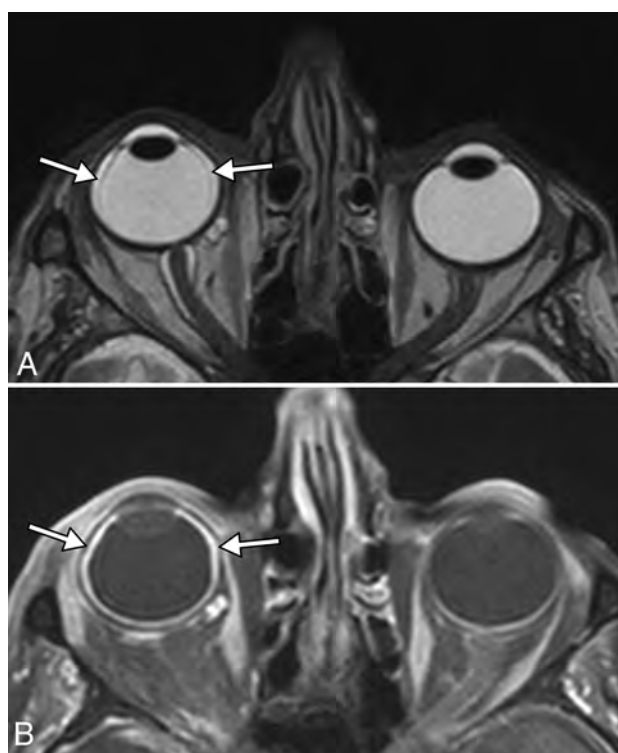


**FIG 1.** Axial MR imaging T2-weighted sequence (A) demonstrating a thin membrane (arrows) in the right globe extending anteriorly to the ciliary body, with corresponding enhancement on postcontrast T1-weighted sequence (B, arrows), consistent with a thin peripheral cilio-choroidal detachment. Postcontrast imaging is useful to confirm choro-roidal detachment because the choroid displays frank enhancement as opposed to the retina or sclera.

All MR imaging examinations are performed at 3T. Our protocol is centered on the orbits with high-resolution 3D T1-weighted sequences before and after intravenous injection of gadolinium chelate and a 3D T2-weighted sequence. We obtain high in-plane spatial resolution of the order of 0.45–0.55 mm, which is obtainable on most commercially available MR imaging scanners. Practically, this allows reconstructions in any plane approximating the

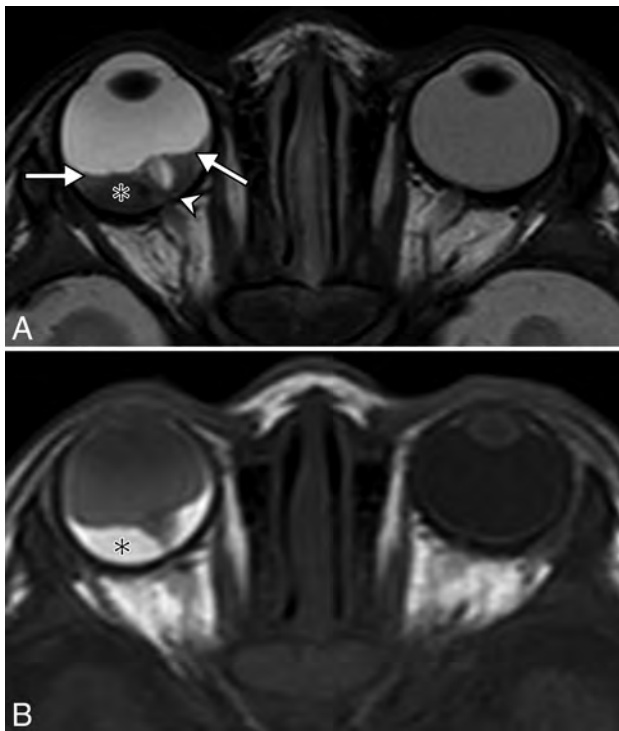


**FIG 2.** Axial MR imaging T2-weighted sequence (A) demonstrating a V-shaped membrane (arrows) converging on the right optic disc posteriorly (arrowhead), limited by the ora serrata anteriorly. This is the classic appearance of total retinal detachment, confirmed at surgery. There is an underlying subretinal hematoma (asterisk); these are intrinsically T1-hyperintense (B). Note the slightly T1-hyperintense vitreous compared to the contralateral side, consistent with vitreous hemorrhage, initially seen at slit-lamp examination.

accuracy of B-mode ultrasound at 10 MHz, which can localize anomalies according to standard field or meridian nomenclature.

Urgent or emergent examinations are determined on an individual basis but include those entities requiring immediate clinical or surgical intervention, often with sight-threatening complications, including ocular trauma, retinal detachment, choroidal detachment, vitreous hemorrhage, and ocular tumors. We illustrate the value of ocular MR imaging in some of these settings (Figs 1–3).

In conclusion, we show that ocular MR imaging can be a useful diagnostic tool as a substitute for ultrasound and a temporary measure during the COVID-19 pandemic. The sensitivity and specificity of MR imaging compared with ultrasound for the investigation of ocular emergencies is not currently known; therefore, further studies are required.

Disclosures: Julien Savatovsky—UNRELATED: Consultancy: Bayer AG; Payment for Lectures Including Service on Speakers Bureaus: Philips, Medtronic; Travel/Accommodations/Meeting Expenses Unrelated to Activities Listed: Bayer AG.

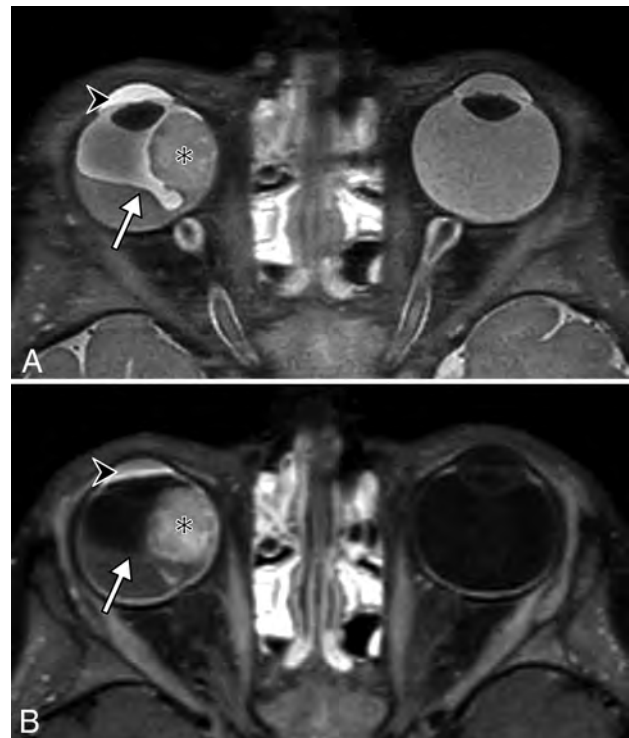


**FIG 3.** Axial MR imaging T2-weighted (A) and T1-weighted post-IV gadolinium (B) sequences demonstrating the classic V-shaped membrane of a retinal detachment (arrow), converging on the optic disc posterior to the right globe, due to an underlying, exophytic, enhancing mass in the nasal quadrant (asterisk). There are also inflammatory changes in the anterior chamber (arrowhead).

## REFERENCES

1. Ji-Peng OL, Shantha J, Wong TY, et al. Preparedness among ophthalmologists: during and beyond the COVID-19 pandemic. *Ophthalmology* 2020;127:569–72 CrossRef Medline
2. Colavita F, Lapa D, Carletti F, et al. SARS-CoV-2 isolation from ocular secretions of a patient with COVID-19 in Italy with prolonged viral RNA detection. *Ann Intern Med* 2020;173:242–43 CrossRef Medline
3. American Institute of Ultrasound in Medicine. Quick Guide on COVID-19 Protections—Patient and Ultrasound Provider Protection. 2020. [https://aium.s3.amazonaws.com/covid19/Covid19\\_Quick\\_Guide\\_PUPP.pdf](https://aium.s3.amazonaws.com/covid19/Covid19_Quick_Guide_PUPP.pdf). Accessed April 24, 2020
4. Qiao C, Zhang H, He M, et al. Symptomatic COVID-19 Infection in Eye Professionals in Wuhan China. *Ophthalmology* 2020;127(9):1268–1270 CrossRef Medline

Y.M. Purcell

O. Bergès

J. Savatovsky

A. Lecler

Neuroradiology Department

Fondation Ophtalmologique Adolphe de Rothschild

Paris, France

## Gadolinium Deposition and the Patient's View on the Problem

**R**arely, radiology journals publish patients' perspectives concerning the gadolinium deposition. Therefore, the editorial by Mallio et al<sup>1</sup> is unique, and I read it with great interest. In addition to mentioned facts, the following points are of great impact, too.

- The decision to inject gadolinium-based contrast agents (GBCAs) or not should be made, if possible, together with the patient. Well-informed patients are able to choose the most suitable imaging procedure. Moreover, patient-centered care leads to satisfaction.<sup>2</sup>
- To realize the first point, the patient should be well informed. This means that the patient should be informed about the potential risk of gadolinium deposition in the brain and within several other organs and, as mentioned by Mallio et al, "patients should be informed that there is no documented clinical risk related to gadolinium deposition. . . ."<sup>1</sup> Moreover, patients should be also informed that delayed adverse events cannot be excluded.
- Symptoms self-reported by patients after exposure to GBCAs should be documented exactly. Currently, documentation of different adverse symptoms related to the application of contrast media is sparse or is missing.<sup>3</sup> This is surprising because an exact documentation facilitated the everyday routine, as well as retrospective analyses.

- Patients with subjective symptoms should undergo a diagnostic procedure and should be closely monitored. To avoid overlooking harmful conditions, it is recommended to check the patient's symptoms.

Disclosures: Ingrid B. Böhm—UNRELATED: Travel/Accommodations/Meeting Expenses Unrelated to Activities Listed: Bayer AG Switzerland, Comments: German Radiology Congress (Leipzig) 2019.\* \*Money paid to the institution.

### REFERENCES

1. Mallio CA, Quattrocchi CC, Rovira À, et al. **Gadolinium deposition safety: seeking the patient's perspective.** *AJNR Am J Neuroradiol* 2020;41:944–46 CrossRef Medline
2. Nairz K, Böhm I, Barbieri S, et al. **Enhancing patient value efficiently: medical history interviews create patient satisfaction and contribute to an improved quality of radiologic examinations.** *PLoS One* 2018;13:e0203807 CrossRef Medline
3. Böhm IB, van der Molen AJ. **Recommendations for standardized documentation of contrast medium-induced hypersensitivity.** *J Am Coll Radiol* 2020;17:1027–28 CrossRef Medline

 I.B. Böhm

Department of Diagnostic, Interventional, and Pediatric Radiology, Inselspital  
University of Bern  
Bern, Switzerland

<http://dx.doi.org/10.3174/ajnr.A6826>